भाभा परमाणु अनुसंधान केंद्र
BHABHA ATOMIC RESEARCH CENTRE

BARC NEWSLETTER

Founder's Day

Special Issue - October 2012

BARC NEWSLETTER

Founder's Day

Special Issue - October 2012

भारत सरकार
Government of India
भाभा परमाणु अनुसंधान केंद्र
Bhabha Atomic Research Centre

From the Editor's Desk

Welcome to the 2012 Founder's Day Special Issue of the BARC Newsletter. We bring to you 64 award winning papers by BARC Scientists and Engineers out of which 37 are DAE Excellence Awards for the year 2010 and the others are Merit Awards received in 2011. A broad panorama of the R&D activities at BARC can be seen through these papers.

We would like to place on record our sincere thanks to all those who submitted their award winning papers for this issue well in time. Like last year, 2011, all the articles were submitted on-line and it has considerably simplified the process of publication this year, too. We propose to provide enhanced features and a better interface for uploading all articles for BARC Newsletter soon. Through this forum, I would like to invite the entire BARC fraternity to continue supporting the regular bimonthly issues of the BARC Newsletter through contribution of various types of articles. The R&D work carried out by all of you needs to be showcased and disseminated to a wide audience and also motivate our young scientists and engineers.

Finally, readers' comments, criticisms and valuable inputs have helped the Editorial Committee to further enhance the quality of the articles. We would like to thank both readers and contributors for the 2012 Founder's Day Special Issue of the BARC Newsletter.

Happy reading!

Dr. K. Bhanumurthy
On behalf of the Editorial Committee

CONTENTS

DAE (Excellence in Science, Engineering & Technology) Awards-2010

Merit Awards

CHALLENGES IN DEVELOPMENT OF SAFETY CRITICAL SOFTWARE FOR NUCLEAR PLANTS

R.M. Suresh Babu
Control Instrumentation Division

Shri R.M. Suresh Babu is the recipient of the DAE Homi Bhabha Science & Technology Award for the year 2010

Abstract

This paper provides an overview of the challenges in development of safety critical software for Nuclear Plants, with illustrations showing how the patterns of development, documentation, verification, etc. have evolved in BARC over the last two to three decades.

Introduction

Nuclear Power Plants (NPPs) in India have been using software-based instrumentation & control (I&C) systems for more than 3 decades. But, it was only from late 1980's that software has shown its presence in safety-critical systems – which initiates reactor trip, decay heat removal, etc – of Indian NPPs. Because of their criticality with respect to plant safety, development of these software packages has distinct characteristics from that of commercial software or information system software. BARC has been in the forefront of development of these critical software packages for Indian NPPs. This paper provides a brief insight into the main issues related to its development along with a few snapshots of its evolution in BARC from rudimentary to a more formal and sophisticated development process, illustrated by data from various projects that the author executed over the years.

Safety Critical Software

Safety critical software is one, the failure of which can lead to accidents, which can cause damage to the system/ plant, personnel and the environment. In case of NPP's, this kind of software is used in class IA systems [1], which are responsible to prevent postulated initiating events (PIEs) from leading to accident conditions. Examples of such systems are reactor protection system, safety actuation system, decay heat removal system, etc.

Three important attributes of safety critical software are: safety, security and comprehensibility. To ensure and assure (i.e. to demonstrate) these attributes it is necessary to follow a systematic and controlled software development process. In this paper, to limit the contents, the safety attribute is elaborated with details of its definition, main issues, methods & practices and illustrations based on data/statistics from various projects executed in BARC.

Safety

Definition

'Safety' is the degree of conformance of a system or software to,

- *specified requirements, and,*
- *implied requirements to ensure plant safety, such that "as far possible, under all failures/unspecified conditions, a safe signal trajectory is executed that leads the system being controlled to a safe state"*

Main Issues

The main difficulties in ensuring safety are: incomplete requirements and design verification.

Incompleteness in requirements is due to scenarios not envisaged, and when such conditions occur, the design fails to produce the expected outputs. The omitted scenarios may be failure conditions or even normal conditions. For example, failure of an I/O board that causes a valve to be in both open and closed state, or multiple and possibly contradictory commands arriving simultaneously from operator or process interlocks. There is another class of scenarios that cannot be specified at the system level, but are very crucial: those which arise from the specific implementation chosen. For example, overflow of integers, precision loss in type conversion, array bound violation, etc. While, at system level it may be possible – albeit with arduous efforts - to specify all scenarios for a moderately complex system, it is extremely difficult – if not impossible – to specify all the implementation related scenarios, except for very simple systems. In summary, the software engineer – responsible for safety critical software - should continuously strive to discover new safety requirements throughout the development, i.e., during requirements specification, design, coding and testing. The ability to carry out this is part of the safety culture that the software engineer should possess [2].

Main challenge with design verification is to ensure complete coverage of the design/code in the verification process. This means that the design or code should be checked in all possible scenarios that not only cover all specified system functions, with the software taken as a black box, but all possible paths executed by software, which additionally encompass all possible internal states of the software. While it is fairly straight forward – although cumbersome for complex systems - to test the software with all possible inputs to check if the desired outputs are produced, it is more challenging to design 'negative tests', which ensure that the software does not do anything that it is not supposed to do. For example, if a particular combination of inputs is supposed to trip the reactor, the negative tests create all other combinations of the inputs and check if the system does not trip the reactor.

How to Ensure and Assure Safety?

Fig. 1 illustrates the elements for ensuring and assuring safety. The inner three blocks are the elements related to ensuring safety, i.e. requirements analysis, standards compliance and testing & verification and validation (V&V). Outer two circles indicate the elements that are necessary to assure safety, i.e. planning and documentation. These elements of safety are described in the following sections.

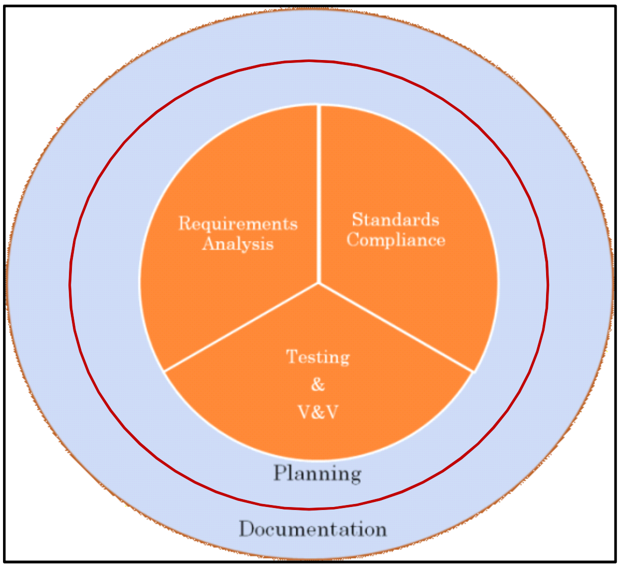

Fig. 1: Elements of Safety

Requirements Analysis

Requirements analysis is one of the most difficult tasks for safety-critical software, as is clear from the description given above. Industry statistics show that typically 25% of software errors are due to erroneous requirements. It is also quoted that if the effort to correct an error in requirements analysis phase is 1, the effort for correction during testing is 100 and after deployment it gallops to 400.

The software bugs detected during development is developer's perspective, while the software bugs detected after deployment is user's perspective; these may not be considered as bugs by the developer. These conflicts between developer and user arise because of misinterpretation or incompleteness in the requirements. Hence, it is prudent to involve users during requirements analysis. This is especially important in case of Human-machine interface (HMI) requirements.

A good software requirements document should be: complete, correct and unambiguous. Correctness and completeness are to be ensured thorough reviews, especially by the users. Usage of natural language, such as English, is one of the main sources of ambiguities, which can be reduced by using semi-formal (e.g. UML) or formal language (e.g. Z). We have evolved from software requirements written in English to use of data flow techniques [3], and currently we use Unified Modeling Language[4] (UML). Fig. 2 shows how, in our projects, the documentation effort and document size have multi-folded over the years, illustrating growing emphasis and importance given to the requirements analysis.

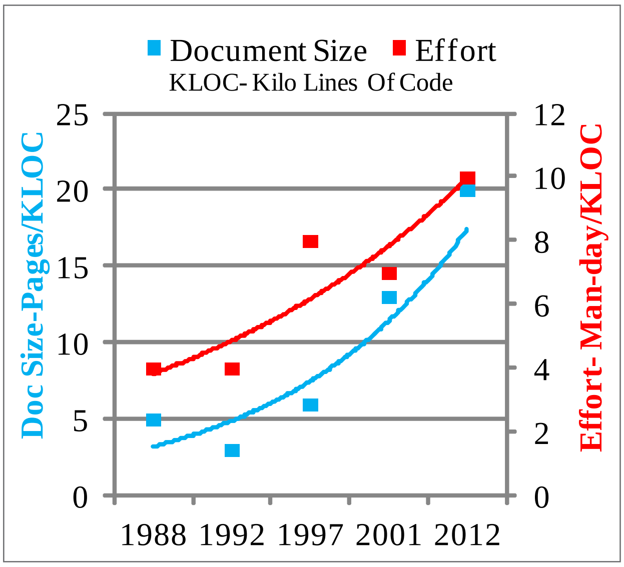

Fig. 2: Evolution of Software Requirements Analysis

Standards Compliance

The second element related to ensuring safety is compliance to relevant and applicable standards. The standards specify:

- Requirements for development, V&V, quality assurance and change management
- List of documents to be produced
- do's and don'ts in the design
- Important design criteria (e.g. connecting systems of different classes)

Depending on safety class of the system, i.e. IA, IB, IC, there are different standards. AERB-D-25[5] is the guide to be used for safety systems of an Indian NPP. Other widely used international standards are: IEC 60880 (for IA systems)[6] and IEC 62138 (for IB & IC systems).

Testing and V&V

The third element related to ensuring safety is testing and verification & validation (V&V). Verification checks if product of a software development phases meets the requirements set forward in a previous phase, while validation checks if the software meets the software requirements.

Fig. 3 illustrates how V&V methods have changed over the years. Initially, review was done at the end of software development, which does not provide any scope for improving the software quality. Later years, the reviews were done at the end of each phase. Manual reviews are now supported by tools and formal methods for better coverage and to reduce human errors.

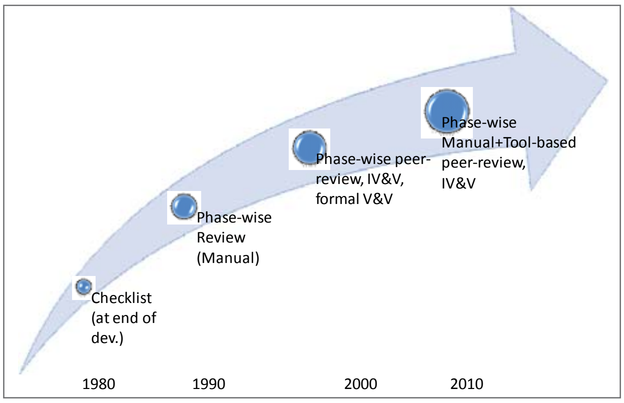

Fig. 3: Evolution of V&V Methods

From the last decade we have successfully been using peer-reviews, in which software team members review each other's software designs. Also, independence V&V (IV&V) was introduced for critical software, in which a team independent of the user and designer executes the V&V tasks. Fig.4 shows the comparisons of Peer V&V and IV&V in terms of their effectiveness, i.e. the percentage of errors detected in a phase. The Peer V&V is found to be more effective as it is executed in line with the development and because of better motivation in execution of the V&V activity.

Software testing is conducted at three levels: unit test, integration test and validation test. Fig. 5 shows how the testing methodology has been evolved over the years. Initially, software testing involved only the functional checks based on inputs and outputs.

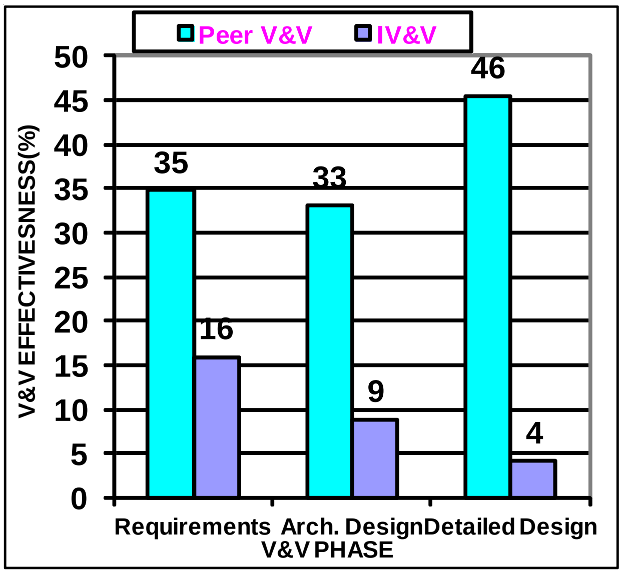

Fig. 4: Comparison of Peer V&V and IV&V Effectiveness

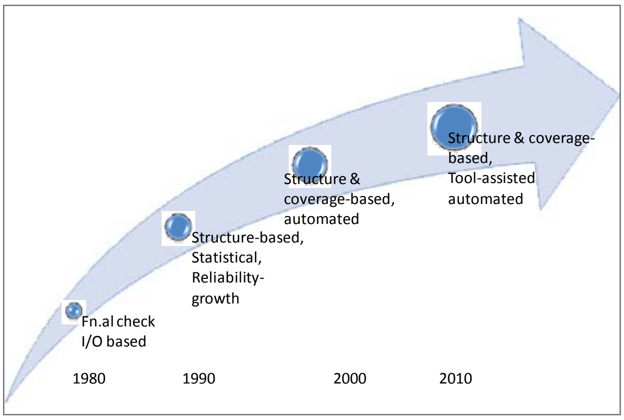

Fig. 5: Evolution of Testing Methodology

Later on, structure-based (coding structure) and coverage-based (path coverage, condition coverage, etc.) tests were introduced. We have also used reliability growth based testing, in which the fault intensity (failures per unit time of test) was used to evaluate software reliability. Also, statistical test was used in one system, in which pseudo-random number based commands were executed continuously over a period of few months and the system response was evaluated. Now software tools are used to make the software testing more effective and efficient.

Software Planning

A documented software development plan at the beginning of a project is a very important element in assuring software quality. Various software plans and their inter-relationship are illustrated in Fig. 6. The plans consists of Software project management plan (SPMP), software quality assurance plan (SQAP), software V&V Plan (SVVP) and software configuration management plan (SCMP). These plan documents not only stream line the development, but specify the activities to be performed (e.g. QA checks) and reports to be generated to provide documentary evidence (e.g. for regulatory body) that the development indeed was executed as planned.

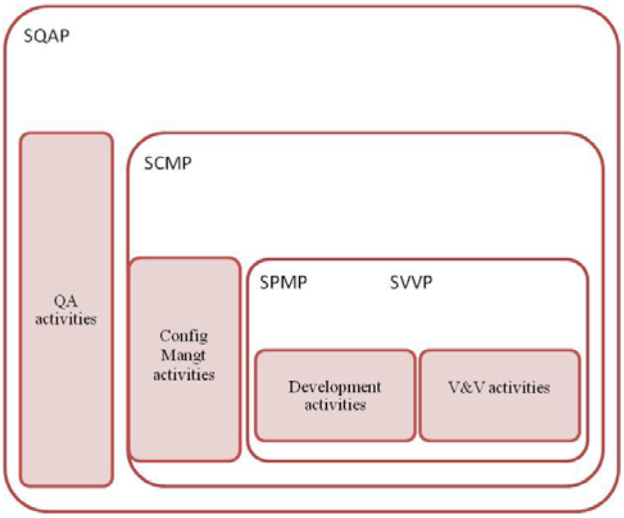

Fig. 6: Software Planning

Documentation

Documentation is very often neglected, but it is one of the most crucial elements to assure or demonstrate safety. Documents not only include design documents, but, test documents, V&V reports, etc.

Documentation provides evidence that an appropriate system of development and V&V has been used. It also

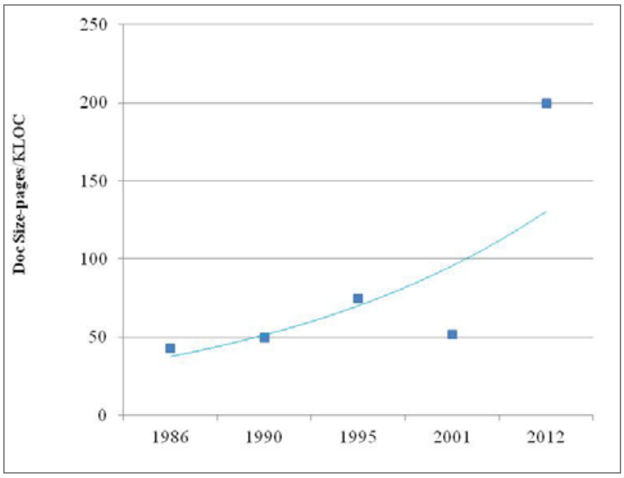

Fig. 7: Evolution of Software Documentation

makes the products (requirements, design) amenable to review - by V&V team and users - so that anomalies are resolved at the earliest.

Fig. 7 shows how the software documentation has multifolded over the years, indicating that the importance and efforts of documentation have considerably gone up over the years.

Parallel Trends

There are also methodologies other than that described above. Formal verification can be effectively used for hardware design, where the specification is clear, but is not mature enough to handle fairly complex control/safety software, where, requirements are very complex and have to be understood from a plant perspective.

Model-based development reduces coding errors and cuts-down the development and V&V time. But, one requires very high confidence on the tool (as manual intervention in V&V is cut-down drastically) and software models can become extremely difficult to review. Besides, from security point of view, software produced through some of these tools are more vulnerable (e.g. Stuxnet).

Conclusion

This paper briefly discussed the important elements for ensuring and assuring safety attribute of critical software to be deployed in NPPs. In BARC, the software development process and methodology used for NPP safety systems have evolved considerably over the years. Using our current development process, we are able to produce software with less than 0.05 faults per KLOC after deployment, which is better than the internationally published data for similar software[7][8].

Acknowledgement

I express my sincere gratitude to Shri G Govindarajan, former Director, E&I Group and Shri GP Srivastava, Director, E&I Group for their encouragement and support while carrying out the projects covered in this paper. I also thank all my colleagues in CnID and RCnD with whom I was associated in these projects.

References

1. Safety Classification, AERB/NPP-PHWR/SG-1, AERB, 2003.
2. Software for Computer based systems important to safety in NPPs, NS-G-1.1, IAEA, Vienna.
3. Hatley et al., Process for System Architecture and Requirements Engineering. New York, NY: Dorset House Publishing.
4. Grady Booch, Ivar Jacobson & Jim Rumbaugh, OMG Unified Modeling Language Specification, March 2000.
5. Computer Based Systems of Pressurised Heavy Water Reactor, AERB Safety Guide, AERB/SG/D-25, January 2010.
6. IEC 60880 2006-05, “Nuclear power plants – Instrumentation and control systems important to safety – Software aspects for computer-based systems performing category A functions”.
7. Kelly, Tim, McDermid, John A, Software in Safety Critical Systems: Achievement and Prediction, Volume 2, No. 3, Nuclear Future, June 2006.
8. Hatton, L., Estimating Source Lines of Code from Object Code: Windows and Embedded Control Systems, 2005.

DEVELOPMENT OF C & I SYSTEMS FOR COMPACT LWRS: OVERVIEW, CHALLENGES & SPIN OFF'S

P.P. Marathe
Control Instrumentation Division

Shri P.P. Marathe is the recipient of the DAE Homi Bhabha Science & Technology Award for the year 2010

Abstract

Compact C&I (control and instrumentation) systems are characterized by low foot print – space & weight. Smaller space implies higher heat density in electronic cabinets. Lesser weight implies high order of integration. Requirement of high availability and high reliability along with above constraints requires a different philosophy for C&I systems compared to conventional C&I systems.

This paper describes the triple modular redundant (TMR) configuration designed and developed for control system applications e.g. reactor regulation, reactor protection and process control for compact LWR. Based on the computer based hardware currently being used for Indian NPPs, new set of hardware was developed having low power consumption, improved diagnostic capability, lower time to maintain. Configurations were made to achieve the reliability and safety targets at the same time keeping the high availability. The designs shall be fail-safe.

The spin offs of this work have resulted into development of special connectors, low power electronic modules, high availability networked architecture, special cabinets and creation of test facilities at BARC & ECIL.

Introduction

The primary plant control system of a compact LWR comprise of Reactor Control & Protection Systems, Process control systems for Power Plant. Reactor control & protection systems & process control systems configured using customized C & I hardware satisfies the single failure criterion. A common set of hardware for computer based control system which is configured to implement IA/IB functions and incorporate typical features like galvanic isolation, physical separation, fault tolerance, failsafe output generation, ease of maintenance with improved diagnostic and human machine interface (HMI) capabilities has been developed. The configurations formed for IA class incorporates features for fault tolerant, on line testability for critical trip parameters, fault detection & indication for reactor control protection hardware up to module level. In order to reduce cabling in the plant, Process control system is distributed having plant wide communication network and supports built in pre-start check facility to check continuity & Insulation resistance for actuators/feedback control lines. Hardware designed in modular form support extensive diagnostic features to achieve MTTR of 30 minutes. This article briefly describes the typical primary plant control system unit, henceforth referred to simply as "system" and brings out issues & challenges for the development & qualification and spin-offs of the development.

General system specifications and I & C requirements

General System specifications

Broad specifications of the commuter based system are given in the table 1 below, along with I & C requirements.
Table 1

Table 1: Broad specifications of the computer based systems

Type of system	Processor based, fault tolerant, TMR system
Analog inputs	4-20 mA; 0-10V; thermocouple
Analog outputs	4-20 mA
Digital inputs	24V
Digital outputs	Dry relay contacts; 24V signals
Data links for communication– for control, plant wide data exchange, DAS and remote I/O	• MIL 1553B serial links for control & data exchange, • CAN for interchannel communication • Ethernet for diagnostics & DAS
Accuracy of analog I/O	±1% full scale (approx)
I/O's per channel	200, analog(50) + digital (150 approx)
Response time	100-200 milliseconds

I & C Requirements

The compact LWR systems are designed to meet IA/IB/IC regulatory norms and specific qualification requirements as per Quality Assurance Plan (QAP) defined for the project. The qualification requirements to be met by these systems are:

- Environmental norms- as per JSS 55555
- Mechanical-shock & Vibration
- EMI/EMC-MIL STD 461 C/E
- Enclosure protection-IP21/55/68

In addition to conventional functional attributes for NPP's, these systems are designed to meet the following Functional & Non-Functional attributes given in Table 2:

System Overview

The Fig. 1 given below shows overview of the Reactor Control & Protection system and control rod drive system. The system for generation of reactor period, reactor power & reactor inlet/outlet temperature has three identical channels. Each channel processing hardware receives signal inputs of that channel and implements the required functions and generates outputs for that channel. The trip generation hardware receives all triplicated signals (analog & digital) outputs and implements 2/3 coincidence voting for generation of reactor trips on various plant trip parameters or conditions. The control rod drive system is customized system which implements control rod drive logics and also generates drive signals for control rod drive mechanisms. The setback signals required as per pre defined algorithms are received from process control systems for power reduction. This triplicated channel scheme is referred to as the "Triple Modular Redundant" (TMR) scheme. Each of the three channels has it's own power supply and is galvanically isolated from the other two channels. I/O's of all three channels are isolated. The hardware is modular in construction and the modules (printed circuit boards) housing electronic circuits are qualified as per qualification requirements stated in section 2.2 above. The trip generation and processing hardware is built in with on line testability for testing and equipped with diagnostic capability to detect and locate fault for such modules and its indication on console to the operator.

Table 2: Functional & Non-functional attributes for Nuclear Power Plants

Functional Attributes	Non-Functional attributes
Control philosophy-A mix of NPP & Aircraft philosophy	Dependability
High level of pre-start checks (Off-line checks)	Low power requirement
High Availability	No additional cooling (Fanless)
Diagnostic & Online testability	Low weight (Preferable)
Detection of un-authorized withdrawal of control rods	Small size

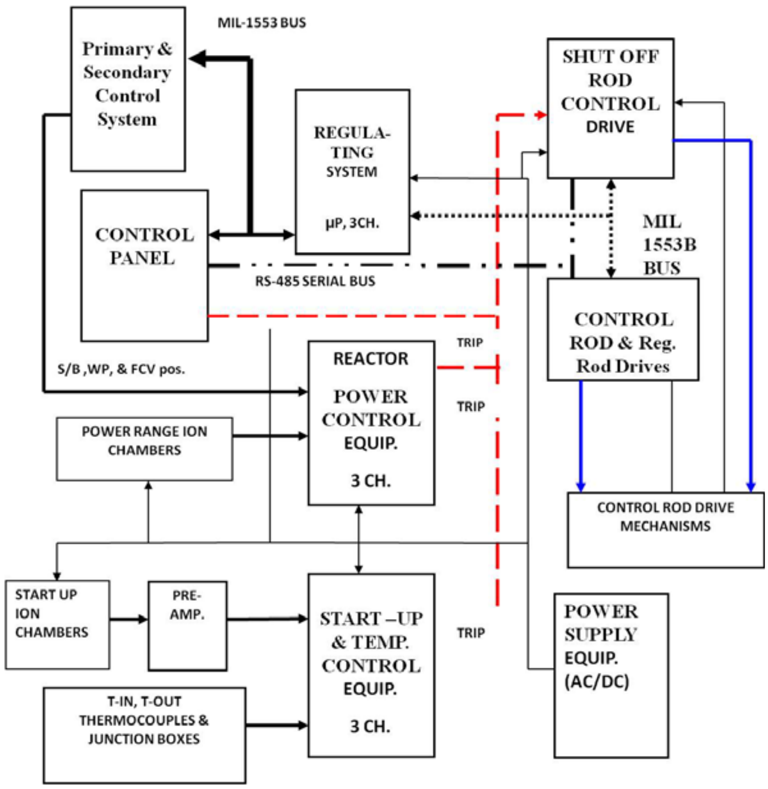

Fig.1: Reactor Control & Protection System Architecture

The Fig. 2 given above shows overall architecture of the Process control systems. These are also triplicated channel computer based units consisting of Logic controllers which implement the process control algorithms & Output Drivers which pass on drive signals for control of plant equipments & valves of primary & secondary plant. In order to improve the availability of the system, each logic controller channel consists of dual redundant hardware for processing the I/O signals. These logic controllers process the input data received from plant sensors, signalling devices and plant equipments and initiate a control action on the control organs using control algorithms. The controllers which are part of the system are inter connected by six channel serial MIL 1553 B data buses. Exchange of data between all units of process control system is also through the controller channels of primary and secondary via six redundant MIL1553 channels. The plant wide data and information about the plant is passed on to these data buses. Network Controllers control these MIL1553 B data buses. They coordinate the control of the data buses and the data information flow between the system control cabinets of primary and secondary plant. The information from controllers is also sent to control panel via these data buses. While the information from control console to Centralized DAS is sent via Ethernet links and to other systems via hardwired links.

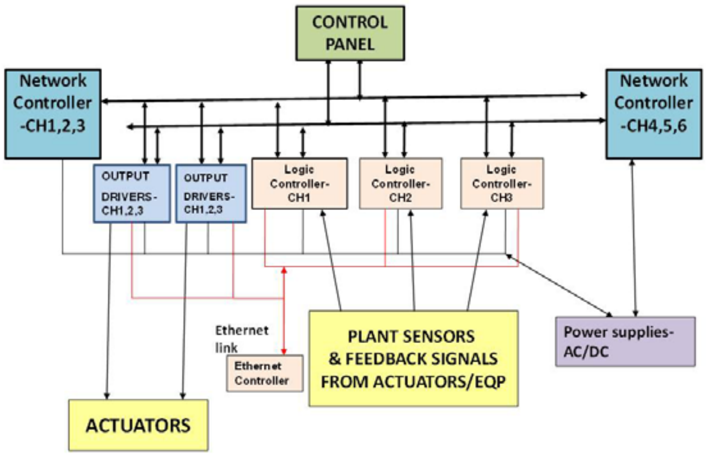

Fig.2: Plant Control System Architecture

Challenges for hardware development

The hardware designed & developed shall meet the I & C requirements given in section 2.2 above. The architecture designed for safety critical requirement shall satisfy basic principles like single failure criteria, diversity, common cause failure etc. The design shall incorporate features like physical separation wherever applicable, galvanic isolation, fail safeness etc. The selection of components and hardware used in designing Control systems depends on the quality requirements related to operating temperatures, environmental requirements, seismic requirements, power supply requirements, EMI/EMC requirements, structural, mechanical requirements etc.

To design the control system satisfying non functional requirement-**dependability** is a challenge in itself. Control systems are characterized by four fundamental properties: functionality, performance, cost and dependability. One of the essential properties which determine suitability of a system for a given usage/application is its dependability. Dependability of a system is the ability to deliver service that can justifiably be trusted. Correct service is delivered when system is free of failures(s). A systematic exposition of the concepts of dependability consists of three parts: the **threat** (an understanding of things can affect the dependability) to, the **attributes (a way to assess the dependability)** of and the **means** (ways to increase dependability) by which dependability is attained is shown below in Fig3. Dependability is an integrative concept that encompasses the following attribute: **availability**: readiness for correct service; **reliability**: continuity of correct service; **safety**: absence of catastrophic consequences on the user(s) and the environment; **confidentiality**: absence of unauthorized disclosure of information; **integrity**: absence of improper state alteration; **maintainability**: ability to undergo repairs and modifications.

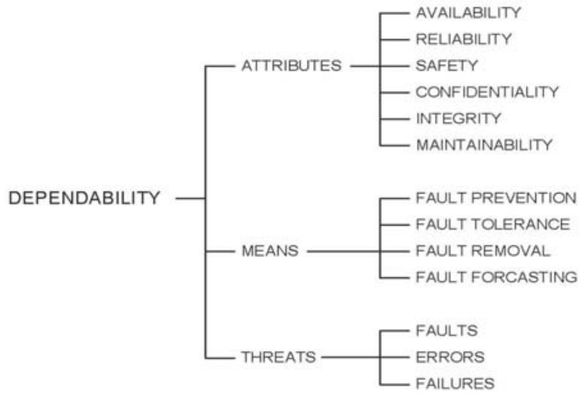

Fig 3: Dependability tree

The development of a dependable system calls for the combined utilization of set of four techniques: **fault prevention**: to prevent the occurrence or introduction of faults (this can be achieved by good safety margins in design, by using proven designs, by stringent quality control and qualification plan, by operation in controlled environment); **fault tolerance**: capability to deliver correct service in the presence of faults (this can be achieved by providing sufficient redundancy into the system); **fault removal**: to reduce the number or severity of faults (this is achieved by periodic/repeated testability, efficient diagnostics and also by having On/line-off line repairs/replacements); **fault forecasting**: to estimate the present number, the future incidence, and the likely consequence of faults.

The electronic modules used in the design of regulation, control rod drive & process control systems can be categorized in three major types:

a) Power supplies for control systems of reactor regulation & protection and process control systems.
b) Control circuits for generation of drive control and protection requirements.
c) Circuits for non computer & computer based system.

As conventional items available in markets or COTS items for the following special hardwares types did not meet the qualification norms given in section 2.2, these items were also developed to satisfy qualification requirements:

a) Special connectors (for cable termination, electronic modules, PCB connectors)
b) Test jacks, LED holders, intelligent monitors & displays
c) Racks, JB's, Consoles, Module cages with required strength, low weight qualifying for our requirements and efficient thermal design.

The design issues involved for above types of hardwares (electronic modules & special hardware) and design considerations are briefly described below. These issues themselves become challenges as the implemented design is required to satisfy the qualification requirements, low footprint and optimum weight consideration and also satisfying the important requirement of low power consumption and efficient thermal designs for compact LWRs.

Power supplies for control systems of reactor regulation & protection and process control systems

The power supplies forms the important hardware for any C & I system. The ultimate DC power required should be derived from 3 independent AC sources having diverse principle of operation. e.g. battery, DG/MMG, TA. Power supplies shall be galvanically isolated and to be physically separated from control system in separate units so that excessive heat generating sources do not affect the control system performance due their presence within same unit/cabinet and thereby increasing the internal ambient temperatures wherever they are located. All high power consumption components like DC/DC or AC/DC converters of power supplies are mounted on heat sinks which are placed in contact with side covers or walls so that heat can be directly transferred by conduction thereby reducing contribution of heat within cabinets and by employing efficient thermal designs. AC-DC converter modules with high MTBF figures are preferable because of their compactness compared to linear types. The DC drive/control supplies derived from AC/DC to be made as redundant or parallel configurations for increasing availability. The control power supplies to be provided with EMC filters for suppression of conducted noise and RF noise, protection from surge voltage/inrush currents, short circuit protection, over voltage protection, Thermal cutoff due to heat sink over temperature for power devices etc. Special provision of very highly redundant monitoring supply to monitor health of all power supply modules is desirable.

Control circuits for generation of drive control and protection requirements

The selection of logic family with high noise immunity and low power consumption is more preferred. Design should be configured to incorporate the features given below:

- Provision of noise filtering/de-bouncing for drive commands
- Generation of pulses by validating multiple signal commands instead of single command and avoid generation of pulses without a command.
- On failure of any component of the logic, impose failsafe output for pulse generation or to impose no operation state.
- Independent watch keeping circuit to ensure the proper pulse generation.
- Generate a self-healthiness signal on fulfillment of the built in design functionality. The control circuit should also provide the circuits for processing the representative drive power signals for the drive motor /coils for detection of:
- Short circuit of the load & Over current (due to excess torque) in the load
- Open load due to loss of connecting cable.

For implementation of the scram/trip logics, coincidence logic is built by using 2 out of 4 OR 2 out of 3 networks depending on the reliability and availability requirements. In the circuits feeding high current, to avoid single failures, combination of series and parallel contacts is desirable. The testability for checking the health of important contacts initiating safety action shall be built into the logic.

Circuits for non computer & computer based system

Hardware for computer based system consists of bus based I/O modules, communication modules, modules designed to meet special interfacing requirements. Computer based I/O modules shall support bus based architecture, better diagnostic capability, built in/external testability & meeting the performance requirements of the system and features like geographical addressing, failsafe etc. The I/O bus selected shall be industrially rugged, proven bus architecture and shall be lasting in the industry for long period so as to beat obsolescence. I/O modules design to have low power consumption, PCB layouts satisfying efficient thermal & EMC requirements. Signal conditioning & I/O processing hardware to have very low offsets and temp. drifts so as to meet desired conversion accuracies; galvanic isolation requirements; built in ref check/self check/test facilities. Communication modules designed also should meet the required performance, isolation, diagnostic requirements and shall have proper shielding, grounding and earthing termination for connection with field communication cables.

Spin offs

During the course of development, it lead to development of products, methods and facilities.

Products:1.VMEbus I/O module with low mean time to repair (not requiring any jumper or pot setting), 2. MIL-STD-1553B modules for implementation of standard as well as star topology networks, 3. Special connectors (rack, module and PCB) & LED holders fit to be used in harsh environment (high temp, shock and vibration), 4. Rugged mechanical enclosures (module cages, bins, racks and junction boxes)

Methods: Reliability estimation, spare estimation

Facilities:EMI/EMC facility at ECIL, K-200 at CnID

Conclusion

The group has concentrated on generic I & C indigenous developments- first of its kind- for compact LWR's. In its series of activities, the first set has been developed & deployed at PRP Kalpakkam. The advanced designs are at hand and the hardware for reactor regulation, control rod drive system & process control system has been successfully developed and qualified as per QAP of the project. The elaborate integrated testing of the reactor control & protection system with process control system of primary & secondary plant using the integrated test facility is also planned before final deployment.

Acknowledgement

The author is thankful to Shri G.P Srivastava, Director E & IG, and Shri Y.K.Taly (Head CnID, BARC) for their continuous encouragement and extensive support. And special thanks to Shri U.Mahapatra, Ex Head, CnID for his guidance and support for the development of the hardware.

Reference

1. A. Avizienis, J.-C. Laprie, and B. Randell, "Fundamental concepts of dependability," in Proc. of 3rd Information Survivability Workshop, pp. 7-11, Oct. 2000.
2. Anuradha Mayya, M.K. Singh, Manoj Kumar, K.C. Madala, P.P. Marathe, P.Ramakrishna, M.R.KGiri, Arun Bikkina "MIL-STD-1553B sub-system for strategic applications", ", *Indian Nuclear Society News,* Vol 8 (3&4), pp. 57-61, 2011.
3. P.V. Varde, M. Aggarwal, P.P. Marathe, U. Mahapatra, R.C. Sharma and V.N.A. Naikan, "Reliability and Life prediction for Electronic connectors for control Applications", Proc. of 2nd Int. conf. on Reliability, Safety and Hazard (ICRESH - 2010), pp. 63-67, Mumbai, 2010.
4. MIL-STD-461E, Requirements for the control of Electromagnetic Interference characteristics of subsystems and equipment, 1999
5. JSS 55555: 2000, Joint Services Specification on Environmental Test Methods for Electronic and Electrical Equipment, Rev. 2, 2000
6. IEC 60529, Degree of protection provided by enclosures (IP code), 2001-02.

DYE-SENSITIZED SOLAR CELL: DESIGN AND SYNTHESIS OF NEW SENSITIZERS (SOLAR DYE) AND ULTRAFAST ELECTRON TRANSFER DYNAMICS

Hirendra N. Ghosh
Radiation & Photochemistry Division

Dr. H.N. Ghosh is the recipient of the DAE Homi Bhabha Science & Technology Award for the year 2010

Introduction

Fossil fuels, the world's conventional energy supplies have a limited lifetime as the major source of energy. Depleting fossil fuel and the environmental concern have actually initiated the search for sustainable, clean and secure energy sources. It has been argued by several researchers from various areas that among different possibilities, solar, wind and biomass are the most suitable alternatives. Earth receives a huge amount of energy from sunlight ($4.3\text{x}10^{20}$ J h^{-1}) and perhaps is the best alternate for renewable energy resource for the future either by direct conversion into electrical power or by transformation into useful fuels. Thus, harnessing the solar energy, which is clean is the main objective of an alternative energy strategy. Several inorganic complexes and organic compounds absorb sun light to initiate excited state redox reactions. It has been argued that appropriately designed and coupled processes, along with these photo-induced redox reactions could eventually led to yield electrical power generation or developing useful fuels such as hydrogen gas. Photoinduced redox reactions initiate the generation of a charge separated species and thus provide a molecular basis for the conversion of light into free energy in the form of oxidized-donor and reduced-acceptor equivalents. However, in general this energy is only transiently formed as thermodynamically downhill charge recombination or back electron transfer (BET) occurs to regenerate the ground-state products. This deleterious process actually limits the possible application of many inorganic or organic dye molecules for being used as a sensitizer dye for efficient conversion of solar to electrical energy.

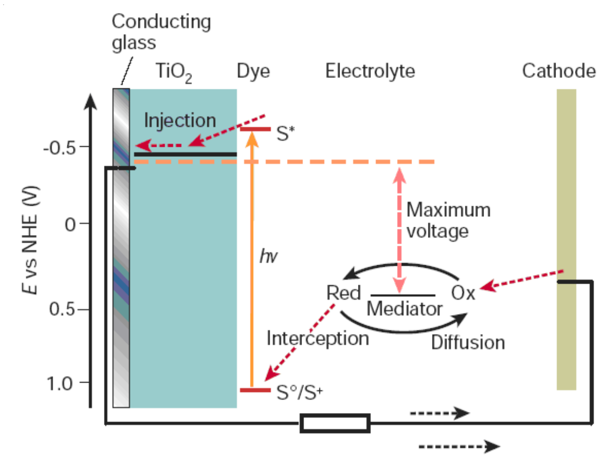

Scheme 1: Schematic Diagram of Dye-Sensitized Solar cell and different Electron Transfer reactions.

Among various photoactive inorganic complexes or organic dye molecules, Ru(II)-polypyridyl complexes have received enormous attention during past four decades and in particular after the report by Gratzel et al[1] in 1991 (Nature) on photocurrent generation using a Ru(II)-polypyridyl complex, supported on anatase form of mesoporous TiO_2. Since then, numerous sensitizers have been prepared, and their performance has been tested. Best conversion efficiency of up to 11% and 12% was achieved till date by using a derivative of cis-di(thiocyanato)bis(2,2'-bipyridyl-4,4'-dicarboxylate) ruthenium(II) (N3) as a photosensitizer[1] and a porphyrin-based carboxylate derivatives[2], respectively. Slow back electron transfer (BET) from the conduction band ($[CB]e^{-}_{TiO2}$) to the photooxidized Ru(III) is believed to be the most important that helps in achieving this higher efficiency. Weakly basic carboxylates do not have a sufficiently high affinity for the Ti(IV) ions and the weaker interaction contributes to this slower BET process. Weaker interaction also has demerits. In presence of water, slow desorption of the photosensitizers can occur which can limit the long-term stability of the cell. Additionally, dynamics of the eˆ transfer involving the $Ru_{d\pi} \rightarrow dcbpy_{\pi*}$-based ^{1}MLCT and/or ^{3}MLCT states and $[CB]_{TiO2}$ was multi-exponential due to a competitive ISC and a vibrational cooling processes. Weaker coupling between the TiO_2 and carboxylate is ascribed to the reason for such slower electron injection dynamics. Possibility of using phosphonate or sulphonate as the anchoring functionality has also been investigated. Phosphonates ($pK_a \sim 6.5$) provide stronger binding than carboxylates ($pK_a \sim 4$) and sulphonates. However, these anchoring functionalities also have some intrinsic problems and did not lead to the design of an efficient sensitizer dye molecule for DSSC. This has actually led us to the search for an alternate anchoring functionality, which shows more efficient binding to the TiO_2 surfaces.

It is well documented in the literature that catechol forms a strong charge transfer complex with TiO_2. Their studies revealed that interfacial reaction dynamics was mediated by the excited electronic states of the dye, rather than the electron being injected into the semiconductor material directly from the ground electronic state of the adsorbate. The primary process of the interfacial electron-transfer dynamics for this strongly coupled catechol-TiO_2 system was found to involve an ultrafast electron-injection event ($\tau_1 = 6$ fs), which was subsequently followed by efficient charge diffusion along the semiconductor surface. In our previous studies we have shown that catechol[3-4], pyrogallol red (PGR)[5], alizarin[6-7] and porphyrin molecules[8-10] bind strongly with TiO_2 nanoparticles through catechol moiety and found to have large electronic coupling with the TiO_2. In the present article we have discussed interfacial electron transfer dynamics of Ru(II)-Os(II)-polypyridyl-catecholate and their different derivatives[11-20] with TiO_2 nanoparticles also to understand the influence of molecular structure on ET dynamics using ultrafast femtosecond transient absorption spectroscopy.

Overview of Different Electron-Transfer Processes in Dye-Sensitized Solar cell (DSSC):

In Scheme 2 we have shown all the electron transfer reactions which take place in working DSSC. Although in our spectroscopic measurements we monitor only forward electron transfer from photoexcited dye to TiO_2 semiconductor particles and back ward ET from TiO_2 to dye cation, however we felt that it is important to discuss different electron transfer reactions which take place in DSSC ranging from sub-10 fs to millisecond.

One of the most amazing observation in DSSC research is the ultrafast injection from the photoexcited excited Ru-complex in the TiO_2 conduction band. Although the detailed mechanism of the injection process is still under debate, it is generally accepted that a fast femtosecond component is observed for this type of sensitizer directly attached to an oxide surface. In the study of ultrafast spectroscopic studies we made significant contribution to unravel the charge transfer dynamics in dye-sensitized nanoparticle systems. However it has been realized that through our and other investigations For DSSC device performance, the time scales of the injection process should be faster compared to the decay of the excited state of the dye to the ground state. This is given by the excited state lifetime of the dye, which for typical Ru-complexes used in DSCs is more than 100 ns.

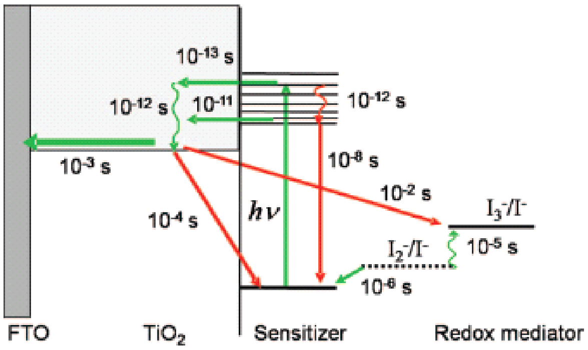

Scheme 2: Schematic diagram showing different Electron Transfer reactions in DSSC showing their times scales. The favorable kinetics are indicated by green line, where as intercepting kinetics are shown by red lines.

Other than electron injection and back ET reaction charge transfer reaction takes place between oxidized dye and electrolyte normally I-, which takes place in microsecond time domain. Electron transport through the mesoporous oxide film is also very important process to achieve very high efficient solar module. Finally, reduction of electron acceptors in the electrolyte at the counter electrode is also very important electron transfer reaction. However using our expertise in femtosecond spectroscopy we will be discussing ultrafast electron injection and back electron transfer dynamics using newly designed and synthesized different ruthenium and osmium polypyridyl complexes.

Femtosecond Transient Absorption Studies

The femtosecond tunable visible spectrometer has been developed based on a multi-pass amplified femtosecond Ti:sapphire laser system supplied by Thales, France (Scheme 3). The pulses of 20 fs duration and 4 nJ energy per pulse at 800 nm obtained from a self-mode-locked Ti-Sapphire laser oscillator (Synergy 20, Femtolaser, Austria) were amplified in a regenerative and two-pass amplifier pumped by a 20W DPSS laser (Jade) to generate 40 fs laser pulses of about 1.2 mJ energy at a repetition rate of 1 kHz. The 800 nm output pulse from the multi-pass amplifier is split into two parts to generate pump and probe pulses. In the present investigation we have used frequency doubled 400 nm as excitation sources. To generate pump pulses at 400 nm one part of 800 nm with 200 μJ/pulse is frequency doubled in BBO crystals. To generate visible probe pulses, about 3 μJ of the 800 nm beam is focused onto a 1.5 mm thick sapphire window. The intensity of the 800 nm beam is adjusted by iris size and ND filters to obtain a stable white light continuum in the 400 nm to over 1000 nm region. The probe pulses are split into the signal and reference beams and are detected by two matched photodiodes with variable gain. We have kept the spot sizes of the pump beam and probe beam at the crossing point around 500 and 300 micron respectively. The noise level of the white light is about ~0.5 % with occasional spikes due to oscillator fluctuation. We have noticed that most laser noise is low-frequency noise and can be eliminated by comparing the adjacent probe laser pulses (pump blocked *vs* unblocked using a mechanical chopper). The typical noise in the measured absorbance change is about <0.3%. The instrument response function (IRF) for 400 nm excitation was obtained by fitting the rise time of the bleach of sodium salt of *meso* tetrakis (4 sulfonatophenyl) porphyrin (TPPS) at 710 nm and found to be 120 fs . The <N>(jσ) was maintained <1 to prevent multiexciton formation due to higher pump intensity. All the samples were dissolved in nanopure water. The Quantum dot solution was circulated to avoid sample bleaching during the course of the experiment. The data analysis and fitting at individual wavelengths were carried out by Lab-View program.

Molecular structures of Newly Synthesized Sensitizer Molecules.

To address the above issues on electron transfer reaction we have designed and synthesized a series of transition metal complexes (both Ru and Os) and the structures and

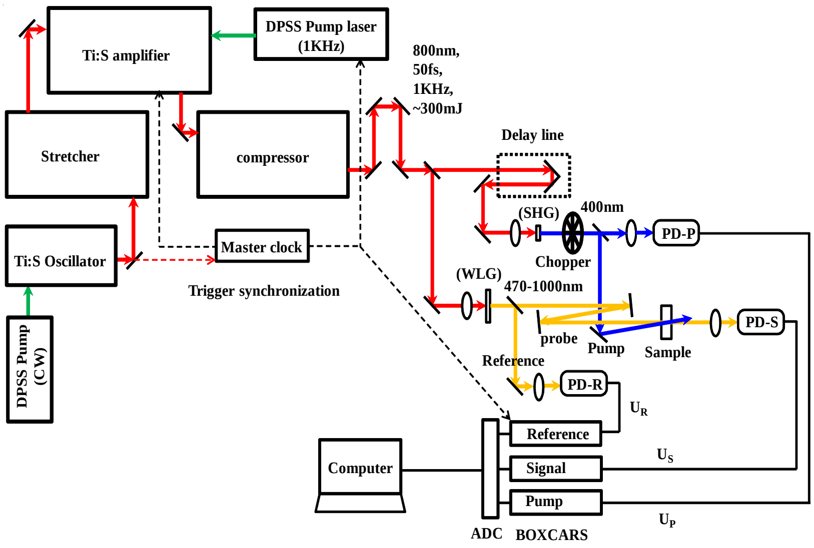

Scheme 3: Schematic Diagram of Femtosecond Transient Absorption Spectrometer developed in Radiation & Photochemistry Division.

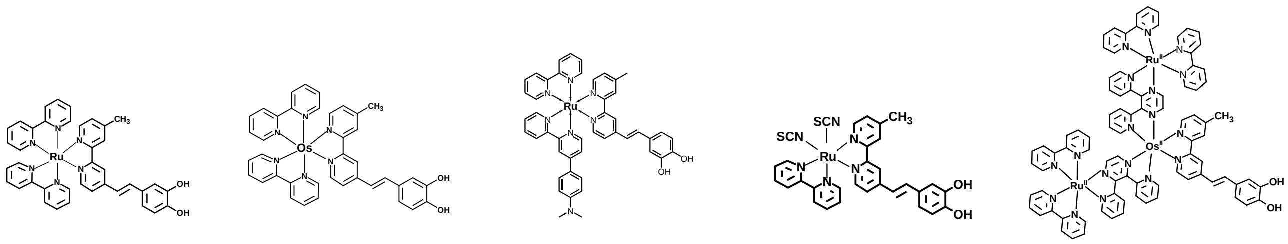

Chart 1: Molecular structure of different ruthenium and osmium polypyridyl complexes which have used as sensitizer molecules on TiO_2 nanoparticle surface.

are shown for few of them in Chart 1. It is interesting to see that all the sensitizer molecules can bind with TiO_2 nanoparticles through catecholate binding. All the dye molecules have been synthesized by Dr. Amitava Das and his co-workers of Central Salt & Marine Chemicals Research Institute (CSMCRI) Bhavnagar, Gujarat (India) under BRNS collaborative project.

Optical Absorption Studies of Sensitizer Molecules.

To study interfacial electron transfer dynamics it is very important to monitor the optical absorption of the senstizer molecules. Fig. 1 (Left panel) shows the optical absorption spectra of all 5 complexes in water. Let us discuss optical absorption behaviour of Ru complex[11]. Fig. 1a shows low energy band at 426 and 456 nm. Band at 426 nm can be attributed to a $d_{Ru(II)} \rightarrow \pi^*_{(bpy)}$ -based metal to ligand charge transfer transition (MLCT). The other band at 456 nm is to attributed to $d_{Ru(II)} \rightarrow \pi^*_{(L1/L2)}$-based MLCT transition. Now let us discuss the optical absorption behaviour of Os which is shown in Fig. 1b. Broad absorption bands with maxima at 443 and 486 nm (Fig. 1b) are assigned to two $d_{Os(II)} \rightarrow \pi^*_{(bpy)}$ (at ~ 443 nm) and $d_{Os(II)} \rightarrow \pi^*_{(L1/L2)}$-based (at ~ 486 nm) MLCT transitions[12-13]. The broad absorption feature exhibited by Os^{II} complex in 550-750nm region is attributed to spin-forbidden MLCT transitions, which gain intensity in the osmium complexes because of enhanced spin-orbit coupling—a common feature for heavy metal centers.[12]

Now, interestingly for Ru-NMe_2, the introduction of N,N'-dimethylaminophenyl moiety to ancillary bpy ligand broadens the MLCT band from 400 to 700 nm region with a significant increase in its molar extinction coefficient (shown in Fig.1c). The broadening can be due to presence of electron donor bp-ph-NMe_2 ligand which raises the HOMO level of Ru-NMe_2 in comparison of its homoleptic Ru complex (Fig. 1a). The electron donor strength of ph-NMe_2 group depend on its rotational conformer with respect to bpy plane and contribution from all possible conformer produces a broad distribution in HOMO level of Ru-NMe_2 which ultimately reflected in its broadened optical absorption spectra[14-15]. Additionally, the presence of electron -donor and -acceptor (L_2 and L_1) ligands in Ru-NMe_2 can give rise to LLCT absorption band in 350-700nm region (Fig.1c). This is evident in Fig. 1 that the absorbance of Ru-NMe_2 is significantly high at 400nm as compared to Ru and can be assigned to LLCT transitions.

Interestingly the absorption spectrum of Ru-SCN in the visible region is dominated by different metal to ligand charge transfer transitions (MLCT)[16]. Effect of incorporation of –NCS on the electronic spectra is clearly visible when that is compared to that for Ru complex (Fig. 1a). A significant red shift in the absorption maxima along with the appreciable absorption tail extending to ~650 nm could be achieved for Ru-SCN (Fig.1d). The onset absorption of Ru-SCN also shifts drastically from 600 nm to 750 nm ensuring much broader absorption of solar radiation. This can be explained that on introducing

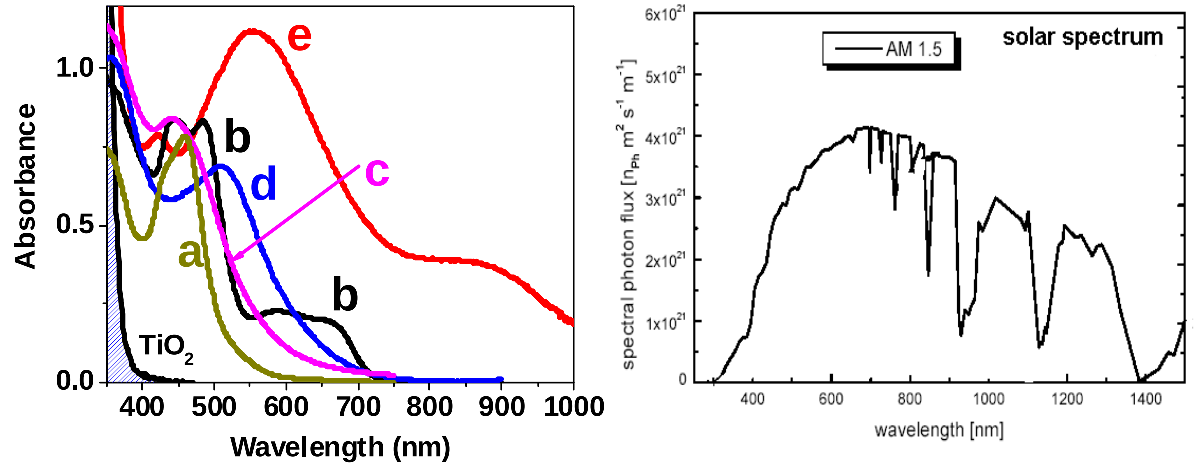

Fig. 1: Left Panel: Optical absorption spectra of a) Ru, b) Os, c) Ru-NMe_2 d) Ru-SCN and e) Ru_2Os polypyridyl complexes in water. Right Panel: Solar spectrum which falls on Earth under the condition AM 1.5.

electron donating -NCS ligand, energy level of t_{2g} orbital is pushed to a higher energy ($\sim$ 0.3 V) and as a result an appreciable red-shift in optical absorption of Ru-SCN is observed as compared to Ru complex[16].

Finally Fig. 1e shows the optical absorption spectrum of Ru_2Os_1 complex which covers the entire visible and near IR region[20]. The broad absorption of Ru_2Os_1 complex is attributed to "$t_{2g} \rightarrow \pi^*_{bpy}$" and "$t_{2g} \rightarrow \pi^*_{dpp}$" MLCT transitions of Ru(II)- and Os(II)- complex fragments. The dpp ligand is a strong π-acceptor than the bpy ligand. Therefore, the "$t_{2g} \rightarrow \pi^*_{dpp}$" ^{1}MLCT transitions contribute largely in 510-750nm region whereas "$t_{2g} \rightarrow \pi^*_{bpy}$" ^{1}MLCT transitions appear in the lower wavelength region (<510nm). The broad band in 750-1000nm region is assigned to "$t_{2g} \rightarrow \pi^*_{dpp}$" ^{3}MLCT transitions of core Os(II)-complex fragment. A large spectral shift in the absorption spectrum of the Ru_2Os_1 complex (^{1}MLCT band; 550-750nm region) in comparison to $Ru_2 {}^\frown Ru_1$ complex represents redox asymmetry of heterometallic Ru/Os ions pair[20].

Ultrafast Interfacial Electron Transfer Dynamics: Femtosecond Transient Absorption Studies

To monitor interfacial electron transfer dynamics we have carried out femtosecond transient absorption spectroscopy by exciting dyes at 400 nm laser light after sensitizing on TiO_2 nanoparticle surface. Fig. 2 shows the transient absorption spectra of Ru complex-sensitized TiO_2 nanoparticles at different time delays. The spectrum at each time delay consists of bleach below 500 nm wavelength region, an absorption band 510-630 nm peaking at *ca* 550 nm and another broad positive absorption band in 6501000 nm region. The absorption peak at 550 nm can be attributed to $Ru^{\bullet+}$ (cation radical). The broad absorption band in 650–1000 nm region has been attributed to the conduction band electrons in the nanoparticles. Similarly we have also carried out transient absorption studies by exciting all the sensitizer molecules after sensitizing on TiO_2 nanoparticles. We have compared the electron transfer dynamics for both Ru and Os-complex after sensitizing on TiO_2 nanoparticle surface. To monitor electron injection dynamics we have monitor the kinetics at shorter time scale and are shown as inset in Fig. 3. It is evident from the curve A of Figure 3 that the electron injection kinetics in Ru/TiO_2 is single exponential with pulse-width limited (< 100 fs) time constant. This single exponential electron injection for Ru/TiO_2 has been attributed to injection from non-thermalized MLCT states. Here due to strong coupling through catecholate moiety, electron injection competes with ISC rate which leads thermalized ^{3}MLCT states. On the other hand, in Os/TiO_2 system (shown in curve 3B) electron injection dynamics is found to be bi-exponential with time-constants $\tau_{inj}^1 <$ 100 fs (42%) and $\tau_{inj}^2 = 1.7$ ps (58%). Here the shorter component has been attributed to the electron injection from non-thermalized MLCT states and the longer component could be attributed to electron injection predominantly from thermalized ^{3}MLCT states[13].

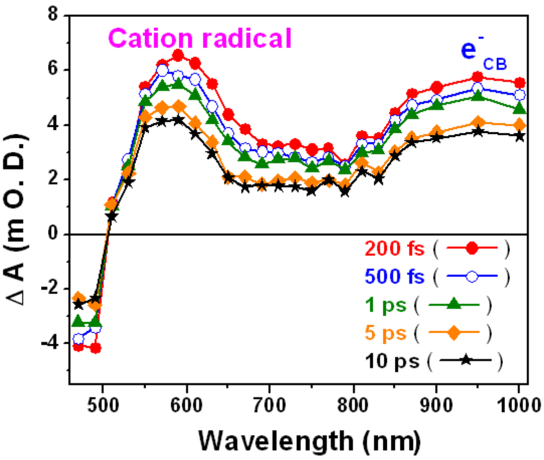

Fig. 2: Transient absorption spectra of Ru-complex sensitized TiO_2 nanoparticle in water at different time delay after excitation at 400 nm.

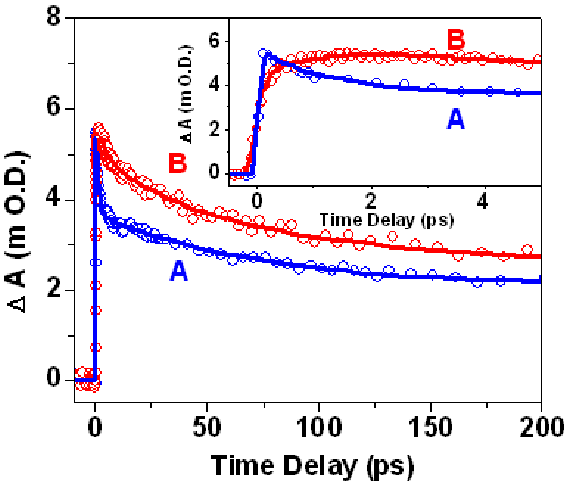

Fig.3: Kinetic decay trace of the injected electron in the conduction band at 1000 nm in A) Ru/TiO_2 and B) Os/TiO_2 following excitation with 400 nm laser pulse. [Inset shows the kinetic trace at shorter time scale].

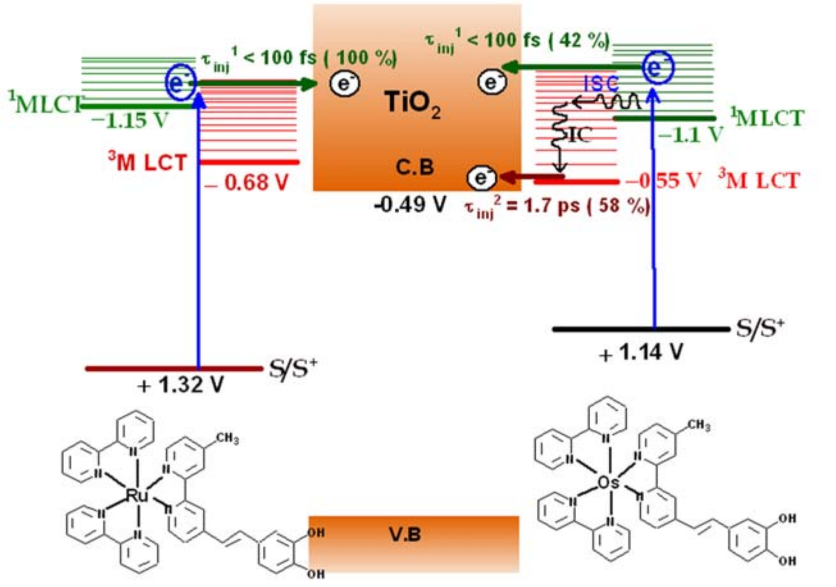

Scheme 4: Mechanistic scheme showing three-level model which consists of the ground state (S_o), excited triplet state (^{3}MLCT) and excited singlet (^{1}MLCT) state of 1 and 2 adsorbed on TiO_2 nanoparticles.

In Scheme 4 we have shown the mechanistic path ways of electron transfer and relaxation dynamics of both dyes (Ru and Os) bound to TiO_2 surface. The ground and excited state energy levels of these complexes were determined by cyclic voltametry and optical absorption spectrum of MLCT-based singlet and triplet states. It is interesting to see that ET path ways are different for two complexes, though the energy levels of the complexes do no differ appreciably. Os being the heavier transition metal, spin orbit coupling for Os(II)-complexes is larger compared to analogous Ru(II)-complexes and thus for Os, ISC process is expected to be much faster and more efficient[13]. Thus on photoexcitation, ^{3}MLCT state gets populated much faster through an efficient ISC process from initially populated ^{1}MLCT states as compared to the analogous Ru(II)-complex and electron injection takes place from both the states with different time constants (Scheme 4).

Now we have monitored ET dynamics in Ru-NMe$_2$/TiO$_2$ system by exciting the sample at 400 nm laser pulse and compared the dynamics with Ru/TiO$_2$ system and shown in Fig. 4. The BET dynamics is followed by monitoring kiteics at 900 nm for injected electron and fitted multiexponentially with time constants of 2ps (11.8%), 200ps (20.7%) and > 1ns (67.5%) for complex-Ru-NMe$_2$/TiO$_2$ system[15] and 1ps (37%), 100ps (26%) and > 1ns (37%) for complex Ru/TiO$_2$ system. It is interesting to observe a slow BET dynamics in complex Ru-NMe$_2$/TiO$_2$ system as compared to complex-Ru/TiO$_2$ system despite the fact that both the complexes are strongly coupled to TiO$_2$ surface via catehcolate linkage. In complex Ru-NMe$_2$, the electron donating dimethylaminophenyl group act as secondary electron donor to Ru$^{(III)}$ central ion which is produced after electron injection from photoexcited MLCT states into TiO$_2$ NP.

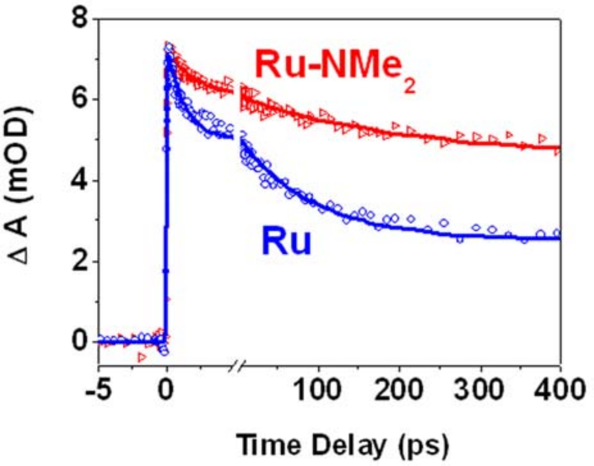

Fig. 4: BET kinetics monitored by TA of e$^-$(C.B. TiO$_2$) at 900nm in (a) Ru-NMe$_2$/TiO$_2$ and (b) Ru/TiO$_2$ system.

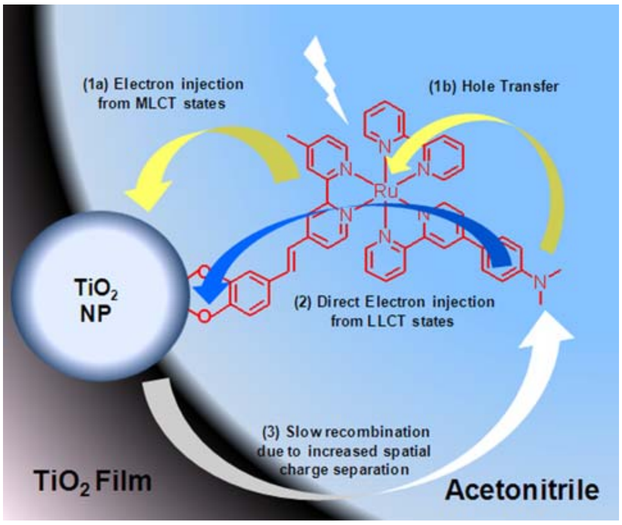

Scheme 5: Schematic representation of interfacial electron transfer in Ru-NMe$_2$/TiO$_2$ system.

Here the charge separation due to populating LLCT state can be viewed as direct hole localization on electron donor dimethylamino moiety with a simultaneous electron localization on electron acceptor **L_1** ligand. So, in presence of TiO_2 NP, 400nm excitation results a direct electron injection from **L_1** ligand to conduction band of TiO_2 NP and the hole is localized away from the TiO_2 surface as shown in sheme-5. As a result, the electron injection yield is observed to be 20% more in Ru-NMe_2/TiO_2 system as compared to Ru/TiO_2 system. Further, the increased spatial charge separation between e^-(C.B. TiO_2) and hole (residing at -ph-NMe_2 moiety of Ru-NMe_2) causes a slow BET in Ru-NMe_2/TiO_2 system as compared to Ru/TiO2 system[15]. It is clear from Figure 1 that optical absorption spectra of Ru-SCN is much red shifted as compared to that Ru-complex. So it was very important to study ET dynamics of Ru-SCN/TiO_2 system and compared the dynamics with Ru/TiO_2 system. We have also carried out transient absorption studies to monitor ET dynamics in Ru-SCN/ TiO_2 system[16]. Charge recombination reaction was determined by monitoring the transient kinetics at 900 nm (Fig. 5). It is interesting to see that although both the sensitizers are strongly coupled with TiO_2 nanoparticles still BET reaction is much faster in Ru-SCN/TiO_2 system as compared to Ru/TiO_2 system. The free energy of reaction (-ΔG^0) for Ru-SCN/TiO_2 and Ru/TiO_2 systems calculated to be 1.47 eV and 1.81 eV respectively[16]. Again we can imagine that electron coupling between dye-nanoparticle systems are same as both the ruthenium complex (Ru-SCN and Ru) bound to TiO_2 through pendant catecholate functionality. So BET reaction rate will mainly depend on free energy of reaction of dye-nanoparticle system. According to Marcus ET theory, with increasing thermodynamic driving force (-ΔG^0), the ET rate initially increases to reach a maximum value and then starts decreasing. This high exoergic region is often termed as "inverted regime". BET processes in dye-sensitized TiO_2 nanoparticles surfaces fall in the Marcus inverted regime for its high free energy of reaction. In this region with increasing driving force (-ΔG^0) of the reaction, the rate of BET decreases. As the free energy for BET reaction in the case of Ru/TiO_2 is higher than that of Ru-SCN/TiO_2 system, BET rate in Ru/TiO_2 system will be slower as compared to that Ru-SCN/TiO_2.

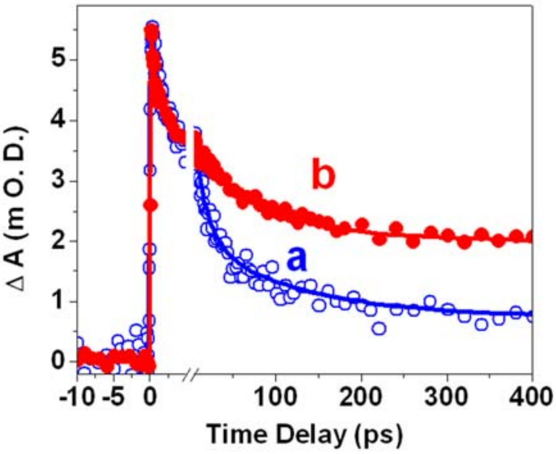

Fig. 5: BET kinetics monitored by TA of e^-(C.B. TiO_2) at 900nm in (a) Ru-SCN/TiO_2 and (b) Ru/TiO_2 system.

Finally we have compared charge transfer dynamics in Ru_2Os_1/TiO_2 system and compared the dynamics with Os_1/ TiO_2 system. The rise of 1000nm kinetics corresponds to an electron injection process. It shows a bi-exponential electron injection in Os_1/TiO_2 system (<100fs, 1.5ps) which is attributed to electron injection from the MLCT manifolds (thermalized and unthermalized)[13]. On the other hand the Ru_2Os_1/TiO_2 system exhibits multiexponential electron injection (<100fs, 1ps, 20ps) dynamics[20]. The strong catecholate binding on TiO_2 surface initiates electron injection in < 50fs time scale. Subsequently, the "peripheral-to-core" energy transfer excites the core Os(μ-dpp)$_2$(bpy-CH=CH-catechol) complex. So, the electron injection process is observed to be multiexponential in Ru_2Os_1/TiO_2 system. The decay of 1000nm kinetics corresponds to the charge recombination process. It is apparent from Fig. 6 that the charge recombination is

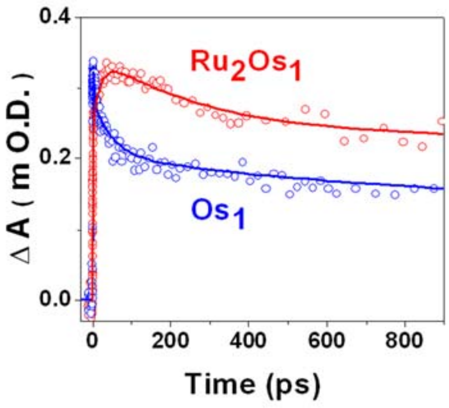

Fig. 6: Transient absorption kinetics at 1000nm; a) Ru_2Os_1/TiO_2 system and b) Os_1/TiO_2 system.

comparatively slower in Ru_2Os_1/TiO_2 system as compared to Os_1/TiO_2 system. This may be due to partial hole delocalization in mono-oxidized $[Ru_2Os_1complex]^{+\bullet}$ cation radical. It is one of the possible reason that causes better interfacial charge separation in Ru_2Os_1/TiO_2 system.

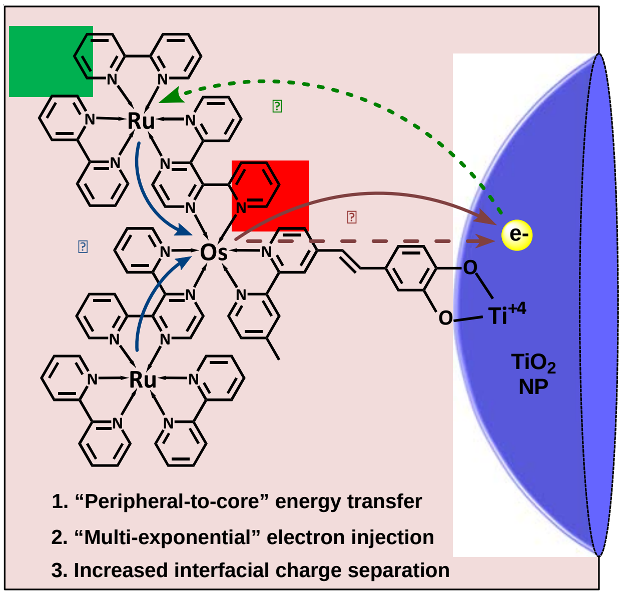

Scheme 6: "peripheral-to-core" energy transfer in Ru_2Os_1 complex causes multiexponential electron injection on TiO_2 surface. The electronic coupling between poly-metallic centres stabilizes the interfacial charge separation in Ru_2Os_1 sensitized TiO_2 nanoparticles.

A comparison of the transient absorption kinetics of Ru_2Os_1, Ru_2Ru_1 and Os_1 complexes reveals a "peripheral-to-core" energy transfer in the Ru_2Os_1 complex[20]. The directional energy transfer occurs in ultrafast time scale (400fs, 8ps and 40ps). The transient absorption study shows that energy transfer is much faster than non-radiative relaxation processes (*viz.* vibrational relaxation; ~10ps). Such complex mimics the antenna function of natural light harvesting complexes in which energy transfer occurs very efficiently. The antenna function is useful in improving the core activity of the complex. It is evidenced in interfacial electron transfer study of Ru_2Os_1/TiO_2 NP system. The study shows multiexponential electron injection and a longer lived charge separation in Ru_2Os_1/TiO_2 NP system as compared to that in monomer-Os_1complex/TiO_2 NP system. This reveals that the ground and excited state electronic coupling between different M^{II}-complexes (M=Ru/Os) facilitates a better interfacial charge separation. This investigation reveals the potential of polynuclear complexes which can show panchromatic effects, unidirectional energy and electron transfer properties.

Dye-Sensitized Solar Cell (DSSC) Module

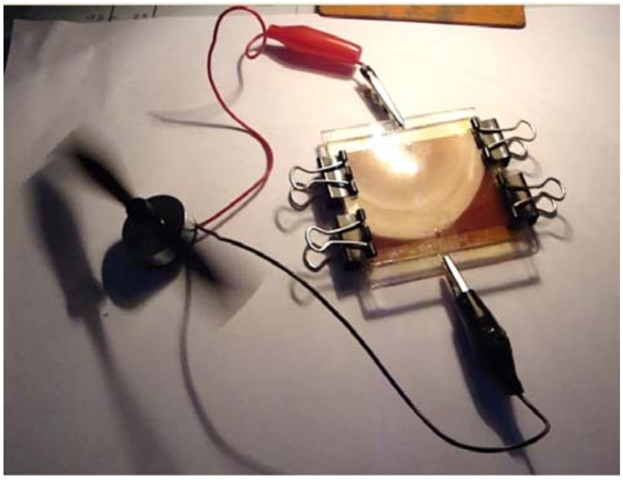

Scheme 7: Working Dye-Sensitized Solar Cell (DSSC) Module designed and fabricated out of Ru-complex as sensitizer in Radiation & Photochemistry Division, BARC.

Conclusion

In conclusion we have reported the design and synthesis a series of mono-nuclear and trinuclear ruthenium and osmium polypyridyl complexes and their derivatives with catecholate binding group which can bind with TiO_2 nanoparticle surface through pendant catechol moiety. As the pK_a value for the catecholate ruthenium/osmium polypyridyl complex is as high as > 9.5, these dye-nanoparticle systems give more stability even at higher pH conditions unlike other carboxylate ruthenium polypyridyl complexes. On modification of their molecular structures it reveals that the solar absorption spectra of poly-nulclear Ru/Os complexes can go beyond near IR region. Femtosecond transient absorption measurements have been carried out to study interfacial ET dynamics in dye/TiO_2 systems. On excitation with 400 nm laser pulse, a bleach of the adsorbed dye, transient absorption for the dye cation and broad absorption band for the conduction band electron have been observed for the above dye-nanoparticle systems. By monitoring the transients in ultrafast timescale electron transfer dynamics (both electron injection and back electron transfer) have been determined in dye/TiO_2 systems. A detailed ultrafast electron transfer studies on the dye-TiO_2 systems unrevealed suitability of the newly designed and synthesized mono and poly-nuclear ruthenium and osmium complexes in dye-sensitized solar cell.

Acknowledgement

I cordially thank my younger colleague Dr. Sandeep Verma and my collaborator Dr. Amitava Das of Central Salt & Marine Chemicals Research Institute (CSMCRI) Bhavnagar, Gujarat (India) for scientific discussion and fruitful suggestions. We also thank Dr. D. K. Palit, Dr. S.K. Sarkar and Dr. T. Mukherjee for their encouragement.

References

1. B. O'Regan and M. Graetzel. *Nature*, 1991, 353, 737.
2. A.Yella, H.Wei Lee, H.N. Tsao, Chenyi Yi, A.K.Chandiran, M. K. Nazeeruddin, E. W. Guang Diau, C.- Yu Yeh, , S.M Zakeeruddin, , M. Grätzel, *Science,* 2011*: 334,* 629*.*
3. M.C. Rath, D. K. Palit, T. Mukherjee, H.N. Ghosh *J. Photochem. Photobiol A: Chemistry* 2009, *204*, 209.
4. S. Kaniyankandy, S. Rawalekar, A. Sen, B. Ganguly, and H. N. Ghosh *J. Phys. Chem. C* 2012, *116, 98.*
5. G. Ramakrishna, H.N.Ghosh, A.K. Singh, D.K. Palit and J.P. Mittal, *J.Phys.Chem.B.* 2001, *105,* 12786.
6. G. Ramakrishna, A. K. Singh, D. K. Palit and H.N.Ghosh, *J.Phys.Chem.B* 2004, *108,* 1701.
7. K. Sreejith, S. Verma, J. A. Mandal, D. K. Palit and H. N. Ghosh, *J. Phys. Chem. C* 2009, *113*, 3593.
8. G. Ramakrishna, S, Verma, A. D. Jose, D. Krishnakumar, A. Das, D.K. Palit and H.N. Ghosh *J.Phys.Chem.B* 2006, *110*, 9012.
9. S.Verma, A. Ghosh, A. Das and H. N. Ghosh, *Chem. Eur. J.*, 2011, *17*, 3458.
10. S. Verma. H. N. Ghosh *J. Phys. Chem. Lett.*, 2012, *3*, 1877.
11. G. Ramakrishna, Amilan D. Jose, D. Krishnakumar, Amitava Das, D.K. Palit, and H.N. Ghosh *J. Phys. Chem. B* 2005, *109,* 15445.
12. S. Verma, P. Kar,. A. Das, D. K. Palit, H. N. Ghosh, *J. Phys. Chem .C,* 2008, 112, 2918.
13. S. Verma, P. Kar, A. Das, D. K. Palit, H. N. Ghosh, *Chem. Eur. J.*, 2010, *16*, 611.
14. S. Verma, P. Kar, A. Das, and H. N. Ghosh, *Dalton Trans.*, 2011, *40*, 9765.
15. S. Verma, P. Kar, A. Das, and H. N. Ghosh, *Chem. Eur. J.*, 2011, *17*, 1561.
16. P. Kar, S. Verma, A. Das, H. N. Ghosh *J. Phys. Chem. C* 2009, *113,* 7970*.*
17. P. Kar, S. Verma, A. Sen, A. Das, B. Ganguly, H. N. Ghosh, *Inorg. Chem.*, 2010, *49*, 4167.
18. T. Banerjee, S. Rawalekar, A. Das, and H. N. Ghosh, *Eur. J. Inorg. Chem.* 2011, 4187.
19. P. Kar, T. Banerjee, S. Verma, A. Sen, A. Das, B. Ganguly and H. N. Ghosh, *Phys. Chem. Chem. Phys.,* 2012, *14*, 8192.
20. S. Verma, P. Kar, T. Banerjee, A. Das, and H. N. Ghosh, *J. Phys. Chem. Lett.* 2012, *3*, 1543.

DEVELOPMENT OF RADIATION EMERGENCY RESPONSE SYSTEM FOR NATIONAL LEVEL PREPAREDNESS FOR RESPONSE TO NUCLEAR AND RADIOLOGICAL EMERGENCIES

Pradeepkumar K.S. and Probal Chaudhury
Radiation Safety Systems Division

Dr. K.S. Pradeepkumar is the recipient of the DAE Homi Bhabha Science & Technology Award for the year 2010

Abstract

As identified by various international agencies, in addition to nuclear and radiological accidents, threats from orphan sources and nuclear and radiological terrorism are to be addressed in the preparedness for nuclear and radiological emergencies. DAE is the identified nodal agency for technical support for response to any radiation emergency. For the preparedness at national level, nuclear disaster and various nuclear and radiological emergency scenarios and their impacts are identified. To reduce their consequences, mobile and aerial radiation monitoring systems, methodologies for detection and quick impact assessment, aerial and ground based validation trials, trained First Responders and Quick Response Teams(QRTs) and twenty two DAE- Emergency Response Centers etc. are developed under 'Radiation Emergency Response System'

Introduction

World over large number of nuclear facilities including nuclear power reactors are in operation and usage of radioisotopes for medical and other applications are on increase. Though probability of occurrence is small, radiation emergencies, either due to releases following major accidents[1,2] or due to orphan sources[3] or malicious acts involving radioactive material[4] can lead to radiological and psychological consequences in addition to economic losses. Adequate measures are required for the prevention and response to these emergencies. For the preparedness at national level, various potential nuclear/radiological emergency scenarios[5,6] including transboundary emergencies and nuclear disaster[7,8,9,10,11] were taken into account addressing their possible impact.

Identification and Impact Assessment of Potential Nuclear and Radiological Emergency Scenarios

The radiological impact following release of radioactivity to the atmosphere depends on[12] (i) accident scenario, (ii) quantity and type of releases (radionuclides), (iii) elevation of the release, (iv) meteorological conditions under which the releases take place, (v) topography of the site, (vi) living habits of the population. In addition to radiation related health effects, Nuclear and Radiological emergencies are likely to lead to psychological, social, economic and environmental consequences.

The following nuclear and radiological accidents and emergency scenarios were identified for national level emergency preparedness:

a) Accidents in facilities with release of radioactivity to the environment (Reprocessing facility, Nuclear reactor etc, e.g. Kystim, Chernobyl, Fukushuima)
b) Accident during the transport of radioactive material affecting the container or package
c) Theft or loss of radioactive material from hospitals or industrial radiographic institutions.
d) Accidents involving medical or industrial sources (e.g. Yanango, Mayapuri)

e) Fire incident involving radioactive material
f) Loss, unauthorized removal or misuse of radioactive sources (e.g. Goiania)
g) Undetected melting of radioactive sources into metal products (e.g. Mexico, Thailand)
h) Malicious use of radioactive material
i) Explosion of Radiological Dispersal Device (RDD)
j) Nuclear disaster/nuclear threats[7]
k) Crash of a nuclear powered satellite (e.g. Cosmos954)

Impact prediction carried out for 'Nuclear Disaster' when any major city is affected demonstrates the requirement of systems and software for the quick assessment of radioactive fallout over large area and radiological status of the affected area for the implementation of protective measures. 'Intervention and Action Levels' for the Quick Response Teams (QRTs) and 'First Responders' during large scale Nuclear Disaster/Radiological emergencies are optimized based on the projected dose for public and the rescuers.

Our study related to radiological threats and simulated RDD experiments conducted using stable isotopes indicates that radiation levels for distances more than 50m will not be very high as hotspots may be restricted to nearby area. The biggest challenge from an RDD explosion will be handling of the radioactive contamination and 'fear factor' compared to radiation exposure to public or First Responders. Level and pattern of radioactive contamination on ground following releases during nuclear accidents and minimum strength of orphan radioactive sources to be detected are taken into account for optimizing systems and monitoring methodology required for emergency preparedness.

Development of 'Radiation Emergency Response System'

Based on the study and analysis of the 'potential challenges' and the preparedness required for impact assessment and response, the following systems/techniques are developed:

State-of-the-art systems for quick assessment of radiological impact in case of any large scale nuclear disaster or radiological emergency in public domain: This includes

i) Aerial Gamma Spectrometry System (AGSS)[13] to be installed in aircrafts for aerial radiation monitoring for quick impact assessment
ii) Compact Aerial Radiation Monitoring System (CARMS)[13] for remote aerial surveys using Unmanned Aerial Vehicles (UAVs)
iii) Installed environmental radiation monitoring and warning systems with data transfer facilities to Emergency Response Centre
iv) Mobile Radiological Impact Assessment Laboratory (M-RIAL) installed with monitoring systems with online computation and data transfer capability

Methodology for mobile monitoring for the assessment of radiological status which includes :

a) Aerial survey methodology for (i) quick assessment of large scale ground contamination [Fig.1], (ii) search for locating and identifying radioactive orphan sources and (iii) tracking of radioactive plume [Fig.2]. Installing the AGSS in MI-8/MI-17/ ALH Helicopters, aerial gamma spectrometric mapping of simulated 'large area contamination' and 'orphan source search' exercises were conducted at Kalpakkam, Pune and Delhi as well as Argon-41 plume tracking and scanning of Emergency Planning

Lat 12 deg 33.85 min N
Long 80 deg 07.74 min E
Lat : 12deg 34.47min
Long : 80deg 08.71min
ROI : Co 60-2
START CHN : 209
END CHN : 235
🟥 > 500
🟪 > 300
🟦 > 80
🟩 < 80
SPECT. NO : 149
Height (m) 80
DETECTORS : 1
COUNTS : 518
ACTIVITY (kBq/m.sq) : 2.84E+1
DOSE (uR/hr) 2.82E+1
Lat : 12deg 33.09min
Long : 80deg 07.03min

Fig.1: (a) AGSS installed in a Helicopter for aerial radiation mapping above 'simulated contamination' using combination of radioisotopes on ground. (b)AGSS screen display during an Aerial Survey above 'Simulated Radioactive Contamination on Ground'- spectrum showing Co-60 detected along with location displayed.

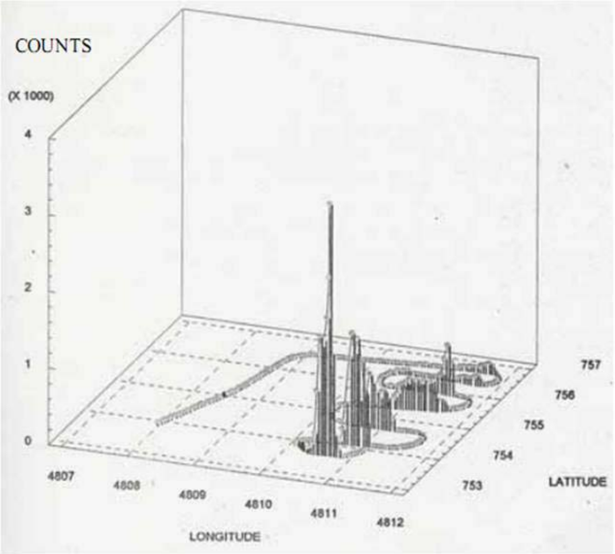

Fig.2: 3D distribution of counts recorded in Ar-41 window during plume tracking carried out by AGSS around a NPP

Zones(EPZs) of NAPS and MAPS. The results are used to establish the flight pattern, speed, flight line spacing and altitude of flying for different monitoring requirements [Fig.3] during emergencies. Paramotors based aerial radiological scanning methodology, tested using CARMS and Gamma Tracer is found to be very effective for complex topography with variable heights of flying [Fig.4].

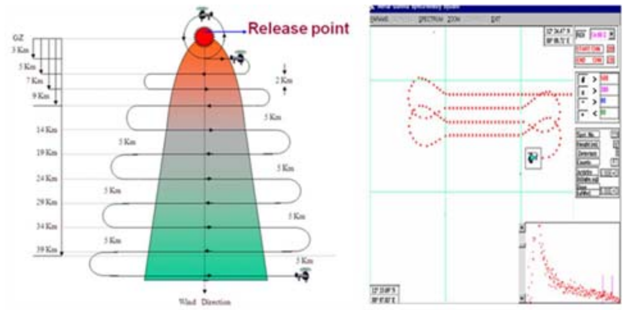

Fig.3:Aerial survey flight paths (a) for mapping of radiological fallout following a Nuclear disaster and (b) 'source search'

Fig.4:'Para Motor' based aerial trials using CARMS –for the assessment of ground level contamination and search of 'orphan sources'

b) Ground based mobile monitoring by using state of the art monitoring systems CARMS and AGSS. Radiological mapping of 14 major cities and EPZs of NPPs carried out demonstrated the method of searching for orphan sources in vulnerable area. Fig.5 shows the mobile radiological survey of Delhi City carried out to rule out 'RDD usage' in the terrorist threat.

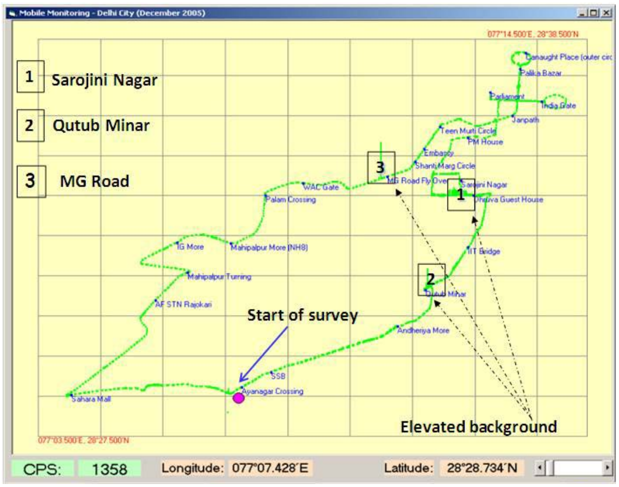

Fig.5: Mobile radiological survey of Delhi City to rule out any 'RDD usage' in the Terrorist attack

Methodology for search and recovery of orphan sources from metallic scrap, handling of contaminated soil and investigation procedures for the finding out the origin of the orphan source etc. were demonstrated during Mayapuri radiological emergency[Fig.6].

Fig.6 Search and recovery of Co-60 sources by DAE-ERC team during Mayapuri radiological emergency.

Impact Assessment Software (IAS) developed and integrated with Geographical Information System (GIS) for prediction of the affected area following any nuclear disaster to help authority in planning of countermeasures and rescue operations. IAS is used by NDMA to predict the possible impact of a nuclear disaster for the preparedness required for response.

First Responders, Quick Response Teams (QRTs) and Emergency Response Teams (ERTs) of DAE - ERCs. Many field exercises simulating nuclear / radiological emergency scenario including 'nuclear and radiological threats' were conducted with participation of the 'First Responders' for nuclear/radiological emergencies.

Portable Personal Decontamination Unit (PPDU) useful for decontamination following any major radiological emergency in public domain. This system after getting transported to the required site can be erected within 30minutes and has the capability of decontaminating 15 persons /hour with facility for handling the contaminated water.

Impact assessment due to dispersion of Argon-41 plume within the BARC site was carried out by installing Gamma Tracer at different receptor locations in and around the BARC site. Assessment was carried out to correlate the behavior of the Ar^{41}plume in the complex topography. This study is used to understand the impact of any accidental releases within the complex topography of Trombay site.

DAE- Emergency Response Centres

Fig.7: Locations of 22 DAE ERCs and 8 proposed new NDRF-ERCs

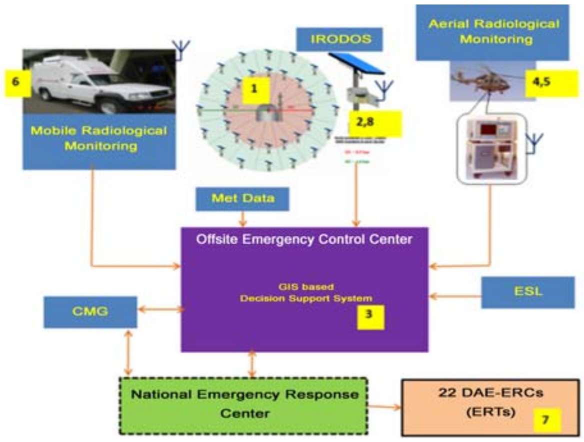

1. Exhaust Monitoring System
2. Indian Real Time Online Decision Support System (IRODOS)
3. GIS Supported Impact Assessment
4. Aerial Gamma Spectrometry System (AGSS), Software & Methodology for Assessment of Large Area Contamination
5. Compact Aerial Radiation Monitoring System (CARMS) for remote aerial surveys using UAVs
6. Mobile Radiological Impact Assessment Lab(M-RIAL)
7. Twenty-two DAE Emergency Response Centers (ERCs)
8. Indian Environmental Radiation Monitoring Network (IERMON)

Fig.8: DAE-ERCs and Systems for Preparedness and Response to nuclear Emergencies

A network of 22 DAE-Emergency Response Centres [Fig.7, Fig.8] spread over country was planned with a nodal centre at BARC for responding effectively to any nuclear or radiological emergency anywhere in the country. ERCs having various monitoring systems, protective gears, software etc in readiness with expertise in the field of assessment of 'Radiological Impact' following any nuclear accident/radiological emergency in public domain is developed and the up-gradation is in progress. Coordination with the DAE-ERCs and the state and district administrations are being taken up by the respective ERCs. Emergency Response Teams of DAE-ERCs responded to the following radiological and other suspected radiation emergency situations; e.g. Mayapuri radiological emergency, Kolkata AMRI Hospital fire, Kakinada fire near to a Ir^{192} source, detailed monitoring of a ship intercepted at Andaman, response to cases of confiscated Depleted Uranium, monitoring of sites of Terrorist attacks for response to any radiation emergency or /to rule out possibility of usage of dirty bombs (26/11 Mumbai attack, Mumbai Train explosions, Delhi, Jaipur, Mumbai, Bangalore etc.), and ERC response to transboundary emergency situation due to Fukushima releases. As suggested by IAEA for major public events[14], DAE-ERCs ensured radiological safety and security along with preparedness for response during Commonwealth Games (CWG-2010) at Delhi [Fig.9]. Detailed mobile radiation monitoring of Delhi city using AGSS, CARMS, Gamma Tracer etc and radiation screening of CWG stadia and

Fig.9: Ensuring 'Radiological Security and Safety' during Commonwealth Games (CWG-2010) through mobile radiation mapping (radiation level with positional coordinates and route followed) using AGSS and CARMS and screening of CWG stadia

Games Villages using PRD and portable spectrometers were carried out to rule out any malicious usage of radioactivity.

Conclusion

Preparedness for quick detection, assessment and response capability to meet any nuclear or radiological emergency situation is very essential to reduce the consequences. Identification of various nuclear and radiological emergency scenarios and possible consequences including nuclear disaster are used for deciding the requirements for emergency preparedness.State of the art radiation monitoring systems, associated software, methodology for quick assessment of radiological status, GIS supported impact assessment programs for the decision makers and 22 DAE-Emergency Response Centres are developed to strengthen national level preparedness for response to nuclear disaster and nuclear and radiological emergencies. Coordinated efforts by Defence, medical, paramilitary, administrators and various security agencies with the support of media and NGOs can ensure effective response to nuclear disaster or radiological emergencies anywhere in the country and can create deterrence against nuclear and radiological threats.

Acknowledgement

We are thankful for the constant encouragement and support from Dr A.K.Ghosh, Director HS&E Group,BARC, Dr D.N.Sharma, Associate Director, HS&E Group, collegues from Emergency Response Systems & Methods Section, RSSD, Heads of DAE Units, members of DAE-ERCs and Emergency Response Teams. We also like to express our gratitude to MOD, MHA, NDMA and State Authorities for their support during the experiments, field trials and aerial survey exercises.

References

1. IAEA, Preparedness and response for a nuclear or radiological emergency, IAEA Safety Standards Series No.GS-R-2 (2002).
2. IAEA, Method for developing arrangements for response to a nuclear or radiological emergency — EPR method, Vienna (2003).
3. Gonzalez, Lost and found dangers - orphan radiation sources raise global concerns, timely action, strengthening radiation safety and security,2-17,*IAEA Bulletin*, Vol 41, No.3, (1999)

4. Criteria for use in preparedness and response for a nuclear or radiological emergency, IAEA Safety Standards Series No. GSG-2, (2011)
5. IAEA, Arrangements for preparedness for Nuclear or Radiological Emergency, IAEA Safety Standards Series No. GS-G-2.1 (2007).
6. Protecting People against Radiation Exposure in the Event of a Radiological Attack, ICRP Publication 96, (2005).
7. Preparedness and response to radiological and nuclear threats, planning guidance for response to a nuclear detonation, FEMA., June 2010.
8. Effects of Nuclear War on Health and Health Services, 2nd , WHO Geneva, (1987).
9. Planning Guidance for Response to a Nuclear Detonation, Federal Emergency Management Agency (FEMA), (2010)
10. A Nuclear Explosion in a City or an Attack on a Nuclear Reactor, Richard L.Garwin, Volume 40, number 2 , 2010, THE BRIDGE, National Academy of Engineering, P20-27.
11. Reducing the Consequences of a Nuclear Detonation: Recent Research, Brooke Buddemeier, P28-38, Volume 40, number 2, THE BRIDGE, National Academy of Engineering, (2010).
12. Nuclear and Radiological Threats and Emergency Preparedness at National Level, K.S. Pradeepkumar, *Bulletin of Radiation Protection and Environment, journal of IARP,* pp48-53, Vol.31, No: 1-4, (2008).
13. Probal Chaudhury and Pradeepkumar K.S., State-of-the-art Monitoring Systems and Software for Assessment Radiological Impact, BARC Founder's day Special Issue, (2012)
14. Nuclear Security Systems and Measures for Major Public Event, Nuclear Security Series No. 18, IAEA, (2012)

DEFECT CHARACTERIZATION FROM MAGNETIC FLUX LEAKAGE SIGNAL OF INSTRUMENTED PIPELINE INSPECTION GAUGE

Shilpi Saha, D. Mukherjee, Salek Chand, Sangeeta Dhage, S.K. Bahuguna,
S.K. Lahiri, S. Mukhopadhyay and U. Mahapatra
Control Instrumentation Division

and

S. Bhattacharya and G. P. Srivastava
E & I Group

Smt. Shilpi Saha is the recipient of the DAE Scientific & Technical Excellence Award for the year 2010

Abstract

An Instrumented Pipeline Inspection Gauge (IPIG) is used for non-destructive, in-line inspection of buried carbon steel pipelines. It magnetizes pipe wall and detects corrosion and mechanical damages from the leakage flux pattern. Characterization of the defects and sentencing according to the severity is extremely important for organized maintenance of pipelines. This paper addresses the issue of automated analysis of Magnetic Flux Leakage (MFL) data collected by an instrumented pig.

Introduction

Pipelines are economical and environmentally safe mode of transportation of petroleum products over long distances in bulk quantities. These pipelines are buried below the ground surface and are installed for providing service for a period above 50 years. Although protected by right-of-way surveys, cathodic protection surveys, leak detection programs, excavations to look for pipe corrosion or protective coating failures etc. it is mandatory to do inline inspection of the pipelines at a regular interval, by in-line inspection tools popularly known as IPIG, leading to yearly inspection of several kilometers of pipelines. Preventive maintenance based on the inspection report avoids accidental loss of hazardous and costly petroleum products. In this regards the area of inline pipeline diagnostics involving accurate defect detection, identification, measurement and final assessment of pipeline health has become highly important. IOCL approached BARC for the development of various sizes of pipe inspection gauges under Memorandum of Understanding. In the past decade BARC has successfully developed the IPIG for 12", 14", 18" and 24" nominal bore (NB) pipelines [1]. The technology involved multidisciplinary developments in engineering and has matured through a number of field trials in test rigs and actual pipelines and dig site verification thereafter. This demanded not only intense research and development but also hardship of the site activities for the sake of proving the technology in actual field conditions. This paper focuses on the development of in-house data acquisition electronics and analysis software for characterization of metal loss defects from MFL signals.

Technique

A section of pipe is axially magnetized with strong rare earth (NdFeB) permanent magnets. In case of any break in pipe geometry (internal or external) due to metal loss level of leakage flux changes near the wall. The magnetic flux leakage is sensed by two sets of hall sensors. The first set detects both the internal and external defects, whereas, the second set of sensors is used for differentiating them. The measured leakage field depends on the percentage wall loss, axial length, circumferential width, and shape of the defect, as well as on the magnetic properties of the pipe material. As the instrument moves along the pipeline propelled by the product flowing in the pipeline, the hall sensors sense the leakage flux density continuously and the outputs are acquired, digitized and stored in the on-board data acquisition and storage system of the in-line instrument.

The Instrument

The IPIG consists of magnetic module, data acquisition system module (DAS), battery module and pig locator module housed in one or two pressure vessels. The polyurethane cup mounted on IPIG, seals the pipe and oil pressure gives required propelling force for its movement. Front cups are sealing cups and other cups are supporting cups. It also consists of 3 odometers to record actual distance traveled by the instrument inside the pipeline. Imprecise location of defect due to inherent slippage of these odometers can make it necessary to excavate a large length of the pipeline, resulting in much greater repair cost. The pipeline inspection tool achieves the stipulated location accuracy with the help of Inertial Navigation Technology aided by odometer system and DGPS readings of fixed installations like Magnetic Markers. An inclinometer circuit is used to measure the inclination of IPIG to determine the clock position of the defect.

Test rigs

Various test rigs such as static test rig, rotary test rig, dry pull-through rig and wet test loop were planned and built to test the developed components. After several trial runs at these test rigs a good amount of data bank was generated as baseline for defect characterization as well as calibration of sensor systems. These trial runs also enabled several alterations in mechanical components of the instruments to enable the tool to achieve its desired functionalities in the several hundred kilometers of run inside the pipeline. Several configurations of IPIG and CPIG were tested to prove the mechanical negotiability through the wet test loop

Development of Data acquisition system

The data acquisition system started with a single board computer and has now progressed to a multiprocessor low power compact system. The system has evolved through several iterations keeping to meet the prime requirement of very low power consumption in addition to stringent environmental condition and space restrictions. Major specifications of the system are listed below.

- Multiprocessor for high speed data acquisition and online compression
- Control logics implemented in FPGA
- On board storage on flash chips (ICs)
- Flange mounted cards for cleaner interconnections and compact packaging
- Low power consumption for achieving 400km run length

Data analysis technique and in-house software development

MFL data interpretation involves analyzing large volume of data within a limited time-schedule with stipulated accuracy. The task can only be handled with very high level of sophisticated automation, reducing the time for offline assessment of data as well as increasing the reliability of the same. Prior to storage, the data collected by IPIG is processed on-line by thresholding its projection coefficients on a set of wavelet basis (Fig. 1), to retain useful information regarding pipe features and metal loss defects.

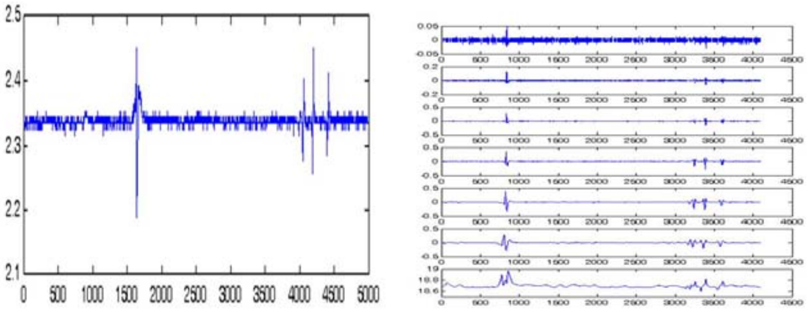

Fig. 1: Raw MFL signal and the signal decomposed in Time Scale

Locating defects and pipe features

The first step of data analysis is to locate magnetic markers placed approximately every one or two kilometers along the pipe. These markers are placed to correct the error in distance measurement due to slippage of odometers. Other pipe features are located with reference to magnetic markers. The distance error due to odometer slippage is compensated at each weld so as to get zero error at each marker and thus absolute weld log distance is found. Nearest weld log distances (preceding and succeeding) are used to locate any other feature placed between them. The log distance of markers is corrected by using INS system along with DGPS and odometer readings. A trial run of this multisensory system was carried out at Wet Test Loop and gave encouraging results. This system is now being incorporated in the instrument for actual pipeline trial.

Characterization or sizing of defects

The compressed MFL data is de-compressed and de-noised off-line using undecimated discrete wavelet transform to form an image of the pipe surface (Fig. 2). Pipe features and defects are detected from the pipe image using image segmentation technique. The analysis software uses signal from radial sensors to extract defect parameters. The radial MFL signal for a defect is bipolar and is characterized by three primary parameters 1) peak to peak span, 2) number of sensors and 3) maximum peak to peak flux density B_{max}. [2]

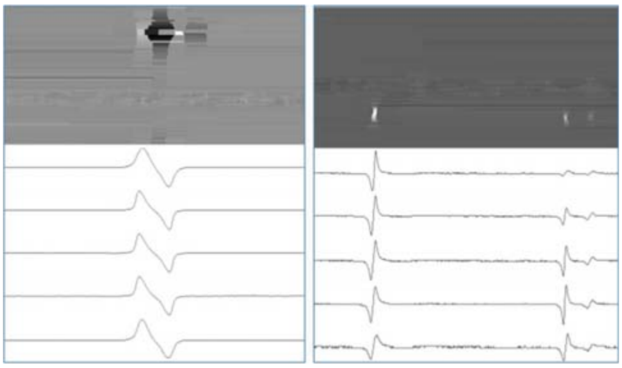

Fig. 2: MFL signatures of magnetic marker and corrosion defects

In addition to these parameters the secondary parameters like shape of the circumferential flux pattern and its spread are also considered. These parameters are then used in the classifier module of software to finally predict the defect feature dimensions namely length, width and depth.

Report generation and presentation

An unsupervised defect characterization algorithm works on the segmented image and automatically generates a

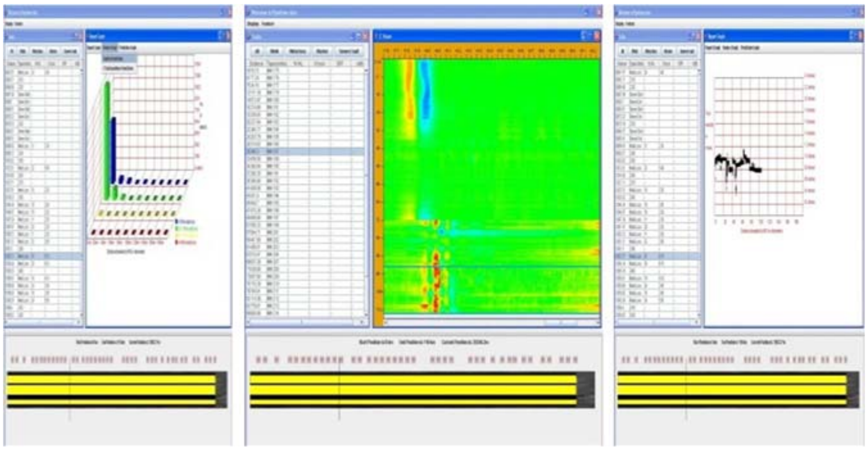

Fig. 3 Data visualization package

report giving details of the size and shape of the defect. This package along with an automatic feature and defect characterization package is used for analysis of large volume of data and generation of report. Finally a table is formed and presented in a data visualization package with associated statistics (Fig. 3) having all detected pipe features with its log distance from nearest magnetic marker. The algorithm to detect features is mostly rule based and is validated by matching with pipe features from a number of field trials and dig-site verifications (Fig. 4) in actual oil pipelines.

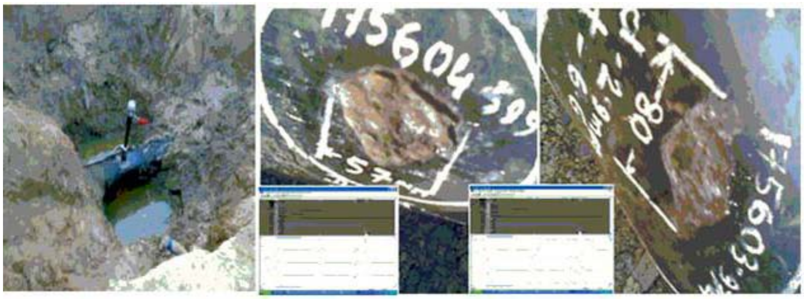

Fig. 4: Actual corrosion defect, its signature and a pilferage point in 14" buried oil pipeline

Conclusion

Major achievement of this work has been successful employment of advanced signal preprocessing techniques for analysis of MFL signal. Defect characterization technique has been validated more than once by dig site inspections based on which corrective measures have been taken for the repair of the pipeline. About 2000 Km length of pipeline section has been already inspected by using 12" IPIG. The 14" tool has taken the three trial runs in Delhi – Panipath section of MJPL pipeline and in addition to the corrosion defects, the runs have revealed illegal tappings from which pilferage of oil was taking place. The diagnosis, confirmed by the dig site verifications has prevented huge loss of revenue.

Acknowledment

The contribution of all team members in the development work of this technology is gratefully acknowledged.

References

1. Mukhopadhyay S, Srivastava G P, Characterization of metal loss defects from magnetic flux leakage signals with discrete wavelet transform, *NDT&E International,* 2000, vol. 33, pp. 57-65.
2. Saha S, Mukhopadhyay S, Mahapatra U, Bhattacharya S, Srivastava G P, Empirical structure for characterizing metal loss defects from radial magnetic flux leakage signal, *NDT&E International,* 2010, vol. 43(6) pp. 507-512

DEVELOPMENT OF TOOLS FOR LIFE MANAGEMENT OF VARIOUS REACTOR COMPONENTS

Kundan Kumar and J.N. Kayal
Reactor Engineering Division

Shri Kundan Kumar is the recipient of the DAE Scientific & Technical Excellence Award for the year 2010

Abstract

Reactor components are subjected to harsh operating conditions, due to which their ageing is very fast. The ageing needs to be monitored in timely manner for incident-free operating life of the component in particular and the reactor as a whole. The ageing is due to degradation mechanisms, which need to be identified and addressed. Methodologies and techniques have been developed for assessment of ageing their disposition. Reactor Engineering Division (RED) has been associated with ageing management of many reactor components since long. Techniques have been developed for life assessment & life extension of Coolant Channel of 220MWe PHWRs, life assessment of Core Shroud of Boiling Water Reactors at TAPS-1 &2 and improvement of thermal efficiency of heat exchangers of Indian PHWRs. The techniques developed include Integrated Garter Spring Repositioning System, Sliver Sample Scraping Tool, Boat Sampling Technique and Sludge Lancing Equipment. This paper is limited to the brief description of development of these techniques, related tool heads and their application at various reactor sites.

Introduction

The life management techniques namely Integrated Garter Spring Repositioning System (INGRES) and Sliver Sample Scraping Tool have been developed for assessment of integrity of Coolant Channels of Indian PHWRs. INGRES, Fig. 1, was developed for the rehabilitation of coolant channels of original core of MAPS-1 & 2 and RAPS-2 reactors, which were having problems of reducing the creep contact time due to shifting of the loose-fit garter springs spacers. INGRES was deployed in these reactors for extending their creep contact time by way of repositioning the Garter Springs, in a remotely manner, to an optimised location in order to increase the operating life of the coolant channels. Sliver Sample Scraping Technique (SSST) was developed considering the hydrogen pick-up tendency of Zr-2 and Zr-2.5%Nb pressure tubes, causing reduction in fracture toughness value and problem of delayed hydride cracking. By SSST, sliver samples of 90-120mg are obtained from the bore of the pressure tube and are analysed for the hydrogen/deuterium value. Various need-based versions of scraping tools have been developed, which include, SSST-1, SSST-2 (both for operation in water-drained coolant channels), Wet Scraping Tool (WEST), Multi-head scraping tool and Circumferential Scraping Tools. All tools, except last one is used for obtaining samples in axial direction, whereas the last one is used for obtaining samples in circumferential direction.

Apart from life management tools for coolant channels, the Boat Sampling Technique (BST) was developed for obtaining boat shaped samples from the core shroud of TAPS-1&2 BWRs, in order to insure its integrity. Sludge Lancing Equipment (SLE) was developed for improving the thermal efficiency of the steam generator by way of removal of sludge from secondary side of the mushroom type steam generator of Indian PHWRs. The following paragraphs describe these techniques, the tooling developed and their application in actual reactor site.

Fig. 1: INGRES Tool Head

Sliver Sample Scraping Technique

Sliver Sample Scraping Technique, Fig. 2, was developed for obtaining statistically significant number of samples without damaging the integrity of the tube, *in situ*, i.e. without removing it from the service. The sliver sample, having weight 90-120 mg and thickness about 100 microns are obtained by this technique. The sampling is done in two tandem steps, with the help of two tool bits, one followed by another. Front tool-bit removes the outer surface of the bore of the tube, which may contain oxide layer or foreign particles, while rear tool-bit obtains actual metal sample from the underneath, by following the same path.

Wet Scraping Tool (WEST)

The latest version of Scarping Tool, WEST, operates with the help of fuelling machine for obtaining samples from six different axial locations within the bore of the pressure tube. Special provisions in the tool make it suitable for operation in shut-down flow of the reactor. SSST, since inception, have been used at various reactor sites and have obtained sliver samples from a large numbers of pressure tubes of 220MWe PHWRs.

Multi-head Scraping Tool

The WEST tool requires as many visits to the channel as the number of sliver locations. Generally, four to six locations, along the channel length, are required to be scraped for determination of peak location. This requires four to six visits of the scraping tool to the channel resulting in higher time consumption as well as repetition of procedure. In order to minimize the time and procedural steps, a new scraping tool, namely Multi-head Scraping Tool has been developed. Using the new tool, scraping operation can be conducted at four different locations inside the coolant channel in a single visit to the channel. These samples can be easily identified and collected after the tool is taken out from the coolant channel. The tool is operable under water and with the help of a new system, called Tool Delivery System (TDS), being developed by RED.

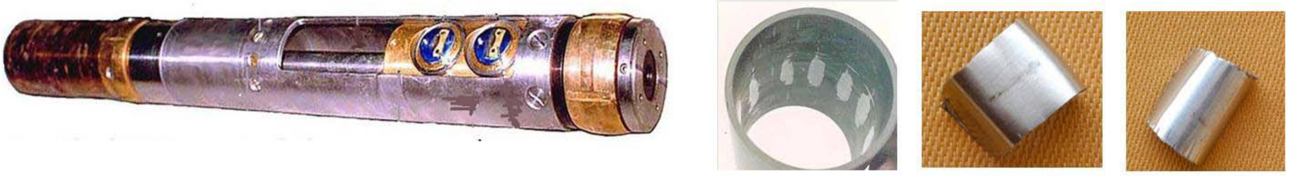

Fig. 2: Wet Scraping Tool (WEST) and sliver samples

Fig. 3: Multi-head Scraping Tool

Circumferential Scraping Tool for Pressure Tubes

The Zr-2.5%Nb alloy material of pressure tubes of PHWRs exhibit considerably high hydrogen concentration near rolled-joint regions with steep variation in comparison to central region, Fig. 4,. The steep variation in the concentration of hydrogen near the rolled joint regions needs to be verified by way of sampling at close intervals. To fulfill the requirement, circumferential scraping tool, Fig. 5, has been developed for 220MWe PHWRs. The typical dimension of metal sample is 110 mm long and 6 -8 mm wide. The tool is operable in water filled condition of the coolant channel. Two versions of tool have been developed, one which can be operated with the help of Fuelling Machine and the other with the help of TDS.

Circumferential scraping Tool pressure Tubes for 540MWe

Circumferential scraping Tool, Fig. 6, has also been developed for 540MWe Pressure tubes which can be operated through Advance drive machine (under development).

Vertical Scraping Tool for CIRUS PWL

Scraping tool for operation in vertical coolant channels, such as AHWR coolant channel, was developed and technique was demonstrated. For the purpose a scraping tool for existing vertical coolant channel of Pressurized Water Loop (PWL) in CIRUS reactor was developed for 57mm ID. The tool, Fig. 7, was successfully deployed in the dummy PWL pressure tube at Hall No.-3 and technology was demonstrated by obtaining in-situ sliver samples, Fig. 8, from four different axial and circumferential locations within the bore of the tube.

Boat Sampling Technique

Boat Sampling Technique (BST) was developed for obtaining metal samples from the HAZ of H4A weld of the core shroud for assessing the integrity of Core shrouds of BWR at Tarapur Atomic Power Station (TAPS) as these reactors belong to the early class of Boiling Water Reactors, having AISI-304 as core shroud material. BST is remotely operable and is non-destructive sampling technique, as sampling operation does not lead to loss of integrity or reduction in residual service life of the core shroud.

The contour of the scooped region merges smoothly with the surface profile of the base material. A typical sample is removed in about three hours.

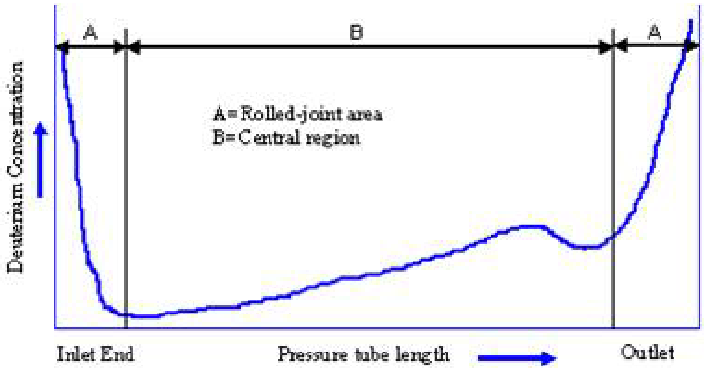

Fig. 4: Typical Profile of Deuterium Concentration along the Length of Zr-2.5%Nb Pressure Tube

Fig. 5 : Circumferential Scraping Tool for 220MWe PHWRs

Oxide Sample

Metal Sample

Fig. 6: Circumferential Scraping Tool for 540MWe PHWRs

Scraped tube

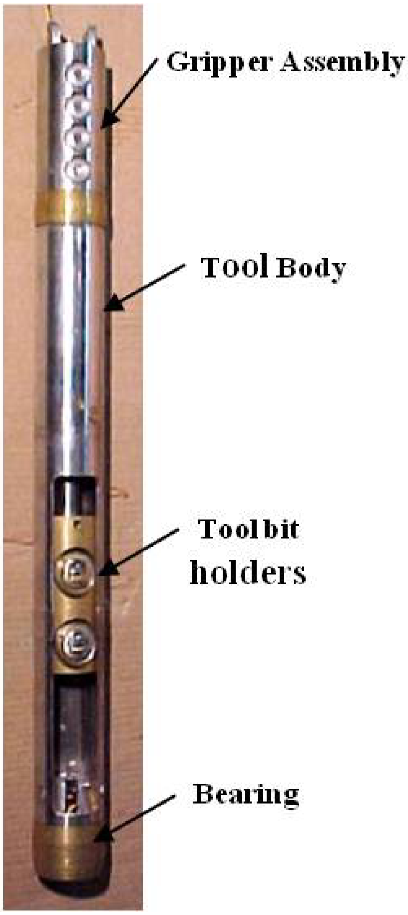

Fig. 7: Vertical Scraping Tool

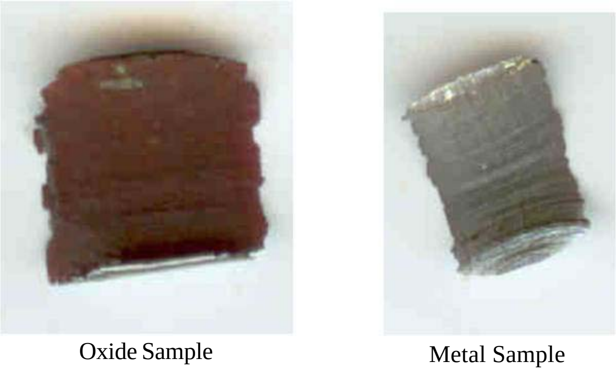

Fig. 8 : Sliver Samples obtained from dummy

The sampling is a scooping process, which is done with the help of a specially developed device, known as Sampling Module, developed at RED. For operation of the Sampling Module at TAPS a handling manipulator has been developed by DRHR.

Fig. 9: Mock-up Sampling Trial at TAPS

Fig. 10: Scooped Region

Fig. 11: Boat Sample

Development of Miniature Specimen Testing Technology

The samples, obtained through the sampling technique mentioned above, are further used for preparing miniature test specimen. The samples can be precisely waferred and machined for obtaining a number of test specimen of various types. One schematic layout of miniature test specimens is shown in Fig. 12. Provision should be there for cutting allowances and cutting sequence to be followed for preparing the test specimens. Fig. 13 show photographs of some of the miniature test specimens of SS 304 material, prepared from the sample.

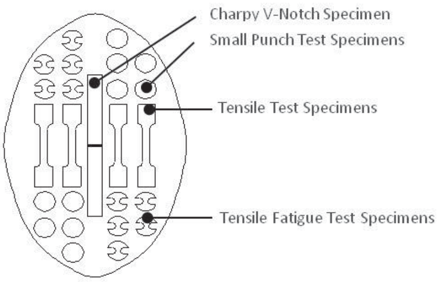

Fig. 12: Layout of miniature specimens within a Boat Sample

Fig. 13 : Photographs of Miniature Specimens

Development of Jet Manipulator & Remote Visual Inspection System for Sludge Lancing Equipment

The steam generators (SG) of recent Indian Pressurised Heavy water Reactors, are compact mushroom shaped with inverted vertical U-tubes housed in a single vertical cylinder shell heat exchanger with integral feed water pre-heater. The U-tubes are made of Incoloy-800 and having 16mm OD and 1mm wall thickness. The tube bundle consists of 1834 such U-tubes. Due to prolong operating years, the steam generator may face sludge accumulation in secondary side of the SG, which may lead to loss of thermal efficiency and corrosion etc. In order to minimize such effects, sludge should be removed for safe and enhanced operating life of the steam generators. A sludge lancing system has been developed for sludge removal from the secondary side of the steam generators. Jet Manipulator and Remote Visual Inspection Systems have been developed to enter into the no-tube lane of the steam generator and carry out the sludge lancing operation.

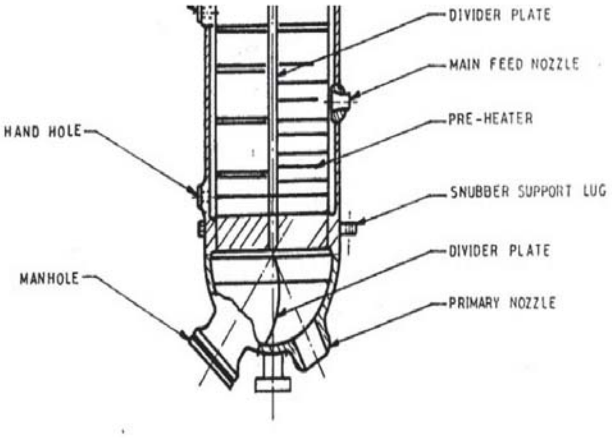

Fig. 14: Partial view of Steam Generator

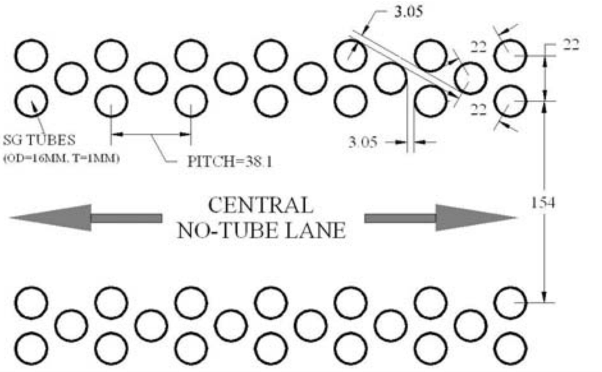

Fig. 15: SG Tube Layout

Jet Manipulator

The mechanical assembly of jet manipulator (JM), Fig. 17, consists of three modules, namely walker, elevator and nozzle head. The Nozzle head has four nozzles on each side of the nozzle head oriented at various angles such as 30°, 90° and 150° directed towards the narrow no–tube lanes. All three modules of JM are assembled in-situ after insertion of the entire modules one-by-one through the hand hole. The jet manipulator moves in

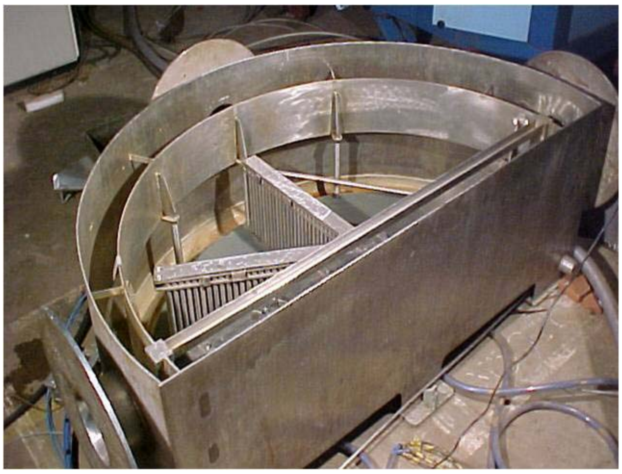

Fig. 16: SG Mock-up

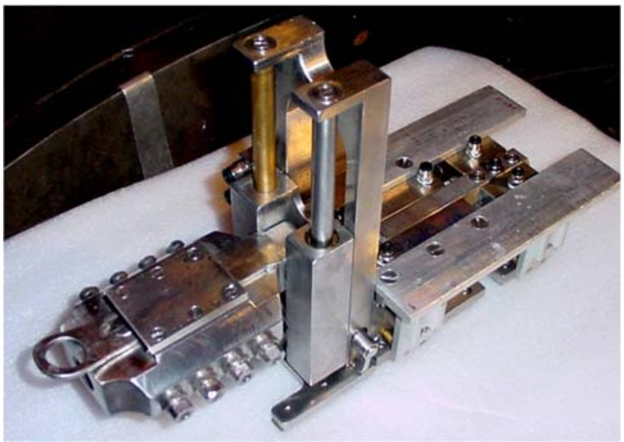

Fig. 17: Jet Manipulator

forward or backward direction along the central no-tube lane of steam generator. The nozzle head directs the multiple water jets along the narrow inter tube gap having 3 mm width, Fig. 15, on both sides of the central no-tube lane, to dislodge the sludge and deposits from the tube sheet of the secondary side of steam generator. The nozzle head can be set to move at different elevations such that the multiple jets will graze along the narrow tube lane to create the sludge lancing action.

Remote Visual Inspection System (RVIS)

Remote Visual Inspection System (RVIS) has been developed for carrying out inspection inside the SG before and after the sludge lancing operation. The system is used to obtain information about the condition of tube sheet and tubes before and after lancing. This information provides handful tool to take operation decision to carry out lancing, to increase lancing time etc. The RVIS consists of four different modules, namely Camera Housing, Pan & Tilt unit, Lighting Assembly and Walker. Apart from these, there is separate control panel to operate RVIS and to view images. All three modules are assembled in-situ on the steam generator tube sheet after insertion of the entire modules one-by-one through the hand hole.

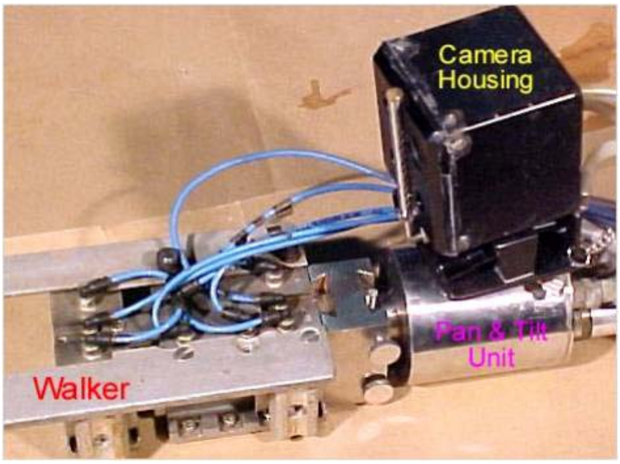

Fig. 18: RVIS Assembly

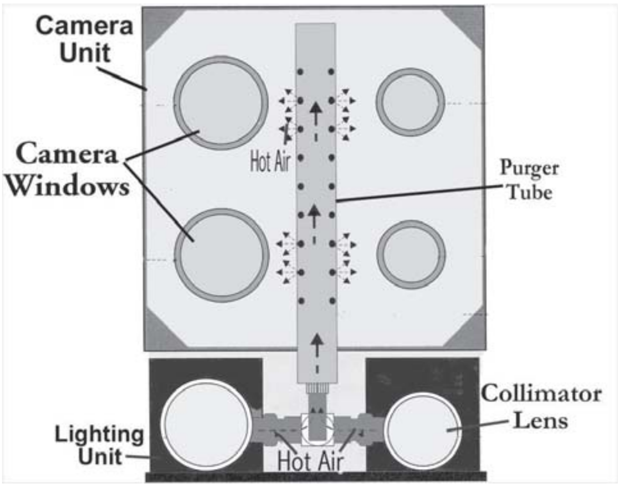

Fig. 19: Camera Housing with Lighting Unit

Deployment of JM and RVIS at KAPS

Jet Manipulator and Remote Visual Inspection System were successfully deployed in the steam generators 1 to 4 in KAPS-1 during September-October, 2009 and sludge was removed.

Conclusion

The technologies developed for the life management of various components of PHWRs and BWRs have been need based developments and their usefulness has been proven by their successful deployment at various reactor sites. These technologies have not only extended the service life of the critical components of the reactor but at the same time have set a milestone in the Indian nuclear power programme by way of completing 40 years of almost incident free operation of power reactors.

Acknowledgement

Authors are grateful to Dr. R.K. Sinha, Chairman, AEC for continuous guidance and encouragement provided by him during the development of the techniques for life management of Coolant Channels and other reactor components. We are also thankful to our colleagues in RCCS, RED who have been part of the development of these techniques and their deployment at various reactor sites. We are also thankful to our colleagues in CDM, RTD and DRHR for their support for site deployment of these techniques. We are also grateful to NPCIL officials at Mumbai headquarter, specially Shri S. Vijayakumar and Shri A.K. Sinha and officials at various reactor sites for their support in implementation of these life management techniques at various reactor sites.

References

1. BARC Internal Report No. BARC/I/2000/005 titled "Development of Sliver Sample Scraping Technique for Pressure Tubes of Indian Pressurised Heavy Water Reactors" by Kundan Kumar and B.B. Rupani, RCCS, RED, BARC
2. BARC Internal Report No. BARC/I/2004/009 titled "Evolution of Scraping Tools for Coolant Channels of 220 MWe Indian PHWRs" by Kundan Kumar; Nirupam Das; B.B. Rupani
3. Internal Report BARC-2002-I-013 titled "Development of Boat Sampling Technique" by Kundan Kumar, T.V. Shyam, B.S.V.G. Sharma, J.N. Kayal, B.B. Rupani
4. BARC Internal Report No. BARC/I/2006/006 titled "Development of Jet Manipulator and Remote Visual Inspection System for lancing of Mushroom type Steam Generators" by Kundan Kumar, D.K. Nathani, J. Aparna, J.N. Kayal and B.B. Rupani

EVOLUTION OF DYNAMICS IN SDS SURFACTANT IN SOLID PHASE AND MICELLES

S. Mitra, V.K. Sharma and R. Mukhopadhyay
Solid State Physics Division

Dr. S. Mitra is the recipient of the DAE Scientific & Technical Excellence Award for the year 2010

Sodium dodecyl sulphate (SDS), $C_{12}H_{25}OSO_3^- Na^+$, is a common surfactant used extensively in a number of applications such as cleaning agents, removal of oily stains and residues, engine degreasers, etc [1]. Amphiphilic molecules such as SDS exhibit a rich variety of phases in aqueous solution. Micelles are important to a number of physical and technological processes such as in detergents, pharmaceutical formulations, biomedical applications, materials synthesis, and phase transfer catalysis, amongst others. It is important to understand the specific macroscopic properties of these systems that are of direct consequence of the behaviour at the molecular level. This includes the rate of release of solubilised drugs and other molecules from micelles, micellar breaking time, etc. Hence, it is of great interest to obtain a detailed description into the molecular dynamics in such systems which can be best probed by Quasi-elastic Neutron Scattering (QENS) technique [2-6]. In a quasielastic neutron scattering experiment, the measured intensity is proportional to the double differential scattering cross-section, representing the probability that a neutron is scattered with energy change $\hbar\omega$ into the solid angle $d\Omega$, which in turn is proportinal to the scattering law $S(Q,\omega)$, Q being the the wave-vector transfer. In general, the scattering law can be written as a combination of elastic and quasielastic components. The variation of quasielastic width provides information about the time scale of the motion and the fraction of elastic component in the total spectra, also known as Elastic Incoherent Structure Factor (EISF), gives information about the geometry of the motion. QENS technique in particular offers a unique possibility of analyzing spatial dimensions of atomic or molecular processes in their development over time. For a hydrogenous sample, scattering cross section of H atom is much greater than the scattering cross section of any other atom. So contribution of others species present in the system is almost negligible and can be neglected.

Dynamics of sodium dodecyl sulfate (SDS) in powder as well as in micellar form are studied using Quasi-elastic Neutron Scattering technique. In case of micellar solution, contribution from D_2O, was subtracted after measuring the QENS spectra from pure D_2O. Measurements were carried out at different temperatures to delineate the microscopic understanding of the dynamics in details.

Micelles in solution have the freedom to undergo a variety of motions including whole body diffusion known as global diffusion and internal motions within the micelle corresponding to the dynamics of the individual monomers. It is these two dynamical processes which are expected to contribute within the time scales of the neutron scattering technique (10^{-9} - 10^{-12} sec). Considering the existence of these processes, the generalized scattering law for micelles can be written as

$$S_{micelles}(Q,\omega)=e^{-Q^2\langle u^2\rangle}\left[A(Q)L_G(\Gamma_G,\omega)+(1-A(Q))L_{in}(\Gamma_{in}+\Gamma_G,\omega)\right] \quad (1)$$

Here, the Lorentzian, $L_G(\Gamma_G,\omega)$ corresponds to the global motion of the whole micelle and the Lorentzian, $L_{in}(\Gamma_{in}+\Gamma_G,\omega)$ represents the combination of global micellar motion and internal motions of the micelle. A(Q) is nothing but the EISF which can provide information about the geometry of the internal motion of the micelles. QENS spectra for the micelles are fitted with the generalised scattering law defined in Eq. 1. To gain more insight into the nature of the two dynamical processes, the parameters such as HWHM of the Lorentzian and A(Q) were analysed as a function of temperature and Q. The variation of the HWHM, Γ_G, of the 1st Lorentzian, with Q^2 at different temperatures, is shown in Fig. 1, which we assign to the global dynamics of the micelles. The result can be described by a simple Brownian motion following Ficks law, $\Gamma_G = D_G Q^2$. Here D_G is the global diffusion coefficient. Obtained global diffusivity for SDS micelles is found to vary from 2.5×10^{-6} cm²/s at 300 K to 3.1×10^{-6} cm²/s at 330 K [4].

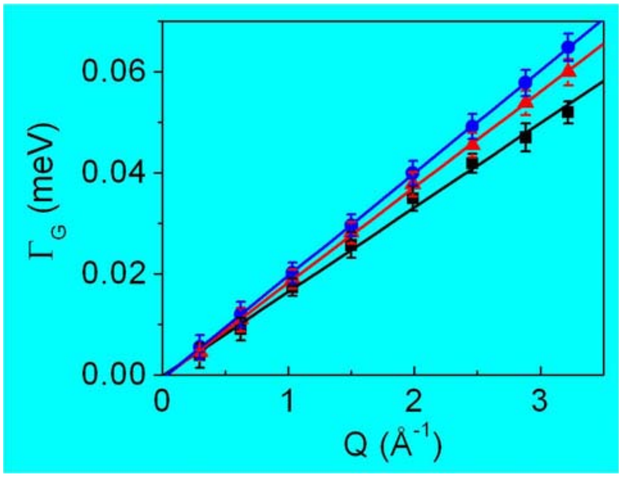

Fig. 1: Variation of HWHM of the Lorentzian representing global motion, Γ_G with Q^2 at temperatures of 300K, 315K and 330 K. The lines correspond to a fit with Fick's diffusion

The Q-dependence of the EISF at different temperatures is shown in Fig. 2. To get the information about the geometry of the motion, it is essential to model the dynamics and compare that with that obtained from the experiment. Considering various factors like, conformational changes of the monomer chains, bending and stretching of the chemical bonds etc., our proposed model considers that the hydrogen atoms in each CH_2 unit undergo localised translational diffusion motion inside a small spherical volume. This volume increases linearly as a function of CH_2 position along the length of the chain, with the hydrogen atoms closer to the head group moving within smaller spheres and with lower diffusion constants, than the hydrogen atoms away from the head group. A sketch to demonstrate the proposed model is shown in Fig. 3a where the CH_2 units in the monomer are shown to diffuse within a spherical volume of different sizes, which increases linearly from the head towards tail. Solid lines in Fig. 2 shows the fit with the proposed model. The fact that fits are found to be reasonably good at all temperatures confirms that the proposed model is an appropriate description of the internal dynamics of the SDS monomers in the micelles. Minimum radius of the sphere (R_{min}) corresponding to CH_2 units close to the head group and the maximum radius of the sphere (R_{max}) corresponding to terminal CH_3 groups are obtained from the fit. At 300K the localized motions of hydrogen atoms along the SDS chain are restricted to spheres of radii between 0.4 Å to

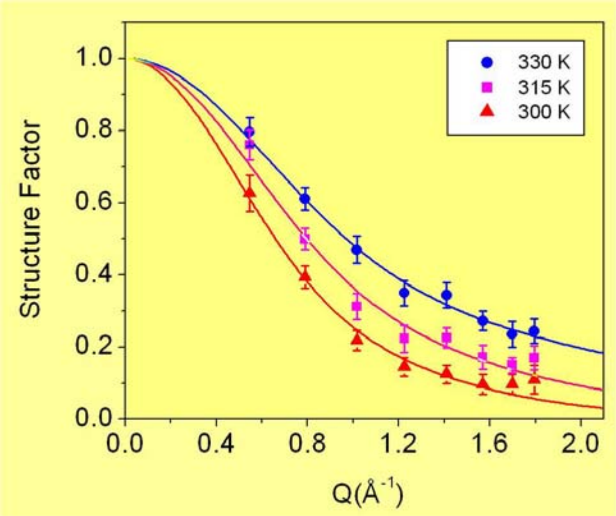

Fig. 2: Variation with Q of the EISF for the 20% (w/w) SDS micellar solution. The solid lines represent calculated values using the model described in the text

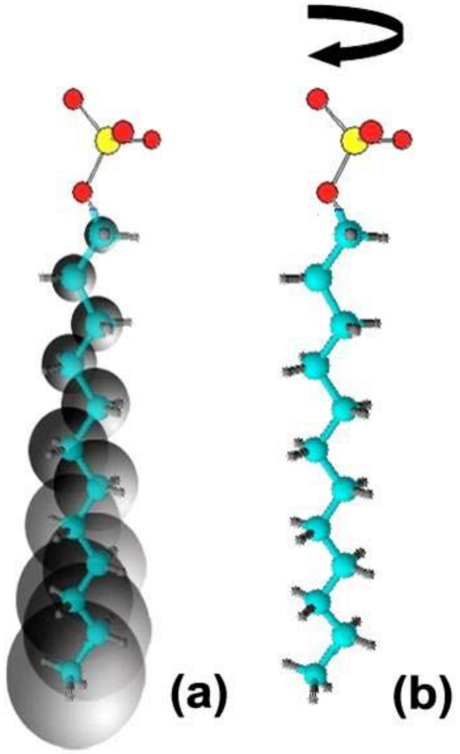

Fig. 3: Schematic of the proposed model for the chain dynamics in (a) SDS micelles and in the melt state of anhydrous SDS powder (T > 360 K) (b) SDS powder below transition (T < 360 K).

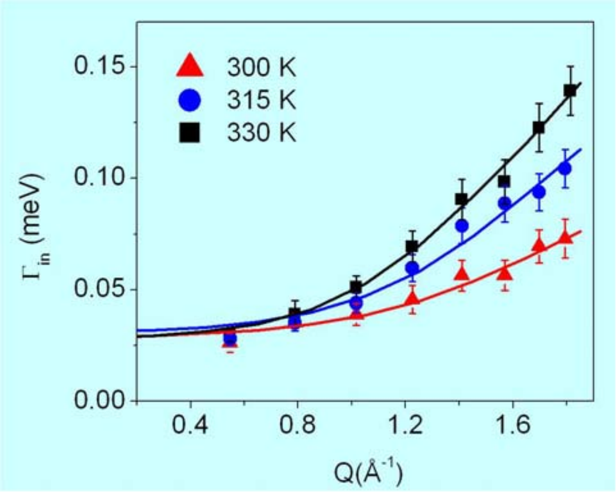

Fig. 4: Variation with Q of the HWHM of the Lorentzian representing the internal motion, for the 20% (*w*/*w*) SDS micellar solution. The solid lines are fits with a model in which the hydrogen atoms at the different CH_2 positions along the of SDS chain are moving within spheres of varying radii and with varying diffusion coefficients.

3.4 Å, and increase to 1.2 Å and 4.4 Å at 330K. The behaviour of HWHM corresponding to internal motion as a function of *Q* at different temperatures is shown in Fig. 4. Solid lines are the fit with our proposed model. Minimum diffusivity (D_{min}) corresponding to CH_2 units close to the head group and the maximum diffusivity (D_{max}) corresponding to terminal CH_3 groups are obtained from the fit. D_{min} and D_{max} are found to be 0.1×10^{-5} cm^2/sec and 1.5×10^{-5} cm^2/sec at 300 K respectively [4].

After describing the microscopic dynamics of the SDS micelles with a suitable model, it is also interesting to understand the dynamics of SDS in crystalline solid phase. Elastic scans probe the mobility in samples by determining the amount of elastic scattering as a function of temperature within the resolution of the spectrometer used [5]. Elastic scan was performed in the temperature range 175 - 400 K on solid SDS and shown in Fig. 5. Important features observed are, the monotonic decrease of elastic intensity (almost linearly) with increase in temperature up to 360 K, and a step decrement in intensity is observed at 360 K indicating presence of a dynamical transition.

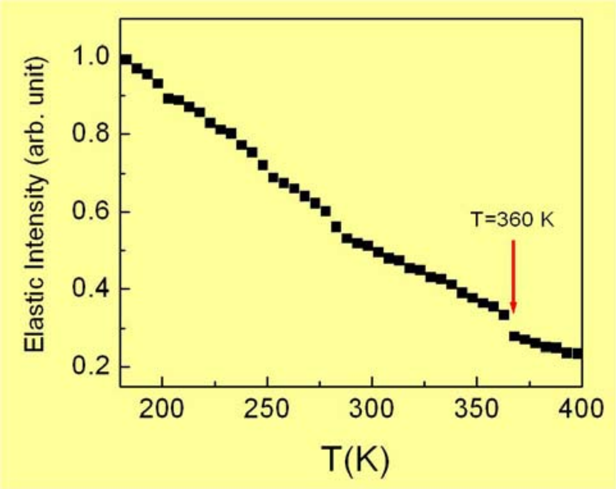

Fig. 5: Temperature dependence of elastic intensity (normalised to T=178 K) for, average over Q = 0.45 to 1.84 Å^{-1}. A melting transition is evident at T=360 K

Since the QENS spectra from solid SDS showed significant quasielastic (QE) broadening over the resolution function of the instrument at 210 K and above, QENS spectra are analysed in detail. It is found that SDS molecules undergo fractional dynamics following uniaxial rotation model (as shown in Fig. 3b) in the temperature range 210-350 K. The fraction of SDS molecules taking part in the dynamics is found to increase linearly with temperature. Rotational diffusion coefficient also found to increase with temperature and follows the Arrhenius behaviour. An activation energy of 0.9 (± 0.2) kcal/mol is obtained from the Arrhenius plot of D_r in the temperature range of 210 – 350 K. A dynamical transition takes place at 360 K as seen in the elastic scan is also seen in QENS spectra. Observed dynamical transition can be understood in conjunction with Raman spectroscopy and XRD studies on SDS powder where a structural transition is seen around 360 K. This transition is accompanied with an increase in molecular area by 20%. Therefore, at high temperature, there exists more space for the chains and therefore the molecules have more freedom to rotate which leads to more disorder. Therefore, phenomena such as bending, stretching modes of chemical bonds, large amplitude oscillations, reorientation of SDS chain etc. would take place. Due to all these various motions, the hydrogen atoms of each CH_2 unit are expected to undergo diffusion but limited within a small volume of space as the crystal structure still remains intact. Both the width of the quasielastic part (shown in Fig. 6) and the EISF at T > 360 K have been successfully described by localized translational diffusion model.

It is interesting to compare the SDS chain dynamics observed in both solid and micellar phases. At room temperature, in case of solid phase, chains are found to

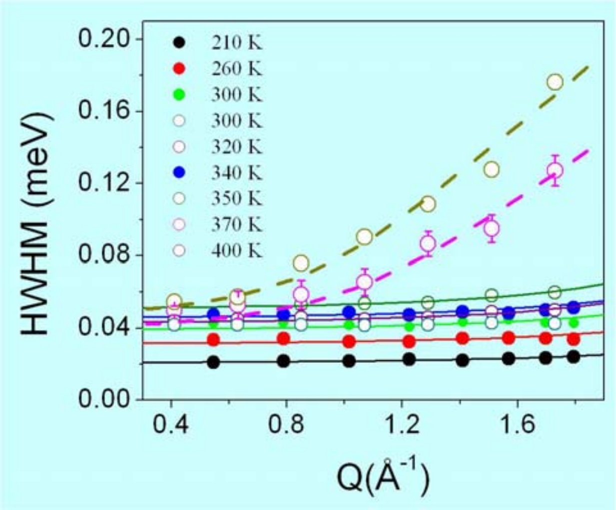

Fig. 6: Variation of HWHM of a Lorentzian representing internal motion SDS powder with Q. Solid and empty circles represent data obtained with IRIS and FOCUS spectrometer respectively. Solid lines are the fits with a fractional uniaxial rotational model. Dashed lines are the fit with a model based on localised translational diffusion (see text).

undergo fractional uniaxial rotational diffusion, however in micellar phase, localised translational diffusion describes the chain dynamics. It is therefore worthy to note that dynamics of SDS chain in anhydrous powder at chain melt state (> 360 K) is more or less similar to that in the micellar phase. This gives us a valuable insight in understanding the evolution of chain dynamics from dry SDS powder to micellar solution.

Acknowledgement

Fruitful discussion with Dr. P.A. Hassan is gratefully acknowledged.

References

1. J. C. T. Kwak, *Polymer-Surfctant Systems*, Marcel Dekkar: New York 1998.
2. S. Mitra, V. K. Sharma, V. Garcia Sakai, J. Peter Embs and R. Mukhopadhyay, *J. Phys. Chem B*, **115** (2011) 9732.
3. V. K. Sharma , S. Mitra ,V. Garcia Sakai , P. A. Hassan, J. Peter Embs and R. Mukhopadhyay , *Soft Matter*, **8**, (2012) 7151
4. V. K. Sharma, S. Mitra, G. Verma, P. A. Hassan, V. Garcia Sakai, and R. Mukhopadhyay, *J. Phys. Chem. B* **114** (2010) 17049
5. V. K. Sharma, S. Mitra, V. Garcia Sakai and R. Mukhopadhyay, *J. Phys. Chem* B, 116 (2012) 9007.
6. V. K. Sharma, Gunjan Verma, S. Gautam, P. A. Hassan, S. Mitra and R. Mukhopadhyay *Z. Phys. Chem*., 2010, **224**, 253-261

FLEXIBLE CONDUCTING POLYMER NANOCOMPOSITES FOR TOXIC VAPOUR SENSING

Y.K. Bhardwaj, K.A. Dubey and L. Varshney
Radiation Technology Development Division

Dr. Y.K. Bhardwaj is the recipient of the DAE Scientific & Technical Excellence Award for the year 2010

Abstract

Incorporation of conducting fillers in insulating polymer matrices is an effective strategy to synthesize chemi-resistive vapor sensing arrays for rapid detection of hazardous volatile organic compounds (VOCs) and gases. However, synthesis of such conducting polymer composites warrants trade off between conductivity, flexibility and sensitivity towards VOCs. This paper describes synthesis of novel polymer nanocomposites having high conductivity, good mechanical properties, easy processability and fast sensing response by selective percolation of conducting component in different multiphase polymer alloys. The composites were prepared by melt compounding of conducting carbon black (CCB) and different polymers such as nylon, ethylene vinyl acetate (EVA), low density polyethylene (LDPE), polypropylene (PP), and ethylene propylene diene monomer (EPDM). Multiple walled carbon nanotubes (MWNTs) and organoclays were used to modify conductivity and sensing behaviour. With proper morphology and composition optimization, different VOC sensing matrices were developed for almost entire spectrum of toxic VOCs from non-polar benzene to highly polar formic acid.

Introduction

Blending of two or more components offers an economically viable and versatile way to produce new engineering materials with the desired properties from the parent components [1,2]. Selective percolation of a conducting filler in an insulating polymer/polymer blend matrix is an effective strategy to develop conducting formulations for several advanced applications such as EMI shielding, over current protection devices, self regulating devices, piezoelectric devices, phase transfer catalysis material and gas sensors [3-5]. Commonly used fillers are carbon black, carbon nanotubes, carbon fibers, graphite, conducting polymers, conducting ceramics and metallic micro and nanoparticles. The conductivity of such composites depends on characteristics of fillers such as length, diameter, volume fraction, homogeneity of dispersion; on molecular weight , crystallinity and geometry of polymer; processing method and conditions and finally on final morphology.

Aromatic hydrocarbons such as benzene, toluene, ethylbenzene, xylene (BTEX) are widely used as solvents and are released from exhaust of motor vehicles and industries. They have low flash point, produce CO and CO_2 on burning, are highly carcinogenic and can be a serious health hazard at concentration <0.1%. Acetone, chloroform, formaldehyde and isopropyl alcohol are among major polar VOCs that pose serious health hazard. The ability to monitor and identify small quantities of these VOCs has therefore become a prime requirement to counter the hazards and sensors for the detection of organic vapors are required in several industrial and environmental applications [6-8].

This paper reports our recent findings on the synthesis of multiphase conducting polymer nanocomposites for the detection of toxic VOCs. EPDM has been used as a matrix for developing non-polar VOC sensors; whereas nylon has been used as a matrix for sensing polar VOCs. Sensing matrices having multiple non-conducting and conducting synergistic fillers have also been developed to improve the electrical conductivity and to fine tune the sensing response.

Materials and methods

A series of nanocomposites were prepared by mixing the components homogeneously in Brabender plasticordar at 30 rpm for 20 minutes. The homogeneous mix was compressed into sheets of size 10x10 cm of different thicknesses in range 0.1-1 mm using compression-molding machine at 150 kg/cm^2 pressure for 5 minutes. The vapor sensing studies were carried out in self designed glass gas chamber of capacity ~2 L equipped with heating arrangement and fan assembly for instantaneous dispersal of toxic vapors inside the chamber. To sense vapors the resistance of the composite was measured through a computerized logging arrangement.

Results and discussion

Electrical properties and phase continuity

Achievement of high conductivity and fast sensing response are the prime requirements for developing smart sensing devices. Efforts were therefore made to impart high electrical conductivity at the lowest possible loading of the conducting phase and to incorporate a phase that responds substantially to the external stimuli (VOCs). Nylon and EPDM phases were used to target polar and non polar stimuli respectively, and selective percolation as well as synergistic interactions between fillers were used to induce high selectivity and sensitivity.

Fig. 1(a) represents the variation in the conductivity with the variation of EVA/nylon blend for the 10 wt%, 25 wt% and 30 wt% carbon black loading. The conductivity of the blends with 30 wt% CCB loading was higher than that of 25 wt% loading at all compositions; however the difference was not as high as was observed between 10 wt% and 25 wt% loading. This observation suggests that the selective localization of CCB in incompatible blends, strongly depends on the blend composition and percolation can be achieved at low CCB loading by carefully architecting the blend morphology. Fig. 1 (b) represents change in the conductivity with increase in the MWNT content, in EPDM/CCB/organoclay nanocomposites, such an increase in the conductivity was attributed to the synergistic interactions among fillers (CCB/organoclay/MWNT).

To get the best mix of conductivity and sensitivity, different type of polymer nanocomposites were prepared. The conductivity increased for different nanocomposites with increase in CCB fraction (figure 2 a&b). It can be seen from the profile that the percolation threshold for EPDM was much higher than that observed for LDPE or PP and followed the trend EPDM/CCB >LDPE/CCB >LDPE/PP/EPDM/CCB >PP/CCB. It was therefore expected that with increase in EPDM volume fraction the conductivity of the matrix would decrease. On the other hand, the conductivity of EVA/nylon 50:50 blend/CCB composites showed three peculiar features (1) the conductivity is much higher for the blend/CCB than for the individual blend constituents (2) the blend shows two step percolation behavior, a phenomenon of high importance for

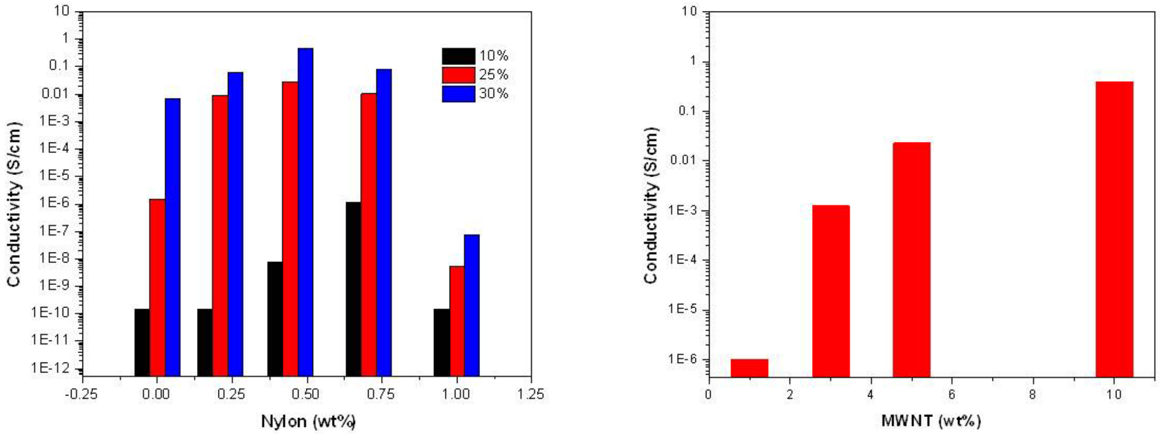

Fig.1: Variation in the DC conductivity for different systems (a) in EVA/Nylon with CCB content (b) in EPDM/CCB/organoclay with MWNT content

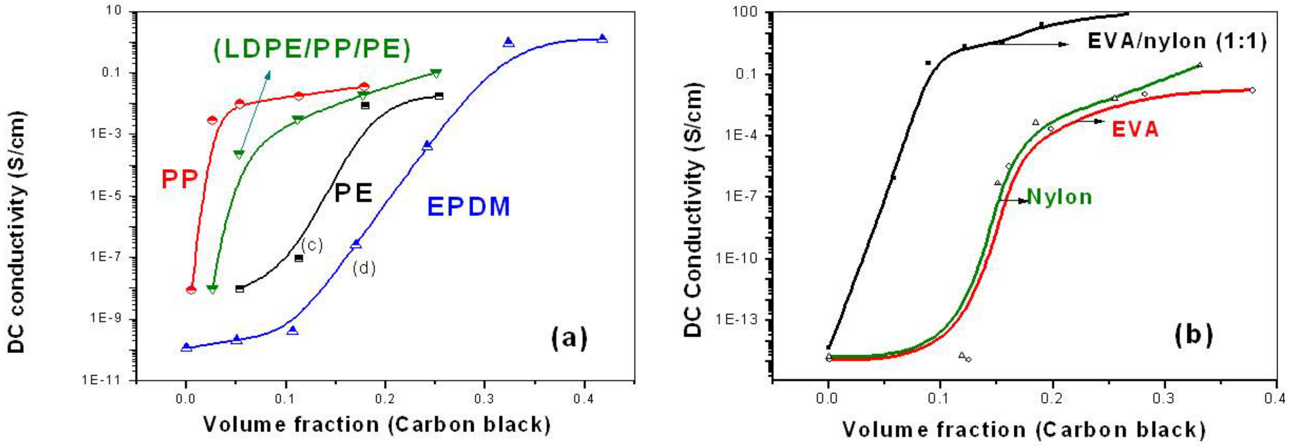

Fig. 2: Variation in the DC conductivity with CCB volume fraction for different composites (a) LDPE/PP/EPDM/CCB composites (b) nylon/EVA/CCB composites

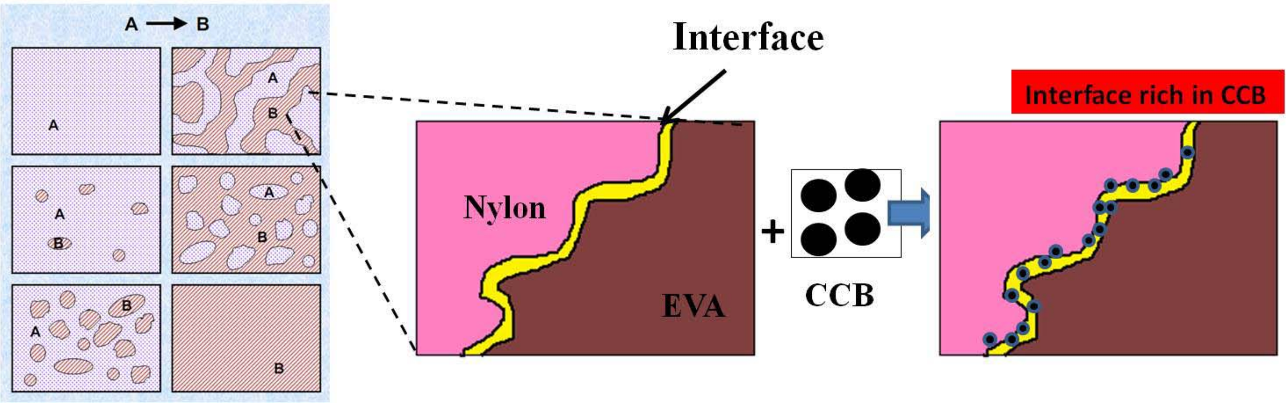

Scheme 1: Selective percolation in multiphase polymer alloys

fabrication of electrical devices (3) the transition in the first step is much more prominent than the second step transition

Similar discontinuity was inferred from the mechanical properties, hardness and melt viscosity of the composites. High conductivity of nylon/EVA/CCB composites was also attributed to the selective percolation, in interfacial region (Scheme 1).

VOCs sensing response

Fig. 3 shows the electrical response i.e. relative change in the resistance (R/R_o) of different composites. The conducting polymer assembly was subjected to a cycle of VOC vapor absorption (purging) and desorption (evacuation) to analyze the sensitivity and reproducibility of the electrode. After a five minute exposure to a fixed concentration of VOCs, the sensor was exposed to laboratory air for five minutes.

Fig. 3 (a) represents sensing response for benzene for a flexible sensor based on EPDM/MWNT/CCB/organoclay nanocomposites {conductivity profile shown in Fig. 1 (c)} for several cycles. In Fig. 3(b), the sensing response of EPDM/CCB nanocomposites for different BTEX compounds has been shown. It is clear from the profiles that the composites have highest response for xylene; though the change for toluene and benzene is also significant, suggesting with proper algorithm and device design this formulation can be used to detect the entire BTEX group. Fig. 3 (c) shows sensing response of the sensors made from EVA/nylon composites for formic acid and chloroform. The sensor had reproducible sensing response for these highly toxic compounds. In Fig. 3 (d), the sensing response of a BTEX sensor has been depicted. It can be seen that this sensor can be used over a wide concentration range (20-200 ppm). These results suggest that a range of sensing polymer alloys can be designed by carefully architecting the morphology and composition of the composites.

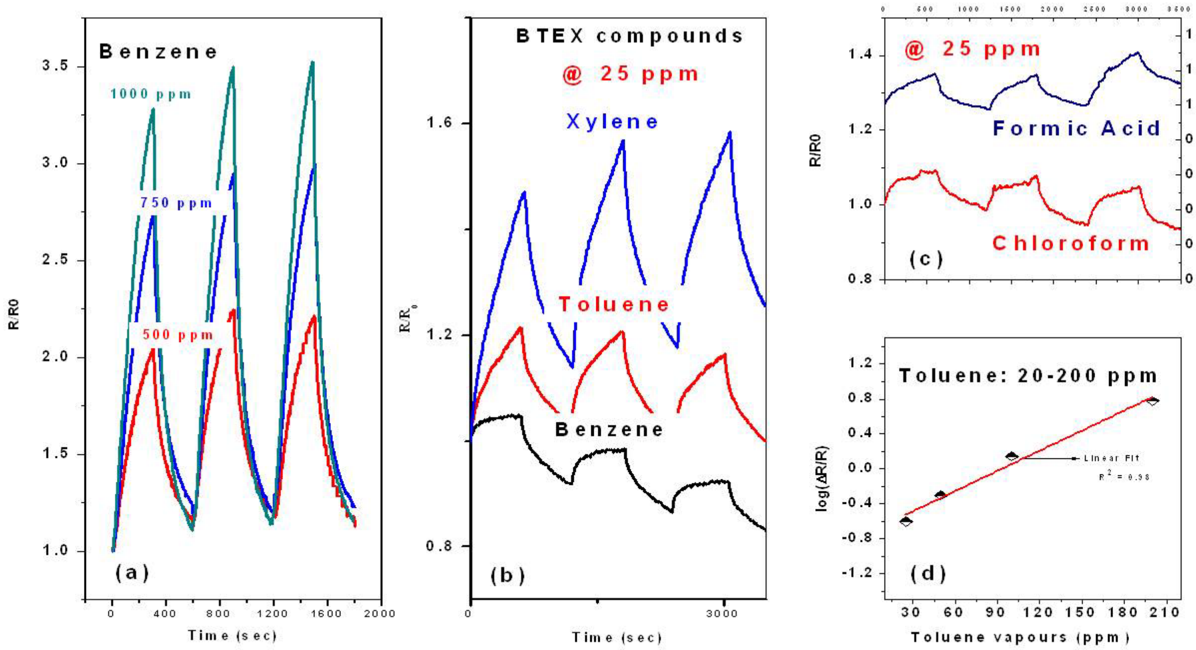

Fig. 3: Sensing response of different sensors (a) EPDM/CCB/organoclay/MWNT for benzene (b) EPDM/CCB for benzene, toluene and xylene 25 ppm (c) EVA/nylon/CCB for chloroform and formic acid (d) Linear fit of the sensing response of one of the sensor for toluene

Conclusion

The study suggests that high conductivity along with good flexibility can be achieved by tuning the compositional characteristics polymer alloy based nanocomposites. EPDM/CCB/organoclay/MWNT composites also showed good sensing response for BETEX compounds. For polar toxic VOCs, nylon/EVA was found to be a better matrix. Experiments are on for further improvement in selectivity and sensitivity with an aim of developing field sensors for different industries.

References

1. Dubey KA, Bhardwaj YK, Chaudhari CV, Sabharwal S. Polym Composite 2011; 32(5):737-746.
2. Dubey KA, Bhardwaj YK, Chaudhari CV, Goel NK, Sabharwal S, Rajkumar K, Chakraborty SK. Polym Adv Technol 2011; 22:1888-1897.
3. Costa LC, Chakki A, Achour ME, Graa MPF. Physica B Condensed Matter 2011;406(2):245-249.
4. Lu H, Yu K, Liu Y, Leng J. Smart Mater Struct 2010;19(6):065014.
5. Moriarty GP, Whittemore JH, Sun KA, Rawlins JW, Grunlan JC. J Polym Sci Pol Phys 2011;49(21):1547-1554.
6. Young CR, Menegazzo N, Riley AE, Brons CH, Disanzo FP, Givens JL, Martin JL, Disko MM, Mizaikoff B. Anal. Chem. 2011;83(16):6141-6147.
7. Hanyecz V, Mohácsi Á, Puskás S, Vágó Á, Szabó G. Meas Sci Technol 2011;22(12):125703.
8. Li H, Meng F, Liu J, Sun Y, Jin Z, Kong L, Hu Y. Sensor Actuat B Chem 2012;166-167:519-525.

FUSION AT DEEP SUB BARRIER ENERGIES FOR WEAKLY BOUND NUCLEI

A. Shrivastava
Nuclear Physics Division

Dr. Ms. A. Shrivastava is the recipient of the DAE Scientific & Technical Excellence Award for the year 2010

Abstract

In weakly bound nuclear systems, correlation among nucleons and pairing is manifested, among others, as an emergence of strong clustering and exotic shapes. Recent studies with weakly bound nuclei have focused on the understanding of the role of novel structures on the reaction dynamics. First measurement of fusion cross-section at deep sub barrier energies using a new sensitive off-beam technique is reported for weakly bound ^{6}Li on ^{198}Pt. The present results for a system with weakly bound projectile confront the current understanding of the fusion hindrance at these low energies, underlying the role of internal reorganization on the dynamical path towards fusion.

Introduction

The fusion of complex nuclei is governed by a delicate balance between the attractive nuclear and repulsive Coulomb interactions. During the last three decades of sub-barrier fusion studies, the important observations made are the discovery of sub-barrier fusion enhancement associated with couplings to the intrinsic excitations and nucleon transfer of the participating nuclei, measurements of the spin-distributions of the fused-compound nuclei and their theoretical description and the introduction of the concept of barrier distributions and their subsequent detailed measurements. Excellent reviews are given by Ref. [1].

Recently a new phenomenon of hindrance in fusion reactions has been reported in medium-heavy systems at deep sub barrier energies [2]. Measurements with medium-heavy nuclei highlighted the change of slope of the fusion excitation function at deep sub-barrier energies compared to coupled channels calculations [2]. The energy where these deviations begin referred to as the threshold energy for observing fusion hindrance has been parameterized and its implications on the fusion with light nuclei of astrophysical relevance have been discussed [2,3]. It has been pointed out that the cross-sections at deep sub-barrier energies could be used as an unique tool to obtain the value of the nuclear potential at small distances [3]. More recently it was shown [4] that the potential energy at the touching point strongly correlates with this threshold energy. Micsicu and Esbensen proposed a potential with a shallow pocket (as compared to that obtained from Woods-Saxon parametrization) based on a sudden approximation, where the reaction takes place so rapidly that the colliding nuclei overlap with each other without changing their density [5]. A repulsive core included to take into account the nuclear compressibility arising due to Pauli Exclusion Principle, modifies the depth and the shape of the minima of the inter-nuclear potential at small distances. The nucleus-nucleus interaction potentials extracted from the microscopic time-dependent Hartree-Fock theory indicate that at low energies the frozen density approximation breaks down underlying re-organization of the internal degrees of freedom. Based on an adiabatic picture, a dynamical two-step model was proposed by Ichikawa et al. [4] to explain the deep sub-barrier fusion data.

The fusion of weakly bound nuclei, which is a subject of current interest, has yet not been investigated at energies far below the barrier due to challenges involved in measuring low cross-sections. The possible effects that explain the change in slope of the measured fusion cross-sections are expected to be a general phenomenon. Hence measurements of fusion cross-sections at low energies for a completely different entrance channel are necessary to understand the tunneling process at energies well below the barrier.

Experimental Details

A new sensitive off-beam-gamma-spectroscopy method to obtain the cross-section of residues from fusion, utilizing a coincidence between characteristic KX-rays and gamma-rays from the daughter nuclei, has been developed [6] for the present measurement. This coincidence measurement permitted the accurate and precise determination of the residue cross-sections by reducing the background.

The experiment was performed at Pelletron Linac Facility-Mumbai, using beams of ^{6}Li on a ^{198}Pt target in the range of 20 to 35 MeV. Two efficiency calibrated HPGe detectors with a Be window were placed face to face for performing KX-gamma-ray coincidence of the decay radiations from the irradiated sample. The sample was positioned symmetrically at the center, between the two detectors in a close geometry (1.5 mm from the face of each detector). The measurements were performed in a low background setup with a graded shielding. The reaction products were uniquely identified by means of their characteristic gamma-ray energies and half-lives which in the case of fusion lead to $^{199-202}$Tl residues. The gamma-ray yields of the daughter nuclei were extracted by gating on their KX-ray transitions. Due to the increased sensitivity of the KX-gamma-coincidence method, cross-sections down to a few nano-barns could be measured. The fusion cross-sections, obtained from the sum of the measured compound nuclear evaporation residue cross-sections, are plotted in Fig. 1 for ^{6}Li+^{198}Pt. The cross-sections for the sum of deuteron-capture and neutron-transfer (plotted as open squares) are larger than those for fusion by orders of magnitude at deep sub-barrier energies. In the present work the average angular momenta (<l> have been derived from the fusion excitation function and are plotted in Fig. 2a.

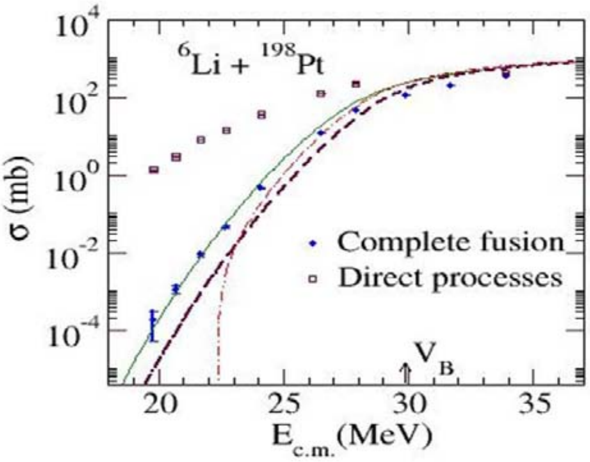

Fig.1: Cross sections for compound-nucleus formation and direct processes obtained from a sum of the partial cross sections. The results of the coupled-channels calculations using the WS potential (solid line), along with single-channel calculations using the WS potential (dashed line) and the M3Y potential with a repulsive core (dot-dashed line), are shown

Results and discussions

Calculations using the coupled-channels (CC) code CCFULL were performed with the ingoing-wave-boundary condition. Two sets of calculations, one using a standard Woods-Saxon potential (WS) ($V0=110$ MeV, $r0=1.1$ fm and $a=0.63$ fm) and the other based on the M3Y folded potential are presented. The potentials are plotted in Fig. 3. The results of the calculation with and without the inclusion of the couplings are shown in Fig. 1. At energies above the barrier the calculations overestimate the data, as expected from earlier studies involving weakly bound nuclei [8]. As can be seen in the figure, the CC calculations reproduce the data for energies around and well below the barrier. Plotted in Fig. 2b is the logarithmic derivative of the fusion cross-section ($L(E)=d[\ln(\sigma E)]/dE$). This representation provides an alternate way to illustrate any deviations in the slope of the fusion excitation function independent of the weight of the lowest barrier. The CC calculations reproduce well both the experimental slope L(E) and the <l> values (Fig.~2(b)) over the entire range of energy. Thus for ^{6}Li + ^{198}Pt, the CC calculations successfully explain the fusion excitation function along with the average angular momentum, consistently implying absence of the fusion hindrance at deep sub-barrier energies.

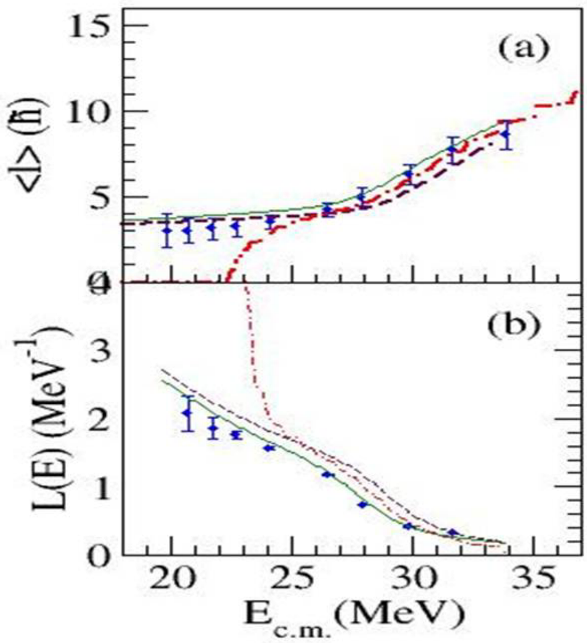

Fig.2 (a) Average angular momentum and (b) logarithmic derivative of the fusion excitation function. The calculated curves are as in Fig. 1

The lack of the fusion hindrance observed in the present system from the above calculations is also possible if the threshold value for the onset of fusion hindrance was not reached. This is not the case, as shown below. The threshold energy computed following two independent approaches sudden approximation (M3Y+repulsive core) and adiabatic methods; was found to 21 MeV and to be 22.3 MeV (Fig. 3) respectively. The present measurements extend down to Ecm = 19.8 MeV, which is well below the threshold energy computed from both the approaches.

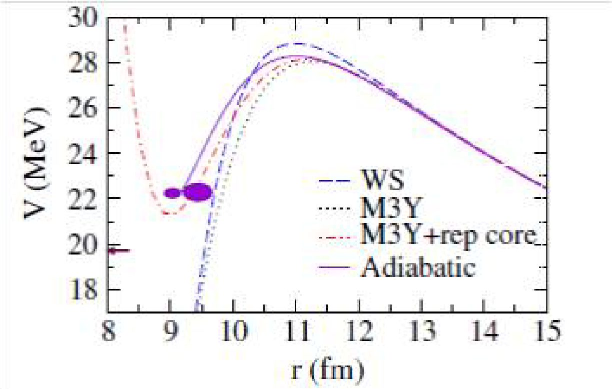

Fig.3: Inter nuclear potentials for ^{6}Li+^{198}Pt using the WS (long dashed line), the M3Y-double folding (dotted line), and the M3Y with a repulsive core (dash-dotted line). The adiabatic potential is shown as a solid curve up to the formation of a neck configuration. The arrow indicates the lowest center of-mass energy where

Single-channel calculations using the above M3Y potential with a repulsive core were also performed as suggested in [5] and the results are shown in Figures 1,2. The calculated fusion cross-sections, for energies lower than 22~MeV, fall off steeply and are orders of magnitude lower than the corresponding single channel calculations using the WS potential (Fig. 1). The effect of coupling on the calculated fusion cross-sections are found to be small from the CC calculations as seen in the same figure. A similar behavior was observed in Ref. [8]. Hence at these energies, even including the effect of coupling the calculated fusion cross-sections using the M3Y+repulsive core potential will be much lower than the measured fusion cross-sections. The calculated L(E) values also do not agree with the data and rise more steeply at low energies (Fig. 2b). The corresponding mean angular momentum drops to zero around an energy of E=22 MeV which is also inconsistent with the experimental data (Fig. 2a).

A shallow potential obtained using the M3Y interaction with a repulsive core successfully describe the fusion cross-sections at deep sub-barrier energies for symmetric, asymmetric and positive reaction Q-valued systems [5,7]. But for the present system with a weakly bound projectile this potential does not reproduce the trend of the fusion excitation function, L(E) and <l>. The present results suggest that the inner part of the interaction potential becomes deeper, going from symmetric to weakly bound asymmetric system, implying reduced contribution of the repulsive core. A plausible reason for this could be as follows: as the nuclei start overlapping, due to the weak binding of one partner, the Fermi energies of the two interacting nuclei are "very" different and will tend to equilibrate rather fast. Thus the Pauli blocking is expected to be less effective for asymmetric systems involving weakly bound nuclei as compared to two overlapping Fermi levels of symmetric systems [5]. The actual form of the repulsive core is expected to depend also on the extent of the adiabatic nature of the collision [7]. At energies well below the barrier the adiabatic approximation is expected to be more appropriate where nuclear reactions take place following the minimum energy path allowing for the readjustment of the densities as a function of collective variables. The predictions based on the adiabatic model of Ichikawa [4] already appear to give the correct behavior for the average angular momentum in the medium-mass symmetric systems though currently such calculations are not possible for asymmetric systems.

Summary and conclusion

We have presented the fusion excitation function for very asymmetric system involving weakly bound projectile at energies well below the barrier using a novel sensitive technique developed for this measurement. This study shows the absence of fusion hindrance, pointing to the limitation of the sudden approximation for modeling reactions in such systems. It would be of interest to see whether this arises solely from the effect of weakly bound cluster structure or also due to difference in transition from the sudden to the adiabatic potential.

References

1. A.B. Balantekin, N. Takigawa, Rev. Mod. Phys. 70, 78 (1998), M. Dasgupta et al., *Ann. Rev. Nucl. Sci.* 48, 401 (1998).
2. C.L. Jiang et al., *Phys. Rev. Lett.* 89 052701 (2002).
3. C. H. Dasso and G. Pollarolo, *Phys. Rev. C* 68, 054604 (2003).
4. T. Ichikawa, K. Hagino, and A. Iwamoto, *Phys. Rev. C* 75, 064612 (2007).
5. S. Misicu and H. Esbensen, Phys. Rev. Lett. 96, 112701 (2006); *Phys. Rev. C* 75, 034606 (2007).
6. A. Shrivastava et al, Phys. Rev. Letts. 103, 232702 (2009).
7. H. Esbensen and S. Misicu, *Phys. Rev. C* 76, 054609 (2007).
8. M. Dasgupta et al., *Phys. Rev. C* 66, 041602(R) (2002).

HIGH PULSE REPETITION RATE DYE LASER SYSTEM

S. Kundu
Laser & Plasma Technology Division

Shri Soumitra Kundu is the recipient of the DAE Scientific & Technical Excellence Award for the year 2010

Abstract

An overview of a copper vapor laser pumped dye laser system, operating at high pulse repetition rate (PRR), is presented. Some of the specific problems & solutions pertaining to sustained & efficient high average power operation are briefly discussed.

Introduction

Narrow bandwidth, widely tunable dye lasers (DL) pumped by copper vapor laser (CVL) find extensive applications in many fields such as photo-ionization spectroscopy, medicine and isotope separation [1,2,3]. One of the major activities of the Laser & Plasma Technology Division involves the application of high average power, precisely tunable, dye laser systems, operating at multi-kilohertz PRR, in the field of laser based material processing. Higher repetition rate of the laser system ensures higher process yield. Both CVL and DL are chosen as they are relatively inexpensive, indigenous system having inherent power scaling capability. Hence multiple units of both types of laser systems are arranged sequentially in master oscillator power amplifier (MOPA) configuration to produce high average power laser outputs. However, there are many challenges in sustained, efficient, and reliable operation of CVL pumped DL system for a process facility. Thus, considerable research and developmental effort has been directed towards improving the performance and availability of the system. In this paper, some of the salient features of the CVL pumped DL system installed in our departmental facility is presented.

System overview:

Copper Vapor Laser system

Copper vapor lasers belong to the family of metal vapor lasers and emit pulsed output at two wavelengths (510 nm & 578 nm) simultaneously. They are high temperature, low pressure, and high voltage fast discharge devices generating laser pulses of 50-70 nanosecond duration with energies of few milli-Joules per pulse at kilo-Hertz PRR. In a CVL MOPA chain, low average power oscillator output with requisite optical characteristics, amplified in following amplifier modules for boosting power levels as per the requirement. The optical gain media of these amplifiers are aligned spatially and synchronized temporally with the propagating oscillator output pulse. Large numbers of reflecting and transmitting optics were used for beam transportation within the MOPA chain. Several MOPA chains are installed and have completed more than thousand hours of cumulative operation in our facility. Outputs of these chains are appropriately mixed using optical beam splitters for temporal multiplexing and excitation of DL modules at twice the PRR.

The CVL oscillator output beam is normally un-polarized and contains significant amount of highly diverging ASE (amplified spontaneous emission) during the build-up of the laser pulse. Both features are unsuitable for efficient operation of dye lasers. Thus, in our setup, the CVL oscillator output was made linearly polarized by using Brewster window in conjunction with an intra-cavity plate polarizer, custom designed for polarizing both CVL wavelength components at 511 & 578 nm. Simultaneously, the CVL amplifiers were equipped with Brewster windows, substantially reducing window reflection losses and enabling high power extraction from a multi-stage MOPA. Spatial filtering was used after the oscillator to remove the ASE, which also reduced the pulse rise-time of the MOPA output (Fig.1) enabling faster build up of the DL pulse and improving DL efficiency. Production of polarized beams further allowed us to extensively use a combination of half wave plate and plate polarizer for variable and precise splitting of the pump beams for optimal distribution of pump power for different DL modules.

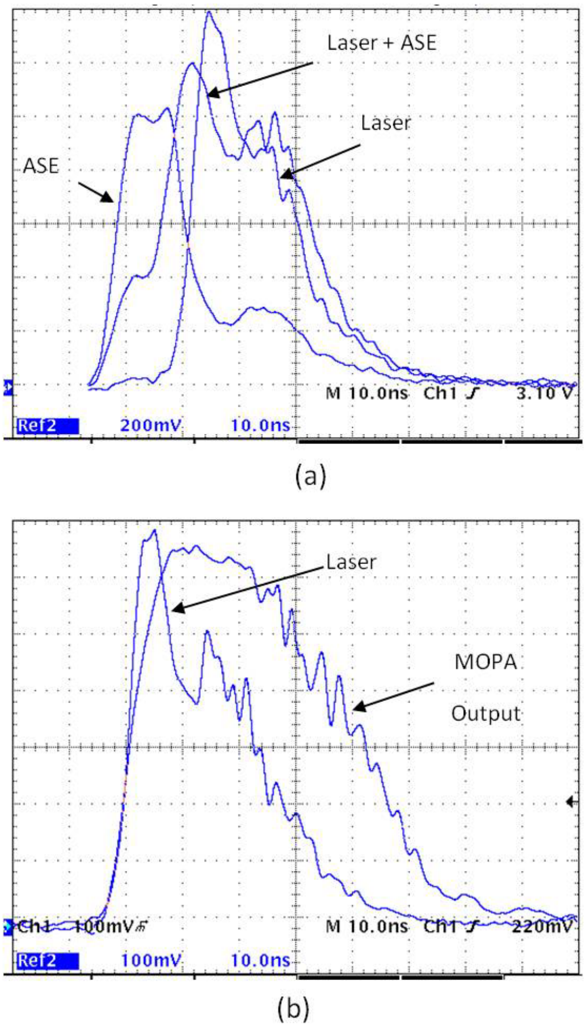

(a)

(b)

Fig. 1: Temporal pulse shapes of (a) CVL oscillator output showing laser and ASE components and (b) CVL MOPA chain output.

Dye Laser system

Dye lasers using organic dyes dissolved in suitable liquid solvents as the gain medium are the most versatile devices for generating high average power, frequency tunable, narrow-band radiation at visible and near infrared wavelength region. Transversely pumped dye laser oscillators and amplifiers perform more efficiently if both pump and dye laser beams are linearly polarized with electric field vectors oriented orthogonal to the plane containing the two beams. By inserting a polarization rotator at an appropriate location to decouple the oscillator cavity into two parts (see fig. 2) which exhibit higher preferences for orthogonal polarizations, we could achieve substantially higher efficiency while simultaneously producing the appropriate polarization for efficient extraction from downstream amplifiers. The dye oscillator efficiency and output pulse duration, which is inherently shorter than that of the pump, changes significantly over the wavelength tuning range. In MOPA systems, it is thus essential to stretch the pulsed oscillator output in time to

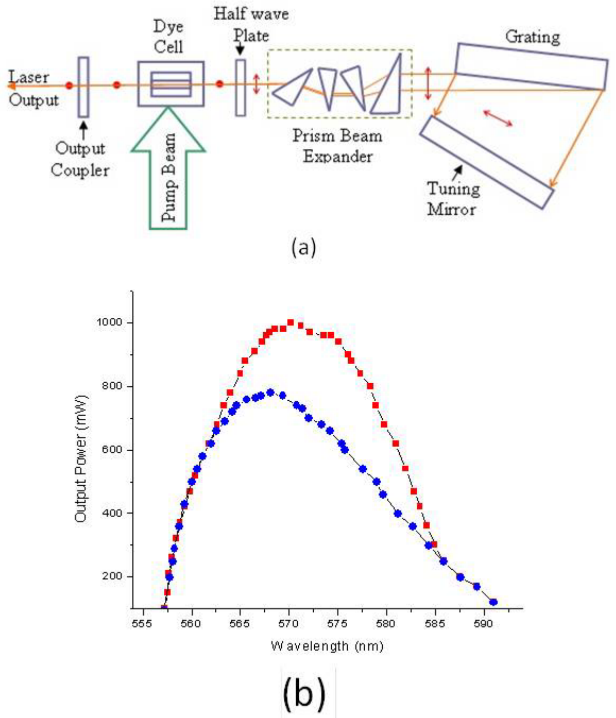

(a)

(b)

Fig. 2. (a) Top view of DL oscillator setup with intra-cavity half wave plate. Red dots and double headed arrows indicate directions of polarization for intra-cavity DL beam. Polarization direction for pump beam is perpendicular to the plane of the paper. (b) Performance of DL oscillator with red and blue points are for with and without half wave plate.

match the pulsed gain of the following amplifier in order to achieve maximum amplification and suppress broadband ASE component. This stretching was accomplished by splitting the oscillator pump beam into a 'prompt' and an optically 'delayed' beam for pumping a common gain line at the oscillator dye cell. Synchronizing amplifier gain timings aptly with the stretched DL oscillator output, the fraction of ASE content in the final amplified DL MOPA chain output was reduced to a negligible amount.

Dye molecules absorb energy in the form of photons both at pump as well as at DL wavelengths. Some part of this absorbed energy is converted into heat and not only perturbs the refractive index of the dye solution locally within the gain volume, but in principle, can damage cell window(s). Efficient heat removal by fluid flow through thin channel ensures complete replacement of the excited gain volume between successive pulses and thus provides stable high PRR operation of DL system with good output beam quality. High speed, safe and centrally controlled dye circulation systems, essential for reliable operation of the large scale high PRR DL systems, were designed, deployed, and used extensively.

Optimized operation of pulsed, narrow-band DL at required wavelengths requires a detailed knowledge of the photo-physical characteristics of the dye molecules. Also, photo-degradation of dye molecules is a major concern for continuous operation of high PRR DL system. Thus, dyes, solvents and additives, which are at times used to enhance the DL performance [4], were selected on the basis of their photo-stability characteristics and sustained operation capability through a series of performance tests. A glimpse of the CVL pumped high average power DL system, installed in our facility, is shown in fig. 3.

Numerical code for DL oscillator:

The efficiency and spatio-temporal evolution of a pulsed DL oscillator output depend on various parameters such as cavity losses, wavelength-dependent photo-physical constants of the dye, on the pump laser characteristics (power and pulse shape), and on processes such as gain saturation. Thus, comprehensive tests are needed to ascertain the performance of various dyes at required wavelengths in a given oscillator setup. Hence a numerical code was developed to simulate the DL oscillator in terms of its efficiency and output characteristics in order to narrow down test conditions and save experimental time and equipment life. The code, based on a time dependent, two dimensional (in space) rate equation model of a transversely pumped pulsed DL [5], incorporates coupled and inter-dependent orthogonal propagation of pump and DL radiation inside the gain medium. The model incorporates complex processes arising from excited state absorption of dye molecules, both at pump and DL wavelength, presence of broad band ASE components, and simulated diffraction loss within the cavity. The good

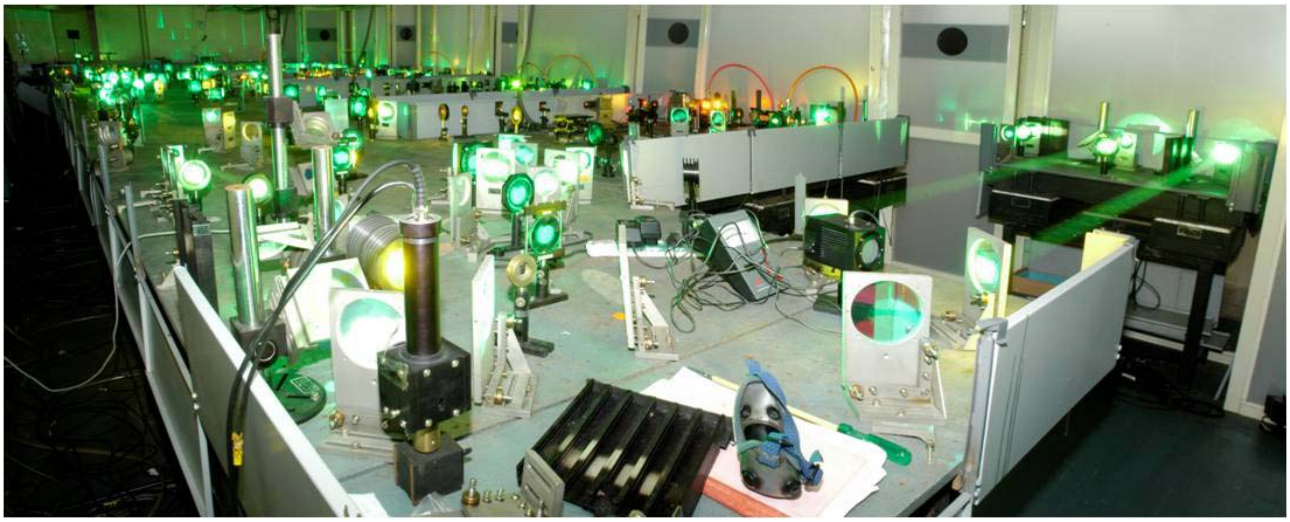

Fig. 3: High average power CVL pumped DL systems at our departmental facility during continuous round the clock operation

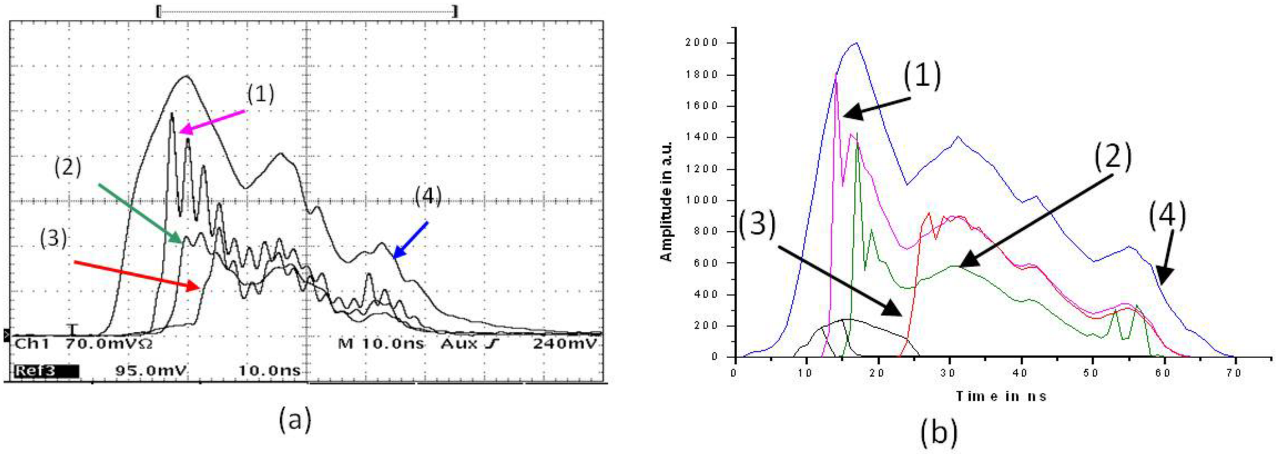

Fig. 4: DL oscillator output pulse evolution with respect to pump pulse for dye R6G. Experimental (a) and model outputs (b) at wavelengths: (1) peak of the tuning range; (2) half-maximum, short wavelength point; (3) half-maximum, long wavelength point; (4) pump wavelength. Computed ASE at different wavelengths are shown by traces in black, and appear as pedestals at the start of a recorded pulse.

agreement of the simulated pulses and efficiency of a DL oscillator with experimental results at different wavelengths (Fig. 4), validates the basic capability of the code. The code, after further validation under diverse test conditions and possible refinement, would be useful in designing the oscillator cavity as well as in predicting the performance of downstream amplifiers of a DL MOPA chain.

Conclusions

A brief discussion on CVL pumped DL systems have been presented. Some of our efforts to improve the overall system efficiency and availability for high average power operation of both types of laser systems are briefly discussed.

Acknowledgement

I would like to thank Dr. K. Dasgupta, and all other members of Tunable Laser Section, L&PTD, for their sincere, valuable guidance and intense participation in installation, operation & maintenance, and experimental tests of the laser systems. I would also like to thank Dr. A.K. Das, Head, Laser & Plasma Technology Division and Dr. L.M. Gantayet, Director, Beam Technology Development Group for their stimulating inputs and constant encouragement. Finally, I would like to acknowledge the continuous cooperation of the members of the LSE Section at RRCAT, Indore.

References

1. Letokhov, V. S., Laser Photoionization Spectroscopy. New York, Academic, 1987.
2. Goldman, L., Dye Laser in Medicine, in Dye Laser Principles, F J Duarte and L W Hillman, eds. New York, Academic, 1990 Chapter 10.
3. Greenland, P.T., Laser isotope separation, Contemporary Physics, 31(1990): 405–424.
4. Ray, A.K. et al, A binary solvent of water and propanol for use in high-average power dye lasers, Appl. Phys. B, 87 (2007): 489 – 495.
5. Kundu, S. et al, Rate equation simulation of temporal characteristics of a pulsed dye laser oscillator, Pramana, J. of Phys., 75, 5 (2010): 947 – 952.

INKJET PRINTED BIFUNCTIONAL $Zn_{0.98}Mn_{0.02}O$ FILMS

O.D. Jayakumar
Chemistry Division

Dr. O.D. Jayakumar is the recipient of the DAE Scientific & Technical Excellence Award for the year 2010

Abstract

Inkjet printed films and patterns of ZnO and $Zn_{0.98}Mn_{0.02}O$ have been developed on Si and polyimide substrates with a drop-on-demand inkjet printer, using their precursor inks. $Zn_{0.98}Mn_{0.02}O$ film printed on Si after processing showed enhanced bi-functional properties, like room temperature ferromagnetism and ultraviolet sensing, compared to diamagnetic and the ultraviolet sensing properties of a pristine ZnO film. Thus, this process opens up new possibilities of patterning advanced multifunctional materials.

Introduction

Novel functional nanomaterials are the basis of newly emerging nanotechnologies for various device applications. Nanotechnology deals with engineering and creating new materials in the dimension of up to 100 nm that can have new and unique physical or chemical properties differ significantly from the bulk materials. This revolutionary technology is already applied in many fields and it is expected to be dominant in numerous industrial processes. One of the most interesting classes of materials that nanotechnology deals with belongs to nanoparticles possessing functional properties. Magnetism, luminescence, sensing and drug delivery are some of the major applications among wide variety of functionalities. Inkjet printing technology is a simple and low cost method which has recently become an attractive technique for the patterning and printing of thin films of semiconductors, conductive polymers and organic LEDs, electronic circuits and bio-nanoparticles at ambient conditions (1,2). Its versatility to deliver small volumes of inks with spatial accuracy and its direct-writing ability in a non-contact deposition mode makes it a novel patterning technique (3). Further, there are hardly any reports on the bifunctionality studies of Mn doped ZnO films developed by inkjet printing.

Recently, inkjet printed films and patterns (dots, lines and junctions) of wide band gap semiconductor and their derivatives were developed on Si and polyimide substrates using their precursor based solvent inks (4, 5). These nano-inks were fine tuned to match the desired viscosity (10–12 centipoises at room temperature), surface tension (35 dynes/cm at room temperature) and adhesive properties by adding suitable additives. Inkjet printed 'c' axis oriented films (3 pass printed) on Si have been characterized for their magnetic, structural and UV sensing properties. The 3 pass printed film of $Zn_{0.98}Mn_{0.02}O$ on Si showed bifunctional properties after processing, such as a fast ultraviolet (UV) sensing capability along with enhanced ferromagnetism compared to pristine diamagnetic UV sensing ZnO film. This tailored rheological formulation of precursor based inks and their subsequent printing opens up a new processing route for the patterning of various dimensional forms of crystalline TM doped ZnO and other oxide based advanced multifunctional materials like $BiFeO_3$, TiO_2, $PbZr_{1-x}Ti_xO_3$ etc.

Experimental

Metal acetates dissolved in organic solvents along with additives, surfactants and binders form printable inks with the desired viscosity and surface tension. The ZnO precursor ink solution (0.25 M) is prepared by mixing a 1 : 1 molar solution of zinc acetate dihydrate and 2 ethanolamine (99.99%) in 2 propoxy ethanol with vigorous stirring at 60 °C for 1 h. The nominal concentration of $Zn_{0.98}Mn_{0.02}O$ is also prepared in a similar manner by adding an appropriate amount of manganese acetate tetra hydrate (99.99%) with zinc acetate. Particle concentration, ink viscosity, surface tension and adhesive properties were tuned using various concentrations of precursors, surfactants and binders (4). The substrates Si and polyimide were cleaned by rinsing them in acetone followed by rinsing in isopropanol and subsequently dried by blowing with dry nitrogen. In a typical printing process of different patterns of ZnO, the ZnO ink was inkjet printed on top of the cleaned Si or polyimide, at 60 °C and dried on a hot plate at 200 °C, followed by annealing at selected temperatures in a preheated furnace for 30 min. Additional layers were deposited and heat treated in a similar manner after each deposition. Most of the films were 3 pass printed while the dots and other patterns were printed with only one pass. The resulting patterns, films in particular, were characterized using XRD, SQUID, SEM, XAS, XES, AFM, high resolution digital camera and UV sensing (4). Three pass printed films were made only after completing the 1 and 2 passes of printing followed by drying and heating. Cu-Kα radiation of a Philips Diffractometer (model PW 1071) was used for XRD studies. A quantum designed SQUID (model MPMS2) was used for the magnetization studies. SEM was done on a Hitachi 3000N machine. For most of the experiments described in this work, a Dimatix 2800 printer attached with a motorized X, Y, Z movable substrate holder and 10 pl (drop volume) print head with a printing resolution of 600 dpi was used. The soft X-ray absorption (XAS) and emission (XES) experiments were performed in the undulated beam-line 8.0.1 at the Advanced Light Source, Lawrence Berkeley National Laboratory, California, USA. The beam-line is equipped with a spherical grating monochromator. The XAS data were measured in the total electron yield (TEY) mode by monitoring the drain current, and the XES data were measured with a spherical grating X-ray emission spectrometer. The slits of the beam-line were set to 40/40 mm for the O K XAS and 50/50 mm for the Mn L XAS. For the XES measurements, 100/100 mm slits were chosen. Atomic force microscopic (AFM) measurements were performed using an NT–MDT solver model instrument with a 50 mm scanner head and silicon nitride tip in contact mode. The photo-response was measured by a custom-designed setup, using copper contacts in a coplanar gap (0.5 mm) configuration with high precision Keithley measurement instruments, by irradiation with a light emitting diode (LED, wavelength 363 nm and optical power 1.5 mW at a forward current of 20 mA). The UV response measurement was performed using a synthesized functional analyzer in the frequency of 50 Hz with a high resolution oscilloscope (Tektronix 7503).

Results and Discussion

A schematic steps used for the printing (Fig.1 top), processing and patterning (Fig.1a bottom) of these developed inks on the preheated substrates and its characterization using x-ray diffraction and cross-sectional SEM is shown in Fig.1. These samples were further characterized using Atomic Force Microscopy (AFM), X-ray absorption (XAS) and emission spectroscopy (4) (XES). XRD patterns of ZnO and $Zn_{0.98}Mn_{0.02}O$ revealed that films were highly oriented along 'c' axis and showed no evidence of any possible secondary phases that can be detected on the resolution of XRD (Fig. b). The average crystallite size obtained (by Scherer equation) for ZnO and $Zn_{0.98}Mn_{0.02}O$ were ~20 nm, which is in agreement with the SEM results (Fig. 1c, d).

Fig. 1a depicts the photographs of films and patterns of printed ZnO and $Zn_{0.98}Mn_{0.02}O$ on Si and polyimide substrates. These films were heated at 400 °C for 30 min and were found to be homogenous with significant adhesive properties. Fig. 1a also shows photographs of the printed patterns of these inks in the form of dots (200 μm in diameter), lines of ZnO and $Zn_{0.98}Mn_{0.02}O$ with widths ranging from ~150 to ~400 μm and their junctions with ~250 and ~300 μm widths. Atomic Force Microscopy (AFM) images of the 3 pass printed film of $Zn_{0.98}Mn_{0.02}O$ indicate that the film surface is highly homogenous and smooth with a mean square roughness (Rms) value of ~2.5 nm ± 0.2 nm. The AFM image of the ZnO film also showed a Rms value of ~2.5 nm ± 0.2 nm (4).

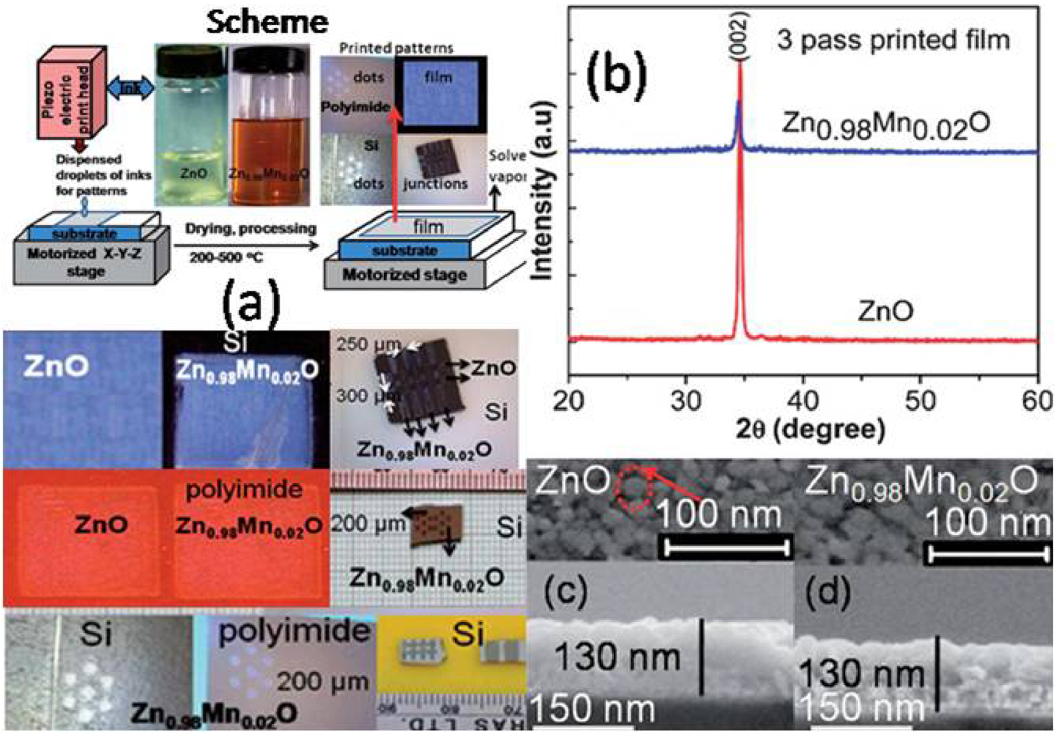

Fig. 1: Scheme and photographs of printing, processing and patterning of ZnO based inks (a), XRD pattens of ZnO and $Zn_{0.98}Mn_{0.02}O$ films (b), cross sectional SEM of ZnO (c) and $Zn_{0.98}Mn_{0.02}O$ (d) films

The room temperature ferromagnetism of these films were measured using a quantum design SQUID magnetometer and showed ferromagnetic characteristics. While ZnO film showed a typical diamagnetic behavior, $Zn_{0.98}Mn_{0.02}O$ film showed ferromagnetic nature with decreasing Ms value when heated above 400°C (Fig.2), which was attributed to mixed-valent states of Mn, confirmed from the electronic structure of the ZnO and $Zn_{0.98}Mn_{0.02}O$ films, probed by X-ray absorption (XAS) and emission spectroscopy (XES) (4). The photo-response was measured by a custom-designed setup, using copper contacts in a coplanar gap (0.5 mm) configuration with high precision Keithley measurement instruments, by irradiation with a light emitting diode (LED, wavelength 363 nm and optical power 1.5 mW at a forward current of 20 mA). The UV response measurement was performed using a synthesized functional analyzer in the frequency of 50 Hz with a high resolution oscilloscope (Tektronix 7503). For the

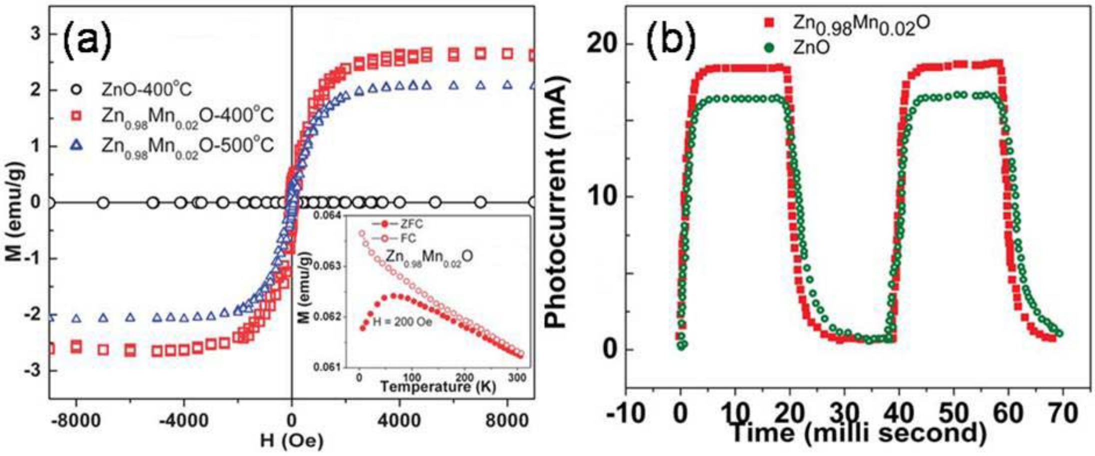

Fig. 2: M vs H at RT (a) and M vs T (inset of (a)) curves of $Zn_{0.98}Mn_{0.02}O$ films. For comparison, M vs H curve of ZnO is also given. UV response of ZnO and $Zn_{0.98}Mn_{0.02}O$ films (b)

$Zn_{0.98}Mn_{0.02}O$ film a fast decay time of around 0.55 milliseconds is observed compared to that of 0.63 millisecond observed for the ZnO film. Furthermore, the $Zn_{0.98}Mn_{0.02}O$ film showed a marginally increased photocurrent than the ZnO film. The observed faster response and decay times of the ferromagnetic $Zn_{0.98}Mn_{0.02}O$ film than those of the diamagnetic ZnO film is interesting and needs detailed investigation. This enhanced UV sensing capabilities and ferromagnetic behavior of $Zn_{0.98}Mn_{0.02}O$ film (Fig.2 right) compared to pristine ZnO paves the way for multifunctional devices (4).

Conclusion

In summary, films and patterns of semiconductors ZnO and $Zn_{0.98}Mn_{0.02}O$ have been inkjet printed on Si and polyimide substrates, using their precursor based inks. The $Zn_{0.98}Mn_{0.02}O$ film on Si showed both enhanced ferromagnetism and UV sensing capabilities compared to pristine ZnO film on Si thus paving the way for multifunctional devices.

References

1. De Gans, B.J. Duineveld, P.C. and Schubert, U.S. *Adv. Mater.* **16** (2004): 203.
2. Holdcroft, S. *Adv. Mater.* **13** (2001): 1753.
3. Sirringhaus, H. *Adv. Mater.,* 17 (2005): 2411.
4. Jayakumar, O. D and Tyagi, A.K. *J. Mater. Chem.* 21 (2011): 12246.
5. Jayakumar, O.D., Sudarsan, V and A.K. Tyagi, *Nanoscience and Nanotechnology Lett.* 3, (2011): 136.

MULTIWAVELENGTH STUDY OF VHE γ-RAY FLARE FROM MRK 421 DURING FEB. 2010

R.C. Rannot, P. Chandra, K.K. Yadav and R. Koul
Astrophysical Sciences Division

Dr. R.C. Rannot is the recipient of the DAE Scientific & Technical Excellence Award for the year 2010

Abstract

VHE Observations on Mrk 421 were made using TACTIC gamma-ray telescope during February 6 - 23, 2010 for 50 hours during which we find evidence for 712±87 VHE γ-ray photons with a statistical significance of 8.18σ at $E\gamma \geq 1$TeV. The time averaged differential energy spectrum obtained in the energy range 1.0 - 16.44 TeV follows a power law function of the form $dF/dE = f_0 E^{-\Gamma}$ with $f_0 = (2.23 \pm 0.58)10^{-11}$ $cm^{-2} s^{-1} TeV^{-1}$ and $\Gamma = 2.25 \pm 0.22$. The source light curves obtained from satellite based experiments at x-ray and γ-ray energies indicate a correlation between TACTIC observed and x-ray light curves during these observations, thereby supporting the SSC model in which a relativistic electron population produces the x-rays by synchrotron radiation and the γ-ray component by inverse Compton scattering. In addition, the fitted single zone SSC model parameters also supports the mentioned source model for the production of observed γ-rays.

Introduction

Active Galactic Nuclei (AGNs) are super-massive black holes accreting matter and, in some cases, emitting ultra relativistic particles by means of two collimated jets. Blazars class of AGNs are radio loud with a relativistic jet pointing towards the observer. The majority of extragalactic γ–ray sources belongs to this class of AGNs with their Spectral Energy Distribution (SED) dominated by the non-thermal continuum produced within the jet and boosted by relativistic effects, exhibiting fast variability at all wavelengths and amplified by beaming effect. The SED of blazars displays two broad peaks in the frequency(ν) and νxFlux representation, widely interpreted as due to synchrotron (low frequency peak) and inverse Compton (high frequency peak) mechanisms. There are two models proposed for the origin of the photons of the high energy bump observed in the SED of blazars, based on the leptonic and hadronic interactions with the ambient photons and magnetic fields. Leptonic models propose the Inverse Compton(IC) scattering as leading mechanism for explaining the energetic photons origin. In the Synchrotron Self Compton (SSC) model, the energetic photons observed in blazars are produced by IC scattering of synchrotron photons by the same electron population emitting them. In the hadronic models, energetic photons are expected in jets via hadronic interactions, such as synchrotron emission of pair cascades triggered by photo-meson process and/or by direct synchrotron emission of protons and mesons [1].

Mrk 421 belongs to the blazars class of AGNs located at a distance of about 135Mpc and was the first extragalactic source detected at TeV energies in 1992 using imaging atmospheric Cherenkov telescopes [13]. The source has been observed extensively by various groups since then [5,6]. These observations have shown that the TeV γ-ray emission from Mrk 421 is highly variable with variations of more than one order of magnitude and occasional flux doubling time as short as 15 mins [11, 2]. It is widely recognized that one of the most effective ways of studying the physics of blazars is through the use of multi-frequency data that is ideally contemporaneous. In this paper we present multi-wavelength view of the Mrk 421 flaring state observed during February 2010 using TACTIC atmospheric Cherenkov telescope [12], and RXTE(ASM)[4], Swift(BAT)[15] and Fermi(LAT)[10] satellite based instruments.

Observations and data analysis

Mrk 421 was observed with the TACTIC γ-ray telescope in February 2010 for 50 hours. Details of these observations and data analysis procedure followed are given in [5]. The data analysis chain involves a number of steps

Table 1: γ-ray image selection criteria used while analysing TACTIC data.

Parameter	Cut value
LENGTH(L)	$0.11^0 \le L \le (0.235 + 0.0265 \times \ln S)^0$
WIDTH(W)	$0.065^0 \le W \le (0.085 + 0.0120 \ln S)^0$
DISTANCE(D)	$0.5^0 \le D \le (1.27 \, \mathrm{Cos}^{0.88} \ln\theta)^0$ (θ =zenith angle)
SIZE(S)	$S \ge 485$ dc (6.5 Dig counts = 1.0pe)
ALPHA(α)	$\alpha \le 18^0$
FRAC2(F2)	$F2 \ge 0.38$

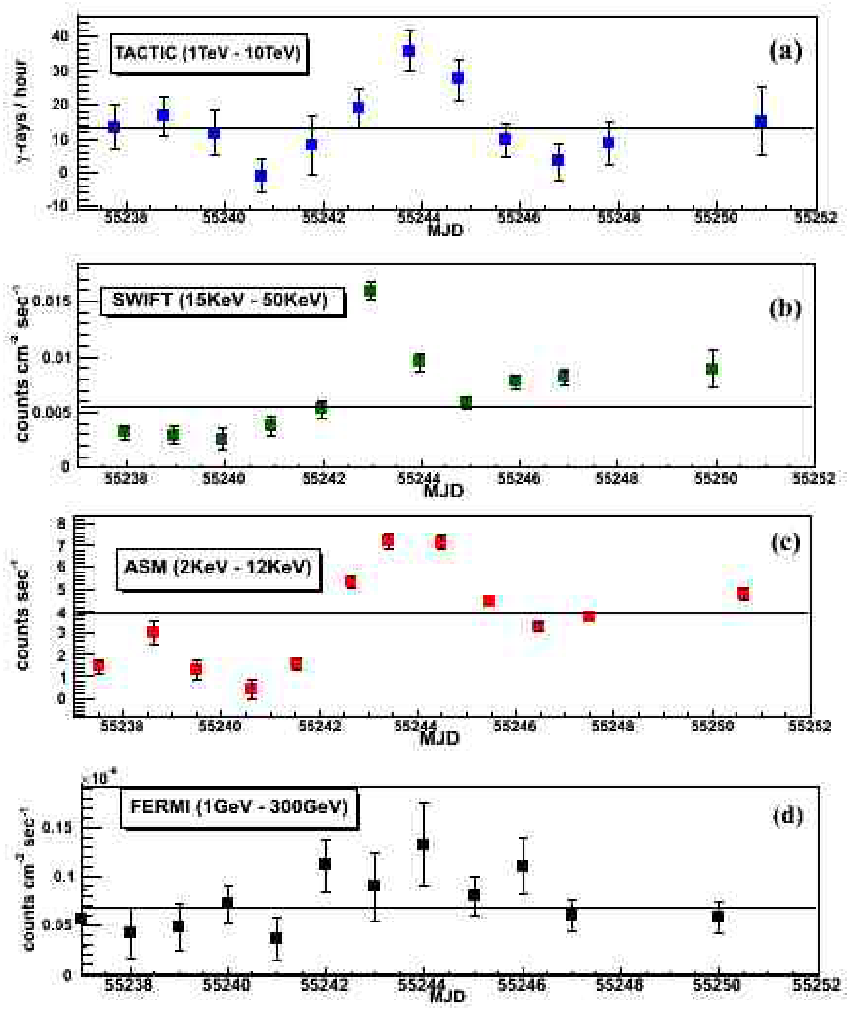

Fig. 1: Mrk 421 light curves at x-ray and γ-ray energies for February 2010 observations.

including filtering of night sky background light, accounting for the differences in the relative gains of the PMTs, finding Cherenkov image boundaries, image parameterization, event selection, energy reconstruction etc. Each recorded Cherenkov image is characterized using a moment analysis methodology given in[8], wherein the roughly elliptical shape of the image is described by the LENGTH and WIDTH parameters and its location and orientation within the telescope field of view are given by the DISTANCE and ALPHA parameters respectively. The gamma-ray selection criteria used in data analysis is given in Table 1 and has been obtained by using Monte Carlo simulation studies of the TACTIC telescope. The ALPHA parameter distribution is expected to be flat for the isotropic background of cosmic ray events, whereas for the γ-ray events, the distribution is expected to show a peak at smaller ALPHA values. This range for the TACTIC telescope is ≤18°. The contribution of the background events is estimated from 27° – 81° ALPHA region which is expected to be flat. The number of γ- ray events is then calculated by subtracting the expected number of background events, calculated on the basis of the background region, from the γ- ray domain events. During February 2010 source observations we have detected 712±87 VHE photons with

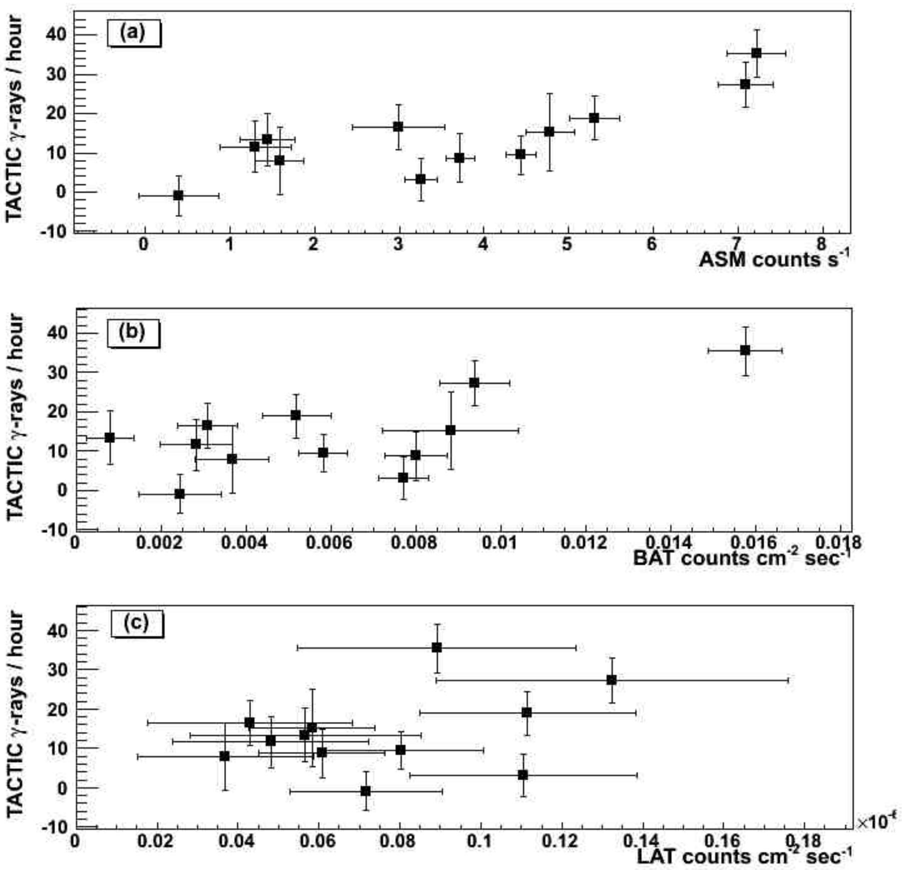

Fig. 2: TACTIC hourly γ-ray rate versus (a) ASM counts s^{-1} (b) BAT counts cm^{2} s^{-1} and (c) LAT counts cm^{-2} s^{-1} .

Table 2: Single zone SSC model[9] parameters obtained by fitting spectral energy distribution data from various observations in different energy bands[15,7].

Magnetic field(G)	Doppler factor(δ)	Size (R)	log(E_{min}) eV	log(E_{max}) eV	log($E_{br.}$) eV	n1	n2	Ue ergs cm^{-3}	Sy$_{peak}$ (x10^{17} Hz)	IC$_{peak}$ (x10^{25} Hz)
0.09	31	2.0E+14 m	9.1	12	10.9	-2	-3	1.45E-3	8.08	8.46

their time averaged differential energy spectrum following a power law function of the form dF/dE= $f_0 E^{-\Gamma}$ with f_0 = (2.23 ± 0.58)10^{-11} $cm^{-2} s^{-1} TeV^{-1}$ and $\Gamma = 2.25 \pm 0.22$. In Fig. 1 we show Mrk 421 light curves in four energy bands from TeV γ- ray to soft x-ray energies. TACTIC observed source light curve shown in Fig. 1a has been obtained after analyzing February, 2010 data on nightly basis. It is characterised by a reduced χ^2 value of 33.46/11 (χ^2/dof) with respect to a mean value of 13.1 ± 1.7 gamma-ray photons per hour and yields a corresponding probability of 0.00044 thereby indicating that the light curve is consistent with a variable signal.

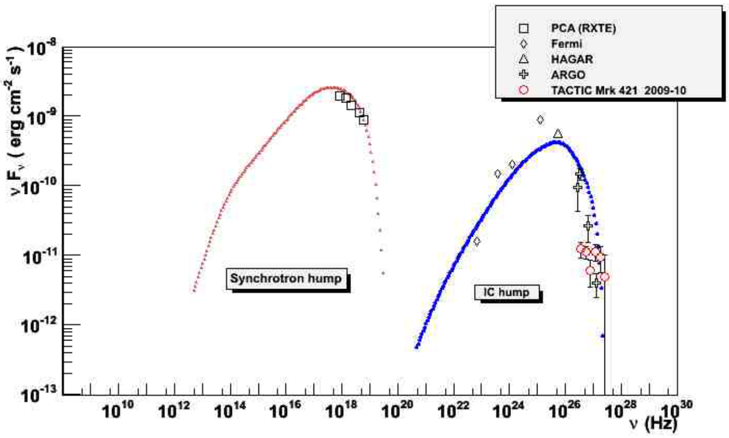

Fig. 3. Spectral energy distribution of Mrk 421 derived during its February 2010 high state. The dotted curves show a fit to the observed spectra[7,14] using an homogeneous single zone SSC model[9].

We have also used Mrk 421 data obtained by three satellite based telescopes namely; Fermi(LAT), *Swift*(BAT) and RXTE(ASM) which operate in 30MeV -300GeV, 15-50keV and 2-12keV energy bands respectively. The *SWIFT/BAT* x-ray light curve shown in Fig. 1b has been obtained using publically available data from [15] and is characterized by a reduced χ^2 value of 298.2/11 with respect to mean value of 0.00055 ± 0.0002 counts $cm^{-2} s^{-1}$ which yields a corresponding probability close to zero thereby indicating that the *SWIFT/BAT* hard x-ray light curve is consistent with a variable signal as well. Further, the RXTE/ASM [4] light curve in the energy range of 2-12keV is shown in Fig. 1c also indicates source high state during TACTIC observations. This light curve is characterized by a reduced χ^2 value of 459.4/11 with respect to mean value of 3.87 ± 0.07 counts s^{-1} which again yields a corresponding probability close to zero indicating that the RXTE/ASM soft x-ray light curve is consistent with a variable x-ray source state. Next the Fermi/LAT[10] light curve shown in Fig. 1d is characterized by a reduced χ^2 value of 12.4/11 with respect to mean value of 0.066e-06 ± 0.0064e-6 counts $cm^{-2} s^{-1}$ which yields a corresponding probability of 0.33. All the source light curves show an enhancement in corresponding signal around 15- 17 February, 2010 (MJD 55242.73913 – MJD55244.75948) as is clear from Figures 1a,b,c and d. In order to explore a possible correlation between the source emission at VHE and lower energies we show three correlation plots in Fig. 2. Figs. 2a and b indicate a possible correlation between TeV and x-ray emissions from this source direction. In Fig. 3 we show spectral energy distribution of the source using source spectra obtained by different instruments [7,14 and references therein]. These data fits well with the single zone SSC model [9] as is clear from the figure and the parameters obtained are given in Table 2, thereby lending a possible support to the SSC model in which a unique electron population produces the x-rays by synchrotron radiation and the gamma-ray component by inverse Compton scattering.

Discussion and conclusions

Mrk 421 is a very interesting blazar having relatively high flaring frequency as compared to other similar objects making it an excellent candidate for the study of the jet physics in AGNs. Using the TACTIC γ-ray telescope the source was observed for 12 nights during February, 2010 and 712±87 VHE γ- ray photons were detected at 8.18σ statistical level. The time averaged differential energy spectrum has also been obtained for these photons in the energy range 1.0 - 16.44 TeV which is consistent with a power law function of the form dF/dE= $f_0 E^{-\Gamma}$ with f_0 = (2.23 ± 0.58)10^{-11} $cm^{-2} s^{-1} TeV^{-1}$ and $\Gamma = 2.25 \pm 0.22$ indicating a relatively harder spectrum as compared to those observed earlier from this source using the TACTIC telescope. Further, TACTIC, Swift(BAT) and RXTE(ASM) light curves of February, 2010 observations indicate a possible correlation of TeV and x-ray emissions of the source as is shown in Figs. 2a and b. Therefore these observations possibly support the SSC model in which a relativistic electrons population produces the x-rays by synchrotron radiation and the γ-ray component by inverse Compton scattering. This scenario is also reflected in Fig. 3 which shows fitted synchrotron and inverse Compton peaks using SSC single zone model described in [9] and source spectra at x-ray and γ-ray bands observed by various groups [7,14 and references therein].

Acknowledgements

Authors would like to acknowledge the excellent team work of the technical staff at the Mt. Abu observatory.

References

1. Aharonian, F.A., (2000), *New Astronomy*, 5, 377–395.
2. Aharonian F. et al. (2002), A&A, 393, 89
3. Atwood, W. B., Abdo, A. A., Ackermann, M., et al. (2009), ApJ, 697, 1071
4. ASM http://xte.mit.edu
5. Chandra P., et al.(2012) *J. Phys. G: Nucl. Part. Phys.* **39** 045201
6. Chandra, P., et al., et al.(2010), *J. Phys. G: Nucl. part. Phys.* 37, 125201
7. He H.H. et al. (2011), 32nd ICRC, Beijing, China
8. Hillas, A. M. (1985), in Proc 19th ICRC, 3, 445
9. Krawczynski, H. 2004, *New A Rev.,* 48, 367
10. Fermi(LAT) http://fermi.gsfc.nasa.gov/ssc/data/access/lat/msl_lc/
11. Gaidos J.A. et al.(1996), *Nature,* 383, 319
12. Koul, R. et al. (2007) *Nucl. Instrum. and Meth. A.,* 578 548
13. Punch M., et al.(1992), *Nature,* 358, 477
14. Shukla A., et al. (2012), A&A, 541, A140
15. *SWIFT* http://swift.gsfc.nasa/docs/swift/results/transients

NMR AS A TOOL FOR THE CHARACTERIZATION OF GLASSES AND NANOMATERIALS

V. Sudarsan
Chemistry Division

Dr. V. Sudarsan is the recipient of the DAE Scientific & Technical Excellence Award for the year 2010

Abstract

Structural configurations of boron and silicon present in borosilicate glasses have been identified and quantified by ^{29}Si and ^{11}B solid state nuclear magnetic resonance (NMR) technique. Physico-chemical properties like thermal expansion coefficient, glass transition temperature, leach resistance etc., strongly depend on nature and relative concentration of different structural units constituting the glass. ^{31}P NMR can be very effectively used to find out and quantify the different P structural units present at the interface region of a representative core-shall nano-material having hexagonal $GaPO_4$ phase as core covered by psudo-hexagonal $AlPO_4$ phase as shell.

Introduction

Nuclear magnetic resonance (NMR) spectroscopy is based on magnetic properties of atomic nuclei and is only possible with nuclei having non-zero value of nuclear spin ($I \neq 0$). The technique can give valuable information about structure, dynamics and chemical environment around a particular nucleus in a molecule/material [1]. Recently, different solid state NMR techniques gained considerable interest for the characterization of different types of materials. Unlike solution state NMR, where there is continuous averaging of different types of inter nuclear interactions, in solid state NMR, interactions do not get averaged out and this results in significant line broadening and appearance of feature less spectra. In earlier times this prevented the use of solid state NMR for understanding structural changes taking place in solids. After the discovery of Magic Angle Spinning (MAS) NMR technique, significant extent of line narrowing was achieved in solid-state NMR line shapes resulting in sharp NMR lines from solids which eventually helps one to understand the structural changes taking place in solids. In the present manuscript, initially basic principle of MAS NMR technique is briefly described. This is followed by discussion on the structural characterization of glassy and nanomaterials by MAS NMR.

Basic principle of MAS NMR technique

MAS NMR technique involves rotating powder samples at high spinning speeds (of the order of few kHz), at an angle of 54.7° (magic angle) with respect to applied magnetic field direction (B_0). When $\theta = 54.7°$, the term $3\cos^2\theta$ becomes unity. Since Hamiltonian for different anisotropic interactions like dipole-dipole, quadrupolar and chemical shift, have $3\cos^2\theta - 1$ term in their expression, such anisotropic interactions get averaged out (becomes

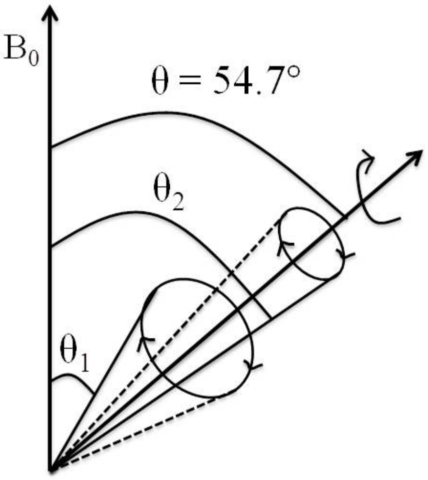

Fig. 1: Schematic representation for the averaging effect of NMR interaction tensors with two different angles of orientations θ_1 and θ_2

very small) in time during fast spinning. Further, under fast spinning conditions, NMR interaction tensor orientations with initial angles of θ_1 and θ_2 relative to applied magnetic field (B_0) will also have orientational averages of 54.7° (Fig. 1). This results in sharp NMR peaks which are quite sensitive to changes in the local environments and hence can be correlated with corresponding chemical shift values obtained from different samples.

Results and Discussion

In this manuscript, NMR studies have been carried out on two representative samples. First one is a sodium borosilicate glass and the second one is core-shell nanoparticles having $GaPO_4$ core covered with $AlPO_4$ shell. Sodium borosilicate glasses have been chosen in the present study as it has got potential application as host matrix for incorporating of high level nuclear waste generated from the reprocessing of spent fuels from different type of nuclear reactors. The main constituents in borosilicate glasses are boron and silicon, the local environment around both of them can be investigated by recording ^{29}Si and ^{11}B MAS NMR patterns. It is worth while to mention here that, as both B and Si are low atomic number (Z) elements, techniques based on diffraction will not be very useful for understanding minor structural changes around the nuclei. In the case of structural characterization of nanomaterials, core-shell nanomaterials having $GaPO_4$ core and $AlPO_4$ shell is chosen as a representative compound since ^{31}P is a nucleus with spin = ½ and is very sensitive to the structural changes taking place around the nucleus.

The glass with composition $(Na_2O)_{0.36}(SiO_2)_{0.39}(B_2O_3)_{25}$ was prepared by conventional melt-quench method (at 900°C) starting from analytical grade reagents of Na_2CO_3, H_3BO_3 and SiO_2. Figure 2 shows ^{29}Si MAS NMR pattern of $(Na_2O)_{0.36}(SiO_2)_{0.39}(B_2O_3)_{25}$ glass. The pattern is characterized by a broad asymmetric peak with maximum around -100 ppm. The broad asymmetric peak can be de-convoluted into two peaks based on Gaussian fit with individual peaks around -102 and -89 ppm which are characteristic of Q^4 and Q^3 structural units of silicon respectively (where Q^n represents silicon structural units having "n" number of bridging oxygen atoms attached with it) [2]. The structural uints schematically represented in Fig. 2 (a and b). With increase in network modifier concentration, it is observed that the silicon structural units undergo de-polymerisation to form Q^2 and Q^1 structural units. The physicochemical properties like, thermal expansion coefficient, glass transition temperature, leach resistance etc have got strong influence on the nature and relative concentration of different structural units present in the glass. Our studies have revealed that as the Q^4 structural units of silicon get converted to Q^3, Q^2 and then to Q^1 structural units sequentially, the thermal expansion coefficient of glass increases and the glass transition temperature decreases. This is explained based on the conversion of more rigid structural units to less rigid ones brought about by the bridging to non-bridging oxygen atoms conversion. As mentioned earlier, ^{11}B MAS NMR also can give valuable information regarding the coordination environment around boron atoms in the glass and this is discussed in the following section.

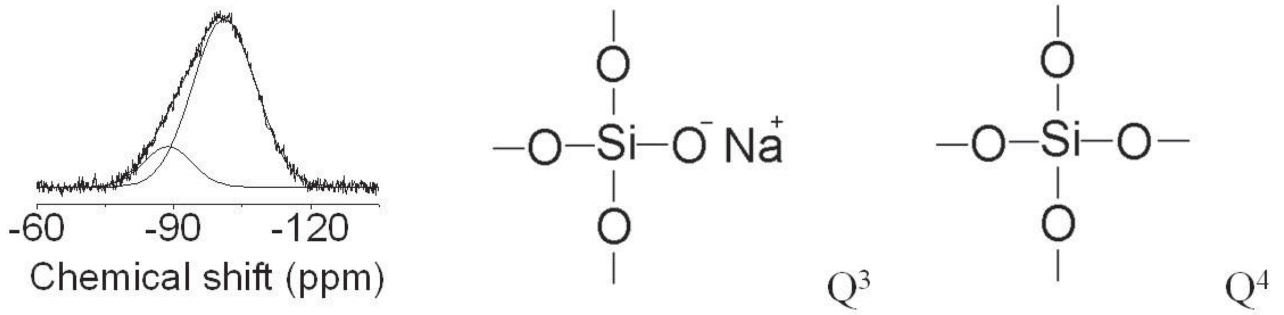

Fig. 2: ^{29}Si MAS NMR pattern of (a) $(Na_2O)_{0.36}(SiO_2)_{0.39}(B_2O_3)_{25}$ glass. Schematic representation of Q^3 and Q^4 structural units are shown in Fig. 2 (b) and (c) respectively. (All chemical shift values are expressed with respect to tetra methyl silane (TMS)). Spinning speed was 5 kHz.

^{11}B MAS NMR patterns of sodium borosilicate glass having composition $(Na_2O)_{0.36}(SiO_2)_{0.39}(B_2O_3)_{25}$ is shown in Figure 3. The pattern consists of a sharp peak around -1 ppm and a broad peak around 11 ppm. Based on the previous ^{11}B MAS NMR studies [2] the sharp peak has been attributed to boron in tetrahedral coordination and broad peak to boron in trigonal coordination. As ^{11}B is a qudrupolar nucleus with spin I = 3/2, quadrupolar interaction around the nuclei will be quite significant when it occupies a site with non-cubic symmetry, like that in trigonal configuration (BO_3 structural units). Unlike this, in tetrahedral configuration (BO_4 structural units) boron is having cubic symmetry and hence negligible quadrupolar interaction. Thus BO_3 structural units give rise to broad NMR line shape and BO_4 structural units give rise to sharp NMR line shape. Taking in to consideration of intensity of spinning sidebands and the detector efficiencies of BO_3 and BO_4 structural units (using the standard compound like borax), relative concentration of the two types of born structural units in the glass can be calculated. Schematic representation of BO_3 and BO_4 structural units attached with silicon structural units in sodium borosilicate glass is also shown in Fig. 3. The relative concentration of BO_3 and BO_4 structural units are also found to have strong influence on the thermo-physical properties of glasses like thermal expansion coefficient and glass transition temperatures. In the following section use of NMR to understand the structural aspects of representative $GaPO_4$-$AlPO_4$ sample in nano-size dimensions is given.

Structural characterization of nanomaterials using solid state NMR

$GaPO_4$, $AlPO_4$ and their solid solutions have got potential application as piezo-electric materials. Nanoparticles of $GaPO_4$-$AlPO_4$ with core shell geometry and having an average crystallite size of 50 nm were prepared by precipitation in ethylene glycol medium followed by heating at 900°C. Figure 4 shows ^{31}P MAS NMR patterns for $AlPO_4$, $GaPO_4$ and core-shell nanoparticles having $GaPO_4$ core and $AlPO_4$ shell. For $GaPO_4$ a single peak, with a chemical shift value of -9 ppm is observed. This peak is characteristic of P in hexagonal $GaPO_4$ phase. ^{31}P MAS NMR pattern for $AlPO_4$ sample is characterized by a slightly broad and asymmetric peak around -27 ppm, which is characteristic of pseudo-hexagonal trydimite phase of $AlPO_4$. ^{31}P MAS NMR pattern for core-shell nanoparticles exhibits three additional low intensity peaks around chemical shift values -14, -18 and -22 ppm, in addition to the intense peaks placed around -9 and -27 ppm. These three peaks correspond to P structural uints having varying number of Ga^{3+} and Al^{3+} as the next nearest neighbors. From the detailed ^{31}P MAS NMR studies on $AlPO_4$-$GaPO_4$ solid solutions having different composition [1] it is inferred that for the core shell particles, there exist mixed configurations of the type P_{3Ga1Al}, P_{2Ga2Al}, P_{1Ga3Al} with varying concentrations. This can happen only at the interface of the core shell particles, where the two compounds chemically interact with each other. It is of interest to

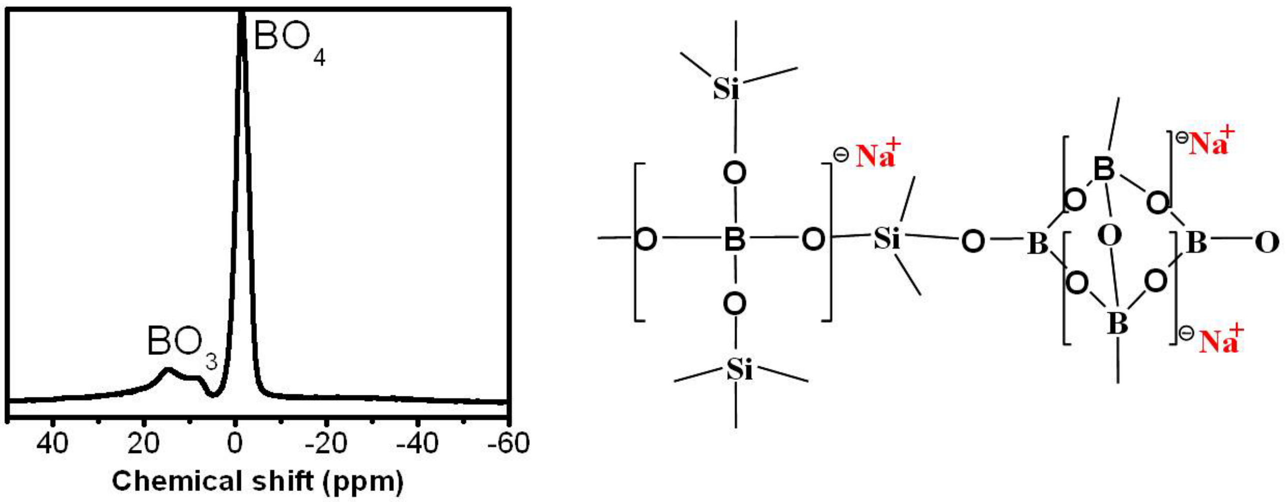

Fig. 3: ^{11}B MAS NMR pattern (left) of $(Na_2O)_{0.36}(SiO_2)_{0.39}(B_2O_3)_{25}$ glass. Schematic representation of BO_4 and BO_3 structural units attached to silicon is shown in the right. (All chemical shift values are expressed with respect to 0.1M aqueous solution of H_3BO_3). Spinning speed was 10 kHz.

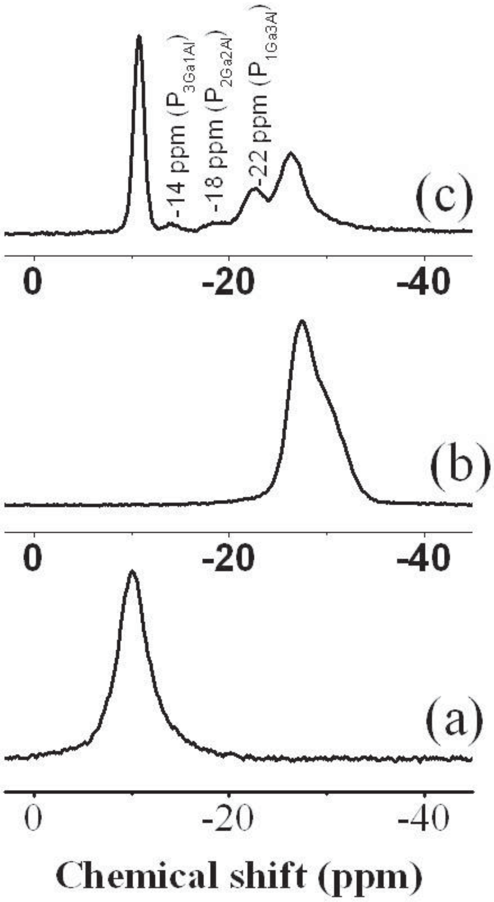

Fig. 4: ^{31}P MAS NMR patterns for nanomaterials of (a) $GaPO_4$ (b) $AlPO_4$ and (c) core shell particles with $GaPO_4$ core and $AlPO_4$ shell. (All chemical shift values are expressed with respect to 85%H_3PO_4). Spinning speed was 5 kHz

mention here that this information is quite unique and can be obtained only by solid state NMR technique. Form the above studies it is concluded that MAS NMR can be very effectively used to understand the structural aspects of glassy materials and nanoparticles.

References

1. Kulshreshtha S K, Jayakumar O D, Sudarsan V..Non-random cation distribution in hexagonal $Al_{0.5}Ga_{0.5}PO_4$. *J. Solid State Chem.* 183 (2010): 1071-74
2. Mishra R K, Sudarsan V, Tyagi A K, Kaushik C P, Kanwar Raj, Kulshreshtha S K, *Journal of Non-Cryst. Solids* 352 (2006): 2952–2957.

NOVEL EXTRACTANTS IN THE BACK-END OF NUCLEAR FUEL CYCLE

P.N. Pathak
Radiochemistry Division

Dr. P.N. Pathak is the recipient of the DAE Scientific & Technical Excellence Award for the year 2010

Abstract

Extensive studies have been carried out on the evaluation of novel extractants in the back-end of the nuclear fuel cycle. A process flow sheet has been proposed for the reprocessing of AHWR spent fuels employing *N,N*-dialkyl amides as alternative extractants to TBP. Whereas branched chain *N,N*-di(2-ethylhexyl) isobutyramide (D2EHIBA) has been found promising for selective extraction of U-233 from irradiated Th; straight chain *N,N*-dihexyl octanamide (DHOA) appears attractive for the recovery of U-233 and Pu from $(Pu,Th)O_2$ spent fuels. Co-processing of U and Pu from spent fuels has also been investigated which is of interest from non-proliferation perspective. The conditions for selective recovery of U, Pu and Np from high-level waste (HLW) solutions prior to actinide partitioning have been optimized. Tetraalkyl diglycolamides have been evaluated for the partitioning of minor actinides from simulated HLW solutions. A method for Np estimation in spent fuel dissolver solution of PREFRE Plant, Tarapur was developed. *Tert*-butyl hydroquinone (TBH) was evaluated as a reductant for plutonium for partitioning cycle of the reprocessing. An analytical method has been developed and adopted for analysis of uranium in PuO_2 samples at PREFRE, Tarapur.

Introduction

Nuclear power has to play an important role to meet the world energy demand with the diminishing resources of fossil fuels. There are now over 430 commercial nuclear power reactors operating in 31 countries, with 372,000 MWe of total capacity. They provide about 13.5% of the world's electricity as continuous, reliable base-load power. In India, a large potential exists for the resource conservation through introduction of thorium fuel cycle. Proven natural uranium reserves of India are ~172,000 tonnes of U_3O_8 and those of thorium are ~650,000 tonnes. In view of this, future of India's nuclear power programme is based on a unique mix of U and Th resources available in the country and is broadly divided in three stages: (i) First stage based on natural uranium in PHWRs, (ii) Second stage based on Pu and U in Fast Breeder Reactors (FBRs), and (iii) Third stage based on extensive use of Th/^{233}U in Advanced Heavy Water Reactor (AHWRs)/Molten Salt Breeder Reactor. India has opted for a closed fuel cycle wherein the generated fissile isotopes such as ^{239}Pu (from natural U) and ^{233}U (from Th) isotopes will be reused in the reactors for power generation to effectively use U and Th resources and to minimize environmental burden.

Evaluation of N,N-dialkyl amides for reprocessing

Conventionally, PUREX and THOREX processes have been proposed for the reprocessing of U and Th based spent fuels employing TBP as an extractant. However, based on the experiences gained over last five-six decades on the reprocessing of spent fuels, some major drawbacks of TBP have been identified, such as (i) lower distribution ratio (*D*) of Pu(IV) compared to U(VI), which can lead to Pu losses to raffinate, (ii) third-phase formation tendency during the extraction of tetravalent metal ions such as Th((IV) (*relevant for Th fuel cycle*) and Pu(IV) (*relevant for fast reactor reprocessing*), (iii) deleterious nature of degradation products (mono- and dibutyl phosphoric acids) leading to decreased decontamination of U and Pu from fission products, loss of U and Pu to organic phase during stripping, and (iv) production of large volumes of secondary radioactive waste. Evaluation of alternative extractants is, therefore, desirable which can overcome at least some of these problems. In this context, completely incinerable high molecular weight *N,N*-dialkyl amides have drawn considerable attention of radiochemists as potential green extractants for actinides and have been proposed as alternatives to TBP for the reprocessing of irradiated fuels. Whereas spent fuels emanating from PHWRs and FBRs will contain U, Pu along with minor actinides such as (Np, Am, Cm) and fission products; the AHWR spent fuel assembly will require the separation of Th-^{233}U in (Th-^{233}U)O_2 fuel-pins and of Th-^{233}U-Pu in (Th-Pu)O_2 fuel-pins. Therefore, AHWR spent fuel reprocessing adds new step of segregation of (Th,Pu)O_2 and (Th,^{233}U)O_2 pins. This suggests that additional provisions are required in reprocessing plants wherein the integration of PUREX and THOREX processes can be realized. An attempt was made on the identification of *N,N*-dialkyl amide based extractants alternative to TBP in the THOREX as well as in the PUREX processes.

Branched chain *N,N*-di(2-ethylhexyl) isobutyramide (D2EHIBA, Fig. 1) was found as a promising alternative extractant to TBP under THOREX process conditions where ppm concentration of ^{233}U, the fissile isotope produced on the irradiation of ^{232}Th, needs to be separated efficiently from the bulk of Th and large number of fission products. Laboratory batch as well as mixer settler studies were performed under THOREX feed conditions using 0.5 M D2EHIBA as well as 0.18 M TBP (5 %) solutions in *n*-dodecane as extractants. Significant improvement in the separation of ^{233}U from Th and fission products was achieved by employing 0.5 M D2EHIBA in *n*-dodecane as compared to that of 0.18 M TBP (the THOREX solvent) (Fig. 2). In addition, a process flow sheet was developed for the reprocessing of three component (comprising U, Pu and Th) AHWR spent fuel feed solution using straight chain *N,N*-dihexyl octanamide (DHOA, Fig. 3) as an alternative to TBP.

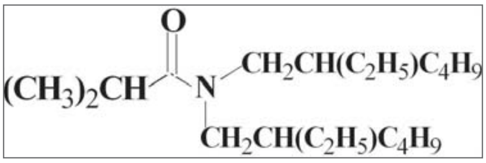

Fig.1: D2EHIBA

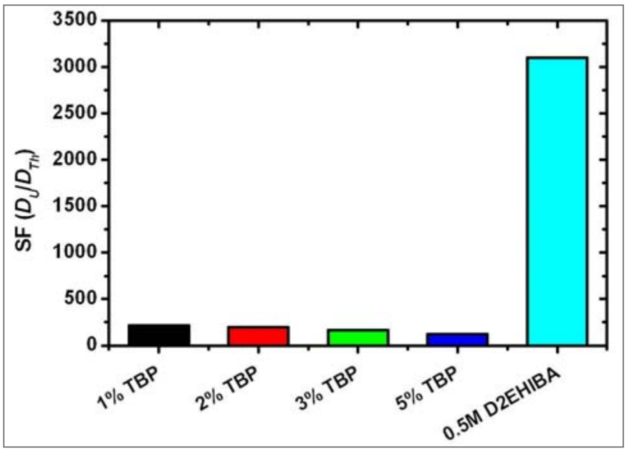

Fig.2: Comparison of SF values for TBP and 0.5M D2EHIBA under Thorex feed conditions

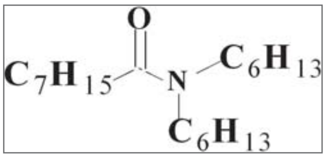

Fig.3: DHOA

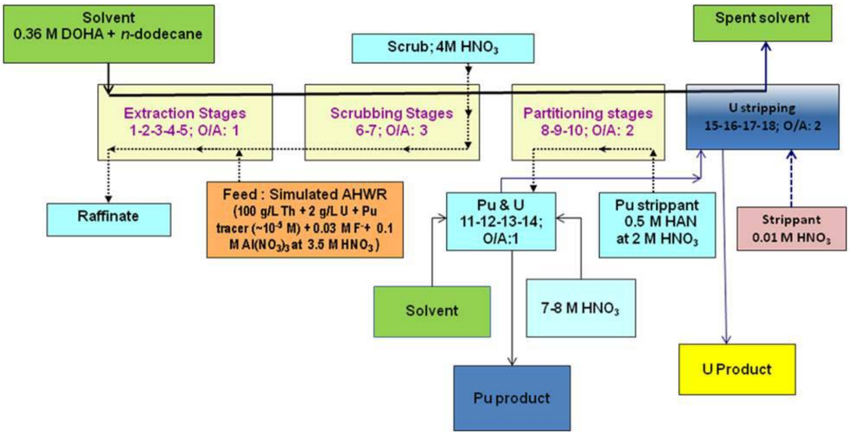

Fig. 4: Proposed flow sheet for AHWR spent fuel reprocessing using 0.36 M DHOA/*n*-dodecane

The experimental data demonstrated that 0.36 M DHOA/*n*-dodecane appears an attractive alternative of 0.18 M TBP/*n*-dodecane with respect to number of stages required for extraction, scrubbing and stripping of U and Pu (Fig. 4). In addition, the organic waste volume generation in the case of 0.36M DHOA was approx. half of that generated using 0.18 M TBP. The evaluation of hydrodynamic parameters and radiolytic degradation behavior also suggested that 0.36 M DHOA can be used as solvent for the reprocessing of AHWR spent fuel.

Advanced fuel cycle scenarios have led to a renewed international interest in the development of separation schemes for co-recovering U/Pu from spent fuels. Based on batch as well as mixer settler studies, DHOA (Fig. 3) was identified as a promising candidate for the reprocessing of spent fuels.

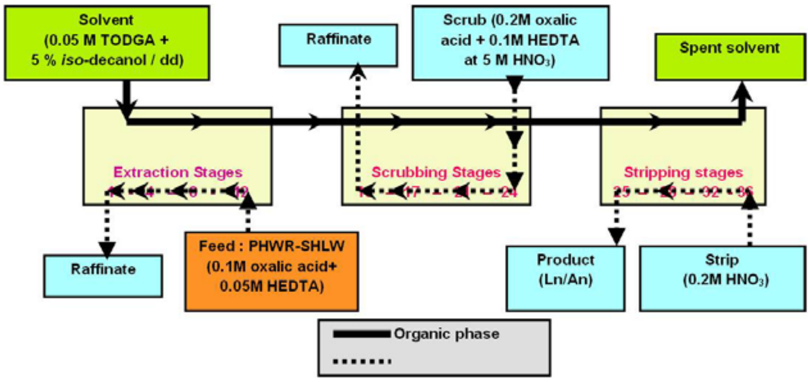

Fig. 5: Proposed flow sheet for actinide partitioning

Batch as well as mixer settler studies were carried out to evaluate DHOA and TBP for the coprocessing (co-extraction and co-stripping) of U and Pu from spent fuel under varying concentrations of nitric acid and of uranium as well as under simulated PHWR and Pu rich spent fuel feed conditions relevant for fast reactor fuel reprocessing. DHOA displayed better recovery of Pu and DF of U/Pu with respect to fission product/structural materials. Radiolytic degradation studies suggested that performance of DHOA was better than that of TBP under PUREX process conditions.

Actinide partitioning studies

The conditions for selective recovery of U, Pu and Np from high-level waste (HLW) solutions prior to actinide partitioning were optimized employing TBP or DHOA as extractants. Extensive evaluation of tetraalkyl diglycolamides (*including batch extraction, mixer settler runs and hydrodynamic parameters*) viz. *N,N,N′,N′*-tetraoctyl diglycolamide (TODGA) and *N,N,N′,N′*-tetra(2-ethylhexyl) diglycolamide (TEHDGA) was carried out for the partitioning of minor actinides from simulated HLW solutions, as a part of the taskforce constituted for the selection of suitable extractant system for actinide partitioning. Based on these studies, a process flow sheet (Fig. 5) has been proposed employing TODGA as the extractant.

Analytical separations

Experimental conditions were optimized for the estimation of Np in spent fuel dissolver solution at PREFRE, Tarapur using 2-thenoyltrifluoroacetone (HTTA) as extractant and its estimation was carried out by ICP-AES. The method is precise and accurate yielding Np analytical recovery of 99±1 %. *Tert*-butyl hydroquinone (TBH) was evaluated as a plutonium reductant for reprocessing and analytical applications. A method was developed for the separation of trace concentrations of U from PuO_2 (products) and is adopted for U analysis by ICP-AES.

Acknowledgements

Author wishes to thank Dr. P.K. Mohapatra, Head, Actinide Chemistry Section (ACS), Radiochemistry Division for his keen interest in this work. He thanks all colleagues of ACS for their valuable support. He gratefully wishes to thank Dr. K.L. Ramkumar, Director, RC&I Group, Dr. S.K. Aggarwal, Associate Director, RC&I Group, and Dr. A. Goswami, Head, Radiochemistry Division for their constant encouragement.

References

1. P.N. Pathak, D.R. Prabhu, A.S. Kanekar, P.B. Ruikar, A. Bhattacharyya, P.K. Mohapatra, V.K. Manchanda. *Ind.& Eng. Chem. Res.,* 43 (2004) 4369.
2. P.N. Pathak, A.S. Kanekar, D.R. Prabhu, and V. K. Manchanda, *Sep. Sci. Technol.*, 44(15) (2009) 3650.
3. Neelam Kumari, P.N. Pathak, D.R. Prabhu, V.K. Manchanda. *Desalination & Water Treatment*, 38 (2012) 159.
4. S.A. Ansari, P.N. Pathak, P.K. Mohapatra and V.K. Manchanda, *Chem. Rev.*, 112 (2012) 1751.
5. S.A. Ansari, P.N. Pathak, P.K. Mohapatra and V.K. Manchanda, *Sep. Purif. Rev.*, 40 (2011) 43.

PROBING MESOSCOPIC STRUCTURES IN TECHNOLOGICALLY RELEVANT MATERIALS USING SMALL-ANGLE NEUTRON AND X-RAY SCATTERING

D. Sen
Solid State Physics Division

Dr. D. Sen is the recipient of the DAE Scientific & Technical Excellence Award
for the year 2010

Abstract

Density fluctuation in mesoscopic length scale (1-1000 nm) is crucial as far as the functionality of the materials is concerned. Mesoscopic inhomogeneities in various technologically relevant materials have been investigated using small-angle neutron and x-ray scattering. A double crystal based medium resolution SANS facility has been developed indigenously at the guide tube laboratory of Dhruva. This facility has been being used to probe various porous materials, ceramics, cements, nuclear alloys, self assembled nanostructures etc. In some cases, experimental results on evolution of mesoscopic structures have been compared with results obtained from computer modeling.

Introduction

Mesoscopic structures (1-1000 nm) in various technologically important materials decide, to a great extent, the application of those materials for some specific purposes. Such structural features include precipitates in an alloy, pores in porous media, nanostructures, self assembled structures etc.

Small-angle neutron (SANS) and x-ray scattering (SAXS) are powerful techniques [1], which provide statistically averaged information on mesoscopic structures. Typical information obtained from small-angle scattering are size, shape, size distribution, spatial correlation, number density etc. Further, SANS/SAXS can provide quantitative measure of self-similarity/self-affinity in fractal systems. For probing porous materials, small-angle scattering has special advantage that it probes both closed and open pores unlike porosimetric techniques. Small-angle scattering and electron microscopy are complementary to each other. While Scanning electron microscopy (SEM) or transmission electron microscopy (TEM) provides direct information about the density fluctuations over a local zone, small angle scattering provides statistically averaged information in bulk samples.

SANS and SAXS have been used [2-10] extensively to investigate various technologically relevant materials such as, membranes, nanocomposites [2-5], nuclear materials like Zircaloy-2 fuel cladding tube, Maraging steel, 13-8 Mo PH steel [6], ceramics [7], cements [8], etc. Some useful naturally occurring materials like coal, porous rocks etc. have also been dealt with.

A double crystal based Bonse Hart type medium resolution SANS instrument (MSANS) (Fig. 1) has been indigenously developed [9] at the guide tube laboratory of Dhruva reactor, Trombay. This instrument has been calibrated with respect to the Ultra SANS instrument S18 at Institute Laue Langevin, Grenoble, France. The accessible wave vector transfer (q) for MSANS instrument is ~0.003 to 0.173 nm^{-1}. SANS experiments are performed primarily using this facility. In a few cases, the pinhole collimation SANS instrument, at guide tube laboratory, DHRUVA and SANS instruments at JCNS, Germany have also been used to obtain scattering data over a wide q range. For SAXS

Fig. 1: MSANS facility at the guide tube laboratory, DHRUVA and schematic diagram of MSANS

experiments, either laboratory based SAXS instrument or SAXS beamlines at synchrotrons have been used. Results from some of our recent work are discussed below.

Carbide precipitates in solution quenched PH 13-8 Mo stainless steel

PH13-8 Mo, because of its high strength and toughness, coupled with good corrosion resistance, is often used in aircraft, nuclear reactor, petrochemical plants and many other challenging applications. SANS data [6] from solution quenched (from 1000° C) sample for two different sample thicknesses are shown (Fig. 2a). Single scattering profile has been estimated (inset of Fig. 2a) from the experimental profiles of specimens of different thickness. TEM (inset of Fig. 2a) shows the presence block like precipitates. The size distribution of the parallelepiped block precipitates, estimated from SANS, is shown in Fig. 2b.

Hierarchical structure in spray dried nanocomposites:

Spray drying is regarded as an indispensable industrial process since long time because of its wide use in various industries. Recently, this method has embellished [2-5] itself in nano-science and nano-technology. For slow drying rate, a spray dryer is built [10] indigenously and for faster drying rate, LABULTIMA spray dryer is installed. Using this spray drying technique and *E.coli* as template materials, porous silica nanocomposites have been synthesized. It has been found [11] that a coloumn of

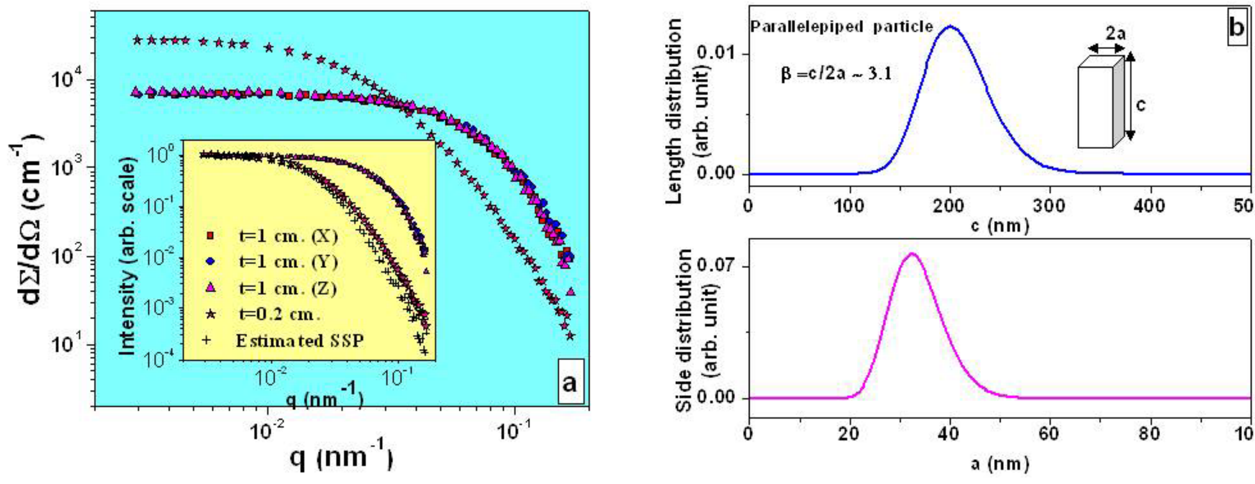

Fig. 2. (a) SANS profiles from PH 13-8 Mo stainless steel. Inset shows the TEM micrograph of the block type precipitates. (b)Estimated size distribution of the precipitates.

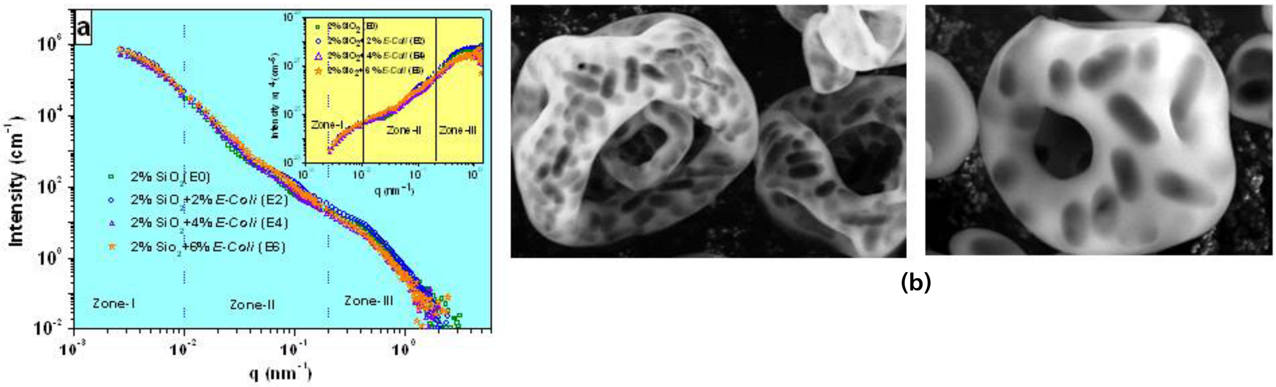

(b)

Fig. 3: (a) SANS profiles from E. coli templated grains. (b) SEM micrographs of the grains.

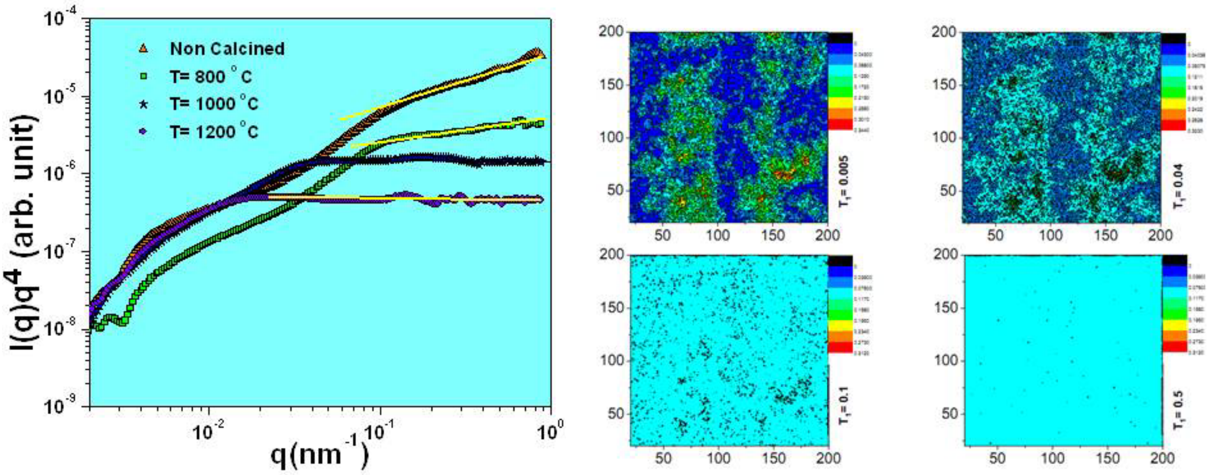

Fig. 4: SAXS profiles of Non Euclidean surface of nanoceramics in Porod representation (left panel). Colour map of the height of simulated rough surface at different stages of smoothening

such porous grains can efficiently filter out *E. coli* from drinking water. Various issues on evaporation induced self assembly have been addressed [12] using SANS/SAXS.

Smoothening of non Euclidean surface under calcinations

Smoothening of fractal rough surface, in Nd_2O_3 doped CeO_2 ceramic, under calcination has been observed [7] by SAXS. Surface-fractal dimension (2.6), in the non-calcined specimen reduces with calcination temperature and gradually attains a value of 2.0 (implying a smooth surface) at high enough temperature. A Monte Carlo based computer simulation has been performed in order to explain the smoothening process of such rough surface due to the diffusion based surface transport of the materials from region of positive curvature to that of negative curvature.

Acknowledgement

I thankfully acknowledge the guidance, continuous support and encouragement received from Dr. S. Mazumder. I am also grateful to Mr. J. Bahadur and my all other collaborators.

References

1. A. Guinier and G. Fournet; *Small-Angle Scattering of X-rays* (Wiley, New York 1955).
2. D. Sen *et al.* 'Nanocomposite Silica Surfactant Microcapsules by Evaporation Induced Self Assembly: Tuning the morphological buckling by modifying

viscosity and surface charge' *Soft Matter* **8** (2012): 1955-1963.

3. D. Sen *et al.* 'Arrest of Morphological Transformation during Evaporation-Induced Self-Assembly of Mixed Colloids in Micrometric Droplets by Charge Tuning' *Soft Matter* **7** (2011): 5423-5429.
4. D. Sen et al. 'Evaporation driven self-assembly of a colloidal dispersion during spray drying: Volume fraction dependent morphological transition' *Langmuir* **25**(12) (2009): 6690-6695
5. D. Sen *et al.*, 'Buckling driven morphological transformation of droplets of a mixed colloidal suspension during evaporation induced self assembly by spray drying' *European Physical Journal-E*, **31** (2010): 393-402
6. D. Sen, A.K. Patra, S. Mazumder, J. Mittra, G.K. Dey, P.K. De 'Morphology of carbide precipitates in solution quenched PH13-8 Mo stainless steel: A small-angle neutron scattering investigation' *Materials Science and Engineering A* **397** (2005): 370–375.
7. D. Sen et al.'Smoothening of non-Euclidean surface of Nd_2O_3 doped CeO_2 nanoceramic grains under sintering: an ultra-small angle x-ray scattering investigation and a computer simulation study' *J. Phys.: Condens. Matter* **20** (2008): 035103.
8. D. Sen, S. Mazumder, and J. Bahadur, "Temporal evolution of characteristic length and fractal dimension for a non-Euclidean system". Phys. Rev. B. **79** (2009): 134207 (1-8).
9. S. Mazumder, D. Sen, T. Saravanan and P.R. Vijayaraghavan, "Performance and calibration of the newly installed medium resolution double crystal based small-angle neutron scattering instrument at Trombay". *J. Neutron Research*, **9** (2001): 39-57.
10. Arshad Khan, D. Sen, P. Kothalkar, B.K. Sapra, S. Mazumder, Y.S. Mayya 'Design and performance of a laboratory spray dryer to realize evaporation induced self-assembly of nanoparticles' *Drying Technology* **30** (2012): 679–686.
11. J.S. Melo, D. Sen, S. Mazumder and S.F. D'Souza Microbial imprinted silica nanoparticle spheres for filtration of bacteria:*IDA & APDA Conference on desalination and water purification* pp 411-417, 2010.
12. D. Sen, J. Bahadur, S. Majumdar, s. Bhattacharya (Formation of hollow spherical and doughrut microcapsules by evaporation induced self -assembly of nanoparticles: Effects of pro size and polydispersity Soft Matter. 8 (2012) 10036-10044

REACTOR COMPONENT INTEGRITY: LEAK-BEFORE-BREAK DEMONSTRATION, WELDING DEVELOPMENT AND MATERIAL AGEING DEGRADATION

P.K. Singh, V. Bhasin, K.K. Vaze and H.S. Kushwaha
Reactor Design & Development Group
and
A.K. Ghosh
Health Safety & Environment Group

Shri P.K. Singh is the recipient of the DAE Scientific & Technical Excellence Award for the year 2010

Abstract

Reactor Safety Division had undertaken large-scale piping component integrity assessment programme, to resolve issues in structural integrity, Leak-Before-Break (LBB) and ageing degradation. In this programme, reactor components of primary pressure boundary, like pipes, pipe welds and elbows, of operating Indian PHWRs and those proposed for AHWR, were tested under normal operational loads. The aim of this programme was direct verification of LBB applicability to Indian reactors and ageing assessment of Nuclear Power Plants (NPPs). One of the unique features of this programme was that components and its welds of actual or near actual size were tested under different loading conditions for direct verification and realistic quantification of safety margins. In addition, the data has helped in benchmarking of existing analytical methods for fatigue life prediction. In this prorgramme, thrust was also given to quantify the life limiting mechanisms, identify measures and develop technologies to enhance the operating life of the components. Automated Ball Indentation (ABI) technique has also been developed for the in-situ measurement of material properties of components.

Introduction

The Leak-Before-Break (LBB) assessment of pressurized nuclear components, for example Primary Heat Transport (PHT) piping, is done for two reasons. First, to provide assurance of early warning before any major break in pressure boundary occurs. In this regard the calculations also help in serving design basis for leak monitoring devices, etc. Secondly, to achieve design simplifications, this in turn, leads to minimization of design and operational penalty. This is due to the fact that, if LBB is demonstrated, then dynamic effects resulting from rupture of the pipe need not be considered as design basis loads. This results in lesser operational stresses and improves the accessibility to pipes for in-service inspection. This in turn reduces the men-rem exposure during maintenance and inspection.

For verification of LBB (in case of Indian PHWRs and AHWR) three categories of tests were conducted. In the first category, the aim was to assure intrinsic toughness of material and rule out any material degradation owing to long-term ageing. In the second category of LBB verification tests, large size components were subjected to fatigue loading of amplitudes anticipated in normal operation of NPPs. In the third category of LBB verification tests, components having pre-machined through wall cracks were subjected to high amplitude loads and it was demonstrated that ultimate fracture load is adequately higher than the postulated design basis accident loads. These three categories of tests clearly demonstrated the LBB applicability to Indian NPPs and have helped in identifying the measures and technologies for assuring longer life of new generation reactors.

Material Property Database Generation: LBB Level 1

In level-1 it is ensured that materials are ductile, components have adequate design margins and there are no unacceptable sized flaws. Specimen level tests, [1-3], were conducted to assess the intrinsic toughness of material and to quantify the material degradation owing to long-term ageing and exposure to reactor environment. Specimens were machined from different product forms such as pipes, elbows, reactor inlet/outlet header forgings and corresponding weld joints. The variability also included different orientations of crack and loading, such as longitudinal and circumferential directions, along with different heats (or mill lots) of material. Tests on specimens were conducted to generate the material property database, which included tensile properties/stress-strain curves, low cycle fatigue curves, cyclic stress strain curves, fatigue crack growth rate constants, monotonic and cyclic fracture properties (i.e., J-resistance curves) and impact toughness.

Fatigue Investigations: LBB Level 2

The large size components were subjected to fatigue loading of amplitudes anticipated in normal operation of NPPs. In all 47 tests, [4-6], on pipes and elbows were conducted on sizes varying from 6″ NB to 16″ NB and made of carbon steel or stainless steel materials. In these tests part through thickness notches were machined in circumferential direction (for pipes) and circumferential or axial direction for elbows. The fatigue crack initiation and crack growth tests were conducted under varying notch sizes (aspect ratio), in air and water with controlled chemistry and different load combinations. A typical test setup (Fig.. 1) and the measured crack growth versus cycles in different tests have been shown in Fig.. 2. The Fig. 4 clearly shows that the crack growth in depth direction is much faster than in surface direction. These investigations constitutes Level-2 LBB and it was concluded that in any combination of load, environment and crack shape / size the fatigue crack growth would always produce small leak and sudden break is ruled out. This is one of the important requirements of level 2 LBB qualifications. The fatigue crack growth tests performed

Fig. 1: Actual Pipe test set up

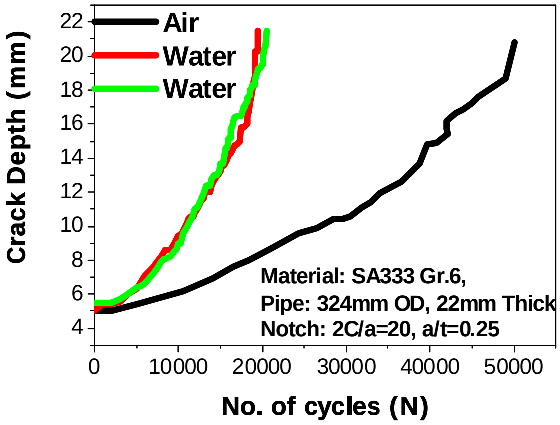

Fig. 2: Crack growth in pipe in air and water environment

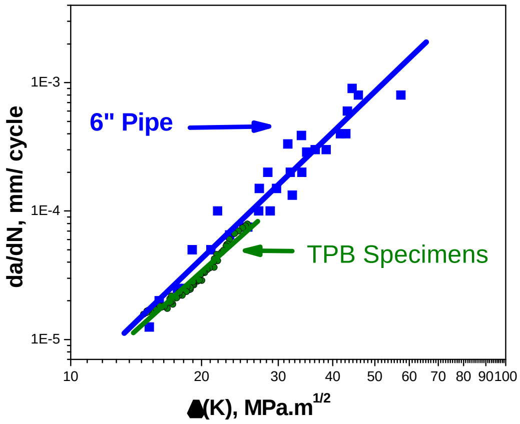

Fig. 3: Crack growth rate in pipe and TPB specimens

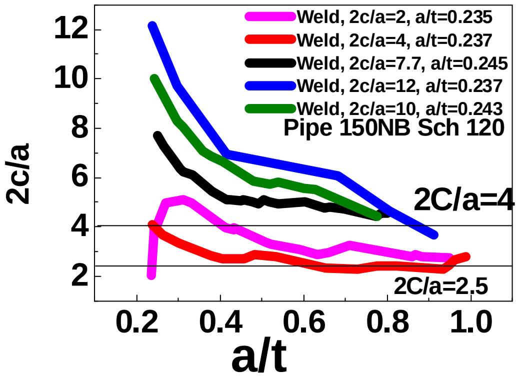

Fig. 4: Clearly shows that the crack growth in depth direction is much faster than in surface direction

on specimens and components, depicts that the transferability of fatigue crack growth rate data, from specimen to component, is not a major issue, see Fig..3. This demonstrates the Leak-Before-Break design criteria of high energy piping system of PHWR and AHWR. It has been also found that the fatigue life of the notched pipe subjected to vibration+cyclic loading is reduced by 70% compared to that subjected to cyclic loading only. This finding is not reported in the available literature so far.

Fracture Investigations on Pipe Welds: LBB Level 3

The austenitic stainless steel pipe and pipe welds having pre-machined cracks were subjected to monotonically increasing loads and the test results helped in demonstrating that ultimate fracture load is adequately higher than the postulated design basis accident loads, thereby validating LBB Level 3. 37 numbers of fracture tests, [7], were conducted on pipes and elbows to directly determine the ultimate fracture load and validate the analytical procedures used to for its evaluation. To address the fracture resistance characteristics pipe welds, tests were conducted on various sizes of full-scale pipe and pipe welds.

The fracture tests (Fig.s. 5-8) demonstrated that the load bearing capacity of a cracked pipe is higher than the maximum anticipated load during a Safe Shutdown Earthquake, thus verifying the level 3 criterion of LBB. The experimental database was used for validating the existing correlation for limit load calculation for pipes. Although the available limit load expression gives reasonable prediction for the base metal, it is not conservative for pipe welds. Suitable correction factors have been suggested for GTAW and GTAW+SMAW welds. Advantage of the Gas Tungsten Arc Welding (GTAW) over Shielded Metal Arc Welding (SMAW) process for welding of pipes of SS304LN material has been brought out with reference to the fatigue, fracture and metallurgical properties.

Development of Narrow Gap Welding Technique

In order to minimize the failure due to IGSCC austenitic stainless steel pipe welds, it is desirable to have compressive stress or low tensile stress achievable at the weld root and reduced sensitization. To address this issue the work on development of welding technique and suitable welding process for welding of stainless steel pipe was carried

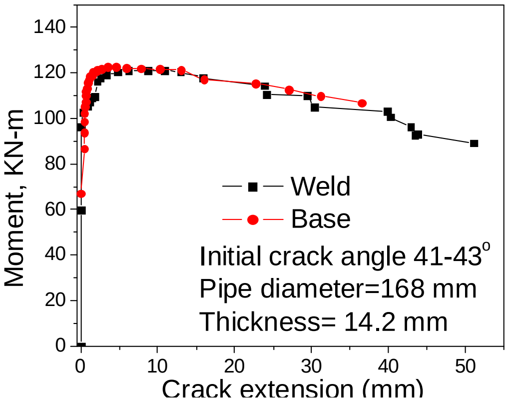

Fig. 5: Fracture resistance in168 mm OD

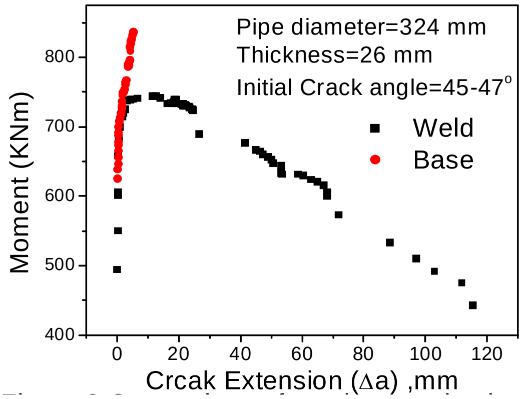

Fig. 6: Fracture resistance in 324 mm OD

Fig. 7: Crack Growth in Pipe Base of 168 mm OD

Fig. 8: Crack Growth in Pipe Weld of 168 mm OD

out. In this study [8], widely used welding processes such as Gas Metal Arc welding (GMAW), Gas Tungsten Arc Welding (GTAW) and Shielded Metal Arc welding (SMAW) and Hot wire GTAW with narrow gap welding technique were considered.

It was shown that residual stress is significantly reduced (Fig. 9). The reduction in residual stress is due to the low heat input because of the adopted welding process and technique. Sensitisation resistance is further improved by adopting high deposition rate welding (hot wire GTAW) and narrow gap technique. Lower heat input leads to higher cooling rate (Fig. 10) giving more margins on sensitization during welding. This has been confirmed by measuring temperature in HAZ of the weld joints. Finally it has been demonstrated that use of hot wire GTAW with narrow gap technique is most desirable technique for welding of stainless steel pipes in terms of low residual stress, less sensitization and low embrittlement.

Life Related Issues: AHWR

In view of the proposed 100 years life of the AHWR, and unavailability of the material data and experience to ensure the designed life of the main heat transport system piping made of stainless steel, there was need to demonstrate the proposed life by carrying out studies considering the life limiting degradation mechanism of the material. These types of tests are usually done at accelerated ageing at higher temperature, which may call for extrapolation of data at operating temperature. The unique feature of these are that exposure temperature is kept near to operating temperature. This in turns calls for long exposure temperature but ensures prediction of realistic scaling of damage. Studies on low temperature sensitization (LTS) and low temperature embrittlement (LTE), which are the life limiting degradation mechanisms in AHWR piping was carried out to assure the long life [9].

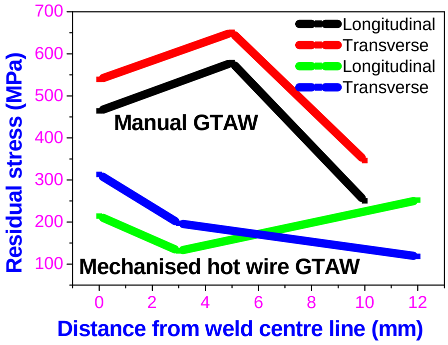

Fig. 9: Residual stress in Manual GTAW and Hot Wire GTAW

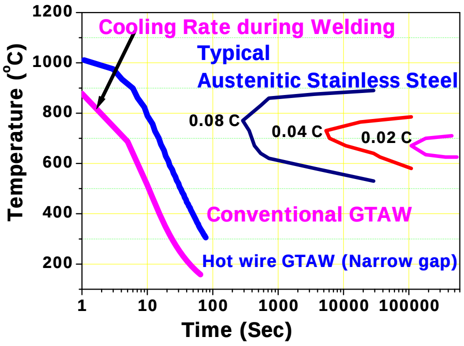

Fig. 10: Temperature vs. Time plot shows Narrow Gap Welding leading to high margin against sensitization

For LTS, duration of 1300 and 8000 Hours at 450°C and 400°C respectively simulates the 100 years at 300°C. Thermal ageing at 350°C at 50000 hours is also planned. Thermally aged materials were tested for susceptibility to sensitization by carrying out the tests as per ASTM A262 and Electo-Potentiokinetic Reactivation (EPR) method. It was concluded that degree of sensitization increases with ageing time. However, it was less than acceptable limit. LTE studies were carried out to confirm that austenitic stainless steel (SS 304LN) welded by E308L/ER308L would not have problem of loss in toughness during service of the plant. The ageing durations planned are of 5000, 10000, 20000 and 50000 Hours at temperatures 400°C, 350 and 300°C. Loss in toughness has been quantified by carrying out the impact test. The result indicates no reduction in toughness for the ageing duration of 5000 hours at various temperatures.

In-situ Measurement of Material Properties: Portable Automated ball Indentation (ABI)

Portable ABI system for monitoring the degradation in mechanical and fracture properties in situ was developed. The system has been designed and fabricated in different modules such as base for attaching on the component, grinder for cleaning, actual indentation system, control and display. These modules can be assembled on the piping components insitu in plants (Fig.11) and thereafter measurements (Figs. 12-13) can be made. Carrying out the conventional tests and comparing the properties obtained from the ABI system validated the ABI system. Various types of material such as steel, zircalloy, copper, weld joints etc has been tested for validation of system

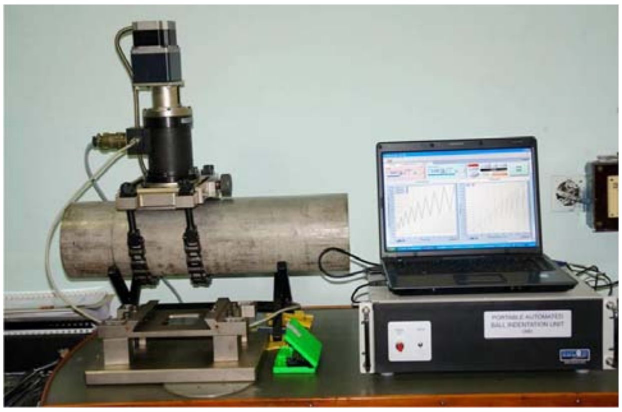

Fig. 11: Portable ABI System

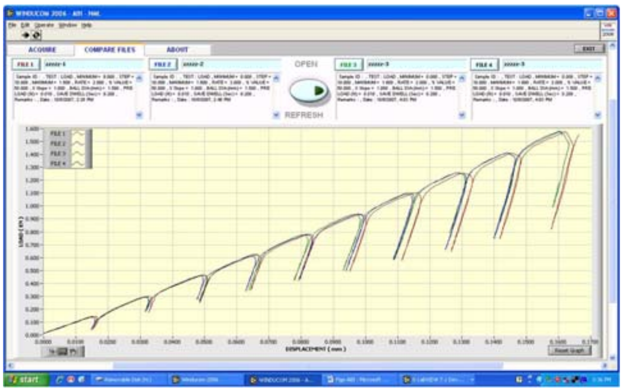

Fig. 12: Load-Indentation depth

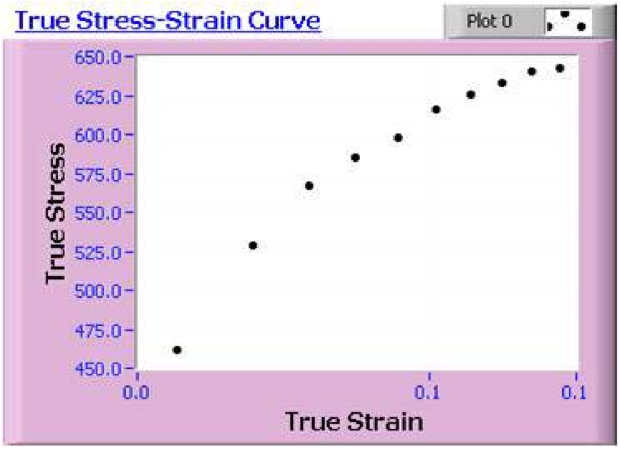

Fig. 13: True stress-strain plot

Summary

The component integrity assessment programme has assured the overall structural safety and LBB applicability to Indian PHWR and AHWR. It has helped in identifying the measures and technologies for assuring longer life of new reactors. The studies were useful in benchmarking and modifying existing analytical methods for prediction of crack growth, ultimate fracture loads and ageing assessment.

References

1. Singh P.K., Chattopadhyay J., Kushwaha H.S; Tensile and Fracture properties evaluation of PHT system piping material of PHWR; *International Journal of Pressure Vessel and Piping* 75 (1998) 271-280
2. Singh P.K., Dubey J.S., Chakrabarty J.K., Vaze K.K., Kushwaha H.S "Evaluation of fatigue crack growth and fracture resistance of SA350 LF2 material" *ISIJ International,* Vol. 43 (2003) No. 8, pp 1274-1279
3. Singh P.K., Ranganath V., Tarafder S., Prabha Prasad, Bhasin V., Vaze K.K., Kushwaha H.S. "Effect of cyclic loading on elastic-plastic fracture behavior of PHT system piping material of PHWR" *International Journal of Pressure Vessel and Piping* 80, Issue 10, October 2003) 745-752.
4. Singh P.K., Vaze K.K., Kushwaha H.S., Pukazhendi D.M., seetharaman S., Murthy D.S.R., "Fatigue crack growth and fracture behaviour of carbon steel elbows", *Journal of Aeronautical Society of India,* Vol. 54, No. 4, pp 374-382, November 2002.
5. Singh P.K., Vaze K.K., Bhasin V., Kushwaha H.S, Gandhi. P., Murthy D.S.R "Crack initiation and growth behaviour of cuircumferentially cracked pipes under cyclic and monotonic loading" *International Journal of Pressure Vessel and Piping* 80, Issue 9, September 2003 629-640.
6. P.K.Singh, V.Bhasin, K.K.Vaze, A.K.Ghosh, H.S.Kushwaha, P.Gandhi, D.S.R.Murthy, S.Sivaprasad "Fatigue studies on carbon steel piping materials and components: Indian PHWRs" *Nuclear Engineering & Design,* Volume 238, Issue 4, April 2008, pp 801-813.
7. P.K.Singh, K.K.Vaze, A.K.Ghosh, H.S.Kushwaha, D.M.Pukazhendi, D.S.R.Murthy "Crack resistance of austenitic stainless steel pipe and pipe welds with circumferential crack under monotonic loading" *Fatigue and Fracture of Engineering Material and Structures* Vol. 29 (11), November 2006, 901-915.
8. P.K.Singh, V.Bhasin, K.K.Vaze, A.K.Ghosh, H.S.Kushwaha, "Structural integrity of main heat transport system piping of AHWR" *BARC Newsletter* Issue No. 299 December 2008.
9. Raghuvir Singh, Gautam Das, P.K. Singh, I. Chattoraj "Low temperature sensitization behavior of base, heat affected zone and weld pool in AISI 304LN" *Metallurgical and Materials Transactions A:* Volume 40, Issue5 (2009), Page 1219

RESONANCE IONIZATION (MASS) SPECTROSCOPY OF SAMARIUM ATOM & LASER IONIZATION MASS SPECTROMETRY OF BIOMOLECULES

T. Jayasekharan
Applied Spectroscopy Division

Dr. T. Jayasekharan is the recipient of the DAE Scientific & Technical Excellence Award for the year 2010

Traditionally quantum states of an atoms and molecules are investigated using single photon absorption and emission spectroscopic technique. However these techniques has some serious limitations, for example (i) An excited state having the same parity as that of the ground state is not accessible through single-photon absorption from the ground state. (ii) Absorption cross sections become poorer as one goes to higher-energy states. (iii) Cumbersome vacuum spectrometers must be used if the absorption/emission photon happens to lie in the vacuum-ultraviolet region. These limitations are overcome by the application of stepwise excitation of the atoms using more than one photon of tunable lasers. The spectrum of lanthanide and actinide atoms is highly complex due to its partially filled f^N shell. A complete characterization of its atomic levels in terms of multiplicity, orbital (L) and total angular momentum (J), is not an easy task. As a consequence, the information available in the literature on high-lying, Rydberg, and autoionizing states of same parity as of the ground state is scanty and limited.

Resonance Ionization Mass Spectrometry (RIMS)

Resonance Ionization Mass spectrometry (RIMS) is a highly selective and sensitive technique, in this technique atoms/molecules are selectively excited to different intermediate quantum states and finally ionized using photons of tunable laser. The photo ions are further subjected to mass analysis, RIMS thus enables both optical and mass selectivity in atoms/molecules. The spectrum of the samarium atom is highly complex because of its less-than-half-filled 4*f* shell. The ground term of Sm (I) is [Xe] $4f^6\,6s^2\ {}^7F_J$, $J=0\text{–}6_,$ and the seven low lying ground-state multiplets are readily populated when the sample is heated. Typically the percentage of population in various ground state multiplets of ${}^7F_J$, $J=0\text{–}6$ are 21.03, 37.83, 25.45, 10.89, 3.55, and 0.25 respectively at 800 k. This further complicates the identification of spectra by conventional spectroscopic techniques. The information on high-lying even-parity states of Sm (I) is limited to energies of ~31,300 cm^{-1}, and scanty data are available between 32,000 and 45,519 cm-^{1}, the first ionization potential. In order to investigate the excited quantum states of samarium atom we have designed, fabricated, and commissioned a RIMS set up in our laboratory, and the photograph of the setup is shown in Fig. 1. The data acquisition/integration of RIMS is done through a box car average and software was developed for the calibration of the unknown wavelength of the spectra. After extensive performance testing the spectrometer was used to probe the excited quantum levels of samarium atom with the objective of determining absolute energies and total

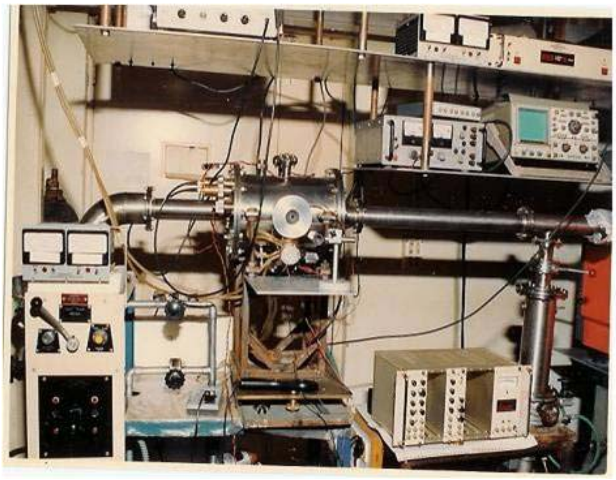

Fig. 1: Photograph of indigenously built Resonance Ionization Mass Spectrometer

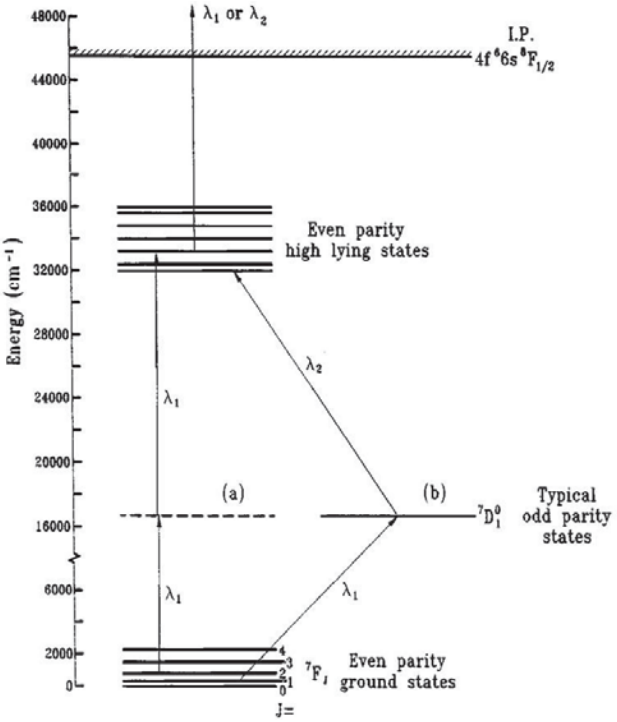

Fig. 2: Schematic of the excitation process: (a) single-color two-photon-resonant three photon ionization, (b) two-color stepwise excitation and photoionization.

angular momenta of high-lying even parity levels, as no data for such levels are available in the literature. We have used different two color two step excitation and three photon ionization scheme to map the excited energy levels of samarium atom. The schematic of the excitation process used are shown in Fig. 2. Typical photoionization spectra obtained along with reference Uranium hollow-cathode discharge lamp and Fabry-Perot etalon spectra are shown in Fig. 3. Fig. 4 shows the time of flight mass spectra of naturally occurring isotopes of samarium atoms.

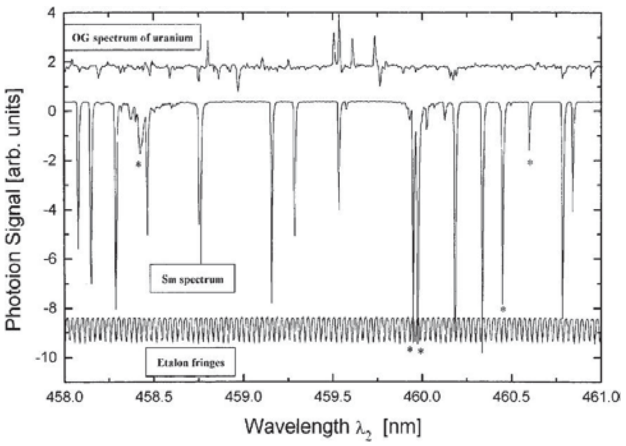

Fig. 3: Typical two-color photoionization spectra of Sm atom along with reference optogalvanic (OG) spectra of uranium and Fabry–Perot etalon transmission fringes.

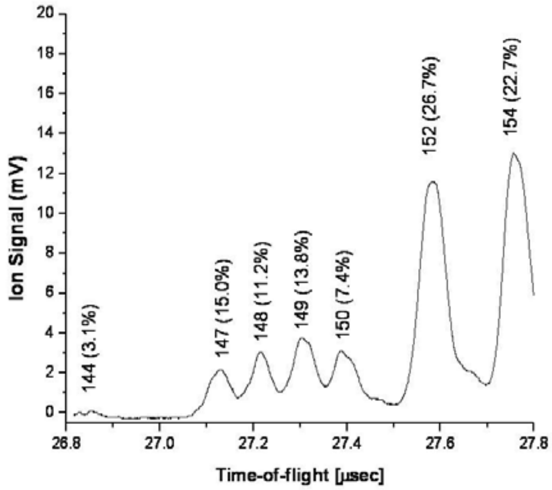

Fig. 4: Natural Isotopes of Samarium atoms resolved using RIMS

Using excimer pumped dye lasers we have recorded several single and two color photoionization spectra of samarium atoms in the wavelength region 355-615 nm. The wavelength region is covered using different dyes viz., Butyl-PBD, PBBO, Stilbene 3, Coumarin 47, Coumarin 307, Coumarin 153, Rhodamine B, and Rhodamine 6G. Analysis of thousands of spectral data results the discovery of 650 new even parity energy levels in the energy region 34850-45300 cm^{-1}, 1 bound and 3 auto ionizing Rydberg series. The energies of these levels were measured with a precision of 0.3 cm^{-1} and the energy levels were assigned unique total angular momentum (J) value after extensive and careful analysis spectral data obtained from several multiphoton excitation and ionization schemes. Analysis of Rydberg series lead to a more precise determination of first ionization potential of samarium atom 45519.64 ± 1.39 cm^{-1}, which has less uncertainty than the previously reported value and is taken as the reference data by NIST. The new energy level data will be useful in many applications like laser isotope separation, new laser transitions, trace analysis etc. Further, the data can also be used for the theoretical calculation of the atomic structure and parity non conservation experiments on Sm atom.

Laser Ionization Mass Spectrometry of Biomolecules (LIMS)

Mass spectrometry in principle is mass dispersive, and the mass spectrometers are widely used to measure mass-to-charge ratio (*m*/*z*) and abundance of ions moving at high speed in vacuum. Typically the mass spectrometer consists of an ion source, mass analyzer, and an ion detector. Ion motion in the mass analyzer can be manipulated by the application of electric and/or magnetic fields to direct the ions to a detector in an *m/z*-dependent manner. In a time of flight mass spectrometry (TOFMS) ions are accelerated in an electric field and are directed into field free drift tube where they separated according to their *m/z* value and detected by the detector. Several techniques are available to generate ions of atoms/ molecules, for example thermal ionization, spark source, plasma source, glow discharge, and ICP are usually employed to generate atomic ions for mass spectrometry. Molecular ions of volatile compounds are produced using electron impact ionization, chemical ionization, photo ionization and field ionization techniques. However the application of mass spectrometers for the analysis of biological molecules posed a greater challenge due to their poor volatility, polar, and charged nature. The development of two new ionization techniques viz., Matrix Assisted Laser Desorption Ionization (MALDI) and Electrospray Ionization (ESI) translated the biomolecules into gas phase ions without significant fragmentation, and revolutionized the range of organic molecules that can be analyzed using modern mass spectrometers as well as contributed significantly in proteomic and genomic research. MALDI is a laser based technique which produces intact protonated/deprotonated molecular ions of non volatile, thermally fragile, and massive bio molecules in gas phase. In this technique analyte macro molecules are embedded in UV/VIS/IR radiation absorbing low molecular weight organic molecules (matrix) and are deposited on a solid target and air dried. A low power UV/VIS/IR laser beam of nanoseconds pulse duration is used to desorb and ionize the analyte macromolecules from condensed phase to gas phase without much fragmentation. The ejected molecular ions are then mass analyzed using linear and/ or reflectron TOF analyzers and detected by microchannel plate detectors (MCP). The schematic of the laser desorption ionization (LDI) mass analyzer is depicted in Fig. 5.

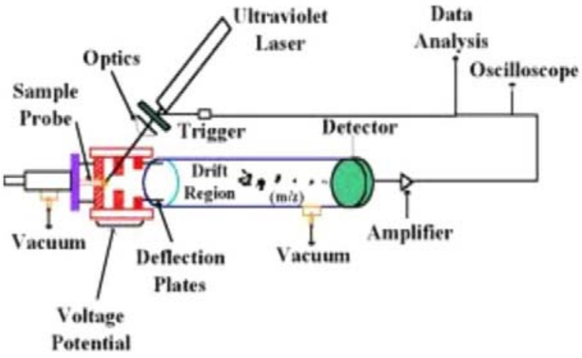

Fig. 5: Schematic of the Laser Desorption Ionization Mass Spectrometer

We have designed, fabricated and commissioned a state of the art LDI-MS equipped with both linear and reflectron TOFMS for the detection, identification and characterization of peptides, proteins, clusters, DNA, and other molecular complexes. The performance of the mass spectrometer has been tested extensively by recording the mass spectra of many different class of molecules (inorganic, organic, and biomolecules) of mass range up to 50,000 Da. The detection sensitivity of the spectrometer for peptide and proteins is in the sub picomole range. The photograph of the fully functional home built LDI mass spectrometer is shown in Fig. 6.

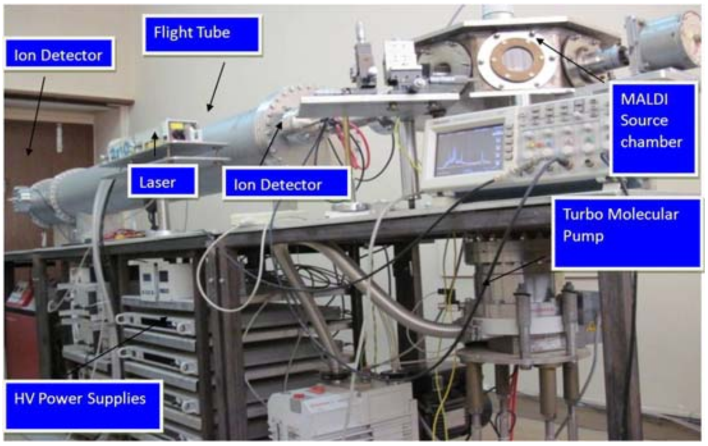

Fig. 6: Photograph of home built LDI Mass Spectrometer

Fig. 7 show the mixture of different peptides/proteins analyzed using this spectrometer. The mass spectra of proteins of higher masses obtained using this spectrometer is also shown in Fig. 8.

In addition, laser desorption ionization technique is applied for the separation of isotopes of different elements as well as molecular mass measurements of different molecules. Typical Ag isotopes resolved from silver salt is shown Fig. 9. Fig. 10 shows the LDI spectra of fullerene molecule.

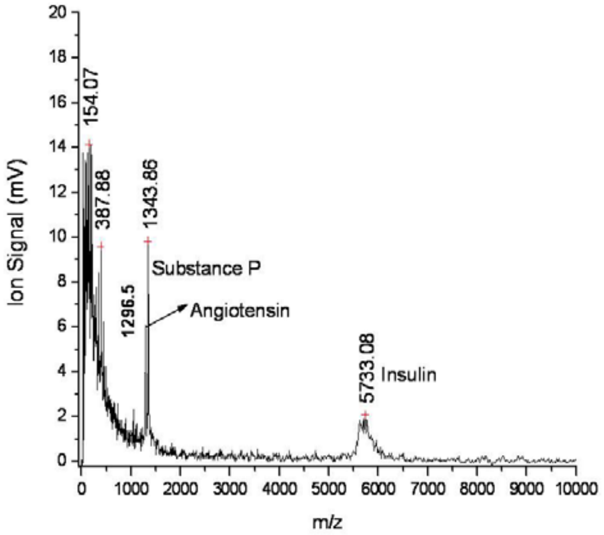

Fig. 7: Mass Spectra of peptide/protein mixtures

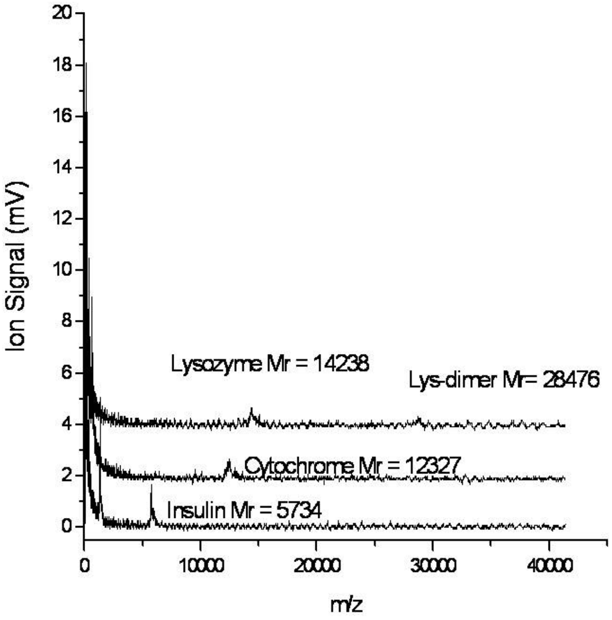

Fig. 8: Mass Spectra of higher mass proteins

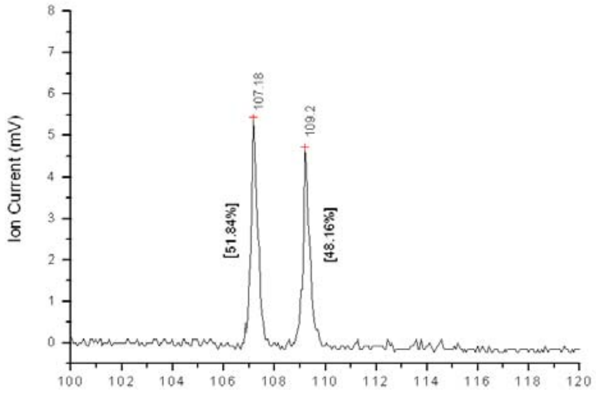

Fig. 9: Isotopes Ag^+ resolved from LDI spectra of Silver nitrate

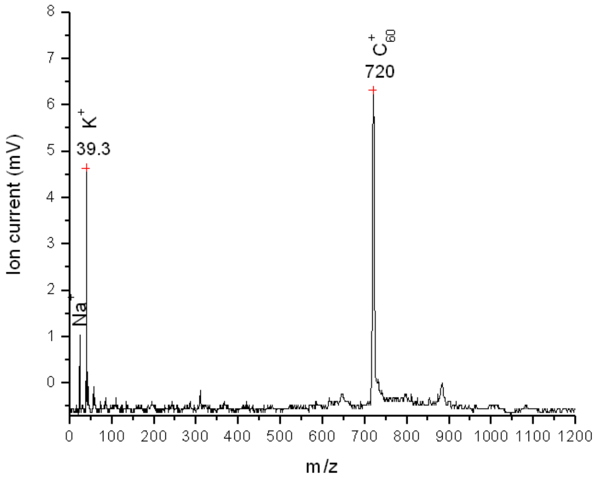

Fig. 10: LDI spectra of fullerene molecule

Acknowledgements

I am grateful to Dr. N. K. Sahoo, Head Applied Spectroscopy Division for his constant encouragement and support. I am also thankful to the personnel of Machine and Optics workshops who greatly assisted in the development of the instruments.

Publications

1. Observation of new even parity states of Sm I by resonance ionization mass spectrometry. T. Jayasekharan, M. A. N. Razvi and G. L. Bhale, J. Opt. Soc, America B: 13, 641, (1996)
2. Investigations of high lying even parity energy levels of samarium atom below its first ionization limit. T. Jayasekharan, M. A. N. Razvi and G. L. Bhale, J. Opt. Soc, America B: 17, 1607, (2000)
3. New even parity bound and autoionizing Rydberg series of samarium atom. T. Jayasekharan, M. A. N. Razvi and G. L. Bhale, J. Phys B: Atomic, Molec, and Optical Physics. 33, 3123, (2000)
4. Characterization [Peptide + $(Ag)_n$]$^+$ complexes using matrix-assisted laser-desorption/ionization time-of-flight mass spectrometry. T. Jayasekharan and N.K Sahoo, Rapid Commun. Mass. Spectrom. 24, 3562 (2010)
5. Matrix Assisted Laser Desorption Ionization Mass Spectrometry (MALDI-MS). T. Jayasekharan and N.K Sahoo, BARC News Lett. 321, 18 (2011)

STATE-OF-THE-ART MONITORING SYSTEMS AND SOFTWARE FOR ASSESSMENT OF RADIOLOGICAL IMPACT

Probal Chaudhury and Pradeepkumar K.S.
Radiation Safety Systems Division

Shri Probal Chaudhury is the recipient of the DAE Scientific & Technical Excellence Award for the year 2010

Abstract

A large number of radioactive sources are in use and are transported across the globe on a daily basis to meet the requirements in medical, industry, agriculture and research and a transport accident or a deliberate theft of such sources can lead to radiological emergency in the public domain. Furthermore, there is an increasing global radiological threat due to orphan sources or malicious acts using radioactive material. Though probability of occurrence is extremely small, a nuclear emergency at a nuclear facility, say reactor or reprocessing facility can lead to release of radioactivity into public domain. It is essential to assess the radiological impact following such emergencies for planning the appropriate emergency response to mitigate the consequences. Aerial and mobile radiation monitoring systems, software, methodologies and GIS support are developed for impact assessment following nuclear and radiological emergencies.

Introduction

There is a continuous increase in the nuclear and radiation related applications in the public domain and a large number of nuclear power reactors and research reactors are in operation. The radioactive sources in use are having different half-lives and have various strengths depending upon the application. Though all the sources are transported and used under regulatory control, there is always a possibility of some of the sources landing with the well trained and committed anti social non state actors. This gives rise to increase in the global radiological threat as the non state actors may be looking for an opportunity to use radiation in malicious activity or to create a psychological threat in the public domain. Considering the requirement of nuclear and radiological emergency preparedness[1], systems, software and methodologies have been developed.

Aerial radiation monitoring is an effective tool for rapid assessment of the impact of radioactive deposition over a large area. Due to the speed, height and access to any terrain, aerial survey is the most efficient and effective tool for deciding on response during nuclear and radiological emergencies. Aerial Gamma Spectrometry System and Compact Aerial Radiation Monitoring System are two systems developed for using in aerial platforms to carry out radiological mapping of an affected area. The systems are shown in Fig.1 and Fig.2. The systems are also used for ground based mobile monitoring as has been demonstrated in several exercises and operations[1].

Aerial Gamma Spectrometry System (AGSS)

AGSS has been developed for quick assessment of radioactive deposition over large areas following nuclear emergencies and searching of orphan sources in public domain. The system is mounted in a helicopter for carrying out the monitoring and has the capability of quantitative and qualitative (identification of radionuclide) assessment of radionuclides deposited on ground. Aerial survey technique ensures minimal exposure to the monitoring personnel. The Air to Ground Correlation Factor (AGCF) of the AGSS has been established through calibration exercises carried out over simulated ground contamination. The level of contamination on ground is computed on-line based on the altitude of flying and spectrum details and using the AGCFs.

Major components of AGSS are NaI(Tl) Detector, Pulse Height Analyzer, GPS receiver, Radioaltimeter, Radiomodem and Roentgenometer. The minimum detectable activity (MDA) of AGSS is 25 kBq/m^2 (90 nGy/h at 1 m) for Cs-137 from 100 m altitude while using four 3"x3" NaI(Tl) detectors. The integrated software package developed for AGSS includes system software with data acquisition and processing. The system acquires gamma ray spectral data and the corresponding positional co-ordinates through a Global Positioning System (GPS) receiver at an interval of two seconds and then it maps the computed activity level or counts profile on-line onto a stored digitized sitemap or using Geographical Information System (GIS). The on-line mapping enables easy demarcation of the contaminated area based on the activity levels indicated by colour codes and in identification of any hot spots instantly. AGSS has been used in several aerial monitoring of Emergency Planning Zone (EPZ) of NPPs, source search at Georgia on IAEA's request, ground based surveys of many cities[2] and during Mayapuri radiological emergency.

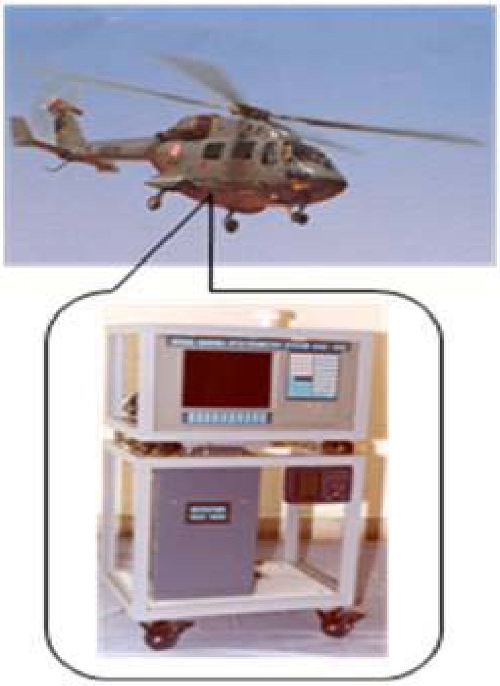

Fig. 1: AGSS installed in Helicopters and tested in many aerial gamma spectrometric monitoring

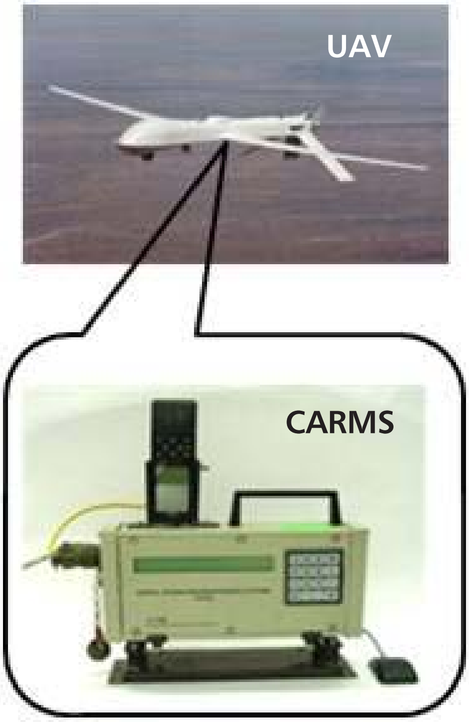

Fig. 2: CARMS to be integrated with Unmanned Aerial Vehicles (UAV) for remote aerial radiation monitoring

Compact Aerial Radiation Monitoring System (CARMS)

CARMS has been developed for gamma radiation dose rate monitoring based on GM detectors. It has been specifically designed and developed for automatic dose rate data logging for integration with Unmanned Aerial Vehicle (UAV). The dose rate data is tagged with positional information received from GPS receiver and continuously data is trasmitted online to a ground station using radiomodem. The data processing software developed for CARMS generates radiological profile of the surveyed area. The sensitivity of the system is 40 CPS per μGy/h for Cs-137. The system operates on 12-30 V DC and weighs approximately 2 kg. The system has been / can be used in various road, rail and aerial surveys to obtain radiological map of the surveyed regions and for the source search or confirmation of absence of elevated radiation level following terrorist threat[1].

Geographical Information System (GIS)

GIS for major cities and areas around NPPs have been developed to enhance the capability of quick decision making on the implementation of countermeasures

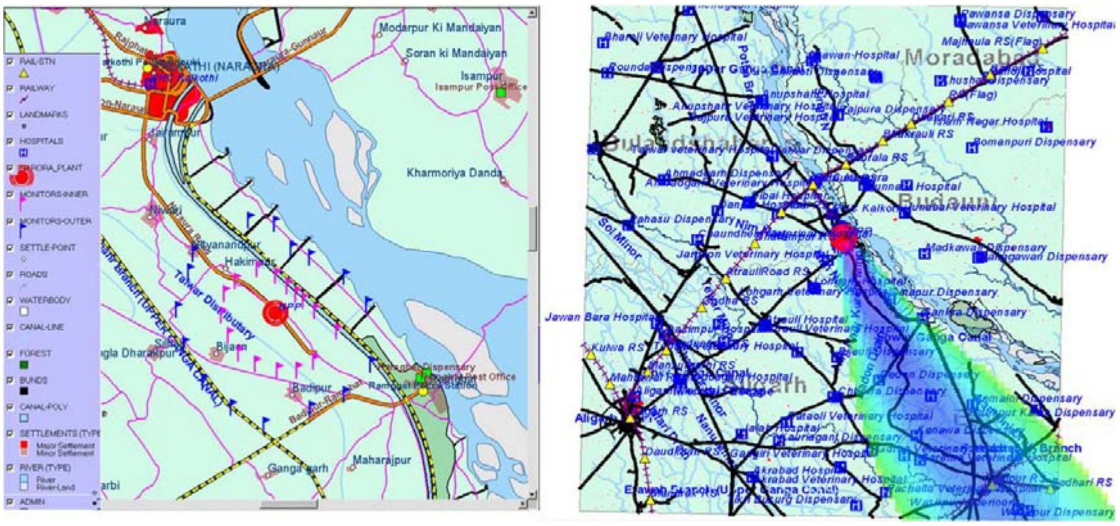

Fig. 3: Geographical Information System around Narora Atomic Power Station showing various layers with 'Radiological Forecast' (simulated) superimposed on it

following any nuclear or radiological emergency[3,4]. The important GIS layers pertaining to a nuclear emergency are roads and railway network, settlements, hospitals, shelter locations, rallying points, water bodies, land use land cover, demography etc. Various GIS layers and radiological forecast is shown in Fig.3.

A software package has been developed for computing and display of iso-doserate contours[5] on a digitized map using the data collected by mobile monitoring systems, which may be irregularly spaced. The entire area covered by the aerial or ground survey is mapped with varying color gradients corresponding to the level of contamination or dose rate in the area. The mapping feature facilitates demarcation of contaminated land and the 'hot spots', strengthening the decision support for effective implementation of countermeasures.

Survey methodologies have been designed using these aerial surveys. Fig.4 shows an ideal flight path for an aerial survey for radiological impact assessment following any nuclear disaster and Fig.5 shows aerial radiological mapping of NAPS-EPZ carried out at an altitude of 120 m by installing AGSS in a MI-17 Helicopter.

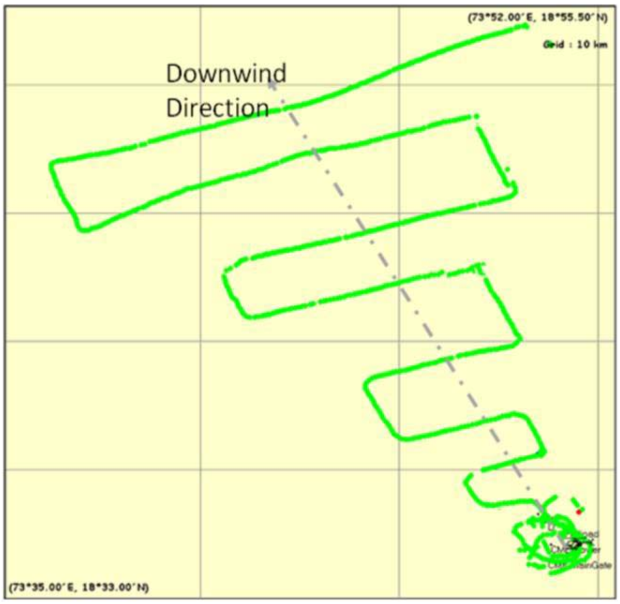

Fig.4: Ideal Aerial Radiation Mapping Flight Path for Impact Assessment as demonstrated during an aerial monitoring exercise using AGSS installed in an Advanced Light Helicopter

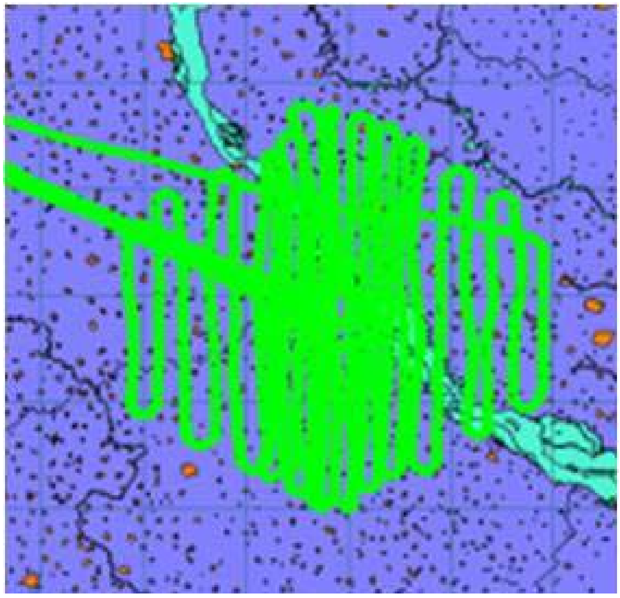

Fig.5: Online Display on the AGSS screen with the route followed during the aerial radiation scanning of NAPS – EPZ (survey conducted at an altitude of 120 m from ground)

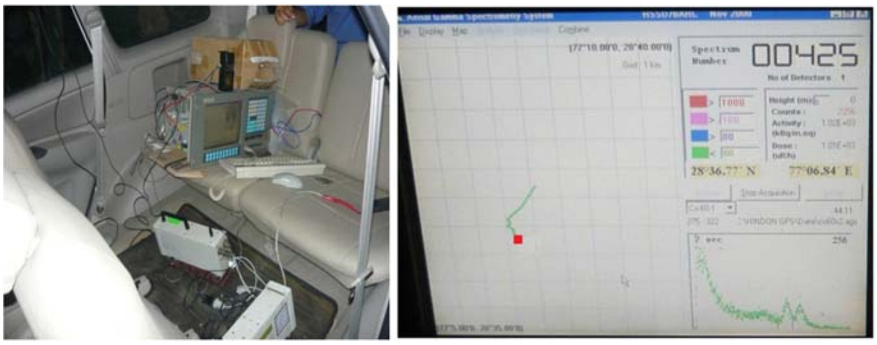

Fig. 6: AGSS and CARMS installed in a vehicle for the mobile radiological mapping of Mayapuri and display on AGSS screen showing the route followed and location of Co-60 contamination.

Mobile Radiation Mapping following Mayapuri Radiological Emergency

Radiological emergency at Mayapuri, Delhi had generated concern of presence of contamination and inadvertent exposure. A mobile radiation monitoring of Mayapuri Industrial Estate and surrounding was carried out to detect the presence of any radioactive source or possible traces of radioactive contamination due to the inadvertent breaking and transportation of the contaminated scrap. AGSS and CARMS were used by installing in a vehicle for generating the radiological mapping of the area. The radiation profile of the area generated by these systems showed presence of Co-60 contamination and the radiation profile was effectively utilized for the planning and execution of decontamination operation. The installation of the systems in the vehicle and the route followed during the mobile monitoring along with the identified location of contamination are shown in Fig.6.

Conclusion

Radiological emergency in public domain cannot be ruled out due to potential orphan sources, radiological accidents or malicious acts using radioactive materials. The developed state-of-the-art monitoring systems, software and GIS support provide efficient tools for the assessment of radiological impact following such nuclear or radiological emergency.

Acknowledgements

We are grateful to Dr. A.K. Ghosh, Director, Health, Safety and Environment Group, BARC, Dr. D.N. Sharma, Associate Director, HS&EG for their constant encouragement and guidance. The support rendered by our collegues from Emergency Response Systems & Methods Section, RSSD, BARC and various government agencies is gratefully acknowledged.

Reference

1. Pradeepkumar K.S. and Probal Chaudhury, Development of Radiation Emergency Response System (RERS) for National Level Preparedness, BARC Founder's day special issue, 2012.
2. Probal Chaudhury, N. Padmanabhan, Rajvir Singh, K.S. Pradeepkumar and D.N. Sharma, Gamma Spectrometric Monitoring of Delhi City to Demonstrate the Methodology for the Assessment of Ground Contamination and Search and Detection of Orphan Sources,. 12th International Congress of the International Radiation Protection Association, Buenos Aires, Argentina, (2008).
3. Probal Chaudhury, K. S. Pradeepkumar and D. N. Sharma, GIS Technology for Radiological Impact Assessment and Quick Response during Nuclear or Radiological Emergencies, National Workshop on Role of Armed Forces in Disaster Management, College of Military Engineering, Pune, (2006).
4. A. Vinod Kumar, R.B. Oza, P. Chaudhury, M. Suri, S. Saindane, K.D. Singh, P. Bhargava and V.K. Sharma, Online Decision Support System (IRODOS) – An Emergency Preparedness Tool for Handling Offsite Nuclear Emergency, International Conference on Peaceful Uses of Atomic Energy, New Delhi (2009).
5. Rajvir Singh, Probal Chaudhury, K. S. Pradeepkumar and D.N. Sharma, Radiological Mapping for Impact Prediction and Response during Emergency, 12th International Congress of the International Radiation Protection Association, Buenos Aires, Argentina, (2008).

STRUCTURE AND DYNAMICS OF COMPLEX FLUIDS AT THE NANOSCALE: MOLECULAR DYNAMICS SIMULATION STUDY

Niharendu Choudhury
Theoretical Chemistry Section, Chemistry group

Dr. N. Choudhury is the recipient of the DAE Scientific & Technical Excellence Award for the year 2010

Abstract

Predicting properties of various materials from a molecular perspective is an important aspect of modern chemical physics. Understanding various phenomena in condensed phase by using theoretical and computational methodologies is the major focus of the present investigation. In particular, various complex fluids at the nanoscale interfaces and in the bulk have been studied with the help of multiscale modeling, theory and large-scale molecular dynamics (MD) simulations. A brief account of our recent research efforts on development of new methodologies, implementation of MD simulations to understand different phenomena and predict properties of condensed phase is presented here.

Introduction

The field of theory and computation has progressed so significantly over the last two decades that now it is able to address important questions in the core areas of the physical and chemical sciences, including questions lying on the interface among chemistry, physics, biology, and engineering. In order to study properties of material in condensed phase at finite temperature, many-body statistical mechanical theories and simulations are required. A large fraction of computational chemical physics is now associated with the development and use of powerful computational tools[1] such as molecular dynamics and Monte Carlo simulations to predict structural, thermodynamic, and dynamical properties of many-body ordered and disordered systems.

However, one of the main unresolved problems in computational chemical physics is the gap in time-scale and length-scale between computational and experimental methods for studying many-body systems. For example, in systems where lengthscale heterogeneity is inherent, atomistic modeling still remains a challenge due to prohibitively high computational requirements and in order to bridge the gap in the lengthscale, coarse graining is essential. For example, hydrophobic C_{60} or carbon nanotube (CNT) in water because of their much larger dimension as compared to water, induce lengthscale heterogeneity and therefore coarse-graining (CG) approaches[2] are required to simulate such a system with multiple C_{60}s or CNTs in water. In this article, we present a new CG model to study large solutes in solution and its implementation in MD simulations to investigate hydration and aggregation phenomena of fullerenes in a polar solvent.

It is well known that hydrophobic effect[3] plays a crucial role in the hydration and self-assembly processes over the entire length scales ranging from solubility of inert gases in water to folding of proteins and other macromolecules in aqueous solution. However, precise role of water in the process remains unclear till date.[4] It is believed that water behave differently at an extended hydrophobic surface and induce dewetting,[5,6] which is believed to be responsible for the self assembly of hydrophobic nanoscopic objects in water. In this article, we intend to reveal the subtleties in the behavior of water at the nanoscopic hydrophobic solute-water interface caused by minute details of solute topology.

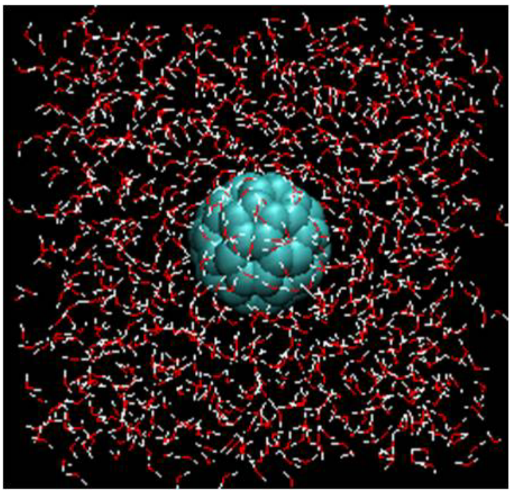

Fig. 1: A snapshot of a simulation box with an atomistic C_{60} in water.

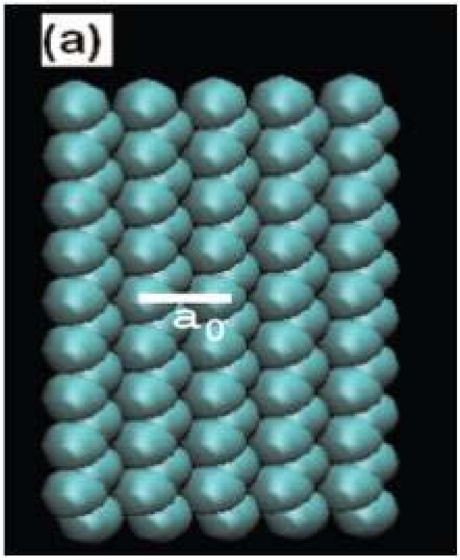

Fig. 2: (a) VDW representation of the paraffin like plate. Intermolecular distance a_0 of the plate is shown by a white line.

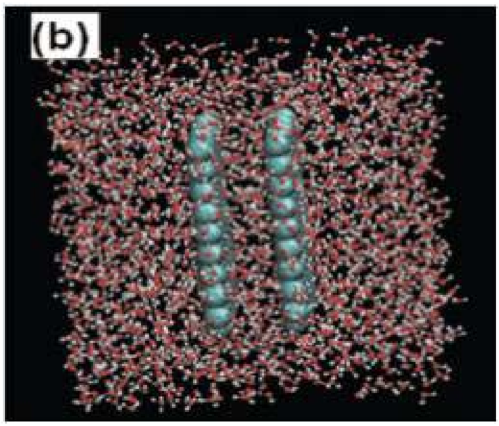

Fig. 2: (b) A snapshot of a simulation box with a pair of paraffin plates in water.

Models and methods

We present here results of our molecular dynamics simulations of two different systems, namely, *(i)* C_{60} in water and *(ii)* hydrophobic model paraffin plates in water, typical system configurations for which are shown in Fig. 1 and 2 respectively. For C_{60}-water systems, both atomistic and CG MD simulations have been carried out. We compare the results of CG modeling with those from atomistic modeling by calculating various structural and dynamical quantities. In the other case, we investigated behavior of water in and around two large, hydrophobic paraffin plates using atomistic MD simulation. Each of the hydrophobic solute was modeled as paraffin-like plates,

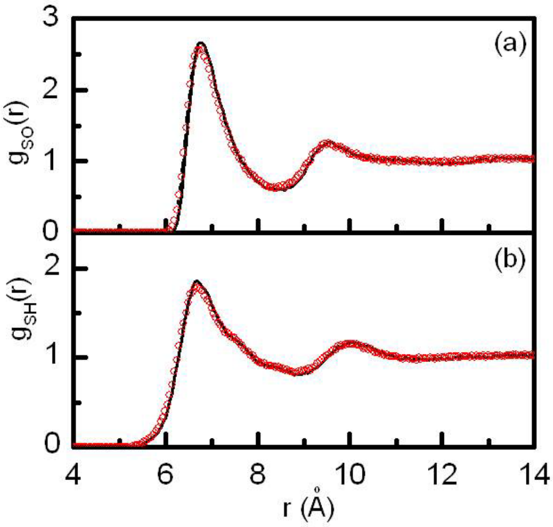

Fig. 3: Solute-water radial distribution functions for the (a) oxygen $g_{SO}(r)$ and (b) hydrogen atoms $g_{SH}(r)$ of water as a function of the radial distance r from the fullerene center. Solid lines and symbols represent CG and the atomistic models, respectively.

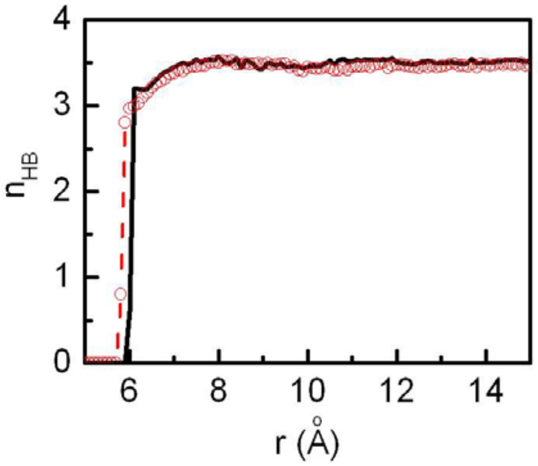

Fig. 4: Average number of hydrogen bonds n_{HB} per water The key is the same as in Fig. 3.

consisting of n-$C_{18}H_{38}$ molecules. The topology of the plate was varied by changing the intermolecular spacing, a_0 (see Fig.2(a)), between different C_{18} molecules in the plate. Three plates with a_0 values of 4, 5, and 6 Å were used. In all the cases water molecule was modeled with standard SPC/E model[7]. The simulations were performed in isothermal-isobaric (NPT) ensembles.

Results and Discussions

C_{60} in water

In order to investigate distribution of water molecules around the fullerenes, radial distribution functions have been calculated. The calculated C_{60}-oxygen and C_{60}-hydrogen (of water) radial distribution functions are shown in Fig. 3(a) and (b) respectively for atomistic as well as CG models. In both the cases results from the CG model are in excellent agreement with those obtained from the atomistic model. The RDFs show that the water near the fullerene surface is densely packed relative to the bulk. The almost coincident first peaks of oxygen and hydrogen distribution functions indicate that the plane of the water molecule is tangential to the fullerene surface. To quantify the loss of hydrogen bonds due to the presence of a mesoscopic nonpolar solute in water, we have also calculated and shown in Fig. 4 the average number of hydrogen bonds per water molecule as a function of radial distance from the center of the fullerene for both the models. The average number of H-bonds in the bulk is around 3.5 for both models and it reduces to 2.8 and 3.0 near the atomistic and the CG buckyballs, respectively. Although not shown here, we have also compared[8,9] orientational and dynamical quantities of the surrounding water molecules, details of which can be found in Refs. 8 and 9. The results from the present CG model are in excellent agreement with those from atomistic description.

Hydrophobic paraffin plates in water

We present results of our atomistic MD simulations on paraffin-plates immersed in water (see Fig.2). In order to assess effect of topology of plate on the behavior of interfacial water, three different paraffin like plates differing from each other only in the intermolecular spacing (a_0) between two adjacent paraffin molecules within the plate have been considered. The normalized ensemble averaged number density, $\rho(z)/\rho_0$ profiles (ρ_0 being the bulk density) of water in and around the two-solutes system with a_0 = 4, 5 and 6 Å at an intersolute separation r_0 = 7.2 Å corresponding to one-layer of intervening water molecules have been presented in Fig. 5. It is observed that for a_0 = 4 and 5 Å plates (see to ρ and middle panels of Fig. 5) the peak heights in the middle of the two plates are quite high, but for a_0 = 6 Å plate, there is almost no density

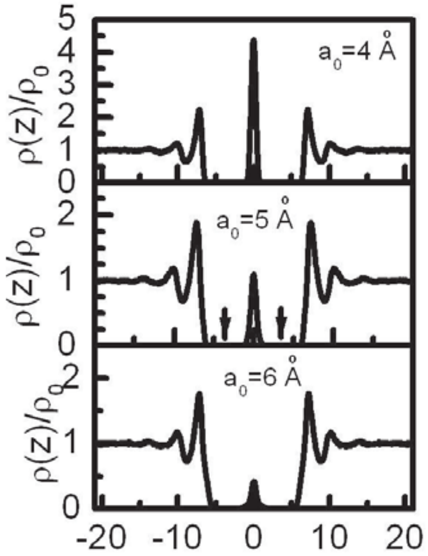

Fig. 5: The normalized single particle density $\rho(z)/\rho_0$ of water oxygen in and around three different plates with intermolecular spacing (a) a_0 = 4 Å (b) 5 Å and (c) 6 Å.

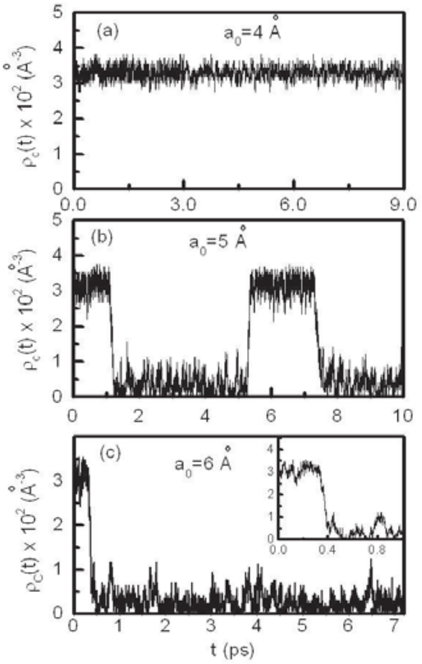

Fig. 6: Plot of the instantaneous number density of water, $\rho_c(t)$ in the intersolute region corresponding to Fig. 5.

accumulation in the middle, indicating a dry inter solute state. In hydrophobic soute-water interfaces, density fluctuations play an important role and in order to monitor that, instantaneous number density $\rho_c(t)$ of water in the intersolute region have been calculated (see Fig. 6) for the three different systems. It is found that for $a_0 = 4$ Å, there is no sudden fluctuations in the density, where as for $a_0 = 5$ Å, the inter plate region fluctuates between wet and dry states with a timescale of about 2-3 ns. Similar wet-dry oscillations have been observed in other investigations involving hydrophobic solutes and biological ion channels.[5,6] For $a_0 = 6$ Å plate, however, interplate region remains dry throughout the entire simulation time.

Dynamics of confined water

Our intention is to investigate the effect of solute plate topology (intermolecular distance a_0) on the dynamics of water in the interplate region. The calculated diffusivities for these three systems as calculated from mean square displacements (MSD) and velocity correlation functions (VCF) are tabulated in Table I. Faster diffusion of water in case of $a_0 = 6$ Å plate as compared to the other two cases has been observed. The larger intermolecular distance (a_0) within the plate dilutes the dispersion interaction with water and has depleting effect on the water structure. Faster translational dynamics of water in the intersolute region of the plate with larger a_0 value can be justified in the context of excess entropy scaling[12] of the dynamical quantities.

Table 1: Diffusion coefficients of water for different solute-water systems as calculated from MSD and VCF

a_0 (Å)	D (cm^2 sec^{-1})	
	MSD	VCF
4.0	1.65	1.70
5.0	1.94	1.84
6.0	2.24	2.47

In summary, the new coarse-grained model for C_{60}-water interaction has been tested against atomistic description. For hydrophobic plate-water system, it has been found that behavior of water in the inter plate region is guided by the interplay of the short-ranged interaction with the solute and the long-ranged interaction with the bulk water. The present study clearly demonstrates that the structural and dynamical characteristics of the intersolute water depend on the minute details of the solute.[9,10] The present observation can be used to tailor new materials with required wettability and channels with desired water accessibility and also help to understand the environment near a protein surface.

Acknowledgements

It is a pleasure to thank Dr. Swapan K Ghosh for his guidance at various stages of my research and for numerous fruitful discussions. I am benefited from many insightful discussions with Prof. B. M. Pettitt. I thank Dr. Tulsi Mukherjee for his kind interest and encouragement. I am thankful to Computer Division, BARC for providing Anupam supercomputing facility and related support.

References

1. M. P. Allen and D. J. Tildesley, *Computer Simulation of Liquids.* Oxford University, New York, 1987.
2. L. A. Girifalco, J. Phys. Chem. **96**, (1992). S. Izvekov, A. Violi, and G. A. Voth, *J. Phys. Chem. B* **109**, (2005) 17019.
3. C. Tanford, *The Hydrophobic Effect: Formation of Micelles and Biological Membrane.* John Weiley: New York, 1973.
4. P. Ball, *Nature* **423**, (2003) 25. *ChemPhysChem* **9,** (2008) 2677.
5. D. Chandler, *Nature* **437**, (2005) 640. X. Huang, C. J. Margulis and B. J. Berne, *Proc. Natl. Acad. Sci. U.S.A.* **100**, (2003) 11953.
6. N. Choudhury and B. M. Pettitt, *J. Am. Chem. Soc.* **127**, (2005) 3556. *J. Am. Chem. Soc.* **129**, (2007) 4847.
7. H. J. C. Berendsen, J. R. Grigera, and T. P. Straatsma, *J. Phys. Chem.* **91**, 6269 (1987).
8. N. Choudhury, *J. Chem. Phys.* **125**, (2006) 034502; *J. Phys. Chem. B* **111,** (2007) 10474-10480.
9. N. Choudhury, *J. Phys. Chem. C* **111** (2007) 2565-2572**.**
10. N. Choudhury, *J. Phys. Chem. B* **112** (2008) 6296–6300.
11. N. Choudhury, *J. Chem. Phys.* **132**, (2010) 064505. *J. Chem. Phys.* **131**, (2009) 014507.
12. M. Dzugutov, *Nature* (London) **381**, (1996) 137.

STUDIES ON ION-EXCHANGE MEMBRANES USING RADIOTRACERS

A.K. Pandey
Radiochemistry Division

Dr. A.K. Pandey is the recipient of the DAE Scientific & Technical Excellence Award for the year 2010

Abstract

Radiotracers have been used for understanding the intrinsic properties of the membrane and tuning them for the specific applications. Several robust and stable functionalized membranes have been developed by *in situ* photo-polymerization in pores of host membrane, nanocomposites by controlled incorporation of metal nanoparticles in the membrane matrix, and tailor-made polymer inclusion membrane. The color changeable optode and scintillating membrane made by polymer inclusion method could be used for monitoring ultratrace concentration of uranium and α/β-emitting radionuclides in complex aqueous samples, respectively. The EGMP-grafted fibrous membrane developed take up uranium from variety of aqueous media including seawater with fast kinetics.

Introduction

The fundamental properties of the ion-exchange membranes and sorbents are measured in terms of ion-exchange capacity, ion-exchange isotherms, partition coefficients and diffusion coefficients. In RCD, the radiotracers have been used to understand the diffusional transport properties of the home-made membrane as well as commercially available Nafion-117 membrane.

Physico-chemical Characterization of Ion-exchange Membranes Using Radiotracers

The self-diffusion coefficients ($D^{m}_{H_2O}$) of different valence counterions and water in Nafion-117 and polymer inclusion membrane were measured using appropriate radioactive isotope and tritiated water, respectively.[1-5] While self-diffusion coefficient provides information about the mobility of individual ions, the counterion-exchange involves inter-diffusion of the two counterions in the membrane. During the ion exchange, the process of self - diffusion is complicated due to coupling of interchanging ions fluxes. In order to understand the inter-diffusion process involved in the counter-ions exchanges, the rates of forward $(\mathrm{Li}^{+}/\mathrm{Na}^{+}_{\mathrm{mem}} \leftrightarrow \mathrm{M}^{n+}_{\mathrm{aq}})$ and reverse $(M^{n+}_{\mathrm{mem}} \leftrightarrow \mathrm{Li}^{+} / Na^{+}_{\mathrm{aq}})$ exchanges of metal ions ($M^{n+} = Ag^+$, Cs^+, Ba^{2+} or Eu^{3+}) in poly(perfluorosulfonic) acid membrane (Nafion-117) equilibrated with a well-stirred aqueous salt solution were experimentally measured using the radioactivity tagged counter-ions.[4] The nonlinear inter-diffusion equation for counter-ions exchange, based on Nernst-Planck model of inter-diffusion, was used to interpret the experimental exchange rate profiles. Na^+ ion was used as a reference counter-ion with other interchanging ions (Ag^+, Cs^+, Ba^{2+} and Eu^{3+}) in forward $(\mathrm{Na}^{+}_{\mathrm{mem}} \leftrightarrow \mathrm{M}^{n+}_{\mathrm{aq}})$ and reverse $(M^{n+}_{\mathrm{mem}} \leftrightarrow Na^{+}_{\mathrm{aq}})$ exchanges to test the validity of the nonlinear inter-diffusion equation. The self-diffusion coefficients of Na^+, Cs^+, and Ba^{2+} ions were also determined in Nafion-117 membrane having mixed cationic compositions to understand the effects of competing ions on their diffusion mobility.[5]

Polymer inclusion membranes (PIMs) are used in chemical sensors as these membranes can be tailor-made.[6] PIMs were used to developed chemical sensors as described below.

Optodes based on PIMs

The word "optode" or "optrode" is derived from Greek, meaning "the optical way" of generating signal in the sensing layer. These chemical sensors generate an optical response to the chemical reaction that results from the interaction of the analyte with the receptor. Most of the optode designs involve simultaneous preconcentration and determination of the target analyte, and are therefore amenable for continuous monitoring of toxic species in aqueous environment. A color changeable optode for UO_2^{2+} ions in the aqueous samples has been developed by physical inclusion of a chromophore 2-(5-bromo-2-pyridylazo)-5-diethylamino phenol (Br-PADAP) in a plasticized cellulose triacetate matrix.[7] Color of this optode changes depending upon UO_2^{2+} ions preconcentrated in its matrix.

Fig.1: Color changeable optode for UO_2^{2+} ions in the aqueous samples

The preconcentration efficiency of the optode from 100 mL aqueous sample indicated that 50 ng g^{-1} concentration of uranium in the optode can easily be quantified. The optode was found to be fully reversible and can be regenerated with 0.1 mol L^{-1} HNO_3. Iodine species (I^-, IO_3, I_3^- and I_2) specific polymer inclusion membranes have also been developed.[8]

Scintillating PIMs

The scintillating membranes have been developed for selective extraction and detection of trivalent radionuclides like ^{147}Pm, ^{154}Eu, and ^{241}Am in our laboratory.[9] These scintillating membranes were prepared by using dioctyl phthalate (DOP) plasticized cellulose triacetate (CTA) membrane containing optimum amounts of extractant bis(2-ethylhexyl)phosphoric acid (HDEHP), scintillator 2,5-diphenyl oxazole (PPO) and wavelength shifter 1,4-bis(2-methylstyryl)benzene (MSB). The plasticized anion-exchange membrane based scintillating membrane for simultaneous preconcentration and detection of $^{99g}TcO_4^-$ ions was also developed.[10] It was found that the membrane takes up TcO_4^- ions quantitatively (95±5%) from a solution having pH ≥ 2, tap water and seawater. The pulse height of the membrane was slightly higher than that of the Liquid Scintillation Cocktail. The β-counting efficiency of the membrane was found to be 72 % for ^{99g}Tc.

Nanoparticles embedded membranes

The radiotracer tagged nanoparticles has been used to study the galvanic reactions of Ag nanoparticles with Hg^{2+}, Rh^{3+}, and $AuCl_4^-$ ions in the membrane matrix.[11] The TEM analyses showed that the spatial distributions of Ag nanoparticles in the ion-exchange membrane could be controlled by using ionic or non-ionic reducing agents. It was also observed that shape of nanoparticles in the membrane is also dependent on the nature of precursor ions, see Fig. 2. For example, the clusters are formed with Rh^{3+} ions and non-spherical nanoparticles are formed

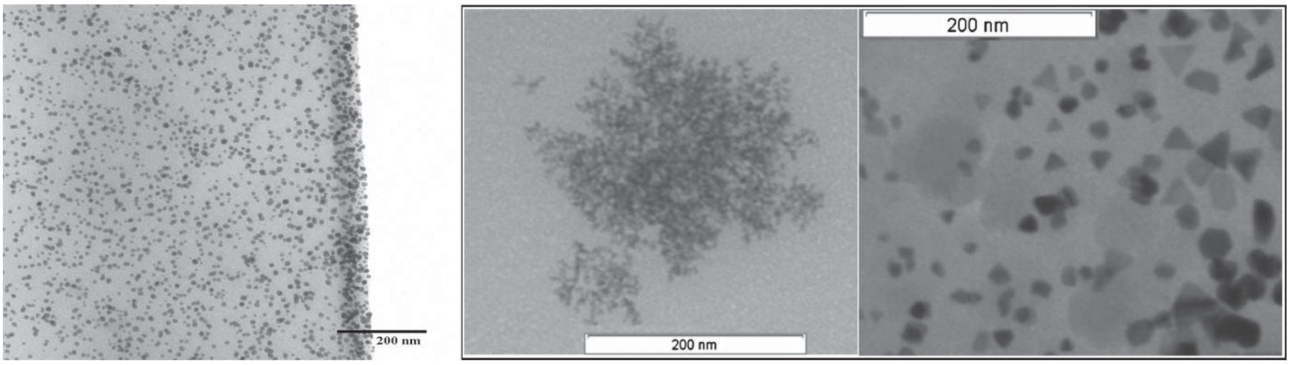

Ag nanoparticles Rh Cluster Au nanostructures

Fig.2: Cross-sections of membrane samples showing distributions of nanoparticles in Nafion-117 matrix.

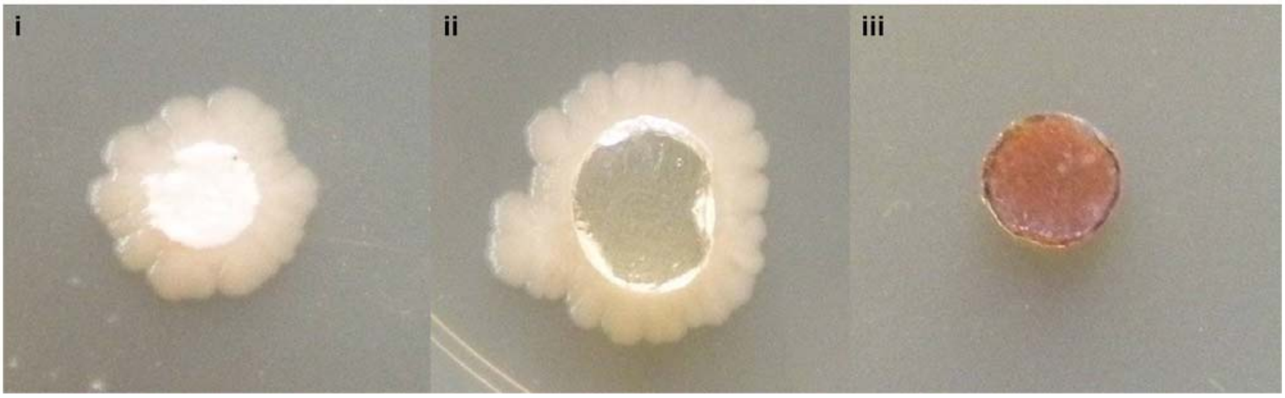

Fig. 3: Growth of bacteria adhered to different membranes was evaluated by planting the discs on Luria agar plates. (i) Whatman filter disc, (ii) Blank PEGMP sorbent, (iii) ME-1 (PEGMP sorbent with 1.6 wt.% Ag).

with $AuCl_4^-$ ions in the Nafion-117 membrane. These metal nanoparticles embedded membranes can be utilized for modifying the transport properties of the membrane and as a base material for developing the membrane based chemical sensors. For example, blue shift and decrease in the intensity of surface plasmon absorption band (SPB) of Ag nanoparticles can be used for generating the response signal for detection and quantification of Hg^{2+} ions by the using galvanic reaction.

It was observed that the presence of Ag nanoparticles in the polymer matrix impart the bio-resistivity to the matrix.[12] As can be seen from Fig.3, Ag nanoparticles (1.6 wt.%) in PEGMP composite sorbent did not exhibit growth at all after incubation with pre-grown E. *coli* cells, and showed non-adherence of this bacteria to the composite. This will be quite useful in preventing the fouling of membrane in bio-aggressive aqueous media like seawater.

Conclusions

Radiotracers have been found to be ideal tool for studying the transport properties of the functionalized membranes. Two types of functionalized membrane have been developed in our lab. These are polymer inclusion membranes and pore-filled membranes. Polymer inclusion membranes were used for developing optodes and scintillating membranes. Fibrous EGMP-membrane was found to promising for uranium recovery from seawater. The incorporation of metal nanoparticles in the membrane enhances functional property of the membranes. These nano-membranes are new generation of the membrane that can lead to more advance applications of the functionalized membranes.

References

1. Goswami, A.; Acharya, A.; Pandey, A.K. "Study of self-diffusion of monovalent and divalent cations in Nafion-117 ion-exchange membrane". *J. Phys. Chem. B* 105 (2001): 9196-9201.
2. Suresh, G.; Pandey, A.K.; Goswami, A. "Self-diffusion coefficients of water in Nafion-117 membrane with multivalent counterions". *J. Membr. Sci.* 284 (2006): 193-197.
3. Suresh, G.; Sodaye, S.; Scindia, Y.M.; Pandey, A.K.; Goswami, A. "Study on physical and electrostatic interactions of counterions in poly(perfluorosulfonic) acid matrix: Characterization of diffusion properties of membrane using radiotracers". *Electrochimica Acta* 52 (2007): 5968-5974.
4. Sodaye, S.; Suresh, G.; Pandey, A.K.; Goswami, A."Inter-diffusion of exchanging counterions in poly(perfluorosulfonic) acid membrane", *J. Phys. Chem. B* 113 (2009):12482–12488.
5. Chaudhury, S.; Agarwal, C.; Pandey, A.K.; Goswami, A. "Self-diffusion of ions in Nafion-117 membrane having mixed ionic composition". *J. Phys. Chem. B* 116 (2012): 1605"1611.
6. Kumar, R.; Pandey, A.K.; Sharma, M.K.; Panicker, L.V.; Sodaye, S.; Suresh, G.; Ramagiri, S.V.; Bellare, J.R.; Goswami, A. "Diffusional transport of ions in plasticized anion-exchange membranes". *J. Phys. Chem. B* 115 (2011) 5856–5867.

7. Kalyan, Y.; Pandey, A.K.; Naidu, G.R.K.; Reddy, A.V.R. "Membrane optode for uranium(VI) ions preconcentration and quantification based on a synergistic combination of 4-(2-thiazolylazo)-resorcinol with 8-hydroxyquinaldine". *Spectrochimica Acta Part A* 74 (2009): 1235-1241.
8. Bhagat, P.R.; Pandey, A.K.; Acharya, R.; Natarajan, V.; Rajurkar, N.S.; Reddy, A.V.R. "Molecular iodine selective membrane for iodate determination in salt samples: Chemical amplification and preconcentration", *Anal. & Bioanal. Chem.* 391 (2008): 1081-1089.
9. Sodaye, S.; Scindia, Y.M.; Pandey A.K.; Reddy, A.V.R. "Studies on the optimisation of optical response of scintillating optodes". *Sensor and Actuator B: Chemical* 123 (2007): 50-58.
10. Das, S.; Chakraborty, S.; Sodaye, S.; Pandey, A.K.; Reddy, A.V.R. "Scintillating adsorptive membrane for preconcentration and determination of anionic radionuclides in aqueous samples". *Anal. Methods* 2 (2010):728–733.
11. Kumar, R.; Pandey, A.K.; Das, S.; Dhara, S.; Misra, N.L.; Shukla, R.; Tyagi, A.K., Ramagiri, S.V.; Bellare, J.R.; Goswami, A. "Galvanic reactions involving silver nanoparticles embedded in cation-exchange membrane". *ChemComm.* 46 (2010): 6371-6373.
12. Das, S.; Pandey, A.K.; Athawale, A.A.; Subramanian, M.; Seshagiri, T.K.; Khanna, P.K.; Manchanda, V.K. "Silver nanoparticles embedded polymer sorbent for preconcentration of uranium from bio-aggressive aqueous media". *J Hazard. Mat.* 186 (2011): 2051–2059.

SYNTHESIS OF A COBALT SELECTIVE POLYMERIC SORBENT THROUGH METAL ION IMPRINTING AND ITS EVALUATION

Anupkumar B.
Water and Steam Chemistry Division

Shri B. Anupkumar is the recipient of the DAE Scientific & Technical Excellence Award for the year 2010

Abstract

A polymeric sorbent with high selectivity towards cobaltous ions was synthesised for the first time, using the technique of metal ion imprinting. The Co(II) imprinted polymer was found to sorb cobaltous ions present in ppb levels while completely rejecting ferrous ions present in large excess. The imprinted polymer has been demonstrated to selectively remove cobalt under typical PHWR decontamination conditions. The selectivity of the polymer has also been investigated through theoretical calculation of the formation energies of metal ion complexes of synthesised imprinted sorbents, which showed relative instability of ferrous complex within the sorption site.

Introduction

Selectivity is an important aspect in effective handling of radioactive waste generated in the nuclear industry. Nuclear power plants are routinely subjected to clean up operations, otherwise known as decontamination campaigns, to reduce the radiation field in the coolant systems. During decontamination, solution containing a mixture of complexing agents is circulated through the system to be decontaminated to bring out the corrosion products and thereby release and trap the active ions [1]. In Pressurised Heavy Water Reactors (PHWR), whose major corroding surface is made of carbon steel, the process typically brings out large excess of ferrous ions (which predominantly are non-active) into the solution. Along with the excess ferrous ions, ppb to sub ppb levels of active cobaltous ions are removed into the solution. The conventional IX resins do not differentiate between them and trap both the ions (Fig.1a). In addition, ferrous and cobaltous ions have largely similar complexation chemistry..

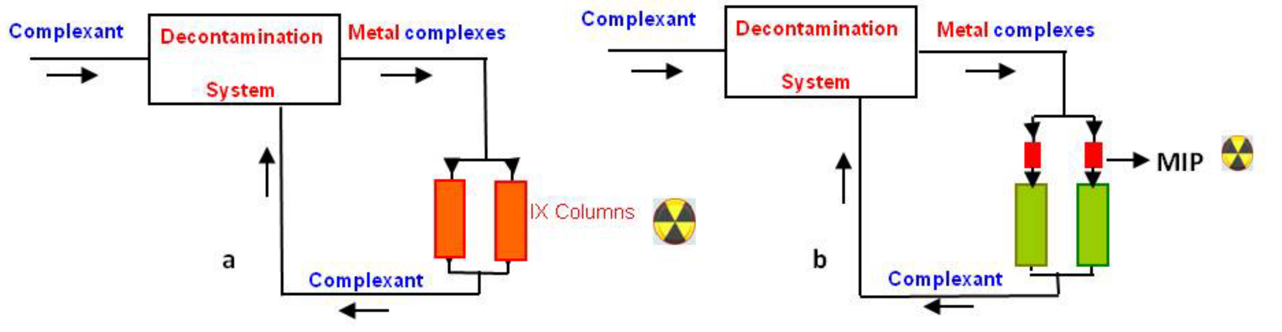

Fig.1: Schematic of a typical PHWR decontamination process a) Current scenario wherein IX resins are used for trapping the metal ions b) Desired ideal scenario wherein radioactive metal ions (cobalt is generally the major source of activity) are selectively isolated by a selective sorbent

On the other hand, with a selective resin that could trap Co^{2+} ions but completely exclude Fe^{2+} ions, the radioactive cobalt ions present in small chemical quantity (but the major source of radioactivity) can be isolated from the ferrous ions, which form the bulk of the metal ions removed (and hence the resin volume used). This will lead to significant reduction in the volume of spent resin containing cobalt activity (Figure 1b). Such segregation is highly desired, as cobalt activity is of very high concern in nuclear industry because of its high gamma energy coupled with long half life. With this objective investigations were initiated into exploring the feasibility of developing what are known as imprinted polymers suitable for this purpose.

Molecular imprinting is a technique that yields selective sorbents and aspires to mimic the extreme selectivity achieved by many biological systems [2]. The technique involves synthesis of a highly crosslinked polymer in presence of the chosen metal ion or a molecule (or a suitable analogue of the molecule) as template and functional monomers that can complex with the template (Fig.2). The geometry of the complex formed is fixed within the polymer matrix by the crosslinkers that polymerise around the complex.

The template is removed after polymerisation, thereby yielding a polymer with a preset configuration that can selectively accommodate that particular molecule or metal ion. Metal ion imprinted polymers are prepared in presence of the chosen metal ion as the template, which directs the geometric arrangement of the functional monomers (polymerisable ligands) through complex formation. The selectivity achievable depends largely on the functional monomers chosen, which should form a complex stable enough to retain the geometry but labile enough to facilitate removal of the template. The relative stability of the competing metal ions within the geometry fixed in the imprinted sites is the major driving force towards selectivity. Using this concept, we have prepared an imprinted polymer, with vinylbenzyliminodiacetic acid (VbIDA) as the functional monomer, which sorbs Co^{2+} ions while completely rejecting excess Fe^{2+} ions from complexing media (Fig. 3) [3, 4].

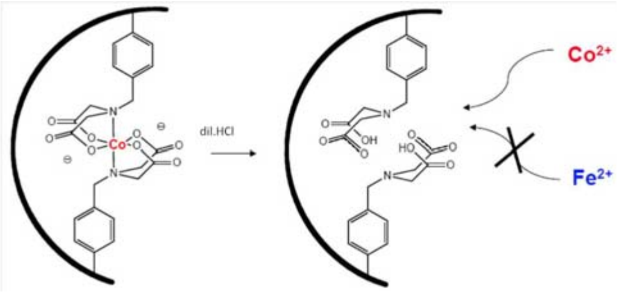

Fig.3: Selectivity of the cobalt imprinted polymer: The polymer sorbs cobaltous ions and rejects ferrous ions

Results & Discussion

Based on detailed investigations with different functional monomers such as vinyl imidazoles and pyrazolones, vinyl pyridines, EDTA, etc., it was found that vinylbenzyliminodiacetic acid (VbIDA) was the most suitable fucntional monomer for achieving the stated objective [5]. VbIDA was synthesised through a condensation reaction. The cobalt imprinted polymer was synthesised through two methods 1) two step synthesis in which the cobalt – VbIDA complex was synthesised and isolated, which was crosslinked with ethylene glycol dimethacrylate by thermal polymerisation in the second step; and 2) one step in-situ synthesis in which complexation and crosslinking polymerisation were done

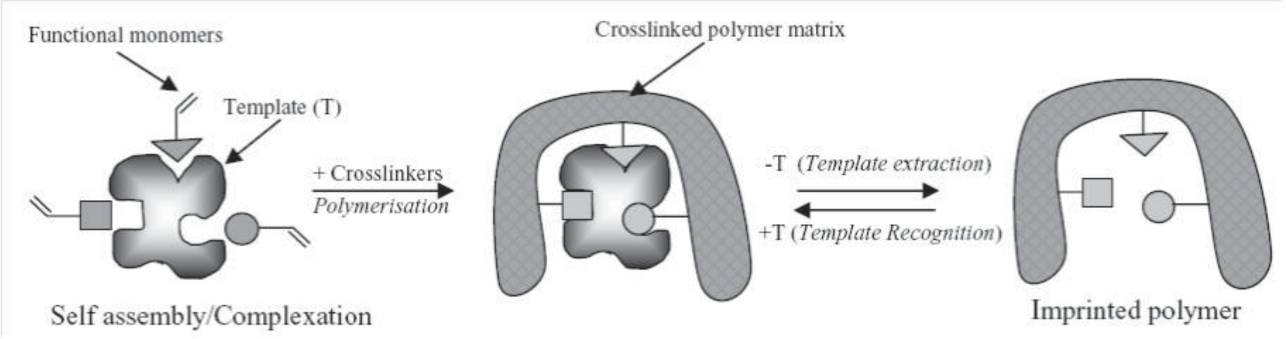

Fig.2: Concept of synthesis of imprinted polymers

in one pot wherein an organic base, namely tetrabutyl ammonium hydroxide, was used to aid the complexation. Polymers synthesised through both the methods were found to show similar sorption behaviour. The in-situ method, however, is simple to perform and easier to scale up. The template (cobalt) ions were removed from the synthesised polymers using dilute acid to obtain the metal ion (Co^{2+}) imprinted polymer (MIP). The theoretical capacity calculated (108.3 μmol/g) indicated that more than 90% of the originally added template ion has resulted in functional binding sites. Non-imprinted polymers (NIP) were prepared, as reference polymers, by a similar procedure but in the absence of the template ion (Co^{2+}). Spectroscopic analysis confirmed the incorporation of the ligand groups in the polymers.

Rebinding studies

Rebinding (sorption) studies of the Co^{2+} imprinted polymer (MIP) have been done in citrate buffer under various solution conditions. The equilibrium was found to be attained within 10 min and the maximum capacity was achieved at a pH of 4.8. The key observation (Tables 1 & 2) was that the polymer completely rejects Fe^{2+} ions irrespective of the solution concentration, while it sorbs Co^{2+} ions even at ppb levels in presence of strong complexant, Nitrilotriacetic acid (NTA). Unlike the MIP, the NIP did not sorb any of the metal ions under complexing conditions. This is due to the lack of organised functional cavities in the NIP which makes it an unfavourable choice for the metal ions present in a complexing medium. The cobalt bound by the MIP could be quantitatively, and almost instantaneously, removed by dilute acid. The polymer was found to retain the capacity and selectivity on repeated reuse (tested for more than 4 cycles of reuse). Sorption experiments were also carried out under typical PHWR decontamination conditions with radioactive cobalt. From a solution containing cobalt activity of 0.8 mCi/L and 225 ppm of Fe^{2+} ions in a typical decontamination formulation containing NTA (1.4mM), ascorbic acid (1.7 mM) and citric acid (1.4 mM), more than 55% of cobalt activity was removed by the MIP, while there was no pick up of Fe^{2+} ions. This indicates that the MIP retains its cobalt selectivity under typical PHWR decontamination conditions.

Table 1: Sorption of the cobalt imprinted polymer (MIP) for Co^{2+} and Fe^{2+}

Exp.No.	M^{2+}	Concentration (mM)		Capacity*
		M^{2+}	NTA	(μmol/g)
1	Co	4.24	-	58.0
2	Fe	4.48	-	BDL
3	Co	4.24	4.0	59.3
4	Co	8.40×10^{-2}	0.1	9.8 (70% uptake)

*BDL: Below detectable level

Table 2: Competitive sorption of Co^{2+} present in ppb levels from strong complexing medium

Exp.No.	M^{2+}	Concentration (mM)		Sorption*
		M^{2+}	NTA	%
1	Co	0.16×10^{-3} (9.4 ppb)	-	57
	Fe	0.89		BDL
2	Co	0.16×10^{-3}	1.0	55
	Fe	0.89		BDL

*BDL: Below detectable level

On comparison with a commercially available iminodiacetate containing resin, Amberlite IRC-718, it was found that the latter does not have exclusive selectivity towards Co^{2+} ions in presence of excess Fe^{2+} ions present in complexing medium. The MIP on the other hand was very specific towards Co^{2+} ions against Fe^{2+} ions in complexing medium.

Theoretical studies on selectivity

The selectivity of the imprinted polymer, especially the ferrous ion exclusion, was further probed through theoretical calculation of the formation energies of respective complexes within the sorption sites by using the ab-initio density functional theory (DFT) code SIESTA (Spanish Initiative for Electronic Simulations with Thousands of Atoms) [6]. The calculations were performed on the three dimensional structures generated for the complexes involving the functional monomers arranged in a specified geometry as is expected to be formed by the Co^{2+} ion within the sorption site. Few crosslinking units were also incorporated into the structure. The energy values obtained showed a positive formation energy value (+ 0.078 eV) for Fe^{2+} while it was -0.477 for Co^{2+} and thus indicated the instability of the Fe^{2+} complex in the fixed sorption site geometry.

Conclusion

This is the first report of a polymeric adsorbent capable of sorbing low level cobaltous ions while rejecting excess ferrous ions. Moreover, the synthesis was realised through a simple and reproducible "one pot" synthesis procedure. The polymer was designed predominantly with an objective of selective removal of activity generated due to cobalt during decontamination of PHWR wherein carbon steel is the major structural material in the primary system. Nevertheless, most of the nuclear reactor types used world wide use iron based alloys (eg., SS) as structural materials and face the problem of radioactive cobalt being present along with excess iron [7]. The MIP has been found to reject Cr^{3+} ions also under complexing conditions [3]. Thus its utility has a broader appeal. The cobalt imprinted polymer can also be used in effecting separation of radioactive waste generated due to cobalt activity during decommissioning as well. Similar concept can be made use of in devising selective sorbents for various other radioactive metal ions, such as antimony, cesium, etc., which are otherwise difficult to separate. Though the utility of the concept of imprinting has been proved in lab scale through this work, it will be challenging to synthesise the sorbent in formats suitable for large scale operations without losing the selectivity. Nevertheless, this is an important proof of concept based on which many separation problems can be tackled effectively.

Acknowledgement

I sincerely thank all the co-authors of the published works (3,4,6) that are summarised in this article. I also thank Dr S Velmurugan, Head, WSCD and Dr. T Mukherjee, Director, Chemistry Group for their encouragement and support.

References

1. Rufus A L, Sathyaseelan V S, Velmurugan S, Narasimhan, S V. *Nucl. Energy*, 43 (2004): 47 – 53.
2. Wulff G, *Angew. Chem. Int. Ed. Engl*. 34 (1995): 1812 - 1832.
3. Anupkumar B, Narasimhan S V, Sellergren B. *Ind. Eng. Chem. Res.* 48 (2009): 3730-3737.
4. Anupkumar B**,** Narasimhan S V, Sellergren B *Nuclear Engineering International* (2010): 22-24.
5. Anupkumar B. "Synthesis and Characterisation of Metal Ion Imprinted Polymers for Selective Metal Ion Sorption and Molecularly Imprinted Polymers for Catalysis" Thesis submitted to University of Madras, 2011.
6. Anupkumar B**,** Chandra S, Narasimhan S V, Sellergren B. *Biosens. Bioelectron.* 25 (2009): 558-562.
7. Venkateswaran G. Proceedings of the Symposium on Emerging Trends in Desalination, Reactor Water Chemistry and Back-End Technology for Nuclear Fuel cycle, Kalpakkam, India, (2007): 43 - 51.

IN VITRO CULTURE AND RADIATION INDUCED MUTATION TECHNIQUES FOR CROP IMPROVEMENT

Suprasanna Penna
Nuclear Agriculture and Biotechnology Division

Dr. P. Suprasanna is the recipient of the DAE Scientific & Technical Excellence Award for the year 2010

Abstract

Genetic variability is the main stay for plant breeders to create novel plant gene combinations and select crop varieties better suited to diverse agricultural systems. Mutation induction has become a potential and alternative method for the induction of novel genetic variability for use in crop improvement. Physical and chemical mutagens have been applied in many laboratories to induce mutations, among which gamma rays have become the sought after mutagen, as majority of the mutant varieties have been developed using gamma rays in different plant species. Plant cells and tissues cultured *in* vitro provide an efficient system for large scale propagation and genetic modification. *In vitro* mutagenesis of cultured explants, cells and tissue cultures is a feasible method for the induction of genetic variability. Somaclonal variation in combination with mutagenesis followed by cellular level selection has been employed for the isolation of agronomically desirable mutant lines in seed and vegetatively propagated plants. This article draws different features of *in vitro* mutagenesis and selection for applications in crop improvement.

Introduction

The improvement of crop plants has been a primary human pursuit since cultivation began. Of the world's approximately 200 000 plant species that have been found suitable for domestication, only 200 are domesticated as crops and only 15-20 of these have assumed importance as major food crops [1]. Traditionally selection, hybridization and recombination have been employed in the improvement of crop varieties. These methods continue to enrich the germplasm base of crop plants by evolving genetically superior varieties (Fig. 1). However, current population-increase and limiting natural resources demand that new and innovative technologies need to be in place to step up agricultural production in an environmentally sustainable manner. The use of induced mutations has played a key role in the improvement of superior plant varieties [2, 3]. More than 3000 improved mutant varieties have been released for commercial cultivation in different crop species demonstrating the economic value of the mutation breeding technology [4]. Several of the mutant crop varieties have been released in economically important plants and these occupy majority of the cultivated areas in the World. Radiation induced mutations have been obtained for modification in plant architecture, root characteristics, oil and protein quality, seed size, color and flowering time besides yield.

The approach of increasing the productivity by genetically altering the crop plants appears to be more economically favorable and eco-friendly and growing such genetically improved varieties along with the best cultural practices can significantly boost productivity. Compared to crossbreeding methods, mutagenesis has the ability to modify only a very few characters in an otherwise promising cultivar without altering significantly the remaining and often unique genetic background. Most important considerations are availability of mutagenized

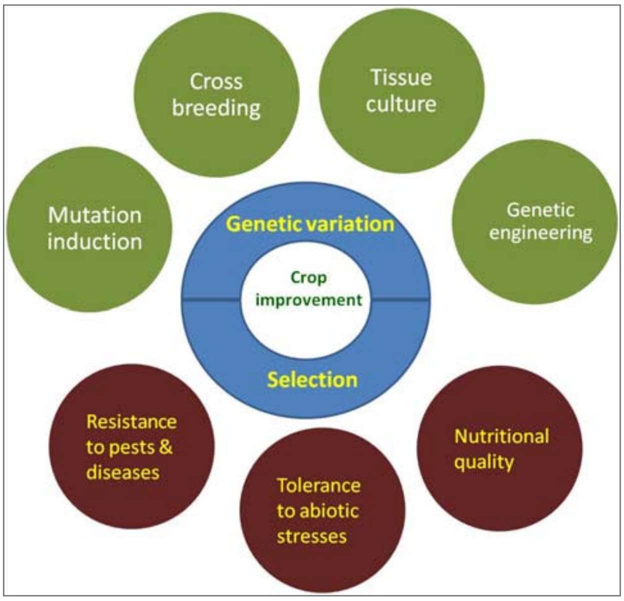

Fig. 1: Integration of methods of induction of genetic variation and selection in crop improvement

populations, methods for screening and selection which have become critical for achieving higher mutation frequency. Mutation breeding, therefore, can be considered as a viable option to genetically modify existing commercial clones and, mutagenesis using *in vitro* plant cell and tissue cultures offers as a feasible method for generating novel genetic variability [5].

Rapid developments in cell and tissue culture and genetic engineering have generated great interest to plant biologists. The major principle underlying the use of *in vitro* techniques is "totipotency" which means that isolated plant cells have the ability to divide, proliferate and develop into complete plants. Plant cell and tissue culture has emerged as a tool for a number of basic and applied research problems of relevance to plant improvement. To date several plant species including annuals and perennials, herbaceous and woody species, monocots and dicots, self and cross-pollinated groups that are vegetatively propagated and apomictic forms have been cultured *in vitro* and regenerated into complete plants. High value horticultural plants are routinely multiplied, at commercial scale, using tissue culture techniques. Several in *vitro* techniques have been developed with great potential in the propagation, creation of genetic variability and improvement of crop plants.

Cell and tissue culture techniques can improve the effectiveness of mutation induction in several aspects [6]. One of the major advantages of tissue culture is that a large number of plants can be regenerated. *In vitro* methods can be applied to a wide range of plant material, e.g. axillary buds, organs, tissues, protoplasts and cells. In case of haploid cell cultures, selected single haploid cells can be regenerated and diplodized to isolate desirable mutants as double haploids. Mutagenized cell suspension, microspores and protoplast cultures have the greatest potential for *in vitro* selection owing to their uniformity. The success of *in vitro* mutagenesis depends on established and reproducible *in vitro* plant regeneration procedures, optimization of mutagenic treatments, and efficient screening of the mutagenized populations for desired variations. Importantly, the developmental patterns of cultured cells, organs and tissues can be synchronized allowing for replication of treatment, mass *in vitro* selection and, as a consequence, provide consistency and a high frequency of mutants reproducible results. The methods are relatively inexpensive, simple and rapid and can be performed in a laboratory thus saving space and at any time of the year.

Plant cells cultured *in vitro* also provide an opportunity for the selection of useful mutations at cellular level [6]. It is possible to select cell lines tolerant or resistant to selective agents such as pathogens, pathogenic products or agents, aminoacid analogues, salts, herbicides etc. Often mutagenesis using physical and chemical mutagens is adopted in tissue cultures so as to enhance the recovery of the selected variants. Using patho-toxins or fungal culture filtrates, resistance has been observed in cell lines and regenerated plants in potato, maize, rice, wheat, barley, tobacco, alfalfa, sugarcane, peach and oats [6]. Salt and drought tolerance has been induced in rice, tobacco, oats, by subjecting cell lines to increased levels of sodium chloride, mannitol and polyethylene glycol in the medium. Likewise, tolerance to herbicides, heavy metals and other abiotic stresses like cold and high temperature has been successfully attempted. Mutant selection in plant cell and tissue cultures is interesting and offers considerable scope for generating genetic variability.

The development of improved varieties for the staple food crops has been achieved, however, in case of vegetatively propagated crops like banana, apples, cassava and sugarcane constraints of heterozygousity, systemic disease and pest incidence have posed as drawbacks to the application of induced mutagenesis. For this important group, manipulation with somatic tissue has great relevance and hence, *in vitro* protocols need to be established for mutagenesis, production and handling of large population to detect desirable mutations. The evaluation of putative mutants will also require more time and physical resources. Biologically, some peculiarities of vegetatively propagated plants include the absence of meiotic sieves, the concurrent fixation of deleterious allele, pathogen transmission to subsequent generations, and most importantly, the prevalence of chimeras [7].

R & D activities in sugarcane

In vitro culture methods in sugarcane have a great impact both on basic research and applied commercial interest. These include micropropagation of elite clones, production of disease-free planting material, generation of agronomically superior somaclones, screening methods for biotic and abiotic stress tolerance, and conservation of novel and useful germplasm. Somatic embryogenesis has been useful for propagating large number of uniform plants in less time, for obtaining virus resistant plants through somaclonal variation, mutagenesis and *in vitro* selection and developing transgenic plants [8, 9]. Our R & D activities in sugarcane include development of different *in vitro* culture systems and their application. This has provided a focused support to the DAE-BRNS funded collaborative research projects on the application of radiation mutagenesis for the isolation of useful mutants in sugarcane. Two such programmes are underway at Dr. Panjabrao Deshmukh Krishi Vidyapeeth (PDKV), Akola and Vasantdada Sugar Institute (VSI), Pune. Somaclonal variation in combination with *in vitro* mutagenesis has been used for the isolation of salinity and drought tolerant lines in a short duration employing *in vitro* selection [10]. Radiation induced mutagenesis has been undertaken using embryogenic callus cultures followed by the *in vitro* selection and field evaluation of selected lines. A general outline of the strategy is depicted in Fig. 2. Calli irradiated at different doses (10 – 50 Gy) of gamma rays showed decreasing percent survival with increasing dose [11]. Irradiated embryogenic calli were

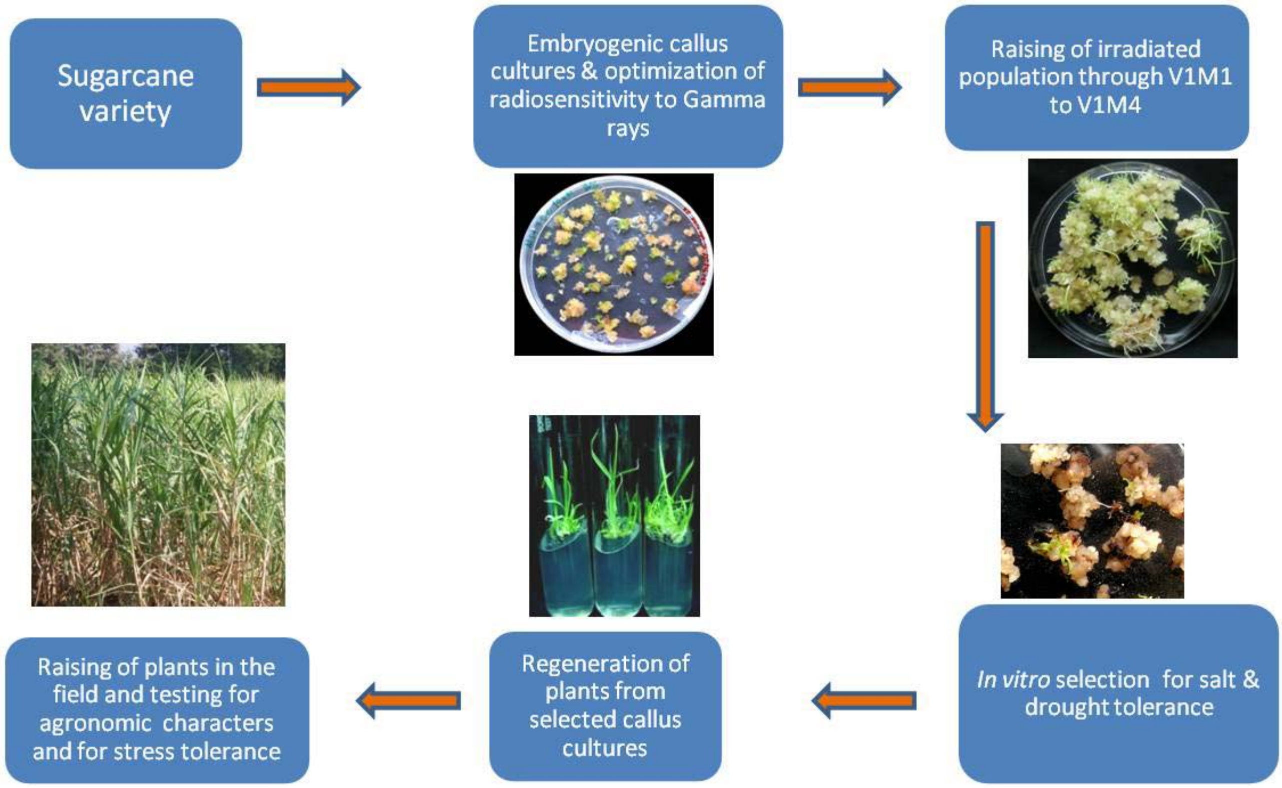

Fig. 2: Radiation mutagenesis followed by *in vitro* selection in sugarcane

exposed to different concentrations of NaCl (42.8, 85.6, 128.3, 171.1, 213.9 and 256.7 mM). The survival response decreased with increasing salt concentrations. In case of 10 and 20 Gy irradiated cultures, plant regeneration was observed up to 171.1 mM NaCl selection medium whereas in 40 Gy irradiated calli, regeneration was observed only upon 85.6 mM NaCl selection. Cell viability decreased and higher levels of osmolytes like free proline and glycine betaine were found to be accumulated in stressed calli as compared to control. Higher electrolyte leakage (2.8 times over control) was observed under salt stress, and leached out Na^+ and K^+ was much more than that of retained in tissue in both adapted and unadapted callus cultures. The results indicated that physiological and biochemical attributes are critical in alleviating salt stress effects and in improving salt tolerance in sugarcane.

Gamma irradiated, embryogenic calli of commercial sugarcane cultivars (CoC-671, Co 86032 and Co 94012) were raised in 2004-2005 and 7500 regenerated plants were hardened for field planting. Field trials of the plants were conducted at the Sugarcane Research Station, Dr. Panjabrao Deshmukh Krishi Vidyapeeth, Akola, India over a period of four years (2007-2011), and elsewhere in Maharashtra. About 900 mutant clones were then selected in 2007 on the basis of quality and phenotype. A wide range of agronomically desirable mutations was observed for characters like morphological, quality and yield contributing etc [12]. The spectrum of mutations was broader in Co 94012 for morphological characters whereas, cultivar Co 86032 exhibited wider range of mutations for quality and yield characters. Range of mutations obtained for cane yield attributing characters was 0.09 to 0.38 % for different doses of gamma rays and cultivars. In case of yield attributing characters, maximum mutations obtained for cane weight per plant (0.023 %) followed by cane diameter and cane height. The desirable mutants are now being evaluated in rod-row trials for genetic stability. Twenty one sugarcane mutant clones were found to be promising for agronomic and biochemical characters and, those mutant clones that vary from their parents are being looked into for registration under PPV & FR Act. The research emphasis is on mutant characterization using molecular markers and transcriptomic studies, creation of mutant collections for germplasm enhancement (biotic stress tolerance) and identification of genes for stress tolerance and sugar-related traits. Presently efforts are being made to characterize and evaluate these clones under advance varietal trials and to test for biotic stress resistance for exploiting these promising clones.

The isolation and deployment of mutations can be augmented through a strategic use of cell and tissue culture techniques in vegetatively propagated and other crops while molecular biological tools can help in the rapid genotyping of the mutational events. In recent years, there have been technological developments in the induction, screening and utilization of mutated genes in crop plants. By employing the genomic information and genomic-related technologies, approaches can be made for mutagenic treatments to significantly enhance the mutation frequency. Continued research in mutation induction and screening will enable researchers to harness the potential of 'genetic variation' in crop improvement.

Acknowledgements

The author is grateful Dr. S. F. D'Souza, Associate Director (A), BMG & Head, NABTD for his constant encouragement and support.

References

1. Novak FJ and Brunner H (1992) Plant breeding: Induced mutation technology for crop improvement. IAEA Bulletin 4:25-33.
2. Ahloowalia BS, Maluszynski M and Nichterlein K (2004) Global impact of mutation-derived varieties. Euphytica 135, 187-204
3. Jain SM (2005) Major mutation assisted plant breeding programs supported by FAO/IAEA. Plant Cell Tissue and Organ Culture 82, 113–123
4. Kharkwal MC, Shu QY (2009) The role of induced mutations in world food security. In: Shu QY (Ed) Induced Plant Mutations in the Genomics Era. Food and Agriculture Organization of the United Nations, Rome, pp 33-38
5. Brar DS and Jain SM (1998) Somaclonal variation: mechanism and applications in crop improvement.

In: Jain SM, Brar DS and Ahloowalia BS (eds.). Somaclonal variation and induced mutations in crop improvement, Kluwer Academic Publishers, Dordrecht, The Netherlands. pp15-38.

6. Suprasanna P, Jain SM, Ochatt SJ, Kulkarni VM, Predieri S (2010) Applications of *in vitro* techniques in mutation breeding of vegetatively propagated crops. In: Shu QY (Ed) *Plant Mutation,* IAEA, Vienna, pp 369-383
7. Mba C, Afza R, Jankowicz-Cieslak J, Bado S, Matijevic M, Huynh O and Till B J (2009) Eenhancing genetic diversity through induced mutagenesis in vegetatively propagated plants. Q.Y. Shu (ed.), Induced Plant Mutations in the Genomics Era. Food and Agriculture Organization of the United Nations, Rome. Pp 262-265.
8. Suprasanna P. (2010) Biotechnological interventions in sugarcane improvement: Strategies, methods and progress. BARC Newsletter 316: 47-53
9. Suprasanna P, V Patade, Desai NS, Devarumath RM, Kawar PG, Pagariya MC, Ganapathi A, Manickavasagam M and Babu KH (2011) Biotechnological Developments in Sugarcane Improvement – An Overview. SugarTech. 13: 322-335
10. Patade YV and Suprasanna P. 2008. Radiation induced *in vitro* mutagenesis for sugarcane improvement. Sugar Tech. 10(1):14-19.
11. Patade VY, Suprasanna P. and Bapat VA (2008) Gamma irradiation of embryogenic callus cultures and *in vitro* selection for salt tolerance in sugarcane (*Saccharum officinarum* L.) Agri. Sciences (China) 7(9):101-105
12. Suprasanna P, Patade VY, Vaidya ER and Patil VD (2009) Application of radiation induced *In Vitro* mutagenesis for the improvement of sugarcane. Proc. International Conference on Peaceful Uses of Atomic Energy, September 29- October 1, 2009. New Delhi. Pp 548-549.

DEVELOPMENT OF HIGH POWER RADIO FREQUENCY (RF) SYSTEMS FOR ION ACCELERATORS IN BARC

Manjiri Pande
Ion Accelerator Development Division

Smt. M.M. Pande is the recipient of the DAE Scientific & Technical Excellence Award for the year 2010

Abstract

Bhabha Atomic Research Centre (BARC) is developing proton, deuterium and heavy ion accelerators for its own scientific program. These accelerators require radio frequency (RF) power for their beam acceleration. So, a number of high power RF systems at various frequencies and power levels are being developed for this purpose & are explained below.

For RF ion source of 14 MeV neutron generator, a solid state rf amplifier has been developed and integrated with ion source to generate deuterium plasma. For heavy ion RFQ, a 1 kW, 76.58 MHz RF system has been designed, developed and successfully integrated with it.

As a part of accelerator driven sub-critical system (ADS), a low energy high intensity proton accelerator (LEHIPA) (20 MeV, 30 mA) is under development. It needs a total of around 2.4 MW of RF power at 352.21 MHz. So, three klystron based RF systems will be developed to fulfil this requirement. Simultaneously, a 400 KeV, deuterium based radio frequency quadrupole (RFQ) accelerator is being developed, which needs around 68 kW of RF power at 350 MHz. So two tetrode based RF systems are under development for this. First RF system has been tested up to 56.6 kW in CW mode and up to 48 kW in pulse mode. Second RF system has been tested up to 40 kW in CW mode and up to 38 kW in pulse mode.

As a technology development under XI and XII plan program, high power solid state rf amplifier development at 350 MHz and 325 MHz has also been taken up. This paper gives an overview of details and current status of these different high power rf systems.

Introduction

Accelerators

Accelerators were invented to provide energetic particles to investigate the structure of the atomic nucleus. They speed up and increase the energy of a beam of particles by generating electric fields that accelerate the particles and magnetic fields that steer and focus them. The main components of an accelerator are:

Radiofrequency (RF) cavities and electric fields: These provide acceleration to a beam of particles. RF cavities are located intermittently along the beam pipe. Each time a beam passes the electric field in an RF cavity, some of the energy from the radio wave is transferred to the particles.

Vacuum chamber: This chamber maintains ultra high vacuum inside the RF cavities. Inside the beam pipe, a beam of particles travels. It is kept at an ultrahigh vacuum to minimize the amount of gas present to avoid collisions between gas molecules and the particles in the beam.

Magnets: Various types of magnets are used to serve different functions. Dipole magnets are usually used to bend the path of a beam of particles that would otherwise travel in a straight line. The particle with more energy needs more magnetic field to bend its path. Quadrupole magnets are used to focus a beam, gathering all the particles closer together.

RF power for accelerators

An RF accelerator uses electromagnetic fields to propel charged particles to high speeds and to contain them in well-defined beams. All particle accelerators with energies greater than or equal to 20 MeV require high-power radio-frequency (r.f.) sources / systems. These sources must normally be amplifiers in order to achieve sufficient frequency and phase stability. The frequencies employed range from about 50 MHz to 30 GHz or higher. Power requirements range from 10 kW to 2 MW or more for continuous sources and up to 150 MW for pulsed sources. The power amplifier converts direct current (D.C.) input power into r.f. output power whose amplitude and phase is determined by the low-level r.f. input power. The r.f. amplifier extracts power from high-charge, low-energy electron bunches. The transmission components (couplers, windows, circulators etc.) convey the r.f. power from the source to the accelerator. The accelerating structures use the r.f. power to accelerate low-charge bunches to high energies. Thus the complete r.f. system can be seen as an energy transformer which takes energy from high-charge, low-energy electron bunches and conveys it to low-charge, high-energy bunches of charged particles. When sufficient power cannot be obtained from a single amplifier, then the output from several amplifiers may be combined. In some other cases, power is supplied to a number of accelerating cavities from one amplifier.

RF power sources / systems

For an overall optimised system design of an RF power system (inclusive of its cost factor), the fundamental RF criteria’s are; RF power range, wall plug efficiency, reliability and maximum voltage standing wave ratio (VSWR) that it can withstand. Other important criterias are operating frequency, bias parameters (which consume maximum energy), RF transmission line design and gain of final power stage. RF sources can be designed and classified in terms of their class of operation, configuration of the power source and overall system power gain. The choice of RF power device depends upon a range of parameters like high reliability, size, long life, easy replacibilty, possibility of modulation and proven feasibility. Using such criterias, we have developed some high power RF systems which are described in detail in this paper.

KLYSTRON BASED RF SYSTEM (1 MW AT 352 MHZ) FOR LEHIPA (For ADS)

As a part of accelerator driven sub-critical system (ADS) program [1] LEHIPA is being developed As per the accelerator physics design, RF power requirement for RFQ is about 530 kW of radio frequency (RF) power and for 10 MeV and 20 MeV DTL around 900 kW each. Each accelerating cavity will be driven by a one- megawatt (CW) klystron based RF system at 352.21 MHz.

The RF system [2] has been designed around five cavity klystron tube TH2089F, (Thales make) capable of delivering 1 MW continuous wave power at 352.21 MHz. Each RF system comprises of a low power driver, klystron tube, associated HV and LV bias supplies, harmonic filter, directional coupler, Y-junction circulator and WR2300 wave guide based RF transmission line. It includes other subsystems like interlock and protection circuits, dedicated low conductivity water-cooling, pulsing circuitry / mechanisms, special mechanical support structures and special RF grounding. This proton accelerator will be operated initially in pulsed mode and then will be gradually switched to continuous (CW) mode. The required pulse parameters are, Pulse repetition rate (PRR) (Hz): 1, 10, 100 and Pulse width (PW): 20 microseconds. Hence, the RF system is being designed to operate in above-mentioned both modes. The performance and reliability of klystron depends on performance of the power supplies connected to it, specially its DC bias supplies. So the essential features like tight voltage regulation, low ripple voltage, better voltage stability, low stored energy and high efficiency are included in all the bias supplies. The installation of RF system will start soon.

TETRODE BASED RF SYSTEM (60 KW AT 350 MHZ) FOR 400 KEV RFQ

A 400 KeV deuterium based RFQ is being developed to study neutronics behaviour and RF coupling to accelerator before going for ADS.

Fig.1: Photograph of 350 MHz RF system

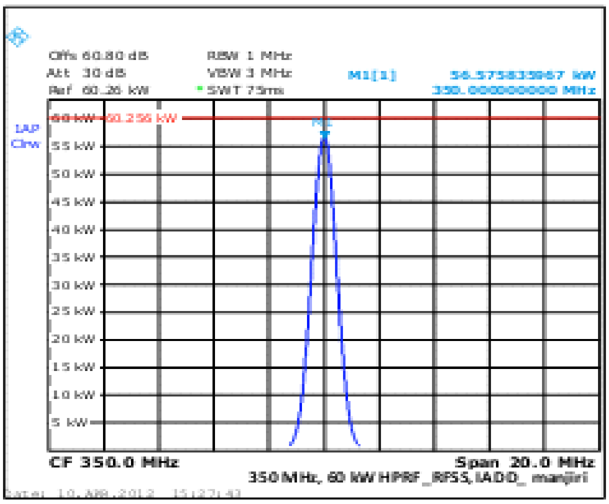

Fig.2: RF power Waveform

This RFQ requires around 68 kW of RF power. Hence, two RF power amplifiers [3] are developed to feed the RF power to this RFQ at two ports. Each RF system (figure 1) comprises of a high power tetrode TH 571B, its driver amplifier (TH 393), dual directional couplers, rigid coaxial transmission line (6 1/8", 50 ohm), other bias supplies, air and water cooling set up. All the bias supplies, RF driver and cooling circuits are being switched ON/OFF in a predefined time sequence to prevent damage to the high power RF devices by a suitable PLC based interlock and protection circuit. This RF system is operating in class AB and grounded cathode configuration. The RF system - set up-I, has been tested up to 40 kW CW output power with efficiency 60% and gain 15 dB. The amplifier was also tested in pulse mode up to 38 kW with 20 %, 10 %, 5% and 1 % duty cycle. The RF system set up -II has been tested in CW mode up to 56.6 kW (figure 2) with efficiency 65% and gain 14.8 dB and in pulse mode up to 48 kW with 20%, 10 %, 5% and 1 % duty power gain. This RF system will be coupled to 400 KeV RFQ.

PENTODE BASED RF SYSTEM (76.58 MHZ, 1 KW) FOR HEAVY ION RFQ

A heavy ion RFQ is being developed by NPD at TIFR. The RF system (figure 3) has been developed for testing the prototype heavy ion RFQ. Because of non availability of circulator at this frequency and power range, a pentode (5CX 1500) based power stage has been designed and developed. Its solid state driver (200 watt) comprises of pre driver and final stage is based on MRF 141G. The entire RF amplifier [4] has been tested up to 1008 Watt with 51.7 % efficiency and 63dB overall system power gain. One more identical solid state driver has been developed and coupled with prototype RFQ (without vacuum). In the coupled stage, it has achieved 0.4 W of reflected power and 80 W of forward power. Recently, the 1 kW RF system has been coupled successfully with the RFQ and reflection achieved is less than 10 %.

Fig.3: Photograph of 1 kW, 76.58 MHz RF system

SOLID STATE RF SOURCE (100 MHz, 256 W) FOR NEUTRON GENERATOR

14 MeV neutron generator uses a RF coupled ion source for deuterium plasma generation.

Fig. 4: 100 MHz RF source

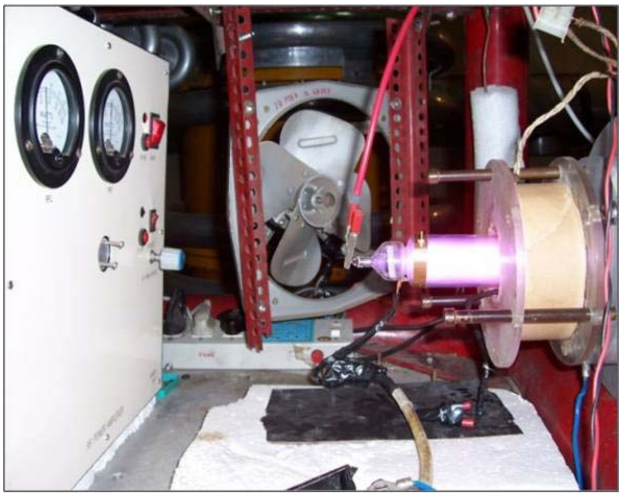

Fig.5: RF source with deuterium plasma

For this purpose, a solid state RF source (Fig. 4) operating at 100 MHz has been developed. It is capacitively coupled [5] with the ion source to generate deuterium plasma (Fig. 5). The D^+ beam current of the order of 170 microampere is extracted from this and impinges upon a Tritium target which in turn generates 14 MeV neutrons from DT reaction. This RF source consists of an oscillator, a driver (18 Watt) designed around transistor BEL S 12-28, a power amplifier based on MOSFET MRF 141G biased in class 'C', input/output matching networks, a circulator and biasing techniques. This RF source has achieved an overall efficiency of 63.5 % and 13.7 dB of power gain.

HIGH POWER SOLID-STATE RF AMPLIFIER

As a technology development under departmental plan programs, high power solid RF amplifier at 352.21 and 325 MHz are being developed. The overall configuration of amplifier includes basic 300 watt or 1000w modules based on LDMOSFET or VDMOSFET, a no. of power splitters / combiners with different configurations depending upon various power stages, compact DC supplies and an interlock and protection circuit. Initially an attempt has been made to combine eight such modules and has been tested at a total of 2100 watt power level. Another approach based on single 1000 watt RF device, a 1 kW RF amplifier module has been developed. This is being further combined together to generate higher RF power.

RF GENERATOR 2 kW AT 27.12 MHZ FOR ICP-MS

A number of RF generators have been developed for inductively coupled plasma based mass spectrometers for various DAE units like RMP, Mysore, HWP, Manuguru, BARC etc. This RF generator (Fig. 6) is capable of delivering 2000 Watt at 27.12 MHz to argon gas to produce its plasma at atmospheric pressure. The RF generator [6] has 20 dB gain and 78 % efficiency.

Fig. 6: RF generator: 27.12 MHz, 2 kW and (RF) argon plasma

Acknowledgement

Author wish to thank Dr.S.Kailas, Director, Physics group and Dr. P. Singh, Head IADD for their constant encouragement and support.

References

1. BARC internal report 'Road map for development of accelerator driven sub-critical reactor systems, S.S Kapoor
2. Klystron based high power RF system for proton accelerator Manjiri Pande, Sandip Shrotriya, Sonal Sharma, Niranjan Patel and Verander Handu Technical Physics Division, Bhabha Atomic Research Centre, Mumbai 400085, India, IEEE-IVEC (International Vacuum Electronics Conference) -2011, Bangalore, Feb 21 to 24, 2011
3. Development of 35 kW power amplifier at 350 MHz for RFQ based neutron generator" Manjiri Pande, Atul Soni, Niranjan Patel and V.K.Handu WEPMA 145, Asian Particle Accelerator Conference (APAC) 2007, RRCAT, Indore,
4. Design and development of 75MHz 1KW RF system with micro-controller based protection and control Sherry Rosily, Manjiri Pande and V.K. Handu, Indian Particle Accelerator Conference (InPAC) 2011, IUAC, New Delhi Feb 15 to 18, 2011.
5. Measurement and analysis of the radio frequency radiation (non ionizing) in dc accelerator based 14 MeV neutron generator facility at BARC, Manjiri Pande, Niranjan Patel, Indian Journal of Pure Applied Physics (IJAP), vol 50 (2012), p 478-481 and CARS-2011
6. A high power RF system for Inductively Coupled Plasma source Mass Spectrometry Manjiri Pande, K.R.Shinde, Niranjan Patel and V.K.Handu, TPD, BARC, 13 th ISMAS symposium cum work shop, Jan 27-31, 2008 at BARC, Mumbai

DESIGN & DEVELOPMENT OF CHANNEL ISOLATION PLUG FOR 540 MWE PHWRS

M. Chaturvedi, M. Dev and R.J. Patel
Refuelling Technology Division

Shri M. Chaturvedi is the recipient of the DAE Young Engineer Award for the year 2010

Abstract

The Coolant Channels of PHWRs is sealed at both the ends using sealing plugs. Sometimes situation arise in which sealing plug starts leaking due to some damage on closure seal face of coolant channel. The problem is rectified by lapping of the seal face. To approach the closure seal face for lapping, scheme was developed for 220 MWe PHWR in which a Fuelling Machine (FM) based Channel Isolation Plug (CHIP) is installed in coolant channel by FM to seal the coolant channel. However this design requires manual removal of some components of CHIP after installing in coolant channel. The components are again reassembled after completion of the repair operation. As the manual operation results into considerable radiation exposure and also chances are there for human error which can result into malfunctioning of the CHIP. To address this problem, a new concept of CHIP is developed for 540 MWe PHWR which is operated by FM and completely eliminates the manual operation on the CHIP before approaching the closure seal face. Design, manufacturing and testing of the CHIP is completed successfully at FM test facility, Hall-7, BARC and also in CMF facility, TAPS 3&4. The CHIP has been handed over to NPCIL for reactor use. This paper highlights the design aspects and operation of the 540 MWe Channel Isolation Plug.

Introduction

540 MWe PHWR is a horizontal pressure tube type reactor having 392 Nos. of coolant channels. Each channel consists of one seal plug at each end of the channel. The sealing plug is a pressure boundary component which seals the coolant channel using a metallic face seal (seal disc) which butts against a closure seal face provided on end fittings of the coolant channels (Fig. 1). Closure seal face is a stepped diameter provided in the end fitting. During refuelling, seal plugs at each end of channel are removed by FMs and are again installed after completion of refuelling. Effectiveness of proper sealing by seal plugs is checked by FMs before unclamping.

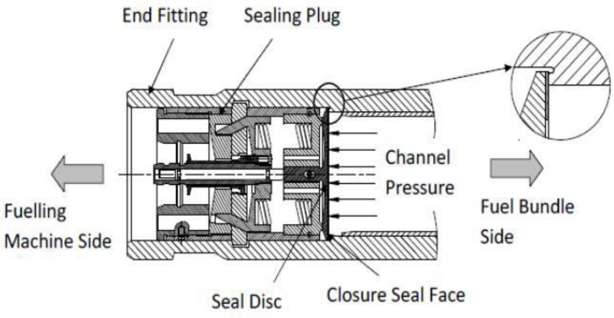

Fig.1: Schematic of sealing plug in coolant channel

Sometimes it is observed that some foreign material get trapped between sealing plug seal disc & closure seal face which results in damage of closure seal face. This damage may cause leakage through seal plug. To rectify this problem, closure seal face is approached for lapping operation during planned shut down and a thin layer of material from closure seal face is removed.

Making this surface approachable for lapping tool without draining and drying of coolant channel, a FM operated Channel Isolation Plug (CHIP) is developed. The CHIP along with its delivery adaptor is first loaded in the FM. The FM is then clamped to leaky coolant channel and installs the CHIP in the coolant channel with the help of Delivery Adaptor (DA) after removing the sealing plug & shielding plug from the channel. In installed condition, the 'O' ring provided on CHIP sits onto the small clear area in End Fitting available just after the closure seal face before the liner tube. After confirming the leak tightness of CHIP, the FM is then unclamped from the channel. This operation makes the closure seal face accessible for lapping operation to get it repaired.

Background

Approaching the closure seal face for repair without CHIP is a difficult task. This requires isolation of channel from the particular feeder which involves shut down of reactor, defueling of coolant channel, formation of ice plug in the feeder and draining & drying of the coolant channel. This entire operation required lot of shut down time and man rem expenditure. Initially some concepts were used by RAPS / MAPS for 220 MWe PHWR but these could not be used to its full extent due to non availability of safety features in these concepts. Subsequently a new concept of FM operated CHIP was developed by Refuelling Technology Division for 220 MWe PHWR with adequate safety features to isolate the channel without draining and drying of coolant channel. This tool is being extensively used in 220 MWe PHWRs however this tool requires manual removal of some of its component before approaching to closure seal face. These components are again need to be manually reassembled after completion of the lapping operation. This manual operation results in extra man rem consumption, also the manual operation always has possibility of human error. The new concept of CHIP developed for 540 MWe PHWR completely automate its operation using FM and this concept enables immediate approach to closure seal face after its installation in coolant channel.

Design requirements / features:

1. Sealing of coolant channel pressure boundary in cold shutdown condition without blocking the flow path.
2. Availability of adequate clear space to repair closure seal face after installing the CHIP.
3. Compatibility with FM for its operation.
4. Safety features to avoid unintended detachment of the CHIP from coolant channel.
5. Elimination of all the manual operation to install / uninstall the CHIP.

Description and operation:

As described earlier, CHIP is installed and removed from the channel with the help of Delivery Adaptor (DA). Both the subassemblies are kept joined with each other outside the channel with the help of manual plug operation tool. The CHIP and DA when attached to each other is called Integrated CHIP. The details of CHIP and Delivery Adaptor are shown below in Fig.2.

Before starting the closure seal face seal repair campaign, the Integrated CHIP is installed manually in the FM. To install the CHIP in channel, the Integrated CHIP is picked from the FM magazine using FM rams and advanced into the channel. After installing the integrated CHIP in the coolant channel, the DA is separated from the CHIP and stored in magazine. The detachment of DA from CHIP provide a clear space to access the damaged closure seal face for repair immediately after unclamping of FM. After completing the repair operation, the FM is again clamped

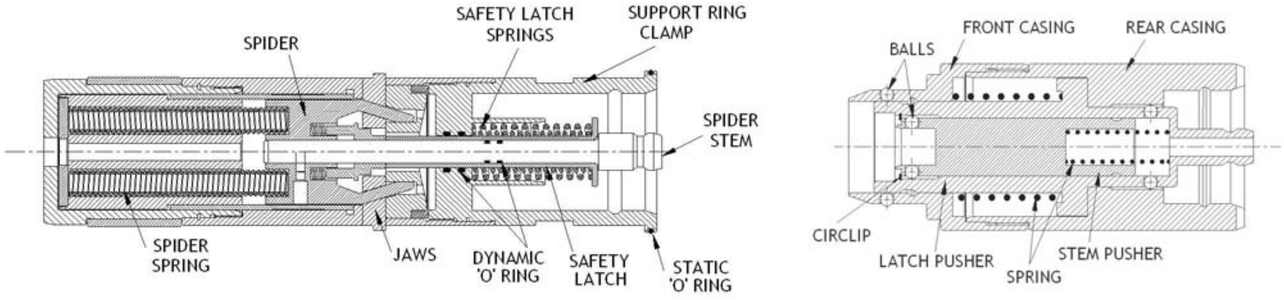

Fig.2: Sketch of CHIP and Delivery Adaptor

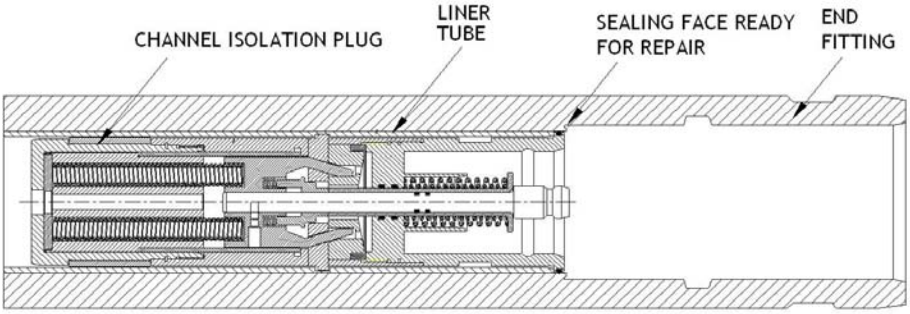

Fig.3: Channel Isolation Plug after installing in coolant channel

onto the channel, DA is picked by FM rams and advance to attach with CHIP. The Integrated CHIP is then removed from the channel and taken into the FM. Sketch of CHIP after installing in end fitting is shown (Fig.3).

The movement of latch pusher of DA (using FM latch ram) is used to perform different functions of CHIP during the operation. Total 50 mm movement of latch ram is required for complete CHIP operation. Five different positions of latch ram are defined for different operations like Picking of CHIP in FM, locking of CHIP & DA, unlocking of CHIP & DA, installing CHIP in Channel and Releasing CHIP in FM.

Performance Testing

After completing the manufacturing (Fig. 4), detail fuel handling operating procedure along with prerequisites were finalized to take up the tasting activity. As the CHIP will be used in reactor shutdown condition, pressure testing was done at 10 kg/cm^2 water pressure and all the critical parameters were checked.

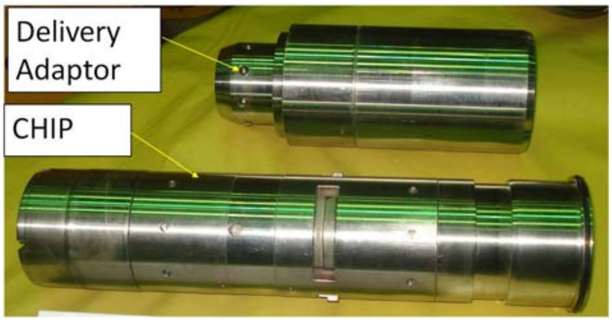

Fig.4: Photograph of Channel Isolation Plug & Delivery Adaptor

The CHIP was tested in simulated shut down condition at FM test facility Hall-7. After taking necessary safety clearances, the CHIP was also tested successfully at Calibration & Maintenance Facility (CMF), TAPS 3&4 using FM. The CHIP is handed over to TAPS 3&4 for reactor used.

Conclusion

In operating PHWRs, sometimes need arises to repair the closure seal face of coolant channel assembly. It is required to defuel, drain & dry the coolant channel for the repair of closure seal face. This consumes considerable time & man ram. To facilitate closure seal face repair in water filled condition, a FM operated channel Isolation Plug (CHIP) has been developed for PHWRs and being used in 220 MWe PHWRs. A new concept has been developed for 540 MWe, which has various improved features over 220MWe CHIP. The 540 MWe CHIP eliminates all the manual operation before approaching damaged closure seal face for repair. Design, development and testing of 540 MWe CHIP completed successfully and handed over to NPCIL.

DEVELOPMENT OF BORIDE BASED ADVANCED CERAMIC MATERIALS

J.K.Sonber, T.S.R.Ch.Murthy, C. Subramanian, R.K. Fotedar,
R.C. Hubli and A.K. Suri
Materials Group

Shri J.K. Sonber is the recipient of the DAE Young Engineer Award for the year 2010

Abstract

Borides are candidate materials for control rod applications in nuclear reactors. In this programme, processing scheme was developed for synthesis and consolidation of borides. Pure powders of ZrB_2, HfB_2, CrB_2, EuB_6, LaB_6 and NdB_6 were successfully prepared. Densification studies were carried out by using hot pressing technique. Hot pressing temperature and pressure were lowered by using suitable additives such as silicides. Effect of sinter additives on mechanical properties and oxidation resistance were studied.

Keywords: borides, synthesis, densification, fracture toughness, oxidation resistance

Introductions

Borides of refractory and rare earth metals are potential materials for neutron absorber applications in nuclear reactor. Neutron absorbing behavior is attributed to high neutron absorption cross section of ^{10}B isotope (3800 barn). Natural boron contains 19.8% ^{10}B which could be enriched to higher values. Besides high neutron absorption cross section, borides also have high melting point, good thermal conductivity, low thermal expansion coefficient, good thermal shock resistance, high temperature strength and stability in extreme environment.

ZrB_2 and HfB_2 have superior high temperature properties and thus can be utilized in high temperature reactors. CrB_2 forms solid solution with other borides and can be used as additive for improving densification and properties of other borides. Rare earth borides such as EuB_6, NdB_6 and LaB_6 are excellent control materials due to high neutron absorption cross section of rare earth elements. EuB_6 with enriched boron would be the best neutron absorber material for fast neutrons. Although these borides are known to have good potential, their actual applications are still very limited due to processing difficulties. Due to very high melting point and high brittleness these materials can be processed only by powder metallurgy route.

In this programme, studies were carried out on synthesis, densification, mechanical property evolution and oxidation of different boride materials which include ZrB_2, HfB_2, CrB_2, EuB_6, LaB_6 and NdB_6 materials. Effect of sinter additives on processing, properties and microstructure were investigated. Present paper gives only highlights of the programme. More details are available in published articles.[1-6]

Powder synthesis:

Boride powders were synthesized by boron carbide reduction of metal oxides in vacuum according to reaction (1) (2) and (3).

$MO_2 + 1/2B_4C + 3/2C \rightarrow MB_2 + 2CO$……[M= Zr, Hf]………………..(1)

$M_2O_3 + B_4C + 2C \rightarrow 2MB_2 + 3CO$……….[M=Cr]…………………….(2)

$M_2O_3 + 3B_4C \rightarrow 2MB_6 + 3CO$ ………….[M= La, Eu, Nd]………….(3)

Effect of temperature and charge composition on product obtained were studied. The optimized synthesis conditions to obtain pure boride powders are presented in Table (1). In the case of CrB_2 and ZrB_2, the charge was modified to obtain single phase diboride. Stoichiometric charge results in the formation of boron deficient phases (ZrB, Cr_3B_4) due to loss of boron in the form of its oxides. To compensate the loss, excess boron is added in the charge and carbon is accordingly reduced.. Though reaction starts at lower temperature, pure boride powder with low oxygen content is obtained only at high temperature.

Table 1: Optimized synthesis conditions and charge composition for preparation of pure borides (holding time: 2 hour, Vacuum: $1x10^{-5}$ torr)

Boride	Molar ratio of reactants	Temperature
HfB_2	$HfO_2 : B_4C : C = 2:1:3$	1875 °C
ZrB_2	$ZrO_2 : B_4C : C = 2:1.1:2.7$	1875 °C
CrB_2	$Cr_2O_3 : B_4C : C = 1:1.2:1.21$	1700 °C
EuB_6	$Eu_2O_3 : B_4C = 1:3$	1400 °C
LaB_6	$La_2O_3 : B_4C = 1:3$	1500 °C
NdB_6	$Nd_2O_3 : B_4C = 1:3$	1500 °C

Densification of borides:

Studies were carried out on densification of borides by vacuum hot pressing. Effect of sinter additives such as $TiSi_2$ and $CrSi_2$ on densification and properties were investigated. Results of densification studies alongwith some of the properties of the densified products are summarized in Table 2. Densification of monolithic ZrB_2 requires a temperature of 1850 °C. For HfB_2 only 80% density is obtained even at 1850 °C. High temperature required for densification of monolithic borides is due to the poor sinterability of powder. Borides are predominantly covalently bonded and hence self diffusivity is low. Silicide addition brings down the hot pressing temperature by liquid phase sintering. EuB_6 or NdB_6 addition also brings down hot pressing temperature by formation of solid solution. From Table-2 it can be noted that hardness of dense monolithic borides are higher than 20 GPa (23.9 GPa for ZrB_2). Silicide additions decreases the hardness due to their relatively lower hardness compared to borides. Hexaboride addition improves the hardness by formation of solid solution.

Fracture toughness values of dense monolithic borides are in the range of 3-4 MPa.$m^{1/2}$. Composite materials with sinter additives have shown higher values of fracture toughness compared to monolithic borides. Fig.1 presents the crack propagation behavior in boride-silicide composite. Crack deflection was observed which explains the higher fracture toughness.

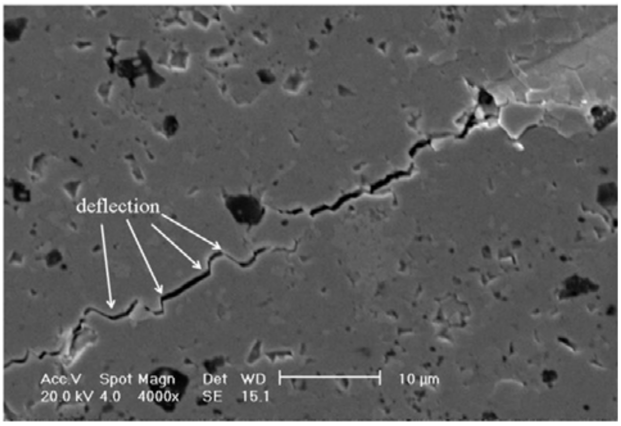

Fig.1: Crack propagation pattern in HfB_2+5%$TiSi_2$

Oxidation study

Borides are susceptible to oxidation at high temperature and so investigation was carried out on oxidation behavior of these materials. Isothermal oxidation was carried out at 900 °C in air for 64 hours. It was found that $TiSi_2$ and $CrSi_2$ addition improved oxidation resistance by formation of borosilicate based glassy layer which protect from further oxidation. Fig. 2 presents the effect of additives on oxidation behavior of ZrB_2 material. Addition of rare earth borides was also found effective in improving the oxidation resistance.

Conclusion

Technology was developed for synthesis of pure boride powders. Different borides (ZrB_2, HfB_2, CrB_2, EuB_6, LaB_6

Table 2: Summary of densification studies on borides (Holding time: 2 hour)

Material	Temperature (°C)	Pressure (MPa)	Density (%)	Hardness (GPa)	Fracture Toughness (MPa.m$^{1/2}$)
HfB_2	1850	35	80.0	11.5	5.7
HfB_2+15 wt.% $TiSi_2$	1650	20	99.9	27.4	6.6
HfB_2 + 10wt.% $CrSi_2$	1650	20	99.5	24.8	5.8
ZrB_2	1850	35	99.8	23.9	3.3
ZrB_2 + 10 wt.% $TiSi_2$	1650	20	98.9	19.4	6.4
ZrB_2 + +10 wt.% $TiSi_2$ 10% HfB_{2-}	1650	20	99.6	23.1	6.4
ZrB_2 + 10 wt.% $TiSi_2$ +20% HfB_{2-}	1650	20	98.4	23.7	6.6
ZrB_2+10 wt.% $CrSi_2$	1650	20	98.9	19.8	4.1
ZrB_2+2.5 wt.% EuB_6	1750	35	98.3	24.8	5.94
ZrB_2+2.5 wt.% NdB_6	1750	32	99.3	26.4	4.25
CrB_2	1600	35	99.8	22.12	3.67
LaB_6	1900	35	~100	20.34	3.02
EuB_6	1750	32	86	18.11	-
EuB_6 + 10%$TiSi_2$	1750	32	96	18.49	3.2

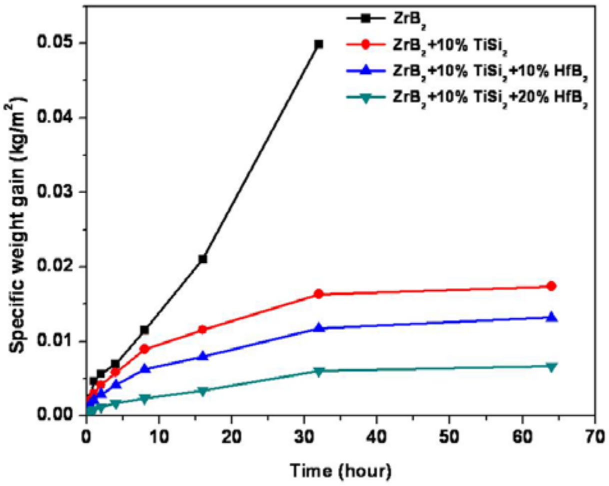

Fig. 2: Oxidation plot of ZrB_2 based materials oxidized isothermally at 900 °C in air

and NdB_6) were prepared in 100 gm scales. Dense shapes of borides were prepared and characterized. Effect of sinter additives on densification and some of the properties were investigated.

References

1. Sonber J.K., Murthy T.S.R.Ch., Subramanian C., Hubli R.C., Suri A.K., Effect of EuB_6 on densification and properties of ZrB_2 . *International Journal of refractory metals and hard materials.* doi. :10.1016/ j.ijrmhm.2012.04.012 (2012)
2. Sonber J.K., Murthy T.S.R.Ch., Subramanian C., Krishnamurthy N., Hubli R.C., Suri A.K., .Effect of $CrSi_2$ and HfB_2 addition on densification and properties of ZrB_2 . *International Journal of refractory metals and hard materials* 31 (2012) : 125-31.
3. Sonber J.K. and Suri A.K. .Synthesis and consolidation of zirconium diboride.. Advances in Applied Ceramics 110 [6], (2011) : 321-34
4. Sonber J. K., Murthy T. S. R. Ch., Subramanian C., Sunil Kumar, Fotedar R. K., Suri A. K. Investigations on synthesis of ZrB_2 and development of new composites with HfB_2 and $TiSi_2$.. *International Journal of refractory metals and hard materials* 29 (2011): 21-30.
5. Sonber J. K., Murthy T. S. R. Ch., Subramanian C., Sunil Kumar, Fotedar R. K. , Suri A. K. Investigation on synthesis of HfB_2 and development of a new composite with $TiSi_2$. *International Journal of refractory metals and hard materials,* 28 (2010): 201-10.
6. Sonber J. K., Murthy T. S. R. Ch., Subramanian C., Sunil Kumar, Fotedar R. K. and Suri A. K.. Investigation on synthesis, pressureless sintering and hot pressing of chromium diboride. *International Journal of refractory metals and hard materials* 27 (2009) 912-18.

QUALIFICATION OF INSITU PROPERTY MEASUREMENT SYSTEM USING HEAT TREATED SPOOL PIECES OF Zr 2.5 WT% Nb PRESSURE TUBE WITH DIFFERENT MECHANICAL PROPERTIES

S. Chatterjee, K. Madhusoodanan, Sanjay Panwar and J. N. Kayal
Reactor Engineering Division

Shri Subrata Chatterjee is the recipient of the DAE Young Engineer Award for the year 2010

Abstract

Material properties of Zr 2.5 wt% Nb pressure tube undergo change during service due to environmental conditions. Measurement of mechanical properties of the pressure tubes is important for assessing their fitness for service. As it is not possible to remove sizable samples from an operating pressure tube for doing the measurement in laboratory, insitu technique for measurement of mechanical properties has great significance. Hence an Insitu Property Measurement System (IProMS) based on cyclic ball indentation technique has been designed and developed in house. For qualification of IProMS a number of experimental trials have been carried out. One of the most important tests was to carry out IProMS trials inside spool pieces of Zr 2.5 wt% Nb pressure tube having different mechanical properties. This paper highlights the basic theory of measurement, qualification tests carried out using IProMS inside pressure tube spool pieces with different mechanical properties and the results obtained.

Keywords: In-situ, mechanical properties, ball indentation, pressure tube

Introduction

Material properties of Zr 2.5 wt% Nb pressure tube undergo gradual change during service due to severe environmental conditions. In order to assess the fitness of the component for continued operation, it is necessary to estimate its mechanical properties. Insitu measurement of the properties is the only option available in this situation. Hence an Insitu Property Measurement System (IProMS) based on cyclic ball indentation technique has been designed and developed in house. For qualification of IProMS extensive experimental trials have been carried out on several materials with known mechanical properties [1, 2, 3]. As per the design intent it was mandatory to conduct experimental trials inside Zr 2.5 wt% Nb pressure tube. Hence pressure tube spool pieces with different mechanical properties have been developed through heat treatment and tested subsequently using conventional test method and IProMS for its qualification.

Ball Indentation Technique

Cyclic ball indentation involves multiple indentation cycles (at the same penetration location) on a metallic surface by a spherical indenter. Each cycle consists of indentation, partial unload and reload sequences. The load and corresponding deformation are recorded during the test. Post-processing of the data recorded gives an estimate of the yield strength, ultimate tensile strength (UTS), strain hardening exponent and Brinell hardness of the material. The parameters involved in ball indentation technique are shown in Fig. 1.

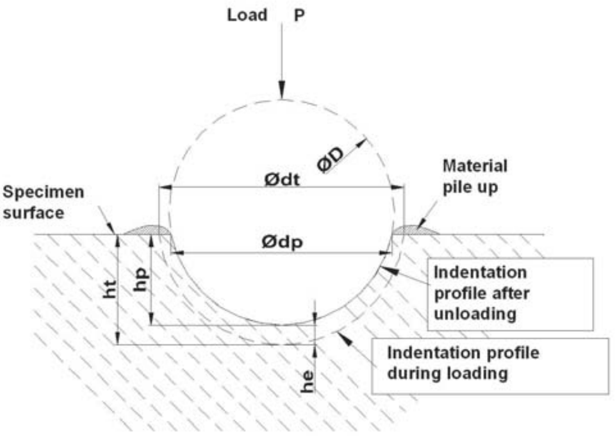

Fig. 1: Illustration of parameters of ball indentation geometry

Estimation of mechanical properties

The methodology used for estimation of mechanical properties from ball indentation test, is described in ref. [4, 5]. From the data recorded during the test, values of peak load, total depth of indentation and plastic depth of indentation, corresponding to each unload cycle are used to estimate the mechanical properties.

Description of IProMS

IProMS, which is remotely operable, consists of a tool head (Fig. 2), Data acquisition system, Display system and Control system. Indentation is carried out using a 1.5 mm diameter tungsten carbide ball and load is applied using a pressurising device. Depth of indentation is measured using a LVDT (Linear Variable Differential Transducer) and pressure is monitored using a pressure switch. Load and depth of indentation (deformation) data during the experiment is recorded in a computer and analysed later to estimate the mechanical properties.

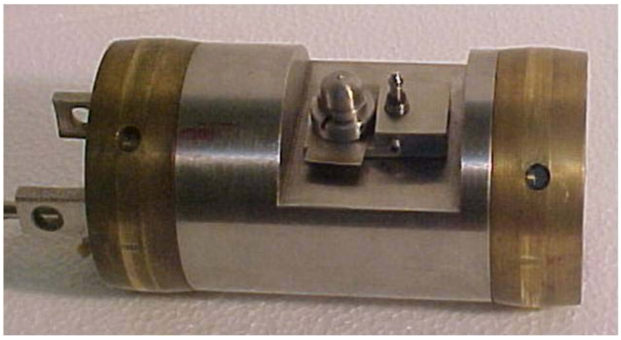

Fig. 2: IProMS tool head

Qualification trials using IProMS

For qualification of IProMS, pressure tube spool pieces having different mechanical properties have been prepared by heating them to different temperatures and time periods in a vacuum furnace as given in Table1. After heating, the spool pieces were cooled inside the vacuum furnace itself. Tensile specimens have been prepared from these spool pieces and the mechanical properties have been measured by conventional tests. A plot of load vs. extension up to failure in conventional tests is shown in Fig.3. IProMS trials have been conducted in the spool pieces and load-deformation curves acquired from the tests for five different material IDs are shown in Figs. 4-5. The results of IProMS trials have been compared with those from conventional tests and the same are presented in Figs. 6-9.

Table1: Details of heat treatment carried out on Zr 2.5 wt% Nb pressure tube spool pieces for IProMS trials

Material ID	Heat treatment condition
1	As received (No heat treatment)
2	Heat treated at 550 °C for 6 Hrs.
3	Heat treated at 625 °C for 4 Hrs.
4	Heat treated at 700 °C for 2 Hrs.
5	Heat treated at 800 °C for 0.5 Hrs.

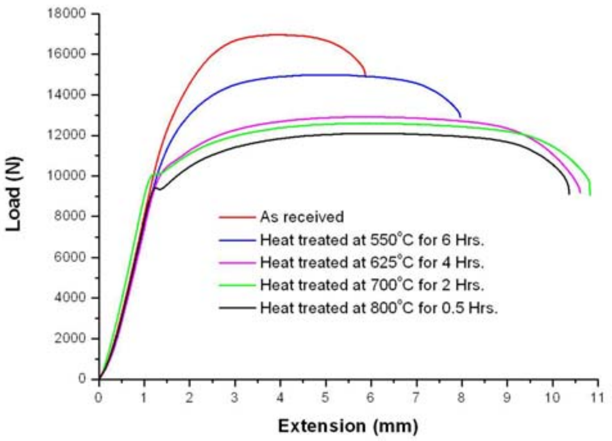

Fig. 3: Load vs. extension up to failure of heat treated Zr 2.5 wt% Nb materials

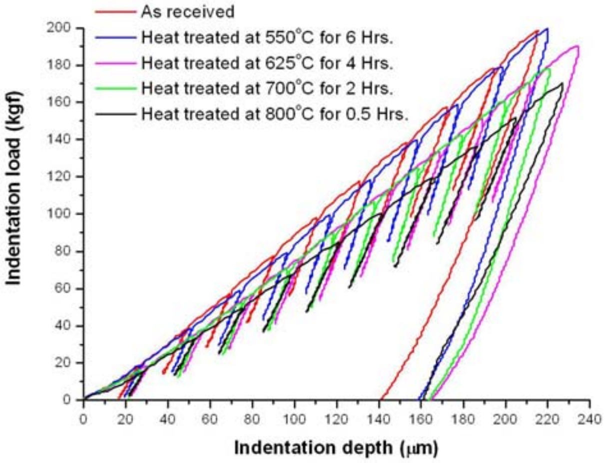

Fig. 4: IProMS load vs. indentation depth plot of different heat treated Zr 2.5 wt% Nb materials

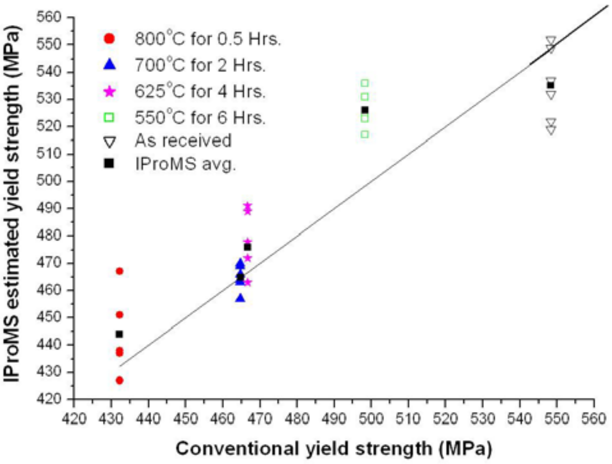

Fig. 7: Comparison between conventionally measured and IProMS estimated yield strength

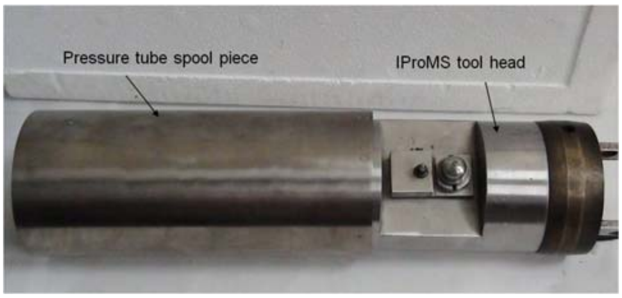

Fig. 5: IProMS tool head being inserted inside a heat treated spool piece of pressure tube

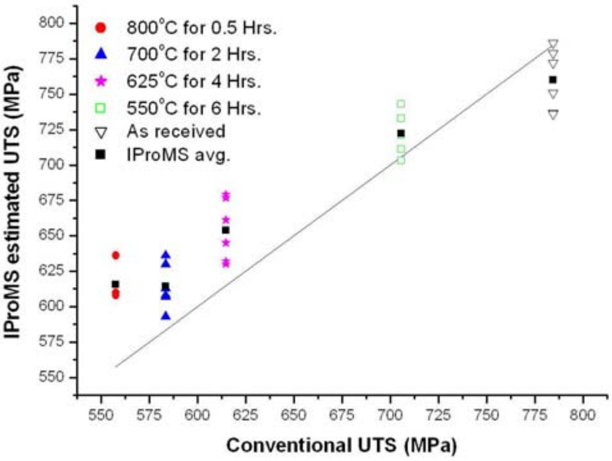

Fig. 8: Comparison between conventionally measured and IProMS estimated UTS

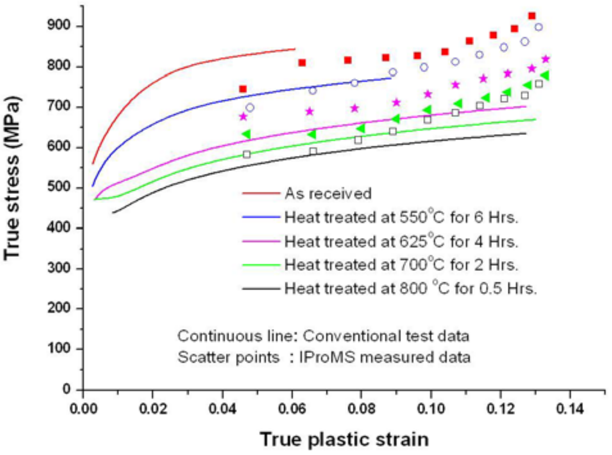

Fig. 6: Comparison of true stress vs. true plastic strain between conventional and IProMS estimation

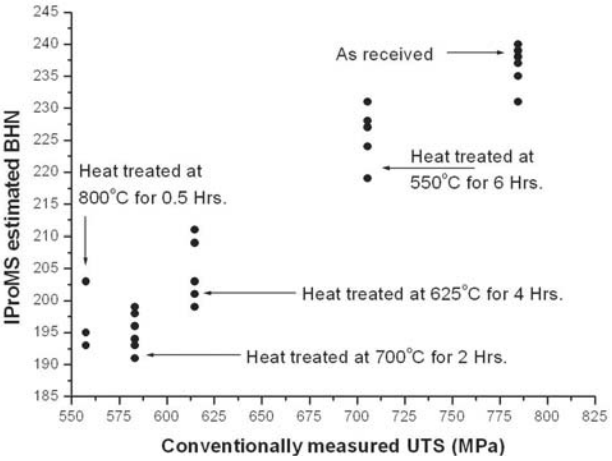

Fig. 9: IProMS estimated BHN vs. conventionally measured UTS

Conclusion

A number of qualification trials have been carried out using in-house developed IProMS inside spool pieces of Zr 2.5 wt% Nb pressure tube having different mechanical properties. Tests carried out using IProMS are highly repeatable and the difference between the mechanical properties estimated using IProMS and conventional tensile tests is about ±10%. It is also observed that IProMS can be used to estimate the mechanical properties of pressure tube material with different mechanical properties using same material specific constants. Hence the system is capable to capture the variation in mechanical properties of the same material due to service induced conditions.

Acknowledgements

Authors are grateful to Head, EISD for allowing us to use their vacuum furnace facility for heat treatment jobs. The authors do convey the extent of gratitude to Head, CDM and RED workshop for machining of specimens using wire EDM. The authors are also grateful to Head, MMD for allowing us to use their UTM for conventional tests.

Authors express their deep sense of gratitude to Director, RD&DG and Head, RED for their constant encouragement and support during the course of the work.

References

1. S. Chatterjee, K. Madhusoodanan, Sanjay Panwar, Nirupam Das, J. N. Kayal, B. S. V. G. Sharma And B. B. Rupani: Development Of In-Situ Property Measurement System, BARC Internal Report No.: BARC/2005/I/C01/2005.
2. S. Chatterjee, K. Madhusoodanan, Sanjay Panwar and B.B. Rupani: Design of in-situ property measurement system, Proceedings international conference on advances in mechanical engineering-2006 (AME-2006), December 1-3, 2006, Baba Banda Singh Bahadur Engineering College, Fatehgarh Sahib, Punjab, India.
3. S. Chatterjee, K. Madhusoodanan, Sanjay Panwar and B. B. Rupani: In-situ measurement of mechanical properties of structural components using cyclic ball indentation technique, Theme meeting on modern developments and practices in mechanical testing of structural materials, Bhabha Atomic Research Centre, Trombay, October 10-11, 2007: 121-126.
4. Haggag. F.M.: In-Situ Measurements of Mechanical Properties Using Novel Automated Ball Indentation System: ASTM STP 1204 (1993): 27-44.
5. Murty K.L., Mathew M.D., Wang Y., Shah V.N., Haggag. F.M.: International Journal of Pressure Vessels and Piping 75 (1998): 831-840.

Nomenclature

d_t - Total indentation diameter during loading,
h_t - Total depth of indentation during loading,
d_p - Plastic indentation diameter after unloading,
h_p - Plastic indentation depth after unloading,
D - Ball diameter,
h_e - Elastic component of indentation depth

THERMAL HYDRAULIC SAFETY ANALYSIS INCLUDING UNCERTAINTIES QUANTIFICATION FOR INDIAN NPPs

A. Srivastava , H.G. Lele and K.K. Vaze
Reactor Safety Division

Shri A. Srivastava is the recipient of the DAE Young Engineer Award for the year 2010

Abstract

Deterministic safety analysis is an important tool for confirming the adequacy and efficiency of provisions within the defence in depth concept for the safety of nuclear power plants. For safety evaluation, design capabilities of a nuclear plant are assessed for different level of defence in depth, which includes operating transients, design basis events, and beyond design basis events including severe accidents. In the beginning, conservative approach was used to assess the different accident scenarios and output was compared with set of acceptance criteria to assure plant safety. In this approach, conservatism in the code models as well as boundary and initial conditions were used to envelop all uncertainties associated with calculation. With advent of knowledge, now best estimate code are used to assess the plant safety. These Best Estimate (BE) analyses are supported by uncertainty analysis to take into account all uncertainties associated with the calculation. In the present paper, different levels of defence in depth approach are addressed along with uncertainty estimate for LOCA scenario for different Indian NPPs.

Introduction

Nuclear Power Plant (NPP) performance evaluation during off-normal conditions has been the main issue of safety research in the thermal-hydraulic area since beginning. Several Design Basis Events (DBEs) are analyzed in order to ensure the effectiveness of the engineered safety features and to satisfy the regulatory requirement of the proposed plant design.

The thermal hydraulic analysis for different Indian reactors such as Advanced Heavy Water Reactor (AHWR), Pressurised Heavy Water Reactor (PHWR) and VVER-1000 are presented in this paper highlighting the use of best estimate codes primarily RELAP5 and also CATHARE. The paper also highlights the uncertainty estimate for LBLOCA for these reactors. The paper discusses the application of

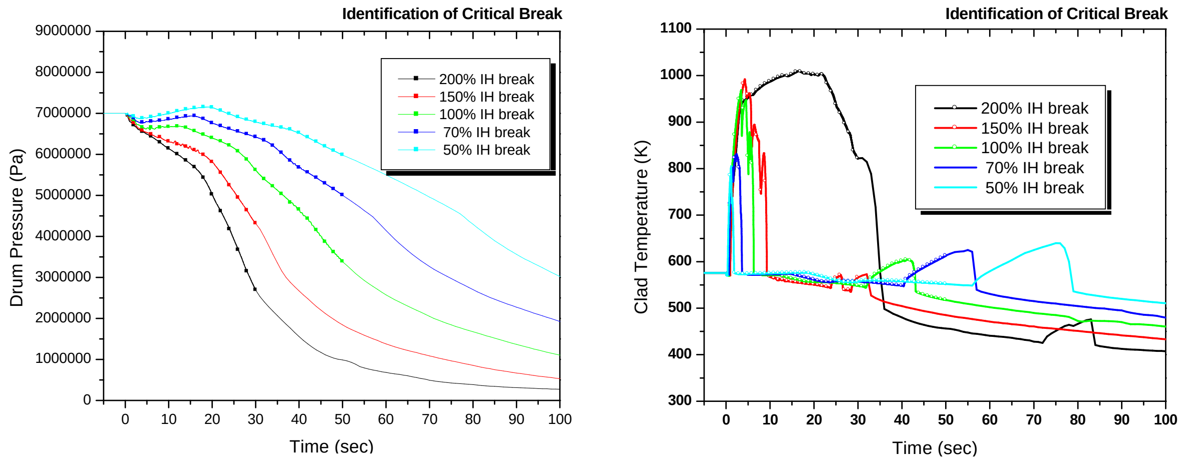

Fig. 1: Identification of critical break for AHWR

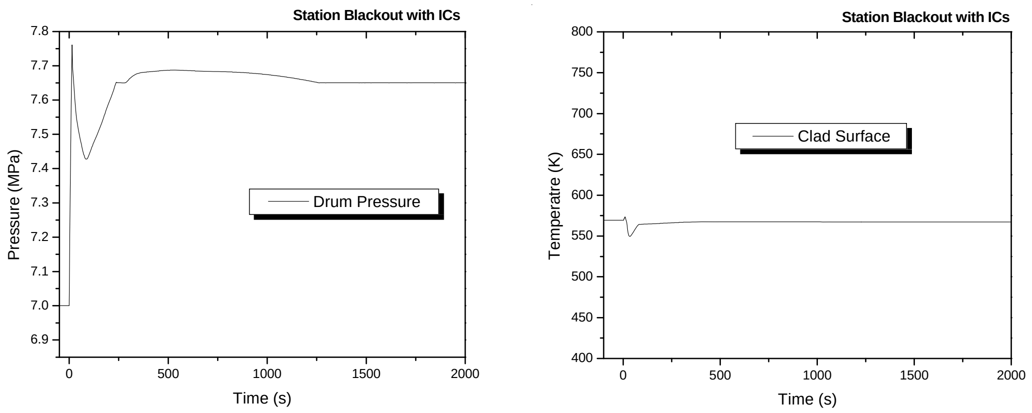

Fig. 2: Performance of IC under Station blackout for AHWR

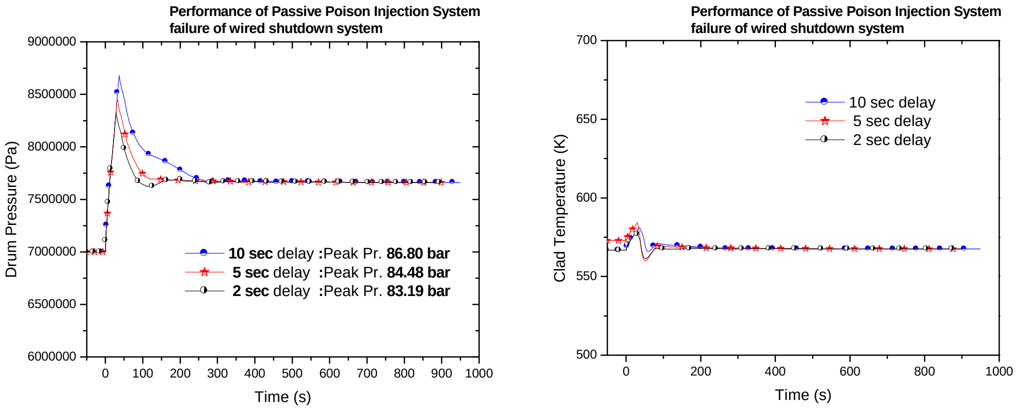

Fig. 3: Performance of PPIS under wired shutdown system failure for AHWR

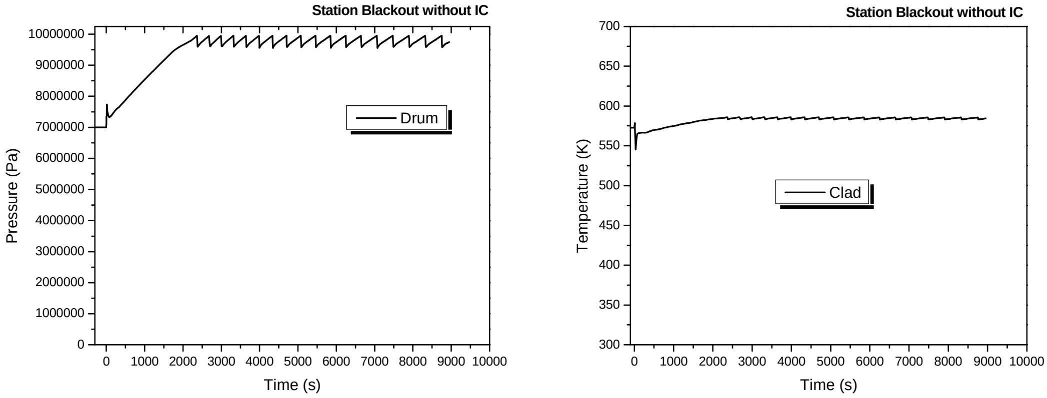

Fig. 4: Performance of SRV during SBO without IC for AHWR

integrated MHT-Turbine-condenser model for AHWR. The paper further highlights the severe accident analysis done for TAPS-1 & 2 BWR type reactors. This analysis shows the response of the reactor during extended SBO scenario.

AHWR Safety Analysis

An input model of AHWR in RELAP5 has been developed [1], which has been used for the safety analysis work of AHWR. Number of transients under different categories have been analysed and results of analyses are compared with acceptance criteria.

Important contribution in AHWR safety analyses are identification of critical break, performance evaluation of Isolation Condenser (IC) under station blackout, performance of Passive Poison Injection System (PPIS) in reactor shutdown under external threat situation, adequacy of safety –relief valve to limit the system pressure under station blackout without IC and analysis of LORA with

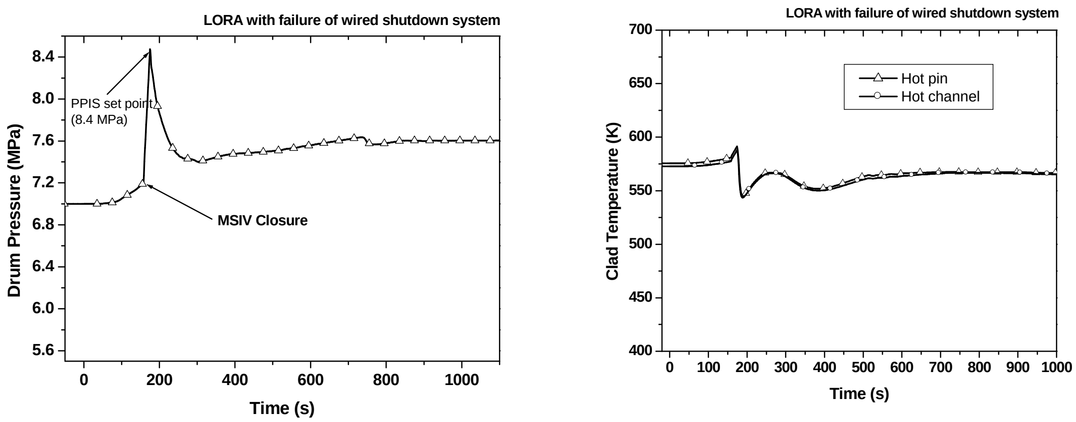

Fig. 5: LORA with failure of wired shutdown system for AHWR

failure of wired shutdown system. The results are given in Fig. 1-5.

Uncertainty analysis has been carried out for the 200% break in inlet header for AHWR using RELAP5 [1]. Two important techniques i.e. first based on 95/95 PCT evaluations from Wilk's theorem and second based on response surface followed by Monte Carlo method to evaluate the 95th percentile PCT. The result is shown in Fig. 6.

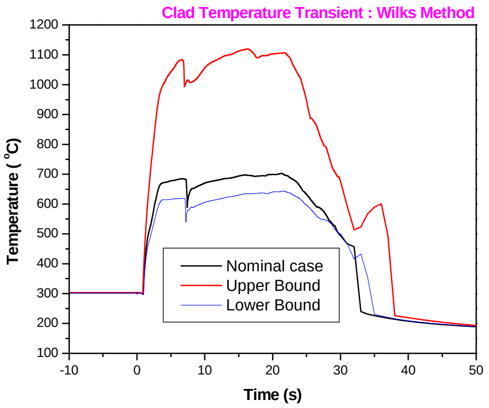

Fig. 6: Results of uncertainty analysis for Clad Temperature for AHWR

An Integrated AHWR MHT + turbine-condenser model has been developed in RELAP5. This model has been tested for power manoeuvring from 100% to 85% and back to 100% transient as shown in Fig. 7. This model will be used for ongoing plant analyser development work.

Safety Analysis for Indian PHWR

An input model has been developed for Indian PHWR in RELAP5 [2]. Spectrum of break sizes ranging from 200%, 160%, 120%, 100%, 75%, 60%, 40% and 20% in four combinations of inlet and outlet header break with and without ECC system are analysed [2] to generate the time variation of the 37 COIS variables for each case for training and further testing of ANN to identify the break size, its location etc. A typical result of one combination of different break sizes at inlet header is shown in Fig. 8. The findings of these analyses forms a database to train the neural network based diagnostic tool useful for emergency planning and management [3].

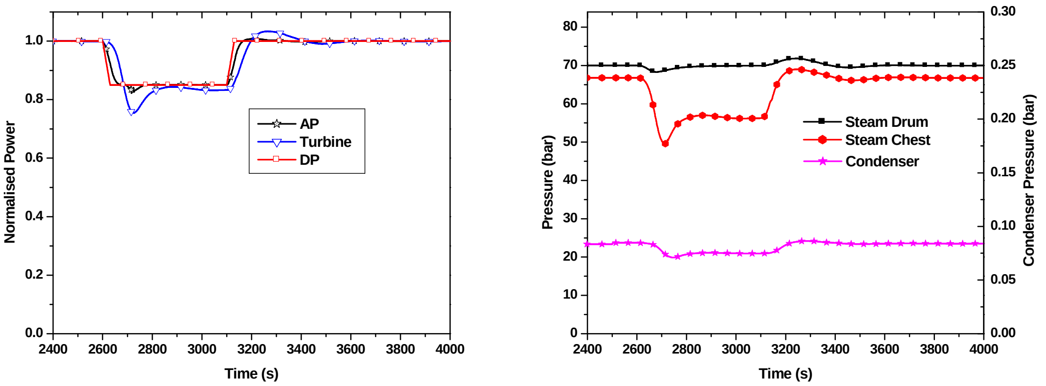

Fig. 7: Results of Power manoeuvring transients for AHWR

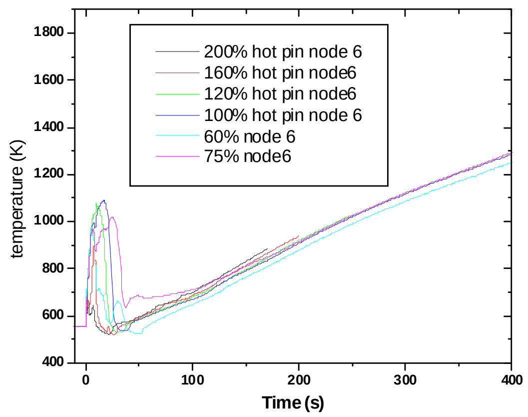

Fig. 8: Clad temperature (broken pass) transients for LBLOCA at IH with no ECC

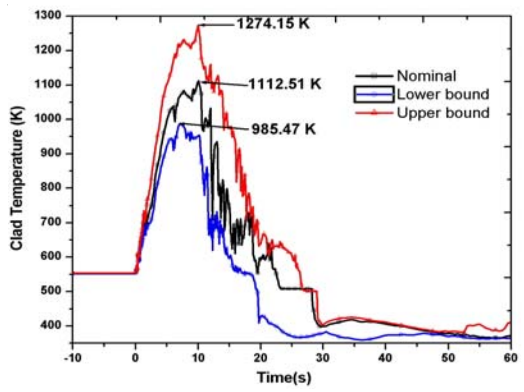

Fig. 9: Bounding Hot pin temperatures for PHWR LOCA analysis

Best estimate plus uncertainty analysis for LBLOCA for PHWR has been done. In this critical break at inlet header of PHWR has been first identified and uncertainty analysis has been performed [4]. For 160% inlet header break for PHWR, the 95th percentile PCT with 95% confidence is 1274 K. The upper, nominal and lower bound clad temperatures are plotted in Fig. 9.

Cold Leg LOCA Assessment for VVER-1000 Plus Uncertainty Analysis

A CATHARE model for the KK-VVER reactor simulating different systems and components has been developed and cold leg LOCA analysis has been carried out along with uncertainty evaluation [5]. The main purpose of this analysis is to have independent verification of predictions with Russian results. The results of best estimate cold leg break LOCA is shown in Fig. 10 and uncertainty analysis findings are highlighted in Fig. 11.

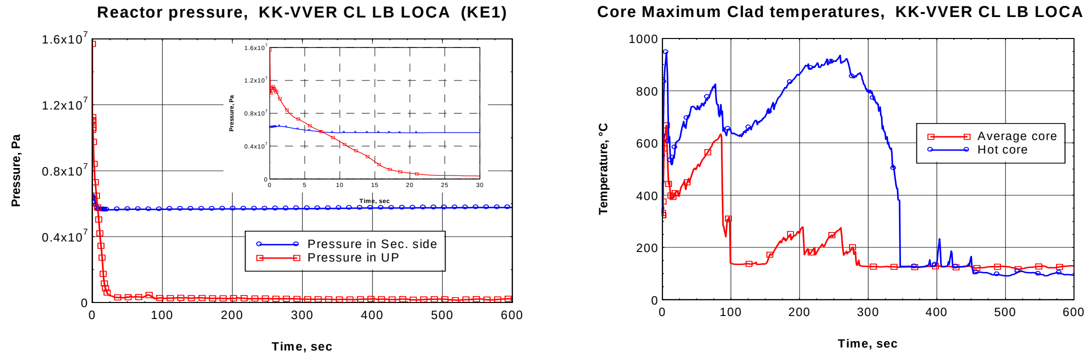

Fig. 10: Results of double-ended cold leg break of KK-VVER

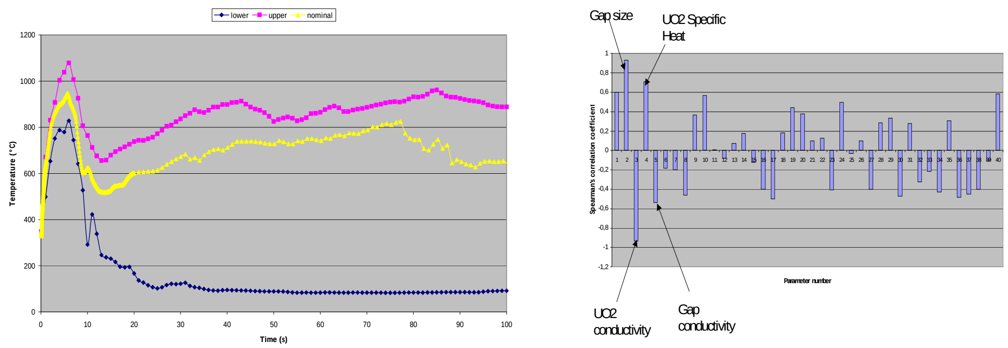

Fig. 11: Results of uncertainty and Sensitivity analysis for double-ended cold leg break of KK-VVER

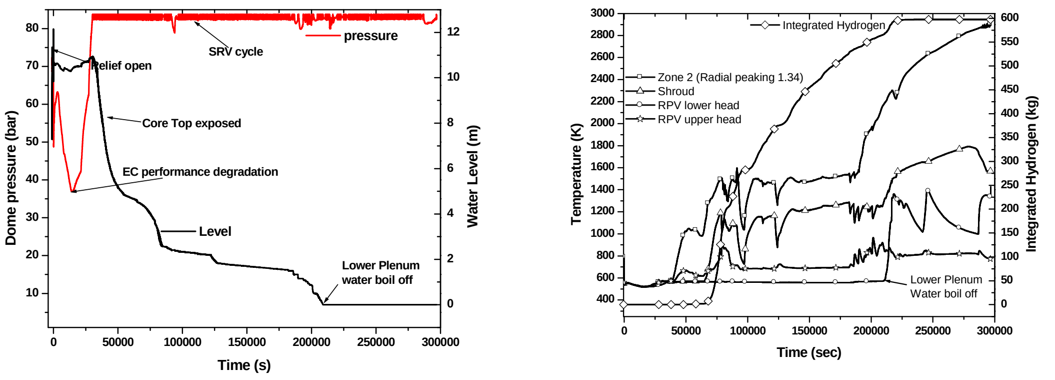

Fig. 12: Fuel, shroud, RPV temperatures and Hydrogen generation during SBO for TAPS

TAPS-BWR Station Blackout Analysis in RELAP5/ SCDAP

A detailed model of TAPS-1/2 NPP has been developed to simulate extended Station Blackout (SBO) severe accident analysis using RELAP-SCDAP code which highlights the accident progression by initial core heat up, material interaction, debris formation and heat transfer, slumping, molten pool thermal hydraulics. This analysis is useful in accident management and timely operator action. A typical result is shown in Fig. 12.

Conclusion

The paper addressed the analyses highlighting the safety aspects for different level of defence in depth for Indian reactors. The use of best estimate code RELAP5 for operating transients, DBEs for AHWR along with its application for simulation of LBLOCA scenario for Indian PHWR for development of diagnostic system is presented. The use of CATHARE code is highlighted for the cold leg LOCA analysis for VVER-1000. The TAPS-BWR SBO analysis highlights the severe accident progression. The paper also brings out the uncertainty estimate for LBLOCA scenarios for these reactors.

References

1. A. Srivastava, H.G. Lele, A.K. Ghosh and H.S. Kushwaha, "Uncertainty analysis of LBLOCA for Advanced Heavy Water Reactor", *Annals of Nuclear Energy,* 35 (2008), Issue 2: 323-334.
2. B. Gera, Mithilesh Kumar, I. Thangamani, H. Prasad, A. Srivastava, P. Majumdar, Anu Dutta, V. Verma, S. Ganju, B. Chatterjee, H.G. Lele, V.V.S.S. Rao, A.K. Ghosh, "Estimation of source term and related consequences for some postulated severe accident scenarios of Indian PHWR" *Nuclear Engineering and Design,* 240 (2010): 3529-3538.
3. T.V. Santhosh, M. Kumar, I. Thangamani, A. Srivastava, A. Dutta, V. Verma, D. Mukhopadhyay, S. Ganju, B. Chatterjee, V.V.S.S. Rao, H.G. Lele, A.K. Ghosh, "A diagnostic system for identifying accident conditions in a nuclear reactor", *Nuclear Engineering and Design,* 241 (2011): 177-184.
4. A.K. Trivedi, A. Srivastava, H.G. Lele, M.S. Kalra, P. Munshi, "Uncertainty analysis of large break LOCA for pressurized heavy water reactor" *Nuclear Engineering and Design* 245 (2012): 180-188.
5. Luben Sabotinov, A. Srivastava and Pierre Probst, "Best Estimate Simulation and Uncertainty Analysis of LB LOCA for KudanKulam VVER-1000 NPP", Proceedings of the 17th International Conference On Nuclear Engineering (ICONE-17) (2009), Brussels, Belgium, July 12-16.

SEPARATION OF ACTINIDES AND FISSION PRODUCTS RELEVANT TO NUCLEAR WASTE MANAGEMENT

S.A. Ansari
Radiochemistry Division

Dr. S.A. Ansari is the recipient of the DAE Young Scientist Award for the year 2010

Abstract

Actinide partitioning has been a proposed strategy for the safe disposal of High Level Waste (HLW) generated during reprocessing of the spent nuclear fuel. In this context, development of new extractants for actinide partitioning has been one of the challenging areas of research for the radiochemists / separation chemists. Amongst different extractants studied for actinide partitioning, *N,N,N′,N′*-tetraalkyl diglycolamides (DGA) have been found to be the most promising [**1**,**2**]. At Radiochemistry Division, DGA extractants have been extensively studied for actinide partitioning up to mixer-settler stage, and the results have been the most promising reported so far internationally. Extensive work has been carried out on hollow fiber supported liquid membrane (HFSLM) technique for possible application to several separations relevant at the back end of the nuclear fuel cycle. The separation of Am(III) from simulated HLW by HFSLM technique has been demonstrated for the first time. A pilot scale run was carried out at 20 L scale for the actinide partitioning using surrogates in simulated HLW solution. The HFSLM method was successfully demonstrated for lanthanide/actinide separation using Cyanex-301 as the carrier. The HFSLM method was also demonstrated for the recovery of Cs(I) and Sr(II) from Simulated HLW on litres scale using macrocyclic ligands. A highly efficient HFSLM method was developed for the recovery of plutonium from analytical waste at a significantly lower personnel exposure and very high recovery percentage and purity of the product.

Solvent Extraction Studies

Extensive actinide partitioning studies have been carried out using extractants such as CMPO (octyl-(phenyl)–*N,N*-diisobutylcarbamoyl methylene phosphine oxide), TRPO (trialkyl phosphine oxide), DMDBTDMA (*N,N′*-dimethyl-*N,N′*-dibutyl tetradecyl malonamide), TEHDGA (*N,N,N′,N′*-tetra-2-ethylhexyl diglycolamide) and TODGA (*N,N,N′,N′*-tetraoctyl diglycolamide) (Fig. 1). Batch extraction and mixer-settler runs demonstrated with simulated HLW suggested TODGA as the most promising for actinide partitioning. With 0.1M TODGA, quantitative extraction (forward and backward) of lanthanides was observed in four stages, and the results were the most promising reported so far internationally. Reusability of the organic phase in five successive cycles suggested excellent hydrolytic stability of the reagent. Negligible effects of radiolytic degradation of solvent (100 kGy) were observed on the extraction as well as on the stripping of lanthanides.

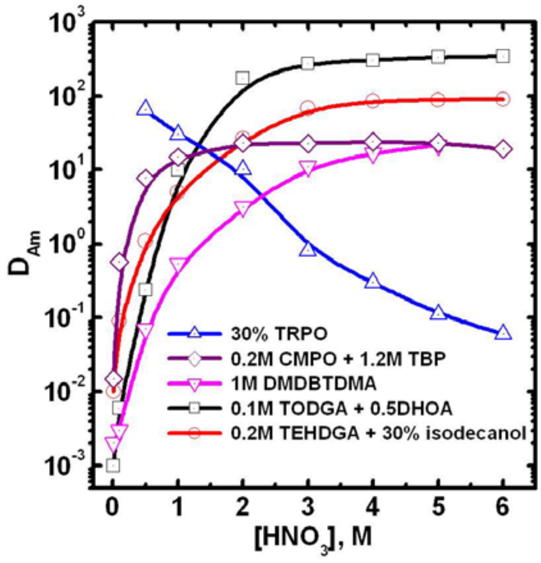

Fig. 1: Extraction behavior of Am(III) by different extractants

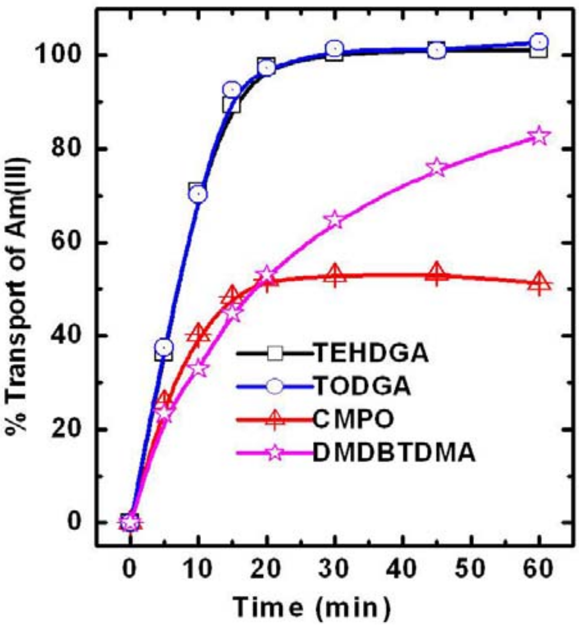

Fig. 2: Transport of Am (III) by HFSLM of different solvents

Actinide Partitioning Studies with Hollow Fibre Membrane

The transport of trivalent actinides by hollow fibre supported liquid membrane (HFSLM) was measured using different extractants proposed for actinide partitioning, viz. CMPO, DMDBTDMA, TODGA and TEHDGA. For different solvents, the transport followed the order: 0.1M TODGA ~ 0.2M TEHDGA > 1M DMDBTDMA > 0.2M CMPO. This order was primarily influenced by the co-transport of acid and the distribution ratio of metal ions at the acidity encountered in the strip phase. The transport of Am(III) with TODGA and TEHDGA yielded quantitative transport of Am(III) within 30 minutes (Fig. 2). Under identical conditions of feed and strip solutions, only ~65% and 50% Am(III) transport were observed for DMDBTDMA and CMPO, respectively. Investigation of acid transport revealed ~0.25M HNO_3 transport in 15 minutes with TODGA, T2EHDGA and DMDBTDMA systems, and ~0.6M HNO_3 in the case of CMPO. The Distribution ratio of Am (D_{Am}) values for these extractants at 0.5 M HNO_3 were 0.2, 0.5, 0.07 and 8, respectively. High D_{Am} value in case of CMPO at relatively lower acidity (0.5-1M HNO_3) hindered the stripping of metal ions in the receiver phase, which restricted the Am(III) transport.

Transport of lanthanides from SHLW was demonstrated with TODGA-HFSLM on 20 liters scale, where quantitative and selective transport of lanthanides was achieved in 18 hrs. The product could be concentrated two times by maintaining the feed to strip volume ratio of 20:10 litres. However, as the feed to strip volume ratio increased, acid build up in the receiver phase increased which was neutralized by adding NaOH and the acidity of the strip phase was maintained around 0.5M HNO_3. The final feed composition of the two times concentrated product was: 0.2M $NaNO_3$ at 0.5M HNO_3, which was suitable for the subsequent lanthanide / actinide separation as described latter in this report. Physical and chemical stability of TODGA-HFSLM was demonstrated to be excellent for 72 hrs of continuous operation. Radiation stability of the carrier (0.1M TODGA + 0.5M DHOA) and hollow fibre lumen was satisfactory up to 500 kGy dose. The present studies revealed that TODGA-HFSLM system offers a promising alternative approach for 'actinide partitioning', where the use of organic solvent inventory could be drastically reduced.

Lanthanide / Actinide Separation with Hollow Fibre Membrane

The HFSLM technique was successfully applied for the selective recovery of trivalent actinides over lanthanides using Cyanex-301 (bis(2,4,4-trimethyl pentyl) dithiophosphinic acid) as the carrier. The feed solution was 1g/L total lanthanides (spiked with tracers such as ^{140}La, ^{160}Tb, ^{166}Ho, ^{175}Yb and ^{177}Lu) along with ^{241}Am tracer at 1M

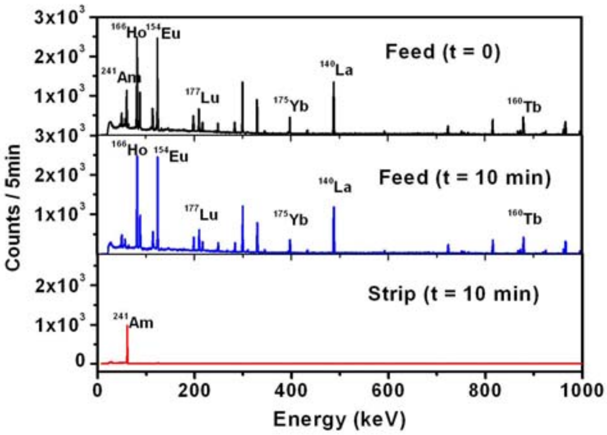

Fig. 3: Gamma spectrum of the Am and lanthanides in the feed, strip and raffinate solutions showing selective transport of ^{241}Am

$NaNO_3$ buffered to pH 3.5 with sulphanillic acid. The strip solution was 500mL of 0.01M EDTA. Quantitative (>99.9%) transport of Am(III) was possible in 10min with 0.5M Cyanex-301 as the carrier with negligible presence of the rare earth tracers (Fig. 3). The decontamination factors for all the lanthanides were ~100. The work revealed that the product obtained during actinide partitioning with TODGA-HFSLM (which contains lanthanides and trivalent actinides) can be directly used for lanthanide/actinide separation by Cyanex-301-HFSLM system, after suitable feed adjustment.

Recovery of Cesium and Strontium by Hollow Fibre Membrane

Calix[4]arene-bis-2,3-naphthocrown-6 and di-*tert*-butyl dicyclohexano 18-crown-6 ligands are reported to be extremely selective for Cs(I) and Sr(II), respectively in the presence of large concentrations other metal ions. However, pertaining to very high cost of these ligands, their applications in solvent extraction process has practical difficulty. Nevertheless, liquid membrane techniques can be applied for such system which has the advantage of using very small amount of ligands. In this context, the HFSLM technique was applied on litres scale for the recovery of radio-cesium and radio-strontium using target selective macrocyclic ligands. The transport data from Simulated HLW revealed the selective recovery of Cs(I) or Sr(II) over other radiotracers (^{214}Am, ^{154}Eu, ^{59}Fe and ^{51}Cr) with decontamination factors of ~100 for all the metal ions present in HLW. High decontamination factors as well as throughputs suggested possible application of the HFSLM system for the recovery of radio-cesium and strontium from HLW.

Recovery of Plutonium from Analytical Waste

An efficient HFSLM method was developed for the recovery of plutonium from analytical waste on litres scale, which contains grams level of U and Pu, and milligram level of Am. In this method, pure fraction of U is also obtained along with Pu. The technique is faster and gives lower radiation exposure to the working personnel with lower volume of secondary waste generation as compared to traditional precipitation technique. The recovery of Pu was carried out in two stages. In the first stage, Pu(IV) and U(VI) were selectively recovered by TBP-HFSLM leaving all the Am and metallic impurities in the raffinate. In the second stage, Pu was reduced to Pu(III) and U(VI) was selectively transported into the receiver phase, separating Pu fraction from U. By following the above procedure, about 50 g Pu could be recovered from 10 litres of analytical waste (Fig 4).

Fig. 4: The recovered plutonium and uranium from the analytical waste; (a) Waste, (b) U(VI), and (c) Pu(III) solutions

Acknowledgements

Author acknowledges Dr. P.K. Mohapatra, Head, Actinide Chemistry Section (ACS), Radiochemistry Division for his guidance. Thanks are due to all the members of ACS for their valuable support in these studies. Dr. K.L. Ramkumar, Director, RC&I Group, Dr. S.K. Aggarwal, Associate Director, RC&I Group and Dr. A. Goswami, Head, Radiochemistry Division are sincerely acknowledged for their constant encouragement.

Reference

1. S.A. Ansari, P.N. Pathak, P.K. Mohapatra and V.K. Manchanda, Chemistry of diglycolamides: Promising extractants for actinide partitioning, ***Chem. Rev.***, 112 (**2012**) 1751-1772.
2. S.A. Ansari, P.N. Pathak, P.K. Mohapatra and V.K. Manchanda, Aqueous partitioning of minor actinides by different processes, ***Sep. Purif. Rev.***, 40 (**2011**) 43-76.

DESIGN AND DEVELOPMENT OF WATER HYDRAULIC MULTI-STAGE PILOT OPERATED PRESSURE CONTROL VALVE FOR AHWR FM

S.B. Pandharikar, N.L. Soni and R.J. Patel
Refuelling Technology Division

Shri S.B. Pandharikar is the recipient of the DAE Young Applied Scientist & Technologist Award for the year 2010

Abstract

During refuelling, the Fuelling Machine (FM) is attached to the end fitting of the coolant channel and it becomes part of reactor pressure boundary. FM pressure is maintained 1 to 2 kg/cm^2 above the channel pressure to prevent the entry of hot water in the FM. The FM pressure control is carried out using pressure sensor, controller and conventional control valves. A compact multi-stage pilot operated pressure control valve has been designed to carry out pressure control of AHWR FM which will eliminate the controller, sensors, control valves and associated components making the system simple and compact. The same valve can be used for pump pressure control of FM head water supply system.

Introduction

AHWR is a light water cooled, heavy water moderated, vertical pressure tube type reactor. Refuelling of the reactor is carried out using a Fuelling Machine (FM). The FM is capable of carrying out on-power refuelling operation. In the on-power refuelling scheme, the FM is attached to the end fitting of reactor coolant channel and becomes a part of reactor boundary. The FM houses many mechanisms, seals etc. which cannot be operated at high temperature. So, to prevent the entry of hot water from reactor coolant channel in the FM, its pressure is maintained 1 to 2 kg/cm^2 above the coolant channel pressure. This FM pressure control is carried out using sensors, controller and conventional control valves. A compact, multi-stage, fast acting, water hydraulic, pilot operated pressure control valve (POPCV) has been designed to control the FM pressure. The single valve will eliminate sensors, controller, control valves, large accumulators and associated piping making the system more compact and easy to maintain. The same valve can be used for pump pressure control of head water supply system of FM.

Existing Pump pressure and FM magazine pressure control circuit

Fig.1 shows simplified circuit of existing FM supply pump and FM magazine pressure control system. The FM requires 125 lpm flow at maximum pressure of 150 kg/cm^2. This requirement is catered by the high pressure FM supply pump. The FM pump pressure is controlled using bypass flow control method. FM pump pressure control system has a pressure transmitter which senses the system pressure. The pressure is given as feedback to a controller. The required pump pressure is given to the controller as set point. The comparator in controller compares set point with the feedback pressure and generates error signal equivalent to the difference between set point and feedback. Using this error signal, the PID controller generates a corrective signal. This output of controller is given to an E/A convertor, which generates an equivalent pneumatic pressure signal. This pneumatic pressure is supplied to the positioners of control valve, which control their opening. Change in opening of control valves will change the system pressure.

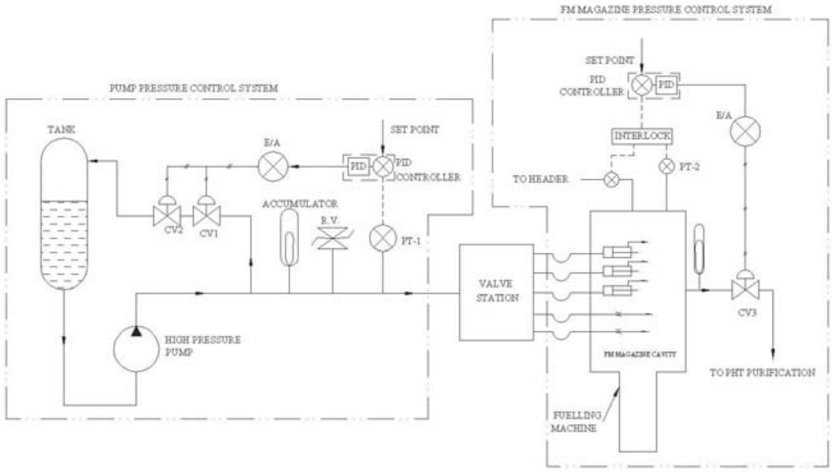

Fig. 1: Simplified circuit of existing FM supply pump and FM magazine pressure control

This pressurised water is supplied to FM magazine cavity, seals and various water hydraulic actuators of FM. This distribution of water takes place in valve station. The outlets of all actuators, seals are finally connected to magazine housing. A control valve in magazine return line controls magazine pressure. Magazine pressure is controlled to 20 kg/cm^2 in Park mode and fuel discharge mode using feedback from pressure transmitter. It is maintained 1 to 2 kg/cm^2 above channel pressure in off-reactor and on-reactor mode using a feedback from differential pressure transmitter connected between fuelling machine magazine and header.

Design and working of Pilot Operated Pressure Control Valve

A pilot operated pressure control valve is designed for FM pump pressure control and FM magazine pressure control. The cross section of valve is shown in Fig.2. The valve consists of a main valve, a pressure compensated flow control valve and a pilot relief valve. The upstream of main valve is connected to the FM pump or Magazine and downstream is connected to return line or PHT purification line. So, very high pressure drop takes place across the main valve control trim. The working medium for valve is water. Since vapour pressure of water is high, cavitation can occur at the control trim. To avoid cavitation, the pressure drop in the valve is carried out in four stages. The stages are sized so that the pressure at any stage shall be always more than the vapour pressure, thus avoiding cavitation.

The inlet pressure to the valve is acting on one side of a balance piston as shown in Fig.2. The other side of balance piston is connected to a pilot relief valve. Flow to this pilot relief valve is maintained constant using a pressure compensated flow control valve as shown in Fig.3. A force is also applied on balance piston using a light spring. The pilot valve also has a piston. One side of this piston is subjected to pressure of spring side of balance piston of main valve. A force is applied on this piston is using a lever. The other side of lever is connected to a spring loaded cylinder. The force generated by this spring loaded cylinder can be changed by changing pneumatic pressure supplied to the cylinder. The pneumatic pressure can be remotely changed using a E/A convertor mounted on POPCV. The force generated by pneumatic pressure opposes the spring force. Thus, with increase in pneumatic pressure, the set pressure of pilot relief valve of POPCV shall be reduced, which in turns reduce the pressure in spring side of balance piston of main valve, and hence the pressure of system, and vice versa. Pilot operated configuration has been adopted for this valve to avoid use of large and heavy spring and reduce the pressure over-ride due to change in opening of the valve at various operating conditions. The pressure compensated

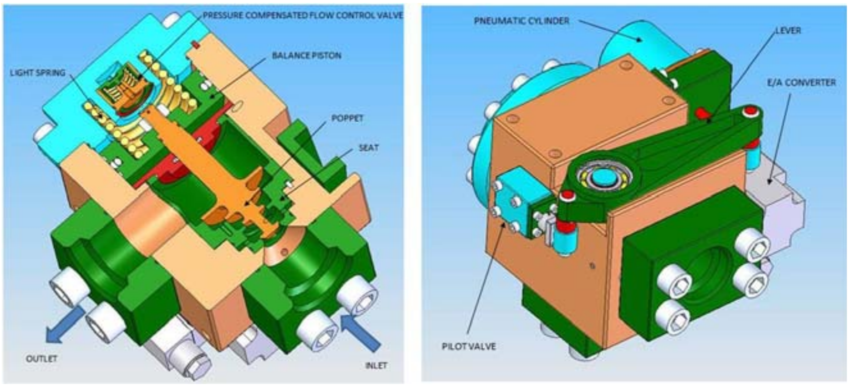

Fig. 2: Pilot Operated Pressure Control Valve

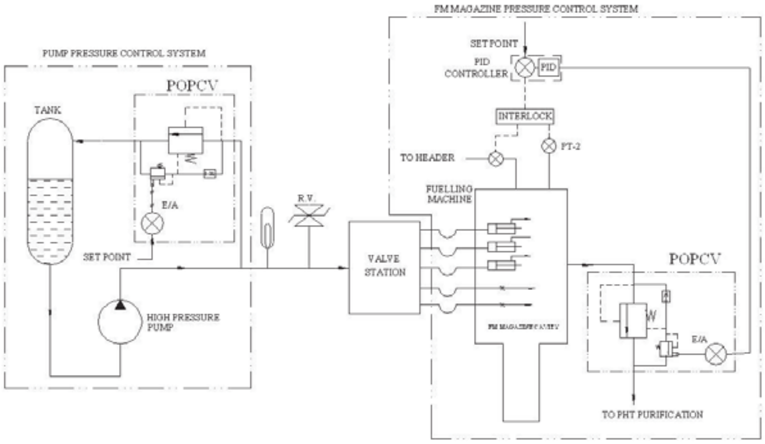

Fig. 3: FM supply pump and FM magazine pressure control circuit using POPCV

flow control valve in the pilot line maintains constant flow to the pilot relief valve thus further reducing the change in operating position of pilot valve resulting in more accurate pressure control.

The valve is designed for a maximum flow of 185 lpm and 160 bar pressure. 4-20 mA signal is given as set point to the valve. The valve can be operated in open loop as well as closed loop control.

Pump pressure and FM pressure control circuit using POPCV

New pressure control circuit for FM pump and FM magazine pressure control is shown in Fig.3. The POPCV used for pump pressure control is used in open loop control. POPCV internally senses the pressure and compares with the set point and changes the position of its poppet to maintain the pressure as per the set point. In FM magazine pressure control, POPCV can control pressure to 20kg/cm^2 in open loop as well as close loop. But during off-reactor and on-reactor mode, the machine pressure is required to be controlled 1 to 2 kg/cm^2 above channel pressure. So a close loop control is preferred.

Advantages

The valve is an indigenous and compact. A single valve can replace sensor, controller, control valves and associated piping and accessories in the system making it compact and easy to maintain. The corrective forces acting on valve poppet are very large, thus making it a fast acting and thus reducing the size of accumulators in the system. The valve can be used in open as well as closed loop control.

Conclusion

An indigenous, compact multi stage pilot operated pressure control valve has been developed which can be used for pump pressure control of Fuelling Machine supply pump as well as for Fuelling Machine magazine pressure control. The single valve can replace controllers, sensors, control valves and other accessories in the system, making the system compact and easy to maintain. The performance of Pilot Operated Pressure Control Valve will be proved by implementing it in AHWR FM test facility. Once the design of Pilot Operated Pressure Control Valve is proven, it has potential for deployment in in operating / future PHWR fuel handling systems.

DESIGN, DEVELOPMENT AND COMMISSIONING OF 9 MeV RF LINAC AT ECIL, HYDERABAD FOR CARGO SCANNING APPLICATIONS

K.C. Mittal, D.P. Chakravarthy, V.T. Nimje, K.P. Dixit, P. Roychowdhury, V. Yadav, Shiv Chandan, P.C. Saroj, Mukesh Kumar, S.R. Ghodke, D. Bhattacharjee, A.R. Tillu, R.B. Chavan, D. Jayaprakash, R.L. Mishra, N. Chaudhary, R.R. Tiwari, S.S. Barje and N.K. Lawangare
Accelerator & Pulse Power Division

and

A.K. Sinha and S.B. Jawale
Centre for Design & Manufacture

and

Amar Sinha
Neutron & X-ray Physics Facilities

Dr. K.C. Mittal, Electron Beam Centre and his team received the
DAE Group Achievement Award for the year 2010

Abstract

A 9 MeV RF Electron linac for cargo-scanning has been successfully commissioned at Electronic Corporation of India Limited (ECIL), Hyderabad. The pulsed coupled-cavity on-axis linac operates at a frequency of 2856 MHz with pulse width of 5.8 μs and 250 Hz repetition rate. This linac has been RF-conditioned up to a peak power of 2.6 MW. Peak beam current of ~ 60 mA has been measured at the output of the linac. X-ray dose of ~ 24 Gy/min has been measured at one meter distance from the tantalum target. Beam size of ~2 mm has been obtained on the target. A primary collimator is designed for slicing the x-ray beam. The accelerated electron beam hits a tantalum target and x-ray generated though the target is fed to the primary collimator. Thereafter, collimated high energy x-ray will be used for cargo scanning. This paper highlights the features of the 9 MeV linac, its performance with RF power, behaviour of the linac under beam loading, design of primary collimator for the imaging purpose and measurements done to determine the x-ray dose rates.

Introduction

Cargo-scanning systems require a linac to produce high energy electrons, which bombard a high Z target to generate bremsstrahlung radiation. These x-rays penetrate high density cargo and the resulting high quality images enable the detection of hidden, contraband goods, weapons, undeclared goods, etc.

A 9 MeV RF Electron linac for cargo scanning has been designed and developed by APPD/BARC at ECIL, Hyderabad [1]. The linac system has been designed to satisfy the specifications listed in Table 1.

System Description

An LaB_6-based electron gun serves as the injector of electrons into the on-axis coupled cavity linac, which is powered by a klystron-based RF source [2]. The electrons are accelerated up to of 9 MeV in a length of ~1m. Fast current transformer at the end of the linac is used to measure the beam current. A solenoid is used to focus the accelerated beam to the required size on the water-cooled tantalum target placed at the end of the beam tube. The thickness of tantalum target is 2 mm. The entire system from gun to target is maintained at a vacuum level of 10^{-7} mbar with the help of sputter-ion pumps.

Remote operation of the linac system, situated in the radiation shielded area, is performed through PC located in the control room [3]. The linac system is in the horizontal position and a view of the linac is shown in Fig. 1.

Table 1: Specifications of 9 MeV RF electron linac

Beam Energy	9 ± 0.1MeV
Average Beam Current	0.2 mA
Peak beam current	100 mA
Average Beam power	1.0 kW
X-ray beam focal spot size	2 mm
X-ray symmetry	±5% at 7.5° off the central axis
Leakage of radiation	0.1 %
X-ray field size	Standard 30 °cone
Length of accelerator	~1 metre
Pulse Width	5.8 μs
Pulse repetition rate	250 Hz
Injection voltage	50-70 kV
Microwave Frequency	2856 ± 2 MHz
Peak klystron power	2 – 3 MW (2.6 MW nominal)
Average klystron Power	2 – 3 kW (2 kW nominal)

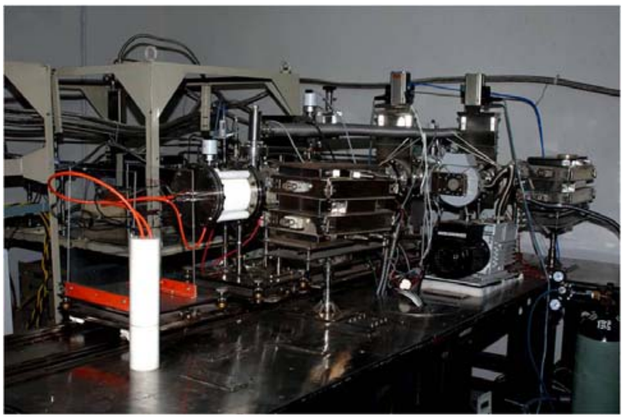

Fig. 1: View of the linac system used for cargo-scanning

X-rays produced from the target are then collimated to form a thin column of ~ 4 mm and allowed to fall on the cargo. The x-rays penetrate through the thickness of the cargo and fall on the detectors placed on the other side of the cargo. At a given time, one column of the image is captured by the detectors. The horizontal dimension of the image is produced by moving the cargo at a given speed. The complete image is then reconstructed by using proper software toolkits.

Safety Interlocks

Various safety interlock has been implemented for safe operation of the microwave source. The klystron modulator has been interlocked with water flow, arc detector, klystron electromagnet current, klystron modulator door and SF_6 gas pressure. In case of any of the interlock getting activated, the input trigger pulse to klystron modulator is blocked thus no output RF power is generated. The klystron electromagnet supply is interlocked with water flow, as there is high current, which can damage the electromagnet in absence of water.

A relay based hardwired interlock unit has been used for implementing the above-mentioned interlocks.

For the safe operation of the system, the sync trigger generator is interlocked with vacuum and arc. In case of vacuum pressure falling or arcing, the trigger pulse to the system is stopped. The vacuum data is continuously monitored and recorded.

Primary Collimator Design

The primary collimator will complement the existing system to get collimated fan beam. A collaborative effort has been made to identify novel and advanced materials to achieve low coefficient of friction for various lateral and angular movements of collimator plates weighing nearly 5 tons. Complex numerical calculations simulating extreme conditions and experimental tests have been undertaken using ANSYS software toolkit. In parallel, an innovative modular design concept of the assembly has been developed to allow fitting in alternative materials, minimizing the load induced deformations, withstanding accidents and accepting desired radiation doses.

The collimator plates are made up of mild steel blocks of IS 2062A grade ensuring high geometrical stability. The assembly structures for the collimator are made up of high stiffness I-beams ISMB 150. Each plate has been machined with high precision Electric Discharge Machining (EDM) and Surface Grinding processes. The plates are also hard chrome plated to provide corrosion resistance and increase surface hardness. A full scale collimator prototype has been manufactured to validate each feature of the new design.

The primary collimator is actually a series of mild steel blocks which have continuous slits but of increasing width. The first block has a slit of width 4 mm X 4 mm. The last block gives out the x-ray beam with same thickness of 4mm but of more length which has been increased as per a particular angle over the series of MS blocks collimating it. This beam is to be used for non destructive scanning of dense cargo.

Detailed analyses were carried out in ANSYS in two stages. [4] In the first stage of analysis all the plates were modelled together of size 900 mm X 800 mm X 800 mm. The base frame supports were provided in the vertically upward direction. The material elasticity, density are defined for steel. As load is only due to self weight the gravity is defined as 9.81 m/s^2 in the vertically downward direction. Case is solved for the deflection and reaction at the supporting edges. Maximum deflection in plate structure is 0.26 micron.

In the second stage of the analysis wire frame modelling was done. The reaction forces per unit length at the supporting edge of the plate from the first analysis were applied as the load in the second stage. All the supporting frame structures selected are I beam of ISMB 150. Beam element is selected and line meshing is done.

Collimator plate structure along with support structure is assembled at ECIL site. Movement of plate in x, y, z direction and angular movement is also checked.

System Operation

The entire linac system was assembled at the Linac Test Facility (LTF). Evacuation of the system was carried out till a vacuum level of 10^{-7} torr was obtained. RF power of 2.6 MW and peak beam current of 60 mA is required for generation of desired intense photon beam. To operate the linac at high microwave power of 2.6 MW, RF conditioning was carried out. For this purpose, the peak power of klystron was increased up to 500 kW at 10 Hz and then pulse repetition frequency (PRF) was raised till 250 Hz. As PRF is increased, detuning of cavity resonant frequency occurs, due to which the RF reflected power increases. To reduce the reflected power, the RF frequency of the signal generator is varied to match the resonant frequency. The peak power is increased in steps of 100 kW & PRF was increased from 10 to 250 Hz at each peak power level. When arcing was observed (as seen in reflected power pulse) or vacuum deterioration in linac, peak power was reduced by changing the gain of the driver amplifier and conditioning was done at higher PRF for longer duration. During RF conditioning, a vacuum of 3.0×10^{-7} mbar was maintained throughout the complete linac system. Vacuum and reflected power was continuously monitored and controlled during RF conditioning of the linac.

After ~200 hours of RF conditioning, forward power of 2.6 MW and 250Hz PRF could be sustained. Beam trials were then carried out. The planar electron gun configuration (cathode-grid shorted) gave an output current of 60 mA at for 65 kV gun voltage for 250 W filament power. An output beam current of 140 mA was achieved with a positive grid bias of 3.8 kV and V_{KA} = 66.8 kV. An output beam current of 58 mA was achieved with a negative grid bias of 3.8 kV and V_{KA} = 63 kV. [5]

X-ray Measurements

The accelerator is operated in x-ray mode and the beam spot has been observed on photographic film which was kept adjacent to the tantalum target. The photograph of the beam spot as seen on the tantalum target is shown in Fig. 2.

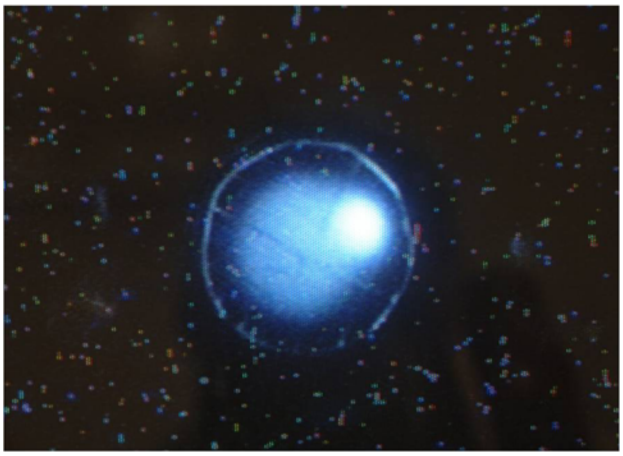

Fig. 2: Beam spot seen on target

The dose rate of x-ray, produced after hitting Ta target has been measured by using air ionization chamber. The radiant energy ionizes the air within the chamber. The ionization chamber used is model no. CC13 make IBA Dosimetry, Germany and its active volume is 0.13 cc.

An electrometer, model Dose1, make- IBA is used for generating bias voltage of 300 V and measuring the ion current. The applied bias voltage results in accumulation of ions and electrons on respective opposite electrodes. The rate of charge accumulated on electrodes gives the dose rate by using a calibration factor having unit in Grey/coulomb (Gy/C).

X-ray dose was measured using ionisation chamber at linac operating parameters of 2.6 MW, 250Hz, 5 .8 μsec, 60 mA peak beam current of 9MeV energy. Dose rate is about 24 Gy/min at 1m from the x-ray converter was measured.

Conclusion

The design and development 9 MeV RF electron linac for cargo-scanning has been completed successfully. X-ray measurements have confirmed required dose rates of 24 Gy/min/m. Beam diameter of ~2 mm has been achieved. Experiments with collimator and imaging system with dummy cargo are in progress. A compact linac for 6 MeV has also being planned along the same lines. These types of compact systems are very useful. It can be transportable systems and installed at any sensitive place on security point.

References

1. Design basis report of ECIL cargo-scanning linac, Internal report
2. V.Yadav, *et al*, "Microwave source development for 9 MeV RF electron linac for cargo scanning", InPAC - 2011, IUAC, New Delhi.
3. R.B.chavan, *et al*, "Linac parameter acquisition system (lipas) for 9 MeV RF linac", InPAC- 2011, IUAC, New Delhi
4. S. R Ghodke, *et al*, "Design and Development of Collimator for 9 MeV BARC-ECIL Linac ", InPAC- 2011, IUAC, New Delhi
5. D. Bhattacharjee, et al, "Design and development of a pierce electron gun", InPAC – 2011, IUAC, New Delhi.

DEVELOPMENT, DEMONSTRATION AND DEPLOYMENT OF ‘BARC ^{125}I -Ocu PROSTA SEEDS’ FOR THEIR USE IN THE TREATMENT OF EYE CANCER

**Ashutosh Dash, Sanjay Kumar Saxena, R.B. Manolkar,
K.C. Jagadeesan and P.V. Joshi**
Radiopharmaceuticals Division

Dr. A. Dash, Radiopharmaceuticals Division, Radiochemistry & Isotope Group and his team received the DAE Group Achievement Award for the year 2010

Abstract

This paper described the development of a technology for the production of titanium encapsulated ^{125}I brachytherapy seed sources for the treatment of ocular cancers. The work entails (i) development of technology for ^{125}I production, (ii) chemical immobilization of ^{125}I into silver carrier rods, (iii) encapsulation of the source in tiny titanium capsules, (iv) quality evaluation of ^{125}I seeds, (v) type approval of the source by AERB, India (vi) collaboration with physicians to deploy BARC ^{125}I-brachytherapy seeds in the clinical arena.

Introduction

Uveal melanoma is the most common primary intraocular malignancy in lightly pigmented persons and is infrequently seen in non-white races. India enjoys a low incidence of malignant melanoma of the uveal tract. Brachytherapy using removable episcleral plaques containing sealed radioisotope sources is one of the treatment modalities extensively used for effective local tumor control, destruction of metastatic potential, and preservation of ocular and visual function. The Radiopharmaceuticals Division with the need based support of other Divisions of BARC, carried out a research which lead to the successful development of a technology for the production of indigenous ^{125}I brachytherapy sources (‘BARC I-125 Ocu-Prosta seed’) [1] in the year 2003 for the management of eye cancer. The driving force behind this initiative was to provide ^{125}I brachytherapy sources to meet the domestic needs and to promote the beneficial use episcleral brachytherapy in India. The work involved three aspects

1. Development of the technology for the production of ^{125}I by gaseous target irradiations in Dhruva reactor followed by chemical reprocessing.
2. Development of technology for the production of titanium encapsulated ^{125}I seed sources conforming to the AERB requirements
3. Collaboration with physicians to deploy BARC ^{125}I-brachytherapy seeds in the clinical arena where patients can benefit from the research.

Production of ^{125}I

An indigenous procedure for the local production of ^{125}I from the neutron irradiated natural Xe target using wet chemical distillation method was developed [2]. The technology development aspects are related to: the design of the irradiation container, its fabrication, cryogenic filling of gaseous Xe target into the container, hermetic sealing of irradiation container, selection of appropriate neuron flux, irradiation time, neutron irradiation of target, target cooling and optimization of distillation parameters to avail ^{125}I of requisite purity and yield. In one batch, typically 4 grams of natural xenon gas was irradiated in the Dhruva reactor of this institution for 15 days with a thermal neutron flux of around 5×10^{13} n/cm^2/s. After irradiation, the targets are left to decay for typically $\sim$ 50 days to reduce the contamination of ^{126}I. The irradiation containers


(a) (b) (c)

Fig. 1: Production of ^{125}I from neutron irradiation of natural Xe gas and a wet distillation process (a) cutting of xenon irradiated container,(b) distillation of ^{125}I, (c) production plant.

was cooled in liquid nitrogen to solidify ^{125}I formed during the neutron irradiation, leached out with 0.03 M Na_2SO_3 solution and purified by wet distillation. In this process, iodine formed was oxidized to non-volatile iodate (IO_3^-) which was then subsequently reduced to molecular iodine by the addition of oxalic acid and distilled out leaving behind the radioactive contaminants in the solution. Iodine-125 liberated was trapped in a small amount (0.5 mL) of 0.01 M NaOH solution. Several batches of ^{125}I were successfully produced using the developed procedure at a level of ~ 18.5 GBq (500 mCi) ^{125}I per batch. The quality of the ^{125}I in terms of radionuclidic purity, radiochemical purity and radioactive concentration were evaluated and found to be acceptable for preparation of ^{125}I brachytherapy sources. Facility used for the production of ^{125}I is shown in Fig.1.

Iodine-125 brachytherapy seeds

An innovative, *efficient*, reliable *and cost-effective* technique was developed and demonstrated for the large scale preparation of ^{125}I-brachytherapy sources of strength 1.665–2.22 GBq (45-60 mCi) in our laboratory [3-4].

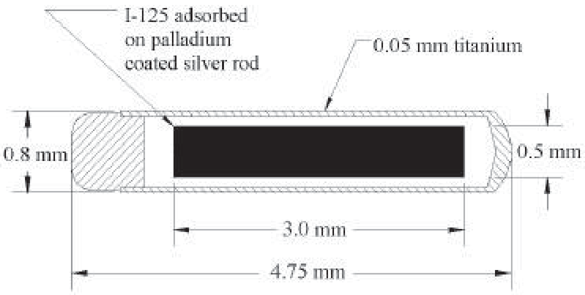

Fig. 2: Schematic diagram of the ^{125}I seed

Schematic diagram of the ^{125}I-brachytherapy source developed is shown in Fig.2. In brief, cleaned silver wires [3 mm (l) × 0.5mm (ϕ)] were treated with 0.05% $PdCl_2$ solution at ~100^{0}C for 30 minutes. Palladium coated silver wires were removed and washed with double distilled water to get rid of traces of loosely held palladium. In a typical batch preparation, 15 Pd coated silver wires were immersed in 750 μL of ^{125}I solution of activity in the range of 1.665–2.22 GBq (45-60 mCi) containing 75 *μ*g KI as carrier at 60–70 °C for 6 h. By this method, more than 80% of the initial radioactivity could be firmly deposited onthe source core and 111-148 MBq (3 - 4 mCi) of radioiodine could be irreversibly adsorbed on the palladium coated silver wires. These source cores were encapsulated in titanium capsules of 4.75 mm (l) × 0.8 mm () and welded in one extremity using a 50 W, Nd:YAG laser welding system [3] as shown in Fig.3. Prior to therapeutic use, each ^{125}I seeds were subjected to numerous quality control tests following the reported procedure [4]. 'Classification Performance Validation' has

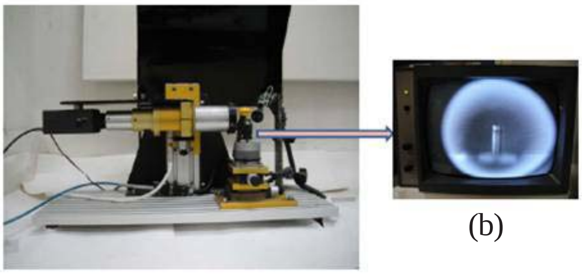
(b)

(a)

Fig. 3: Encapsulation of ^{125}I source in titanium capsule using Nd:YAG laser welding technique (a) Nd:YAG laser welding set-up (b)Magnified view of sample under welding.

(a) (b) (c)

Fig. 4: Titanium encapsulated ^{125}I source (a) Iodine-125 source core, titanium capsule and its lid (left) & laser welded ^{125}I seed (right), (b) Indigenous ^{125}I seed, (c) rice sized simulated ^{125}I seeds

been carried out for renewal of design approval of ^{125}I seeds [4]. The dosimetric studies of sources were carried out at Radiological Physics and Advisory Division (RP&AD) of BARC, which revealed that the 'BARC ^{125}I Ocu-Prosta seeds' is similar to commercial source 6711 Oncoseed of Amersham International [5]. Photograph of the titanium encapsulated ^{125}I source is shown in Fig.4 .

Clinical deployment of ^{125}I brachytherapy seeds

Presently, these sources are supplied to three major oncology centres of India namely Sankara Nethralaya, Chennai, P.D.Hinduja Hospital, Mumbai and Sri Ramkrishna Hospital, Coimbatore. Plaque preparation consists of the assignment of seeds to slots on the plaque to achieve a desired dose rate distribution. For dose calculation, modelling of the eye is done first using computerized tomography or magnetic resonance imaging of axial cut from the centre of the eye. Next, modelling of the tumour is done using the ocular ultrasound. For tumour which are 5 mm or greater in apical height, the tumour dose is prescribed at the apex of the tumour where as for tumours that are 2.5-5 mm in apical height, the prescription point is 5 mm from the interior surface of the sclera. The prescription point was tumor height plus 1 mm for the sclera with calculated dose of 85 Gy. Fig. 5 depicts the dose distribution from a typical plaque. The tumor margins were identified using transscleral illumination and indirect ophthalmoscopy. The placement of the plaque is carried out surgically. The surgical procedure is depicted in Fig.6. The plaque removal is then done after 4 to 5 days, as per the dosimetry. It is pertinent to point out that more than 70 patients have been benefited by this development.

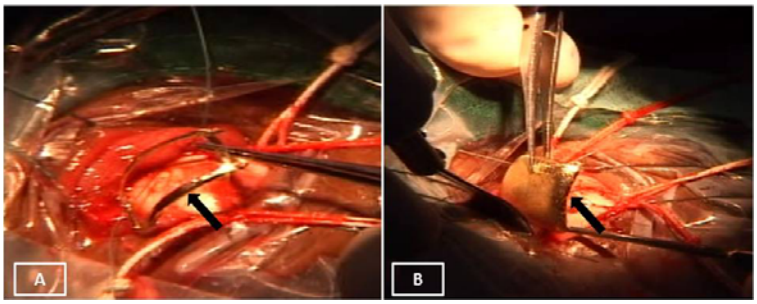

Fig. 6: Surgical procedure A: Dummy gold plaque being inserted. B: Plaque containing ^{125}I-seeds being inserted

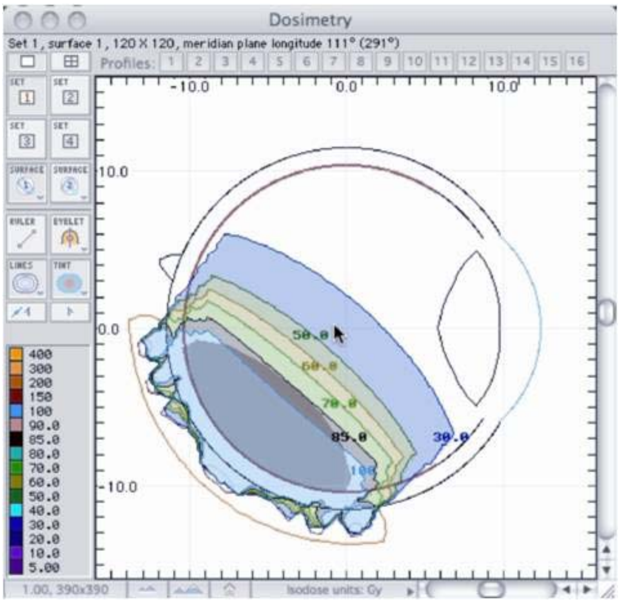

Fig. 5: Longitudinal section of computerised model of the eye ball with posterior choroidal melanoma as seen in the planning software.

Conclusion

This investigation has contributed in building local capability in the production of ^{125}I seeds through a combination of innovative concept, process demonstration and consistent reliable quality control for the management of ocular cancer. While there is still a long path to travel to find the ultimate cure for ocular melanoma, this initiative represents a significant step forward for to provide ^{125}I-brachytherapy sources to meet the domestic needs. for the management of intraocular melanomas. We believe that local availability of 'BARC ^{125}I Ocu-Prosta seed', its favorable characteristic and adaptabilities to specific tumor locations and sizes, cost effective ophthalmic brachytherapy can be offered in India. There is a great deal of anticipation that 'BARC ^{125}I Ocu-Prosta seed' will find their way into many more institution in India in the foreseeable future.

Acknowledgement

The technologies described in this paper are the result of valuable contributions of several scientists. The authors are grateful to Dr. M.R.A. Pillai Head, Radiopharmaceuticals Division for his support to this program. The authors thank all their colleagues from Radiopharmaceuticals Division, BARC for their involvement and contributions at various stages of this work. The authors are indebted to their ex-colleagues Mr. S. A. Balakrishnan, Dr. M. A. Majali and Mr. C. Mathew who carried out the work at the initial stages for the development of the sources. Our special thanks go to Atomic Energy Regulatory Board (AERB), Mumbai India for their help during the 'Classification Performance Validation' of the work.

References

1. S.K. Saxena, C. Mathew, S.A. Balakrishnan, M.A. Majali, R.B. Manolkar, S.U.Sane, Ramu Ram and M.R.A. Pillai, A. Shanta, B.G. Avhad, G.L. Goswami, Development of miniature "BARC I-125 Ocu-Prosta seeds" for the treatment of eye and prostate cancers, BARC News letter, 2004; 243:1-10 available at www.barc.ernet.in/publications/ nl/2004/200404-1.pdf.
2. P.V.Joshi, K.C. Jagadeesan, R.B. Manolkar, A.R. Mathakar, Viju Chirayil, S.V. Thakare,*Ashutosh Dash; M.R.A.Pillai Production of ^{125}I from neutron irradiation of natural Xe gas and a wet distillation process for radiopharmaceutical applications, *Industrial & Engineering Chemistry Research*, **2012**, 51 (25), 8575–8582.
3. Saxena SK, Shanta A, Rajurkar Nilima S, Majali MA. Studies on the production and quality assurance of miniature ^{125}I radioactive sources suitable for treatment of ocular and prostate cancers. Appl Radiat Isot 2006; 64: 441-447.
4. Mathew C, Majali MA, Balakrishnan SA. A novel approach for the adsorption of ^{125}I on silver wire as matrix for brachytherapy for the treatment of eye and prostate cancer. Appl Radiat Isot 2002; 57:359-67.
5. Sanjay Kumar Saxena, Yogendra Kumar and Ashutosh Dash ,Quality Control of ^{125}I-brachytherapy Seeds, *Journal of Radioanalytical and Nuclear Chemistry,* In press
6. Sharma SD, Basu M, Shanta A, Selvam TP, Tripathi UB, Bhatt BC. Dosimetry parameters of BARC OcuProsta I-125 seed source. *Australas Phys Eng Sci Med* 2005;28:14-20

DEVELOPMENT OF AN AGV BASED AUTOMATED MATERIAL TRANSFER SYSTEM

Rahul Sakrikar, P V Sarngadharan, Sanjeev Sharma, Vinay Shrivastava, Vaibhav Dave,
Namita Singh, Vikrant Agashe, Biswajit Das and Prabir K. Pal
Division of Remote Handling & Robotics

Dr. P.K. Pal, Division of Remote Handling & Robotics,
Design, Manufacturing & Automation Group and his team received the
DAE Group Achievement Award for the year 2010

Abstract

This article describes an implemented solution for the material distribution problem in the machining shop of a typical manufacturing unit using Automated Guided Vehicles (AGV). We briefly describe the AGV and its associated material handling system, and then go on to describe the software components and their underlying algorithms, which, when put together, create an automated material transfer system that assesses demands for materials and accordingly plans, prioritizes and executes deliveries. The system has been tested extensively in a mock environment in our Laboratory, the results for which have also been indicated here.

Introduction

Manufacturing requires continuous movement of materials – starting from the point where vendors deliver semi-finished components, up to the point where the finished products are ready for shipment. In between, the semi-finished components are moved to various machining units, to assembly station, testing and quality control, packaging, and so on until the product is complete in all respects. In the past, these movements were performed manually. The idea of deploying one or more Automated Guided Vehicles (AGV) for this purpose is gaining in popularity these days, because they have the potential of making all movements in the manufacturing unit completely autonomous, safe, and extremely efficient, leading to higher productivity and automatic storage management eventually at a lower cost. The system requires design of one or more AGVs that can move and stop precisely along designated trajectories and transfer material using handling mechanisms like powered roller conveyors. The control of the system is managed by the various software modules integrated together. This renders the system extremely flexible. The entire plan can be changed at will by editing trajectories and a few other parameters.

Since the requirement for movement of materials is generic, the need for an automated material transfer system is felt by all segments of industries; more so by those whose processes are well structured to take advantage of automation, or those who are keen to avoid manual handling of hazardous (e.g., radioactive or explosive) materials. The development of Automated Material Transfer System (AMTS) was taken up at DRHR, BARC, to generate an indigenous solution that is affordable to the Indian industries going for modernization of their manufacturing processes, and that can be adapted to the exact requirements of an industry without adding substantially to its cost. The solution can also be readily adapted to automated handling and shipment of radioactive materials in the nuclear establishment.

As a concrete instance around which we can make initial development of the AMTS, we selected the problem of automation of the transfer of semi-finished components from a supply point to several machining centres on the shop floor of a typical manufacturing setup. The semi-finished components are packed into bins, which are stacked up for transfer to and from the AGV. The complete stack is handled by the system and delivered at the designated locations. The automation system so developed has the ability to be scaled to use and control multiple AGVs if the situation demands.

The AMTS can broadly be divided into three major subsystems, namely the AGV, Supervisory controller and the System configuration Software.

Fig. 1 shows the overview of the control architecture of the AMTS [1]. The vehicle is controlled by a Vehicle Control Program (VCP) executing on the PLC, under the guidance of a Plan Executor (PE) program being executed on the onboard single board computer. PE executes plans for transfer orders prepared and assigned by the Supervisory Control Program to the AGV.

A standard PC located conveniently in the Control room or Shop Floor executes the Supervisory Control Program. This program displays current status of the AGV and the field devices such as loading /unloading conveyors etc. It allows an operator to set transfer orders for materials, or to intervene through Emergency-Stop. The supervisory control software interfaces with the field device controller (PLC) which controls all the field devices like conveyors in the loading /unloading stations etc.

Autonomous Guided Vehicle (AGV)

An AGV is a battery powered mobile platform with the ability to interpret and execute a set of motion commands. In a shop floor, it is desirable for the AGV to move along straight paths, curves, turn in place (around its centre) and crab (shift parallel to itself). In order to cater to these requirements, the *quad* configuration, having two steer & drive wheels mounted on the AGV on the centre-line along its length and four support castors on four corners, has been selected. The arrangement of the drive wheels and their modes of operations are as shown in Fig. 2.

Vehicle Control

All the four actuators of the AGV are driven by AC Induction Motors. The control of the motors is achieved using compatible AC Motor Controllers operating on a 48V DC battery supply. A PLC based Vehicle Control Program (VCP) controls the motion of the AGV. It also controls operation of the onboard material handling system, monitors sensors, compiles AGV status data, and executes operational interlocks.

Load Handling Mechanisms

The AGV as well as the loading and delivery stations are provided with motorized roller conveyors for automated transfer of materials to and from the AGV. The AGV conveyors are controlled by the onboard PLC system. The field conveyors have a separate PLC based control system, and the operation of the conveyor sets is coordinated through the Supervisory Control System. Figure 3 shows the actual AGV with various sub-systems.

Safety

The primary safety device for the AGV is a non-contact laser based obstacle detection system, which provides for slowing down or stopping of the AGV depending on the distance of the obstacle much before any contact is

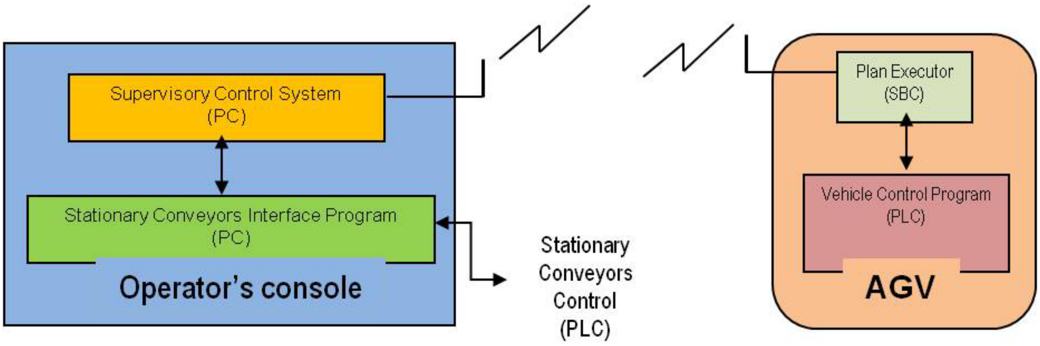

Fig. 1: AMTS Control Architecture

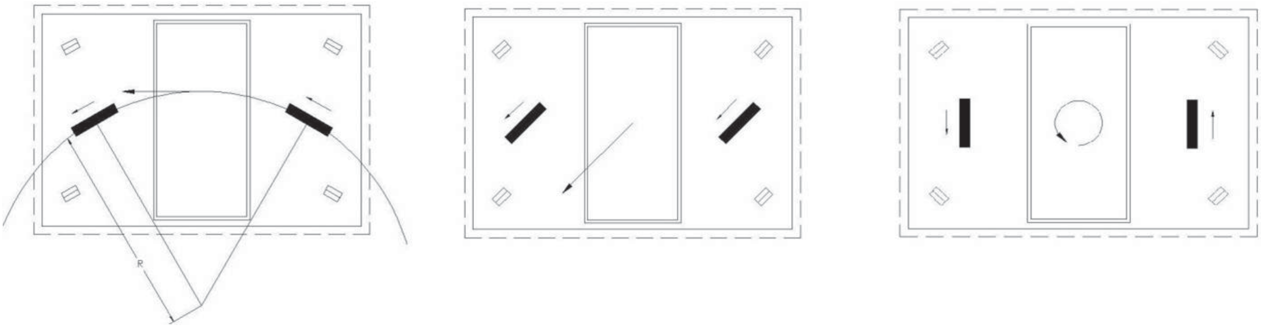

a: Tangential Mode **b: Crab Mode** **c: Differential Mode**

Fig. 2: AGV wheel configurations

established. However the AGV also has a set of bump sensors to be able to stop on contact.

Localisation

The present AGV system detects predefined cylindrical reflectors installed within the work area through an onboard laser ranging device. The laser navigator system, so formed, returns the (*x, y*) coordinates and orientation (θ) of the laser ranging device in the global coordinate system to the AGV controller at the rate of 8 Hz [2]. The instantaneous position and orientation of the AGV is easily computed from this data.

Fig. 3: The AGV

Plan Executor

The Plan Executor (PE) program, running on the Single Board Computer (SBC) of the AGV, carries out execution of the transfer order placed on the AGV by the supervisory control system. The transfer order specifies sources from which materials are to be picked and destinations at which they need to be delivered in a single trip of the AGV. Accordingly, under the control of a trajectory tracking algorithm, e.g., Pure Pursuit Algorithm [3], it keeps issuing motion and activity commands to the Vehicle Control Program (VCP) running on onboard PLC, until the entire plan gets executed.

Supervisory Controller

It is a computer program executing on a standard desktop computer, located either in the operation area or the control room as per convenience. Its function is to manage one or more AGVs with active infrastructure supports for pick-up and delivery stations. The supervisory control system carries out a range of tasks, namely monitoring of field devices, AGV traffic control, communications and AGV dispatching, tracking and tracing.

Communications

The Communication tasks handled by the supervisory controller include messages, such as issue of transfer order to the AGV, insertion of the AGV into the system, and commands to control field devices in the work area. It also includes fault condition detection and reporting based on the 'AGV-heart-beat' monitoring. The Supervisory controller communicates with the AGV on a wireless

Ethernet link and with the field device controller on a wired serial link, using Modbus protocol.

Job Generation & Assignment

The supervisory system is configured to generate a specific, pre-defined transfer order request based on a set of field status conditions. A suitable user interface is provided for the operator to define triggering conditions and corresponding transfer plans to be executed in case the trigger gets activated.

Display and User Interface

The supervisory controller continuously displays the status of systems on the control console. The display includes update of the locations of the AGVs in the system, the status of operation of AGV load handling equipment, AGV battery charge status, field conveyors status and the indication of any warnings and faults generated on any of the sub-systems. The controller also provides user interface for manual intervention.

Trajectory Editor

The Trajectory Editor is a CAD-based software, with the facility to import the layout drawing of the workshop, with outlines of structures, machines and various other entities depicted on it, as a background. The trajectory editor facilitates the creation of routes and loading / unloading stations for the AGV. The software utilizes the drawing facilities of the CAD software for definition of the various entities. The Trajectory Editor generates a database of all the configured entities, which is used by the PE and the Supervisory Controller for their operations. The software provides facilities for editing the existing projects and import of entities for use in a new project. The software also carries out the performance checks based on the defined AGV parameters.

Test runs

Fig. 4 shows the desired and actual path followed by the AGV during execution of a material transfer plan. The small deviations of the actual trajectory from the reference trajectory, particularly at turns, are inherent behaviour of the pure pursuit algorithm. While positioning the AGV for a transfer, errors in alignment, orientation, and distance were measured systematically. It was observed that the errors are within acceptable limits for autonomous operation of the AGV.

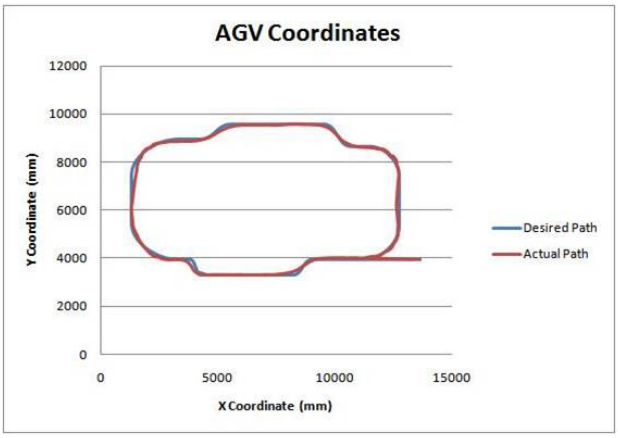

Fig. 4: Path following executed by AGV

Conclusion

We have described the development of an indigenous technology for automation of material transfer in a manufacturing environment. The solutions so generated are of generic nature and may be used with modifications or enhancements to address specific concerns of various application environments.

References

1. Rahul Sakrikar, Sanjeev Sharma, P V Sarngadharan, V K Shrivastava, Vaibhav Dave, Namita Singh, Vikrant Agashe, Biswajit Das, Prabir K Pal, Manjit Singh, "Indigenous Development of an Automated Material Transfer System", National Conference on Robotics and Intelligent Manufacturing Process, Bharat Heavy Electricals Limited, Hyderabad, 2009.
2. SICK NAV-200 & S-3000 series product documents and manuals.
3. Coulter, R.Craig, "Implementation of the pure pursuit path tracking algorithm" (Tech report CMU-RI-TR-9201) Carnegie Mellon University, 1992.

DEVELOPMENT OF CATALYSTS FOR VARIOUS APPLICATIONS RELATED TO DAE PROGRAMS

S.R. Bharadwaj, A.K. Tripathi, B.N. Wani, R. Sasikala, M.R. Pai, Salil Varma, K. Bhattacharyya, A.M. Banerjee, Deepak Tyagi, A.P. Gaikwad and G.S. Mane
Fuel Cell Materials and Catalysis Section, Chemistry Division

and

R.D. Purohit, S.R. Nair, R.P. Corriea, N.M. Avahd and J. Mohan Babu
Energy Conversion Materials Section, Materials Group

Dr. Ms. S.R. Bharadwaj, Fuel Cell Materials and Catalysis Section, Chemistry Division and her team received the DAE Group Achievement Award for the year 2010

Abstract

Catalytic reactions play a foremost role in majority of industrial chemical processes. As an estimate, about 90% of all chemical reactions in industries rely on catalysts. Fuel Cell Materials and Catalysis Section (FCMCS) of Chemistry Division has made significant contributions in the area of catalysis and developed several catalysts for various applications related to DAE programs. Notable among these are (i) development of catalysts for sulfuric acid decomposition and HI decomposition reactions, and (ii) catalysts for mitigation of hydrogen in nuclear power plants under severe accident conditions. In addition, rich contributions were made to the fundamental research in these areas of technological importance viz. studies on photocatalysts for generation of hydrogen by water splitting and photocatalyts for VOC abatement and pollution control. The group at Energy Conversion Materials Section (ECMS), Vashi was instrumental in synthesis of catalysts in large quantities for use in pilot plant scale reactors. This article gives a brief over view of the catalysis development program with respect to the above mentioned activities.

Introduction

Heterogeneous catalysts are extensively used in chemical industries for reactions such as cracking, dehydrogenation, hydrogenation, oxidation, reduction, decomposition, molecular rearrangement, fermentation etc. The main focus of FCMCS is to develop catalysts for various applications related to the Department of Atomic Energy.

In recent past, studies on Sulfur-Iodine (S-I) cycle for large scale nuclear hydrogen generation have been started at BARC in view of availability of high-grade heat from the proposed Compact High Temperature Reactor (CHTR). FCMCS developed catalysts for the sulfuric acid and hydriodic acid decomposition reactions involved in the Sulfur-Iodine cycle for hydrogen generation.

With regard to safe operation of nuclear plants, hydrogen generated under LOCA conditions poses a major threat. The two major nuclear accidents of Three Miles Island (TMI) and Fukushima incident emphasize the hydrogen risk in nuclear power plants. Use of catalysts has been proposed to be one of the alternatives to mitigate this hydrogen. Hence, extensive studies on development of catalysts for hydrogen mitigation were undertaken.

The conversion of solar energy into hydrogen via semiconductor assisted photocatalytic splitting of water, is one of the most promising technologies for clean and sustainable energy solutions. Members of FCMCS have explored various catalysts for this purpose and also for the utilization of solar energy for environmental remediation like VOC's elimination and dye degradation using suitable semiconductor photocatalysts.

Development of catalysts for decomposition of sulfuric acid

With an aim to develop non-noble metal catalysts which are both active and stable, various oxides/mixed oxides and ferrites (MFe_2O_4: M = Co, Ni, Cu) [1, 2] were prepared via different routes like solid state, precipitation/co-precipitation gel-combustion etc. Their performance as catalysts for the decomposition of sulfuric acid was evaluated and compared with that of commercial Pt/Al_2O_3 catalyst, in temperature range of 600-850°C. Textural and structural characterization of both synthesized and spent catalysts was carried out employing various techniques such as XRD, IR, SEM/EDX, TEM, XPS, N_2-BET Surface area, etc. Characterization of fresh and spent catalysts along with thermal decomposition experiments enabled us to propose a plausible mechanism for decomposition of sulfuric acid over these oxides/ferrites which involved the formation and decomposition of metal sulfate, with the metal sulfate decomposition step playing the most crucial role in determining the reaction kinetics. To study the catalytic decomposition of sulphuric acid in temperature range of 600 – 850°C over powder and granular samples two glass setups were indigenously designed and developed in Chemistry division as shown in Fig. 1.

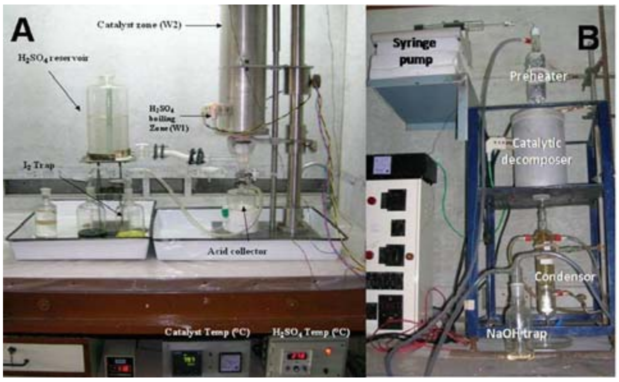

Fig. 1: Experimental set-up in quartz to carry out sulfuric acid decomposition (A) granular catalyst (20 g) and (B) powder catalyst (0.2 g)

The performance of Fe_2O_3, $Fe_{1.8}Cr_{0.2}O_3$ and Pt/Al_2O_3 catalysts in granular form was evaluated for decomposition of sulfuric acid (98 wt %) as a function of time (100 h at 800°C, acid flux of ~0.6 ml/min), temperature (650-825 °C, acid flux of ~0.6 ml/min) and flux of sulfuric acid (0.2-10 ml/min). The SO_2 yield was found to remained close to the equilibrium thermodynamic yield value (~ 80 % at 800°C). Chromium substituted iron oxide and Pt/Al_2O_3 catalysts exhibited almost similar SO_2 conversions at 800 °C which was slightly higher than the unsubstituted Fe_2O_3. No deterioration in the catalyst performance was observed for the oxide samples during 100 h run. Commercially available Pt/Al_2O_3 catalyst works out to be 16 times costlier than iron based catalysts.

On the basis of the overall results obtained from our studies we recommended the $Fe_{1.8}Cr_{0.2}O_3$ catalyst for use in the laboratory scale Sulfur-Iodine demonstration facility at Chemical Technology Division (ChTD), BARC. Synthesis of $Fe_{1.8}Cr_{0.2}O_3$ catalyst in Kg scale was entrusted to ECMS, Vashi.

The group in ECMS has applied co-precipitation method for the preparation of fine powder of catalyst starting from their nitrate compounds. The resulted precipitate was vacuum filtered and calcined in muffle furnace at around 700°C. The calcined material conformed to distinct iron oxide phase. To enhance the surface area of catalyst, the calcined powder was subjected to prolonged duration of milling in conventional roller mill. The powder so produced has specific surface area around 32 m^2 /gm. For making the catalyst suitable to match with S-I decomposition column design, these were shaped into 4-5 mm diameter granules using Polyvinyl alcohol (PVA) as a binder. Kilogram quantities of the catalyst granules prepared as above have been supplied to Chemical Technology Division, BARC for trial runs in their lab scale demonstration plant for hydrogen production. A representative photograph of a batch of catalyst is shown in Fig. 2.

Fig. 2: Iron oxide based catalyst (Spherical granules, ~ 4-6 mm size)

Development of porous Pt/Carbon catalyst for HI decomposition

Different Pt-Carbon catalysts based on high surface area carbon supports have been developed using mesoporous and microporous silica templates and have been employed for HI decomposition step of Sulphur – Iodine thermo-chemical cycle [3]. In this preparation route, carbon precursor like sucrose is impregnated into mesoporous silica template like MCM-41 and SBA-15 and microporous silica template like fumed silica and carbonized by heating at 800 °C, under nitrogen flow. The silica template is removed by hydrofluoric acid to generate porous carbon replica. Platinum has been incorporated in these carbon supports either at initial stage along with sucrose to form a part of carbon framework or by direct impregnation on prepared carbon. Liquid phase HI decomposition at 120°C has been carried out and conversion upto 17% have been obtained in 2 hrs studies. The effluent analysis depicts insignificant noble metal leaching. The efficiencies of these materials for HI decomposition reaction have been found to be dependent on the structural nature of the porous carbon and their surface morphologies. We have concluded that mesoporous Pt/carbon has higher catalytic activity and stability than microporous Pt/carbon catalysts.

Development of catalyst for hydrogen mitigation application

A large amount of hydrogen is generated in nuclear reactor during LOCA conditions. This can be a threat to containment integrity if detonable limit is crossed. Passive autocatalytic recombiner is one of the most feasible remedies for this. New classes of mixed noble metal catalysts, viz Pt + Pd on stainless steel wire gauze have been developed for this purpose [4]. The activity includes development of a novel procedure for preparation of mixed noble metal (platinum-palladium) catalysts by electroless deposition from a single bath containing precursors of both the noble metals and a reducing agent. Evaluation of the deposition steps by SEM-EDAX techniques has clearly indicated that initial nucleation occurs through platinum deposition followed by simultaneous platinum-palladium deposition. These catalysts have been evaluated for their catalytic activity for H_2-O_2 recombination reaction under static air condition, in a 40 litre reactor, in absence and presence of various poisons like carbon dioxide, methane, carbon monoxide and water. The catalytic activity has been found to remain unaffected by the presence of above mentioned poisons. Fig. 3 depicts various forms of supported noble metal based catalysts developed and evaluated for this purpose. Wire gauze supported catalysts have been shortlisted for user evaluation by NPCIL at Hydrogen Recombination Test Facility, Tarapur.

Photocatalytic hydrogen generation from water using solar radiation

With a view to photocatalytic generation of hydrogen using solar type radiation, our group has focused on the development of suitable photocatalytic materials. A number of novel semiconductors have been developed for this purpose and tested for their photocatalytic activity. A series of aliovalent and isovalent ions were substituted at A and B site in indium titanates, In_2TiO_5 (A = Ni^{2+} / Nd^{3+}; B = Fe^{3+} / Cr^{3+}), with an objective to modify their band gap

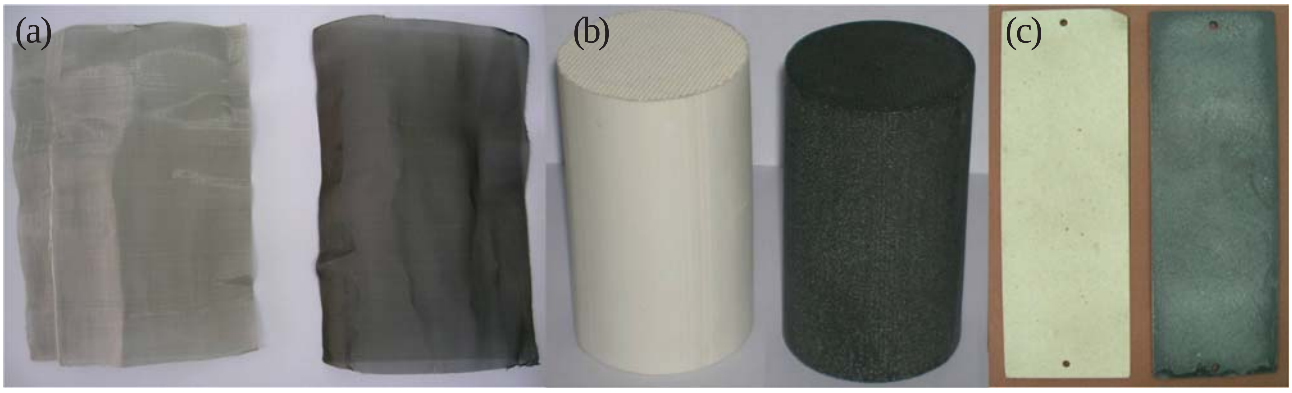

Fig.3: Various catalysts developed for mitigation of hydrogen (a) noble metal on SS wire gauze, (b) noble metal on cordierite honeycomb and (c) Noble metal on cordierite plate.

and extend their photo response in visible light. Effect of metal ion substitution [5] and particle size [6] on band gap and photocatalytic activity of indium titanate has also been explored. TiO_{2-} based photocatalysts like self-doped $(Ti^{3+})TiO_2$ [7], Sn and Eu doped TiO_2 [8], In and N co-doped TiO_2 [9], TiO_2 on various oxides like ZrO_2, Al_2O_3, zeolite and CeO_2 [10] were evaluted to obtain catalyst particles with optimum surface area and crystallinity. Among these oxide catalysts, a composite of TiO_2 dispersed on ZrO_2 inert support exhibited the highest photocatalytic activity with a hydrogen generation rate of 1.1 L/h/m^2/g using solar type radiation. Indium doped CdS dispersed on ZrO_2 was found to exhibits the better activity than oxide catalysts, with hydrogen generation rate of 3.9L/h/m^2/g.

Titania based photocatalysts for abatement of air and water pollutants

Heterogeneous photocatalytic degradation of dyes from waste water and volatile organic compounds (VOCs) from polluted air has become a need of times, as the release of these effluents in the ecosystem forms a primary source of pollution affecting all the flora and fauna in its vicinity. Nano titania, doped titania [11-13], alkaline earth titanates [14] and supported titania [15] systems have been evaluated to understand the structure – activity correlation, influence of oxidation states of dopants, particle size, dopant – titania – support interaction and their physiochemical properties and catalytic activity of these materials. Photocatalytic oxidation of model VOCs like ethane, propene and methane in air and dye like methylene blue in water has been studied in detail. In this context, titania based heterogeneous photocatalysts stands-out to be best methodology that can be effectively exploited for the complete mineralization of various dye and VOC pollutants present in natural environment.

References

1. Banerjee A. M., Pai M. R., Bhattacharya K., Tripathi A. K., Kamble V. S., Bharadwaj S. R., Kulshreshtha S. K., *International Journal of Hydrogen Energy,* 33 (2008) 319.
2. Banerjee A. M., Pai M. R., Meena S. S., Tripathi A. K., Bharadwaj S. R., *International Journal of Hydrogen Energy,* 36 (2011) 4768-4780
3. Tyagi D., Scholz K., Varma S., Bhattacharya K., Mali S., Patil P. S., Bharadwaj S. R., *International Journal of Hydrogen Energy,* 37 (2012) 3602-3611
4. Sanap K. K., Varma S., Dalavi D., Patil P. S., Waghmode S. B., Bharadwaj S. R., *International Journal of Hydrogen Energy,* 36 (2011) 10455.
5. Pai M. R., Majeed J., Banerjee A. M., Arya A., Bhattacharya S., Rao R., Bharadwaj S. R., *Journal of Physical Chemistry C,* 116 (2012) 1458-1471.
6. Pai M. R., Singhal A., Banerjee A. M., Tiwari R., Dey G. K., Tyagi A. K., Bharadwaj S. R., *Journal of Nanoscience and Nanotechnology* 12 (2012) 1957-1966.
7. Sasikala R., Sudarsan V., Sudakar C., Naik R., Panicker L., Bharadwaj S. R., *International Journal of Hydrogen Energy,* 34 (2009) 6105-6113.
8. Sasikala R., Sudarsan V., Sudakar C., Naik R., Sakuntala T., Bharadwaj S. R., *International Journal of Hydrogen Energy,* 33 (2008) 4966-4973.
9. Sasikala R., Shirole A.R., Sudarsan V., Jagannath, Sudakar C., R. Naik, Rao R., Bharadwaj S. R., *Applied Catalysis A: General,* 377 (2010) 47-54.
10. Sasikala R., Shirole A. R., Sudarsan V., Kamble V. S., Sudakar C., Naik R., Rao R., Bharadwaj S. R., *Applied Catalysis A: General,* 390 (2010) 245-252.
11. Bhattacharyya K., Varma S., Tripathi A. K., Bharadwaj S. R. and Tyagi A. K., *J. Phys. Chem. C,* 112 (2008) 19102 – 19112.
12. Bhattacharyya K., Varma S., Tripathi A. K., Tyagi A. K., *J. Mat. Res.,* 25 (2010) 125.
13. Bhattacharyya K., Varma S., Tripathi A. K., Bhattacharyya D., Mathon O., Tyagi A. K., *J. Appl. Phys.* 106 (2009) 093503.
14. Chatterjee S., Bhattacharyya K., Ayyub P. and Tyagi A. K., *J. Phys. Chem. C* 114 (2010) 9424–9430.
15. Hankare P. P., Patil R. P., Jadhav A. V., Garadkar K. M., Sasikala R., *Appl. Catal. B: Environmental* 107 (2011) 333– 339.

DEVELOPMENT OF COLD KITS FOR PREPARATION OF [^{99m}Tc] TRODAT AND HUMAN SERUM ALBUMIN NANOCOLLOIDS

Grace Samuel, Aruna Korde , Usha Pandey, Suresh Subramanian, Drishty Satpati,
Mythili Kameswaran and A.D. Kadam
Radiopharmaceuticals Division

and

H.D. Sarma
Radiation Biology and Health Sciences Division

and

Chanda Arjun
Board of Radiation and Isotope Technology

Dr. Smt. Grace Samuel, Radiopharmaceuticals Division, Radiochemistry & Isotope Group and her team received the DAE Group Achievement Award for the year 2010

Abstract

Research, development, demonstration and deployment of new radiopharmaceuticals for diagnosis and therapy are the major objectives of the Radiopharmaceuticals Division. Work on the development of [^{99m}Tc]TRODAT-1 and [^{99m}Tc]HSA were taken up at the Radiopharmaceuticals Division due to the demand as well as non-availability of the agents locally. [^{99m}Tc]TRODAT-1 is a dopamine transporter (DAT) imaging agent useful in the diagnosis of patients suffering from Parkinson's disease (PD). [^{99m}Tc]HSA is a sentinel node imaging agent useful in the management and staging of breast and prostate cancers. The team has carried out extensive studies to arrive at user friendly, single vial kits wherein ^{99m}Tc radiopharmaceuticals can be formulated at high yields by addition of generator eluted ^{99m}TcO$_4^-$. In preclinical trials, both preparations have yielded good results demonstrating the utility of these agents. The products have been cleared by the Radiopharmaceuticals Committee (RPC) and currently used by nuclear medicine departments.

[^{99m}Tc]TRODAT-1

Neurodegenerative diseases are a group of chronic, progressive disorders characterized by the gradual loss of neurons in discrete areas of the central nervous system (CNS). Parkinson's Disease (PD) is a neurodegenerative disorder characterized by slow progressive loss of dopaminergic neurons resulting in impaired motor and non-motor symptoms. Dopamine transporter (DAT) is a protein located at presynaptic dopamine neuron terminals. A significant reduction in density of the dopamine transporters (DAT) is found in basal ganglia region of the brain of patients suffering from Parkinson's disease (PD). Thus imaging of dopamine transporters provides an important tool in diagnosis of neurodegenerative diseases. Parkinson's disease is caused by a degeneration of neurons that result in uncontrollable tremors, slow movement, stiffness and difficulty in walking. Almost 60% of dopaminergic neurons are lost when the Parkinson's disease is diagnosed by its symptoms, hence early detection of the disease is important. Radiolabeled dopamine transporter ligands when used as tracers to measure the decrease in the DAT provide important information about the functioning of these transporters in the diseased brain. During the past decade, Positron Emission Tomography (PET) and Single Photon Emission Computed Tomography (SPECT) have become the validated tools for evaluation of brain function in normal and disease states.(Mozley *et al*) Radiolabeled cocaine derivatives using radionuclides such as ^{11}C, ^{18}F and ^{123}I have been reported in literature as useful PET and SPECT agents for imaging dopamine transporters. However, these isotopes are cyclotron produced, thus not readily available limiting their use in routine clinical diagnosis. [^{99m}Tc]TRODAT-1 has been proved to be a useful imaging agent for clinical diagnosis and monitoring the effects of therapy in Parkinson's disease. Hence efforts were made at the Radiopharmaceuticals Division to develop a kit for formulation of [^{99m}Tc]TRODAT-1 and demonstrate its usefulness as a radiopharmaceutical with the aim to make it available for clinical studies in India.

Preparation of [^{99m}Tc] TRODAT-1

Detailed studies were carried out to develop a simple procedure with optimum concentration of various reagents as well as the reaction conditions. The freeze dried kit contents included TRODAT-1 (ABx Chemicals, Germany), sodium glucoheptonate, disodium EDTA and stannous chloride. In a typical procedure, 40-50 mCi of $^{99m}\text{TcO}_4^-$, freshly eluted from the generator is added and heated for 40 min at 100°C. The performance of the kit was evaluated based on the quality of the ^{99m}Tc TRODAT-1. The radiochemical purity was estimated by different analytical methods. In solvent extraction using chloroform, percentage distribution of radioactivity in aqueous and organic phase was determined. HPLC analysis was performed on Jasco PU1580 system using a reversed-phase PRP-1 column using 80:20 ACN/3,3-dimethylglutaric acid buffer as mobile phase. Polyamide 6 coated PET strip (Fluka) was used for TLC using the same solvent. After the initial standardisation, the batch formula and step wise production procedures were followed for formulating the kit. Since the product is a radiopharmaceutical and is intended for use in clinics, the complete production was carried out under aseptic conditions. Formulation was dispensed into vials under aseptic condition and lyophilized in clean area. The prepared kits were tested for radiochemical purity, stability as well as pharmaceutical purity. Pharmaceutical purity of the kits was determined by carrying out sterility testing and endotoxin determinations as per pharmacopeia monographs at BRIT QC laboratories.

Preclinical biological studies were carried out in Wistar rats by injecting ^{99m}Tc TRODAT via tail vein. Pharmacokinetics was determined by biodistribution studies at different time points. Scintigraphic imaging using gamma camera was done in rats to ensure brain uptake of the radiolabeled product (Fang *et al*). The dossier enclosing batch formula, production details, quality control methods and results of performance and quality of kits prepared in consecutive six batches were submitted to the 'Radiopharmaceutical Committee' and the approval for production and supply of cold kits was obtained. The cold kits were supplied along with QC reagents to Nuclear Medicine units for preparation of ^{99m}Tc TRODAT to carry out studies in normal human subjects and PD patients

Results

Fig 1 gives the structure of [^{99m}Tc] TRODAT-1. The standardized formulation consisted of 100 μg of TRODAT-1 ligand, 5 mg of GHA, 500μg Disodium EDTA and 40μg of stannous chloride . On addition of $^{99m}\text{TcO}_4^-$, the pH was 6-7. More that 80% was extracted into the chloroform layer indicating the lipophilicity of the preparation. The overall yield was >90% by both HPLC and TLC. The retention time of the complex in HPLC was 13.5 min (Fig. 2).

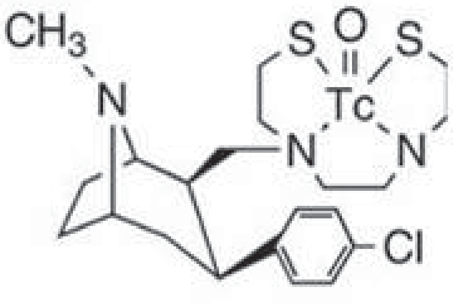

[^{99m}Tc]TRODAT-1

Fig. 1:

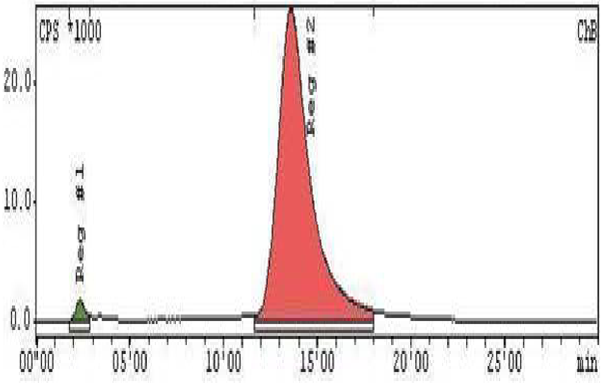

Fig. 2 : HPLC Pattern of ^{99m}Tc- TRODAT-1

The cold kits were stable for a period of six months from the date of production and [^{99m}Tc]-TRODAT-1 prepared using cold kit was stable upto 6h after preparation. Biodistribution studies in normal rat showed 1.3±0.2 %ID of ^{99m}Tc TRODAT-1/gm of brain tissue at 5min post injection (p.i.) which decreased to 0.49±0.09 % at 2h.p.i. The product was mainly excreted by hepatobiliary system. The results were also comparable with imaging studies carried out in normal Wistar rats. The consistent production of cold kits which fulfilled all the laid down criteria of quality such as pH, clarity, radiochemical purity (> 90%), sterility and apyrogenicity of kit contents ensured a safe product suitable for clinical use.

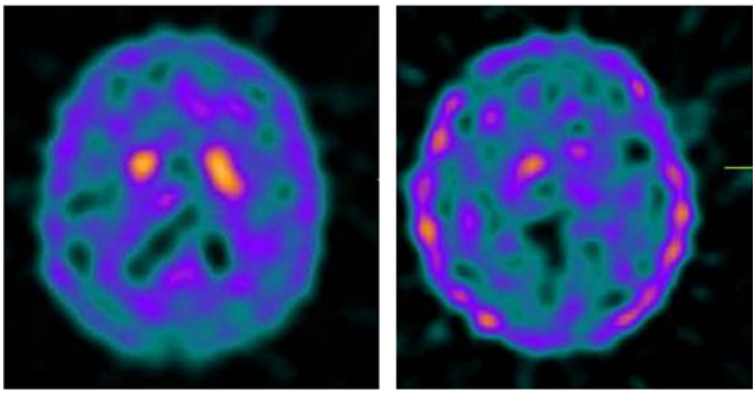

Fig 3b Images in two patients of Parkinson's disease showing varying degree of the disease

Clinical studies

Several batches of kits were manufactured and supplied to nuclear medicine departments. The performance of kits and feedback from Nuclear medicine physicians about the SPECT imaging studies carried out in normal human subjects and PD patients were encouraging. Fig 3a shows brain images of ^{99m}Tc TRODAT in a normal human volunteer while Fig 3b shows the images in patients with varying degrees of Parkinson's disease. Significant reduction in uptake of tracer in striatum region of brain in patients with PD is clearly indicated, thereby facilitating in accurate discrimination between patients with established PD and healthy volunteers.

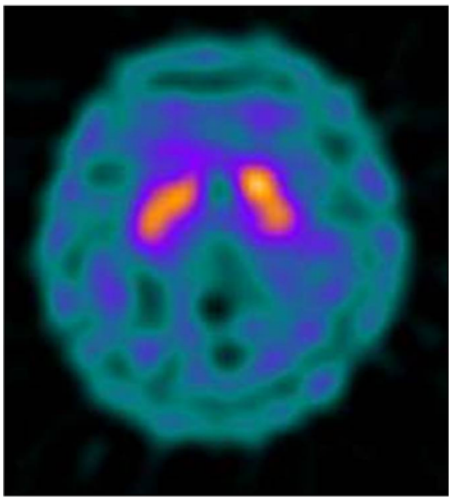

Fig. 3a: Images in a normal volunteer showing uniform distribution of ^{99m}Tc-TRODAT

[^{99m}Tc]-Human Serum Albumin (HSA) nanocolloid

The concept of sentinel lymph node biopsy in breast cancer surgery is that the tumor drains in a logical fashion through the lymphatic system, from the first to upper levels. Therefore, the first lymph node met (referred to as sentinel node) will most likely be the first to be affected by metastasis, and a negative sentinel node makes it highly unlikely that other nodes are affected. Sentinel lymph node biopsy would represent a significant advantage as a minimally invasive procedure, considering that, after surgery, about 70% of patients are found to be free from metastatic disease, yet axillary node dissection can lead to significant morbidity (Morton *et al*) Sentinel lymph node detection (SLND) helps in identification of lymph nodes potentially harbouring cancer cells. The identification of the sentinel lymph node helps in proper staging and management of several malignancies like breast cancer, head & neck cancer.

A nanoparticulate radiopharmaceutical for SLND with a narrow particle size distribution (nm range) shows rapid uptake and retention in the SLN and delivers the minimum radiation dose. With the availability of intraoperative gamma probes and suitable ^{99m}Tc radiopharmaceuticals, SLND has become a routine clinical procedure. The main radiolabeled agents used in SLN detection are sulphur colloid and albumin nanocolloid (Eshima *et al*). Preparation of labeled sulphur colloid is a tedious procedure and has several disadvantages and therefore not preferred by clinicians. Currently, there is no commercially available indigenous kit for preparation of ^{99m}Tc-HSA nanocolloid for sentinel node detection. Efforts were made at

Radiopharmaceuticals Division to develop ^{99m}Tc-HSA nanocolloid and demonstrate its clinical utility as sentinel node imaging agent or lymphoscintigraphy agent.

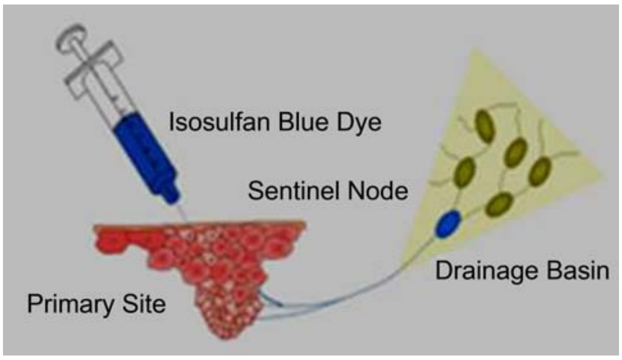

Fig. 4: Drainage of lymphatic fluid from tumor site to the lymph nodes through the sentinel node (blue)

Preparation of HSA nanocolloid

Rigorous standardisation of the reaction conditions for the preparation of HSA nanocolloid were carried out to have a consistent particle size. The main contents of the kit included human serum albumin (HSA certified for human use), $SnCl_2$, Na_2HPO_4 and ascorbic acid along with Tween-20. HSA solution was added stepwise. The resulting solution was filtered and the solution was heated at 55-60°C for 30 min and cooled. The solution was filter-sterilized and 1 mL aliquots were dispensed into suitable sterile vials under aseptic conditions. The vials were lyophilized and stored at 4-8 °C. On addition of $^{99m}TcO_4^-$, the final pH of the solution was ~5.0 to 5.5. Particle size analysis of HSA nanocolloid was performed by Dynamic Light Scattering (DLS) technique. Sterility and BET tests ensured absence of microbial growth and pyrogenicity. Radiochemical purity of ^{99m}Tc-labeled HSA nanocolloid was assayed with paper chromatography (saline), in which the ^{99m}Tc-HSA nanocolloid remains at the point of spotting.

Scintigraphy studies of ^{99m}Tc-HSA nanocolloid were performed in rabbit using the established footpad model to assess popliteal node extraction. Planar static images were obtained at various time points using a gamma camera. Clinical studies of the HSA nanocolloid were carried out in breast cancer patients at Tata Memorial Hospital, Mumbai, after taking the necessary approvals.

Results

Several batches of HSA nanocolloid cold kits could be prepared with consistent quality and reproducibility with respect to particle size, radiolabeling yield and SLN uptake. The kit vials passed the tests for sterility and apyrogenicity. The particle size of the HSA colloid as determined by DLS was ~100 nm. A typical particle size profile of a batch of HSA nanocolloid is shown in Fig. 5 Radiolabeling with $^{99m}TcO_4^-$ using the standardized protocol gave >99% radiolabeling. The radiochemical purity of ^{99m}Tc-HSA remained >95% at 24h. The formulated cold kit was stable

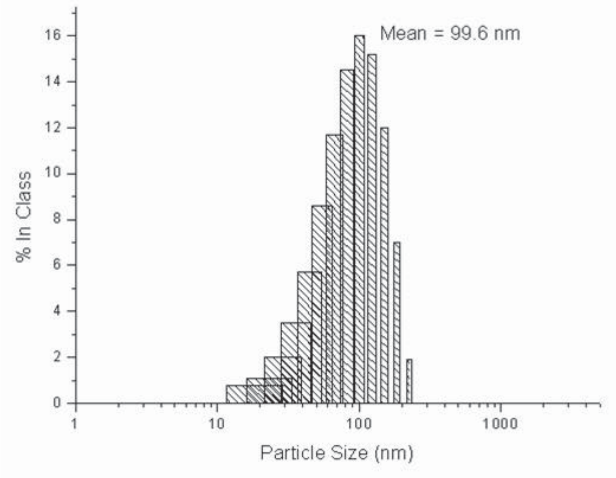

Fig. 5: Particle size analysis of HSA nanocolloid

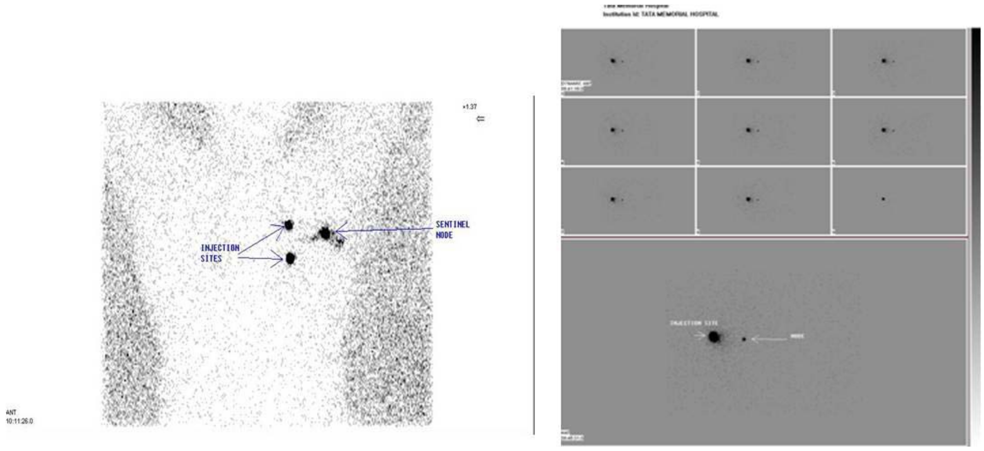

Fig. 6: ^{99m}Tc-HSA nanocolloid in two breast cancer patients

for at least six months when stored at 4°C. Bio-evaluation studies carried out in rabbit model showed clear early visualization of the SLN with retention at least up to 3h post injection and minimal uptake in secondary nodes. Fig. 6 is the image of the ^{99m}Tc-HSA nanocolloid study in a breast cancer patient. The SLN could be successfully localized in almost all the patients. Based on the submission of the dossier containing the preparation, QC and bio-evaluation of the radiopharmaceutical, the Radiopharmaceutical Committee approved the manufacture and supply of HSA nanocolloid cold kits for use in patients for SLND.

Acknowledgements

The authors are grateful to Dr. MRA Pillai, Head, Radiopharmaceuticals Division for the motivation, encouragement and direction given for taking forward this work to clinical users. The authors are thankful to Dr Meera Venkatesh, Former Head Radiopharmaceuticals Division for the valuable guidance and suggestions given during this work. The authors acknowledge clinicians at the nuclear medicine departments at Jaslok, TMH, Bombay hospital and Inlaks hospital, Pune for carrying out the clinical trials.

References

1. Mozley PD, Stubbs JB, Plfssl K, Dresel SH, Barraclough ED, Alavi A, et al. Biodistribution and dosimetry of TRODAT-1, a technetium-99m tropane for imaging dopamine transporters. *J Nucl Med* 39 (1998): 2069–2076.
2. Fang P., Wu C., Liu Z., Wan W., Wang T., Chen S., Chen Z., Zhou X. The Preclinical Pharmacologic Study of Dopamine Transporter Imaging Agent [^{99m}Tc]TRODAT-1. *Nucl Med Biol* 27(2000): 69–75.
3. Morton DL, Chan AD. The concept of sentinel lymph node localization: how it started. *Semin Nucl Med* 30: 4 [2000].
4. Eshima D, Fauconnier T, Eshima L, Thornback JR. Radiopharmaceuticals for lymphoscintigraphy: Including dosimetry and radiation considerations. *Semin Nucl Med* 2000; 30: 25-32.

DEVELOPMENT OF NEUTRON TOMOGRAPHY AND PHASE CONTRAST IMAGING TECHNIQUE

Amar Sinha, Mayank Shukla, P.S.Sarkar, Yogesh Kashyap and Ashish Agrawal
Neutron & X-ray Physics Facilities

Dr. A. Sinha, Neutron & X-ray Physics Facilities, Physics Group and his team received the DAE Group Achievement Award for the year 2010

Introduction

Neutron imaging has proved to be a powerful nondestructive imaging technique. Neutron because of its unique attenuation characteristics is often considered to be complimentary to X-ray based technique. We had earlier shown feasibility of conducting 2D and 3D tomography at APSARA. However it was realized that for obtaining a more precise tomography images, beam quality and neutron flux needs to be improved. This is particularly due to the fact that for tomography reconstruction, projection data need to have good statistics, be free from scattered noise and should have good collimation ratio. With this aim in mind, we designed a neutron tomography assembly at CIRUS. This assembly has been used extensively by us providing very good result for a variety of objects of interest in nuclear and industrial applications.

Traditional imaging methods such as absorption radiography and tomography however have limitations particularly when it comes to imaging objects with low attenuation or distinguishing between objects with minor differences in attenuation. Over the years, a new class of imaging has emerged which overcomes these limitations and uses phase, instead of attenuation, to form images using neutrons. This technique, named as phase contrast imaging, has been used successfully for X-rays. However for neutrons, this technique is slowly gaining importance particularly for objects which are neutron transparent. Such materials include nuclear fuel cladding or deuterium ingress in such cladding etc. The implementation of such a phase imaging for neutron requires a coherent beam of neutrons at least in terms of spatial coherence. This in turn requires a special neutron collimator design. The imaging system also needs especially designed to record high resolution phase images. In order to demonstrate the feasibility of this technique, we have designed a special collimator system and imaging system.

This paper gives brief overview on making of Imaging beamline E12 at CIRUS for neutron tomography and phase imaging and relevant results on neutron tomography, dynamic neutron imaging and neutron phase contrast imaging.

Design of optimized collimator assembly

We have designed a dual purpose use neutron collimator keeping the application of tomography as well as phase imaging. A collimator with L/D=125 has been installed at CIRUS beam hole No.12. It is made up of 1S aluminum tube of length 1921 mm and is kept in between inner and outer gates. The inner aperture of the tube has been defined by B_4C annular disk and gadolinium disk so as to give effective source size of 16mm. A bismuth plug is inserted in the collimator at the inner end to reduce the gamma radiation field.

Experimental Hutch

An experimental hutch as shown in Fig. 1 has been designed for carrying out the neutron imaging experiments. Borated polythene and Lead blocks constitute the basic shielding blocks of the experimental hutch. The sample manipulator has two-translation and one rotational stage. The detector is kept also kept on an adjustable stand and the detector is surrounded by shielding from all sides. The Neutron detector basically consists of lens coupled CCD camera and neutron scintillator. Lead and borated polythene shielding box are also kept on a movable trolley in the rear side of the experimental chamber. This serves as beam-dump when the neutron beam is ON. All the controls are mounted in a separate control cabin. Operation and control of sample manipulator, Detector, monitoring camera etc can be remotely carried out from this cabin.

Fig. 1: Photograph of experimental facility

Experimental results using Neutron tomography and Phase imaging facility at CIRUS

Neutron tomography and phase contrast imaging experiments were carried out at CIRUS reactor for various samples. For neutron tomography, a collimator with collimation ratio of L/D=125 was used. This collimator has the provision to insert an additional collimator to vary the size of neutron entrance hole from 0.5mm and 1mm. This feature was used for conducting experiments on neutron where due to requirement of coherence the neutron beam inlet has to be reduced to pin hole of size 0.5mm to 1mm.

Study of Hydrogen blisters in zircaloy pressure tube

A zircaloy pressure tube sample with hydrogen blisters was especially prepared and used to test the capability of detecting presence of hydrogen and its intrusion within zircaloy matrix, in collaboration with MMD, BARC. Fig. 2 shows the radiographic data of the sample where the dark spots correspond to presence of hydrogen blisters. It may be noted that it is very difficult to do analysis of depth to which hydrogen might have penetrated within the bulk and hence for such purpose the 3D tomography reconstruction is desirable. Fig. 3 shows the tomography reconstructed data. The potential of neutrons to detect hydrogen in high Z material in combination with neutron tomography makes it an important tool for study of hydrogen ingress within the bulk of materials. Fig. 4 shows the reconstructed volume of a single blister which is of inverted ellipsoidal shape.

Fig. 2: Radiograph of zircaloy containing hydrogen blister

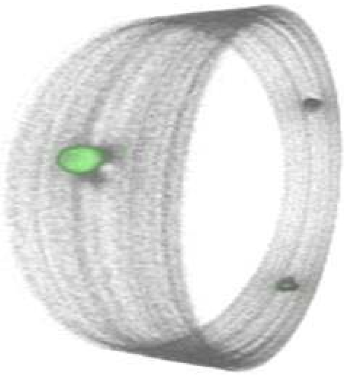

Fig. 3: Reconstructed profile of Hydrogen blister (rendered green) using neutron tomography

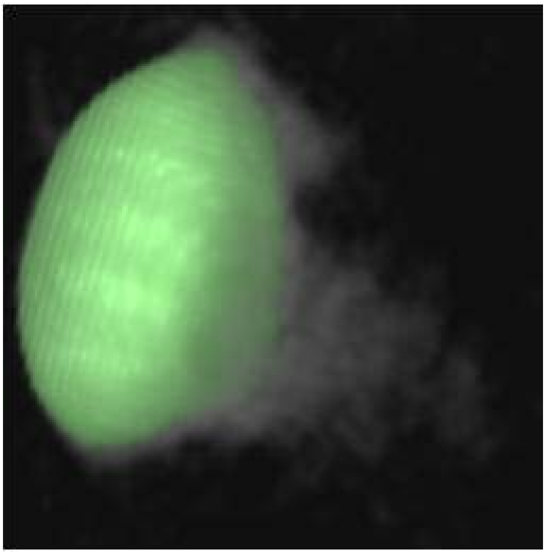

Fig. 4: Reconstructed volume of blister using neutron tomography

Heterogeneous-distribution of Hydrogen on zircaloy

Zircaloy coupons were charged with hydrogen having different concentration by MMD,BARC. The charging process can control both hydrogen concentration and its uniformity. However we have used non-homogenised hydrogen to study the feasibility of detecting hydrogen distribution. Fig. 5 shows the neutron radiograph of three samples mounted on sample manipulator. The hydrogen content of the three sample was 0 ppm, 50ppm and 100ppm. It is very obvious that conventional from neutron radiography one can not detect the presence of minute quantities of hydrogen in samples. However the neutron-tomography reconstruction (Fig. 6) we could detect the distribution of hydrogen even upto 50ppm and also the fact the charging process did not produce uniform hydrogen distribution [1].

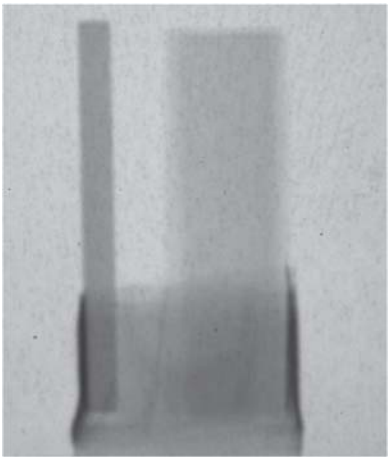

Fig. 5: Neutron radiograph of zircaloy with different hydrogen content

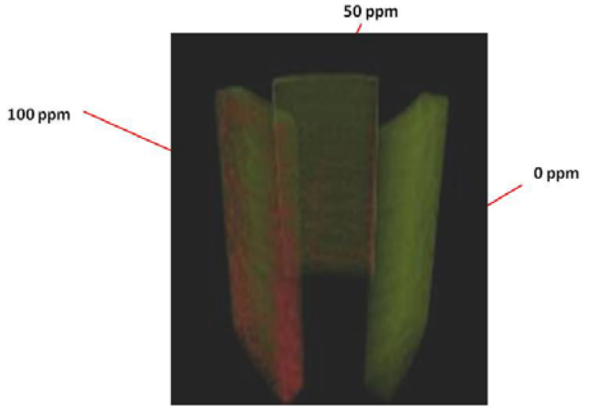

Fig. 6: Neutron tomography reconstruction of hydrogen distribution (rendered Red) in the three different samples (right 0 ppm, middle sample 50 ppm and left sample 100 ppm of hydrogen)

Neutron tomography of a Turbine blade

The first row of turbine blades used in power generating gas turbines has to withstand high temperatures and stress.

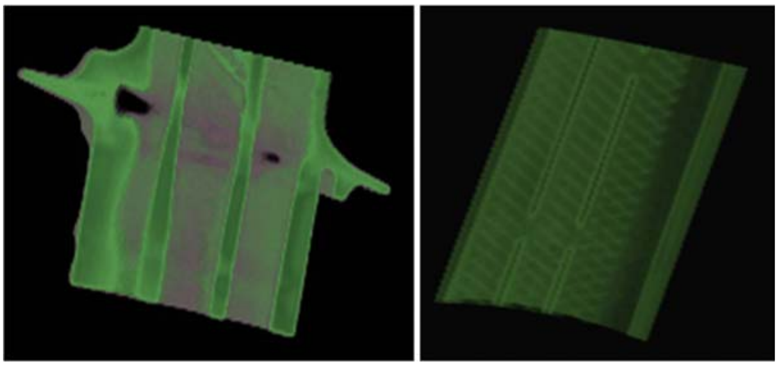

Fig. 7: Neutron Tomography reconstruction upper and lower part of turbine blade

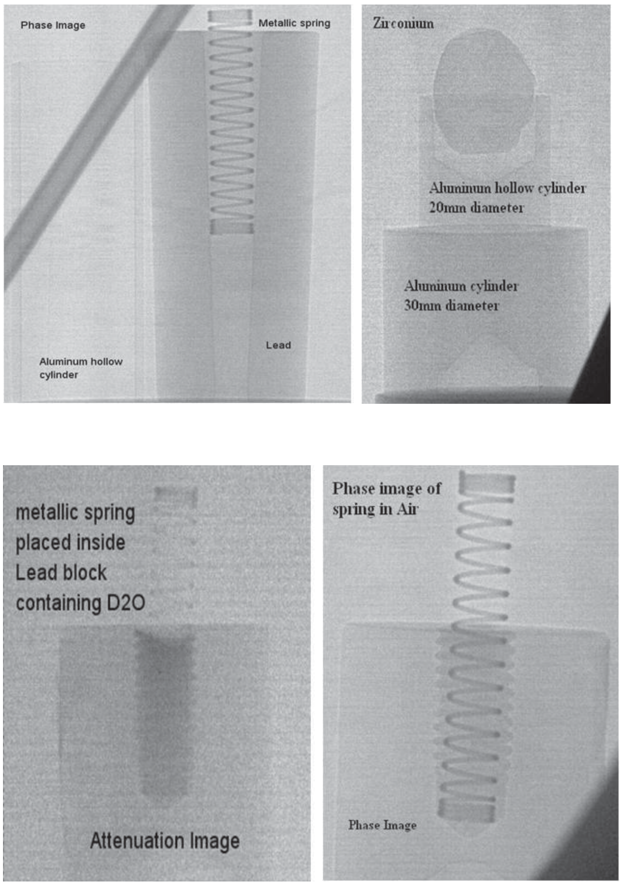

Fig. 8: Neutron absorption and Phase contrast image of various samples

Failure of the blades during operation can lead to very high costs for repair and loss of power-production. To investigate those blades three-dimensional (3D) neutron tomography may be used for non-destructive evaluation (NDE). The reconstruction of the top portion of the blade and reconstructed volume of the body part is shown in Fig. 7.

Neutron Phase contrast imaging

In phase contrast imaging methods images records a special form of contrast generated due to a phase shift induced by the object and determines the phase shift quantitatively [2]. Phase information is generally lost in measuring neutron transmission images due to absence of required coherence for recording interference effect. Specially designed collimators of pinhole sizes 1mm and 0.5mm were used to make a coherent neutron source. The high resolution images were recorded on neutron sensitive image plates. Fig. 8 show some of the results of neutron phase radiography. The acquired images clearly show that there is an increase in sensitivity in phase mode for neutron radiography as compared to conventional neutron radiography.

Dynamic neutron radiography imaging of lead melting

Neutron radiography has been used to online visualization and study of lead melting [3-4] .This work was done in collaboration with RTD, BARC and IIT, Mumbai. Solid lead and liquid lead has a density difference of 6% approximately. One surface of the cubical lead block is heated from one side and temperature is increased from room temperature up to its melting point. Due to heat transmission from the surface in to the bulk of the material, the temperature of the specimen increases with time. The heat transmission is caused by conduction as well as convection hence a definite pattern of melted portion is observed in the meting phenomena which gives the information about the heat transmission process in the bulk. The radiographic images were acquired continuously and melting phenomena was observed (Fig. 9).

Acknowledgements

We are highly indebted to Shri N.K.Mondal and Shri S. Anantharaman of PIED, BARC for providing valuable help in the form of Lead shielding blocks for necessary shielding of experimental facility. We are indebted to Dr. R. N. Singh and Dr. J.K. Chakravartty MMD, BARC for providing zircaloy samples with hydrogen ingress for these experiments. We are also grateful to Shri S. B. Jawale, Head CDM, Shri A.K. Sinha and Shri Sameer Bhatt, CDM for fabrication of high quality collimators for these experiments. We are also grateful to engineers and technicians of CIRUS ROD and RRSD for extending extensive co-operation during installation and commissioning of this beamline. We are grateful to Shri B.S. Manjunath RTD, BARC for his work on lead melting studies. We are also grateful to our colleagues and support staff of NXPF for providing active support during the installation of the beamline. We are indebted to Dr. S. Kailas, Director physics Group and Dr. S. Banerjee, ex-AEC chairman and Homi-bhabha Chair for constant encouragement and support during the setting up of the experimental facility.

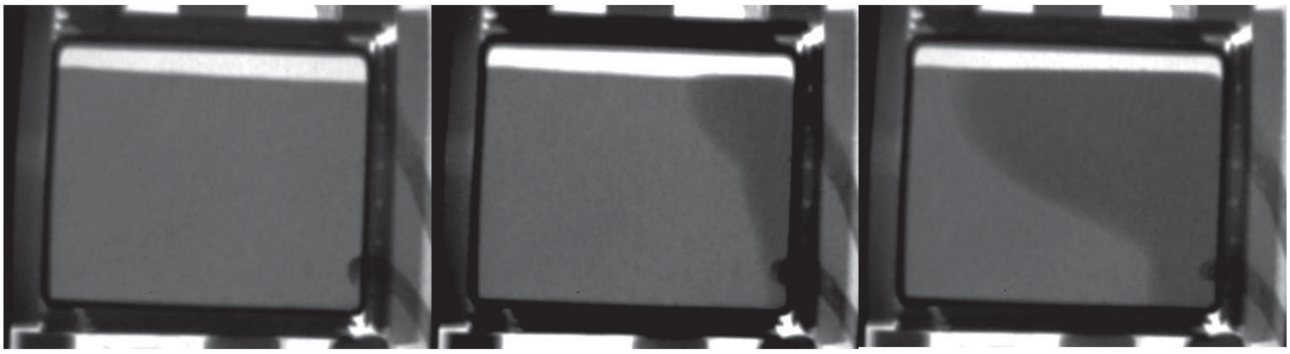

Fig. 9: Radiographs of different stages of a typical melting phenomena in lead. The melting propagation front can be clearly seen

References

1. "Study of Hydride blisters in Zr-alloy using Neutron tomography", Ashish Agrawal, Yogesh Kashyap, P.S.Sarkar, A. N. Behra, M. Shukla, R. N. Singh, Amar Sinha, J. K. Chakravartty, *Journal of Nuclear materials*, 421,47, (2012).
2. "Neutron phase contrast imaging beamline at CIRUS, reactor India", Yogesh S. kashyap, Ashish Agrawal, P.S.Sarkar, Mayank shukla, Tushar Roy and Amar Sinha *Applied Radiation and Isotopes,* 70, 625 (2012).
3. "Visualization of lead melting and solidification using neutron radiography", P.S. Sarkar, Lokendra Kumar, Ashish Agrawal, Yogesh Kashyap, Amar Sinha, B S Manjunath, S V Prabhu and S G Markandeya. Accepted for publication in *International Journal of Nuclear Energy Science and Engineering*
4. Experimental Investigations on Melting of Lead in a cuboid with constant heat flux boundary condition using thermal neutron radiography Lokendra Kumar, B.S. Manjunath, R.J. Patel, S.G. Markandeya, R.G. Agarwal, Ashish Agrawal, Kashyap Y, Sarkar P.S, Amar Sinha, Kannan Iyer and S.V. Prabhu *Accepted for publication in International Journal of Thermal Sciences.*

INDIGENISATION OF REMOTE HEAD METERING PUMPS & BELLOW SEAL BELLOW OPERATED VALVES

T.L. Rao and V.K. Savarkar
Nuclear Recycle Board

Shri V.K. Savarkar, Nuclear Recycle Board and his team received the DAE Group Achievement Award for the year 2010

Introduction

Remote head metering pumps and bellow sealed bellow operated valves are essential equipment for fuel reprocessing and waste management plants. The zero leak feature and reliability of both these equipment, the accuracy and repeatability of the remote head metering pumps are the features which make them essential for handling highly radio-active fluids in these radio-chemical plants.

Development of remote head metering pumps

Any fuel reprocessing plant typically needs 36 metering pumps with capacities ranging from 5 lph to 600 lph. Waste immobilisation plants require about 6 such pumps. These pumps handle highly corrosive and toxic liquids.

The accuracy, repeatability, reliability of pumping required, zero-leak requirement, radioactive nature of the liquids handled and safety aspects there-off make these pumps very special. Till date these pumps were imported as no reliable source was available in India. Difficulties in importing pumps could have led to a major bottleneck for NRB projects.

Fig. 2: Drive Head

Based on the experience with imported pumps, indigenisation efforts were taken up with Indian pump manufacturers.

These pump manufacturers were manufacturing metering pumps for applications not requiring high accuracies. Also pumps only with Teflon diaphragms (i.e. resilient material and not metallic diaphragms as required by us) were being manufactured. These pumps had major problems like unstable metering action, improper leak tightness, and inaccurate flow rate adjustment, excessive pressure drops on suction side, unsatisfactory NRV design, improper suction and discharge connections and unsatisfactory surface finishes. In addition to the above the manufacturers had inadequate facilities in manufacturing, QA and testing.

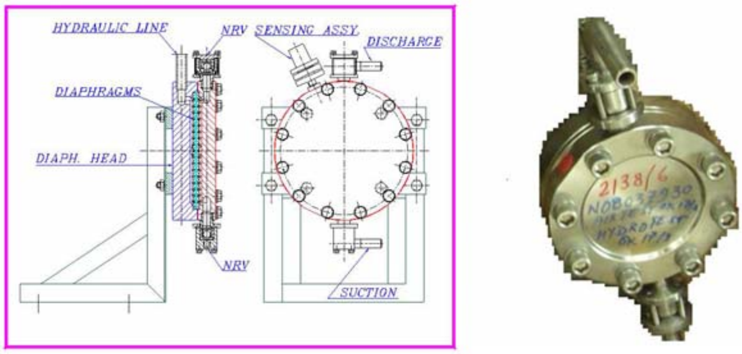

Fig. 1: Remote Head

All the above problems were addressed during development. Manufacturing methods were improved to get proper contouring of remote heads for repeatable performance for a given size of pump. The design of NRVs was changed to sandwich type for ease of maintenance. VRV sizing was done to get good metering stability. VFDs were used for flow control. This led to ease of setting flow rates and quick stabilising of flow rate. The suction / discharge nozzles on the pumps were made with welded design. The internal and external surface finishes were improved by elctro-polishing for ease of decontamination. QA procedures were set for each step of manufacture. Facilities and procedures were set for testing components and performance testing of assembled pumps. Pumps with metering accuracies of ± 1%, Repeatability & Linearity of ±3% have been achieved as required by API standards.

These pumps were tested at vendor's works and in-plant as follows:

A) At vendor's works:
  1) Performance testing on test bed,
  2) Simulated testing,
  3) Endurance testing: 6000 hrs. continuous running under simulated conditions.

B) In-plant Testing:
  1) In-plant testing at PREFRE with process fluids.
  2) In-service testing at PREFRE for scrub solution transfer.

C) Field application:
  1) In-service performance during commissioning
  2) In-service performance during regular operations

About 3 years of effort has gone into the successful development of these pumps. Subsequently, 35 Nos. of these pumps have been installed and commissioned at PREFRE-2, Tarapur and are being used for radioactive service as a part of regular operations. Four pumps have also been installed at WIP(K) & five Nos. at PRTRF Trombay. Further, 30 pumps are being installed at project P3A, Kalpakkam. This development is expected to benefit all users and users like BETDD and PP are also in the process of procuring pumps from the same source.

Commissioning trials of all the pumps installed at PREFRE-2, Tarapur, were carried out. This included performance tests for confirming accuracy, linearity and repeatability in the actual piping system in the field. Pumps of capacities in the lower range viz. 0 to 10 LPH, 0 to 20 LPH and 0-40 LPH and 0-125 LPH for product purification cycles and higher range viz. 0 to 300 LPH, 0 to 500 LPH and 0-600 LPH for organic feed and treatment, were tested at various points in the capacity range. Metering accuracies of ± 1% and linearity within ± 3% has been achieved in actual field trials. Commissioning reports for the same were prepared, reviewed and accepted. For the first time, these pumps were operated and controlled directly from control room using VVVFDs. The satisfactory performance of these pumps was confirmed during integrated water trials in the initial commissioning stage and with actual radio-active process solutions in the hot commissioning stage.

Development of these pumps has also led to a major financial saving e.g. An indigenously manufactured pump costs about Rs.3 to 5 lakhs as compared to Rs.30 to 60 lakhs for a similar imported pump. This has resulted in a saving of about Rs.12 to 13 Crores for a project like PREFRE-2. More importantly development of these pumps in India has led to providing a reliable indigenous source of pumps and spares.

Development of bellow seal bellow operated valves

Any Fuel Reprocessing plant typically needs about 100 to 150 Bellow Seal Bellow Operated Valves of sizes from

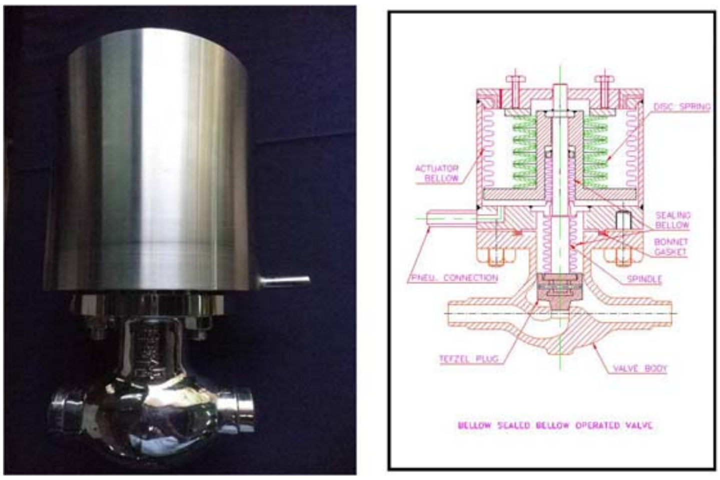

Fig. 3: Bellow Seal Bellow Operated Valve

15 NB to 40 NB. Waste immobilisation plants require about 30 Bellow Seal Bellow Operated Valves in the above sizes. These valves handle highly corrosive and toxic liquids.

The zero-leak and reliability requirement due to the radioactive nature of the liquids handled and safety aspects there-off make these valves very special. Till date these valves were imported as no reliable source was available in India.

Based on the experience with imported items, indigenisation efforts were taken up with Indian manufacturers. Some manufacturers in India manufactured manually operated bellow seal valves. There were no manufacturers for Bellow Seal Bellow Operated Valves.

During development, valve designs were evolved. Experience in working with imported valves was utilized and good design features of various valves were adopted to evolve the final design. Features like full bore, use of Tefzel as MOC for plug and seals, bellow actuator, are some of the features adopted. For the first time valves were made maintenance friendly wherein the actuator along with spindle and plug are made replaceable. This will facilitate replacement of a failed valve in future without cutting pipelines. Compact valve actuators were designed. Selection of liquid sealing bellows and bellows for actuator was an important step in design. Further, selection of disc springs, number of elements to achieve required lift of plug, pre-tension required, etc. were part of the design detailing.

Manufacturing methods were improved at the vendor's works. This includes the critical steps like bellow welding, spindle machining, spindle alignment, etc. The QA procedures were set for each step of manufacture. Facilities and procedures were set for testing components and performance testing of assembled items. Endurance testing rig was specially made for the valves. These Valves have been subjected to rigorous tests like performance testing on test bed, simulated testing, endurance testing for 25,000 cycles and continuous running under simulated conditions. Helium leak test was used for confirming no-leak at various stages like, bellow weld stage, actuator assembly stage and total valve assembly stage.

As a result of the efforts, Bellow Seal Bellow Operated valves meeting Class VI requirements have been achieved.

The valves were further tested for in-plant conditions at PREFRE-1 with process fluids. Subsequently, about 100 Nos. of these valves have been installed and commissioned at project ROP, Tarapur. Valves have also been installed at WIP(K), PRTRF Trombay and P3A, Kalpakkam. The valves installed at PREFRE-2, Tarapur are now in use in radioactive service and giving a good performance.

INNOVATIONS IN DESIGN, CONSTRUCTION AND COMMISSIONING OF ADDITIONAL WASTE TANK FARM (AWTF), TARAPUR

Umadevi K.
Nuclear Recycle Board

Smt. K. Uma Devi, Nuclear Recycle Board and her team received the
DAE Group Achievement Award for the year 2010

Abstract

This paper briely describes all the innovations that has gone into the design, construction and commissioning stages of Additional Waste Tank Farm, Tarapur. This facility is an integral part of the reprocessing plant, PREFRE-II, Tarapur and was commissioned in 2011 along with PREFRE -II. Technology and experience gained so far in the field of high level liquid waste storage is combined with innovative concepts in design and safety in AWTF to make it much more operator friendly and environmentally safe compared to the existing waste tank farms.

General Description of the Facility

Additional Waste Tank Farm (AWTF), Tarapur is a facility meant for the interim storage of the high and medium active waste generated through PHWR spent fuel reprocessing plant PREFRE-II operation, containing almost 100% fission product activity, in such a way that the occupational workers, the general public and the environment is not affected directly or indirectly. Facility design is based on activity of high level waste generated by reprocessing of PHWR spent fuel cooled for more than three years.

After each batch of reprocessing operation, waste generated has to be moved out to this storage facility to ensure continuous plant operation. The waste thus stored is meant for treatment and final disposal depending on the nature of the waste and this is done in the waste treatment facility located nearby the same site.

This waste tank farm facility includes:

a) A shielded transfer facility for transferring waste from the generating point, ie, PREFRE-II to AWTF and also from AWTF to Waste Management facility.

b) A shielded, valveless diversion facility for diverting waste to the desired storage tank and emptying the desired tank without causing any accidental siphoning.

c) A cluster of huge storage tanks of very high integrity located in heavily shielded vaults providing a multi-barrier containment. Refer Fig.1 for General Arrangement of the Tanks.

d) Restricted Access Corridor where all services and utility to the storage tanks are located.

e) Service Building to house a control room where all the operations of the Waste Tank Farm can be carried out, Waste Cooling Water room, off-gas plant room and ventilation air supply fan room and exhaust room. Refer Fig.2 for General Arrangement of the Service Building.

Other than the above, to ensure safe storage and transfer, a no. of systems are provided complying the AERB recommendations to upgrade the engineered safety of the liquid waste storage system. They are :

- Transfer system with adequate stand-by modes and routes.
- Cooling facility for HLLW storage tanks to remove the decay heat generated by the fission products.

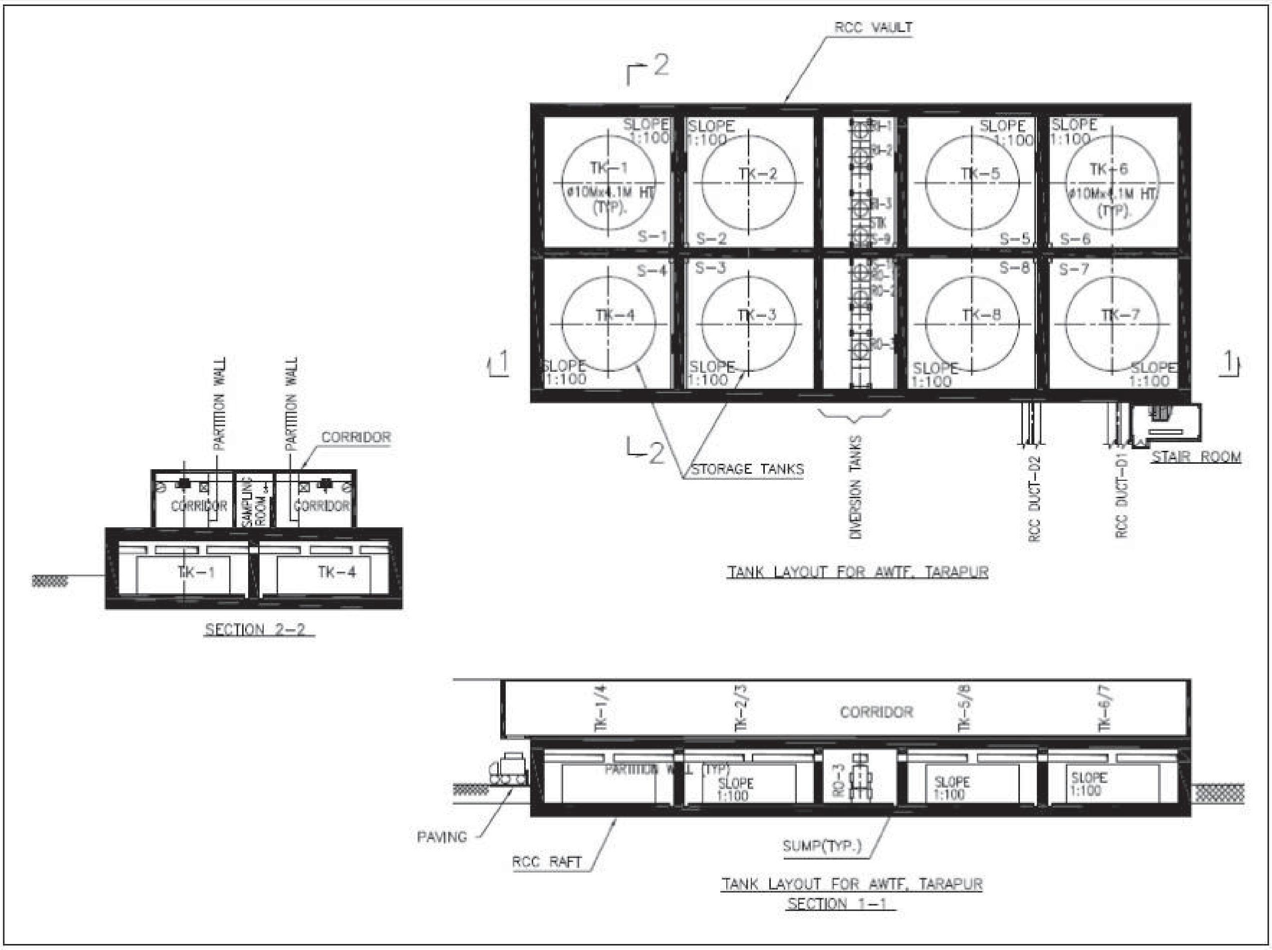

Fig. 1: Plan, Elevation and Side view of AWTF vaults

- Waste agitation and mixing provision by compressed air for all storage tanks.
- Provision of introducing air at the vapor space of al HLLW tanks for diluting any radiolytic hydrogen generated.
- Tank Off-gas treatment and discharge.
- Ventillation system and RCC stack
- Instrumentation system for continuous monitoring of tank conditions.
- CCTV, cameras and Access control system is provided for restricted areas.
- Remote sampling system for taking samples from the tanks and sumps.
- Critical systems such as WCW system, off-gas treatment system, ventillation system, compressed air agitation system etc. are given class III power supply.
- Infiltration gallery all around the vault to maintain underground water table well below the raft automatically.

Innovations in Design for Improved Safety

A number of design innovations are incorporated in AWTF as compared to the existing waste tank farms. They are:

- The tanks, barriers, and the civil structures are designed to withstand the maximum potential earthquake at site, ie, Safe Shutdown Earthquake , in accordance with the provisions of ASME Section-III, Division-I, Subsection-ND.
- Existing horizontal tank design was modified to seismically qualified vertical tank design.
- All tanks are made of Stainless Steel refined grade for long life.
- Overhead shielded duct design with multiple containment was used in place of underground ducts for waste transfer.
- Routing tank concept was used for waste diversion to make the facility valveless.
- The complex AWTF vault piping was analysed through 3- dimensional modeling for SSE qualification.

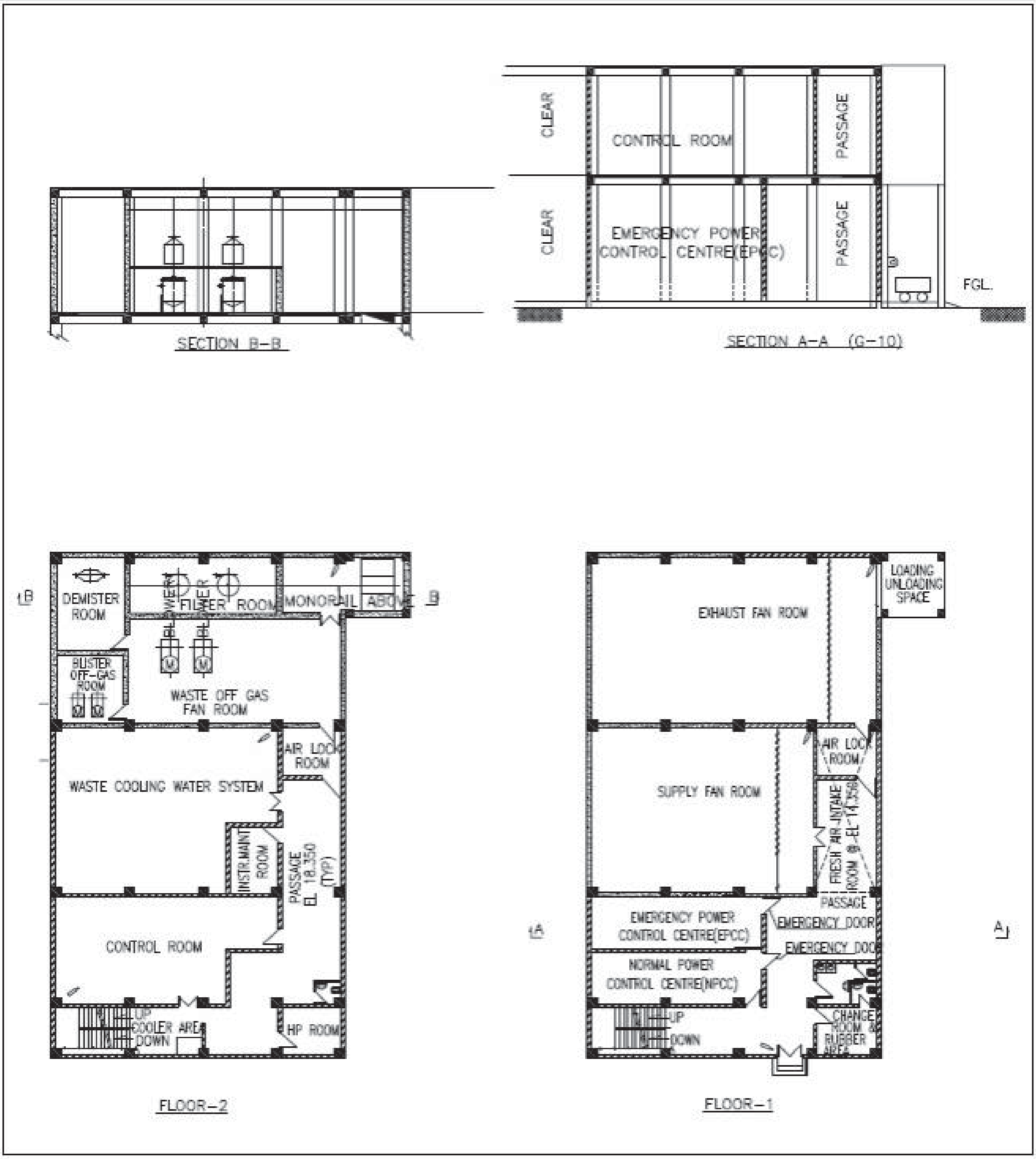

Fig. 2: General Arrangement of AWTF Annexe Building.

- Air-lift recirculator based mixing system which uses very less air compared to the existing systems.
- A complex design of cooling coil removes decay heat and provide uniform cooling to all tank contents, with additional cooling for tank bottom and walls.
- The plant was designed for remote operation using PLC and SCADA from main plant (PREFRE-2) and AWTF control rooms.
- Adequate safety interlocks and cut-offs with back-ups are built into the system.
- VVVF drives were used for ventillation exhaust fans for energy saving and for reduction in DG capacity.
- Shielded plugs for vault lighting.
- An additional portable DG set for power supply to vital systems like cooling water system and off-gas system under post seismic scenario was provided.

- Dedicated UPS with standby for monitoring system was used.
- CCTV and Access control system was incorporated for improved physical protection.

Innovations in construction & commissioning

A unique in-situ fabrication methodology without compromising quality standards was followed to perform the challenging task of installing the huge tanks inside concrete vaults. Laying of overhead shielded duct for waste transfer needs special mention. Routing of the duct at site with minimum change to existing structures, keeping the elevation requirements in open areas and at crossings with existing facilities, integrating with existing facilities without compromising shielding thickness etc. were challenging tasks which were carried out with accuracy. After completion of construction, systematic commissioning activities were undertaken by the commissioning team, following the methodology described below:

- Dividing the facility into 37 sub-systems.
- Defeciency in each system was noted separately and corrected.
- Commissioning procedures for each sub-system was prepared.
- Following the above procedures, pre-commissioning (equipment & line flushing, calibrations and transfer route checking, no-load tests etc) and cold commissioning, (establishing design intent of each system with water as test medium) was done. At this stage, designated operation staff were inducted into the commissioning team.
- Test reports were prepared for each sub-system, which were reviewed by regulatory authority. Recommendations were incorporated..
- Regulatory clearance was obtained for hot commissioning based on the above reports.
- The facility was handed over to the operation group for hot commissioning. Necessary training in the form of classroom lectures and walk-throughs were also given to the operation staff.

Performance

Based on the improved design of the PREFRE-II plant, the waste generation per Ton of fuel processed has come down drastically and as a result, activity of waste is much more than that has been handled so far. AWTF, Tarapur is designed for this level of activity and is giving satisfactory performance in terms of safe transfer, storage and ease of operation.

Acknowledgements

The author thanks Shri S. Basu, Chief Executive, NRB for his valuable guidance , continuous support and motivation in carrying out above activities. Author is also thankful to all the engineers and support staff of NRB, Trombay, Construction directorate, Tarapur and Operation Team of PREFRE-II & WMF, Tarapur who were involved in various stages of design, construction and commissioning and operation of AWTF, Tarapur.

CHARACTERIZATION OF A RADIATION INDUCIBLE EUKARYOTIC TYPE SERINE / THREONINE PROTEIN KINASE FROM *DEINOCOCCUS RADIODURANS*

Yogendra S. Rajpurohit and Hari S. Misra
Molecular Biology Division

Shri Y.S. Rajpurohit was awarded the "FEMS-2011 Young Scientist Award" at the 4th Congress of the Federation of European Microbiological Society (FEMS) held at Geneva, Switzerland, during June 26-30, 2011

Abstract

Serine/threonine protein kinases (STPKs) play important roles in radiation induced signaling processes in case of higher organisms. In bacteria however, the roles of STPKs in radiation resistance and DNA damage response have not been fully understood. A eukaryotic type STPK encoded from *dr2518* gene in the gnome of *D. radiodurans* was characterized and demonstrated that both synthesis and functions of this kinase get induced in cells exposed to γ-radiation *in vivo.* The kinase activity of this enzyme was also stimulated by an antioxidant pyrroloquinoline quinone (PQQ) *in vitro*. The *dr2518* gene was deleted from genome of *D. radiodurans*. The *dr2518* mutant exhibited higher sensitivity to DNA damage and survival of these cells decreased significantly against various DNA damaging agents including gamma and UV radiation. These cells showed DNA repair impairment and change in protein phosphorylation. Through this study, for the first time we demonstrated the role any STPK in bacterial response to gamma radiation and DNA damage using *D. radiodurans* as model organism.

Keywords: Deinococcus radiodurans, DNA damage responsive kinase, radiation induced signaling

Introduction

Deinococcus radiodurans R1 is a bacterium, characterized for its extraordinary tolerance to the lethal and mutagenic effects of DNA damaging agents, including γ rays and UVC radiations, and desiccation (12). These phenotypes are attributed to an efficient DNA strand break repair mechanism (11) and a strong oxidative stress tolerance due to antioxidant enzymes (6) and by the non-enzymatic components like pyrroloquinoline quinine (PQQ) (3), carotenoids (13) and accumulation of Mn (II) (1). This bacterium produces PQQ, a well-characterized antioxidant (7) and role of this compound in radiation resistance and DSB repair beyond its oxidative stress tolerance, has been demonstrated in *D. radiodurans* (9). Database search for the proteins containing PQQ binding motifs shows the presence of five uncharacterized open reading frames (ORFs) DR_0503, DR_0766, DR_1769, DR_2518 and DR_C0015 in the genome of this bacterium (http://smart.embl-heidelberg.de/). All five putative PQQ binding proteins deletion mutant were generated separately and characterization of these mutants' responses to DNA damage was investigated. The Δ*dr2518* mutant was only mutant that showed DNA damage sensitivity. Purified recombinant DR2518 was characterized as a functional kinase and its kinase activity was induced by PQQ and DNA ends *in solution*.

Footnote: Shri Y. S Rajpurohit, Scientific Officer / D, Molecular Biology Division, Bhabha Atomic Research Centre, received FEMS-2011 Young Scientist Award for his work entitled "Characterization of radiation inducible eukaryotic type serine /threonine protein kinase from *Deinococcus radiodurans*" during 4th FEMS congress of European Microbiologists – 2011 held during June 26-30, 2011, at Geneva, Switzerland.

Experimental procedures

D. radiodurans and *E. coli* cultures were maintained as described earlier (8). The *dr2518* gene was cloned in pET28a vector and target protein was purified using metal affinity chromatography as described in (10). Purified DR2518 kinase was used to characterize for its autokinase activity. Deletion mutants were generated by replacement of corresponding gene by nptII gene using protocol as described earlier (5). Knockouts were screen for their survival against DNA damaging agents including γ-radiation, UV, H_2O_2 and MMC (9).

Results and Discussion

Involvement of *dr2518* gene product in *D. radiodurans* survival against DNA damage

Earlier, pyrroloquinoline-quinine synyase (PQQE)mutant of *D. radiodurans* become sensitive to gamma and shows impairment in DNA strand break repair (9) activity. Search of PQQ binding proteins in *D. radiodurans* genome showed the presence of five genes such as *dr0503*, *dr0766*, *dr1769*, *dr2518* and *drc0015* encoding uncharacterized proteins having PQQ binding motifs (Fig. 1A). Amongst others the DR2518 also contains a well-characterized eukaryotic type Ser/Thr kinase (STK) domain. To ascertain the involvement of these genes in radioresistance of this bacterium, they were individually deleted from *D. radiodurans* R1 genomes and these mutants were checked for γ radiation resistance. Only Δ*dr2518* mutant showed nearly 3-log cycle decreased cell survival at 6kGy γ rays (Fig. 1 B) and at $1200Jm^{-2}$ of UVC radiation. These cells also showed ~2.5 log cycle loss of viability upon 14 days desiccation at 5% humidity and 1.5-log cycles less survival in presence of 20μg /ml mitomycin C treated for 30 min, as compared to wild type. Although the precise mechanisms of DR2518 function in radiation resistance and DSB repair are not clear, this protein showed close similarities with two protein kinases (i) YfgL, a periplasmic protein kinase of *E. coli*, which contains multiple PQQ binding motifs and a defined STK domain (4), and (ii) PknB, an oxygen and nutritional stress sensor kinase of mycobacterial two-component system that is associated with cell wall synthesis and cell division in mycobacterium (2). These results however, suggested that DR2518 contribute in radiation resistance and DSB repair of this bacterium.

DR2518 kinase is PQQ inducible Ser/Thr type protein kinase

The *dr2518* was cloned in pET28a+ and recombinant protein was purified using nickel affinity chromatography. The phospho-nature of DR2518 polypeptide and the autokinase activity of this protein were ascertained using phospho-Ser/Thr epitops polyclonal antibodies and by *in vitro* phosphorylation using $[^{32}P]$ γATP. Recombinant DR2518 showed cross reactivity with phospho-Ser / Thr epitops antibodies. Since the DR2518 contains putative

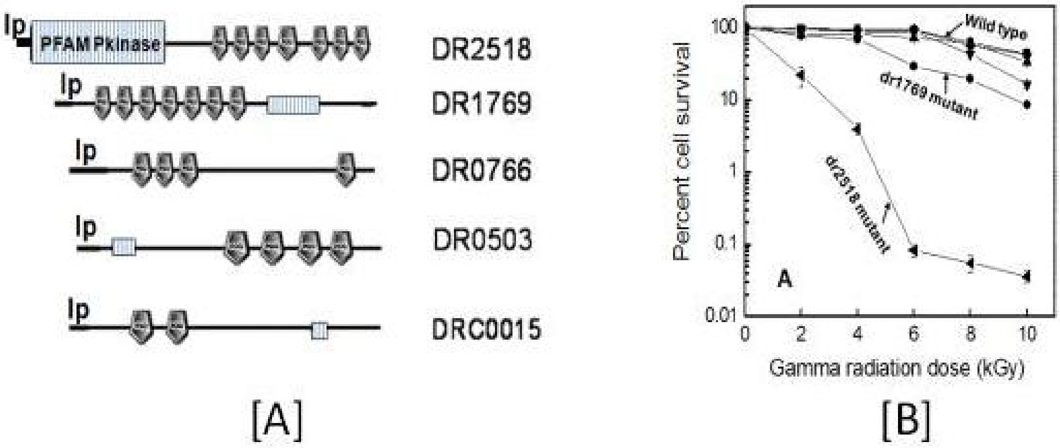

Fig. 1: [A] Diagrammatic representation of individual open reading frames encoding putative quinoproteins in *Deinococcus radiodurans* R1. The DR0503, DR0766, DR1769, DR2518 and DRC0015 ORFs encoding uncharacterized proteins with multiple PQQ binding motifs and N-terminal leader peptides (lp) differ in protein kinase domains. [B] Cells survival of *Deinococcus radiodurans* R1 Wild type (-■-) and D*dr0503* (-▶-), D*dr0766* (-▲-), D*dr1769* (-●-), D*dr2518* (-◀-) and D*drc0015* (-▼-) mutants were exposed to different doses of gamma radiation.

PQQ binding motifs and a well-defined STK domain, the possibilities of this protein interact with PQQ and having autokinase activity were checked. Kinase activity of recombinant DR2518 was assayed using both cold ATP and [^{32}P] γ-ATP in solution. Its kinase activity was stimulated with PQQ by 2.679 ± 0.324 fold (Fig. 2A). This indicated that DR2518 is a phosphoprotein having PQQ stimulated autokinase activity. Circular Dichroism (CD) spectra of DR2518 incubated with increasing concentration of PQQ were different from DR2518 protein alone (Fig. 2B). Since PQQ alone did not show circular dichroism, the change in spectral characteristics as a function of PQQ concentration indicated the conformational change in protein upon PQQ interaction Fig. 2B). Real time PCR analysis for *dr2518* gene expression showed that the level of *dr2518* transcript increase 15.355 ± 0.179 fold within 30 min PIR and maintained closely to this level till 3h PIR and then decreased to nearly unirradiated level in 24h PIR (Fig. 2C). The expression of DR2518 was induced with γ radiation that also produces DNA strand bread; therefore the efect of double-stranded DNA (dsDNA) on autokinase activity of DR2518 was examined by *in vitro* phosphorylation with [^{32}P] γ-ATP. The autokinase activity of DR2518 increased by 2.134 0.321 fold in presence of 1kb linear dsDNA (Fig. 2D) and by only linear plasmid DNA but not in the presence of

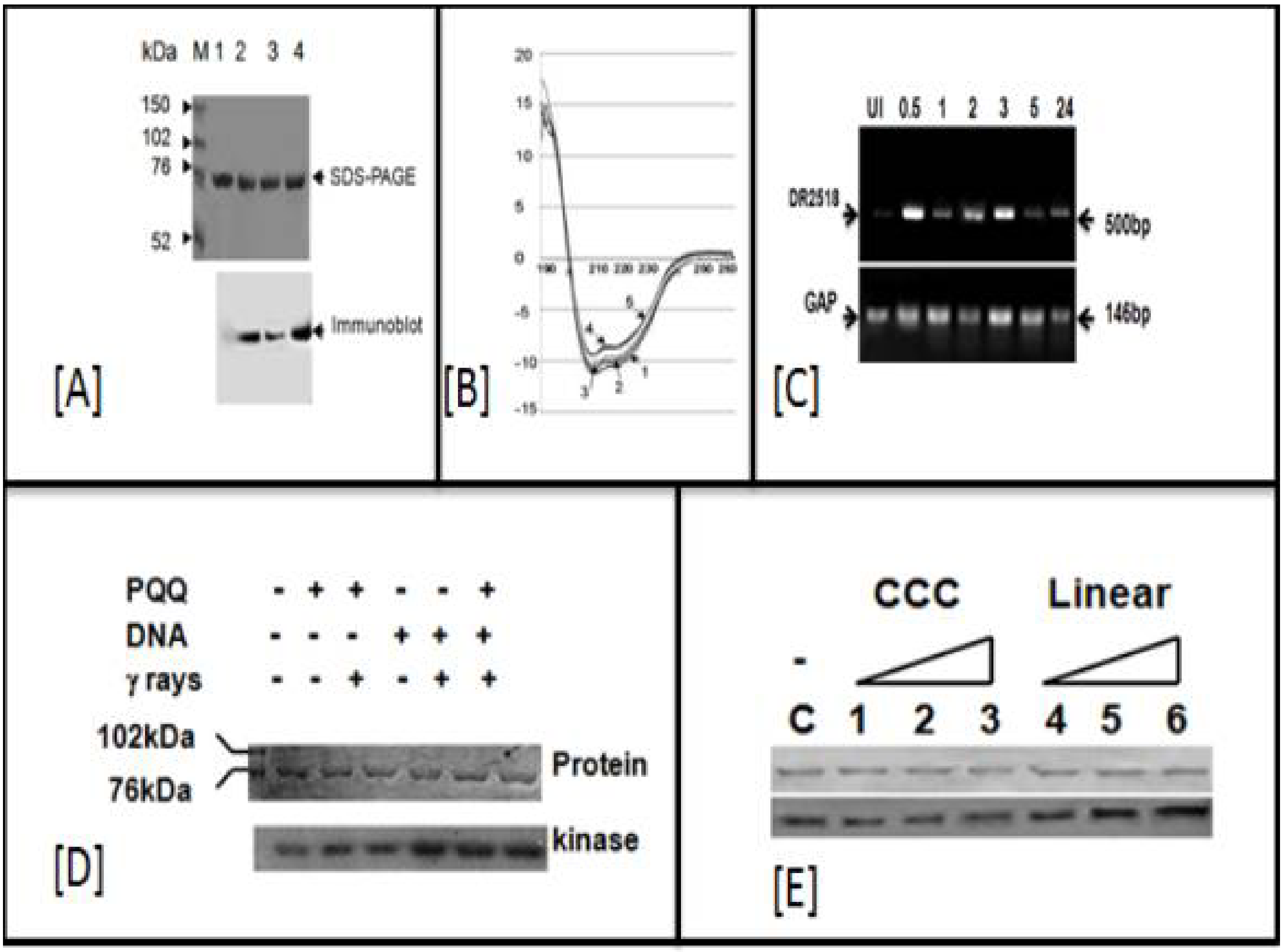

Fig. 2: Biochemical characterization of DR2518A. [A] Purified recombinant protein was treated with alkaline phosphatase (1) and incubated with cold ATP in absence (3) and presence of (4) of PQQ. These samples were separated on SDS-PAGE along with untreated protein (2) and phosphosignals were detected with phospho-Ser/Thr antibodies (immunoblot). [B] Circular Dichroism spectroscopy of purified protein incubated in absence (1) and in presence of an increasing concentration 1nM (2), 10nM (3), 100nm (4) and 1000nM (5), of PQQ was carried out. [C] Effect of DNA damage on *dr2518* gene expression and autokinase activity *in vitro*. The RT-PCR analysis of total RNA of wild type cells collected at different PIR (0.5, 1, 2, 3, 5 & 24h) period and unirradiated (UI) control was carried out using internal primers of *dr2518* gene. [D] Recombinant DR2518 was incubated with PQQ and PCR product in different combinations as indicated and the autokinase activity was detected by autoradiography. [E] DR2518 was also incubated with 100ng of each superhelical form (1, 2, 3) and linear form (4, 5, 6) of plasmid DNA and autokinase activity was detected by autoradiography.

CCC (covalently closed circular) plasmid DNA (Fig. 2E) suggests DR2518 kinase activity is also dsDNA end stimulated *in solution.*

The Δ*dr2518* mutant showed altered phosphoprotein profile and impaired DSB repair:

As DR2518 protein is a functionally active protein kinase involved in DNA repair in *D. radiodutrans*. The possibility of its role in regulation of DNA repair and cellular phosphoproteome were speculated and tested by monitoring the total phosphoproteins profile and DSB repair during post irradiation recovery of *dr2518* mutant and wild type. The Δ*dr2518* mutant showed a major defect in DSB repair and did not recover its unirradiated genome size even up to 24h PIR growth (Fig. 3A). This indicated the role of DR2518 in DSB repair. Similarly, the γ irradiated mutant cells showed significant differences in both levels of total phosphoproteins and their profiles when compared with wild type control. After γ irradiation, the levels of protein phosphorylation decreased significantly in 1h PIR in both wild type and mutant cells (Fig 3B, lane 1). Subsequently, wild type cells showed faster recovery of phosphoproteins as seen in 3 and 4h PIR, which was much slower in mutant cells and similar profile was not observed in these cells even up till 24h PIR (Compare lane 3 and 5 in Fig 3B). Stimulation of DR2518 activity by PQQ and DNA ends, which also increases upon γ irradiation, suggested that both PQQ and DNA fragments act as inducers of this membrane protein kinase. Taken together, the results on the enhanced expression of *dr2518* in response to γ radiation, the stimulation of DR2518 kinase activity by PQQ and DNA ends, and the disappearance of certain phosphoproteins in Δ*dr2518* mutant, collectively suggested this protein as a possible DNA damage sensor kinase, having a role in radiation resistance and DSB repair in *D. radiodurans.*

Acknowledgement

Authors thank Dr. S. K. Apte, Bhabha Atomic Research Centre for his technical comments while pursuing this work. We thank Shri A. D. Das for his assistance in

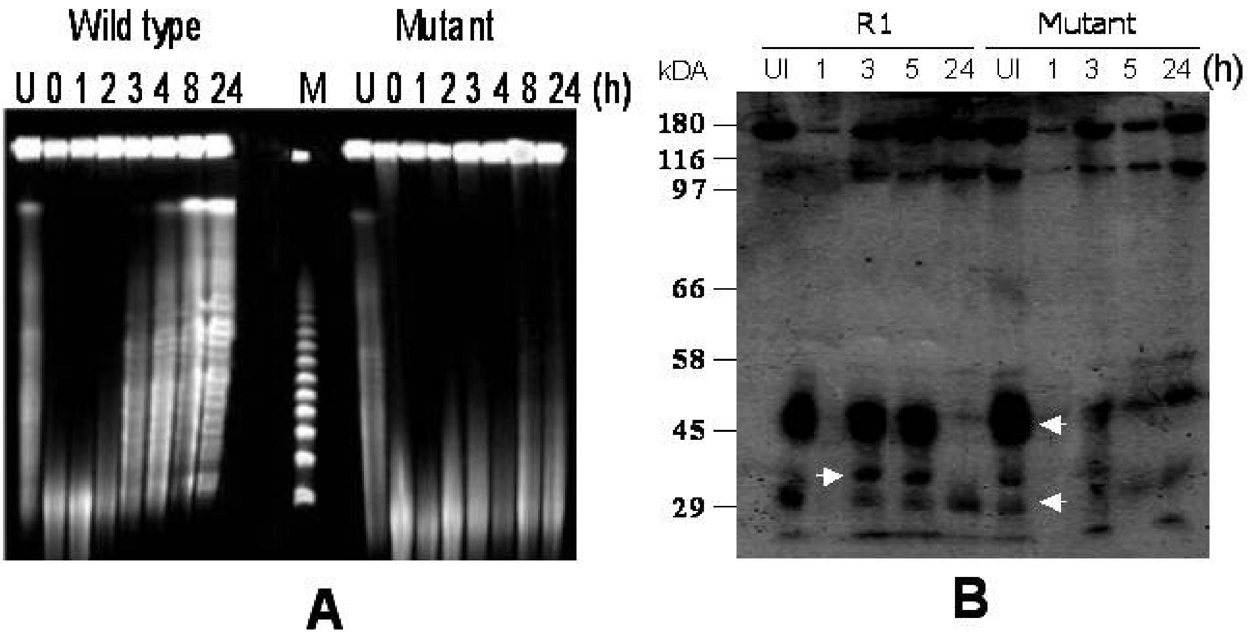

Fig.3 Kinetics of DSB repair and phosphoproteins profiles change during post irradiation recovery of *Deinococcus radiodurans* R1. A. Wild type (wild type) and Δ*dr2518* mutant (mutant) cells were irradiated with 6kGy γ radiation dose and aliquots were collected at different post irradiation recovery period (0, 1, 2, 3, 4, 8 & 24 h) and DSB repair pattern was compared with respective unirradiated (U) controls by monitoring the recovery of wild type *NotI* pattern of genomic DNA from mutant cells. B. Both wild type (wild type) and Δ*dr2518* mutant cells pre-labeled with [^{32}P] were treated with γ radiation and allowed to grow in TGY medium supplemented with [^{32}P]- phosphoric acids. Aliquots were collected at 1, 3, 5, 24 h of post irradiation with 6kGy g radiation and unirradiated (U) controls. Total proteins were analysed on SDS-PAGE and autoradiogram was developed. The phosphoproteins, which are missing in mutant cells, are indicated with arrow.

bioinformatics and Mrs Swathi Kota for her help in the preparation of this manuscript. We acknowledge Shri Subhash Bihani, SSPD, for his assistance in CD spectroscopy.

References

1. Daly M.J., et.al. Accumulation of Mn(II) in *Deinococcus radiodurans* facilitates gamma-radiation resistance. *Science* **306** (2004):1025-1028.
2. Kang C.M., Aboot D.W., Park S.T., Dascher C.C., Cantley L.C. and Husson, R.N. The mycobacterium tuberculosis serine/threonine kinases PknA and PknB: substrate identification and regulation of cell shape. *Genes Dev* **19**(2005):1692-1704.
3. Khairnar N. P., Misra H. S., and Apte S. K. Pyrroloquinoline-quinone synthesized in *Escherichia coli* by pyrroloquinoline-quinone synthase of *Deinococcus radiodurans* plays a role beyond mineral phosphate solubilization. *Biochem Biophys Res Commun* **312** (2003)**:** 303-308.
4. Khairnar N.P., Kamble V.A., Mangoli S.H., Apte S.K., and Misra H.S. Involvement of a periplasmic protein kinase in DNA strand break repair and homologous recombination in *Escherichia coli*. *Mol Microbiol* **65** (2007): 294-304.
5. Khairnar N.P., Kamble V.A. & Misra H.S. RecBC enzyme overproduction affects UV and gamma radiation survival of *Deinococcus radiodurans*. DNA Repair *(Amst)* 7 (2008): 40-47.
6. Markillie L.M., Varnum S.M., Hradechy P., and Wong K.K. Targeted mutagenesis by duplication insertion in the radioresistant bacterium *Deinococcus radiodurans*: radiation sensitivities of catalase (*katA*) and superoxide dismutase (*sodA*) mutants. *J Bacteriol* **181**(1999)**:** 666669.
7. Misra H.S., Khairnar N. P., Atanu B., Priyadarshini I., Mohan H., and Apte S. K. Pyrroloquinoline-quinone: a reactive oxygen species scavenger in bacteria. *FEBS Lett* **578**(2004)**:** 26-30.
8. Misra H.S., Khairnar N.P., Kota S., Shrivastava S., Joshi V.P. and Apte, S. K. An exonuclease I-sensitive DNA repair pathway in *Deinococcus radiodurans*: a major determinant of radiation resistance. Mol Microbiol 59 (2006):1308-1316.
9. Rajpurohit Y.S., Gopalakrishnan R., and Misra H.S. Involvement of a protein kinase activity inducer in DNA double strand break repair and radioresistance of *Deinococcus radiodurans*. *J Bacteriol* **190**(2008): 3948-3954.
10. Rajpurohit Y.S. and Misra H.S. Characterization of a DNA damage-inducible membrane protein kinase from *Deinococcus radiodurans* and its role in bacterial radioresistance and DNA strand break repair. *Mol.Microbiol.* **77** (2010), 1470-1482.
11. Slade D., Lindner A.B., Paul G., and Radman M. Recombination and replication in DNA repair of heavily irradiated *Deinococcus radiodurans*. *Cell* **136**(2009):1044-1055.
12. Slade D. and Radman M. Oxidative stress resistance in *Deinococcus radiodurans*. *Microbiol Mol Biol Rev.* **75**(2011), 133-191.
13. Tian B., Sun Z., Shen S., Wang H., Jiao J., Wang L., Hu Y., and Hua Y. Effects of carotenoids from *Deinococcus radiodurans* on protein oxidation. *Lett Appl Microbiol* **49** (2009):689-94.

PLANT ADAPTIVE RESPONSES TO HEAVY METALS AND IMPLICATIONS FOR PHYTOREMEDIATION

Sudhakar Srivastava, Penna Suprasanna and Stanislaus F. D'Souza
Nuclear Agriculture and Biotechnology Division

Dr. Sudhakar Srivastava received the NASI Young Scientist Platinum Jubilee Award for the year 2011 (Plant Sciences)Annual session held at Thiruvananthapuram, Nov. 24-26, 2011

Abstract

Contamination of the environment by heavy metals has been increasing progressively for the last few decades with the ongoing development of our society and science. The need of the hour is to devise strategies to remediate the heavy metal load of soil and water for the sustenance of environment. The use of plants for the purpose has gained popularity due to low-cost of the technology, namely phytoremediation. However to employ phytoremediation at field scale, we need to understand plants responses to metal(loid) exposure holistically to be able to select suitable plants for a particular area, to use proper strategies and amendments and to develop transgenic plants for improved performance. We have identified various potential aquatic and terrestrial plants and algae in lab and field studies. In addition, we have explored mechanism of toxicity caused by metal(loid)s to plants and also the responses of plants to sense and tackle the stress. This article summarizes the major outcomes of these studies.

Introduction

Anthropogenic and natural activities discharge or induce the release of toxic metals into environment. Both soils and aquatic bodies have thus become contaminated by a variety of metals covering huge areas and affecting millions of people in some cases[1,2]. Metal(loid)s are biologically non-degradable and persist for centuries in environment. Crop plants tend to accumulate these toxic metals. A huge number of people, therefore, remain susceptible to metal(loid) poisoning due to consumption of contaminated drinking water and food. Two perspectives are proposed to cope up the problem[1]. One approach is to remove metals from contaminated environment and remediate the site (particularly suitable for small areas). The plant based approach for this purpose is known as phytoremediation. The other way is to prevent metal(loid) entry into crop plants (particularly for large areas). This may be done through devising strategies to reduce metal(loid) bioavailability and through identifying low metal accumulating varieties. For both scenarios, there is a need to understand mechanistic details of plants responses to metal(loid) exposure and to investigate why plants/varieties show differential metal accumulation. In addition, strategies for modulating metal(loid) bioavailability need to be planned and tested.

We have analyzed potential of plants to accumulate metal(loid)s in laboratory and field conditions. Several potential metal(loid) accumulators (Fig. 1) have so far been identified viz., *Hydrilla verticillata*[3], *Ceratophyllum demersum*[4], *Vicia faba*[5], *Brassica juncea*[6] and *Sesuvium portulacastrum*[7]. We have largely investigated two plant systems, *H. verticillata* and *B. juncea* and the significant outcomes are being presented here.

Hydrilla verticillata is a potential accumulator of As, U and Cu

Hydrilla verticillata is a worldwide distributed aquatic weed having fast growth and adaptability to grow in various habitats with a wide range of light and pH tolerance. This plant has been found to be a potential accumulator of As[3], U[8] and Cu[9] in different studies. In a recent field study, *Hydrilla* plants (100 g) were exposed to As contaminated water (total 8 L) containing 1500 μg L^{-1} As for 45 days. In these conditions, plants could remove about 72% of the total As in 45 days[10] (Fig. 1C). *Hydrilla* plants also showed potential to accumulate U from low-level uranyl raffinate waste (unpublished data). Upon exposure to 10% waste + 10 ppm U treatment for 3 d, plants were found to accumulate a maximum level of 426 μg U g^{-1} dw (Fig. 1D).

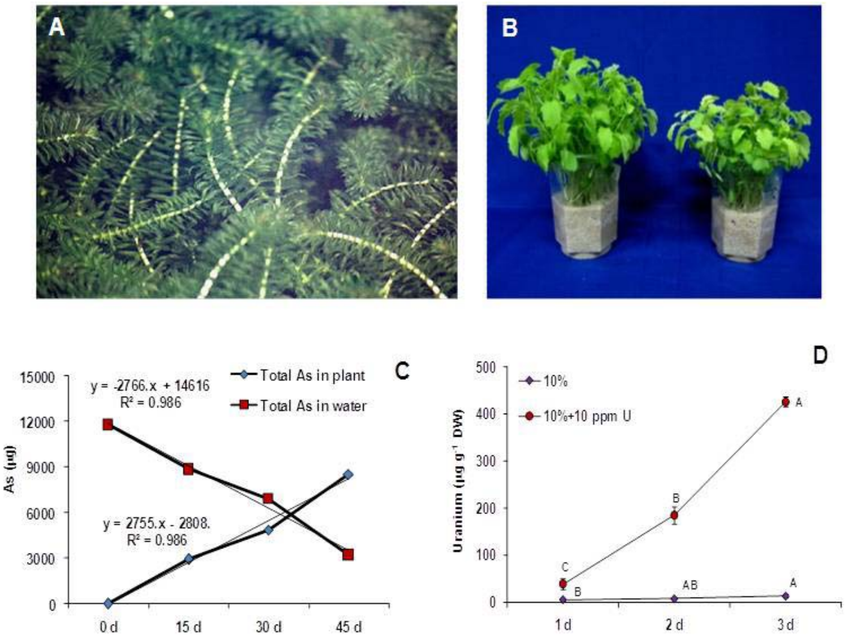

Fig. 1: Potential arsenic accumulator plants, (A) *Hydrilla verticillata* and (B) *Brassica juncea* identified through lab- and field-scale studies. Accumulation of arsenic by *Hydrilla verticillata* grown in simulated As-contaminated water (1500 μg L^{-1}) for 45 d. Total As accumulation in plants and water interpolated for whole plant dry biomass and total volume of water (C). Accumulation of uranium (μg g^{-1} dw) by *Hydrilla verticillata* from 10% waste and 10% waste + 10 ppm U treatments during 3 d exposure (D). No arsenic and uranium were detected in control plant/ water samples.

Arsenic detoxification in plants is achieved by two distinct but interconnected mechanisms

Experiments with *Hydrilla* using As and Cu revealed that mechanisms of metal tolerance in plants may be divided into two levels[3]. Primary detoxification pertains to the complexation of metal(loid) via a ligand like –SH containing compounds glutathione (GSH) and phytochelatins (PCs). This reduces the effective concentration of free ion and hence, the toxicity. It was also established that both components of thiol metabolism viz., synthesis and degradation, work cooperatively to tolerate the stress up to a certain tolerable point. Secondary detoxification signifies the maintenance of oxidative state. This is achieved by coordinated action of various enzymes and metabolites of antioxidant system.

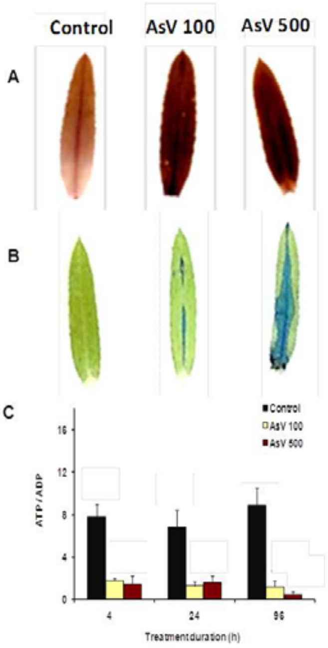

Fig. 2: Effect of arsenate exposure on the level of hydrogen peroxide (A) and cell death (B) after 96 h analyzed through histochemical staining using 3,3'-diaminobenzidine and Evan's blue for hydrogen peroxide and cell death, respectively. The level of ATP/ ADP ratio was analyzed for 4, 24 and 96 h upon arsenate exposure (C). All values are means of triplicates±S.D.

The equilibrium of redox state and energy status determines the extent of stress

To determine the impact of redox state and energetic in stress imposition, plants of *Hydrilla verticillata* were exposed to 100 and 500 μM arsenate (AsV) for 4 to 96 h. A significant increase in the level of reactive oxygen species (Fig. 2), carbonyl, malondialdehyde, and % DNA degradation was observed upon AsV exposure. These parameters collectively indicated oxidative stress, which in turn caused an increase in % cell death. These negative

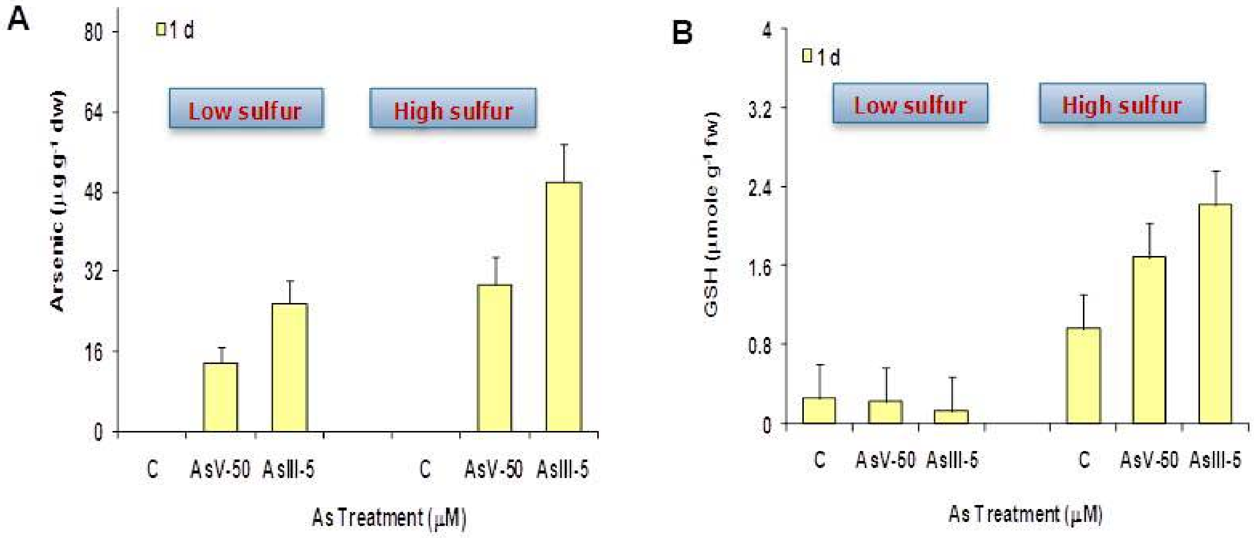

Fig. 3: Effect of low and high sulfur supply on the level of arsenic accumulation (A) and reduced glutathione (B) after 1 d in *Hydrilla verticillata* plants exposed to arsenate (50 µM) and arsenite (5 µM). No arsenic was detected in control plant samples. All values are means of triplicates±S.D.

effects were linked to an altered energetic and redox equilibrium [analyzed in terms of ATP/ADP, NADH/NAD, NADPH/NADP, reduced glutathione/oxidized glutathione, and ascorbate/dehydroascobate ratios]. The study concluded that the magnitude of disturbance to redox and energetic equilibrium upon AsV exposure determines the extent of toxicity[11].

Maintenance of sulfur supply helps alleviate the arsenic stress

Considering the importance of sulfur metabolism in As detoxification, we investigated whether an increase in sulfur supply in a justified manner would modulate plants' tolerance and As accumulation potential. *Hydrilla* plants were exposed to AsV and arsenite (AsIII) under variable S supply: decient (2 μM S, –S), normal (1 mM S, +S) and excess (2 mM S, +HS). Arsenic accumulation in +HS plants was about 2-fold higher than that observed in +S and –S plants (Fig. 3). Despite lower As accumulation, –S plants experienced the maximum oxidative stress owing to significant decline in total thiols. By contrast +HS plants had significant increase in total thiols and an improved redox status, and hence experienced the least increase in oxidative stress parameters. In conclusion, an increase in S supply to plants improved their accumulation capacity for As[12].

Calcium supplementation augments arsenic accumulation in *Brassica juncea*

The effect of AsV exposure either alone or in combination with calcium (Ca) was investigated in *Brassica juncea* at cellular level using hypocotyl-derived callus cultures[13]. The AsV (250 µM) + Ca (10 mM) treatment resulted in a significantly higher level of As (464 µg g^{-1} dw) than AsV without Ca (167 µg g^{-1} dw) treatment at 24 h. Furthermore, AsV + Ca-treated callus had a higher percent of AsIII (24–47%) than calli subjected to AsV treatment (12–14%). Despite this, AsV + Ca-treated callus did not show any signs of hydrogen peroxide (H_2O_2) accumulation or cell death, while AsV-exposed callus had increased H_2O_2, shrinkage of cytoplasmic contents, and cell death. Thus, Ca supplementation holds promise for achieving increased As accumulation in plants.

Perception of the arsenic stress involves various signaling components

Brassica juncea is presently being used as model system to reveal signaling mechanisms under As stress. In a comparative evaluation of two contrasting genotypes of *Brassica juncea*, tolerant variety (TPM-1) had higher accumulation of As and better response of thiol metabolism as compared with the responses observed in the sensitive variety (TM-4)[6]. Transcriptional profiling of selected genes showed an up-regulation of sulfate transporters and auxin and jasmonate biosynthesis pathway genes, whereas there was a down-regulation of ethylene biosynthesis and cytokinin-responsive genes in tolerant variety within 6 h of exposure to As(III). These transcriptional changes were similar to the responses observed in sulfur-depletion studies. The study proposed that an early perception of "As-induced stress to sulfur metabolism" was responsible for As tolerance in TPM-1. In ongoing work, other components of signaling have been revealed viz., microRNAs and mitogen-activated protein kinases (unpublished results).

In summary, our studies reveal the mechanisms employed by plants to perceive and tolerate the metal(loid) stress and to resist any negative impact to redox and energy status. The studies implicate the prospective application of plants like *Hydrilla verticillata* and *Brassica juncea* in phytoremediation efforts. Their potential for metal(loid) remediation can be further enhanced through external application of S and Ca. These plants need to be applied in actual field conditions for the remediation of contaminated soil and water in future.

References

1. Tripathi RD, Srivastava S, Mishra S, Singh N, Tuli R, Gupta DK, Maathuis FJM (2007) Arsenic hazards: Strategies for tolerance and remediation by plants. *Trends Biotechnol* 25:158–165.
2. Sun Y, Zhou Q, Diao C (2008) Effects of cadmium and arsenic on growth and metal accumulation of Cd-hyperaccumulator Solanum nigrum L. *Bioresour Technol* 99:1103-1110
3. Srivastava S, Mishra S, Tripathi RD, Dwivedi S, Trivedi PK, Tandon, PK (2007). Phytochelatins and antioxidant systems respond differentially during arsenite and arsenate stress in *Hydrilla verticillata* (L.f.) Royle. *Environ Sci Technol* 41:2930-2936.
4. Mishra S, Srivastava S, Tripathi RD, Trivedi PK (2008) Thiol metabolism and antioxidant systems complement each other during arsenate detoxification in *Ceratophyllum demersum* L. *Aquat Toxicol* 86:205-215.
5. Srivastava S, Mishra S, Dwivedi S, Baghel VS, Verma S, Tandon PK, Rai UN, Tripathi RD (2005) Nikel phytoremediation of broad bean *Vicia faba* L. and its biochemical responses. *Bull Environ Contam Toxicol* 74:715-72.
6. Srivastava S, Srivastava AK, Suprasanna P, D'Souza SF (2009) Comparative biochemical and transcriptional profiling of two contrasting varieties of *Brassica juncea* L. in response to arsenic exposure reveals mechanisms of stress perception and tolerance. *J Exp Bot* 60:3419-3431.
7. Lokhande VH, Srivastava S, Patade VY, Dwivedi S, Tripathi RD, Nikam TD, Suprasanna S (2011) Investigation of arsenic accumulation and tolerance potential of *Sesuvium portulacastrum* (L.) L. *Chemosphere* 82:529-534.
8. Srivastava S, Bhainsa KC, D'Souza SF (2010) Investigation of uranium accumulation potential and biochemical responses of an aquatic weed *Hydrilla verticillata* (L.f.) Royle. *Bioresour Technol* 101:2573-2579.
9. Srivastava S, Mishra S, Tripathi RD, Dwivedi S, Gupta DK (2006) Copper-induced oxidative stress and responses of antioxidants and phytochelatins in *Hydrilla verticillata* (L.f.) Royle. *Aquat Toxicol* 80:405-415.
10. Srivastava S, Shrivastava M, Suprasanna P, D'Souza SF (2011a). Phytofiltration of arsenic from simulated contaminated water using *Hydrilla verticillata* in field conditions. *Ecol Eng* 37:1937-1941.
11. Srivastava S, Suprasanna P, D'Souza SF (2011b). Redox state and energetic equilibrium determine the magnitude of stress in *Hydrilla verticillata* upon exposure to arsenate. *Protoplasma* 248:805-815.
12. Srivastava S, D'Souza SF (2009) Increasing sulfur supply enhances tolerance to arsenic and its accumulation in *Hydrilla verticillata* (L.f.) Royle. *Environ Sci Technol* 43:6308-6313.
13. Rai AN, Srivastava S, Paladi R, Suprasanna P (2012) Calcium supplementation modulates arsenic-induced alterations and augments arsenic accumulation in callus cultures of Indian mustard (*Brassica juncea* (L.) Czern.). *Protoplasma* 249:725-736.

TECHNOLOGY TO HARVEST URANIUM FROM SEA - DEVELOPMENT OF RADIATION GRAFTING REACTOR SYSTEMS

T.L. Prasad, P.K. Tewari and D. Sathiyamoorthy
Homi Bhabha National Institute
and
N.K. Prasad
Mechanical Design and Prototype Development Section

This paper received the Chinnamaul Memorial Prize and MH Shukla First Prize for the Best Technical Paper presented at CHEMCON-2011, at the 64th Annual Session of the Indian Institute of Chemical Engineers, held at Bengaluru, Dec. 27 - 29, 2011

Abstract

Novel sorbent materials such as Metal Chelate Embedded Polymers (MCEP) are synthesized by post irradiation grafting as a part of technology development to harvest uranium from brine/seawater. Amidoxime groups are embedded into backbone polymers in the form of leaflets, which provides efficient contact patterns with water body in the sea. MCEP's facilitate efficient recovery system design also. Lab scale; Bench scale and Pilot scale systems are being developed for engineering scale studies on radiation grafting of polymeric sorbents. Data has been observed w.r.t time and temperature on pilot scale preparation of metal chelate embedded polymers and are presented in this paper. The paper also highlights design and development features of radiation grafting reactor systems required for preparation of MCEP for use in aquaculture of uranium and other valuables from brine/seawater.

Keywords : Seawater; Brine; Radiation Grafting; Metal Chelate Embedded Polymers; Aquaculture of Uranium

Introduction

Researchers are taking renewed interest on the recovery of uranium from seawater and other alternative resources [1-8] to complement the uranium locally deposited as terrestrial ore. With its lean but clean resource, ocean can serve as a potential source of uranium and other valuable heavy metals for a long run. The uranium content of oceans is of the order 4.5×10^9 tonnes [9 - 11]. Seawater is an electrolyte with pH of 8 to 8.5 and uranium predominantly exists as uranyl tricarbonate complex. The various valuable elements present in seawater are as shown in Table 1 below.

The process of adsorption has been adopted for developing innovative recovery system [8, 10 and 13]. The recovery system design depends on shape (beads/rope/fiber) of adsorbent; mode of operation of adsorbent (fixed/fluidized/floating); contact mode of adsorbent (tidal/pumping). We have developed process flow scheme for efficient recovery system using radiation grafted adsorbents. The objective of the study was to establish the effect of temperature and time parameter on post irradiation grafting. The paper presents design and development of radiation grafting reactor systems required for aquaculture of uranium and other valuables from seawater/brine [9].

Table 1: Valuable elements in Seawater

Sl.no	Element	Concentration (ppb)	Total amount (x 10^8 tonnes)
1	Cobalt	0.1	1
2	Yittrium	0.3	3
3	Titanium	1	15
4	Manganese	2	30
5	Vanadium	2	30
6	Uranium	3	45
7	Molybdenum	10	150
8	Lithium	170	2330
9	Boron	4600	63020
10	Strontium	8000	109600

Design and Development Features for Radiation Grafting Reactor System

Grafting helps to modify the surface of fibers and can be carried out chemically or by radiation. Radiation grafting has many advantages and has been used to synthesize the novel sorbent materials as follows.

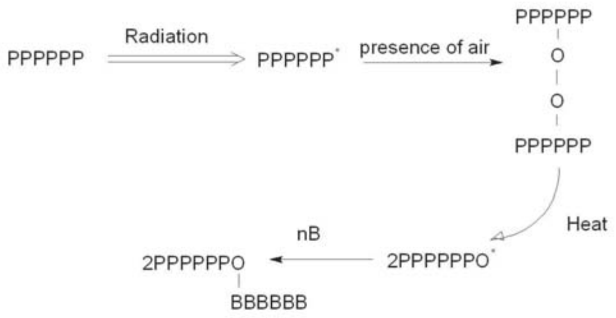

The requirements/features for design of Radiation Grafting reactor systems are as follows:

1. The lead time available for grafting after irradiation is only 12 minutes to achieve maxima in grafting yield.
2. Facilitation of proper contact patterns between solid substrate polymer and liquid monomer.
3. Rate of homopolymerisation of monomer shall be less. Rate of copolymerization between PAN and monofilament/bifilament PP shall be more.
4. Facilitation of proper diffusion of monomer to grafting sites to achieve efficient copolymerisation.
5. Facilitation of Purging of air from reaction media during grafting of acrylonitrile monomer.
6. All along the reaction duration, reaction mixture shall not undergo viscosity variation.
7. From safety and economics, the loss of monomer shall be less and vapor concentration shall be below TLV (2ppm) values.
8. The side reaction and chain transfer to different constituents in the reaction medium shall be less.
9. Shall have dedicated VOG (Vessel Off Gas) system and maintain 2" water column vacuum in grafting reactor system.
10. Flushing arrangement with DMF solvent and draining of the same.

Experimental Methods and Materials

The analytical grade chemicals were used for lab scale studies. Commercial grade chemicals were used for bench scale studies. Nitrogen of purity 99% was used for purging during grafting reaction. The mono filament and bi-filament fibers of polypropylene of various makes and densities were used for the trials [11-13]. The properties of substrate material used for bench scale and pilot scale studies were as shown in Table 2 below.

Lab scale Experimental facilities

The lab scale set up of capacity two litres was made using glass set ups as shown in Fig. 1 below. It can hold substrate tokens of sizes upto 100mm x 100mm. The provision of water condenser is made to study the containment of vapors and minimize vapor losses.

Table 2: Properties of substrate material

Sl.no	Parameter	Description
1	Material	Polypropylene (PP) of bifilament type
2	Form	Non woven thermal bonded fabric
3	Width	1000 mm
4	Length	1000 mm
5	Bulk thickness	1.8 mm
6	Weight	300 gsm
7	Fiber size	1 denier (0.111 e-06 kg/m)
8	Air permeability	250 L/dm^2 /min/20mm WC
9	Bursting pressure	30 kg/cm^2
10	Service temperature	95° C
11	Specific surface area	0.33 m^2 /g

Fig. 1: Lab scale set up for 1.25 MeV energy Electron beam

Bench Scale Experimental facilities

Bench scale set-up is made up of polypropylene material and can hold substrate of sizes up to 1000mm x 1000mm. The details are as shown in figure-2 below. The production capacity of scaled up plant is two adsorbent sheets per shift. Inherent safety of grafting reactors has been achieved with deep bed designs, which render less surface area of evaporation and suppresses the vapor formation. The major unit processes involved in preparation of Metal Chelate Embeded Polymers (MCEP) are: Electron-Beam Irradiation of the substrate; Grafting of acrylonitrile; Dissolving of excess monomer & drying; Oximation;

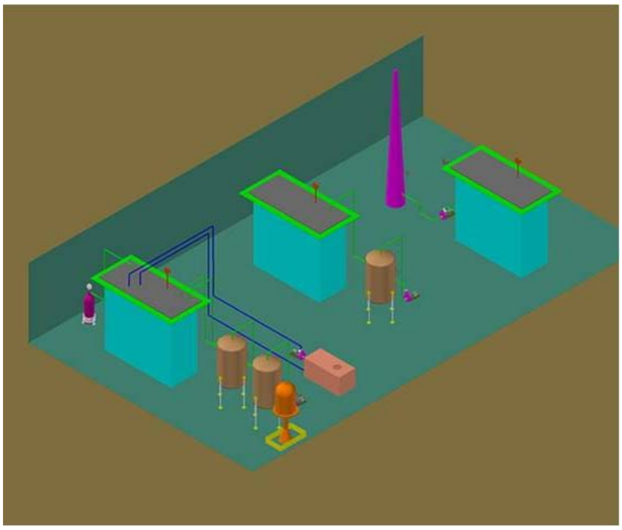

Fig. 2: Bench scale set up for 2 MeV energy Electron beam

Results and Discussions:

4.1 *Lab scale radiation grafting studies*:

These studies were carried out to fine tune the dose and dose rate parameters required for synthesis of metal chelate embedded polymers. Studies were done using 1.25 MeV beam energy on substrates of 100mm x 100mm size with air hold time of 15 minutes. The grafting reactor solution consisting of acrylonitrile and DMF of volume of 600 ml in the ratio of 7:3 was taken for studies. Nitrogen purge

Table 3: Grafting yields observed during lab scale studies

Sl.No.	Dose rate (Mrad/min)	total dose (Mrad)	Initial weight (g)	air hold time (minutes)	Weight after) grafting (g	Grafting level (%)
9	1	20	4.11	15	7.748	88.5158151
10	1	20	3.836	15	8.244	114.911366
1	2	12	4.041	25	4.043	0.0494927
2	2	12	4.187	25	4.189	0.0477669
3	3	18	4.04	25	6.831	69.0841584
5	3	19.8	4.087	15	8.296	102.985075
6	3	19.8	4.207	15	5.646	34.2048966
4	4	20	4.15	25	6.657	60.4096386
7	4	20	4.113	15	8.109	97.1553611
8	4	20	4.036	15	5.065	25.4955401

rate of 0.6 lpm was maintained. The observed results are as shown in table-3 below. With fine tuning of parameters such as dose and dose rate, grafting levels of up to 110% could be achieved. Along with total cumulative dose, rate at which dose is given is also important for achieving optimum results.

Bench scale radiation grafting studies:

Effect of reaction temperature on Radiation grafting at 10kgy:

The post irradiation grafting is a typical chemical reaction involving radicals. Intention of this investigation was to see the effect of temperature for grafting. Fig. 3 below shows the grafting yields as a function of the grafting temperature at cumulative dose of 20 MRad at a dose rate of 10 kGy/pass in air and reaction was carried out for 3 hours. The yields are increased till boiling temperature of the media. Graph also shows the rise in Threshold Limit values for Acrylonitrile vapors, measured at breathing levels in the operating area. The permissible TLV for acrylonitrile vapors is 2 ppm. For safe operation, temperatures are established accordingly for pilot scale operations.

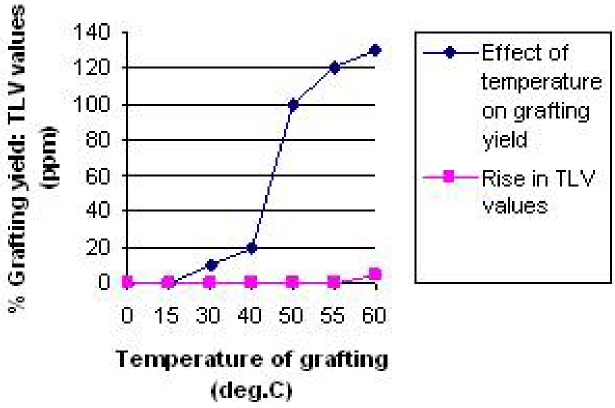

Fig. 3: Effect of Grafting rxn temperature on grafting levels

Effect of Duration on grafting yield:

Fig. 4 below shows the grafting yield as function of reaction time. It gradually increases with reaction time and then leveling off is observed after four hours. Equillibrium grafting reaches in six hours. Optimised durations are established accordingly for regular pilot scale operations.

Metal sorption characteristic evaluation studies:

The developed metal chelate embedded polymers (MCEP's) were used to study the uranium pick up at various

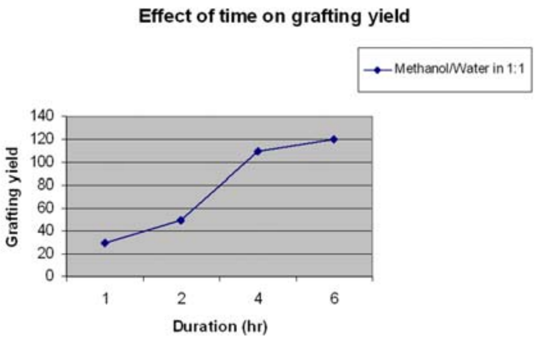

Fig. 4: Effect of time on grafting yield

Table 4: Metal sorption characteristics of MCEP

Sample no	Location	Concentration factors observed (rounded values)	Remarks
LE/A1/F1/1	Cirus jetty	10	Seawater
LE/A1/F1/2	do	11	Seawater
LE/A1/F1/3	do	14	Seawater
DE/CJ/A1/0.05M/F1	do	6	Seawater
DE/CJ/A1/0.5M/F1	do	6	Seawater
DE/CJ/A1/5M/F1	do	4	Seawater
LE/NDDP/0.5M/TK9/F1	Seawater RO, NDDP kalpakkam	6	Desalination effluents
LE/NDDP/0.5M/TK12/F1	do	6	Do
LE/NDDP/0.5M/TK14/F1	do	7	do
LE/NDDP/0.5M/TK16/F1	do	6	Do
LE/NDDP/0.5M/TK18/F1	do	6	Do

locations, both from seawater and as well as desalination effluents [14]. The measured uranium concentrations as per Nuclear Analytical Techniques (NAT) in various locations [15] and concentration factors achieved are as shown in table-4 below:

Pilot scale studies:

Based on the experience gained during the lab scale and bench scale studies, further modification of grafting reactor system has been taken up to increase the throughput capacity upto 5 to 6 sheets per batch with automation for feeding of sheets. VOG (Vessel Off Gas) systems and hold up systems are being augmented to achieve operational safety. Features of pilot scale being set up are shown in Fig. 5 below:

Fig. 5: Pilot scale Radiation Grafting Reactor system

Conclusions

Radiation grafting for synthesis of metal chelate embedded polymeric adsorbents is one of the important industrial application of ionizing radiations. The grafting levels of up to 130% have been achieved. Concentration factors of more than 6 have been observed for the conditions of desalination effluents with tokens of 100mm x 100mm sizes. The sorbent material developed and radiation grafting systems designed have given most optimum uranium pick up compare to any other materials reported in India under actual field trials. As the need of fresh water will increase in future, larger capacity desalination plants will get pressed into service and the coupling for additional value recovery from reject streams will become more feasible as well as desirable.

Acknowledgements

The authors wish to thank Shri. S.K. Ghosh Director Chemical Engg Group for giving constant encouragement to the programme. Thanks are also due to Shri. A.K. Saxena BARC for his valuable periodic discussions. Thanks are also due to RTDD, AChD, HPhD, IDD, REDS, EAD and RChD divisions of BARC for their technical support and sample analysis. We acknowledge the support received from RUSWapp team and staff at NDDP Kalpakkam.

References

1. Kabay, N., Egawa,H., "Behaviour of lightly crosslinked chelating resins containing amidoxime groups for batchwise extraction of UO_2^{2+} " Separation science Technology, Vol 28, 1985-1993, 1993
2. El-Naggar, I.M., El-Absy, M.A., Abdel-Hamid, M.M., Aly, H.F., "Sorption behaviour of uranium and thorium on cryptomelane-type hydrous manganese dioxide from aqueous solutions" Solvent Extraction and Ion Exchange, Vol 7, No. 3, 521-540, 1993
3. Prasad, T.L., "Radiation Grafting Of Adsorbent For Recovery Of Uranium From Seawater" Desalination Divisional colloquim held on September 26, 2006
4. Abbasi, W.A., Streat, M., "Adsorption of uranium from aqueous solutions using activated carbon, Separation Science Technology, Vol 29, No. 9, 1217-1230, 1994
5. Egawa, H., Nonaka, T., Nakayama, M., "Recovery of uranium from seawater with macroreticular resins containing phosphino and phosphono groups" Bull. Soc. Seawater science, Japan, Vol 44, No.5, 316-321, 1990.
6. Ghafourian, H., Latifi, A.M., Malekzadeh, F., "Study for optimization of uranium adsorption by new bacterium MGF-48" Sci.Bull.Atom. Energy Org., Iran, Vol 17, 44-56, 1998.
7. Choi, S.H., Nho, Y.C., "Adsorption of UO_2^{+2} by polyethylene adsorbents with amidoxime carboxyl and amidoxime/carboxyl group" Radiat. Phys.Chem., Vol 57, No. 2, 187-193, 2000.
8. Prasad, T.L., 2nd Desalination Divisional Colloquium on "Plant concept developments for aquaculture of uranium and other valuables from seawater/brine" at Desalination division, BARC Trombay, India 6th November 2009
9. Saxena, A.K., Prasad, T.L., Tewari, P.K., " Value addition to Desalination plants by recovery of Uranium from reject streamsr" Presented at International Symposium on Desalination and Water Purification: Water Resources and their Management, Organised by Malaviya National Institute of Technology Jaipur in association with Indian Desalination Association held at Malaviya National Institute of Technology Jaipur, March 20-21, 2006
10. Prasad, NK, Pathak,K, Kumar, M, Matkar, AW, Prasad, TL and Saxena, AK (2009) "Challenges in the design of a prototype contactor assembly for the recovery of uranium from seawater", Int Jounal of Nuclear Desalination, Vol 3, No.3, pp241-246
11. Saxena, A.K., Prasad, T.L., Tewari, P.K., " Radiation processing for super speciality adsorbent preparation for Uranium extraction from seawater" Presented at Biennial Trombay Symposium on Radiation and Photochemistry (TSRP-2006) held at BARC Mumbai, January 5-9 2006
12. Prasad TL., Tewari PK., Sathiyamoorthy D., "Recovery of uranium from reject streams of Desalination plants" was presented at Eighteenth annual conference of Indian Nuclear Society held at Nuclear Fuel Complex Hyderabad during November 21-24, 2007.
13. Prasad, T.L., Saxena, A.K., Tewari, P.K., Sathiyamoorthy, D., (2009) "An Engineering Scale Study on Radiation grafting of polymeric adsorbents for recovery of Heavy Metal Ions from Seawater ", Nuclear Engineering and Technology, Vol 41, No.8, pp 1101-1108
14. Kalsi, P.C., Chhavi Agarwal, Prasad, T.L., Manchanda, V.K., "Uranium estimation in ppb levels by solid state nuclear track detectors using the pneumatic carrier facility of Dhruva reactor" Presented at NUCAR-2009 (Nuclear and Radiochemistry symposium) Organised by Board of Research in Nuclear Sciences Dept of Atomic Energy in association with Chemistry department of SVKM's Mithibai college of Arts, Chauhan Institute of Science and Aruthben Jivanlal college of commerce and economics held at Vile Parle (W) Mumbai, January 7-10, 2009
15. Prasad, T.L., Tewari, P.K., Sathiyamoorthy D., Kalsi, P.C., Acharya, R., Manchanda, V.K., "Advanced Techniques for measurement of heavy metal concentrations from seawater" Presented at International conference 62nd Indian Chemical Engineering congress CHEMCON-2009, Organised by Indian Institute of Chemical Engineers in association with Waltair Regional Centre held at Andhra University Vishakapatnam, December 27-30, 2009

A NOVEL MEMBER OF THE β-CASP FAMILY OF NUCLEASE IS INVOLVED IN THE SURVIVAL OF *DEINOCOCCUS RADIODURANS*

Anubrata D. Das and H.S. Misra
Molecular Biology Division

Shri A.D. Das received the AMI-Dr. Rana Memorial Best Research Paper Award at the 52nd Annual Conference of Microbiologists of India (AMI), Chandigarh, Nov. 3-6, 2011

Abstract

Deinococcus radiodurans (DEIRA) survives extreme doses of radiations primarily contributed by an efficient DNA repair pathway. This pathway employs panoply of proteins, which orchestrate a coordinated effort to rebuild the shattered chromosomes. The involvement of novel proteins has been implicated in this process. Here we report the activity of a 'hypothetical' protein DR2417, which is a novel member of the β- CASP family of nucleases found widely in all branches of life. Members of this family acting on DNA have been exclusively reported in higher organisms including human being, whilst RNA specific enzymes have been reported in other branches of life. Interestingly, DR2417 is the first example of a DNA specific member of this family found in this radiation resistant bacterium. It shows various activities, which are integral to the repair processes of gamma-shattered genome in living system. *D. radiodurans* cells completely devoid of this protein failed to survive indicating that this novel enzyme is essential for the growth and radiation resistance in this bacterium.

Keynotes: *Deinococcus radiodurans*, radiation resistance, novel DNA repair enzyme

Introduction

Deinococcus radiodurans has a remarkable ability to survive intense doses of γ radiation, dessication and oxidative stress. It survives doses of up to 15 KGy of γ radiation which is a 3000 fold higher dose than the lethal dose for human being (1). During this exposure, the genome breaks down to 150-200 fragments but within 3-4 hours, all this is accurately repaired and no measurable lethality is seen (9). The key player in this resistance is a well-synchronized DNA repair mechanism. The repair process is biphasic and the first phase involves extensive but regulated nucleolytic function. Several studies have earlier implicated the involvement of novel proteins and demonstrated that RecF pathway of homologous recombination (8, 10) plays a crucial role in efficient DNA repair and gamma radiation resistance. DR2417 was found to be present in a cell lysate fraction of DEIRA cells undergoing repair after γ irradiation (5) and a multiprotein DNA processing complex isolated from this bacterium (7). This fraction degraded DNA, but, in contrast to *E.coli,* the degradation was inhibited by ATP (5). Since nucleolytic activity is central to the repair process we wanted to identify the nuclease involved in ATP sensitive nucleolytic processes. Mass spectrometric analysis of this fraction however, showed that no known nucleases were present. We then focused on the 11 hypothetical proteins detected in this fraction. Of these 11, DR2417 had the canonical H-X-H-X-DH motif of the β-CASP family of nucleases and we hence, decided to characterize it. This ORF was wrongly annotated as a genuine frame shift in genome sequence of this bacterium (11). Repeated appearance of DR2417 polypeptide in functional pool of proteins hypothesized the important role of this protein in DNA metabolic functions of this bacterium, and further investigated.

Methodology

Homologues of DR2417 were obtained by PSI-BLAST and these were aligned by T-COFFEE to obtain conserved motifs as described earlier (3). We located new motifs in DR2417, by realigning the protein sequence with the structural homologue RNAse J and a 3-D structure of this protein was generated in SWISSMODEL. The *dr2417* gene from *Deinococcus radiodurans* was cloned in pET28a expression vector and the recombinant protein was produced in *E.coli* BL21 and purified to near homogeneity by Ni^{2+} affinity using manufacturer's protocol. Assays were done in 20 μL by incubating 1 μg of the protein with 1 μg of substrate in a buffer and visualizing on agarose gels. Assays with radio-labeled dsDNA substrates were done by incubating 5 pmol of substrate with 100ng of protein and resolving the products in a denaturing Urea-PAGE gel as described recently (4). A partial genetic knockout of *dr2417* was made, as described earlier (6) and radiation response of mutant and wild type was determined as described earlier (8).

Results and Discussion

DR2417 belongs to the β-CASP family of nucleases

DR2417 was annotated a hypothetical protein in genome of *Deinococcus* and categorized as a nonfunctional pseudogene due to a wrong annotation of a genuine frame shift in this ORF. Nucleotides sequencing of this ORF corrected the mistake and revised sequence of this gene was submitted to GenBank vide accession No. JQ432552. Since DR2417 was found in the pool of proteins involved with DNA processing function, we aligned it with its closest homologues and discovered 2 motifs (motif B and motif C), which predicted it a DNAse. The multiple sequence alignment of this protein with the members of β-CASP family nucleases showed that DR2417 has all the metallo β- lactamase motifs M1-M4 and motif A of the β-CASP fold. Secondary structure prediction as indicated in modelled structure of DR2417 and compared with RNaseJ, showed the long stretches of coils in this region, which seems to be the unique structural feature of this protein. The homology model showed that the conserved motifs formed an active site in 3 dimensions and the valine residue of DR2417, which specifies its DNAse activity. The phylogenetic tree showed that DR2417 is closely related to RNAse J (2).

DR2417 is ATP sensitive DNAse and a hairpin endonuclease

Recombinant DR2417 (~63kDa) was purified to near homogeneity from transgenic *E. coli*. Recombinant DR2417 was checked for DNA binding as well as nuclease functions. It showed a strong binding with both ssDNA and dsDNA in presence of Mn^{2+} ion and on longer incubation it showed nuclease activity in presence of Mn^{2+}. The recombinant DR2417 did not show detectable RNase activity. Interestingly, the DNase activity of DR2417 was inhibited by ATP and GTP but not with either AMP or GMP. DR2417 showed very poor activity with a 5′ labeled 33mer single strand oligonucleotide [99F] substrate. However, it showed relatively faster degradation of dsDNA generated by annealing 99F with equal size complementary oligonucleotide indicating that DR2417 has 3′→5′ exonuclease activity. This was further confirmed by incubating this enzyme with 78mer stem-looped DNA substrate. With this substrate, DR2417 showed a series of typical products that are normally observed during exonucleolytic degradation of DNA labeled at 5′ end. These results suggested that DR2417 has 3′→5′ exonuclease activities and a strong possibility of an endonuclease function at the ss/ds DNA junction, that could produce islands of products of 37nt and 41nt on 5′ labeled HP78. The functional significance of this enzyme in radiation resistance of *D. radiodurans* could be seen as the matter of facts that γ radiation shattered DNA forms secondary structures like hairpin loops which inhibit DNA repair and replication. This enzyme has activity that could process the bad DNA substrate and make it better for efficient DSB repair.

The *dr2417* encodes an essential function in *Deinococcus*

The deletion of *dr2417* gene from the genome of *D. radiodurans* was required for understanding the role of this protein in growth of this bacterium under normal as well as radiation stressed conditions. While attempting to generate deletion mutant of *dr2417*, we observed that the cells approaching complete replacement of *dr2417* with marker gene did not survive under normal growth conditions. Mutants having different copy numbers of this gene showed differential growth rate under normal conditions. These cells, survived less when subjected to gamma radiation stress as compared to the wild type *D. radiodurans*. On the contrary when these cells were grown in absence of selection pressure, the *dr2417* copy numbers increased several folds, which was reflected in growth recovery of these cells. This observation was very much similar to those favoring the essentiality of genes in bacterial system. These results allowed us to conclude the indispensability of *dr2417* gene for the survival and eventually radiation resistance in *D. radiodurans*.

This study has brought forth some interesting findings to suggest that DR2417 ORF encodes a functional and stable protein in *D. radiodurans* that shares considerable similarities with β CASP family nucleases. It showed both exo- and endo-nuclease and needs a 5′ phosphate for its activity akin to Artemis, and inhibited by ATP as observed in hSNM1, a homologue of Artemis. However, uniqueness in DR2417 is the selectivity for DNA for its 3′→5′ exonuclease activity and undetectable activity on tRNA substrate. These results suggested that DR2417 was DNA processing enzyme.

Acknowledgements

We are grateful to Dr. S. K. Apte, Head, Molecular Biology Division, for his constant support and constructive criticism while pursuing this work.

References

1. Battista, J.R. Radiation resistance: the fragments that remain. *Current Biology* 10 (2000): R204-205
2. Callebaut, I., Moshous, D., Mornon, J. P., and de Villartay, J. P. Metallo-beta-lactamase fold within nucleic acids processing enzymes: the beta-CASP family. *Nucleic Acids Res.* 30 (2002): 3592-3601.
3. Das, A.D. and Misra, H.S. Characterization of DRA0282 from Deinococcus radiodurans for its role in bacterial resistance to DNA damage. *Microbiology* **(SGM) 157** (2011)**:** 2196 - 2205.
4. Das A. D. and Misra, H.S. DR2417, a hypothetical protein characterized as a novel β-CASP family nuclease in radiation resistant bacterium, *Deinococcus radiodurans. Biochim Biophys Acta (Gen Subject)* 1820 (2012):1052-1061.
5. Kamble, V. A., Rajpurohit, Y. S., Shrivastava, A. K. & Misra, H. S. Increased synthesis of signaling molecules coincides with reversible inhibition of nucleolytic activity during postirradiation recovery of *Deinococcus radiodurans*. *FEMS Microbiol Lett.* 303 (2010): 18-25
6. Khairnar, N. P., Kamble, V. A. & Misra, H. S. RecBC enzyme overproduction affects UV and gamma radiation survival of *Deinococcus radiodurans*. *DNA Repair (Amst)* 7 (2008): 40-47.
7. Kota, S. & Misra, H. S.. Identification of a DNA processing complex from *Deinococcus radiodurans*. *Biochem Cell Biol* 86 (2008):448-458.
8. Misra, H. S., Khairnar, N. P., Kota, S., Shrivastava, S., Joshi, V. P. and Apte, S. K. An exonuclease I-sensitive DNA repair pathway in *Deinococcus radiodurans*: a major determinant of radiation resistance. *Mol Microbiol* 59 (2006):1308-1316.
9. Slade, D and Radman, M. Oxidative stress resistance in Deinococcus radiodurans. *Microbiol Mol Biol Rev* 75 (2011):133-191.
10. Slade, D., Lindner, A.B., Paul, G. and Radman, M. Recombination and replication in DNA repair of heavily irradiated *Deinococcus radiodurans*. *Cell* 136 (2009):1044-55.
11. White, O., Eisen, J. A., Heidelberg, J. F., Hickey, E. K., Peterson, J. D., Dodson, R. J., Haft, D. H., Gwinn, M. L., Nelson, W. C., Richardson, D. L., Moffat, K. S., Qin, H., Jiang, L., Pamphile, W., Crosby, M., Shen, M., Vamathevan, J. J., Lam, P., McDonald, L., Utterback, T., Zalewski, C., Makarova, K. S., Aravind, L., Daly, M. J., Minton, K. W., Fleischmann, R. D., Ketchum, K. A., Nelson, K. E., Salzberg, S., Smith, H. O., Venter, J. C., and Fraser, C. M. *Science* 286 (1999):1571-1577
12. Zahradka, K., Slade, D., Bailone, A., Sommer, S., Averbeck, D., Petranovic, M., Lindner, A. B. & Radman, M. Reassembly of shattered chromosomes in *Deinococcus radiodurans*. *Nature* 443 (2006): 569-573.

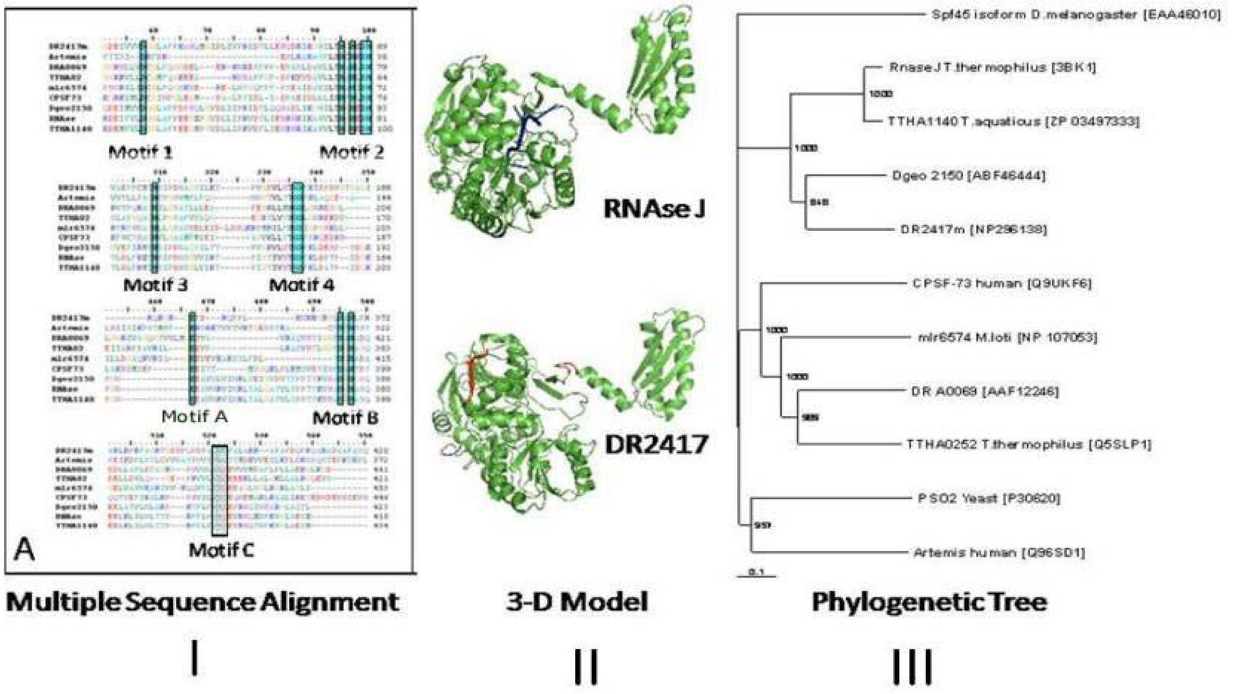

Fig.1: Bioinformatics analysis of DR2417. (I) A Multiple Sequence Alignment of DR2417 with members of β-CASP family highlighting the conserved motifs (1, 2, 3 and 4) specific to nuclease and motif A, B and C form the CASP domain. (II) The 3-D homology model of DR2417 with RNAseJ. The region marked in red is an additional β sheet and a loop specific to DR2417. (III) A nearest neighbor phylogenetic tree of DR2417 with it's homologs, shows that DR2417 is closer to Dgeo2150 from *D.geothermalis* but not it's paralog DRA0069.

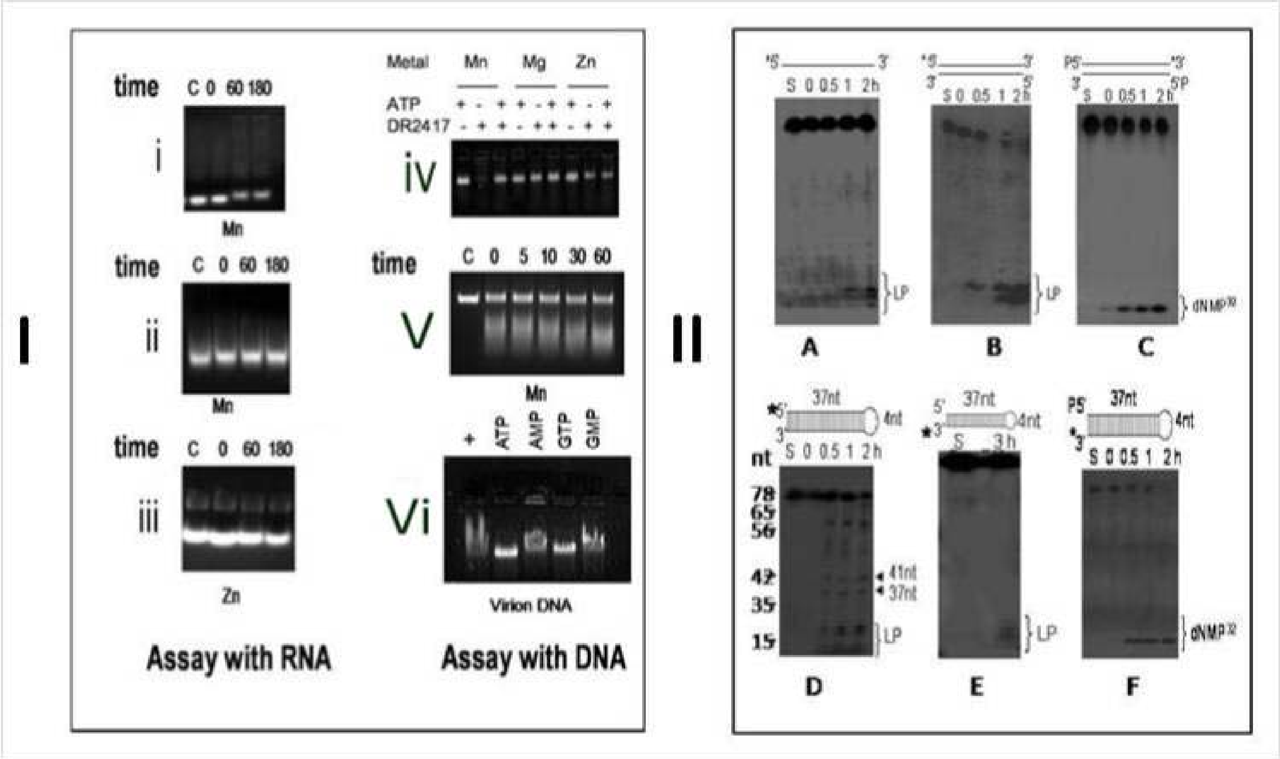

Fig. 2. Nuclease activity characterization of DR2417. (I) Recombinant DR2417 was incubated with M13mp18 virion DNA (ssDNA) or with RNA in assay buffer (10 mM Tris–HCl pH8.0, 50 mM NaCl and 1 mM DTT) in the presence and absence of 1 mM ATP and in different metal ions. The reaction mixture was heated at 85 °C for 15 min in presence of 65% formamide to the break nucleoprotein complex and the products were analyzed on 1% agarose gel and change if any, was compared with respective substrates (S) control. Experiments were repeated at least three times and results of a typical experiment shown (i, ii, iii) Assay with RNA. Total *E.coli* RNA(i) or wheatgerm tRNA(ii) was incubated for upto 180 minutes in presence of Mn. wheatgerm tRNA was also incubated in the presence of Zn(iii) iv,v,vi) Assay with DNA. ssDNA was incubated metal ions Mn, Mg and Zn either in the presence or absence of ATP(iv), 100 ng purified DR2417 was incubated for upto 60 minutes (v) and the effect of ATP, GTP, AMP and GMP on its ssDNA binding activity was also checked(vi). II) DNA processing activity characterization of DR2417 on different types of DNA substrates. DNA substrates like 52 labeled linear 33 bases ssDNA (A), 5' labeled 33 bp dsDNA (B) 3'labelled 33 bp dsDNA (C),5' labelled 78mer stem loop DNA (D), 3 2 labeled 78mer stem loop DNA with 5'-OH end (E), and 3 2 labeled 78mer stem loop DNA with 5'-P end (F) were prepared. These substrates (S) were incubated with DR2417 at different time interval at 37 °C. Reaction was stopped with DNA sequencing dye (50% formamide, 25 mM EDTA, pH8.0) and mixtures were heated at 95 °C for 15 min. Products were analyzed on 16% Urea-PAGE and autoradiograms were developed. Arrow marked showing limit products (LP), terminal mononucleotide (dNMP32) and ss/dsDNA junction endonucleolytic products. Experiments repeated two times and data of a reproducible experiment is shown.

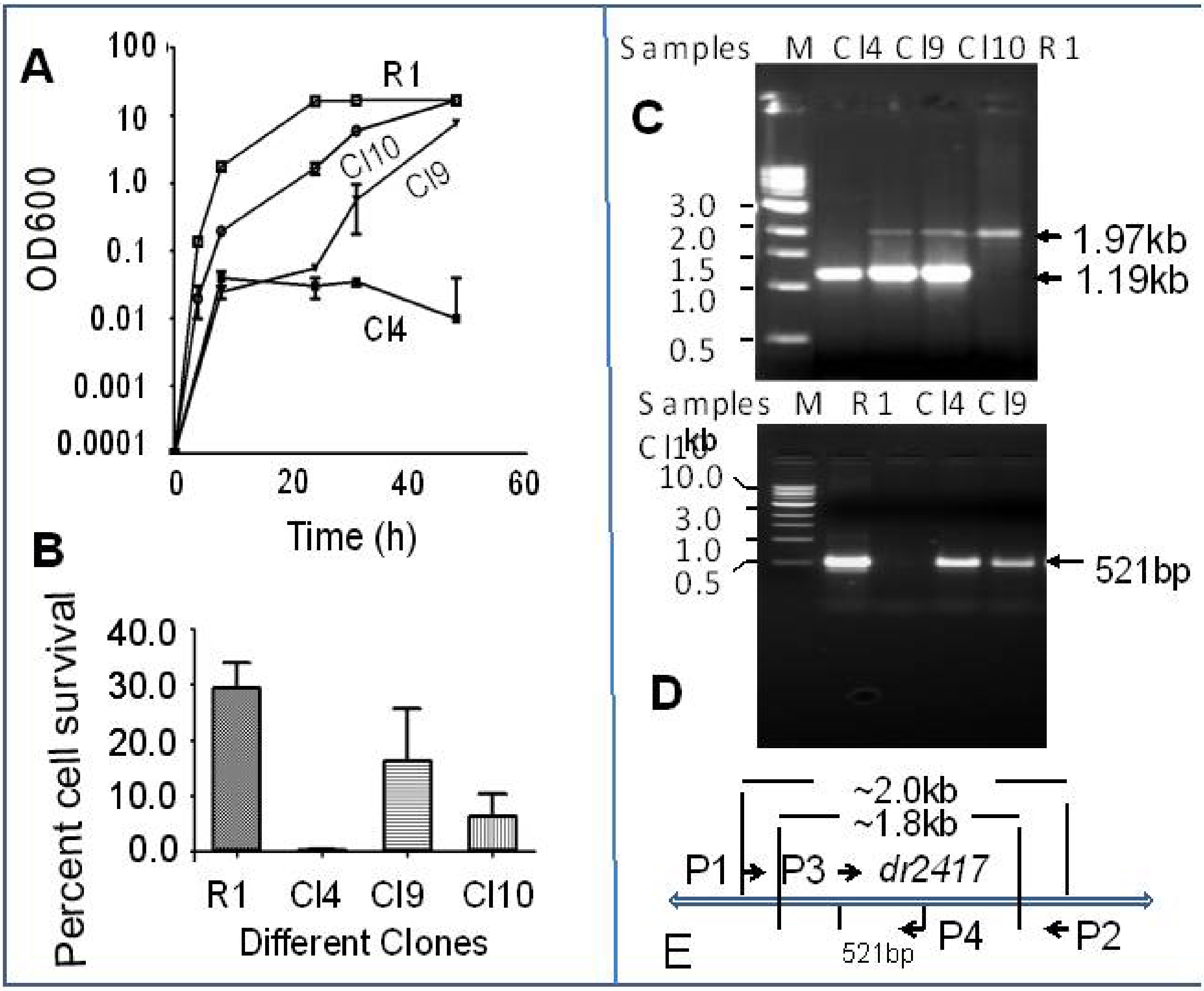

Fig. 3: *In vivo* functional characterization of DR2417. (A) Growth of *Deinococcus radiodurans* R1 and various partial deletion clones of dr2417 monitered by measuring optical density at OD_{600} in a spectrophometer) B) Plot of remaining viable cells of *Deinococcus radiodurans* R1 and various partial deletion clones of dr2417 after 6 kGy of γ radiation dose C, D& E) PCR amplification of genomic DNA from *Deinococcus radiodurans* R1, with flanking primers P1 and P2 (C) and with gene specific internal primers P3 and P4 (D) show that the deletion mutants have gained copies of the shorter *nptII* marker gene and have lost copies of the longer dr2417 gene.

STRUCTURAL PHASE TRANSITIONS IN NOVEL COMPOUNDS

S.K. Mishra
Solid State Physics Division

This paper received the Young Achiever Award at the 56th DAE Solid State Physics Symposium, held at Kattankulathur, Chennai, from Dec. 19-23, 2011

Abstract

Powder Neutron and X-ray diffraction techniques have been used to study variety of phase transitions under various thermodynamical conditions like: temperature, chemical substitution and pressure in $NaNbO_3$ and $SrTiO_3$. High pressure studies on FeAs based compounds show a different phase transition sequence for 1111 and 122 family. I have also contributed towards instrumentation activities related to up-gradation of filter detector neutron spectrometer at Trombay.

Keywords: structural phase transition, diffraction, ferro/antiferroelectric, FeAs based superconductor.

PACS: 77.80.-e, 61.05fm, 77.84Ek, 74.70.-b, 61.50.Ks, 72.80.Ga

Introduction

The importance of materials with novel functionality stems not only from technological applications but also from fundamental interest in understanding structural phase transitions[1]. A vast number of materials are known to exhibit structural phase transformations when subject to changes in thermodynamical conditions like: temperature, pressure, and/or composition, particle size and external stimuli like electric/magnetic field etc. In the present work, we report the systematic investigation of (1) temperature, (2) chemical substitution (composition) and (3) pressure induced structural phase transitions (**SPT**) on technologically important material using diffraction technique. Based on our detailed temperature dependent neutron diffraction studies, the phase diagram of sodium niobate is presented that resolves existing ambiguities in the literature about the different structure. We have also shown for the first time direct experimental evidence of presence of antiferroelectric and ferroelectric instabilities at low temperature. We have also investigated phase transition induced by chemical substitution in (1-x) $NaNbO_3$-x$CaTiO_3$ system and $Sr_{1-x}Ca_xTiO_3$. We found that a variety of phase stabilized ranging from non-polar antiferrodistortive to ferroelectric and antiferroelectric in nature.

High pressure powder synchrotron x-ray diffraction studies of newly discovered FeAs based compounds show that for 122 family, in the Ba-compound, structural phase transition at 300 and 33 K, occurred at higher pressure as compared to the in case of the Ca-compound. We have not found any evidence of a post collapsed tetragonal phase transition in $CaFe_2As_2$ up to 51 GPa (at 300 K) and 37.8 GPa (at 40 K). On the other hand, we find that for 1111 family: CaFeAsF undergoes orthorhombic to monoclinic phase transition at P_c = 13.7 GPa while increasing pressure. SrFeAsF exhibits coexistence of orthorhombic and monoclinic phases over a large pressure range from 9 to 39 GPa. The transition to a lower symmetry phase (orthorhombic to monoclinic) in 1111 compounds under pressure is in contrast with the transition to a high symmetry phase (orthorhombic to tetragonal) in 122 type compounds. We have also involved to up-gradation of the Filter detector neutron spectrometer, which is used for inelastic neutron scattering experiments.

Temperature induced phase transition

The compounds with perovskite structure exhibit interesting structural phase transition due to competition of various instabilities [1]. In this class of materials, sodium niobate ($NaNbO_3$) based solid solutions have shown considerable promise as lead free ceramics with ultrahigh piezoresponse comparable to PZT. It exhibits an unusual complex sequence of temperature and pressure driven structural phase transitions, which are not clearly understood. The highest temperature phase of $NaNbO_3$ (above 913 K) is a simple prototype cubic perovskite and displayed a variety of structural phase transitions as function of temperature (below 913 K), ranging from non-polar antiferrodistortive to ferroelectric and antiferroelectric in nature [2].

We have employed systematic neutron diffraction measurements as a function of temperature (T=12 K to 1050 K) to investigate the temperature induced structures and understand the sequence of structural phase transitions of $NaNbO_3$. Neutron diffraction offers certain unique advantages over x-ray diffraction especially in the accurate determination of positions of oxygen ions, which are crucial for resolving the controversies reported in the literature.

Fig. 1 depicts a portion of the powder neutron diffraction patterns of $NaNbO_3$ at some selected temperature in the range from 12–975 K. At the highest temperature (T= 975 K), all the Bragg reflections present in powder diffraction patterns could be indexed as main cubic perovskite reflections. The reflection labeled as F (d= 2.357 Å) in the diffraction pattern of cubic phase is from the furnace material. Below 950 and 900 K, two new superlattice reflections (S1) appear at d= 2.490 and 2.367 Å, respectively. Further, below 810 K, an additional set of superlattice reflections (S2) appear centered at d= 2.447 Å, and some of them diminish followed by enhancement of the intensity of super lattice reflection (S3) at d= 2.427 Å, which disappears below 680 K. Below 680 K, the super lattice reflections present at d= 2.481, 2.428 and 2.093 Å vanish and new super lattice reflection (S4) appear around d= 2.428 Å. Superlattice reflections, in different temperature regime, are also present at higher angles with prominent intensities. The intensity of these super lattice reflections gradually decreases on lowering the temperature while the some of the peak show drastic changes in the diffraction data. Splitting in peak appear around 2.25 (index as 111 in psedocubic cell) into two with the intensity ratio of 3:1 is an unambiguous signature of rhombohedral distortions and reveals the stabilization of the ferroelectric (***R3c)*** phase at 25 K. Thus, disappearance and reappearance of superlattice reflections in powder neutron diffraction provide unambiguous evidence for structural phase transitions in sodium niobate with temperature and detailed are given in ref. 2.

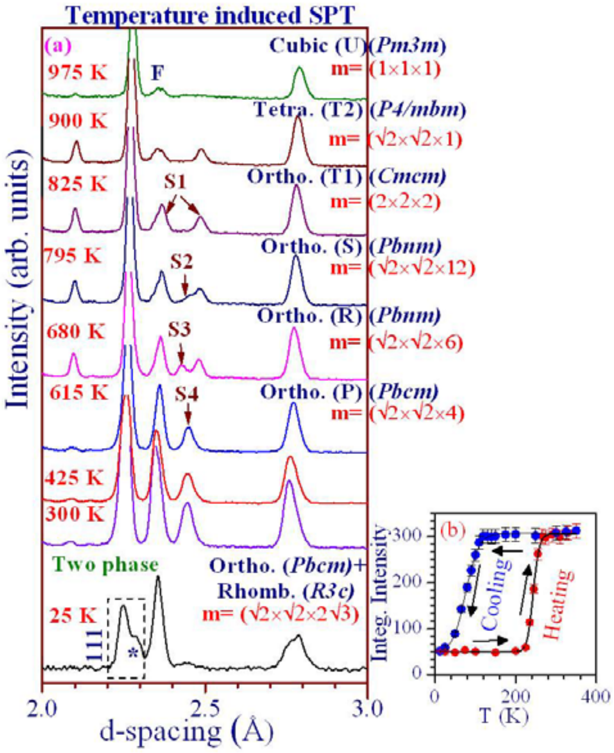

Fig. 1: (a) Evolution of neutron diffraction data and phase stabilities region with temperature for $NaNbO_3$ [2]. Variation of integrated intensity of AFE peak (S4) shown in (b).

To examine the phase stability region we have carried out detailed Rietveld analysis of temperature dependent powder neutron diffraction data. Our studies present unambiguous evidence for the presence of the ferroelectric ***R3c*** phase of $NaNbO_3$ coexisting with an antiferroelectic phase (***Pbcm)*** over a wide range of temperatures below 300 K. Theoretical lattice dynamics calculations of $NaNbO_3$ show well depths and energy barriers from the paraelectric ***Pm3m*** to antiferroelectric ***Pbcm*** and ferroelectric ***R3c*** phases in $NaNbO_3$ are also quite similar. New superlattice reflections appear at 680 K (R phase) and 770 K (S phase) that could be indexed using an intermediate long-period modulated orthorhombic structure whose lattice parameter along <001> direction is 3 and 6 times that of the $CaTiO_3$-like *Pbnm* structure respectively. The correlation of superlattice reflections with the phonon instability is also investigated. The critical exponent (β) for the second order tetragonal to cubic phase transition about 950 K, corresponds to a value $\beta \approx {}^1/_3$, as obtained from the temperature variation of order parameters (tilt angle and intensity of superlattice reflections). It is argued that this exponent is due to a second order phase transition close to a tricritical point. Based on our detailed temperature dependent neutron diffraction studies, the phase diagram of sodium niobate is presented that resolves existing ambiguities in the literature.

Chemical substitution induced phase transition

The properties of materials can be tailored by chemical substitution. The technique has been found to be of special technological significance for preparing new devices. To investigate chemical substitution induced structural phase transition, we select the solid solution (1-x)$NaNbO_3$-x$CaTiO_3$ (NN-xCT) which reveal morphtropic (MPB) like characteristic in a non-ferroelectric system[3]. It is non-ferroelectric and non-piezoelectric MPB system in contrast to the well-known MPB systems which are all ferroelectric and piezoelectric. This is an example of chemical substitution at A and B site of ABO_3 perovskite materials. Due to mismatch the ionic radii of (Na, Ca) and (Nb, Ti) results a stress on system and it exhibit interesting sequence of structural phase transition as function of (Ca, Ti) content. Dielectric studies show an anomalous peak in the composition dependence of the dielectric permittivity of nonferroelectric NN-xCT system for the composition range $0.10 \leq x \leq 0.20$. This is reminiscent of a similar phenomenon in the ferroelectric morphotropic phase boundary ceramics. Fig. 2 depicts the evolution of diffraction patterns as function of composition. The presence of different type of superlattice reflections in diffraction data unambiguously suggests that it undergo a structural phase transition. Detailed Rietveld analysis of the powder x-ray diffraction data for various compositions reveals that this peak is linked with a change of crystal structure from one orthorhombic phase in the *Pbma* space group for $0 \leq x \leq 0.10$ to another orthorhombic phase in the *Pbnm* space group for $x \leq 0.20$ through an intermediate long period modulated orthorhombic phase whose lattice parameter is $c_p \approx 14$ times the lattice parameter of the *Pbnm* phase of $CaTiO_3$ in the [010] direction $q = (0, 1/14, 0)$.

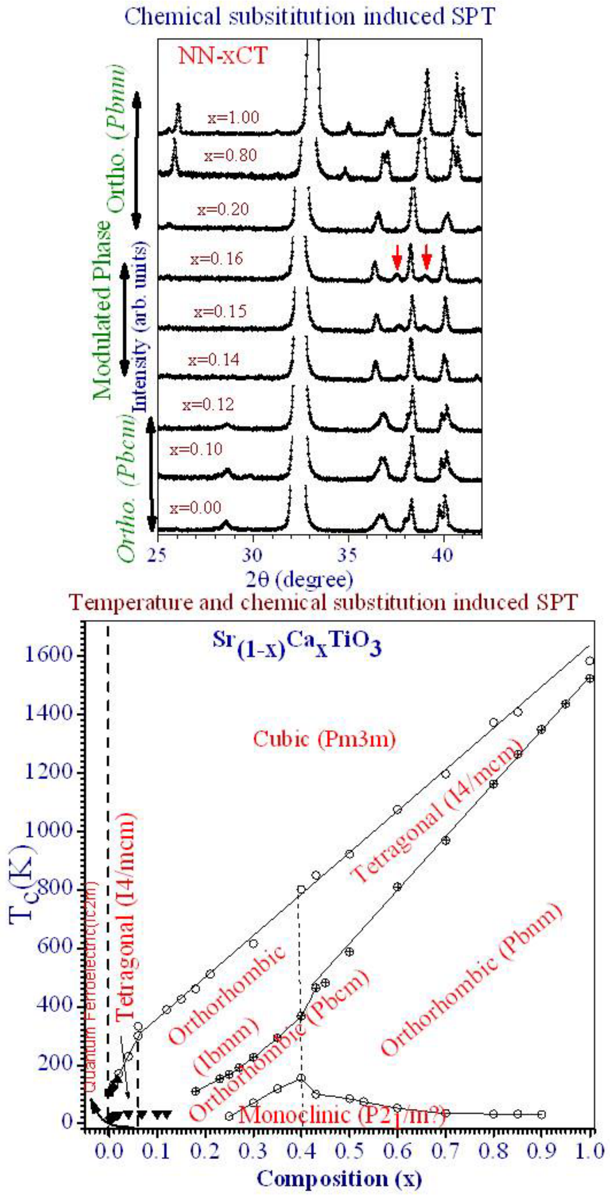

Fig. 2: Stabilization of various phases with composition and temperature for $NaNbO_3$ [3] and $SrTiO_3$ [4] doped with $CaTiO_3$

In addition to this, we have also investigated phase transition of $Sr_{1-x}Ca_xTiO_3$ with temperature and compositions using diffraction with conjunction of dielectric measurements and phase diagram was proposed [4]. We have shown that for the composition x=0.43, the orthorhombic to tetragonal phase transition is of first order in nature. However, the transition from tetragonal to cubic phase seems to be tricritical in nature similar to that reported for $CaTiO_3$ and $SrTiO_3$. A detailed order parameter analysis using Landau type mean field theory has also been carried out[4].

Pressure induced phase transition

The discovery of superconductivity in Fe- based superconductors (FeSCs) has attracted tremendous amount of attention in the quest to understand the mechanism of high transition temperature superconductivity. The generic phase diagram of the FeSCs systems can be produced by manipulating the chemical or structural properties, using chemical doping/substitution or applied external pressure to drive an antiferromagnetic (AFM), non-superconducting parent compound to a superconducting, non-AFM state. The alkaline (Ca/Sr /Ba)-based system so far the most studied of five families.

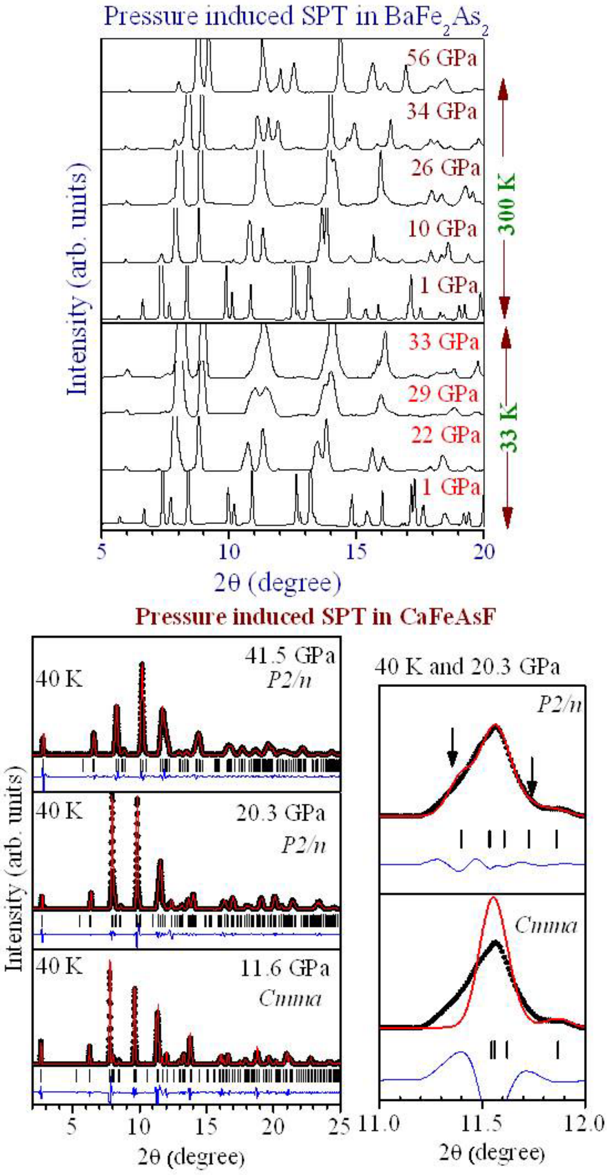

Fig. 3: Evolution of powder synchrotron X-ray diffraction patterns with pressure for $BaFe_2As_2$ and CaFeAsF respectively.

We have carried out systematic investigation of high pressure crystal structures and structural phase transition in 122 family compounds: $CaFe_2As_2$, $BaFe_2As_2$ and 1111 family compounds: CaFeAsF, SrFeAsF using powder synchrotron x-ray diffraction experiments and Rietveld analysis of the diffraction data[5-6]. Fig. 3 depicts a portion of the diffraction patterns at some selected pressure and composition. Rietveld analysis of the high pressure powder x-ray diffraction data showed that at 300 K in the Ba-compound the collapsed tetragonal transition occurs at 27 GPa. The transition pressure value is found to be much higher as compared to the Ca-compound where the transition occurs at 1.7 GPa. However, at low temperature (33K), structural phase transition from the orthorhombic to tetragonal phase in the Ba-compound occurred at about 29 GPa (while increasing pressure), which is much higher than the transition pressure of 0.3 GPa at 40 K as known in case of the Ca-compound. We have not found any evidence of a post collapsed tetragonal phase transition in $CaFe_2As_2$ up to 51 GPa (at 300 K) and 37.8 GPa (at 40 K). On the otherhand, we find that CaFeAsF undergoes orthorhombic to monoclinic phase transition at $P_c = 13.7$ GPa while increasing pressure. SrFeAsF exhibits coexistence of orthorhombic and monoclinic phases over a large pressure range from 9 to 39 GPa. The coexistence of the two phases indicates that the transition is of first order in nature. Unlike in the 122 compounds ($BaFe_2As_2$ & $CaFe_2As_2$) we do not find any collapse tetragonal transition. The transition to a lower symmetry phase (orthorhombic to monoclinic) in 1111 compounds under pressure is in contrast with the transition to a high symmetry phase (orthorhombic to tetragonal) in 122 type compounds. On heating from 40 K at high pressure, CaFeAsF undergoes monoclinic to tetragonal phase transition around 25 GPa and 200 K. Further, it does not show any post-tetragonal phase transition and remains in the tetragonal phase upto 25 GPa at 300 K. The dP_c/dT is found to be positive for the CaFeAsF & $CaFe_2As_2$, however the same was not found in case of $BaFe_2As_2$.

Neutron Instrumentation

In order to understand the microscopic origin of the structural phase transitions, it is essential to study the dynamics of materials which are associated with phonon instabilities and can be investigated using inelastic scattering techniques. For this purpose, we have upgraded the Filter detector neutron spectrometer, which is used for inelastic neutron scattering experiments. The flat PG (0002) single crystal has been replaced with doubly focusing assembly of fifteen Cu (111) single crystals. We found substantial increase of neutron flux at sample position as shown in Fig. 4.

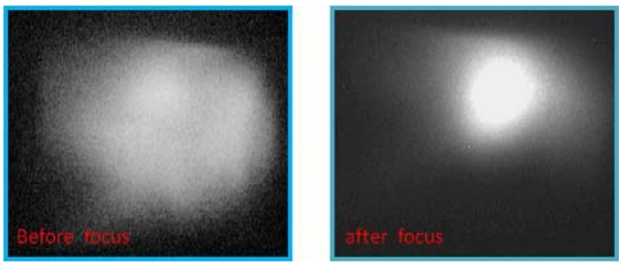

Fig. 4: Photographs of the neutron beam at the sample position of the filter detector neutron spectrometer taken before and after focusing.

The author is grateful to Prof. S L Chaplot and Prof. D Pandey for introducing the subject and P S R Krishna and Dr. R Mittal for useful discussion and scientific collaboration.

References

1. M.E. Lines and A.M. Glass "Principles and Application of Ferroelectrics and Related Materials" (oxford: Clarendon, 1977), E. Bousquet *et al*, *Nature* **452**, 723 (2008); T. Choi, *et al. Nature materials* **9**, (2010) 253 ;Y. Saitoet al. *Nature* **423**, (2004) 84.
2. S.K. Mishra *et al*. *Phys. Rev B.* 83, (2011) 134105 , ***ibid*** 76, (2007) 024110.
3. S. Tripathi et al. *Phys. Rev B.* 77, (2008) 05421041.
4. S K Mishra Ph. D. thesis, Banaras Hindu Unversity, India (2004); S.K. Mishra *et al. Phys. Rev B.* 79, 174111 (2009). ***ibid*** *Apply. Phys. Letter.* 95 232910 (2009), ***ibid*** *Phys. Rev.* B **64**, 092302 (2001).
5. R Mittal, S.K. Mishra *et al. Phys. Rev B.* 83, 054503 (2011), S.K. Mishra *et al. Phys. Rev B.* 84, (2011) 224513. Phys. Rev B. 83, 054503 (2011)

DEVELOPMENT OF SENSOR INSTRUMENTATION FOR VOID AND TWO-PHASE MASS FLUX MEASUREMENTS IN HIGH PRESSURE STEAM-WATER APPLICATION

R. Rajalakshmi, G.J. Gorade, B.S.V.G. Sharma and P.K. Vijayan
Reactor Engineering Division

This paper received the Best Oral Presentation Award at the 16th National Seminar on Physics and Technology of Sensors (NSPTS-16) held at Lucknow, during February 11-13, 2011

Abstract

Multiphase flow/ mass flux measurements have been increasingly important in a variety of processes and power systems such as nuclear reactors, geothermal power stations, pneumatic conveyors, chemical reactors, desalination plants etc. Nuclear reactor related investigations have provided much of the impetus for the recent developments in multiphase flow measurements because of the requirements of design information under steady state operations and also to predict system behaviour under transient and accident conditions. The design and development of sensor instrumentation was carried out for cross section averaged two-phase mass flux measurements with, Pitot tubes rake assembly for velocity measurements and gamma ray densitometer for measurements of void fraction and average mixture density along the horizontal chords. Experimentation was carried out in high pressure steam-water facility and the results were analysed. The sensor developed is simple, rugged, reliable, inexpensive and sturdy sensor for high pressure steam-water applications.

Introduction

Mass velocity and void fraction measurements are required in transient two-phase steam – water flow experiments related to thermal hydraulic studies on reactor safety. An essential feature of two-phase flows is the presence of moving internal interfaces that make theoretical predictions of flow parameters more difficult when compared to single-phase flow. Thus experimental measurements play a key role in providing information for design, analysis and predicting system behaviour. Moreover nuclear reactor safety investigations require reliable thermal hydraulic codes to predict the transient behaviour of power plant under anticipated accident conditions in order to prove the effectiveness of the safety systems and to estimate the possible consequences. Hence for the development & validation of these codes, based on physical modelling of thermal hydraulic phenomena and also to evolve / estimate uncertainties, two-phase instrumentation becomes necessary.

The empirical inputs required for developing models for two-phase flow are conservation of mass, momentum and energy for each phase. As the density and velocity of the two-phase mixture varies across the pipe, we require both velocity and density measurements to obtain the two-phase flow. Development of instrumentation for the measurement of two-phase mass flux in high temperature high pressure steam-water mixture using simple, reliable and inexpensive pitot tube assembly for velocity measurements and void fraction measurements by gamma ray attenuation technique were carried out.

It is observed that mechanical obstruction of the sensing element installed in the flow path can influence the system behavior itself. So an optimum balance between the essential measuring information and flow disturbance must be obtained.

Two-phase Flow Measurement

Two-phase flows show multidimensional characteristics even in a geometrically simple channel. The flow is basically treated as a one-dimensional flow with multidimensional convection effects. The void distribution patterns of two-phase gas liquid flows depends on the pressure, channel geometry, gas & liquid flow rates and orientation of the flow with respect to gravity. These void distributions are characterised as flow regimes namely bubbly, slug, churn and annular flows. The empirical inputs required for developing models for two-phase flow are conservation of mass, momentum and energy for each phase.

The averaged two-phase mixture continuity equation is

$$\frac{\partial\langle\rho\rangle}{\partial t}+\frac{\partial\langle G\rangle}{\partial t}=0$$

Where $\langle\rho\rangle$, $\langle G\rangle$ are the mixture density and mixture mass flux respectively.

$$\langle\rho\rangle = \langle\alpha\rangle \langle\rho_g\rangle + \langle 1-\alpha\rangle \langle\rho_f\rangle$$

$$\langle G\rangle = \langle\alpha\rangle \langle\rho_g\rangle \langle V_g\rangle + \langle 1-\alpha\rangle \langle\rho_f\rangle \langle V_f\rangle$$

While $\langle\alpha\rangle$ is the void fraction i.e. the fraction of the pipe cross section occupied by the vapour (or gas) The subscripts g and f refer to vapour and liquid respectively.

The average velocity for gas and liquid are

$$\langle V_g\rangle=\frac{\langle Q_g\rangle}{\langle\alpha\rangle A} and \langle V_f\rangle=\frac{\langle Q_f\rangle}{\langle\alpha\rangle A}$$

Where A is total cross sectional flow area.

$\langle\rho_g\rangle$ and $\langle\rho_f\rangle$ are related to the pressure and temperature of the vapour and liquid phases. Therefore, if void fraction, average gas velocity, average liquid velocity, phase temperatures and pressures can be measured, then the mixture density **ρ**> and mixture mass flux <G> can be calculated. In dealing with boiling mixtures, the flow can become sufficiently well mixed such that phases can be assumed to be in thermal equilibrium at the saturation temperature. In these cases, $\langle\rho_g\rangle$ and $\langle\rho_f\rangle$ are functions of pressure only. The phases are assumed to be in thermal and mechanical equilibrium i.e. at the same temperature and moving with a same velocity at a given cross section. Therefore, the parameters that must be measured for the multiphase liquids are ***the cross section averaged or global mixture density <ρ> or void fraction<α>, mass velocity (v) and mixture mass flux <G>.*** Void fraction is defined as the cross section of the flow area occupied by the gas phase at any instant.

Sensor Instrumentation

The sensor instrumentation developed in-house for real time two-phase mass flux measurements consists of mass velocity ***(v)*** measurement by in-house developed miniature pitot tubes assembly and void fraction ***(α)*** measurement by traversing gamma ray densitometer. The average mixture densities along the horizontal chord were obtained to compute the cross section area averaged total mass flux. The present instrumentation developed is reliable, inexpensive and sturdy sensor for high pressure applications.

Pitot Tubes Sensor Assembly Description

The Pitot tube rake is formed with a thin stainless steel plate of 66 mm x 18 mm x 3 mm thickness. Six numbers of 1.5 mm diameter miniature pitot tubes were fabricated and assembled in the base plate to form a rake assembly. Five pitot tubes were assembled along the thickness of the plate facing towards the flow direction to sense the impact pressure forming an array of five pitot tubes. The sixth one is assembled perpendicular to these tubes to sense the static pressure.

This Pitot tube rake assembly is fitted into a 50 mm nominal bore pipe through a rectangular bore with the

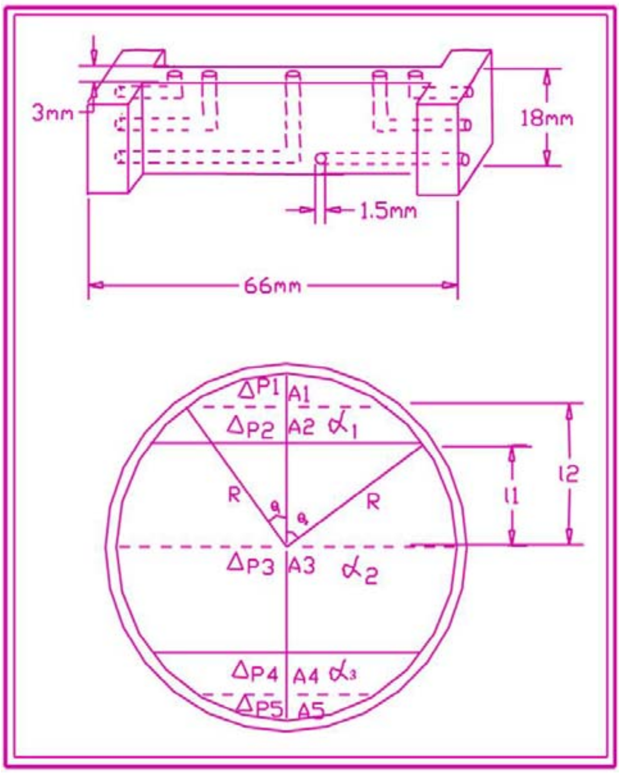

Fig1: Pitot tubes Assembly Construction Details

pitot tubes facing the flow direction. Stainless steel tubing of size 1/8"is silver brazed to the pressure tapping ends and brought out through adapters. Five numbers of differential pressure transmitters are connected through reducer unions and 9.5mm OD impulse lines to measure the difference between the static pressure and the impact pressure. The construction details are shown in fig (1). Impulse lines are routed to ensure that the connecting tubes are always filled with water.

Traversing Gamma Ray Densitometer

The gamma ray densitometer consists of a sealed Cesium-137 gamma source with principal photon energy of 0.662 Mev and NaI(Tl) scintillation detector. The source is positioned in a lead filled shielded source holder with a 2.5mm circular window for the beam to emerge. Lead collimators are used collimate the beam between source and the detector. The scintillation detector is positioned on the other side of horizontal pipe through which the two-phase mixture is flowing, for measuring the intensity of gamma rays. The source holder and detector are mounted on a table in such a way that the gamma beam and detectors are aligned in a line. The construction details of the assembly are given in Fig(2). The detector assembly contains integrated photo multiplier tube and pre-amplifier.

The electronics for gamma ray densitometer consists of amplifier, pulse processing module; HV&LV supply modules and single channel analyser for pulse mode of operation. The single channel analyzer gives output pulse only when the amplifier output pulse falls with in the specified energy window. Hence the background and noise could be reduced. The TTL pulse output obtained from SCA is connected through shielded cables to PC based Data Acquisition System in the control room for event counting.

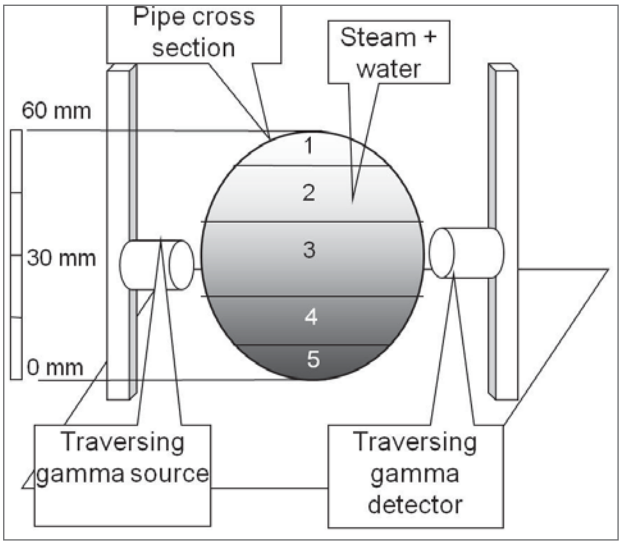

Fig. 2: Traversing Gamma Densitometer Assembly

Design Concept

Pitot tubes are simple rugged and can be used in adverse environment like high-pressure steam water applications. The cross section averaged mass flux measurement using traversing pitot tube and traversing gamma ray densitometer reported in literatures indicated that cross section averaged mixture density could be used to calculate mass flux in high pressure steam water flows. The cross section averaged mass flux calculations using Pitot tubes along the chord were in good agreement if horizontal chordal mixture density was used in place of local mixture density. Also it is relatively easy to measure chordal average mixture densities by gamma ray attenuation.

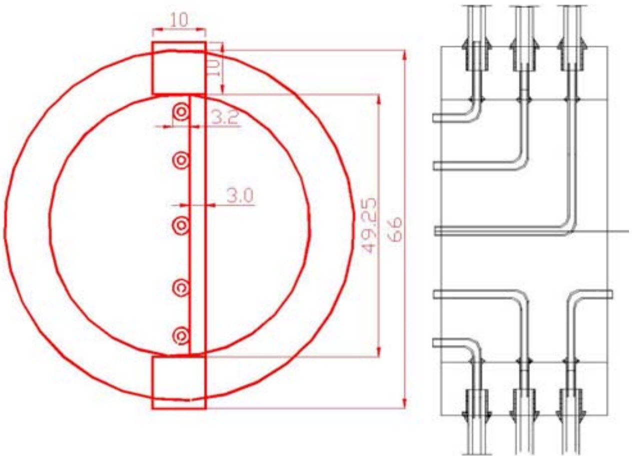

Fig. 3: Pitot Tubes Array for 2" NB Pipe

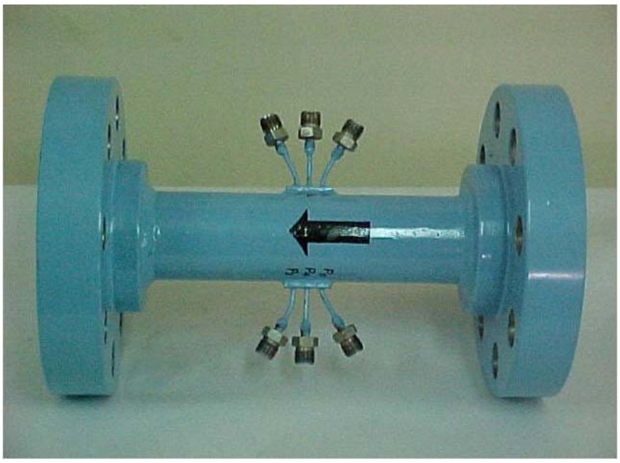

Fig. 4: Pitot Tubes Assembly sensor

Literature survey on the adequacy of average mass flux predictions using pitot tube measurements at only few locations was carried out. A study on the local mixture density distributions and calculated local mass fluxes using algebraic reconstruction techniques reveals that a local measurement near the centre region of the horizontal chord gives good result to predict the chordal mass flux in most flow regimes due to the uniformity of the local mass fluxes along the chord. For axisymmetric and non-axisymmetric flows in vertical & horizontal pipes, as suggested the present design consists of five Pitot tubes located across the pipe section. The pitot tubes are positioned in a vertical line, one at the centre of the pipe, one each at 0.286 diameters and 0.429 diameters above and below the centre of the pipe to ensure that all the flow regimes are covered. Fig-(3) & (4) gives the details of pitot tubes assembly for 2" NB pipe configuration.

Working Priciple Theory

The single phase flow equation using pitot tube pressure drop is given by the following equation.

$$\Delta P = \frac{1}{2}\rho u^2$$

Where, ρ is the fluid density and u is the flow velocity. For two-phase flow, the equation becomes:

$$\Delta P = \frac{1}{2}[\alpha\rho_g u_g^2 + J(1-\alpha)\rho_f u_f^2]$$

Where α is local void fraction, ρ_g and ρ_f are the vapour and liquid densities, u_g and u_f are the local vapour and liquid velocities respectively and J is the momentum exchange factor. The value of J is a function of void fraction and ranges from 1 to 2. Considering J as unity and also no phase slip i.e. $u_g = u_f$ (homogenous flow)
Therefore,

$$u = \sqrt{\frac{2\Delta P}{\alpha\rho_g + (1-\alpha)\rho_f}}$$

Mass flux G = uρ
and the local mass flux is

$$G_j = \sqrt{(2\Delta P_j[\alpha_j\rho_g + (1-\alpha_j)\rho_f])}$$

where ΔP_j and α_j are measured by the Pitot tube and gamma densitometer respectively. Since ΔP_j are local measurements and α_j are averaged over a given volume the data is interpreted in the following manner. Fig (2) shows the locations of the Pitot tubes with respect to the three chordal void fraction measurements. It may be noted that ΔP_3 is associated with α_2 and the two lower and upper Pitot tubes (ΔP_1 & ΔP_2 and ΔP_4 & ΔP_5) are associated with α_1 and α_3 respectively.

The void fraction is calculated from the following equation:

$$\alpha = \frac{\ln[N_\alpha / N_0]}{\ln[N_1 / N_0]}$$

Where N_α, N_0 and N_1 are the count rates for a given void α. When the pipe is full α = 0 and when the pipe is empty α = 1.

The total mass flux is given by

$$G_{(Total)} = G_{12}(a_1 + a_2) + G_3 a_3 + G_{45}(a_4 + a_5)$$

Where

$$G_{12} = [G_1 a_1 + G_2 a_2]/(a_1 + a_2)$$
$$G_{45} = [G_4 a_4 + G_5 a_5]/(a_4 + a_5)$$

a_j is the area ratio associated with the given pitot tube and shown in Fig. 1.

$a_j = A_j/A_t$

Data Acquisition

A USB data acquisition known as USB-4711 100 kS/s, 12-bit Multifunction USB Module has been used for data acquisition. This module has 16 analog input channels, 8 DI / 8 DO, 2 AO and one 32-bit event counter.

The analog input channels have been used for acquiring pitot tubes and temperature data. The event counter is used to measure pulses from gamma chamber.

The data acquisition programming is done using Visual Basic. ActiveX controls are used to acquire the data from the data acquisition device. The ActiveX controls to access the data from the data acquisition device are supplied by the manufacturer.

Experimentation

Test Set up Description

A schematic of the experimental facility in which two-phase flow experiments were carried out is High Pressure

Natural Circulation Loop (HPNCL) and shown in Fig (5). This experimental loop consists of directly heated vertical tubular heater. The cold water enters the heater at the bottom and gets heated as is rises through the test section. Heating takes place in the vertical test section for a length of about 1.2 mtrs by a 80 KW power source. The two-phase steam-water mixture at the heater exit moves into the steam drum wherein the steam gets separated by gravity action and rises to the condenser where it gets condensed. The condensed liquid joins at the bottom of the steam drum. Further the condensate is sub cooled in the double pipe heat exchanger to the desired temperature and recirculated.

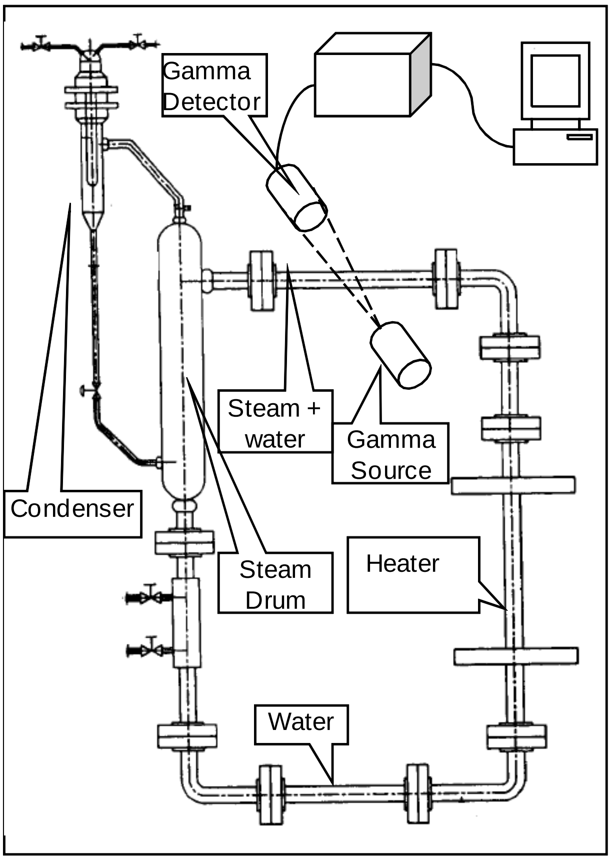

Fig. 5: Steam-Water experimental Facility (HPNCL)

Experimental Procedure

The sensor instrumentation in experimental set up is shown in Fig(6). In this technique a well collimated gamma beam is passed through a test section in which the two-phase mixture is flowing and the intensity of the attenuated beam is measured by the detector kept opposite side of test section. Gamma is attenuated more in water than in steam. From the gamma attenuation we can find out the void fraction in the steam water mixture. For experimental purpose we have divided the pipe in to 5 sections. Gamma attenuation is measured in each section. For measuring steam water mixture velocity pitot tubes are installed in these zones.

The gamma beam is traversed across the pipe cross section and the void fraction was measured across five horizontal chords to obtain the cross section area averaged void fraction. The void sensor was calibrated initially with full water and full air. The pitot tubes assembly was calibrated with water at ambient condition and compared with pipe flow meter located in the single phase inlet section. The calibration results of pitot tubes are shown in Fig (7). The void and velocity measurements were carried out under steady state conditions. The loop was operated at desired pressure and power conditions by adjusting the test section power and secondary flow rate. When the desired steady state is arrived, gamma ray intensity was measured for 5 min for a dwell time of 10 secs across each chord. The experimental data were obtained at various operating process conditions of pressure, temperature and power.

Fig 6: Sensor Instrumentation in Experimental Loop

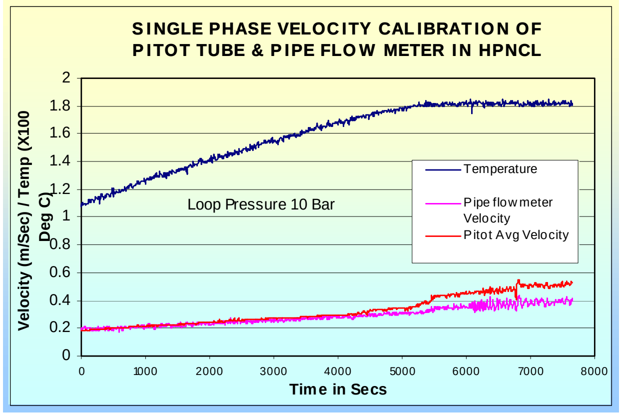

Fig: 7 Pitot Tubes Calibration Results

Experimental Results

Experimental observations for operating conditions of 30 bar, 40 bar and 50 bar pressures at various heater power levels were analysed and the results are given below in Figs (8) to Fig (13).

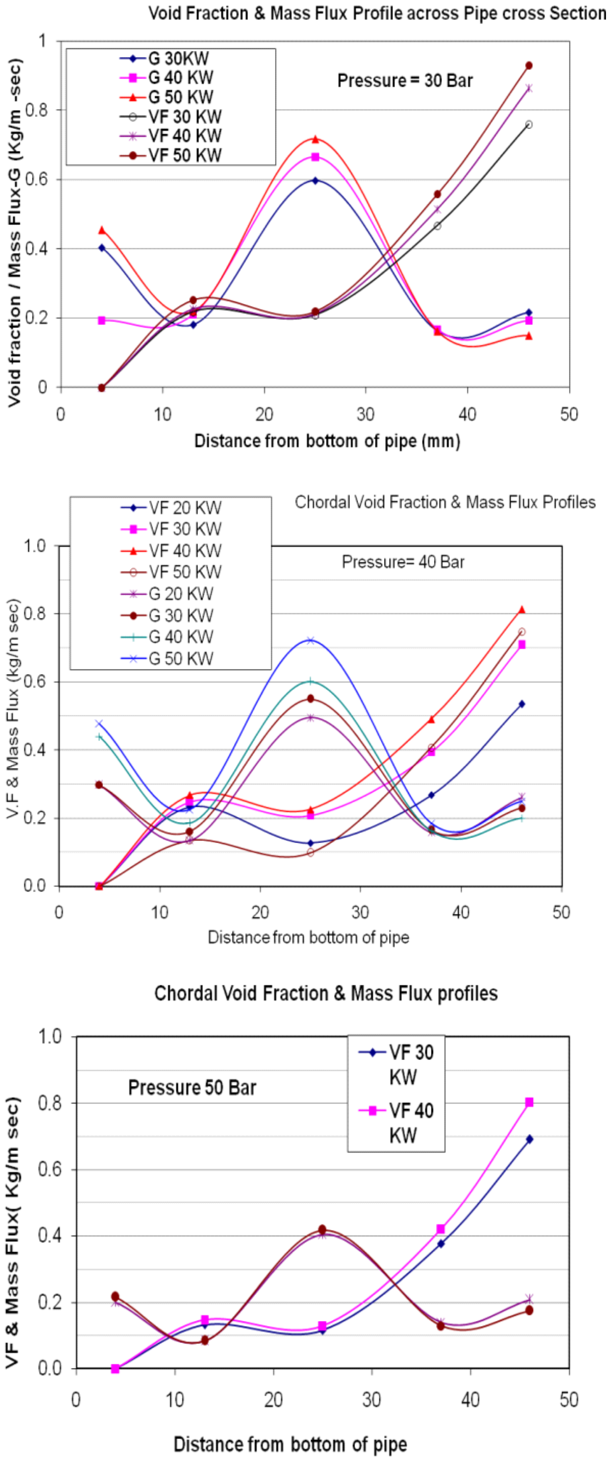

Figs. 8,9,10: Mass Flux & Void Profiles for 30, 40 & 50 bar

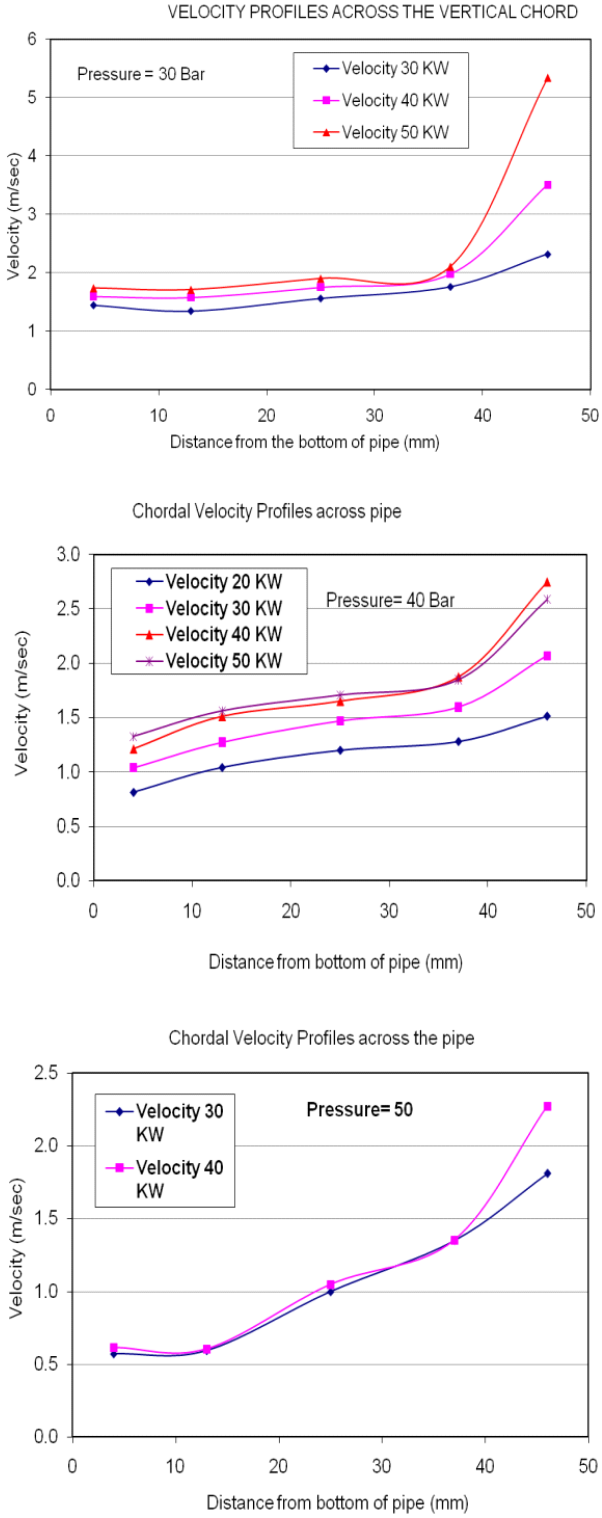

Figs. 11,12,13: Velocity Profiles for 30, 40 & 50 bar

Conclusion

A simple Pitot tube assembly with five Pitot tubes and traversing gamma ray densitometer with point source was designed and fabricated. A relatively simple model assuming unity phase slip ratio and momentum exchange factor for the measurement of cross section averaged mass fluxes was adopted. This method is well suited for two-phase mass flux measurements over wide range of two-phase flow conditions especially in high-pressure steam-water environment. Also the Pitot tube device introduces only very little disturbance compared to other mass flow meters, which is very important for two-phase studies in Natural circulation loops. The present device is developed for simple operation and data interpretation.

Experiments were carried out at 30 bar, 40 bar and 50 bar pressures. Power was varied and pressure was kept constant. Mass flux was found high at the centre region of the pipe. Since the experiments were carried out in horizontal pipe, phase separation takes place due to gravity i.e steam and water phases gets separated at the top and bottom region of the pipe respectively. Hence void fraction is high at the top region of the pipe in the graph. At constant pressures increase in power results in increase in void fraction and mass flux. The velocity profiles in fig (9, 11 &13) shows high velocity steam phase at the top most region of the pipe. Because of large density difference between the densities of two phases at low pressures, a large slip is expected between the two-phases. The slip between two phases accounts for low measured void fraction. However the density difference between the water and steam decreases with increase in pressure. This also reduces the slip between two phases. The experimental observations show good repeatability of the output trend.

References

1. R. Rajalakshmi & L.R.Mohan and R.K.Sinha "Flow measurement for complex Two Phase Flow in High Pressure and High Temperature Loop" Global Conference on Flow Metering & Control for the new millennium at FCRI, Palghat, Sept 2000
2. J.Reimann, H.John and U.Muller, Measurement of two-phase mass flow rate: a comparison of different techniques, Int. J. Multiphase Flow 8 (1982)
3. Anderson, G.H. and B.G.Mantzouranis, "Two-phase (Gas/Liquid) Flow phenomena-II Liquid Entrainment", Chem, Eng. Sci., 12 (1960).
4. Adorni, N.I.Casagrande, L.Cravarllo, A.Hassid and M.Silvestri, "Experimental Data on two-phase adiabatic flow: Liquid film thickness, phase velocity, pressure drops in verticle gas liquid flow" CISER 35.
5. S. Banarjee and R.T. Lahey, Advances in two-phase flow instrumentation, Nuclear Science and technology, 13 (1981).

NEW SYNTHESIS ROUTE FOR DMDOHEMA AND ITS EVALUATION UNDER SIMULATED HIGH-LEVEL WASTE CONDITIONS

Ajay B. Patil and Vaishali S. Shinde
Garware Research Centre, Department of Chemistry, University of Pune
and
P.N. Pathak, P.K. Mohapatra and V.K. Manchanda
Radiochemistry Division

This paper received the Best Oral Paper Award at the Tenth Biennial Symposium on "Nuclear and Radiochemistry" (NUCAR -2011) held at GITAM University, Visakhapatnam, between February 22-26, 2011

Introduction

The long-lived alpha emitting minor actinides (MAs) viz. ^{241}Am, ^{243}Am, ^{245}Cm, and ^{237}Np, and residual Pu, present in High Level Waste (HLW) solutions are of great environmental concern. Actinide partitioning is the proposed strategy for effective mitigation of the long term hazards associated with HLW. Efforts are being made by radiochemists/separation chemists to develop environmentally benign solvents to meet the challenges of radioactive waste management. Amongst these, the completely incinerable pentaalkylmalonamides have distinct advantages. The French DIAMEX (DIAMide EXtraction) process uses a combustible diamide as extractant. In this process actinides and lanthanides are directly extracted from a high acidity PUREX raffinate (3–4M HNO_3). The diamides proposed for this process are *N,N'*-DiMethyl-DiButyl-TetraDecyl Malonamide (DMDBTDMA) and N,N'-DiMethyl-*N,N'*- DiOctyl-2-(2-(HExyloxy) ethyl)- Malonamide (DMDOHEMA). The latter has been chosen as the new reference molecule in view of increased molecular weight resulting in enhanced lipophilicity and limited the third-phase formation problem. The sharing of the alkyl chain length shortens the degradation products and facilitating their elimination by basic scrubbing. Also, the introduction of an ethoxy group on the central alkyl chain enhances the affinity for MA and Ln complexation and thereby extraction efficiency. DMDBTDMA has been studied extensively at BARC and has shown moderate extractability of trivalent Am(III) from simulated high-level waste (SHLW) solution at acidity ~ 3M HNO3. However, no systematic attempt has been made to evaluate DMDOHEMA (Fig.1) as an extractant for actinide partitioning from HLW solutions. The complete synthesis route of DMDOHEMA is not reported in open literature. This paper presents a new synthesis route of DMDOHEMA employing cheaper starting materials, high yield (55-60% as reported in literature) and purities. The synthesized product has been evaluated for the extraction of Am(III), Np, Pu under tracer as well as simulated high level waste condition. The performance has been evaluated vis-á-vis other extractants proposed for actinide partitioning.

Experimental

N-methyl octyl amine and *n*-butyl lithium were obtained from Aldrich chemicals and Chemetall Gmbh respectively. *N*-methyl octyl amine was distilled before use. All the solvents used for reactions and column purifications were distilled and dried. 1M DMDOHEMA solution was prepared in *n*-dodecane (Lancaster) for solvent extraction studies. Purified Pu (principally ^{239}Pu), ^{237}Np, ^{241}Am, and ^{233}U were used for distribution experiments under pure tracer as well as SHLW (at 3M HNO_3) conditions. The composition of SHLW is mentioned elsewhere [1]. All the distribution experiments were carried out at room temperature (25 °C) maintaining organic-to-aqueous phase ratio as 1 and equilibration time about one hour. Distribution ratio of metal ions (D_M) is defined as the ratio of concentration of metal ions (expressed in terms of radioactivity) in the organic phase to that in the aqueous phase. The measurement of radioactivity was carried out by liquid scintillation counting (alpha emitters) and by HPGe detectors (gamma emitters).

Results and Discussion

New route for DMDOHEMA synthesis

DMDOHEMA is synthesized in the following three steps, (i) Synthesis of *N,N'*-dimethyl *N,N'*-dioctyl Malonamide (DMDOMA), (ii) Synthesis of 3-oxanonyl side chain, and (iii) the coupling of 3-oxanonyl side chain with diamides backbone [2]. However, this route was having the limitation of purity essentially due to the reaction of Mesyloxy-3-oxanonane with n-BuLi in step (iii), which affected adversely the purity and consequently the distribution behavior of the final product. Interestingly, the side product was found to have same polarity and close R_f value as that of the DMDOHEMA. Therefore, it was decided to avoid the use of mesylation step by introducing tosyl derivative of 3-oxanonanol maintaining the step 1 as reported earlier [3]. The final step of the synthesis was to couple the tosyloxy 3-oxanonane at the $-CH_2-$ malonyl carbon of DMDOMA in the presence of NaH (instead of *n*-BuLi), which helped in suppressing the formation of side products. Scheme 1-4 shows the complete synthesis scheme.

Scheme1: Synthesis of diamide backbone

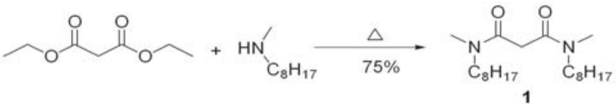

Scheme 2: Synthesis of 3-oxa nonanol side chain (2)

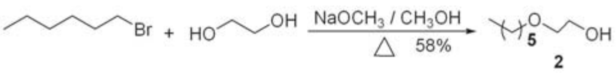

Scheme 3: Synthesis of Tosylated 3-oxa nonanol side chain (3)

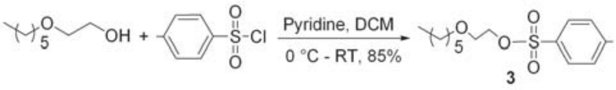

Scheme 4: Coupling of diamide and Tosylated 3-oxa nonanol side chain

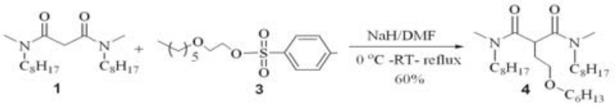

The synthesized product 4 was characterized by CHN, NMR, MS and by distribution data of Am(III) at 0.01 M and 3 M HNO3. **^{1}H NMR** (300MHz, $CDCl_3$): δ0.85(t, 9H, C-CH_3), 1.2-1.3(br s, 26H, $\text{C-CH}_2\text{-C}$), 1.56 (br s, 8H, $\text{-O-C-CH}_2\text{-}$, $\text{N-C-CH}_2\text{-}$), 2.8 (s, 3H, N-CH_3), 3.0(d, 3H, N-CH_3), 3.4 (m, 8H, $\text{-O-CH}_2\text{-}$, $\text{N-CH}_2\text{-}$), 3.9 (m, 1H, -CO-CH-CO-). **^{13}C-NMR**(75MHz,$CDCl_3$):δ49,50(N-CH_3), 69,71($\text{-O-CH}_2\text{-}$), 170(-CO-).

MS m/z:$C_{29}H_{58}N_2O_3$:482.78 (483); It should be noted that majority of the carbon atoms are aliphatic in nature. The peaks corresponding to different carbon atoms are not easily distinguishable. Therefore, only major ^{13}C peaks corresponding to amide (N-CH_3), ethereal (O-CH_3), and carbonyl (>C=O), carbons are listed. **CHNS**: C: 72.08% (71.94%); **H**: 12.01% (12.17%).

Distribution ratio values of Am(III) using 1 M DMDOHEMA/n-dodecane as extractant at 0.01 and 3 M HNO_3 were 1×10^{-3} and 15.5, respectively and were in agreement with the reported values. This method offers product with better yield (55-60%) and a relatively easy purification step. Other important highlights of this route are: (a) the use of diethyl malonate (ester) as a starting material instead of the corrosive/hazardous malonyl dichloride, (b) replacement of *n*-Bu-Li (costly, moisture sensitive and hazardous) with NaH (relatively cheaper).

Solvent extraction studies

Table 1 lists the distribution ratio values for different metal ions using 1 M DMDOHEMA/n-dodecane as extractant at 3 M HNO3 as well as in the presence of SHLW solution. It is evident that D values of Am(III), Np(IV), Np(VI), Pu(IV), U(VI) are high enough for extraction under SHLW conditions. Interestingly, there was an increase in DNp values (without valency adjustment) in the presence of SHLW. This enhancement was attributed to the oxidation of Np to Np(VI), which was independently confirmed by

Table 1: Distribution behavior of different metal ions; Extractant: 1 M DMDOHEMA/n-dodecane; T: 25°C

Metal ion	*D_M*	
	3 M HNO_3	*SHLW*
Am(III)	15.5	12.40
Np[#]	5.4	19.7 (38.9)[##]
Np(IV)	33.0	22.5 (32.5)[##]
Np(VI)	25.0	21.2 (42.0)[##]
Pu[#]	34.5	27.1
Pu(IV)	38.5	23.4
U(VI)	24.0	22.4

[#] No valency adjustment; [##] Values in brackets refer to SHLW containing 0.1 M Oxalic acid + 0.05 M HEDTA (N (2-hydroxyethyl) ethylenediamine triacetic acid)

Table 2: Comparison of D_{Am} of different extractants; Diluent: *n*-dodecane; T: 25°C

Extractant	*D_{Am} at 3 M HNO_3*
1 M DMDOHEMA	*15.5*
1 M DMDBTDMA	10
0.2 M CMPO + 1.2 M TBP	23
0.1 M TODGA+ 0.5 M DHOA	300
0.2 M TEHDGA+ 30 % Isodecanol	100
30 % TRPO	0.8

Table 3: Fission/activation product(s) distribution data

Metal ion	*D_M under SHLW condition*
^{154}Eu	7.0 ± 0.2
^{144}Ce	13.4 ± 0.8
^{106}Ru	0.17 ± 0.02
^{137}Cs	0.06 ± 0.01
^{125}Sb	$<10^{-3}$

spectrophotometry. The extraction data of Am(III) was compared with those of other proposed extractants such as octyl(phenyl)-N,N-diisobutyl carbamoyl methyl phosphine oxide (CMPO), trialkyl phosphine oxide (TRPO), DMDBTDMA, N,N,N,N -tetraoctyl diglycolamide (TODGA), and N,N,N,N -tetra(2-ethylhexyl) diglycolamide (TEHDGA) (Table 2). Table 3 shows the distribution behavior of various fission /activation products under SHLW conditions spiked with diluted aliquot of a high active waste sample from the PUREX process stream (PREFRE plant). As expected, tri-, tetravalent metal ions are extracted under SHLW conditions. Stripping behavior of ^{241}Am loaded in 1M DMDOHEMA/n-dodecane under SHLW conditions was carried out using 0.01 M HNO_3 solution. Two contacts were found sufficient for quantitative stripping (>99.9%).

References

1. S.A. Ansari, et al., Sep. Purif. Technol., 66 (2009) 118
2. Z.W. Zang et al., Chinese J. Inorg. Chem., 22, 1867 (2006)
3. E.G. Knapick et al., Synthesis, 58 (1985).

Acknowledgements

Authors are thankful to Dr. A. Goswami, Head, Radiochemistry Division for his keen interest in this work. Mr. Ajay B. Patil greatfully acknowledges the support for fellowship from Bhabha Atomic Research Centre, Mumbai under BARC-University of Pune, Pune collaborative research programme.

COMPATIBILITY OF STAINLESS STEEL 316L WITH LEAD-17AT%LITHIUM WITH REFERENCE TO INDIAN-TBM

Poulami Chakraborty, Chintamani Das, Sanjay Kumar and R.K. Fotedar
Fusion Reactor Materials Section, Materials Group

This paper received the 1st Prize for Best Poster Presentation at the Second International Conference on Advances in Nuclear Materials (ANM-2011), Mumbai, Feb. 9-11, 2011

Abstract

The present work deals with the study of compatibility of lead-17 at % Lithium ($Pb_{83}Li_{17}$) flowing in thermal buoyancy driven loop made of SS 316L with a thermal gradient of 100°C. The corrosion of SS 316L tube was studied after 1000 of exposure using scanning electron microscope (SEM) and Energy Dispersive X-Ray Analysis (EDX). Preferential dissolution of major constituent elements namely, Fe, Ni, Cr from the tube walls, with the formation of a porous corroded layer was observed in the hot leg maintained at 500°C. Both Ni and Cr rich deposits were found in the cold leg at 400°C but no penetration of $Pb_{83}Li_{17}$ was observed. Chemical analysis of $Pb_{83}Li_{17}$ showed highest concentrations of Ni due to higher solubility.

Keywords: - SS316L, Corrosion, $Pb_{83}Li_{17}$, SEM, Ferrite, Deposits.

Introduction

Various participants to the International Thermonuclear Experimental Reactor (ITER), including India are currently assigned the task of designing their DEMO-relevant Test Blanket Modules (TBMs). All of them are primarily aiming at the designing of a blanket concept, which operates at a tritium breeding ratio of more than one and, also, efficiently extracts the high grade heat generated due to fusion. India has proposed Lead–Lithium cooled Ceramic Breeder (LLCB) as the blanket concept for testing at ITER. The LLCB blanket concept consists of lithium titanate as ceramic breeder (CB) material in the form of packed pebble beds and $Pb_{83}Li_{17}$ eutectic as multiplier, breeder, and coolant for the CB zones [1]. In the initial stages, a number of structural materials, including various classes of stainless steels, have been proposed for the construction of Indian-TBM. The best suited material will be chosen by considering its thermo-mechanical properties, capability to withstand radiation and compatibility with the coolant. $Pb_{83}Li_{17}$ has been found to be more corrosive than pure lithium [2] and the corrosion rate is affected by various factors relevant to the TBM design. With this view, compatibility tests of SS 316L have been performed in molten flowing $Pb_{83}Li_{17}$ in a thermal convection loop with a thermal gradient of 100°C for 1000 Hrs of exposure. Corrosion behaviour of SS 316L has been studied using SEM and EDX.

Experimental

The thermal convection loop used for the experiment was constructed of SS 316L tubes (Fe-17Cr-12Ni-2Mo-2Mn-2Si-0.08C [wt. %]) with I.D of 12 mm and 2 mm thickness as shown in Fig.1. The tubes were initially annealed, then washed with acetic acid and dried with ethanol. The loop circulated 0.8 liter of $Pb_{83}Li_{17}$ with the hot leg temperature of 500°C and the cold leg at a difference of 100°C. The flow rate of liquid metal under this thermal gradient was 6 cm/s. After 1000 hrs of operation, the loop was cooled. SS 316L tube samples from hot and cold leg were cut after draining out the liquid metal. SEM and EDX of the cross-section of SS 316L were carried out without cleaning the inside surface of the tube. Chemical analysis of the

$Pb_{83}Li_{17}$ collected from hot and cold sections of the loop was carried out using Inductively Coupled Plasma- Atomic Emission Spectroscopy (ICP-AES).

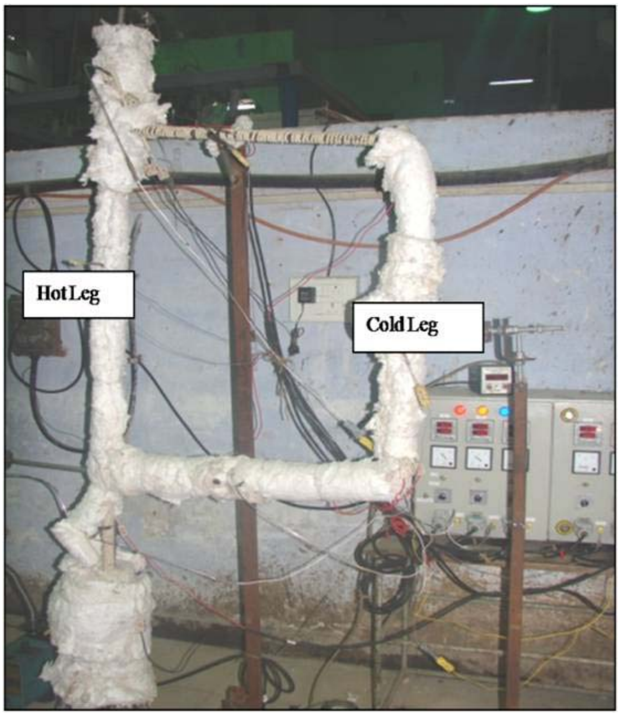

Fig1: The Lead -17Lithium thermal convection loop

Results and Discussions

There was no change in the melting temperature of the $Pb_{83}Li_{17}$, as measured by thermocouple, after the experiment indicating that there was no variation in the stoichiometry or any oxidation of same.

The corrosion of SS 316L at 500°C was characterised by the formation of a distinct corroded layer on the surface facing the liquid metal as shown in the SEM photograph (Fig.2). Similar observations have been made by Tortorelli et.al [3, 4]. The parent austenite grains could be clearly differentiated. Fig. 3 shows the elemental mapping, using EDX, of the same area shown in Fig. 2. The analysis revealed significant depletion of Ni and Cr in the corroded layer (Fig 3a for Ni and Fig 3b for Cr, respectively). Lead was found to be present in the adherent deposit on the surface of SS 316L (Fig.3c). This was further confirmed from the elemental line scans taken across the corroded layer as shown in Fig. 4. EDX analysis on the corroded layer shown in Fig. 5, revealed the presence of around 15% lead in the whitish region on the matrix. Previous studies have reported the formation of a ferrite layer on the surface due to preferential leaching of Ni and Cr by $Pb_{83}Li_{17}$, with Ni dissolution being the higher [4,5].

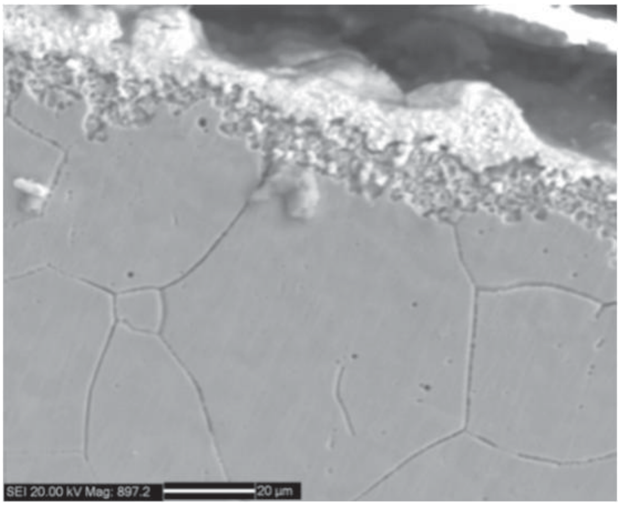

Fig.2: SEM of cross-section of SS 316L tube exposed to Pb-Li at 500°C for 1000 h

No corrosion layer was observed on the cold leg surface due to a comparatively low temperature of 400°C. Deposit of Pb-17Li was found to be adherent to the wall and particles of different compositions were dispersed in the solidified eutectic in a non-uniform manner; their concentration being more, near to the tube surface, as shown in Fig.6. There were two distinctively different phases, one rich in Cr while other rich in Ni and Mn; the

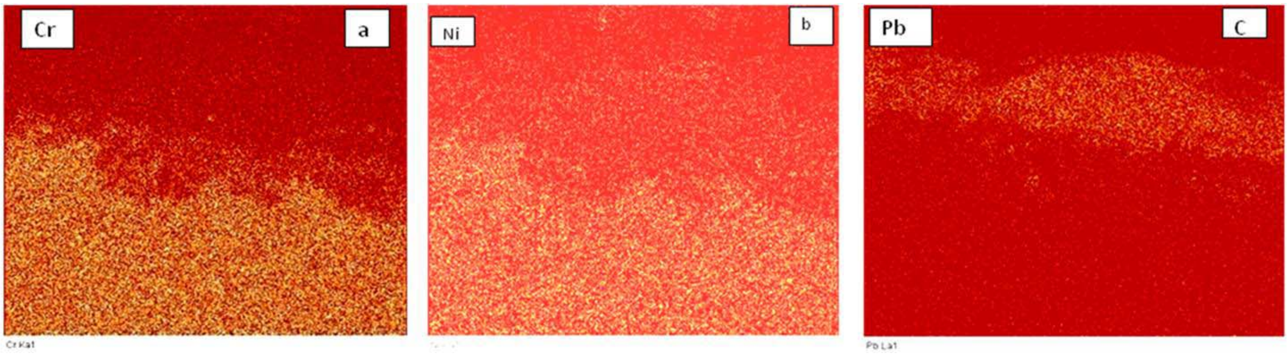

Fig 3: EDX elemental maps of cross section of SS 316L exposed to Pb-17 at% Li for 1000 h at 500°C (a) Chromium (b) Nickel (c) Lead.

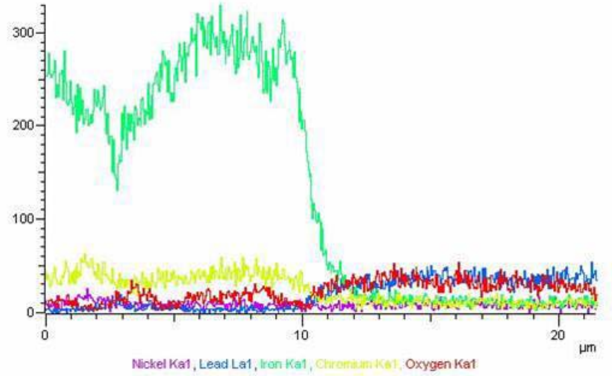

Fig. 4: EDX line scan across the corroded layer in hot leg

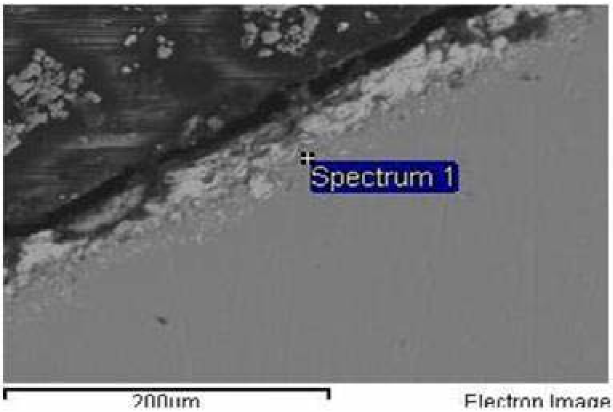

Fig.5: EDX analysis of the corroded layer at spectrum 1 of the hot leg

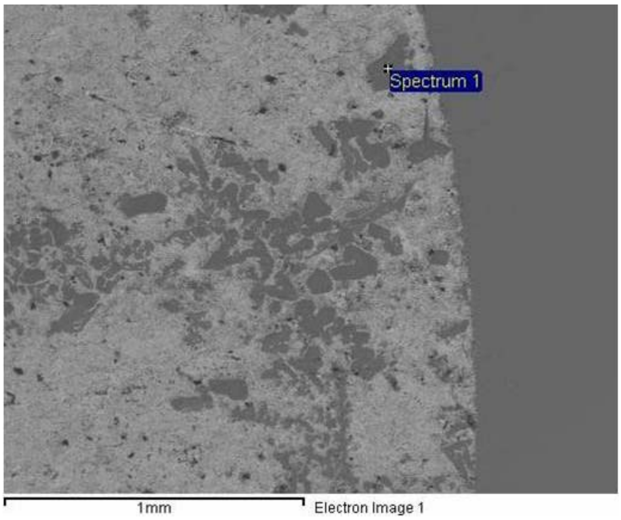

Fig. 6: SEM image of cross-section of SS 316L at 400°C without cleaning

Table 1: EDX analysis of the deposits (spectrum 1 and 2) in weight percentage.

Element	Spectrum 1	Spectrum 2
Fe	33.34	52.05
Cr	65.69	12.88
Ni	0.98	30.65
Mn	-	4.43

compositions are given in Table 1. Some similar observations have been made by Tortorelli [6]. The author has established that chromium rich deposits are formed before the nickel rich ones due to difference in their solubility. However, the distribution of different phases in the present study could be explained only after studying the deposition behaviour with time.

Solidified $Pb_{83}Li_{17}$ taken from the dump or melting tank of the loop after 1000 h of exposure was analyzed using ICP-AES. It was found to contain 409, 395 and 98 ppm of Ni, Fe and Cr, respectively. This was due to the higher dissolution rate of Ni compared to Fe and Cr.

Conclusion

1. The corrosion of SS 316L by $Pb_{83}Li_{17}$ was characterised by the formation of a Ni-Cr depletion layer at 500°C.
2. Both Ni and Cr rich deposits were found at 400°C but no penetration of $Pb_{83}Li_{17}$ was observed.
3. The dissolution rate of Ni is the highest and it was found in maximum quantity in the circulating liquid metal.

Acknowledgements

We would like thank Mr. Bhaskar Paul, BARC for helping us in conducting SEM+EDX on the samples.

References

1. E. Rajendra Kumar et.al., *Fusion Engineering and Design*, 83 (2008) 1169–1172
2. O.K. Chopra And D.L. Smith, *Journal of Nuclear Materials* 155-157 (1988) 715-721
3. P.F. Tortorelli and J.H. Devan, *Journal of Nuclear Materials,* 141-143 (1986) 592-598
4. P.F. Tortorelli, *Journal of Nuclear Materials,* 191-194 (1992) 965-969
5. N. Simon, A. Terlain, T. Flament, *Corrosion Science,* 43,(2001), 1041-1052
6. P.F. Tortorelli, *Fusion Engineering and Design,* 14 (1991) 335-345

USE OF (*n, xn*) REACTIONS TO ENHANCE HIGH ENERGY NEUTRON RESPONSE IN A MODIFIED BONNER SPHERE

Biju K.
Radiological Physics and Advisory Division
and
S. P. Tripathy, Sunil C. and P.K. Sarkar
Health Physics Division

This paper received the Best Poster Award at the International Symposium on Accelerator and Radiation Physics held at Saha Institute of Nuclear Physics, Kolkata during February 16-18, 2011

Abstract

Conventional Bonner spheres with metallic shells are used to enhance the response for the high energy neutrons using (n,xn) reactions. This study provides the enhancement in the neutron response using the low density metallic shells, zirconium and beryllium which has considerably good (n,2n) cross sections. The response with high density metallic shells, lead and tungsten are also studied and compared with zirconium and beryllium. The results of Zr shell over the 9 inch HDPE sphere, at higher energies, seem interesting and can be explored further for the development of low-weight spectrometer whereas Be do not show multiplication that can be used with any reasonable effect.

Introduction

Neutron dosimetric problems in high energy, high current accelerators primarily for the application of accelerator driven technologies like ADSS[1] necessitates spectrum measurement up to few hundreds of MeV or beyond. High-density polyethylene (HDPE) multisphere or Bonner sphere spectrometer using Li-6 thermo luminescence detector at the center is one among the mostly used systems in a high intensity or pulsed radiation field that takes care of the undesirable dead times or pile up effects. Response to high energy neutrons does not increase significantly even by enlarging the sphere diameter further, rather it affects the lower energy part of the spectrum due to over-moderation. Therefore, metallic shells are introduced along with the HDPE spheres to enhance the response via (n,xn) nuclear processes[2]. However, the weight of the spectrometer increases significantly with addition of these metallic shells, which sometimes limit the use of these detectors to measure the neutron field at inconvenient places.

In this work, the response is studied for low density metallic shells such as Zr and Be using Monte Carlo simulation code FLUKA[3]. These materials have considerably good (n, 2n) cross-section and, moreover, Be has much lower threshold energy (~ 3 MeV), which could open up the channel at lower neutron energy leading to enhancement in the overall response. The response with Pb and W are also studied and compared.

Monte Carlo simulations

The geometry as simulated using Monte Carlo code FLUKA is shown in Fig. 1. A parallel monoenergetic beam is made to incident normally on the Bonner sphere. The radius of the beam is kept equal to the radius of the sphere. Neutron fluence spectrum is scored using track length estimator in a sphere of radius 0.5 cm at the centre of the HDPE sphere.

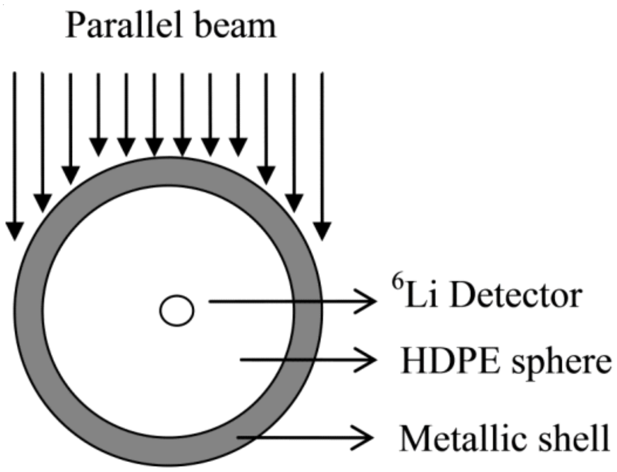

Fig.1 The simulated irradiation geometry

The ^{6}Li detector response was calculated using the formula $R=\int\phi(E)\sigma_{(n,t)}(E)dE*A$, where $\varphi(E)dE$ is the fluence (cm^{-2}) at energy between E and $E+dE$, $\sigma_{(n,t)}(E)$ is the cross section (cm^2) and A is the area of the neutron beam (cm^2).

Initially a bare HDPE sphere of 9 inch diameter is used to estimate the ^{6}Li(n,α) reaction inside the detector cell volume. Subsequently, 1 cm thick metallic hollow spherical shells of the four chosen materials were used to cover the HDPE sphere and the response was calculated again. The ratio of these two results gives the enhancement in the response.

Results, Discussion and Conclusion

The reaction cross section and the threshold energy values were obtained from the ENDF/B-VII cross section data base[4] and were analyzed to identify the elements that could be used as suitable metallic shells. Table 1 presents the density, (n, 2n) reaction cross section and the threshold energy for W, Pb, Zr, and Be.

Of these W and Pb have been well studied and are used in various configurations of extended dose monitors and Bonner spheres. Use of Zr and Be have not been reported in the literature. In the present study, the response of ^{6}Li detector is compared for these four different cover materials. Fig. 2 shows the enhancement in the response of ^{6}Li detector, for the HDPE sphere covered with a 1 cm metallic shell to that of the bare HDPE sphere, in the neutron energy range of 50 - 200 MeV.

Table 1: Useful properties for metallic shell selection

	Threshold energy (MeV)	σ(n,2n) (barn)	Density (g cm^{-3})
^{182}W	9.0	2.02	19.25
^{206}Pb	9.0	2.23	11.34
^{96}Zr	12.5	1.25	6.52
^{9}Be	3.0	0.56	1.85

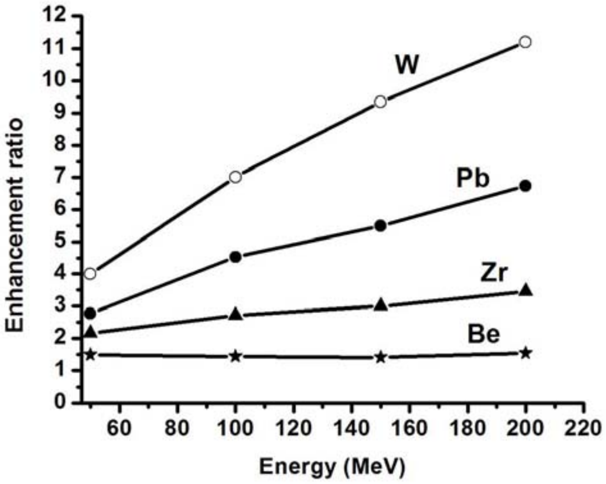

Fig. 2: The ratio of ^{6}Li response with 1 cm shell (W, Pb, Zr and Be) on a 9'' HDPE to Li-6 response with 9 inch HDPE sphere as a function of neutron energy.

From fig. 2, it is clear that W and Pb have better enhancement properties when compared to Zr and Be which is primarily due the higher density of these materials containing more number of reactions. Fig. 3 presents the enhancement of Zirconium as a function of shell thickness. At higher energies for larger thickness, say 2 cm, the enhancement ratio for Zr improves. The results for Be is

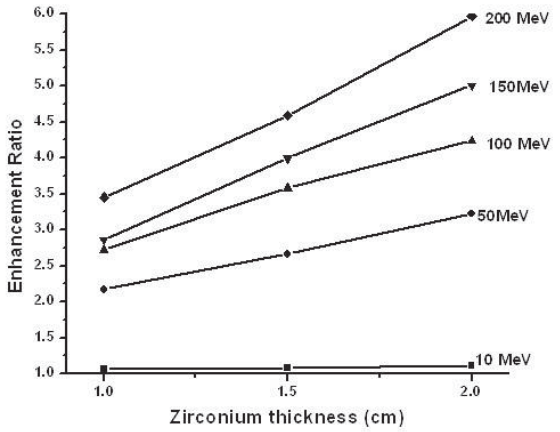

Fig. 3: The ratio of 6Li response with Zr shell on a 9'' HDPE to Li-6 response with 9 inch HDPE sphere as a function of shell thickness.

not as promising as one would expect from the lower threshold and the peak cross section. This is due to the fact that the elastic cross section constitutes 2/3 of the total cross section while the (n,2n) cross section is just 1/3. W and Pb have (n,3n) channel also opening up at higher threshold energies thereby ensuring a constant multiplication while Fermi breakup is the preferred mode in the case of Be at higher energies.

Fig.3 The ratio of 6Li response with Zr shell on a 9'' HDPE to Li-6 response with 9 inch HDPE sphere as a function of shell thickness.

The results of Zr shell over the 9 inch HDPE sphere, especially at higher energies, seem interesting and can be explored further for the development of low-weight spectrometer. However, results from Be do not show multiplication that can be used with any reasonable effect. Further studies are in progress with different detectors to optimize the enhanced response for high energy neutrons.

References

1. Sarkar P. K. Neutron dosimetry in the particle accelerator environment, Radiation measurements (2010) 1476-1483
2. Birattari C. , Ferrari A., Nuccetelli C., Pelliccioni M., Silari M., An extended range neutron rem counter, Nucl. Instrum. Meth. A 297 (1990) 250 Birattari A. Ferrari C. Nuccetelli M. Pelliccioni and M. Silari *Nucl. Inst. Meth*. A (1990) 250-257.
3. Fasso' A., Ferrari A., Ranft J. and Sala P. R., FLUKA: a multi-particle transport code, CERN-2005-10. INFN/TC_05/11, SLAC-R-773 (2005).
4. http://www.nndc.bnl.gov/, (last accessed 21 October 2010)

ELUCIDATION OF MOLECULAR MECHANISM OF RADIOPROTECTION EXHIBITED BY BAICALEIN

R.S. Patwardhan, Rahul Checker, Deepak Sharma,
Santosh Kumar Sandur and T.P.A. Devasagayam
Radiation Biology & Health Sciences Division

This paper received the Best Poster Award, at the International Conference on Recent Trends in Therapeutic Advancement of Free Radical Science, and 10th Annual Meeting of the Society for Free Radical Research, Chennai, January 9-11, 2011.

Abstract

Baicalein, a naturally occurring flavone, present in certain Indian and Chinese medicinal plants has been reported to exhibit antioxidant and anti-inflammatory effects. Experiments were carried out to evaluate its radioprotective efficacy using murine lymphocytes. Baicalein offered concentration dependent protection to murine splenic lymphocytes against radiation (4Gy) induced apoptosis. Mechanistic studies revealed that, radioprotective effects of baicalein were independent of modulation of cellular redox status. It activated cellular pro-survival signaling molecules like ERK, Nrf-2 and NF-κB. Based on these results we propose that ERK/Nrf-2/NF-κB may be responsible for radioprotective action of baicalein.

Introduction

Radiotherapy is the most common treatment modality for cancer patients. Often the dose that can be delivered to tumor tissue for treatment is limited by the sensitivity of surrounding normal tissue [1]. This affects the overall outcome of radiotherapy, since doses above threshold tolerance of normal tissue lead to tissue injury. In order to achieve better tumor cell killing larger doses need to be delivered to tumor tissue without affecting normal tissue. This may be possible using radioprotectors in clinical radiotherapy [2]. Exposure to ionizing radiation (IR) induces ROS (reactive oxygen species) inside cells. About 75% of the damage to the critical biomolecules inside cells caused by IR has been attributed to ROS. This fact has driven researchers in this area to focus their attention on search of molecules that are capable of scavenging radiation derived free radicals.

Further, apart from cellular effects of ionizing radiation, there are dose-dependent and system-specific effects of ionizing radiation in living organisms. Exposure to doses >2Gy induces hematopoietic syndrome which leads to weakened immunity and higher susceptibility tofatal infections leading to radiation induced mortality [3]. These effects motivated scientists to focus on search for molecules that can specifically protect hematopoietic stem cells from radiation. Therefore, hematological targets of radiation damage are of great significance for radiation oncology and protection against normal tissue injury. Till now researchers have employed a number different strategies in the search for radioprotectors which include, compounds that scavenge ROS [4], upregulate antioxidant enzymes, upregulate pro-survival molecules viz. NF-κB [5], inhibit p53, induce cell cycle arrest [6] etc. Despite several years of research there is no syndrome specific radioprotector available for human consumption. Hence, there is a need to develop a radioprotector that would stand the scrutiny for the desired application.

Recent report from our laboratory has revealed that a pro-oxidant could ameliorate radiation induced cell death via upregulation of Nrf-2 pathway [7]. There are reports of wide array of dietary phytochemicals that can upregulate this redox sensitive transcription factor. Nrf-2 is a master regulator of antioxidant defense machinery and is critical for cell survival under conditions of oxidative stress. Hence, phytochemicals that can upregulate this molecule can be investigated for their radioprotective potential.

Baicalein is 5, 6, 7 tri-hydroxy flavone obtained from the dried roots of a herb *Scutellaria baicalensis Georgi.* It has been reported to be a potent antioxidant in cell free and cellular system. It has been reported to exhibit anticancer,

Table 1: Radioprotective effects of Baicalein in lymphocytes and its mechanism of action

Activity	Baicalein Treatment	Radiation expousre	End points	Results
Protection of lymphocytes against ionizing radiation	Cells pre-incubated with 5µM to 100µM baicalein	Exposed to 4Gy IR	Analyzed for apoptosis by PI staining and flow cytometric analysis	Offered complete radioprotection at 100µM.
Modulation of apoptotic machinery and ROS	Cells pre-incubated with 5µM to 100µM baicalein		Cellular redox status and anti-apoptotic genes	Altered cellular redox and upregulated bcl-2.
Effect of baicalein on irradiated human T cell lymphoma	Cells pre-incubated with 5µM to 100µM baicalein	Exposed to 4Gy IR	Analyzed for apoptosis by flow cytometry	Did not offer radioprotection to lymphoma cells.
Induction of ERK pathway	Cells pre-incubated with pharmacologic inhibitors of ERK or JNK or P38 or mTOR or Nrf-2 and then with 100µM baicalein	Exposed to 4Gy IR	Analyzed for apoptosis by flow cytometry	Did not offer radioprotection in presence of inhibitors of ERK or Nrf-2.
Modulation of pro-survival pathways like Nrf2, Erk and NF- κB	Cells pre-incubated with 100µM baicalein for different time intervals (30, 60, 180 min).		Detection of intracellular proteins by flow cytometry and western blotting.	Induced phosphorylation of ERK, its upstream kinase MEK and downstream kinase p90RSK in a time dependent manner.
Effect on Nrf-2	Cells pre-incubated with 100µM baicalein for different time intervals (6, 12, 24h).		Nuclear levels of Nrf-2 were measured by EMSA and western blotting.	Induced nuclear translocation of Nrf-2.
Effect on NF-κB	Cells pre-incubated with 100µM baicalein for different time intervals (6, 12, 24h).		Nuclear levels of NFκB were measured by EMSA.	Induced nuclear translocation of NF-κB.
Mechanism of Nrf-2 and NF-κB activation	Cells pre-incubated with ERK inhibitor prior to incubation with100µM baicalein.		Nuclear levels of NFκB and Nrf-2 were measured by EMSA.	Baicalein induced nuclear translocation of Nrf-2 and NF-κB was suppressed by ERK inhibitor.
Analysis of Nrf-2 dependent gene expression	Cells pre-incubated with 100µM baicalein for different time intervals (6, 12, 24h).		mRNA levels of catalase, GCLC, Mn-SOD and HO-1 were measured by real time PCR.	Induced time dependent increase in gene expression of Nrf-2 dependent genes.

anti-apoptotic, anti-mutagenic, anti-microbial and anti-proliferative properties in different cell types. We tested this molecule for its ability to offer radioprotection in murine splenic lymphocytes. Lymphocytes are the most sensitive cell types in the body to radiation induced cell death. Radiation exposure above >2Gy induces leucopenia. Hence, in the present study we used this model system to test the ability of baicalein to protect against ionizing radiation induced cell death and elucidate the underlying molecular mechanisms. Our study has revealed that, baicalein protected murine splenic lymphocytes against radiation induced cell death.

Results: The experimental models, end points and salient observations are described in Table 1.

- Baicalein offered complete radioprotection to murine splenic lymphocytes at 100µM against ionizing radiation (4Gy) induced apoptosis in vitro.
- It inhibited radiation induced activation of apoptotic machinery in lymphocytes.
- It did not protect tumor cells against radiation induced cell death.
- Baicalein mediated radioprotection is not via alteration of cellular redox.
- ERK and NRf-2 inhibitors completely abrogated baicalein mediated radioprotection.
- Baicalein induced time dependent phosphorylation of ERK, its upstream kinase MEK and downstream kinase p90RSK.
- Baicalein induced nuclear translocation of redox sensitive transcription factor Nrf-2 and pro-survival transcription factor NF-kB.
- Expression of antioxidant enzyme genes viz. catalase, Mn-SOD, GCLC increased in a time dependent manner after incubation of lymphocytes with baicalein.
- Thus, baicalein offered complete radioprotection to murine splenic lymphocytes via upregulation of ERK and Nrf-2 pathway.

Conclusions

Our results demonstrated that baicalein ameliorated radiation induced cell death in lymphocytes through upregulation of ERK-Nrf-2 pathway. This molecule showed good promise to be tested in animal models for radioprotection.

References

1. Greenberger JS. Radioprotection. *In Vivo* 2009;23:323-336.
2. Henni M, Ali D. [Radiation induced side effects]. *Rev Prat*;62:461-466.
3. Prise KM, Saran A. Concise review: stem cell effects in radiation risk. *Stem Cells*;29:1315-1321.
4. Li H, Wang Y, Pazhanisamy SK, *et al.* Mn(III) meso-tetrakis-(N-ethylpyridinium-2-yl) porphyrin mitigates total body irradiation-induced long-term bone marrow suppression. *Free Radic Biol Med*;51:30-37.
5. Burdelya LG, Krivokrysenko VI, Tallant TC, *et al.* An agonist of toll-like receptor 5 has radioprotective activity in mouse and primate models. *Science* 2008;320:226-230.
6. Johnson SM, Torrice CD, Bell JF, *et al.* Mitigation of hematologic radiation toxicity in mice through pharmacological quiescence induced by CDK4/6 inhibition. *J Clin Invest*;120:2528-2536.
7. Khan NM, Sandur SK, Checker R, *et al.* Pro- oxidants ameliorate radiation-induced apoptosis through activation of the calcium-ERK1/2-Nrf2 pathway. *Free Radic Biol Med*;51:115-128.

MEASUREMENT OF COSMIC RAY DOSE IN ANTARCTIC REGION USING SOLID STATE DETECTORS

Rupali Pal, A.K.Bakshi, R. Chilkulwar, M.P.Chougaonkar and Y.S.Mayya
Radiological Physics and Advisory Division

This paper received the Best Poster Award at the Conference on Accelerator Radiation Safety (CARS 2011) held at BARC, Mumbai during November 16-18, 2011

Abstract

In the present study the background radiation dose rate around the Indian base at Antartica named 'Maitri' was measured by TLDs and CR-39 neutron dosimeters. Gamma components were measured using TLDs whereas CR-39s were used for neutron measurements. CR-39 detectors were deployed at 14 locations for two and a half months. The detectors used in the study were calibrated using the simulated cosmic ray spectra at CERN high energy reference field (CERF), Geneva. The average neutron dose rate based on CR-39 was found to about 10.4 nSv h^{-1} which is close to the value 11 nSv h^{-1} reported by UNSCEAR at the poles. The gamma dose rate evaluated by TLDs was found to be 32 nSv h^{-1}.

Introduction

Galactic Cosmic Rays (GCR) incident on the top of the atmosphere consist of 98% nucleonic component and 2% electrons. The nucleonic component is primarily protons (85.5% of the flux) and alpha particles (12%), with the remainder heavier nuclei (1%). These primary cosmic particles have an energy spectrum that extends from 10^8 eV to more than 10^{20} eV. The nucleonic component produced after the interaction of GCR with atmosphere consists of nuclear fragments, mainly neutrons and protons[1].

Another component of cosmic rays is generated near the surface of the sun by magnetic disturbances. These solar particle events are comprised mostly of protons of energies generally below 100 MeV. These particles can produce significant dose rates at high altitudes, but only the most energetic (greater than 100 MeV) affect dose rates at ground level[1].

Geomagnetic effect

Charged particle such as protons, pions etc. from distant stars and sun interact with the magnetic field of the Earth and are deflected. Incoming protons that initiate the cosmic ray neutron field are strongly affected by the Earth's magnetic field resulting with minimum intensities and dose rates at the equator and maximum near the geomagnetic poles.

Neutron contribution to cosmic radiation dose

Due to the nucleonic cascade in the atmosphere, the neutron energy distribution of the cosmic ray shows three broad peaks, a high energy peak at 100 MeV and extending upto 10 GeV, a "nuclear evaporation" peak centered around 1 or 2 MeV, and thermal peak[2].

The dose rates due to cosmic radiation are highest close to the geomagnetic poles, due to orientation of the magnetic field lines of earth at these regions. For example, European Program Package for the Calculation of Aviation Route Doses (EPCARD) code predicts an effective dose rate of only about 2 μSv h^{-1} close to the equator, while it predicts as much as about 7 μSv h^{-1} close to the North Pole, at a flight altitude of about 10,000 m and during solar minimum[3]

Florek et al using the Los Alamos LAHET code system calculated that the equatorial neutron fluence rate at sea level is 20% of the polar fluence rate whereas at 50° latitude, it is 80% of polar fluence rate[4].

In view of the above discussion, it is clear that the ambient dose equivalent [H*(10)] due to cosmic rays at poles will be higher than equator. In the present study, ambient dose equivalent due to cosmic ray background in and around the Indian Station Maitri, Antarctica was carried out and results on the same is reported in this paper,

Material and methods

Gamma detectors

The measurement of gamma component of cosmic rays was done using $CaSO_4$:Dy Teflon thermoluminescent disc[5]. The Dy concentration in the $CaSO_4$:Dy phosphor is 0.05mol%. The TLDs were packed in polythene pouches and further inside a 2 mm thick aluminium box. Three sets of TLDs were deployed around the Maitri Laboratory at Dossier point, Maitri camp and Vitayya Mountains. The readout of the TL discs was carried out in India 15 days after irradiation to Antarctica on a Harshaw 3500 TL disc reader. Heating rate of 5°C/s was used for readout of TL discs. Integrated TL output from 50 to 300 °C for $CaSO_4$:Dy disc was used for the evaluation of the response of TLDs. It may be noted that N_2 was flushed continuously during the readout of TLDs. A set of three TLDs was kept for background TL signal at our laboratory in India and TL corresponding to these background TLDs was always subtracted from the actual signal before determining the TL response.

Neutron detectors

CR-39 detectors of dimensions 3 cm x 3cm x 0.0625 cm, with a 1 mm thick polyethylene radiator of similar dimension in front, is sealed together in an air tight triple laminated aluminized pouch which served as a neutron detector. The CR-39 detectors used were of dosimetric grade, with 32 h curing cycle, manufactured by M/s Pershore Moulding, U.K. The aluminized pouch protects the detector from ambient conditions, makes the detector dust free during handling and prevents entry of atmospheric radon/alpha particles which may produce tracks in the detector. The neutron detectors were deployed at various locations around the Indian station 'Maitri' at Antarctica for two and half months. A representative photograph of the arrangement of dosimeter deployment at one of the location is shown in Fig.1. The neutron detectors received after irradiation were electro-chemically etched using 7N KOH in an electro-chemical cell at 60 °C in an incubator in two step Electro-Chemical Etching (ECE) method (i) low frequency of 100 Hz for 4 h (ii) High Frequency of 3.5 kHz for 40 min at constant applied voltage of 1400 V A.C. The nuclear tracks developed in the detector were counted on an image analysis system. The control for these detectors was kept at the laboratory in Mumbai. The net tracks (after subtraction from control tracks) were evaluated and appropriate calibration factor was applied to estimate cosmic neutron doses.

Fig.1: Photograph of TLD and CR-39 dosimeters deployed at Antarctica at a height of 1 m from the surface with a closer view on the left side.

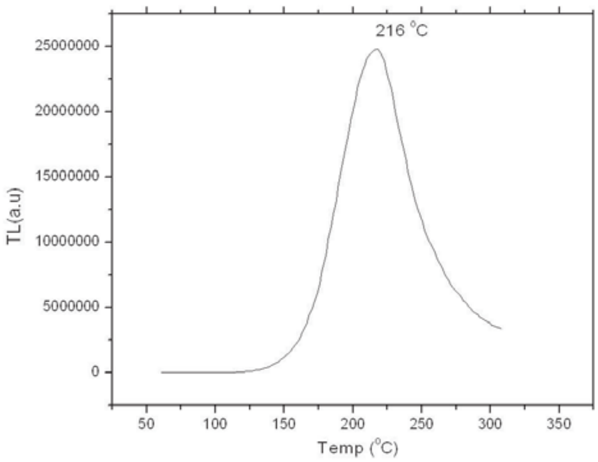

Fig. 2: Glow curve of $CaSO_4$:Dy Teflon TL disc to Cosmic rays

Calibration of the detectors

Neutron detectors were calibrated at high energy reference field (CERF) facility, CERN, Switzerland which simulates cosmic ray spectrum at aircraft altitudes with a mean neutron energy of 70 MeV[6]. The TL detectors were irradiated to 16.70 mSv of dose equivalent at the S1 position (outside the side concrete shield) of CERF facility and CR-39 were irradiated at T1 and T2 positions (top concrete wall) for 3 and 5 mSv respectively. Their response was evaluated and the calibration factor for TLDs was calculated to be 38.18 μSv/TL and that of CR-39 was 0.045 mSv-cm^{2}tracks^{-1} and cosmic neutron dose is found to double for every 1830 m of increased altitude[1]. Thus, using the relation, the neutron fluence is found to be 64 times more at aircraft altitude than at sea level. Therefore, the calibration factor derived from CERF experiment was modified to arrive at a calibration factor for sea level, which is 0.00071 mSv-cm^{2}tracks^{-1} for CR-39 and 0.596 μSv/TL for TLDs. The details on the calculation of response factor of the TLDs and CR-39 to simulated cosmic rays at CERF will be discussed in a separate paper.

Results and discussion

A representative glow curve of CaSO$_4$:Dy Teflon disc irradiated to cosmic rays at Antarctica is shown in figure 2. It shows a peak at around 216°C in the temperature range used for recording the glow curve. The cosmic gamma and neutron dose rates estimated in Antarctica are presented in Table-1.

The dose equivalent rate due to gamma component of cosmic rays estimated by CaSO$_4$:Dy based TLDs were found to be in the range of 24-40 nSv h^{-1} estimated with altitude correction factor. The average cosmic gamma dose rate measured in the present study is 32 nSv h^{-1}. The values of gamma dose equivalent rate measured in the present study agree reasonably well with that of measured by Nambi et al(7).

It has been observed that the neutron dose rate evaluated by applying calibration factor from CERF (at aircraft altitude) directly come in the range of 283-1334nSv h^{-1} in the various locations which is an overestimation. Hence, it was essential to bring the values to sea-level by applying altitude correction factor. The average cosmic neutron dose has been found in the present study is 10.4nSv h^{-1}.

Table 1: Dose rate measurement with CR-39 detectors and TLDs in Antarctica along with respective locations and elevation.

Locations	Elevation (m)	Gamma Dose (nSv h^{-1})	Neutron Dose (nSv h^{-1})
1. Maitri Summer Camp	175	32	17
2. Dossier point	180	24	12
3. Between Shiva Linga mountain & Dossier Pt.	185	—	0
4. Vitayya Mountains	290	40	4.9
5. Near Sankalp	385	—	9.1
6. Between Sankalp & Russian Junction	430	—	4.5
7. Near Russian Junction	464	—	7.5
8. Near Novo Airport	511	—	21
9. White Dessert Area	204	—	14
10. Priyadarshini lake	134	—	14
11. Novo side Priyadarshini lake	126	—	7.5
12. Shirmacher hills shelf ice	154	-	9
13. Shirmacher hills near workshop	130	—	9
14. Living room at Maitri station	175	—	16
Average Dose (nSv h^{-1})		32 ±8	10.4 ±5.6

It is also interesting to note that the highest dose of 21nSv h^{-1} recorded by CR-39 coincides with highest point of elevation at 511 m above sea-level which is Novo Airport. However, the correlation is not seen at all the points. The neutron interactions are complex. Further studies are required for such a correlation.

Conclusions

Background radiation level due to cosmic rays was measured in and around Maitri station, Antarctica using CR-39 and TLDs. The average gamma dose equivalent rate was found to be 32 nSv h^{-1} and average neutron dose equivalent rate was 10.4 nSv h^{-1}. There is good agreement between the cosmic dose rates evaluated in this study with that reported in the literature.

Acknowledgement

The authors wish to acknowledge Dr. A. K. Ghosh, Director, HS&E Group and Dr.D.N.Sharma, Associate Director, HS&E Group for his interest and encouragement in this work.

References

1. UNSCEAR 2008, Volume 1 Annex B, Exposures of the public and workers from various sources of radiation (2010).
2. Gordon M.S, Goldhagen P., Rodbell K.P. et al "Measurement of the flux and energy spectrum of cosmic ray induced neutrons on the ground." IEEE transactions on Nuclear science Vol 51 No.6 (2004), 3427-3433.
3. Mares, V., Maczka, T., Leuthold, G. and Ru¨hm, W. Air crew dosimetry with the new EPCARD.Net code, Radiat. Prot. Dosimetry, Vol. 136, No. 4(2009), 262-266.
4. Florek M, Masarik J, Szarka I, Nikodemova D and Hrabovcova A, Natural neutron fluence rate and the equivalent dose in localities with different elevation and latitude, *Radiat. Protect. Dosim*, Vol.67 , No. 3, (1996) 187-192, .
5. Vohra, K. G., Bhatt, R. C., Bhuwan, C.,Pradhan, A. S., Laxamanan, A. R. and Shastry, S. S, .A Personnel dosemeter TLD badge based on CaSO4:DyTeflon TLD discs., *Health Phys.* 38, (1980),193-197.
6. A. Mitaroff and m. Silari The CERN–EU high-energy reference field (CERF) Facility for dosimetry at commercial flight altitudes and in space. *Radiation protection dosimetry* Vol. 102, no. 1(2002), pp. 7–22.
7. Nambi K S V, Chougaonkar M P and Ramchandran T V, TLD Measurements of Background Radiation Levels in Antarctica - (Letter to the Editor) *Radiat. Protect. Dosim,* Vol.58, No. 1, (1995) 71.

LOW ENERGY PULSED X-RAY ION CHAMBER MONITOR FOR ACCELERATOR SAFETY

P.M. Dighe, L.P. Kamble, D. Das and C.K. Pithawa
Electronics Division

This paper received the Best Presentation Award in the Conference on Accelerator Radiation Safety held at Bhabha Atomic Research Centre, Trombay during November 16-18, 2011

Abstract

Ion chamber sensitive to low energy pulsed X-rays has been developed for area monitoring at the electron accelerators Indus 1 and 2 of Raja Ramanna Centre for Advanced Technology, Indore. Conventional monitors available commercially underestimate the X-ray background because of pulsed nature of the radiation and are not sensitive to X-rays below 100 keV. For this purpose, a high pressure ion chamber made of aluminium with all welded construction has been developed and tested for use in pulsed X-ray background. The chamber has 25 litre sensitive volume, filled with nitrogen at 85 psi and current sensitivity is 12 nA/R/h. The chamber can measure exposure levels from 20 μR/h to 100 mR/h and has uniform energy response within ±12% from 35 keV to 1.25 MeV of X-ray energy. The ion chamber gave more than 86% collection efficiency at 100 mR/h average pulsed X-ray background for 500V operating voltage. Theoretically evaluated collection efficiency values closely match with the experimentally observed values. The design details and characterisation of the ion chamber under different X-ray energy exposures and collection efficiency estimation for pulsed X-ray background have been studied.

Keywords: Ion chamber, Pulsed X-ray, Electron accelerator, Area monitoring

Introduction

Pulsed X-rays of small duty factor are produced in the vicinity of electron accelerators due to scattering of electrons by the molecules of the residual gas in the vacuum chambers of accelerators which are the main constituents of background radiations around electron accelerators and need to be monitored for personnel safety. Instruments that ordinarily respond well to the continuous radiation, fail to work in pulsed radiation because of high peak dose rate delivered during the pulse exposure. Detectors that have dead time problem such as GM counters saturate in pulsed fields and measure one count per pulse irrespective of dose. Ion chambers[1] are most suitable, common and convenient method of on-line radiation area monitoring in continuous as well as in pulsed radiation since they are simple in design, works on average current measurement mode.These are mechanically rugged, have long life and good linearity in signal over a broad range. The Indus-1 and Indus-2 electron accelerator facilities of Raja Ramanna Centre for Advanced Technology, Indore require area monitors in the working areas. X-ray radiation suffers multiple scattering in the labyrinths and the shielding walls due to which the energy in the working area can be well below 100 keV. It has been reported that the transmitted photon-energy spectrum[2] produced by 20 MeV electrons measured at 0° from intermediate thickness target peaks around 80-140keV, while it is suppressed at energies higher than 1-2 MeV. Therefore, for this requirement a special kind of detector is required which is sensitive to low energy X-rays as well as can work with good efficiency in pulsed X-ray background. The present paper describes the development and testing of high pressure ion chamber which can monitor environmental level background radiation and is sensitive to low energy X-rays.

Design

The design criterion of ion chamber is as follows: From the definition of Roentgen per hour, one cc of air produces one esu of charge per hour which is equal to 2.08×10^{9} ion pairs/R/hr or 3.33×10^{-10} Coulombs/hr.This corresponds to 0.93×10^{-13} A/R/h. From this definition,an ion chamber was developed with 25 litre sensitive volume, and filled with nitrogen gas at 85 psi pressure to make it sensitive to environmental gamma background with gamma sensitivity of 0.12 pA/10µR/h. Nitrogen gas is selected to get good electronic equilibrium condition between the chamber aluminium walls and the fill gas. Two mm thick aluminium outer wall gives 91 % transmission to 100 keV X-rays. Fig. 1 shows the schematic of the ion chamber. Table 1 presents the main specifications of the ion chamber. The electrodes were designed to provide uniform electric field within the sensitive volume with the help of guard rings. The uniformity in the electric field ensures signal linearity up to 100 mR/h X-ray radiation. The use of an electrically grounded outer envelope and separate sets of insulators for the two electrodes ensures safety of operation. Great care is being taken during construction of the chamber to maintain insulation resistance between the electrodes more than 10^{15}ohms at 1kV *dc* to have minimum leakage current in the detector so that better signal to noise ratio is achieved. The leakage current was checked in specially erected lead vault of 70 mm thickness to reduce the effect of environmental background radiation. In the lead vault, the ion chamber reading dropped from ambient radiation level of 12 µR/h to 2 µR/h showing that it can monitor environmental radiation level with good accuracy. The chamber has all welded construction which imparts long life to the detector. The all welded configuration became feasible with the use of special SS to Al explosion welded composite plates obtained from the Explosives Research and Development Laboratories (ERDL), Pune, India, as shown in Fig. 2. All the weld joints have been subjected to pneumatic pressure tests and helium leak tests up to 10^{-9}std. cc/sec to ensure the integrity of construction. The ion chamber was also subjected to long term stability tests for a period of 20 days and the signal was stable within ±5%.

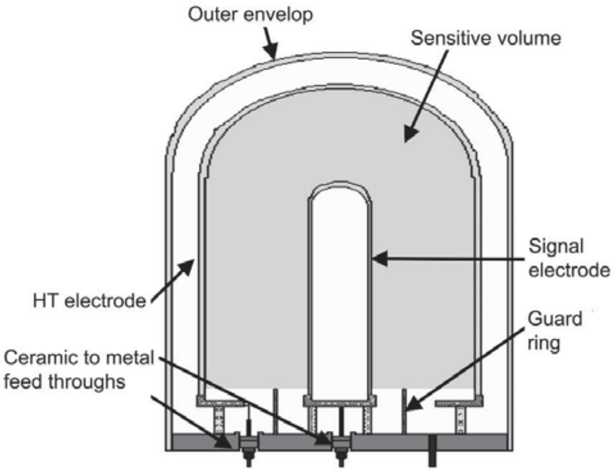

Fig.1: Schematic diagram of low energy ion chamber

Table 1: Main specifications of the low energy ion chamber

Material	Al
Outer housing	320 mm dia X 560 mm ht
Electrode dia	280 mm ht & 80 mm dia
Spacing between the HT and signal electrode	100 mm
Sensitive volume	25 ltr
Gas	Nitrogen
Gas pressure	6 bar
Sensitivity	12 pA/mR/h
Measuring range	20 µR/h-100 mR/h

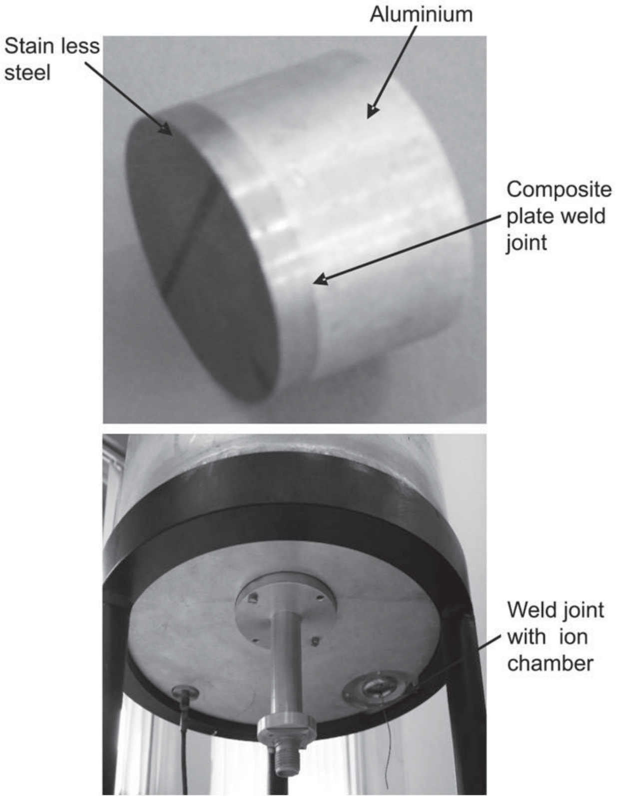

Fig. 2: Photo of SS-Al clad plate and the weld joint

Test and Results

The ion chamber was tested with Co-60 sources of various strengths for different radiation levels using Keithley electrometer to measure current and the current versus voltage curves are shown in Fig. 3. Current sensitivity of the ion chamber is estimated as 12pA/mR/h for Co-60 gamma source for the saturated current value.

Better uniformity in the signal with respect to X-ray energy is achieved in this chamber by filling it with nitrogen instead of argon since the mass attenuation factor of nitrogen and aluminium is similar at lower energies and hence, it gives good electronic equilibrium. With gamma sources energy varying from 35keV (I-125), 60 keV (Am-241), 660 keV (Cs-137), 800 keV (Ra-226) to 1.25MeV (Co-60), ±12% variation in the gamma sensitivity was observed (Fig. 4).

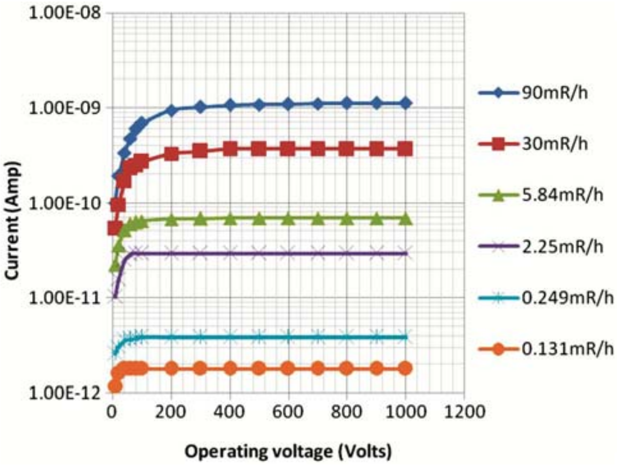

Fig. 3: *V* versus *I* characteristics of low energy ion chamber in continuous radiation

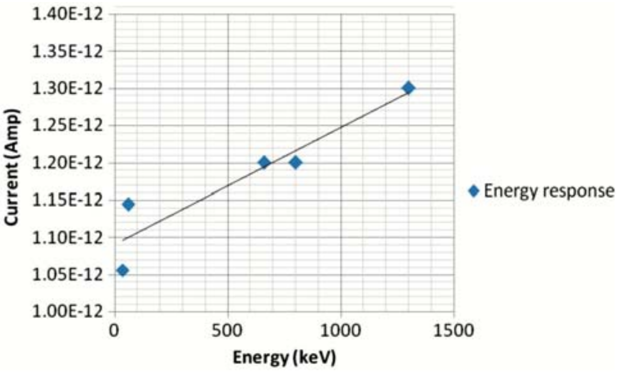

Fig.4: Energy response of low energy ion chamber

The ion chamber was tested for its performance in pulsed radiation in the occupied areas and also in some places where normally people are not permitted at work (outside the shield and inside the labyrinths) at the INDUS-I facility during normal operation and during complete beam loss conditions to cover wider range of X-ray exposure. Since the current produced by the ion chamber in pulsed radiation is also pulsing in nature, the Keithley electrometer, which is normally used for low *dc* current measurements, was also observed to be pulsing. Therefore, measurements were done by a specially designed current electrometer at Electronics Division^3. Before testing the instrument for pulsed radiation, the ion chambers and the monitor were calibrated with a continuous gamma ^{60}Co source of average gamma energy 1.25 MeV. The current measured values by the instrument were identical to the current values measured by Keithley electrometer.

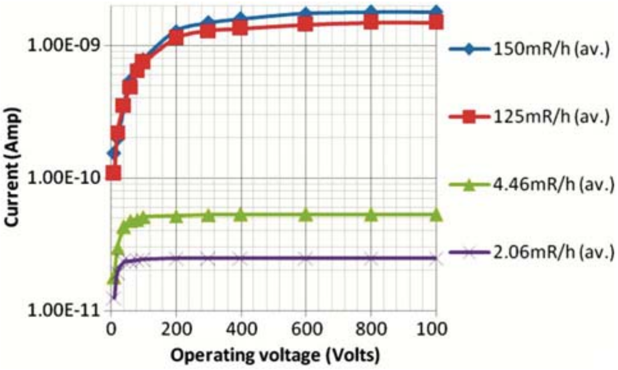

Fig. 5: *V* versus *I* characteristics of low energy ion chamber in pulsed radiation

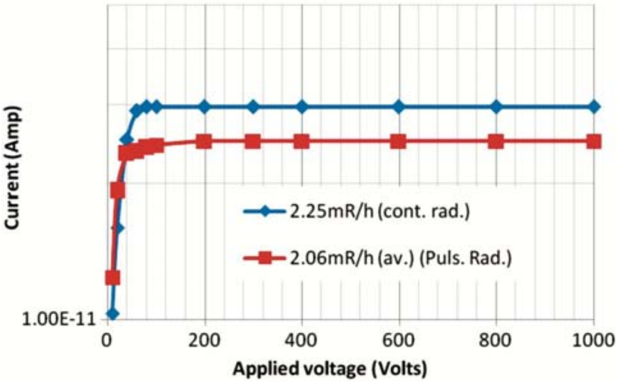

Fig. 6: Comparative *V* versus *I* curves in continuous and pulsed radiation

In pulsed radiation, the *V* versus *I* curves were plotted as shown in Fig. 5. The radiation exposure levels were estimated by taking the ratio of saturated current value and the chamber sensitivity for continuous radiation since at saturated current value the total collected charge is the primary charge generated in the chamber and corresponds to Roentgen value. The saturation curves are similar to those taken in continuous radiation. Fig. 6 shows the *V-I* curve in 2.25 mR/h in continuous radiation and 2.06 mR/h (av.) in pulsed radiation. It was observed that the voltage required to reach saturation current is the same as continuous radiation. For the average radiation background of 150mR/h $V_{0.9}$ equals 400V.

To ensure that there are no recombination losses and the measured exposure is not underestimated due to duty factor of the pulsed radiation the collection efficiency *f* of the chamber in pulsed radiation was estimated theoretically. The collection efficiency *f* is the ratio between the signal current and the saturation current. This depends on the gas-fill, electrode geometry, applied voltage and exposure rate and is estimated as follows[4].

$f = (1/u) \ln (1 + u)$ Here $u = \mu r d^2/V$

where μ is constant and given as $\alpha e/(k_1 + k_2)$, k_1, k_2 are ionic mobilities ($cm^2 s^{-1} V^{-1}$), *r* is the charge density (esu/cm^3) liberated per pulse and is given as $n_0 e$, *e* is electronic charge and *V* is the applied voltage and *d* is equivalent electrode spacing. Fig. 7 shows the solution of *u* of equation by numerical analysis as a function of collection efficiency. From the graph, we can see that to obtain 90% collection efficiency in an ion chamber in pulsed radiation the value of *u* should be less than 0.2. Table 2 presents the estimated collection efficiency of ion chamber. The chamber shows more than 86% collection efficiency at 100mR/h average pulsed X-ray background for 500 V operating voltage. At 90 mR/h continuous radiation the chamber showed 91% collection efficiency at 300 V. Therefore, it was concluded that the collection efficiency values for continuous and pulsed radiation compare well at low radiation level.

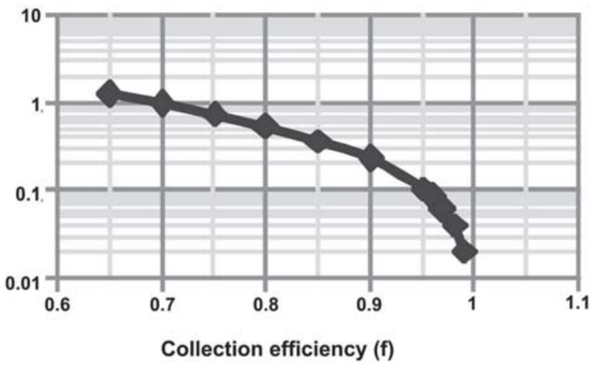

Fig. 7: Collection efficiency versus u

Table 2: Estimated collection efficiency of low energy ion chamber for pulsed radiation

Avg. background	300V	500V	800V	1000V
100mR/h	0.79	0.86	0.90	0.92
50mR/h	0.88	0.92	0.95	0.96
1mR/h	0.997	0.998	0.999	0.999
0.1mR/h	0.9997	0.9998	0.9999	0.9999

Conclusions

The results have shown that the ion chamber developed is capable of carrying out area monitoring tasks in pulsed X-ray background in the working area efficiently. The special explosion welded composite plates imparted long and reliable operation life to the detector.

Acknowledgement

The authors express their thanks to Mr R G Marathe, Mr. K.K. Thakker and Mr. G. Haridas for helping with the experiments at RRCAT, Indore.

References

1. Shambon, A, *Ionization chambers for environmental radiation measurements*, *USAEC Report, HASL*-108 (1963)
2. O'dell A A, Jr Sandifer C W, Knowlen R B & George W D, *Nucl. Instrum & Meth*, 61 (1968) 340.
3. Dighe Priyamvada M & Jakati R K, *Physics Research A,* 578 (2007) 246.
4. Boag J W, *Radiation Dosimetry*, Ed F H Attix & Roesch W C. *Vol.II, Ch.9, Academic Press,* New York (1966).

USE OF MOBILE ROBOTS FOR MAPPING RADIATION FIELD

Sanjeev Sharma, Vikrant Agashe and Prabir K. Pal
Division of Remote Handling & Robotics

This Paper received the Best Presentation Award at the Conference on Accelerator Radiation Safety held at Bhabha Atomic Research Centre during November 16-18, 2011

Abstract

It is a regular requirement in the nuclear industry to locate and assess the radioactivity during maintenance operations, decontamination of areas with radiological spill, and emergency response to unplanned events. Traditionally, field technicians have used hand-held survey meters for such operations with some risk of radiation exposure. This paper describes the development of mobile robots equipped with onboard radiation detectors for mapping such radiation fields. One such robot (ARMER-I), designed and developed by us in consultation with Radiation Safety System Division (RSSD), has a telescopic arm fitted with a light and small GM tube. This can be controlled remotely, and is very useful in remote measurement of radiation from locations, which are difficult to reach otherwise. Another mobile robot (ARMER-II) is a portable mobile robot for identifying locations with radiation levels higher than permissible limits. One more version (ASHWA) has been successfully adapted by VECC, Kolkata, for gamma and neutron radiation profiling in the cyclotron vault area.

Introduction

The urgency to build a mobile robot is felt whenever we confront a situation that requires a human being to be sent to investigate the nature, degree and cause of radiation. The single most important reason why we need robots is that they can be deployed in such situations to reduce harmful exposure of radiation to humans. The robots in these cases are tele-operated from a safe distance [1].

Mobile robots usually have two drive wheels and one castor [2], where steering is realized through differential motion of the drive wheels. Typically, onboard microcontrollers control the motion of mobile robot based on the commands received from remote station. To convert these mobile robots into useful tools for measuring radiation, onboard electronics is integrated and interfaced with radiation detectors. In addition, it may be required to redesign mobile robot by adding telescopic arm for flexibility or fixing the detector at certain height.

This paper describes the development of indigenous mobile robots, including a specially developed mobile robot for Cyclotron [3]. Following subsections of the paper describes the development of different variants of mobile robots developed at Bhabha Atomic Research Centre, Mumbai for remote measurement of radiation.

ARMER-I

This unique mobile robot has been primarily designed and developed for measuring radiation from places that are difficult to reach (Fig. 1).

Fig.1: ARMER-I, Mobile robot with telescopic arm for monitoring radiation

The major sub-systems of this mobile robot are motor controller, supervisor controller, wireless adaptor and GM tubes (Fig.2). The mobile robot and its telescopic arm are controlled remotely through graphical user interface. For giving the real time feedback of the radioactive environment, radiation values along with mobile robot position are displayed online.

Table 1: Sensitivity and range of GM tubes used in ARMER-I

Radiation Sensor	Sensitivity	Range
GM Tube #1	0.2 (counts/sec per μR/hr)	1 μR/hr to 10 mR/hr
GM Tube #2	300 (counts/sec per R/hr)	10 mR/hr to 2000 R/hr

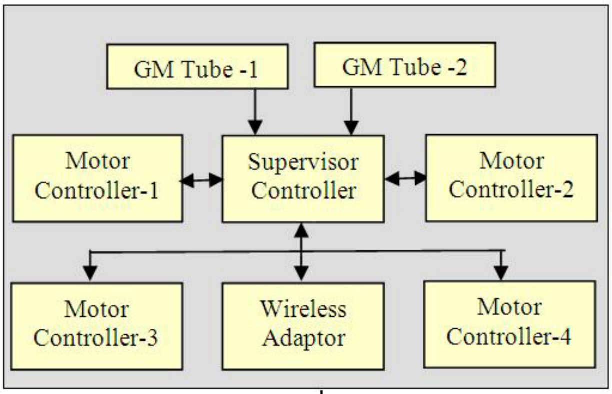

Fig.2: Schematic diagram of the control system for ARMER-I

One of the significant features of this mobile robot is integration of two GM tubes (Table 1). The first GM tube is mounted on telescopic arm tip and can be extended up to three feet. This arm can also be swiveled by +/- 15 degrees. The second GM tube is mounted along with onboard control electronics, and is more sensitive though having less range. This combination is very useful in covering the wide range of radiation.

ARMER-II

ARMER-II (Fig. 3) represents new generation of portable mobile robot designed for searching radioactive sources.

Main objective of this system is to guide the mobile robot towards direction where gradient of intensity of radiation is steepest, which is indicated by blinking arrow in the operator console (Fig. 4). This helps the operator to tele-operate the mobile robot for converging towards radioactive source during the search operation.

Fig.3: ARMER-II, Mobile robot for searching radioactive sources

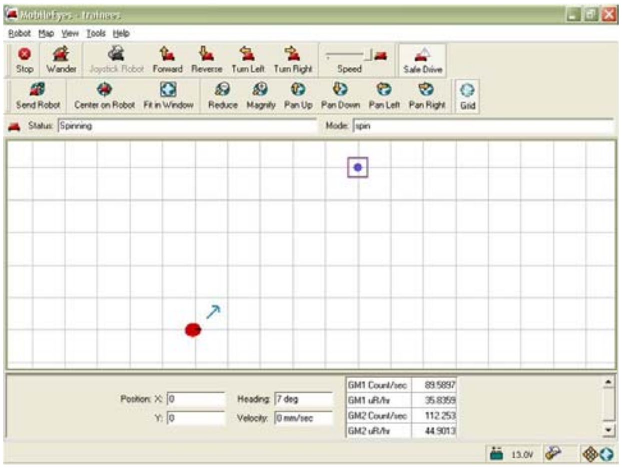

Status: Spinning
Mode: spin

Position: X: 0
Y: 0
Heading: 7 deg
Velocity: 0 mm/sec

GM1 Count/sec	89.5897
GM1 uR/hr	35.8359
GM2 Count/sec	112.253
GM2 uR/hr	44.9013

Fig.4: User interface for locating the direction of maximum direction

Radiation Profiler for K-130 Cyclotron

The K-130 Room Temperature Cyclotron at VECC, Kolkata produces accelerated proton, alpha and other positive heavy ion beams of different energies for beam line experiments. As this accelerator facility has been classified as class IV by AERB, it has potential to produce an accidental dose more than three times the occupational annual dose limit, and may give lethal doses of radiation in case of accidental entry to interlocked beam areas. Therefore, to estimate the distribution of the radiation field prevailing during the operation of the Cyclotron, a mobile robot based radiation dose-rate mapping system has been developed (Fig. 5).

The movements of the mobile robot are controlled by human operator from the control room by using graphical user interface. As mobile robot onboard electronic is integrated with radiation survey meter, it is possible to transmit the measured radiation to control room, while mobile robot is navigating inside the hazardous zone.

Fig.5: Mobile robot carrying Gamma/ Neutron survey meter inside K-130, cyclotron at VECC, Kolkata

This mobile robot has been successfully used to map the prevailing dose rates at different positions inside the vault and experimental areas (Fig. 6). It is also helping in the study of the effects of radiation field on the materials and equipments stationed around the machine.

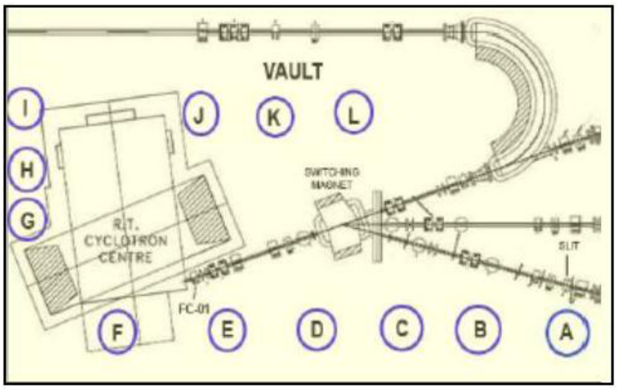

Fig.6: Different locations marked A – L, inside the cyclotron vault where radiation measurements were taken

Conclusion

Three variants of mobile robots have been developed for monitoring and mapping radiation. The development involved integration of radiation measuring detectors with the microcontroller, receiving and processing command packets from the application layer, etc. Several important features like making radiation map as per preset threshold and locating radioactive source using spinning motion of mobile robot have been incorporated and tested.

The radiation profiler mobile robot was successfully deployed at VECC, Kolkata. The experiments using this unique mobile robot were conducted in collaboration with Computer and Informatics Group and Health Physics Unit of VECC at Kolkata. The described mobile robot based dose mapping system has been used to measure neutron and gamma dose rates for different types and energies of the beam. This mobile robot can be used to locate the maximum beam loss positions and thereby improve beam optics for maximum beam transmission efficiency. It can also help in optimization of beam internal parameters to reduce the ambient dose inside vault and pit areas.

Acknowledgement

The authors are thankful to Dr. R. K. Bhandari, Director, VECC, Kolkata and Shri Manjit Singh, Director, DM&A Group, BARC, Mumbai for their constant support and encouragement.

References

1. Prabir K Pal, Asim Kar, Abhishek Mittal, Debasish Datta Ray, K Jayarajan and Manjit Singh; " Remote Survey, Inspection and Operation with Mobile Robot", BARC Newsletter, Aug 2003
2. Sharma S, Jha A N, Das B, Agashe V, Pal P K, and Padmanabhan N, "Mobile robot for radiation monitoring", National Symposium on Nuclear Instrumentation, Mumbai, India 2010.
3. Purakait M, Jena S C, Bhaumik T K, Datta K, Sarkar B, Datta C, Ravishankar R, Mishra S K, Bandopadhyay T, Sharma S, Agashe V, Pal P K, "Online radiation mapping of K-130 room-temperature cyclotron using mobile robot", Proc. 2nd Int. Conf. Computer and Communication Technology (ICCCT), pp. 104-107, DOI: 10.1109/ICCCT.2011.6075176, Allahabad, 2011

STUDY OF IONS EMITTED FROM A PLASMA FOCUS DEVICE USING FARADAY CUP AND SOLID STATE NUCLEAR TRACK DETECTOR

Ram Niranjan, R.K. Rout, Rohit Srivastava and Satish C. Gupta
Applied Physics Division

and

R.V. Kolekar
Radiation Safety Systems Division

Shri Ram Naranjan received the Best Poster Award (1st Prize) in the 26th National Symposium on Plasama Science & Technology (PLASMA-2011), held at Birla Institute of Technology, Patna, during December 20-23, 2011.

Abstract

A compact graphite based faraday cup has been developed for pulsed ion measurements in biased ion collector mode. High energetic pulsed ions (protons, deuterons, ^{3}He ions, ^{4}He ions and nitrogens) are generated in plasma focus device due to plasma pinching action when operated with different gases (deuterium, ^{3}He gas and nitrogen). Ions of energy as low as tens of eV and density up to 10^{17} ions/m^3 were evaluated from the signal observed through the faraday cup. The track densities due to reaction ^{3}He (^{3}He, 2p) ^{4}He were measured using solid state nuclear track detector (CR-39). The track densities observed in CR-39 detector at 16cm from anode tip in axial and radial directions were 2.1 x 10^6 tracks/cm^2 and 3.3 x 10^4 tracks/cm^2 respectively. The details of measurement are reported here.

Introduction

The plasma focus (PF) device is a renowned pulsed plasma producing system that makes use of the self-generated magnetic field. The PF units are used as the intense sources of neutrons, X-ray radiations, ions, and electrons. The studies of ion emission in PF devices have been done extensively when operated with deuterium gas to investigate the correlation between deuterium ion acceleration and neutron production. A few investigations on emission of ions in PF unit operating with other gases e.g. hydrogen, helium, nitrogen, argon etc have also been reported. The PF devices operating at energy range from sub kJs to MJ generate ions with energy more than a few hundred of keV to tens of MeV [1-3]. The characterization of these ions is very important not only in understanding the mechanism of production of high energy ions but also for their applications in different fields like; ion implantation, thermal surface treatment and ion-assisted coatings. The techniques for ion spectrum measurements in PF devices include the use of nuclear activation, particle tracks in dielectric materials, ion time of flight, neutron time of flight and radiation damages. A simple and inexpensive diagnostic to measure the PF ion beam with temporal resolution is Faraday cup (FC) as the electric current produced in FC is proportional to the flux of incident ions. In this article development of FC and study of the temporal and the spatial distribution of the ions in PF devices using the FC and the solid state nuclear track detectors (CR-39) will be reported.

Experimental Setup

The PF device developed here [4] with a 40μF capacity capacitor bank was used to generate high energy ions of deuterium, nitrogen and helium (^{3}He). The energy of the capacitor bank was adjusted through charging voltage for optimized operation with a particular gas. A typical FC for ion measurement with the biasing power circuit [5] mainly comprises of a conical graphite cup as inner electrode (collector of ions) and coaxial cylindrical brass shield as outer electrode. The graphite is chosen because of its low secondary electron emission coefficient and it is given conical shape to redirect the secondary electrons into the collector. A cylindrical teflon tube is used to separate the outer and the inner electrodes. The dimensions of the inner and the outer electrodes are estimated to match the characteristic impedance of 50 Ω using the equation :

$$Z = \frac{60}{\sqrt{\epsilon}} \ln\left(\frac{b}{a}\right)$$

Where b is the inside base diameter of the outer electrode, a is the outside base diameter of the inner electrode and ϵ is the dielectric constant of teflon (= 2.15). The values of a and b are chosen here as 17 mm and 5 mm respectively. The inner electrode is of length 15 mm and the overall length of FC is 43 mm only. The entrance pinhole of 500 μm in diameter is kept at the opening of the FC to control the ion flux. The photographs of the components of the Faraday cup and the assembled FC are shown in Fig.1(a) and Fig.1(b) respectively. A bias voltage of -100 V is applied to the collector and the outer electrode is grounded. RG 75 cable is used for the connection of the Faraday cup assembly to the BNC connector to make it flexible for application. For the time resolved ion emission study the FC is placed along the anode axially at different distances from the anode top. The velocity, energy and density of ions are estimated using time of flight (TOF) technique. The flight time of ion from the anode top to the FC is deduced from the difference of time of the initiation of the post focus phase from the current derivative signal and the rise time of the FC signal. The velocity of ions is evaluated from the ratio of the distance between the anode top and the FC to the ion flight time. The ion energy is calculated using the simple equation :

$$E = \frac{1}{2} m v^2$$

The number density of the ion with velocity v and the charge state q is calculated using the equation :

$$n_i = \frac{V}{RqAv}$$

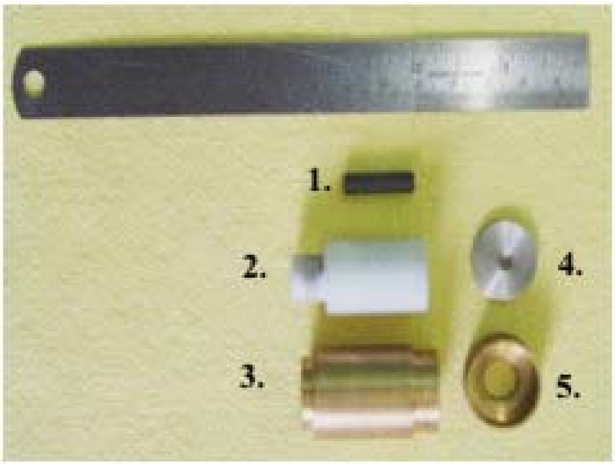

Fig.1(a): Parts of the Faraday cup. 1. Graphite cone, 2. Teflon spacer, 3. Brass housing, 4. Pinhole holder, 5. Brass cap.

Fig.1(b): Assembled Faraday cup

where m is the atomic mass of ion, v is the velocity of ion, V is the maximum voltage of the ion pulse, R is the resistance across which the FC signal is taken and A is the area of the aperture of the pinhole. In order to measure the spatial distribution of helium ions in the PF device, the CR-39 nuclear track detectors (25 mm x 25 mm size) are employed in axial and radial directions. After exposing the detectors to a few PF shots, the detectors are removed and are etched offline under the standard conditions (6N KOH at 60^{0}C) for a period of 4-7 hours to develop visible tracks.

Results and Discussion

The deuterium ions were generated operating the bank at 5.1 kJ (16 kV) and 3 mb filling gas pressure. The density of ions at 6 cm from focus was 4.7x10^{17}/m^3 with the

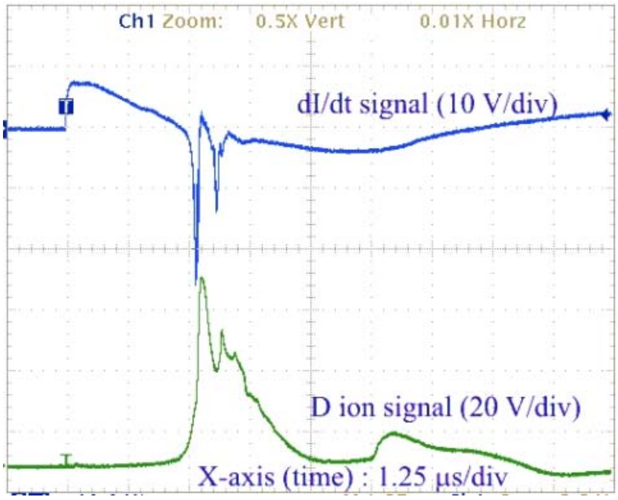

Fig. 2: dI/dt and deuterium ion signals through FC

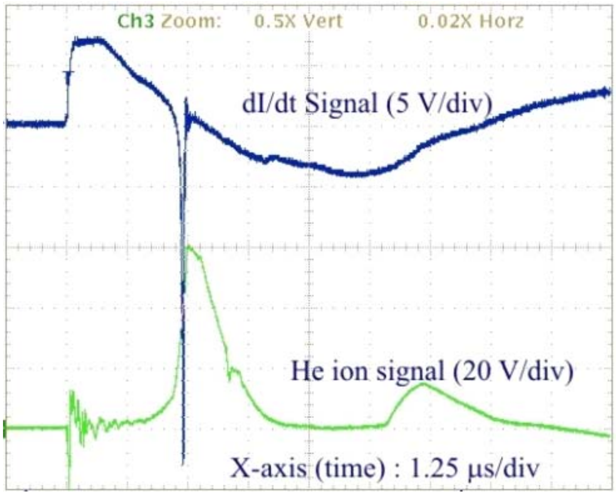

Fig. 3: dI/dt and helium ion signals through FC

maximum energy of 4 keV. Typical signal for the deuterium ion emission is shown in Fig.2. The maximum energy estimated for the helium ion (^{3}He) signal (Fig.3) was 11 keV with the density of $9.95 \times 10^{16}/m^3$ at 6 cm from the PF. The PF device was operated here at 5.1 kJ (16 kV) and 2 mb filling pressure of ^{3}He gas. To generate nitrogen ions, the bank was operated at 5.1 kJ with gas pressure of 0.5 mb. Fig.4 shows oscilloscope signal of current derivative and three FC signals located at distances of 6 cm, 10 cm and 34 cm from the PF for the same discharge. The densities of nitrogen ions were estimated as $1.9 \times 10^{17}/m^3$, $2.4 \times 10^{17}/m^3$ and $3.2 \times 10^{17}/m^3$ respectively. But the energy of nitrogen ions at 6cm distance was 73 keV. The energy of ions at 10 cm was 42 keV. It dropped to 17 eV at 34 cm. The estimated density of nitrogen ions remained almost same but the pulse width of the ions increased and the energy decreased with the distance as they penetrated longer distance in the background plasma. The PF device was operated at a higher bank energy of 11.5 kJ (24 kV) with increased gas pressure (4 mb) of ^{3}He gas

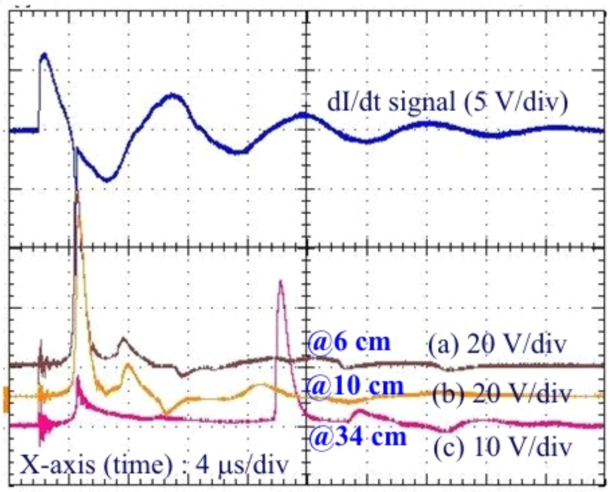

Fig. 4: dI/dt and nitrogen ion signals through FC

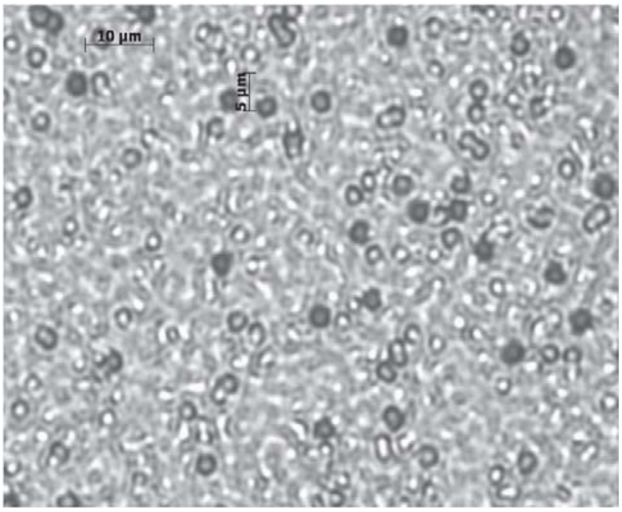

Fig. 5: Tracks of ions in axial direction at 16 cm during fusion of ^{3}He.

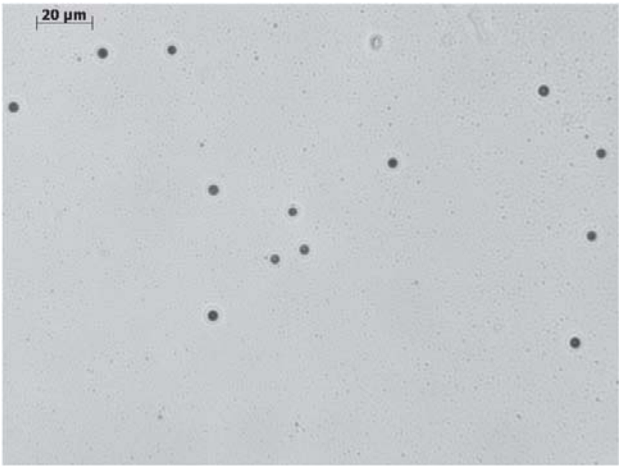

Fig.6: Tracks of ions in radial direction at 16 cm during fusion of ^{3}He

to achieve the fusion reaction ^3He (^3He, 2p) ^4He. The ions were measured with CR-39 nuclear track detector placed axially and radially at a distance of 16 cm from the tip of the anode. The typical images of tracks of the ions are shown in Fig.5 (axial) and in Fig.6 (radial). The CR-39 film was exposed to four PF shots to develop these tracks. The densities of ion tracks were $2.1x10^6/cm^2$ (axial) and $3.3x10^4/cm^2$ (radial). The tracks in axial direction were crowded because of exposure to axially moving plasma, protons, ^3He ions and ^4He ions. The radial direction tracks could be due to fusion products (proton,^4He) as the accelerated ^3He ions in radial direction were too small to generate any track.

Conclusion

Fast response compact and flexible Faraday cups were developed and were used in time resolved study of ions emitted from the PF device by the time of flight analysis. The Faraday cup can register ion energy as low as 10s of eV. The measurements reveal that the energetic ions are confined to axial direction around anode axis and lose energy as they penetrate through the background plasma. The spatial distribution of ions was studied using solid state nuclear track detector (CR-39). The signatures of alpha and proton tracks on CR-39 detectors suggest the possibility of ^3He fusion even through a medium energy (11.5 kJ) PF device.

References

1. Bostick W. H., Kilic H., Nardi V., et al., 'Time resolved energy spectrum of the axial ion beam generated in plasma focus discharges', *Nucl. Fus.,* 33, 1993, 413-420.
2. Sadowski M., Sadowska E. S., Baranowski J., et al., 'Comparison of characteristics of pulsed ion beams emitted from different small PF devices', *Nukleonika,* 45(3), 2000, 179-184.
3. Kelly H., Lepone A., Marquez A., et al., 'Analysis of the nitrogen ion beam generated in alow-energy plasma focus device by a Faraday cup operating in the secondary electron emission mode', *IEEE Trans. Plasma Sci.,* 26, 1998, 113-117.
4. Ram Niranjan, Rout R.K., Srivastava Rohit and Gupta Satish C., 'Development and study of 13kJ capacitor bank and plasma focus device'. 25th Nat. Symp. on Plasma Scien. and Technol. (PLASMA -2010), December 8-11, 2010 , IASST, Guwahati, India.
5. Mohanty S. R., Bhuyan H., Nego N. K. et al., 'Development of multi Faraday cup assembly for ion beam measurements from a low energy plasma focus device', *Jpn. J. Appl. Phys.,* 44(7A), 2005, 5199-5205.

YRAST AND NEAR-YRAST SPECTROSCOPY OF NEUTRON-RICH FISSION FRAGMENTS USING THERMAL NEUTRONS FROM REACTOR

S. Mukhopadhyay, L.S. Danu, D.C. Biswas, P.N. Prashanth, L.A. Kinage,
A. Chatterjee and R.K. Choudhury
Nuclear Physics Division

and

A. Goswami
Radiochemistry Division

This paper received the First Prize for Best Poster Presentation at the DAE Symposium on Nuclear Physics, Visakhapatnam, Dec.26-30, 2011

Introduction

The spectroscopic studies of fission fragments provide direct information on the nuclear excited states, which are related to the shape and structure of the neutron-rich fragment nuclei [1,2]. Thermal neutron induced fission is one of the techniques which allows us to do spectroscopic investigation of such fragment nuclei with a higher neutron to proton ratio. These types of studies help to explore the new regions of nuclear deformations, and to extend the theoretical model(s) to regions which have hitherto been inaccessible. A lot of work has already been done on these set of nuclei by means of spontaneous fission of ^{252}Cf and ^{248}Cm sources [3,4], heavy-ion induced fusion-fission reactions [5], and also using deep-inelastic reactions. It is desirable to extend these measurements to thermal neutron induced fission of ^{235}U as well to investigate those nuclei whose population in the above-mentioned reactions are low, and also to obtain information on the mass regions accessible to all these fissioning systems and compare the results.

Here we report a comparative study in terms of yrast and near-yrast spectroscopy of the neutron-rich fragments that were produced in the thermal neutron induced fission of ^{235}U. It is to be noted that prompt online γ spectroscopy using γ-γ coincidence technique has been attempted for the first time using ^{235}U(n_{th}, f) reaction.

The experiment was done at the CIRUS reactor facility, BARC, Mumbai. The shielding arrangement was made in such a manner so that a collimated radial neutron beam of ~10-mm diameter impinges on the target. The target was uranium aluminide (UAl$_3$, with 17% ^{235}U enrichment) in pellet form, with a material density of ~5.1 gm/cm^3. The 3-mm thick target, fully sealed in a Teflon disk-type capsule, was bombarded by the thermal neutrons from the reactor. The thickness of the Teflon, covering the front face of the target, was measured as 1 mm, whereas the Teflon thickness in the rear (base of the target material) was 5 mm. The neutron flux at the target position was ~4 $\times$ 10^7 cm^{-2} s^{-1}. Deexciting γ rays from the fission fragment nuclei were detected by two clover germanium detectors in coincidence mode, mounted in a vertical ring-type structure with $\varphi = 72^0$. The clover detectors were mounted at a distance of 24 cm from the target along with their anti-Compton shields. The Compton suppressed list-mode data were collected with the condition of firing by both the detectors in a single event. A total of 3×10^6 γ-γ coincidence events were recorded for further off-line analysis.

Results and Discussions

In the offline analysis, several complementary fragments were identified following the γ-γ coincidence technique. The relative yield distribution (Fig. 1) was performed accurately, taking into account the interplay between the neutron and γ absorption in the thick target.

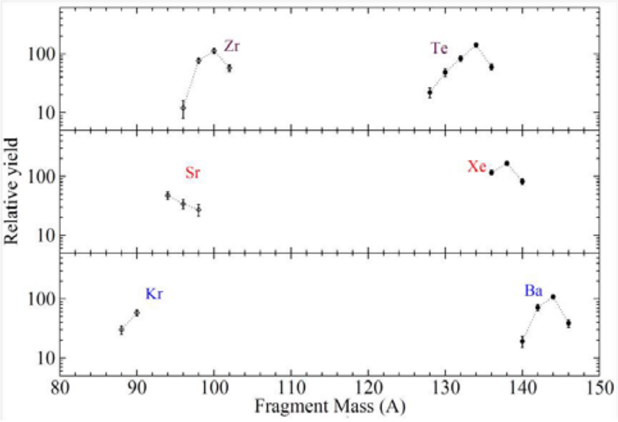

Fig. 1: Relative yield distribution of fragment partners as obtained from the $^{235}U(n_{th},f)$ reaction.

In the thermal neutron induced fission of ^{235}U, the Sr isotopes are the fragment partners of Xe isotopes centered around ^{138}Xe. When gates were pulled on the lower lying strong transitions of ^{138}Xe, the strong γ transitions of $^{94}Sr(4n)$, $^{95}Sr(3n)$ and $^{96}Sr(2n)$ were clearly seen in addition to the strong γ transitions in ^{138}Xe (Fig. 2). Coincidence rates of various Sr isotopes with ^{138}Xe nucleus were obtained. The rates were calculated from the relative intensities of the transitions (first excited to the ground state) in these Sr isotopes from a single spectrum of ^{138}Xe, gated on 484-keV transition. It is very clear from the data that in the case of Xe-Sr fragment pair production, the 3-neutron evaporation channel is dominant. whereas, in the case of Ba-Kr fragment pairs, the 2-neutron evaporation channel has the maximum yield.

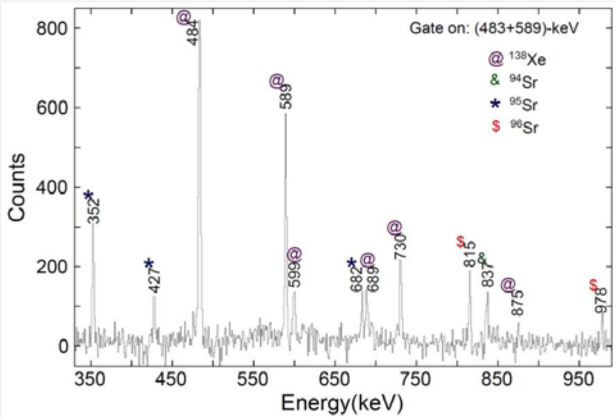

Fig. 2: Representative gated spectrum of ^{138}Xe.

The medium and high-spin states of several isotopes were clearly observed from the present data set, and level schemes were deduced based on coincidence relationship and intensity arguments. In fact, from our analysis of several complementary charge pairs, it has become evident that the Ba chain of isotopes ($^{140-146}Ba$) is the largest that is observed in the thermal neutron induced fission of ^{235}U. The coincidence data have proved to play a crucial role in justifying earlier assignments of the level schemes.

Among the Sr chain of isotopes, we could see the γ lines clearly up to $I = (7^-)\,\hbar$ ($E_x = 3.923$ MeV), $I = (13/2^+)\,\hbar$ ($E_x = 2.344$ MeV), $I = (9^-)\,\hbar$ ($E_x = 3.524$ MeV) in ^{94}Sr, ^{95}Sr and ^{96}Sr, respectively. The level schemes (Fig. 3) obtained agree well with the previous works. In ^{96}Sr, we did not see the excited 0^+ levels at 1229 keV and at 1465 keV, similar to the ^{248}Cm data. Although we could see the quasirotational structure built on a possible 0_2^+ excitation, subsequent experimental non-observation of 0_2^+, 0_3^+ (E_X =1465 keV) and the proposed deformed band built on 0_3^+ render their existences doubtful.

Among the complementary fragments of Sr isotopes, ^{138}Xe was seen to have the highest yield. We could see up to spin $I = (12^+)\,\hbar$ ($E_x = 3.572$ MeV) in its yrast sequence. We could see the first few levels that constitute the proposed gamma vibration band in this nucleus. In ^{140}Xe, levels up to spin $I = (12^+)\,\hbar$ ($E_x = 3.270$ MeV) were observed. This ^{140}Xe happens to be the only nucleus among the Xe isotopes where we could see the first few levels of the octupole band proposed and observed earlier.

Among the Ba chain of isotopes, ^{144}Ba was seen to have the highest yield. The first few levels of the octupole band in ^{144}Ba and ^{146}Ba were seen very clearly. In ^{142}Ba, certain level sequences in the yrast and the octupole band were contradicted previously by Urban *et al*. Our data corroborates the sequence proposed from the ^{248}Cm data set.

Among the Zr chain of isotopes, ^{98}Zr and ^{100}Zr were seen to have maximum yield. We could see up to spin $I = (12^+)\,\hbar$ ($E_x = 4.821$ MeV) and $I = (10^+)\,\hbar$ ($E_x = 2.426$ MeV) in their level sequences, respectively. Although we could not see the 0_2^+ and 2_2^+ states as observed earlier,

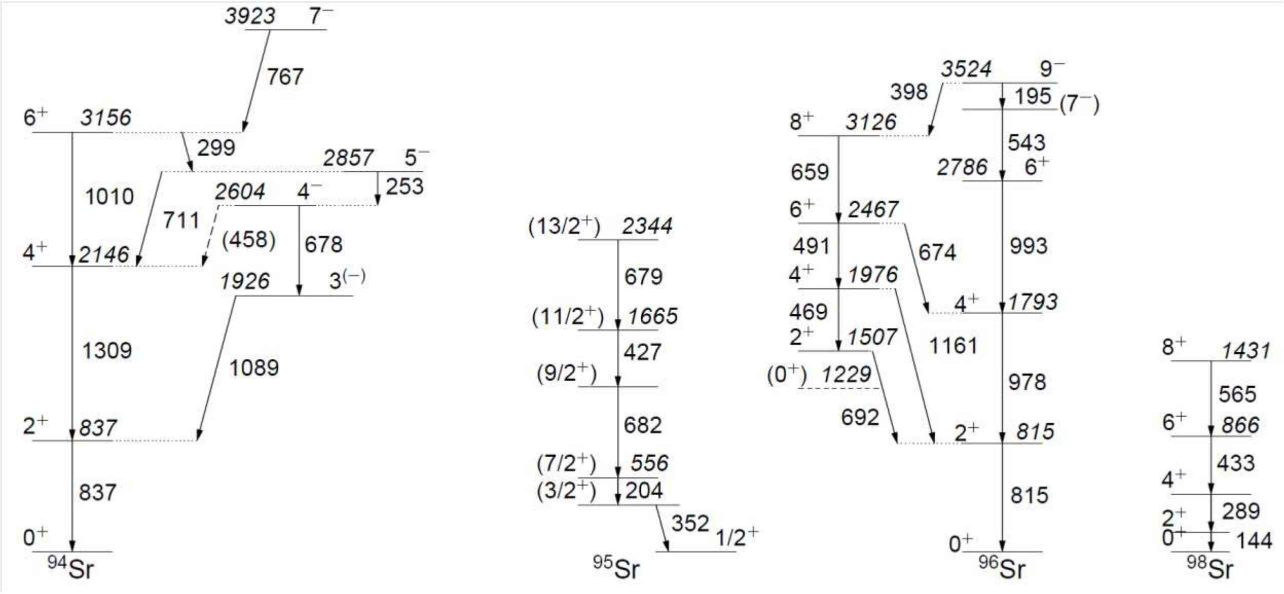

Fig. 3: Partial level scheme of Sr isotopes, as deduced from the present data set

we could see some notable discrepancies with respect to the ^{252}Cf data set. The proposed 0_3^+ level remain elusive like all previous SF data.

Detailed data analysis on relative isotopic yield distribution and yrast and near-yrast level structures of all the fission fragment isotopes were carried out and the results have been published recently [6].

References

1. D. C. Biswas *et al.,* Phys. Rev. C 71 (2005): 011301-05.
2. A. G. Smith *et al*., Phys. Rev. Lett. 77 (1996): 1711-14.
3. J. H. Hamilton *et al*., Prog. Part. Nucl. Phys. 38 (1997): 273-87.
4. W. Urban *et al*., Z. Phys. A 358 (1997): 145-51.
5. L.S. Danu *et al*., Phys. Rev. C 81 (2010): 014311-15.
6. S. Mukhopadhyay *et al*., Phys. Rev. C 85 (2012): 064321-33.

OXIDATION OF TNT USING PHOTO-CATALYSIS PROCESS

S.V. Ingale, A.K. Tripathi, A.S. Dudwadkar, S.S. Gamre, P.T. Rao, Ratanesh Kumar,
I.K. Singh, R.P. Patel, P. B. Wagh and Satish C. Gupta
Applied Physics Division

This Paper received the Best Poster Presentation Award at the National Seminar on Physics of Materials and Materials Based Device Fabrication (NSPM-MDF-2011) held at Shivaji University, Kolhapur during February 17-18, 2011

Abstract

TiO_2-SiO_2 nano composites have been prepared using co-precursor sol-gel method and used in degradation of TNT using photo catalysis process. The 100 ppm TNT solution, irradiated with UV light, was treated with H_2O_2 oxidizer in presence of TiO_2-SiO_2 composites. HPLC analysis showed that the TNT concentration in the treated solution was brought down to less than 1 ppm within two hours whereas the TOC of the treated solution was reduced to less than 1 ppm within 3.5 hours indicating 99% mineralization efficiency.

Introduction

Release of nitro aromatic compounds like trinitrotoluene (TNT) from explosive process plants in the effluents is major environmental concern being TNT a carcinogen and its slow response to biodegradation. TNT in the waste water is generally separated by using granular activated carbon (GAC) filters or is decomposed using chemical methods or advanced oxidation process (AOP). Among these methods, AOP is more favoured as it can be carried out at ambient conditions and result in eco friendly products. Titania (TiO_2) is one of the widely used materials as catalyst in photo oxidation of organic compounds like alcohols, aniline [1] but there are only a few examples of photo oxidation of aromatic compounds using TiO_2. We synthesized high specific surface area TiO_2-SiO_2 nanocomposites and successfully demonstrated that it is promising photo catalyst for oxidation of TNT.

Experimental

TiO_2-SiO_2 gels were prepared by mixing Tetramethoxysilane (TMOS), propanol and water in the molar ratio of 1:24:6, respectively. To this solution Titanium isopropaxide (TIP) was added in desired molar ratio so as to obtain TiO_2-SiO_2 aerogels with 20 and 50 wt % TiO_2 content. After gelation, propanol from gel was extracted using supercritical drying method [2]. The crystalline data for the aerogels were obtained on a Philips X-ray diffractometer (CuKα, 30kV, 20mA). UV–Vis spectra for the aerogels were recorded in 200–800 nm wavelength range on a Jasco V-670 spectrophotometer. Surface area of aerogels was measured by using BET surface area analyzer (Model: Sorptomatic 1990, Italy). For photo oxidation experiments, 100 ppm TNT solution was treated in an UV reactor, which has an UV-C lamp (8W) surrounded by quarts tube in a SS cylindrical vessel. TiO_2-SiO_2 aerogel powder (100 ppm) was dispersed to the TNT solution. H_2O_2 was added at a rate of 35 mM/hour. TNT concentration in the treated solution was measured by HPLC equipped with a HIQ Sil C18W column and UV detector at λ=254 nm. TOC was measured using the ANATOC II SERIES analyzer from SGE, Australia.

Results and discussion

From the XRD patterns of TiO_2-SiO_2 aerogels (Fig. 1), the diffraction peaks were assigned to anatase structure of TiO_2 [3]. The average crystallite size of TiO_2 derived using Scherrer formula is 24 nm for TiO_2-SiO_2 (20/80) aerogels and 17 nm for TiO_2-SiO_2 (50/50) aerogel.

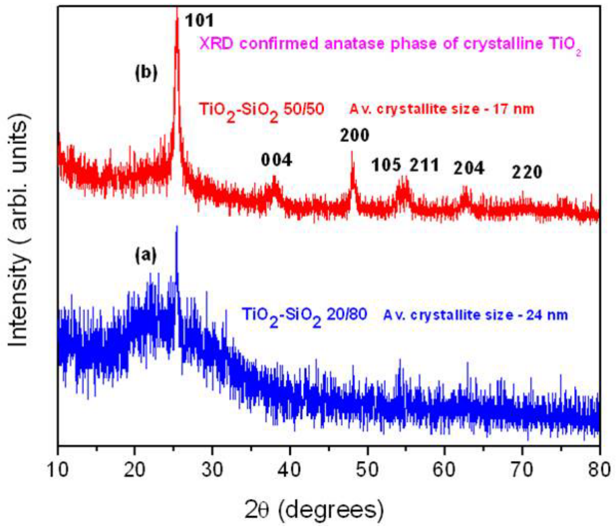

Fig. 1: XRD pattern of TiO$_2$/SiO$_2$ aerogels containing (a) 20 wt% TiO$_2$ (b) 50 wt% TiO$_2$

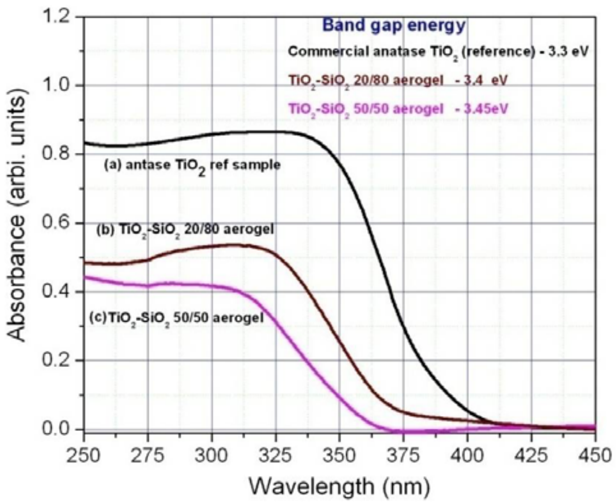

Fig. 2: UV/Vis absorption spectra of: a) anatase TiO$_2$ (reference sample), b) TiO$_2$-SiO$_2$ c) TiO$_2$-SiO$_2$ (50:50) aerogel, and d) TiO$_2$-SiO$_2$ (65:35) aerogel.

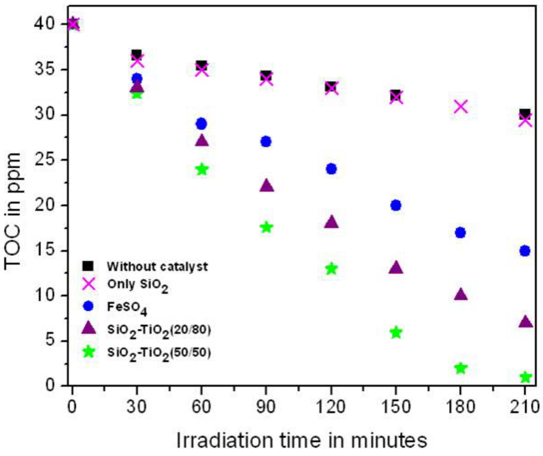

Fig. 3: TOC measurement in photo oxidation of TNT using; % - no catalyst, X - SiO$_2$, % - FeSO$_4$, % - TiO$_2$-SiO$_2$ (20/80) aerogel, * -TiO$_2$-SiO$_2$ (50/50) aerogel

The specific surface area calculated using BET method found to be 1295, 1107 and 485 m^2/g for SiO$_2$, TiO$_2$-SiO$_2$ (20/80) and TiO$_2$-SiO$_2$ (50/50) aerogel, respectively.

The results of TOC measurements for the photo oxidation experiment carried out using H_2O_2oxidizer and SiO$_2$, FeSO$_4$ and TiO$_2$-SiO$_2$ aerogel catalyst are presented in Fig. 3.

For 100 ppm TNT aqueous solution, the TOC recorded was 40 ppm. On treating the TNT solution without any catalyst, didn't show in significant effect on TOC reduction. Using FeSO$_4$ catalyst, TOC reduced to 14 ppm (60% mineralization efficiency) in 3.5 hrs where as TiO$_2$-SiO$_2$ aerogel showed faster and effective degradation of TNT. TOC found to be reduced to 7 ppm using TiO$_2$-SiO$_2$ (20/80) aerogel and it reduced to 1 ppm using TiO$_2$-SiO$_2$ (50/50) aerogel in 3.5 hours indicating 99% mineralization of organic entity. It may be due to high oxidizing and reducing potential of TiO$_2$and very high surface area of the composites.

Fig. 4 shows the typical HPLC chromatograms of the untreated and treated TNT solution. The prominent peak at retention time 9.05 min. (Fig. 4 a) which is attributed to TNT reduced to less than 1 ppm after treating the solution for two hours (Fig. 4 b) indicating oxidative transformation of TNT. The additional peaks emerged at 2.07 and 5.93 min. are due to intermediate oxidation products.

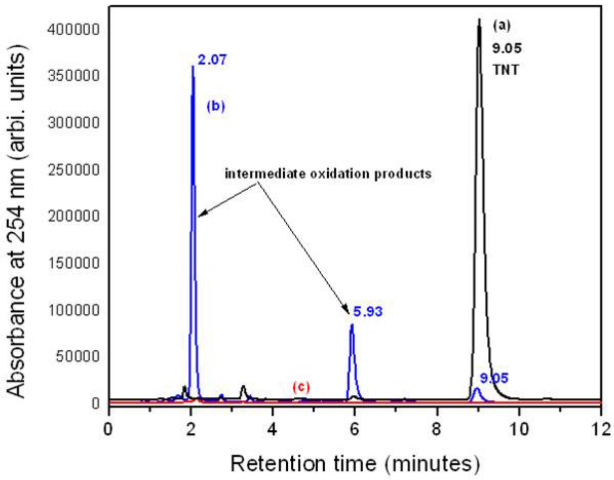

Fig. 4: HPLC chromatograph for TNT solutions; (a) before treatment —, (b) after 2 hours —, (c) after 3.5 hours of treatment — ; using TiO$_2$-SiO$_2$ (50/50) aerogel as catalyst

The chromatograph for TNT solution treated for 3.5 hours (Fig. 4 c) revealed that TNT peak at 9.05 min. and other peaks attributed to intermediate oxidation products disappeared that indicate complete degradation of TNT to CO_2 and H_2O.

Conclusions

High specific surface area TiO_2-SiO_2 nano composites have been prepared using co-precursor sol-gel method and used for complete degradation of TNT. Using the photo-oxidation method for degradation of TNT by using TiO_2-SiO_2 (50:50) aerogel with specific surface area of 485 m^2/g as catalyst, the TOC reduced to 1 ppm within 3.5 hours. This revealed that high surface area TiO_2-SiO_2 nanocomposite prepared by sol-gel method is promising photo catalyst to achieve effective and faster degradation of TNT.

References

1. Kamble S, Sawant S, Pangarkar V, et al. (2003) *J Chem Technol Biotechnol* 78 :865–872
2. Ingale S, Wagh P, Tripathi A, et al. (2011) *J Porous Mater* 18, 567-572
3. Zhao Y, Li C, Liu X, Gu F, Jiang H, et.al. (2007) *Mater Lett* 61:79-83
4. Liu G, Sun C, Yang H, et al. (2010) Chem Commun 46:755–757

PHYTOREMEDIATION OF RADIONUCLIDES FROM SPIKED SOLUTIONS AND LOW LEVEL NUCLEAR WASTE BY *VETIVERIA ZIZANOIDES* L. NASH

Shraddha Singh, Susan Eapen and S.F. D'Souza
Nuclear Agriculture and Biotechnology Division

and

C. P. Kaushik
Waste Management Division

This paper received the Best Poster Award at the 5th International Conference on Vetiver "Vetiver & Climate Change" held at CIMAP, Lucknow (UP) during October 28-30, 2011

Abstract

The potential of *V. zizanoides* was tested for remediation of radionuclides ^{137}Cs, ^{90}Sr, ^{239}Pu and ^{241}Am from spiked solution under controlled conditions. Vetiver plantlets when tested for their potential to remove ^{90}Sr and ^{137}Cs (5×10^3 k Bq L^{-1}) from solutions spiked with individual radionuclide showed that 94% of ^{90}Sr and 61% of ^{137}Cs could be removed from solutions. In case of ^{137}Cs, accumulation occurred more in roots than shoots, while ^{90}Sr accumulated more in shoots than roots. *V. zizanoides* plants could also remediate high levels of ^{239}Pu (65%) and ^{241}Am (62%) from spiked solutions (Initial activity: 100 Bq mL^{-1}) after 30 days. Most of the activity was retained in the roots with a translocation index (TI) of 9.4% (^{239}Pu) and 8.7% (^{241}Am). Plants of *V. zizanoides* could also effectively remove radioactive elements from Low Level Nuclear Waste. The results of the present study indicate that *V. zizanoides* may be a potential candidate plant for phytoremediation of various radionuclides from aqueous bodies.

Introduction

Mining and milling of nuclear fuel, operations typical of nuclear fuel cycle, fall out from nuclear weapon testing and occasional nuclear accidents have contributed to an enhancement in the level of radionuclides in the environment, which can be readily passed onto human beings through the food chain (Shaw and Bell, 1991). Phytoremediation – the use of green plants for remediation of soil and solutions contaminated with low level of toxic metals and radionuclides has received a lot of attention in the last few years due to its environment-friendly nature and aesthetically pleasing qualities. It is a cost effective and eco-friendly strategy that can compliment or replace conventional approaches (Salt et al., 1998, Eapen and D·Souza, 2005).

Vetiver grass (*Vetiveria zizanoides* L. Nash) is a fast growing grass with massive and complex root system coupled with the ability to grow under adverse conditions. This plant has shown the ability to grow under a wide range of edapho-climatic conditions and recognized as a panacea for all environmental problems of the 21st century (Truong, 2000). There are a few reports on the use of *V. zizanoides* for the remediation of metals and organic pollutants. However, there is no report on the use of *V. zizanoides* for phytoremediation of radionuclides from solutions as well as nuclear waste. The present study has been performed to assess the potential of this plant for the remediation of various radionuclides (^{137}Cs, ^{90}Sr, ^{239}Pu and ^{241}Am) from spiked solutions as well as Low Level Nuclear Waste.

Material and Methods

Plant Material

Vetiver grass (*Vetiveria zizanoides* L. Nash) multiplied by axillary bud development *in vitro* was used for the experiments. One month old *in vitro* plantlets having well developed roots were further transferred to Hoagland's liquid medium and plants were incubated at 25°C under white fluorescent light (12.2 μM photon ms^{-2} s^{-1}) for photoperiods of 12 h. For the experiments with Low Level Nuclear Waste (LLNW), hydroponically grown plants were used.

Remediation of ^{90}Sr and ^{137}Cs

The roots of the plantlets were washed thoroughly with distilled water and plants were incubated with roots immersed in 20 ml of distilled water spiked with either ^{90}Sr or ^{137}Cs (5 x 10^3 k Bq L^{-1}) in 50 ml test tubes for a period of 7 days along with one set of control under controlled conditions. Samples were drawn out from the solution at different time intervals and analyzed for radioactivity.

Remediation of ^{239}Pu and ^{241}Am

V. zizanoides plants were incubated with roots immersed in 20 ml of distilled water spiked with either ^{239}Pu or ^{241}Am (100 Bq mL^{-1}) in test tubes for a period of 30 d along with one set of control under controlled conditions. Plants were allowed to grow for 30 d in the spiked solution prior to harvesting. Samples were drawn out from each solution at different time intervals and analyzed for radioactivity.

Remediation of radionuclides from Low Level uclear Waste (LLNW)

Physico-chemical analysis of the waste was carried out (Table 1). Roots of hydroponically grown vetiver plants were exposed to 4 litres of LLNW for a period of 15 days in natural field condition and the activity in the waste at different time periods was checked.

Sample Analysis

At the end of each experiment, plants were thoroughly washed with distilled water, separated into root and shoot, blotted dry and dried in an oven at 60° C for 48 h. The dried plant tissues were digested in HNO_3: $HClO_4$ (5:1, v:v) and analysed for radioactivity. Analysis by gamma spectrometric measurements was carried out for ^{137}Cs using Multi Channel Analyser (MCA) having High Purity Germanium (HPGe) detector. Radio Sr was estimated by extraction of Sr using selective crown ether followed by elution and plancheting the same and checking the activity with a GM counter. For experiments with LLNW, gross β,γ activity was determined using a GM counter.

Activity of ^{239}Pu and ^{241}Am in the hydroponic samples was carried out by plancheting known volume of the samples, drying under IR lamp and planchets were fired to fix the radioactivity on it. Subsequently, the activity was determined using scintillation counter. All the experiments were performed in triplicates, repeated twice and standard error (S.E.) calculated.

Results

When plantlets of *V. zizanoides* were exposed to solutions spiked with ^{90}Sr (5x10^3 k Bq L^{-1}), 50% of ^{90}Sr was removed from the solution within 1 h and thereafter the amount of ^{90}Sr showed a steady and gradual decline (Fig 1). At the end of 168 h, 94% of the ^{90}Sr was removed from solutions by *V. zizanoides* plantlets. When ^{137}Cs (5x10^3 k Bq L^{-1}) was spiked to the incubation medium having *V. zizanoides* plantlets, a steady decline in the activity of the solution

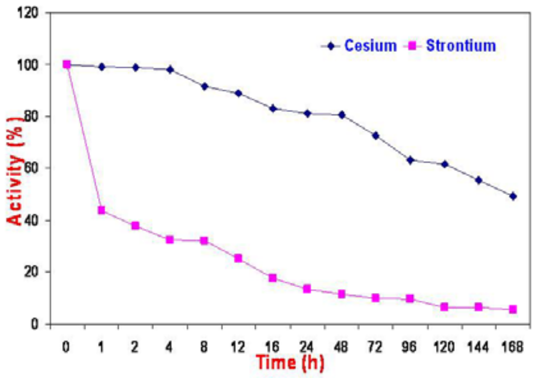

Fig. 1: Activity of ^{90}Sr and ^{137}Cs in solutions after incubation with *in vitro* grown *V. zizanoides* plantlets for different time periods.

was recorded. At the end of 96 h 38% and at 168 h, 61% of ^{137}Cs was removed from the solution when *V. zizanoides* were incubated in the solution (Fig. 1). A large fraction of ^{90}Sr was found to be translocated to the shoots of *V. zizanoides* plants (Fig. 2). For ^{137}Cs, accumulation was recorded higher in roots than the shoots (Fig. 2). When hydroponically grown plants of *V. zizanoides* were exposed to LLNW, 76% of the initial activity was removed after 24 h and 91% of the activity removed at the end of 168h (Fig. 3). Almost all the radioactivity got remediated from LLNW after 360 h (15 d) of exposure. The activity was found more in roots (288 kBq g^{-1} dw) than the shoots (167 kBq g^{-1} dw) of the treated *V. zizanoides* plants.

When *V. zizanoides* plants were exposed to hydroponic medium supplemented with ^{239}Pu (100 Bq mL^{-1}), they were able to survive in ^{239}Pu spiked solution and showed time dependent uptake of this actinide. Plant was able to remediate 23.6% ^{239}Pu from solution in 1d and maximum removal level of 66.2% was observed at 25 d of exposure (Fig 4), after which the level of radionuclide in the solution did not show much change. When the efficiency of *V. zizanoides* for ^{241}Am remediation from solution was studied, it was found that plants could remediate ^{241}Am from spiked solution with a maximum remediation of 63.7% after 25 d.

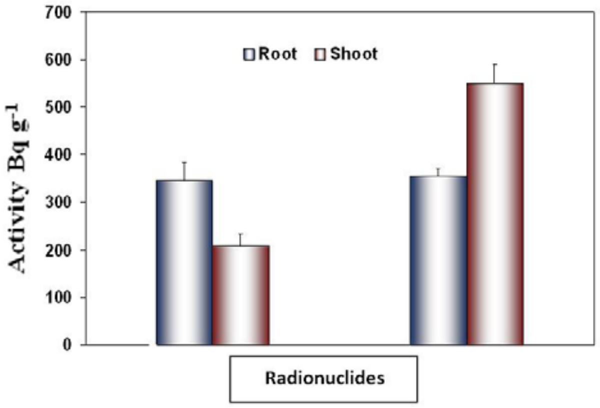

Fig. 2: Distribution of ^{90}Sr and ^{137}Cs in roots and shoots of *in vitro* grown *V. zizanoides* plantlets, when radionuclides were supplemented individually.

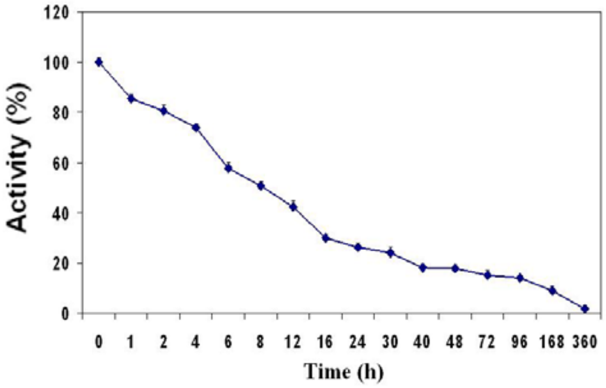

Fig. 3: Activity level in LLNW exposed to hydroponically grown plants of *V. zizanoides* after different time periods.

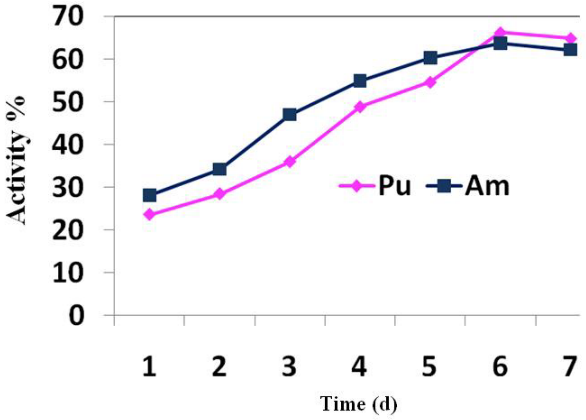

Fig. 4: Activity of ^{90}Sr and ^{137}Cs in solutions after incubation with *V. zizanoides* plantlets for different time periods.

Conclusion

In the present study, *V. zizanoides* was shown to effectively phytofiltrate radionuclides from solutions. Hydroponically grown *V. zizanoides* plants could efficiently remove radionuclides below detection levels within 15 days from LLNW, which makes it a potential candidate plant for removal of radioactivity from LLNW. The results of the present study indicate that *V. zizanoides* may be a potential candidate plant for phytoremediation of various radionuclides from aqueous bodies.

References

1. Eapen S., D·Souza S.F. Prospects of genetic engineering of plants for phytoremediation of toxic metals. Biotechnol Adv. 3 (2005.): 97-114.
2. Salt D, Smith R.D., Raskin I. Phytoremediation. Ann Rev Plant Physiol and Mol Biol. 49 (1998): 643-648.
3. Shaw G., Bell J.N.B. Competitive effects of potassium and ammonium on cesium uptake kinetics in wheat. J Environ Radioact. 13 (1991): 283-296.
4. Truong P. The global input of Vetiver grass technology on the environment. In, Proc. of the second international conference on Vetiver. Office of the Royal Development Project Board, Bangkok. (2000): 46-57

SIGNAL ANALYSIS TECHNIQUES USING DSP FOR FLOW REGIME IDENTIFICATION IN TWO PHASE FLOW

G.J. Gorade, Rajalakshmi R. and B.S.V.G. Sharma
Reactor Engineering Division

This paper received the First Prize for Best Poster Presentation at the National Symposium on Advanced Measurement Techniques and Instrumentation (SAMTI-2011) held at Mumbai from February 2-4, 2011

Introduction

Two-phase gas-liquid flow can be defined as the interacting flow of a gas and a liquid where the interface between the phases is influenced by their motions. For two-phase flows, the respective distributions of the liquid and vapour phases in the flow channel is an important of their description. Their respective distributions take on some commonly observed flow structures, which are defined as two-phase flow patterns or flow regimes, which are determined by the interfacial structure between the two phases and have particular identifying characteristics. The existence of a particular flow regime depends on a variety of parameters, including the properties of the fluids, the flow channel size, geometry and orientation, force field and flow rates. The designation of flow regime has not yet been accurately standardized and depends largely on the individual interpretation of visual observations. Identification and modelling of the flow regime can enhance safety and overall performance in multiphase flow systems.

Flow pattern identification can be performed either by visual inspection of the flow in a transparent pipe or by measuring and quantifying the fluctuations of the flow parameters such as void fraction, which reflects the flow structure. Statistical analyses have been used as efficient tools for two-phase flow regime identification from signal fluctuations. Power spectrum (*PSD*), probability density function (*PDF*) and cross-correlation (*Cxy*) are quite useful statistical tools to attain characteristic signals associated with the passage of the dispersed phase over the probes field. This poster presents the statistical signal analysis techniques like probability density function and Power spectral Density as the mathematical tool using Digital Signal Processing (DSP) for two phase flow regime identification and comparing the experimental data analysis with visual observation.

Why DSP?

DSP has the main advantage of *Fast Processing Of Data.* For fast processing very fast computers, very good memory size and parallel processing architecture all are used effectively to reduce time of processing and control decisions. Statistical Signal analysis functions are stored in the form of algorithms in the hardware memory of DSP system.

Flow Regime Identification in Two-phase Flow

- Two-phase gas-liquid flow can be defined as the interacting flow of a gas and a liquid where the interface between the phases is influenced by their motions.
- Void fraction is one of the fundamental quantities required to describe the flow characteristics of a two-phase mixture. Void fraction is defined as the volume occupied by the gas phase relative to that of the two-phase mixture.
- The distributions of the respective liquid and vapour phases in the flow channel follow some commonly observed flow structures which are defined as two-phase flow patterns or flow regimes

Experiments using High Pressure Natural Circulation Loop

Experiments were carried out at High Pressure Natural Circulation loop in Reactor Engineering Division of BARC.

Steam-Water facility Expt

The void fraction measurements were carried out at high pressure and high temperature steam water mixture using gamma attenuation technique. The experimental data was analyzed using DSP technique and the Probability Density Function were plotted to find out the flow regime.

Bubbly flow regime

In bubbly flow regime gas phase gets dispersed uniformly in the liquid medium in the form of small bubbles in a continuous liquid phase. Bubbly flow regime has distinct bubbles flowing at the centreline of the tube. The void fraction time trace centres around a low average void fraction with small fluctuations corresponding to the passage of the bubbles.

The PDF for bubbly flow shows a single narrow peak at a low void fraction, indicative of the small void fluctuations about a mean value also considerable spread in base of the peak occurring near zero void fractions have been found.

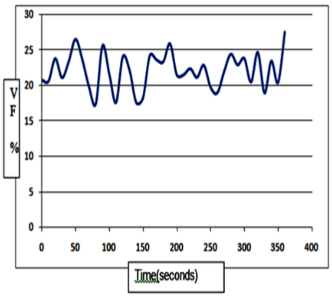

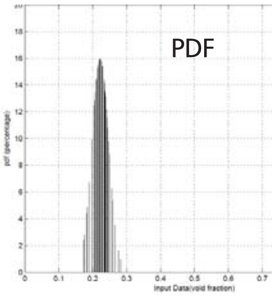

Churn Flow regime

The void fraction time trace of churn flow tends to stay at a high void fraction with random dips into lower void fractions. The PDF for this flow regime shows a single broad peak with maximum void fraction typically between a void fraction of 0.7 and 0.9, with a long tail extending down to low void fractions.

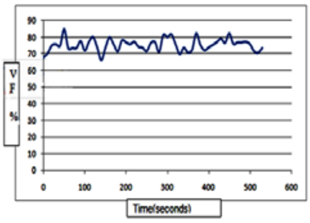

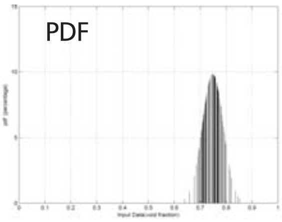

Annular flow regime

A typical PDF for annular flow has a very narrow peak at a void fraction between 0.8 and 0.9, with a short tail extending into lower void fractions. The void fraction time trace for **annular flow** remains constant at a value typically between 0.8 and 0.9. . If PDF has the narrow peak then it indicates that the film maintains a nearly constant thickness between the passing of disturbance waves.

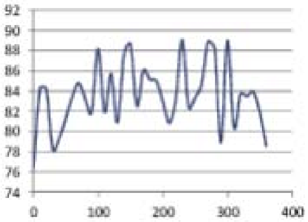

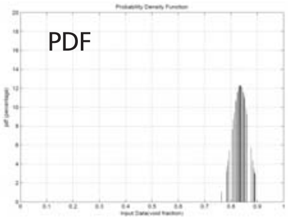

Experiments using air water loop

Air-Water Experimental Set-up

Experiments were conducted in air-water loop for various air and water flow rates and the void fraction was measured with in-house developed Admittance probe. The probe signals were analyzed using FFT for finding out flow regimes. The experiment was conducted at various flow regimes. Since the experimental two-phase section was transparent, the flow regimes were visible and captured with high speed camera for comparing with data analysis and given below.

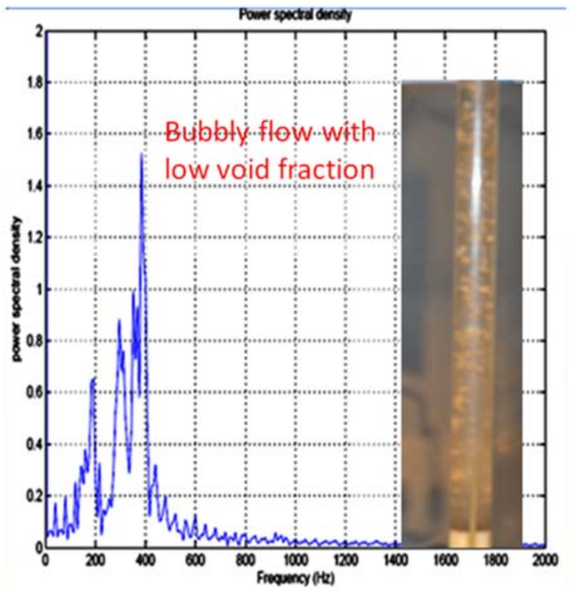

For bubbly flow regime the PSD shows frequencies lying in the range 200-400Hz with peak at around 240-260Hz. There is a single highest peak while other magnitudes are very low compared to it.

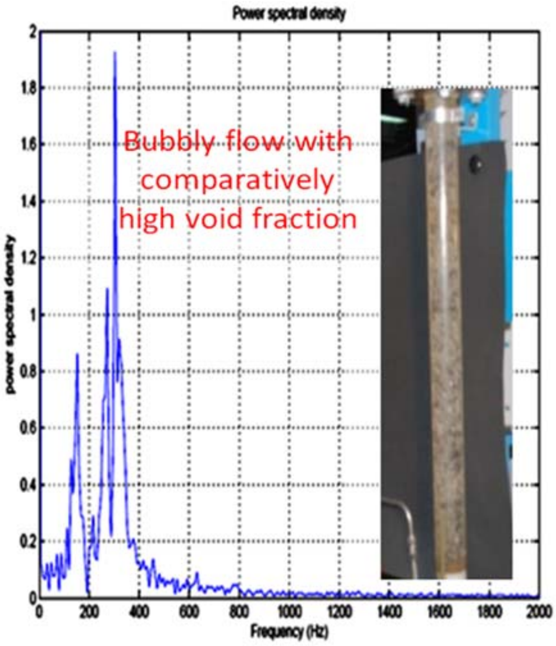

For slug flow regime the PSD shows frequencies lying in the range 350-450Hz. There are a three dominant peaks while other magnitudes are very low compared to it. So, based on various literatures, it can be concluded that this may be slug flow at high void fraction. Visual inspection confirmed it to be slug flow.

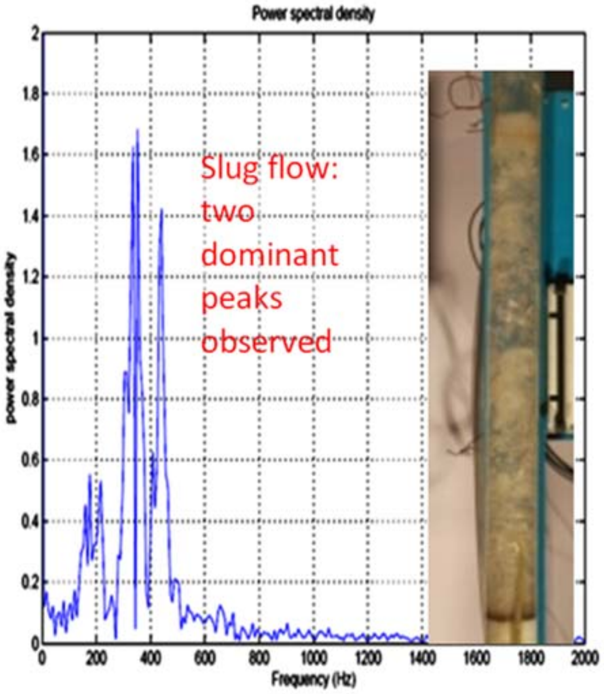

Conclusion

Digital Signal Processing based techniques were studied for flow regime identification. Programming was carried out for implementation of data signature analysis by statistical methods using DSP. The experimental void data obtained from Gamma densitometer and Admittance probe sensors were anaysed using this inhouse developed program and the various flow regimes were evolved. The Air-water void data analysis for bubbly, slug and churn flow were compared with visual image and found good agreement.

NOVEL METHOD OF SYNTHESIS OF RESORCINOL FORMALDEHYDE COATED SPHERICAL BEADS FOR SEPARATION OF Cs^+ FROM ALKALINE WASTE AND THEIR CHARACTERIZATION

Charu Dwivedi, Juby K. Ajish, Krishan Kant Singh and Manmohan Kumar
Radiation & Photochemistry Division

and

Amar Kumar and P.K. Wattal
Process Development Division

and

P. N. Bajaj
Radiation & Photochemistry Division

This paper received the Best Paper Award (Poster Presentation), at the National Symposium on Radiation and Photochemistry (NSRP- 2011), held at Dept. of Chem., JNV Univ., Jodhpur, Rajasthan, during March 10-12, 2011.

Abstract

A novel method of synthesis of spherical RF resin, using pre-formed divinyl benzene cross-linked polystyrene (XAD) microspheres of desired size as a base material, has been developed. These synthesized RF-coated XAD (RF-XAD) beads are characterized, using techniques, such as TGA, SEM, Surface Area Analysis, Universal Testing Machine, etc. Suitable size and mechanical stability, along with their spherical shape, make these beads most appropriate for column operation. The efficiency of these beads is tested for the removal of cesium, from alkaline medium, in batch conditions, using radiotracer technique, employing ^{134}Cs. The effect of sodium ion concentration, the initial cesium ion concentration and the contact time is also investigated. It is observed that, K_d value for Cs^+ ions decreases with increase in Na^+ ion concentration. The ion-exchange capacity of the RF-XAD beads is determined to be 2.35 mmol/g. The equilibrium data are fitted into different isotherm models, and are found to be represented well by the Langmuir isotherm equation, with a monolayer sorption capacity of 2.17 mmol/g. Kinetic modeling analysis, using pseudo first-order, pseudo second-order and intraparticle diffusion equations, show that the pseudo second-order equation is the most appropriate model for description of the sorption of cesium ions onto the RF-XAD beads. The rate constants are determined at different initial concentrations. The process mechanism is found to be complex, consisting of both film diffusion and pore diffusion.

Introduction

During the last several decades, considerable efforts have been directed towards removal and recovery of fission products from nuclear waste streams. Among these fission products, ^{137}Cs is of special concern, because with ^{90}Sr, it constitutes a major source of heat in the waste. This radionuclide has long half-life, and is a biological hazard. So, its removal from the waste streams, before discharge to the environment, is necessary. A variety of methods, such as liquid/liquid extraction, solid/liquid extraction, ion-exchange processes, etc., have been proposed for the recovery/removal of ^{137}Cs from nuclear waste. Because of low-cost, safety, availability, profitability, easy operation and efficiency considerations, only resorcinol–formaldehyde (RF) resin has emerged as a satisfying option for removal of Cs^+ ions from highly alkaline media [1]. RF resin has exceptionally high affinity for Cs^+ ions. Conventionally, RF resin is prepared by bulk polymerization reaction, to get big chunks of the resin, and then, these chunks are ground and sieved, to get desirable mesh size [2]. But, these ground gel particles are of irregular shape, have broad particle size distribution, and exhibit poor column hydraulic behavior. These problems can be solved by using spherical resin material. We have developed a new method for the synthesis of spherical RF resin (RF-XAD), using pre-formed commercially available, divinyl benzene cross-linked polystyrene microspheres (XAD-4) of desired size as a base material. These RF-coated beads are characterized, using TGA technique, SEM, BET surface area analysis and universal testing machine. The sorption and kinetic studies for Cs^+ ions have been carried out in detail, using radiotracer technique. The experimental data are analyzed, using various sorption isotherm and kinetic models.

Experimental

Synthesis of RF-XAD resin beads

Resorcinol formaldehyde pre-condensate was prepared by reacting resorcinol and formaldehyde in aqueous media, using NaOH as a catalyst. An aqueous solution, with resorcinol: formaldehyde: catalyst in the molar ratios of 1:3:6, was prepared, and allowed to react for time till it attained a suitable viscosity. Then, XAD beads were equilibrated with this RF pre-condensate solution, for 2 hours. The equilibrated beads were separated from the rest of the RF pre-condensate solution, and the solution sorbed on the beads was allowed to cure completely. After complete curing at 105 °C, for 4 hours, brown-colored RF-coated XAD beads were obtained. These beads were in sodium form, and hence were dark-colored. The synthesized resin beads were converted into hydrogen form, by contacting these with 0.5M HNO_3 in a 3 to 1

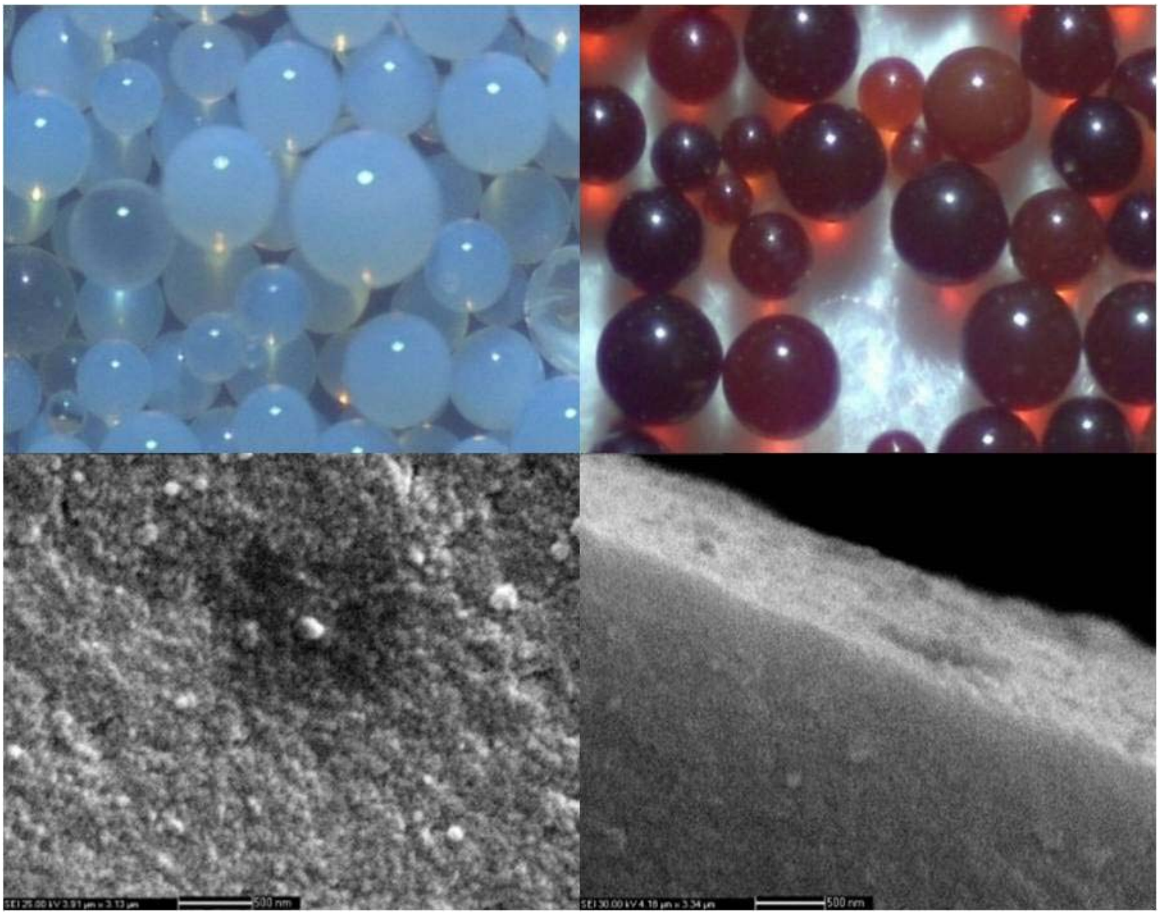

Fig. 1: Optical microscope image of (a) XAD beads, and (b) RF-XAD beads (10X magnifications) and SEM image of (c) surface and (d) a cross- section of a RF-XAD bead (scale bar 500 nm)

ratio of liquid-to-resin volumes for 1 hour, with occasional gentle shaking. After that, the resin beads were separated, and washed with water thoroughly, to remove any residual acid, till pH of the washing became near neutral. This acid treatment brought the resin in light-colored hydrogen form. This hydrogen form of the resin was air-dried, and stored. It was used as such, without any further pre-treatment, in all the sorption experiments.

Fig.1 represents the optical microscope and SEM images of the XAD and RF-XAD beads, and confirms the coating of RF on the pre-formed XAD beads. The SEM image [Fig 1(c)] of the outer surface of these RF-XAD beads shows porosity. This porous nature of the beads, which is also corroborated from the results of the TGA study, is a desirable feature, as it will contribute to better sorption behavior. The SEM image of a cross section of RF XAD beads does not show any distinct boundary or contact between the RF coating and XAD template, indicating that the RF has penetrated inside the XAD-4 beads.

Sorption Studies

^{134}Cs radiotracer ($T_{1/2}$ = 2.06 y; specific activity = 8.44 Ci/ml) was procured from the Board of Radiation and Isotope Technology (BRIT), Mumbai, India. The solution was further diluted to the required concentrations, as and when needed. The batch capacities of the resin were determined, by shaking 0.1 g of RF-XAD resins beads with 10 ml of the $CsNO_3$ solution of appropriate concentration, containing cesium-134 as a radiotracer. The solutions were stirred well, using a mechanical shaker, for 4 hours, which was found to be sufficient for attaining equilibrium. However, for studying kinetics of the sorption, the equilibration time was varied from 0 to 6.5 hours. All the test solutions, containing cesium ions, were prepared in 0.1 N NaOH solutions, to maintain similar alkalinity of the solutions. After the equilibration, a small portion of the aqueous phase (1 ml) was separated, and taken for counting gamma activity. The gamma activity measurements were carried out in a well-type NaI (T1) [ECIL] detector, connected to a single-channel analyzer. Equilibrium sorption capacity, q_e, was determined, using equation (1).

$$q_e = \frac{(C_0 - C_e)V}{m} \qquad (1)$$

Where C_o is the initial cesium ion concentration, C_e is the equilibrium cesium ion concentration, V is volume of the solution equilibrated with m weight of the sorbent.

Results and Discussions

Thermogravimetric analysis (TGA)

Thermo gravimetric analysis (TGA) of the synthesized beads was performed at a heating rate of 10 °C/min in nitrogen atmosphere, from ambient conditions to 900 °C. Fig.2. shows typical TGA profiles of the granular RF particles, XAD and RF-XAD beads. The thermal decomposition profile of pure granular RF particles is continuous, and unlike that of XAD and RF-XAD, it does not show very well-defined decomposition steps (trace a, Fig. 2). After heating upto 110 °C, weight loss of about 8% is observed, which could be due to the absorbed moisture. Additional 7 % weight loss is observed upto 216 °C, which could be due to decomposition of RF. With further increase in temperature, a continuous decrease in the weight takes place, and at the end of the heating cycle, the charred mass is obtained, which is about 37 % of the initial RF weight taken. The thermal decomposition of XAD beads takes place in two major steps (trace b, Fig. 2). In the first step, 30 to 86 °C, there is a weight loss of 8.7%, corresponding to evaporation of the absorbed moisture. Then, the second step starts at 343 °C, in which degradation of XAD matrix takes place, and additional weight loss of ~72% is observed at the end of this step at 560 °C. The TGA profile of RF-XAD beads (trace c, Fig. 2) also can be divided into two main stages. The first stage is from 30 to 118 °C, over which a weight loss of about 36% is observed due to dehydration. The weight loss in the same range of 343-560 °C, as that in the case of XAD beads, is about 38%, due to simultaneous degradation of RF and XAD. The TG profiles of XAD and RF-XAD appear similar, but the extent of thermal degradation of the composite beads is much lower than that of the XAD beads and the moisture content in blank XAD is less than that in RF-XAD beads. The enhanced thermal stability of the composite beads can be attributed to the presence of RF, which is more thermally stable than XAD. The higher moisture content indicates hydrophilic and porous nature of the RF coating. These characteristics of the RF-XAD beads improve the efficiency of Cs^+ ion sorption from alkaline aqueous waste.

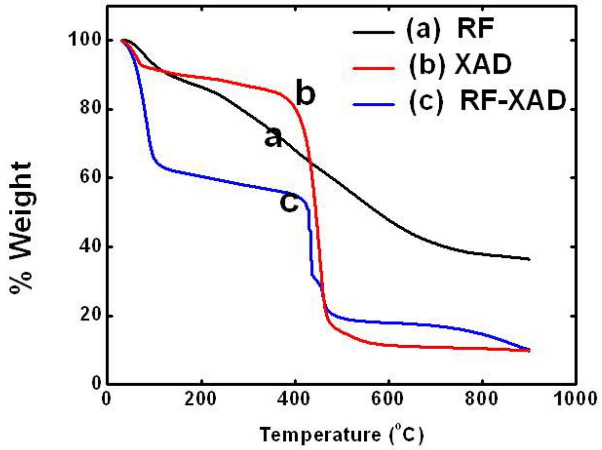

Fig. 2: TGA profile of (a) granular RF particles, (b) XAD beads beads and (c) RF-XAD beads

BET surface area

The specific surface area and pore volume of the beads were determined by BET N_2 adsorption method. The surface area was found to be 170 m^2/g, and the pore volume was found to be 0.19 cc/g. The pore radius was determined to be ~20Å, confirming mesoporous nature of the synthesized beads. The surface area of the blank Amberlite XAD-4 beads, as per specifications is 750 m^2/g, with average pore diameter of 100Å. The reduction in the surface area and shrinkage of the pore diameter of the template beads suggests the presence of the RF inside the pores also.

Mechanical Strength Testing

The mechanical strength of the synthesized RF-XAD beads was tested, by a universal testing machine, by applying a load in the range of 0- 250 N, using 500 N load cell, and compared with that of the conventional ground RF gel particles and blank XAD beads. XAD blank beads showed first breakage at an applied load of 2 N, and second breakage at 4 N. At this stage, the XAD bead was completely compressed, and no machine extension was observed for even higher applied load. Spherical RF-XAD beads showed first break at a load of 13-15 N, for the different samples tested. This increase in mechanical strength of RF-XAD beads suggests that, the RF is present not only on the surface of the XAD template beads, but it has also penetrated in the pores of the XAD beads, and solidified. Under similar experimental conditions, the first breakage for the ground RF gel was observed at 2.5-5 N, and different breakages were seen in the range of 2.5-15 N, depending on the shape and the size of the granular RF particles. The irregular-sized ground gel particles have some sharp and weak edges, which are the most susceptible for breaking under pressure, and result in generation of fine powder, which leads to column choking. While the synthesized RF-XAD beads are spherical in size, and have better mechanical strength as compared to that of the currently used ground RF resin gel particles, making these more suitable for column operation.

Ion-Exchange Capacity and Effect of Na^+ Ion Concentration

About 0.5g of the H^+-form, air-dried RF-XAD resin beads were equilibrated with 100 ml of 0.1M NaOH solution, containing 5% NaCl. From the amount of NaOH consumed, the total H^+-Na^+ ion-exchange capacity was determined to be 2.35 milliequivalents/g, i.e., 2.35 mmol/g of air-dried, H^+-form RF-XAD resin. The capacity of the template XAD-4 beads was also tested, using ^{134}Cs radiotracer, and it was confirmed that blank XAD-4 beads do not pick up cesium from aqueous solution.

The competitive effect of Na^+ ions on the sorption of Cs^+ ions onto the RF-XAD beads was determined, by varying Na^+ ion concentration, at a constant Cs^+ ion concentration of 0.02M, at 300K. The solutions were prepared in 0.1M NaOH solution, and the concentration of Na^+ ions was varied, using $NaNO_3$, as a source of Na^+ ions. The batch distribution coefficient (K_d) was determined, using equation (2)

$$K_d = \frac{A_0 - A}{A} \times \frac{V}{m} \qquad (2)$$

Where A_0 and A are the initial and the final activities, respectively, of the solution, V is the volume of equilibrating solution (10 ml), and m is the weight of the resin taken (0.1g). It is observed that the K_d value for Cs^+ ions decreases quite rapidly with increase in Na^+ ion concentration (Fig. 3), due to the competitive sorption of Na^+ ions onto the available exchange sites.

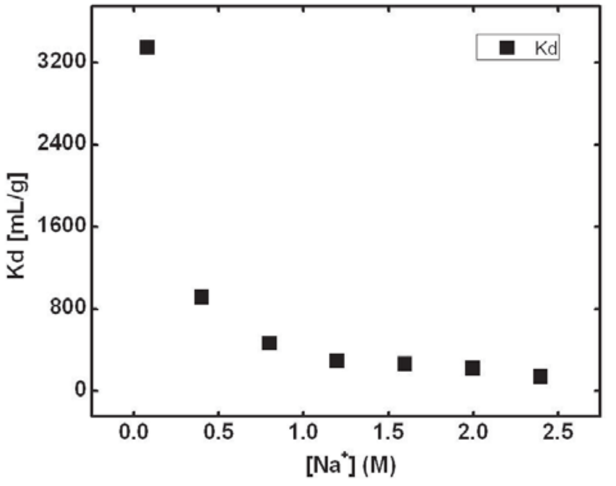

Fig. 3: Effect of the Na^+ ion concentration on the sorption of Cs^+ ion onto the RF-XAD beads at 0.02M Cs^+ ion concentration at 300K

Effect of Cs^+ Ion Concentration

The sorption capacity of the RF-XAD beads for cesium ions was determined, by studying the sorption as a function of cesium ion concentration, at 300K, in a batch experiment. The concentration of the inactive cesium ions in the aqueous solution was increased from 0.1 to 250 mM, and the q_e was determined. It is observed that, q_e increases gradually with increase in cesium concentration, and reaches a saturation value of ~1.5 mmol/g at 250 mM, as shown in Fig. 4. The observed results can be explained by the fact that, with increase in concentration, the incremental increase in cesium ion uptake by sorbent is more initially, as more active sites are available, but it then, decreases as the number of available active sites decreases, and finally, it becomes zero.

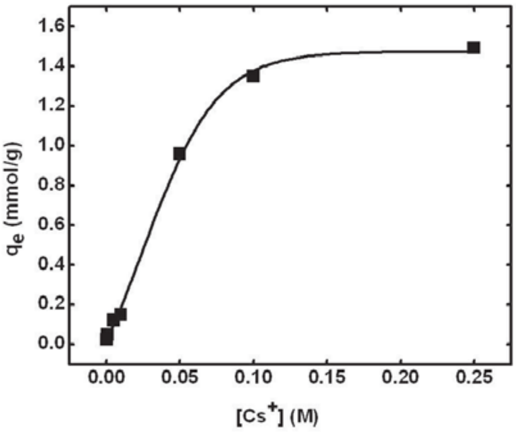

Fig. 4: Effect of the initial cesium ion concentration on the sorption of Cs^+ ions onto RF-XAD beads at 300K

Sorption Isotherms

To evaluate the nature of the sorption, the data were fitted to Langmuir and Freundlich isotherm models.

Langmuir sorption isotherm is the simplest isotherm model for sorption of a solute from a liquid solution, and it is valid for monolayer sorption onto a surface, containing a finite number of identical active sites [3]. It is described by the following equation:

$$\frac{1}{q_e} = \frac{1}{q_m} + \frac{1}{K_L q_m C_e} \qquad (3)$$

Where q_e is the amount of the Cs^+ ions sorbed onto the swollen beads at equilibrium, in mmol/g, q_m is the maximum capacity at complete monolayer coverage of the swollen beads (mmol/g), and K_L is the affinity constant. The plot of $1/q_e$ vs $1/C_e$ is a straight line (Fig. 5). The values of q_m and K_L can be obtained from the intercept and the slope, respectively. The value of correlation coefficient R^2 is 0.99815, which indicates a good agreement between the experimental data and the Langmuir sorption model. The maximum sorption capacity of the RF-XAD beads, for Cs^+ ions, is determined to be 2.17 mmol/g, i.e., 287 mg/g of the resin beads, which is close to the experimental Na^+ ion-exchange capacity value

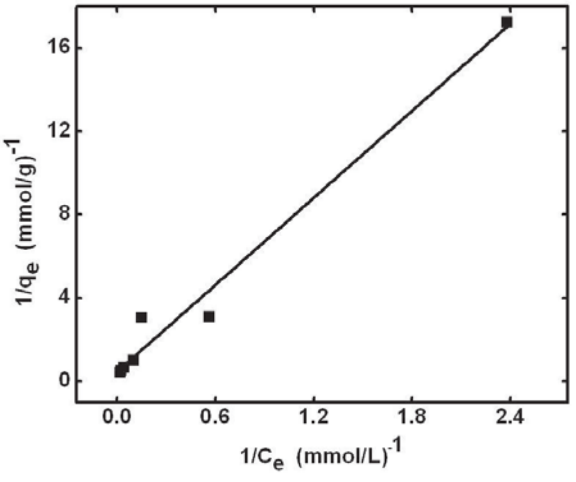

Fig.5: Langmuir isotherm plot for sorption of Cs^+ ions onto RF-XAD beads, at 300 K

of 2.35 mmol/g. The sorption coefficient, K_L, which is related to apparent energy of sorption for Cs^+ ions onto the RF-XAD, is determined to be 0.66 L/mmol. The high sorption capacity of the synthesized beads can be attributed to the high surface area of the RF-XAD beads.

The Freundlich isotherm is the earliest known empirical model and allows the existence of heterogeneous surface. It assumes that the stronger binding sites are occupied first, and that the binding strength decreases with increase in the degree of site occupation. The data were also analyzed, using the linerized form of Freundlich isotherm, which is given by the following equation [4].

$$log\, q_e = \log K_F + \frac{1}{n}\log C_e \tag{4}$$

Where, K_F is Freundlich constant, indicating sorption capacity, and n is Freundlich parameter, which is indicative of the heterogeneity of the sorbent surface. The plot of log (q_e) vs log (C_e) is a straight line, as shown in Fig.6, and from the slope and the intercept, respectively, of this straight line, the values of 1/n and K_F are determined.

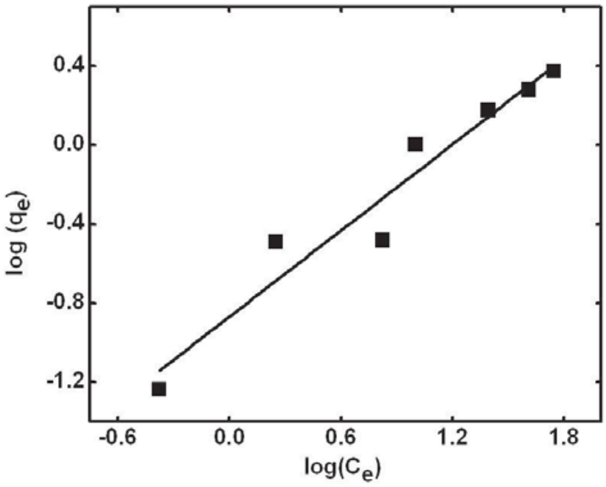

Fig. 6: Freundlich isotherm plot for the sorption of Cs^+ ions onto the RF-XAD beads, at 300 K

The value of correlation coefficient R^2 for this plot is 0.93023, which suggests that the agreement between the experimental data and the Freundlich isotherm model is not as good as that of the Langmuir sorption model. The value of n is 1.378, which lies between 1 and 10, indicating favorable sorption of cesium ions onto RF-XAD beads.

Sorption Kinetics

The effect of equilibration time on the sorption of cesium ions, from aqueous solutions, was also studied. The sorption increases with increase in contact time (Fig.7).

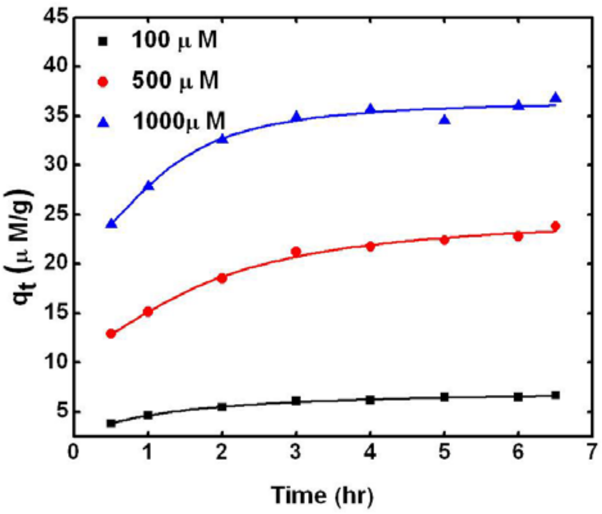

Fig. 7: The effect of equilibration time on the sorption of Cs^+ ions onto the RF-XAD beads, at three different initial concentrations

Uptake of Cs^+ ions is rapid in the initial 2 hours, and the equilibrium is reached in ~ 4 hours, indicating a quite fast sorption rate. The initial rapid sorption can be related to the abundant availability of the active sites in the initial stage. Later on, the process becomes relatively slower, and equilibrium conditions are reached within about 4 hours. At this point, the amount of the cesium ions being sorbed onto the sorbent is in dynamic equilibrium with the amount of the cesium ions desorbing from the sorbent. The time required to attain this equilibrium is termed as the equilibrium time, and the amount of cesium ions sorbed at the equilibrium time reflects the maximum sorption capacity of the sorbent under those operating conditions. As the equilibrium stage is attained in 4 hours, the batch experiments, for uptake determination, were carried out at 4 hours of equilibration time. The experimental q_e values, at the three studied concentrations of 100, 500 and 1000 μM, are found to be 6.7, 23.8 and 36.8 μmol/g, respectively.

Kinetics Modeling

In order to investigate the sorption process of cesium ions onto RF-XAD beads, three kinetic models, namely, pseudo-first-order model, pseudo-second-order model and intraparticle diffusion model and Boyd's plot were used to fit the experimental kinetics data. The values of R^2 for the second order model fitting are higher than that for the pseudo first-order kinetic model, at all the studied concentrations of cesium. And, the q_e values calculated, using the second-order model, are also in good agreement with the actual experimental values. Therefore, the second-order model can be applied to the sorption process in the entire studied concentration range, and we can conclude that the pseudo-second order model explains the kinetics of the process in a better way. The results of the intraparticle diffusion model and Boyd's plot indicate that the sorption process is of complex nature, comprising both the film diffusion and intraparticle diffusion, with the former mainly governing the rate of the process in the studied range of the solute concentration.

Conclusions

The present study shows that the RF-XAD composite beads can be easily synthesized by coating RF onto XAD beads, and can be used as a sorbent for the removal of cesium ions from nuclear waste solutions. The equilibrium data follow Langmuir isotherm, confirming the monolayer coverage of cesium ions onto the composite beads. The maximum monolayer capacity is 287 mg/g. Among the different kinetic equations applied, the kinetics data fit well to the pseudo second-order kinetic model. Analysis of mechanistic steps involved in the sorption process reveals the complex nature of the sorption process. From intra-particle diffusion model and Boyd's plot, it can be inferred that the process mechanism consists of both intraparticle diffusion and film diffusion, with latter as the rate governing step.

Acknowledgements

The author, Charu Dwivedi, is grateful to BRNS, Department of Atomic Energy, for awarding research fellowship. The authors wish to acknowledge Dr. T. Mukherjee and Dr. S.K. Sarkar, for their encouragement during the course of the study.

References

1. N. M. Hassan et al., *Solvent Extraction and Ion Exchange,* 23: 375–389, 2005.
2. S. K Samanta et al., *Separation Science and Technology.*, 27: 255-267,1992.
3. K. R. Hall, L. C. Eagleton, A. Acrivos and T. Vermeulen, *Ind. Eng.Chem.Fundam.,* 1966, 5, 212.
4. D. Das, N. Das and L. Mathew, *J. Hazard. Mater.,* 2010, 184, 765.

EFFECT OF POLYMER MODIFICATION OF SIO_2 DIELECTRIC ON THE PERFORMANCE OF COPPER PHTHALOCYANINE BASED ORGANIC THIN FILM TRANSISTOR

N. Padma, A.K. Chauhan and S.K. Gupta
Technical Physics Division
and
Shilpa N. Sawant
Chemistry Division

This paper received the Best Poster Award at the 56th DAE Solid State Physics Symposium held at Kattankulthur, Tamilnadu during December 19-23, 2011

Abstract

Effect of polystyrene modification of SiO_2 dielectric on the electrical performance of copper phthalocyanine (CuPc) based OFETs was studied. Field effect mobility of holes was found to increase by one order for polystyrene modified dielectric as compared to that on unmodified SiO_2. This is attributed to well connected grains and increased crystallinity of CuPc film. Significantly reduced hysteresis was found in the devices with polystyrene modified dielectric due to almost complete absence of hydroxyl groups at the dielectric/semiconductor interface and hence reduced trap sites.

Introduction

Organic field effect transistors (OFET) have potential use in a variety of applications such as flexible displays, electronic bar codes etc. As most of the modulated charge lies close to semiconductor/dielectric interface, molecular ordering of active layer at the interface is crucial. Modification of dielectric surface with polymers or self assembled monolayers (SAM) are commonly employed techniques to improve molecular ordering of organic semiconductor [1,2]. Since most of the polymers are solution processable, simple method of drop casting or spin coating can be applied to modify dielectric surface. Instability in threshold voltage manifesting as hysteresis in transfer characteristics poses serious limitation to practical use of OFETs. Modifying dielectric with suitable polymer layer minimizes the number of hydroxyl groups at the interface thus reducing trap sites and hysteresis [2]. In this work we have studied the performance of OFETs using SiO_2 as dielectric and chemically and thermally stable copper phthalocyanine (CuPc) as active material. We show that Polystyrene (PS) modified dielectric yields more stable performance with improved mobility.

Experimental

Heavily doped (100) oriented (0.01-0.015 Ωcm) silicon wafers were used as gate electrode with 200 nm thermally grown SiO_2 layer as gate dielectric. For polymer modification, 70 nm thick film of PS was deposited above SiO_2 layer by spin coating 2 wt. % solution of PS in toluene at 4000 rpm and cured under vacuum at 60 °C for 4 hours. 60 nm thick copper phthalocyanine was thermally evaporated above unmodified (device 1) and PS modified SiO_2 (device 2) substrates maintained at room temperature. Top contact OFET devices were fabricated by thermally evaporating gold source (S) and drain (D) electrodes above CuPc film with channel length *(L)* and width *(W)* of 25μm and 2 mm respectively. Capacitance of Au/dielectric/Si(n^{++}) structure and current-voltage *(I-V)* characteristics of OFETs were measured in air at room temperature using Agilent 4284A LCR meter and Keithley meter (model 6487) respectively. Hydrophilic and hydrophobic nature of SiO_2 and PS/SiO_2 surfaces respectively were monitored by measuring water drop contact angle (Data Physics). Surface roughness of SiO_2 and PS/SiO_2 and morphology of CuPc films were verified using Atomic Force Microscopy (AFM) (NT MDT, SOLVER P47). Structure of CuPc films was determined by grazing angle (angle fixed at 0.1°) X-ray diffraction measurements (XRD) (SEIFERT-XRD 3003-TT)

Results & Discussion

Water drop contact angle measured on SiO_2 and PS/SiO_2 were found to be 25 ° and 93 ° respectively and these indicated modification of hydrophilic SiO_2 to hydrophobic nature by PS film. Average surface roughness of dielectric reduced from 1.2 nm to 0.8 nm after coating of PS film. Surface morphology of CuPc film on PS/SiO_2 (Fig.1b) showed larger and better connected grains compared to that on unmodified SiO_2 (Fig. 1a). XRD pattern of CuPc films on both devices (Fig. 2) show a single peak corresponding to (200) plane of α-CuPc indicating π-π stacking of CuPc molecules parallel to substrate surface, and thus resulting in better charge carrier transport across the channel [3].

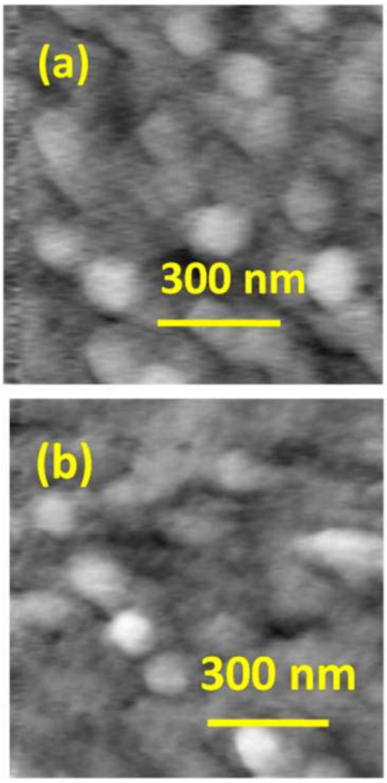

Fig. 1: Surface morphology of CuPc film on a) SiO_2 and b) PS/SiO_2

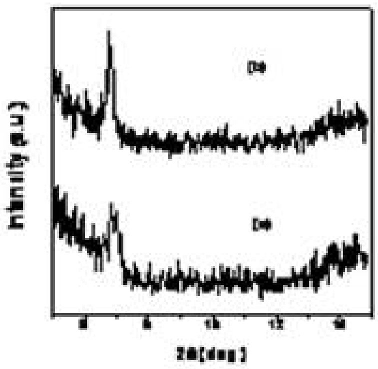

Fig. 2: XRD pattern of CuPc film on a) SiO_2 and b) PS/SiO_2

Output characteristics of both OTFTs and their respective transfer characteristics for gate voltage sweep from 0 to -50 V with constant drain voltage of -50V corresponding to saturation region are shown in Figs. 3 and 4 respectively.

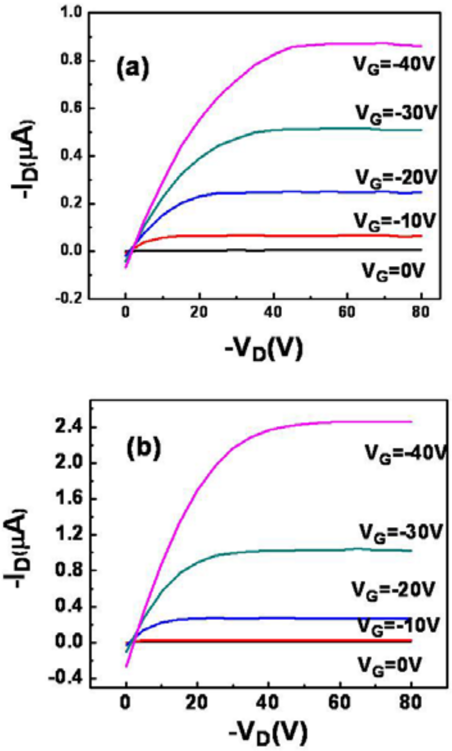

Fig. 3: Output characteristics of OFETS on a) SiO_2 and b) PS/SiO_2

Field effect mobilities (μ) in saturation region were determined using the equation [4]:

$$I_D = (WC_i / 2L)\mu\,(V_G-V_T)^2 \qquad (1)$$

where C_i is capacitance/area of dielectric, V_T is threshold voltage. The electrical parameters of OFETs are summarized

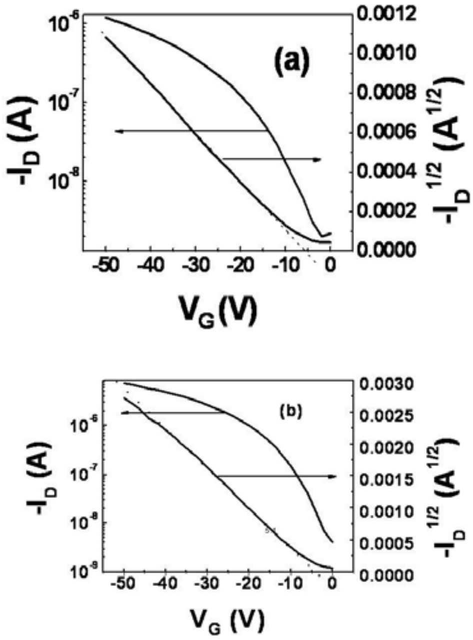

Fig. 4: Transfer characteristics of OFETS on a) SiO_2 and b) PS/SiO_2

in Table 1. Increase in mobility by one order for device 2 could be attributed to well connected grains as seen by AFM investigations, and to increased crystallinity as seen by XRD where reduced FWHM of 0.19° is obtained for film on PS/SiO_2 compared to 0.25° for that on SiO_2

Table 1: Electrical parameters of OFETs

gate ins.	C_i nF/cm^2	(μ) cm^2/Vs	I_{on}/I_{off}	V_T (V)	S V/dec
SiO_2	15	0.001	$1.5x10^3$	-5	7.5
PS/SiO_2	10	0.009	$4x10^3$	-4	5

Hysteresis in transfer characteristics for multiple sweeps of gate voltage is shown in Fig. 5

Large variation in drain current between forward and reverse sweep of gate voltage is seen for device 1. Anticlockwise hysteresis (reverse sweep current less than forward current) is mostly attributed to charge trapping at dielectric/semiconductor interface and/or in semiconductor itself [5]. Si-OH groups on the surface of SiO_2 are known to act as acceptor and donor like traps. For negative and positive gate sweep, hole and electron trapping respectively become dominant causing hysteresis [18]. Negligible hysteresis for device 2 is attributed to absence of OH groups at the interface due to hydroxyl free polymer film and hence more stable performance.

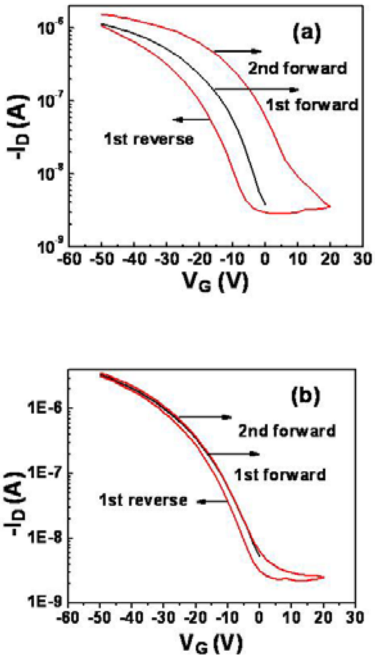

Fig. 5: Hysteresis in transfer characteristics of OFETs on a) SiO_2 (device 1) and b) PS/SiO_2 (device 2).

Conculsions

The field effect mobility of holes increased by about one order while hysteresis in transfer characteristics reduced significantly for OFETs after modification of SiO_2 with polystyrene film. This is attributed to absence of OH groups and increased hydrophobic nature of dielectric surface causing improved ordering of CuPc films.

References

1. K. Xiao, Y. Liu, Y. Guo, G. Yu, L. Wan and D. Zhu, *Appl. Phys.* A, 80, 1541-1545 (2005)
2. A. Yu, Q. Qi, P. Jiang and C. Jiang, *Synth. Met.,* 159, 1457-1470 (2009).
3. N. Padma, A. joshi, A. Singh, S. K. Deshpande, D. K. Aswal, S. K. Gupta and J. V. Yakhmi, *Sens. Actuators B:Chem.* 143, 246 (2009)
4. Y. Jang, H. Seo,Y. Zhang and J. Choi, *Org. elec. ,* 10, 222-227 (2009)
5. D. K. Hwang, K. Lee,J. H. Kim and S. Im, *Appl. Phy. Lett.,* 89, 093507 (2006).

MEASUREMENT OF HIGH ENERGY NEUTRONS (E > 50 MEV) AT INDUS ACCELERATOR COMPLEX USING BISMUTH FISSION DETECTORS

S.P. Tripathy, Sunil C. and P.K. Sarkar
Health Physics Division

and

Dimple Verma and Haridas G.
Health Physics Unit, RRCAT, Indore

This paper received the Best Poster Award at the Conference on Accelerator Radiation Safety (CARS 2011) held at Mumbai, during November 16-18, 2011

Abstract

This paper reports the measurement of high energy neutron component (E > 50 MeV) carried out at Indus-1 (450 MeV) and Indus-2 (2.5 GeV) electron accelerators (RRCAT, Indore). The bismuth fission detector (BFD) stacks are exposed at injection septums of booster synchrotron, Indus-1 and Indus-2 storage rings, where the possibility of dose due to beam loss is expected to be maximum.

Introduction

Indus accelerator complex of RRCAT (Indore, India) consists of a 20 MeV Microtron, a 450/700 MeV Booster, and 450 MeV (Indus-1) and 2.5 GeV (Indus-2) storage rings[1]. Fig.1 represents the layout of booster, Indus-1 and Indus-2. The radiation environment present in these types of accelerators is due to bremsstrahlung photons generated by interaction of high energy electrons with structural materials of accelerator. These photons having sufficient energy ($E_\gamma > 5.0$ MeV), further interact with beam line components like injection lines, collimators, slits, beam stoppers, beam dumps, etc. to produce neutrons of varying energies by means of different photonuclear interactions, viz. giant dipole resonance ($E_\gamma < 40$ MeV), quasi-deuteron ($50 < E_\gamma < 300$ MeV) and photo-pion ($E_\gamma > 140$ MeV).

In accelerators where photon energy and intensity is high compared to neutrons, it is difficult to measure direct photoneutron component. In such accelerators, neutrons and photons contribute to largest percentage of dose even beyond shielding[2]. Since radiation field here is pulsed in nature (ns to μs), measurements using active detectors

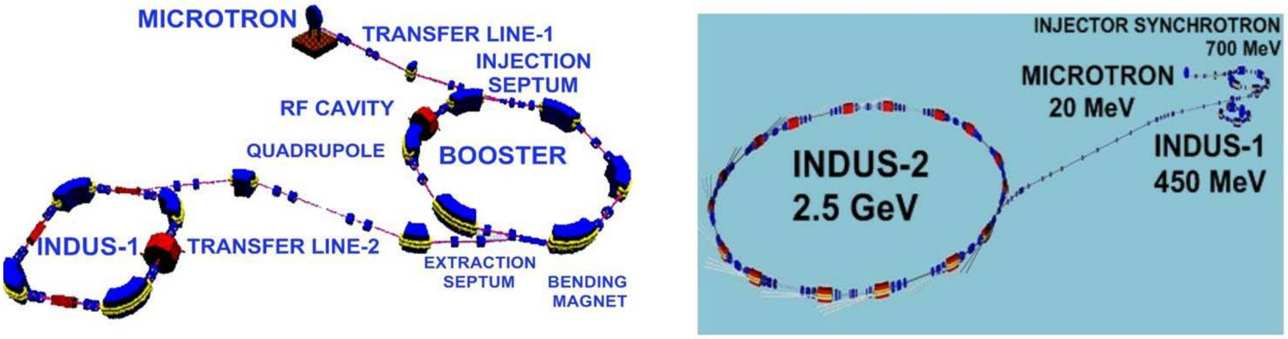

Fig.1: Layout of (a) Booster, INDUS-1, (b) INDUS-2 electron accelerators.

are difficult. In such situations, bismuth fission detectors (BFD) are found to be suitable. In this work, BFD stacks are used to measure photoneutrons above 50 MeV in Indus accelerator facilities at RRCAT, Indore. Attempts are also made to determine the contribution from photofission components.

Bismuth Fission Detector (BFD) stack

Fig. 2 presents bismuth fission detector set up. The neutron-induced fissions in the Bi film are registered in solid polymeric track detector (SPTD). Threshold energy of it is determined from (n,f) cross-section (fig.3). The attractive characteristics of this detector are: insensitive to RF interference, does not respond to low LET particles, smooth variation of cross section with energy, integral mode and almost permanent registration of the signal, mono-isotopic, non-radioactive, light weight and convenient to expose.

Fig.2: Bismuth fission detector

Photofission correction

If gamma field is highly intense in terms of energy and fluence, the photofission component may become comparable to that of neutron fissions. Then dose values need to be corrected for the photofission components. The neutron-induced fission cross section (σ(n,f)) and photofission cross section (σ(γ,f)) for ^{209}Bi are compared in Fig.3. As seen in Fig.3, earlier reported cross section values[3,4] are slightly lower than recent measurements [5,6]. Nevertheless energy threshold is found to be unchanged.

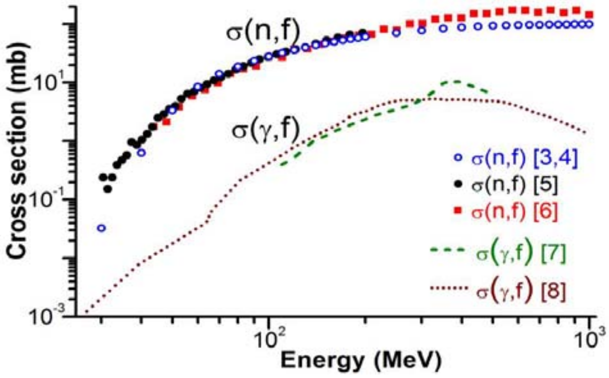

Fig.3: Fission cross-sections in ^{209}Bi induced by neutrons (n,f) and photons (γ,f).

For photofission cross section, measurements up to 500 MeV by Jungerman[7] and calculations up to 1 GeV by Poyser et al.[8] are considered. As seen from these curves, the measured (γ,f) cross section peaks at about 400 MeV photon energy. But, calculated σ(γ,f) values show a smooth variation with energy and is about 20 times less than σ(n,f). Total photofission component can be found by folding bremsstrahlung spectrum with σ(γ,f).

Experimental details

Calibration and measurements

BFDs are prepared by sandwiching polymeric track detectors between Bi radiators. These stacks are calibrated at high energy reference field in CERN, Switzerland and to quasi monoenergetic neutrons at The Svedberg Laboratory (TSL), Sweden. The neutron spectra and other relevant parameters of CERF and TSL are reported elsewhere[9,10]. Measurements at Indus accelerator complex are carried out by exposing BFD stacks at injection septums of the booster, Indus-1 and Indus-2 storage rings, where the possibility of beam loss is expected to be maximum. Three separate experiments are conducted for different time periods (Table 1). The first two experiments are carried out for different durations to check the reproducibility. The third experiment is conducted to determine the signals from photofission components by introducing a Pb block of 3.8 cm between two sets of BFD stacks so as to attenuate the contribution from photon components.

Track development and counting

After irradiation, track detectors are etched with 30% KOH in water at 40°C for 2.5 h. The sparks are counted in spark counter at 500 V after pre-discharge of 900 V. Dose equivalent values are determined using calibration factor (mSv cm^2 spark^{-1}) obtained from CERF.

Results and discussion

Table 1 gives dose equivalent rates and total exposure times. As evident, dose equivalent rates are found to be

Table 1: Dose equivalent rates due to photoneutrons at booster, Indus-1 and Indus-2.

Expt.	Location	Exposure time (h)	Dose equivalent rate (mSv/h)	
1	A	73	0.11±0.02	
	B	35	0.11±0.02	
	C	5	0.65±0.09	
2	B	25.5	0.10±0.01	
	C	18.5	0.62±0.08	
3			BFD-1	BFD-2
	B	180	0.11±0.02	0.10±0.01
	C	164	0.64±0.09	0.63±0.09

Note: A= Booster injection septum, B= Indus-1 injection septum, C= Indus-2 injection septum.

same at booster and Indus-1 injection septums. This is due to gradual ramping of 20 MeV beam, which is injected initially to booster injection septum. In each turn the beam passes through injection septum with amplified energy. So the beam of 20 MeV up to 450 MeV is found to pass through injection septum. The dose rates at the injection septum of Indus-2 (2.5 GeV) are found to be about 6 times higher than Indus-1. Similar results are obtained in second experiment also. Moreover, dose rate values in each location are found to be almost constant even at different periods of exposure. In third experiment, the detectors are exposed for a much longer period. Results obtained from both the detector stacks (BFD-1 and BFD-2 in Fig.4) are found to be almost the same and are comparable to those obtained from the previous two experiments. This indicates that signals from photofission components are too small to be registered in fission track detector.

Conclusion

Bismuth radiators coupled with SPTD are successfully used to measure dose equivalent due to photoneutrons (E>50MeV) at Indus accelerator facilities. Dose rate values are found to be consistent for all sets of experiments. Photofission components are not found to produce any significant changes in the signals registered in BFDs.

References

1. http://www.cat.gov.in/technology/accel/indus/ioapdd/healthphy.html (last accessed: 20 July 2012).
2. Sarkar P K. Radiation Measurements 45 (2010): 1476.
3. Carlson A D et al., IAEA Report INDC (NDS)-368, Vienna, 1997.
4. Tommasino L et al., *Radiation Measurements,* 36 (2003) 307.
5. Shcherbakov O A et al., Int.Sem.on Interactions of Neutrons with Nuclei No.9 (2001) 257.
6. Tarrio D et al. *Phys. Rev. C.* 83 (2011) 044620S.
7. Jungerman A *J., Phys. Rev,* 106 (1957) 585.
8. Poyser W J et al., NASA/TP-2002-211929 (2002).
9. Mitaroff A, Silari M, *Radiat. Prot. Dosim.* 102 (2002) 7-22.
10. Prokofiev A V. et al. *Radiat. Prot. Dosim.* 126 (2007) 18-22.

PprA PHOSPHORYLATION BY Ser/Thr PROTEIN KINASE (STPK) OF *DEINOCOCCUS RADIODURANS* CHANGES ITS *IN VITRO* FUNCTIONS

Yogendra S. Rajpurohit and Hari S. Misra
Molecular Biology Division

Shri Y.S. Rajpurohit received the Best Poster Award at the 6th DAE-BRNS Life Sciences Symposium (LSS-2011), Mumbai, Oct. 12-14, 2011.

Abstract

PprA is unique to *D. radiodurans* and its role in γ radiation resistance and DSB repair has been shown in this bacterium. Phosphomotif search showed that PprA has putative phosphorylation site similar to that is characterized in protein substrates of Ser/Thr protein kinases (STPKs) in eukaryotes. A eukaryotic type STPK (DR2518) of *D. Radiodurans*, could phosphorylate recombinant PprA at threonine amino acid *in vitro.* DR2518 kinase mediated protein phosphorylation of PprA, improves its DNA binding affinity by nearly fourfold and stimulated T4 DNA ligase activity more towards inter-molecular ligation, as compared to unphosphorylated PprA. The putative threonine of 72 position of PprA was replaced with alanine (T72A) by site directed mutagenesis, which resulted in significant reduction of PprA phosphorylation by DR2518 kinase *in vitro* and in the functional complementation of PprA loss in *D. radiodurans*.

Keywords: Deinococcus; DNA repair; protein phosphorylation; radiation resistance

Introduction

The extraordinary survival of *Deinococcus radiodurans* R1 to the lethal and mutagenic effects of DNA damaging agents including ionizing and non-ionizing radiations is result of an efficient DNA double strand break (DSB) repair and a strong oxidative stress tolerance (10). The eukaryotic type STPKs (eSTPK) phosphorylate proteins at serine, threonine and tyrosine residues and play the key roles in regulation of signaling processes involved in development, differentiation, pathogenesis in bacteria (6). Recently, the involvement of DR2518, an eSTPK, in DNA damage tolerance of *D. radiodurans* (8) has been demonstrated. Molecular mechanism underlying sensing of radiation effects and downstream functions of DR2518 to combat γ radiation effects and DNA damage would be worth investigating in this bacterium. In this study, we identified PprA (Pleotropic protein promoting DNA repair), a DNA metabolic protein as a substrate for this kinase and demonstrated that the phosphorylation of PprA occurs at threonine 72 (T72) and such a modification was required for efficient function of PprA *in vitro.*

Experimental procedures

The *pprA* (drA0346) gene was cloned in pET28a vector and recombinant protein was purified using Ni-NTA as described earlier (2). Similarly, recombinant DR2518 kinase was purified as described earlier (8) and was used for the phosphorylation of PprA protein using 50 μCi [^{32}P]-γ-ATP for autoradiography and using 5mM cold ATP for phosphorylation PprA for other experiments like DNA binding and T4 DNA ligase activities. For DNA binding, 33-bp oligomer was radiolabeled at its 5′ end and used for EMSA studies. Ligase activity was performed by preincubation of DNA with PprA, followed by ends joining by T4 DNA ligase as described earlier (3).

Results and Discussion

DR2518 kinase phosphorylated PprA at threonine 72 (T72 *in vitro)*

DR2518 has been characterized as a functional eSTPKs (8), which are known to phosphorylate proteins having conserved phosphomotifs. Therefore, the proteome of *D. radiodurans* R1 was scanned for the presence of "XααααTX(X/V)$(P/R)I" (PMotif), where T is phosphoacceptor site and α is an acidic residues, $ a large hydrophobic residue and X any amino acid (7) using www.scansite.mit.edu motif search tool. Analysis showed a large number of proteins having either exactly or slightly different structure of these phosphomotifs. The notable ones also include PprA. PprA has been shown to be important for radiation resistance of *D. radiodurans* (6). PprA proteins having eSTPK specific phosphomotif was checked for *in vitro* phosphorylation with DR2518 kinase, BSA and single stranded DNA binding protein (drSSB) of *D. radiodurans* were taken as negative controls. The PprA showed relatively higher levels of phosphorylation with DR2518, while drSSB and BSA phopshorylation was not detected (Fig 1A). These results suggested that DNA binding proteins PprA, in *D. radiodurans* could act as phospho-substrates for DR2518 kinase *in vitro*. Since, the mechanisms underlying PprA roles in radiation resistance are better understood as compared to other proteins, the effects of phosphorylation on some of the known functions of PprA including radiation resistance were further investigated. The phosphorylation site (s) in purified PprA incubated with DR2518 kinase, were analysed by mass spectrometry with purified PprA as a control. Unlike recombinant PprA control, the protein incubated with DR2518 showed phosphorylation at threonine 72. These results suggested that DR2518 specifically phosphorylated PprA at T72 position.

Protein phosphorylation modulates PprA functional properties *in vitro*

PprA was shown to be a DNA binding protein. Phosphorylated PprA showed nearly 4 fold higher binding with dsDNA as compared to non-phosphorylated PprA

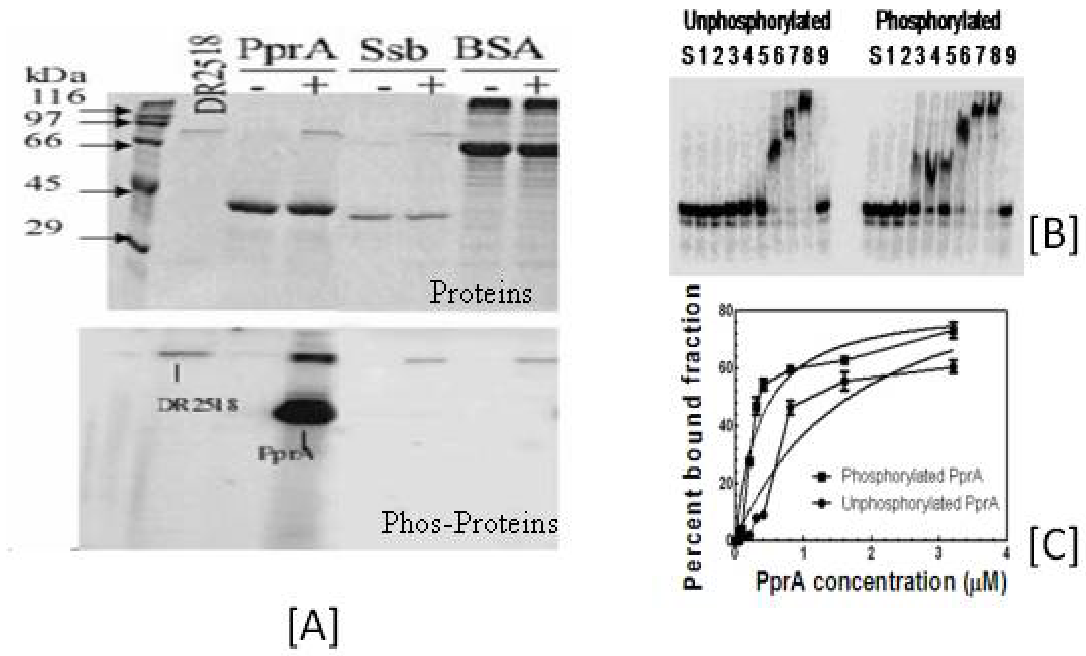

Fig. 1: [A] checking phosphorylation of PprA by DR2518 kinase. Purified recombinant proteins PprA,BSA (Bovine serum albumin), and single stranded DNA binding protein (SSB) of Deinococcus radiodurans were incubated with $[^{32}P]$-γ-ATP in presence, and absence of DR2518 kinase. [B] Effect of phosphorylation on DNA binding activity of PprA. The 0.2pmol of $[^{32}P]$ labeled 33 mer dsDNA (S) was incubated with 0.05 (1), 0.1 (2), 0.2 (3), 0.4 (4), 0.8 (5), 1.6 (6), 3.2 μM (7) and 6.4 μM (8) of unphosphorylated and phosphorylated PprA, separately. [C] Intensity of free DNA and DNA complexes with protein was determined by densitometry scanning. Percent fraction of DNA bound to proteins was calculated and plotted as a function of PprA concentration using Graphpad Prism 5.

(Fig 1B). The Kd values of phosphorylated and unphosphorylated PprAs were 0.348 ± 0.081 μM and 1.766 ± 0.70 μM, respectively (Fig 1C). These results were further supported by competition binding assay of both unphosphorylated and phosphorylated PprA. The log equilibrium dissociation constants (Ki) of both forms of PprA with dsDNA, was calculated by curve fitting using nonlinear regression of competition binding equation of one site Fit Ki, in Graphpad PRISM software. The log Ki for phosphorylated PprA (63.82 ± 0.612) was nearly 4 fold higher than non-phosphorylated PprA (16.3 ± 0.672) (Fig. 2A). The protein phosphorylation mediated increase in DNA binding affinity has been reported earlier for single stranded DNA binding protein (SSB) from *Bacillus subtilis*, where it was shown that tyrosine phosphorylation of SSB increased its affinity for ssDNA by almost 200-fold in *vitro* (4). These results suggested that the phosphorylation of PprA could increase the affinity of this protein for dsDNA.

Earlier it has been shown PprA could stimulate the DNA ligase activity of both ATP type and NAD type DNA ligases (5). Therefore, the effect of PprA phosphorylation on stimulation of DNA ligase activity was examined. Results showed that both phosphorylated and unphosphorylated PprA could improve the total DNA end joining activity of T4 DNA ligase *in vitro* (Fig. 2B) as reported earlier. However, the levels of intermolecular ligation by T4 DNA ligase in presence of phospho-PprA were several folds higher than nonphospho-PprA at 0.4μM concentration (Fig 2B). This might suggest that the phosphorylated PprA could modulate T4 DNA ligase activity for higher levels of intermolecular ligation over the intramolecular ligation.

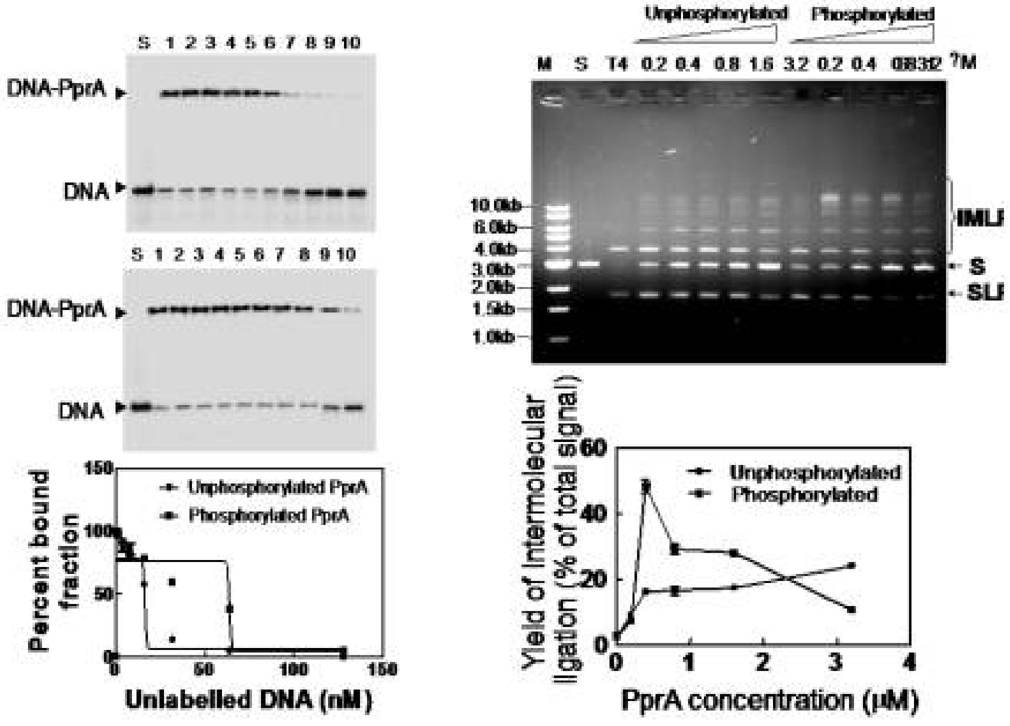

[A] [B]

Fig. 2: [A] The 150nM unphosphorylated (C) and phosphorylated (D) PprAs were incubated with 0.2 pmoles of [32P] labeled 33mer dsDNA (S) in 10ml reaction mixture and chased with 0.25 (1), 0.5 (2), 1.0 (3), 2.0 (4), 4.0 (5), 8.0 (6), 16.0 (7), 32.0 (8), 64.0 (9) and 128 nM (10) cold DNA and products were analysed on 12.5 % native PAGE. Autoradiograms were developed and the intensity of individual bands was determined by densitometry scanning. The percent bound fraction of DNA to protein was calculated and plotted as a function of protein concentration (E). Both Kd and Ki values were determined for curve fitting of individual plot using nonlinear regression equation using Graphpad PRISM software. [B] Effect of PprA phosphorylation on T4DNA ligase activity stimulation. The 400ng BamHI digested pBluescriptSK+ (S) was ligated with T4 DNA ligase (T4) in presence of increasing concentration (0.2M to 3.2μM) of unphosphorylated and phosphorylated PprAs in ligation buffer at 16°C. Products were analysed on agarose gel. The intensity of both self ligated product (SLP) and intermolecular ligated products (IMLP) were determined by densitometry scanning and plotted as a function of protein concentration (B) using Graphpad PRISM 5.

Interestingly, it was observed that the T4 DNA ligase activity stimulation by unphosphorylated PprA increased gradually as a function of PprA concentration, while this activity increase was very rapid with phosphorylated PprA and reached to the maximum at a much lower concentration as compared to nonphosphorylated PprA control. The levels of ligase activity stimulation with 3.2 μM unphosphorylated PprA was always more than similar amount of its phosphoform. Such type of inhibition of T4 DNA ligase activity at higher concentration of PprA has been reported (5) and argued that this effect was due to excessive binding of PprA with DNA molecules. The stimulation of end-to-end joining of linear DNA molecules, resulting in multimer formation has been recently shown in case of native RecN, which has been therefore, named as bacterial cohesin- like protein (9). Therefore, the possibility of phosrylated PprA acting as cohesin –like protein and the phosphorylation regulates this characteristic functions of PprA could be speculated. *D. radiodurans* has both ATP-type as well as NAD-type DNA ligases (1) and the role of PprA in stimulation of its ATP type DNA ligase activity has been shown recently (3). These results suggest that PprA undergoes phosphorylation by DR2518 *in vitro*, which resulted in improved catalytic efficiency on this protein and phospho-PprA possibly supporting the intermolecular DNA end joining activity of DNA ligases during DSB repair, may be suggested.

Acknowledgements

Authors thank Dr. S. K. Apte, Bhabha Atomic Research Centre for his technical comments while pursuing this work. We thank Ms. Swathi Kota for pETpprA and Shri A. K. Ujaoney for SSB, used in this study. We give special thanks to Dr. Steven Patrie and Dr. Tej K. Pandita, UT-Southwestern Medical Centre, Dallas, USA, for their help in mapping of phosphorylation sites in PprA.

References

1. Blasius, M., Buob, R., Shevelev, I. V., and Hubscher, U. Enzymes involved in DNA ligation and end- healing in the radioresistant bacterium, *Deinococcus radiodurans*. *BMC Mol. Biol.* **8**(2007)**,** 69.
2. Kota, S. and Misra, H. S. (2006) A protein implicated in radioresistance of *Deinococcus radiodurans* stimulates catalase activity in *Escherichia coli*. *Appl. Microbiol. Biotechnol.* **72**, 790-796.
3. Kota, S., Kamble, V. A., Rajpurohit, Y. S., and Misra, H. S. ATP-type DNA ligase requires other proteins for its activity *in vitro* and its operon components for radiation resistance in *Deinococcus radiodurans in vivo*. *Biochem. Cell. Biol*. **88**(2010)**,** 783-790.
4. Mijakovic I, Petranovic D, Macek B, Cepo T, Mann M, Davies J, Jensen PR and Vujaklija D Bacterial single-stranded DNA-binding proteins are phosphorylated on tyrosine. *Nucleic Acids Res.* 34(2006), 1588-1596.
5. Narumi, I., Satoh, K., Cui, S., Funayama, T., Kitayama, S., and Watanabe, H. PprA: a novel protein from *Deinococcus radiodurans* that stimulates DNA ligation. *Mol.Microbiol.* **54** (2004), 278-285.
6. Pereira S. F. F., Goss L. and Dworkin J. Eukaryote-Like Serine/Threonine Kinases and Phosphatases in Bacteria. *Microbiol. and Mol. Biol. Reviews* 75(2011) 192-212.
7. Prisic, S., Dankwa, S., Schwartz, D., Chou, M.F., Locasale, J.W., Kang, C.M., Bemis, G., Church, G.M., Steen, H., and Husson, R.N. (2010) Extensive phosphorylation with overlapping specificity by *Mycobacterium tuberculosis* serine/threonine protein kinases *Proc. Natl. Acad. Sci.* USA **107,** 7521-7526.
8. Rajpurohit, Y. S. and Misra, H. S. Characterization of a DNA damage-inducible membrane protein kinase from *Deinococcus radiodurans* and its role in bacterial radioresistance and DNA strand break repair. *Mol.Microbiol.* **77** (2010), 1470-1482.
9. Reyes, E.D.,Patidar, P. L., Uranga, L. A., Boratoletto, A. S., and Lusetti, S. L. RecN is a cohesin-like protein that stimulates intermolecular DNA interactions in vitro. *J. Biol. Chem.* **285**(2010), 16521-16529.
10. Slade, D. and Radman, M. Oxidative stress resistance in *Deinococcus radiodurans*. *Microbiol.Mol.Biol.Rev.* **75**(2011), 133-191.

RADIATION CHEMICAL STUDIES OF WATER-IN-OIL MICROEMULSIONS AND REACTION OF COUNTER ION RADICALS WITH C_{60} AS A PROBE DISSOLVED IN THE ORGANIC PHASE

A. Guleria, A.K. Singh, M.C. Rath, S. Adhikari, S.K. Sarkar and T. Mukherjee
Radiation & Photochemistry Division, Chemistry Group

This paper received the Best Poster Award, at the National Symposium on Radiation & Photochemistry (NSRP-2011), held at JNV Univ., Jodhpur, Rajasthan, during March 10-12, 2011.

Abstract

Radiation chemical studies in quaternary water-in-oil microemulsions (cetyl trimethyl ammonium bromide, CTAB and cetyl pyridinium bromide, CPB) have been performed to characterize the hydrated electrons in these microemulsions having same head group with difference in their hydrocarbon part. Electrons are solvated in two regions; one being the water core other is the interface. Interestingly another species, dibromide radical anion ($Br_2^{\cdot-}$) in CTAB and CPB microemulsions have been observed after electron beam irradiation. Additionally, oxidative electron transfer employing $Br_2^{\cdot-}$ radical has been explored in a situation where inorganic radical is produced in the aqueous core and C_{60} is dissolved in the organic phase of water in oil microemulsions.

Introduction

In four component water in oil microemulsions, surfactant and co-surfactant (commonly medium chain linear alcohols) molecules form a spherical shell with a polar core where water can reside at various concentrations. These core shell structures are dispersed homogeneously in liquid hydrocarbons. As a result, the whole system behaves as a transparent, isotropic and thermodynamically stable solution of water in oil. The water, confined in the cavity controls the size and shape of the micelle and thus the reverse micelles or microemulsions are often characterized by W_0, which is defined as the mole ratio of water to surfactant, $W_0 = [H_2O] / [Surfactant]$. Because of the compartmentalization of reactants into polar and non polar region yet within the reaction zone, the microemulsions have got the importance in its wide applicability in synthesis. Kinetic evidence had shown earlier that the location of the probes in reverse micelles plays an important role in their reactivities. However, in a microemulsion neither the counter ion radical had been observed earlier nor their involvement in redox processes has been reported earlier. In the present article we report important physico-chemical aspects of water in oil microemulsion part of which has already been published [1]. Firstly, the properties of hydrated electron and its decay pattern in the CTAB and CPB microemulsions has been studied to understand the difference in both the environments as both having same head group with difference in their hydrocarbon part. We have also examined, whether oxidative electron transfer employing $Br_2^{\cdot-}$ radical is possible in a situation where the inorganic radical is produced in the aqueous core and C_{60} is dissolved in the organic phase of water in oil microemulsions.

Materials and methods

The pulse radiolysis setup using 7 MeV electron pulses coupled with transient spectroscopy has been employed with 30 Gy dose per pulse. All the surfactants were recrystallized before use. CTAB was recrystallized twice from ethanol. CPB was purified by washing with acetone for 5 times. C_{60} was used as received. All other chemicals were of spectroscopic grade.

Results and discussion

The transient absorption spectra obtained in the pulse radiolysis of a microemulsion containing CTAB /H_2O / *n*-butanol/ Cyclohexane solutions with W_0=40 bubbled with nitrogen are shown in figure where two peaks at 650 nm and at 720 nm are visible. The latter is the typical hydrated electron spectrum one expects in pure aqueous solution. The interesting observation is another absorption maximum at 650 nm. At lower water content (W_0=20) the absorption peak at 650 nm is even more intense than the usual peak at 720 nm at longer times. This absorption peak can be attributed to electrons solvated in the interface of the reverse micelle. It must be noted that the yield of solvated electrons at the interface shows higher value with increase in water content of the system. The electrons at the interface decay slower than the ones in the water pool. Thus, at a particular W_0, due to slower decay, the yield of solvated electrons at the interface might show a higher value at longer time. It is seen from the inset of Fig. 1 that the decay of hydrated electron in these systems is very fast even faster than that in pure aqueous solution and the decay at 720 nm is faster than that at 650 nm. Solvated electrons could not be observed in CPB microemulsion in the present experiments because pyridinium cation reacts very fast with solvated electrons.

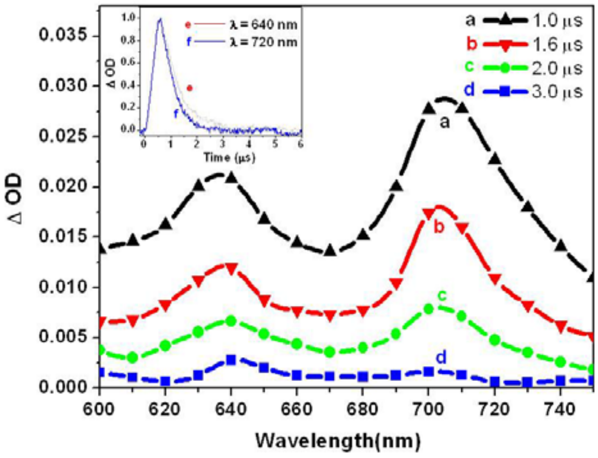

Fig. 1: Transient absorption spectrum of hydrated electrons after the electron pulse of N_2 bubbled solution microemulsion with W_0=40. Inset: e. Decay of hydrated electron at 650 nm, and f. at 720 nm in microemulsion with W_0=40

Counter ion radical: and its reaction with C_{60}.

We have observed another species absorbing in the 300-430 nm region with a maximum around 365 nm (Fig. 2). The bromide ion distribution in CTAB water-in-oil microemulsion has been demonstrated earlier by chemical trapping technique [2,3]. The bromide ion concentrations at the interface and water pool was shown to be as high as 7.0 mol dm^{-3} and 6.0 mol dm^{-3}, respectively, at W_0 =10 in CTAB/*n*-dodecane/$CHCl_3$/water microemulsion.

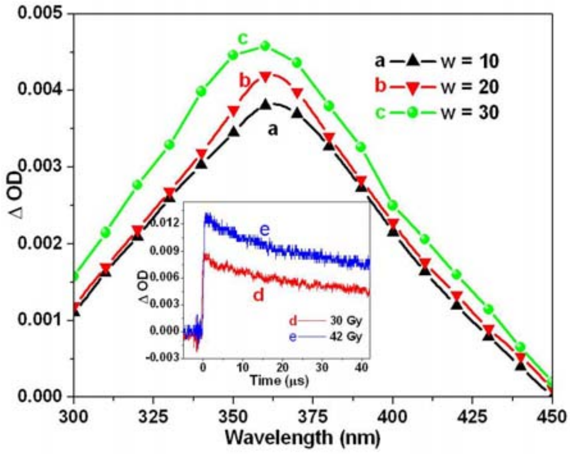

Fig. 2: Transient absorption spectrum of dibromide anion radical (a) W_0=10 (b) W_0=20 (c) W_0=30. Inset: Decay of dibromide anion radical at 360 nm at a dose of (d) 30 Gy & (e) 42 Gy

Direct radiolysis of water in the core of these reverse micelles produces hydroxyl radicals. Molar concentration of bromide ions in the water pool are expected to scavenge these hydroxyl radicals and produce dibromide radical anion ($Br_2^{\cdot-}$). The absorption spectrum matches well with that reported earlier for dibromide radical anion in aqueous solution reported in literature. The faster decay of $Br_2^{\cdot-}$ radical in the microemulsion as compared to aqueous system can be attributed due to the close proximity of the interacting radicals in a small water pool. The $Br_2^{\cdot-}$ radical in pure aqueous solution decays by a second order process .We have also observed a second order decay of the radical as is evident from inset of Fig. 2. The decay at 360 nm becomes faster with an increase in dose from 30 Gy to 42 Gy because of increase in the concentration of the radical at higher dose. $Br_2^{\cdot-}$ radical was also observed in in CPB microemulsion yield being higher in case of CPB. Oxidation of C_{60} by inorganic radicals had been reported in cyclodextrine-C_{60} complex employing $Cl_2^{\cdot-}$ radical anion.

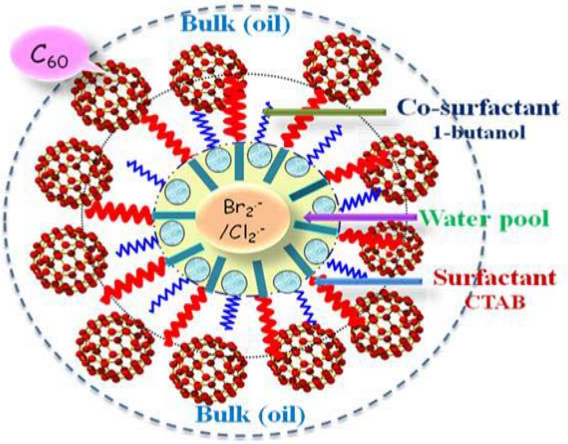

Schematic representation of the CTAB microemulsion containing C_{60}

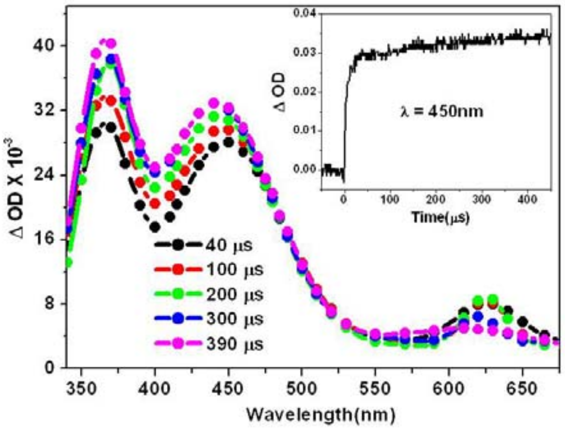

Transient absorption Spectra of N_2O purged CTAB ME with C_{60} dissolved in it

Our aim was to examine whether oxidative electron transfer employing $Br_2^{\cdot -}$ radical is possible in a situation where the inorganic radical is produced in the aqueous core and C_{60} is dissolved in the organic phase as in water in oil microemulsion of CTAB and CPB. We have observed that in both the microemulsions , $Br_2^{\cdot -}$ radical reacts with C_{60} giving rise to absorption maxima at 360 and 440 nm. The formation constants for the species produced the reaction in CTAB and CPB microemulsions were 3.04×10^5 and $2.9 \times 10^5\ s^{-1}$ in CTAB and CPB microemulsions, respectively as measured at 440 nm which are nearly equivalent.

Conclusion

The hydrated electrons could be observed in water-in-oil, CTAB/H_2O/n-butanol/cyclohexane microemulsion. In the microemulsion, the lifetime is shorter than that compared to aqueous solution. The electrons are found to be more stable when they are located at the interface as compared to those present in water pool. Thus, the decay rate constant of the electrons solvated in the interface can provide important clue regarding the physical picture including the rigidity in this region. Moreover, we have presented the first report on the generation of counter ion radical ($Br_2^{\cdot -}$) both in CTAB and CPB microemulsion produced with electron beam irradiation. More interestingly, we were able to demonstrate that a reaction which usually occurs in a two phase chemical system is also possible in a water-in-oil microemulsion.

References

1. Guleria A, Singh A K, Sarkar S K, Mukherjee T, Adhikari S, *J Phys Chem B.* 115, (2011): 10615-10621
2. Das P K, Srilakshmi G V, Chaudhuri A. *Langmuir* 15 (1999)*:* 981-987.
3. Iolanda M, Cuccovia L G D; Fla´vio A M; Chaimovich H. *Langmuir* 17 (2001): 1060-1068.

TUNING THE SHAPE OF CDSE NANOPARTICLES IN *WATER-IN-OIL* MICROEMULSION GROWN *VIA* ELECTRON BEAM IRRADIATION

S. Singh, A. Guleria, M.C. Rath, A.K. Singh, S. Adhikari and S.K. Sarkar
Radiation and Photochemistry Division

This paper received the Best Poster Award, at the National Symposium on Radiation & Photochemistry (NSRP-2011), held at JNV Univ.,
Jodhpur, Rajasthan, during March 10-12, 2011.

Abstract

CdSe nanoparticles of different shapes were synthesized in the water pool of CTAB (Cetyl trimethyl ammonium bromide) based water-in-oil microemulsions through electron beam irradiation. The rod shaped nanoparticles with aspect ratios from 3-5 were formed in microemulsions, $W_0 < 10$ (W_0 = water to surfactant concentrations ratio). In contrast, cubic shaped CdSe nanoparticles were formed in the microemulsions with higher water contents, W_0 values from 20 to 40. Such a transformation of shape from rods to cubes to spheres was attributed to the changes in the hydrophobicity and hydrophilicity of the micro-environment in the medium.

Keywords: Nanoparticles, Electron beam irradiation, Tuning of shapes, Surfactant, Microemulsion

Introduction

Radiation-induced synthesis of nanomaterials has known to be very simple, fast and one step technique with a potential for the commercial scale production of these particles. Various advantages associated with this technique include use of room temperature, atmospheric pressure, devoid of external reducing agent and stringent laboratory conditions. In this process, the synthesis in the aqueous media mainly proceeds through the reaction of the solvated electrons, e_{aq}^-, with the precursor ions. Semiconductor and metallic nanomaterials of different shapes and sizes have been synthesized earlier via radiation chemical routes in aqueous and non-aqueous media using different templates [1–2]. The templates usually determine the shapes and sizes of nanomaterials. Among semiconductors, CdSe is an important one because of its applications in various fields such as photovoltaics, LEDs and other optoelectronic devices. Several groups including us have reported the radiation-induced synthesis of CdSe nanoparticles (NPs) in different condensed phases [1–4]. The yield of CdSe NPs depends on the absorbed dose and the concentration of the precursor ions. Among various templates, water-in-oil microemulsions (MEs) are known as soft templates. CTAB in solution facilitates the formation of different micro-structures under different conditions [5]. In this work, we have used such soft templates i.e. water-in-oil MEs consisting of CTAB as the surfactant, cyclohexane as the oil phase, n-butanol as the co-surfactants and the aqueous phase containing the precursor ions for the synthesis of CdSe NPs via electron beam irradiations.

Experimental

The aqueous solution was prepared separately by adding equimolar (5 mM each) ammoniated cadmium sulfate, $[Cd(NH_3)_4]SO_4$, as the cadmium ion precursor and freshly prepared sodium selenosulfate, Na_2SeSO_3 as the selenium ion precursor in the presence of 1 M tert-butanol. This solution was used as the aqueous phase in the MEs. The de-aerated MEs were irradiated with 7 MeV electron beam obtained from a linear electron accelerator (LINAC). The absorbed dose per pulse was kept at 140 Gy and the samples were irradiated with repeated pulses for a cumulative dose of 25 kGy. The transmission electron microscopy (TEM) measurements were carried out on model no. FEI, TECNAI-F30.

Results and Discussion

Equimolar (5 mM each) concentration of precursors; Cd and Se were dissolved in the water pool of the CTAB MEs and subjected to electron beam irradiation. On irradiation, the colorless MEs changed to greenish-yellow instantaneously, which is the primary indication of the formation of CdSe NPs. As grown CdSe NPs were characterized by optical absorption measurements. The CdSe NPs clearly exhibit excitonic absorption peaks around 420–425 nm as shown in Fig. 1. The band gap values and the sizes of the primary CdSe NPs were estimated from the absorption spectra by using Brus equation (Eq. 1) and are shown in Table 1.

$$E_g = E_g\,(0) + \alpha/d^2 \qquad (1)$$

where, $\alpha = 3.7$ eV nm^2, $E_g(0) = 1.7$ eV, d = particle size (nm) and E_g = band gap value in eV.

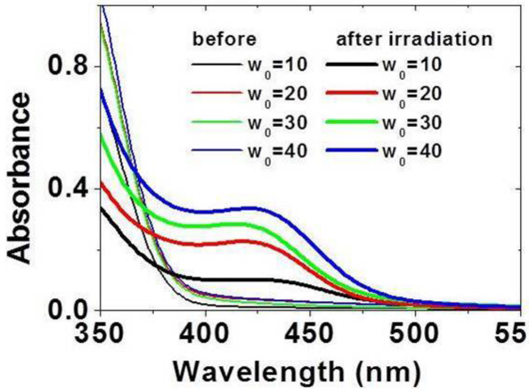

Fig. 1: Optical absorption spectra of CdSe NPs with different W_0 values and [precursor] = 5 mM. Dose = 25 kGy. *Taken from Ref. [6]*

Table 1: Band gap values (eV) and the size of the CdSe primary NPs as estimated from the optical absorption measurements

W_0	Eg (ev)	Particle size (nm)
10	2.50	2.14
20	2.59	2.03
30	2.58	2.04
40	2.55	2.08

It is found that the size of the primary CdSe NPs in all the MEs was about 2 nm. The CdSe NPs were further characterized by TEM measurements.

It was observed that CdSe NPs formed in MEs with lower water content (W_0=10) were of rod shape as seen in Fig. 2(a). The lengths and breadths of the rods were up to 1 μm and 200 nm, respectively with aspect ratios from 3 to 5. From this result it is confirmed that the CdSe primary NPs of size 2 nm get associated to form bigger agglomerates which are entangled within the well structured cavities of CTAB MEs giving rise to rod shaped materials. Here it should be mentioned that CTAB MEs form rod shaped structures when the volume ratio of oil to water is very low [7].

When the volume ratio of oil to water is very low, the hydrophilic groups of surfactant reassemble in order to maximize their contact with water resulting into the formation of cylindrical droplets. As the water content increases, the preference for cylindrical shape decreases. This is due to an increased hydrophilicity in the system which favors the presence of relatively smaller sized water droplets separately instead of staying together, therefore the shape of water droplets changes with the volume ratio of oil to water. And this fact has been proven during the synthesis of CdSe NPs in CTAB based MEs via normal chemical route [8]. A similar phenomenon must be happening here too, which is further facilitated by the electron beam irradiation. Interestingly, the shapes of CdSe NPs formed in the MEs with higher water contents (higher W_0 values) were different from those observed with lower water content. The shapes are no longer rods rather they are of cubical shapes. A typical TEM image of the CdSe NPs formed in the case MEs with W_0=30 is shown in Fig. 2(b).

The cubical shapes have dimensions of about 100 nm and are also well aligned. The TEM image of the CdSe NPs formed in MEs with W_0=40 as shown in Fig. 2(c), clearly exhibits a similar pattern as observed in the case of W_0=30. The only major difference is the particles are more towards spherical shape with increase in the separation between these features. CdSe NPs formed in the present case were fairly stable in ambient conditions. On the contrary, CdSe NPs synthesized in water upon such

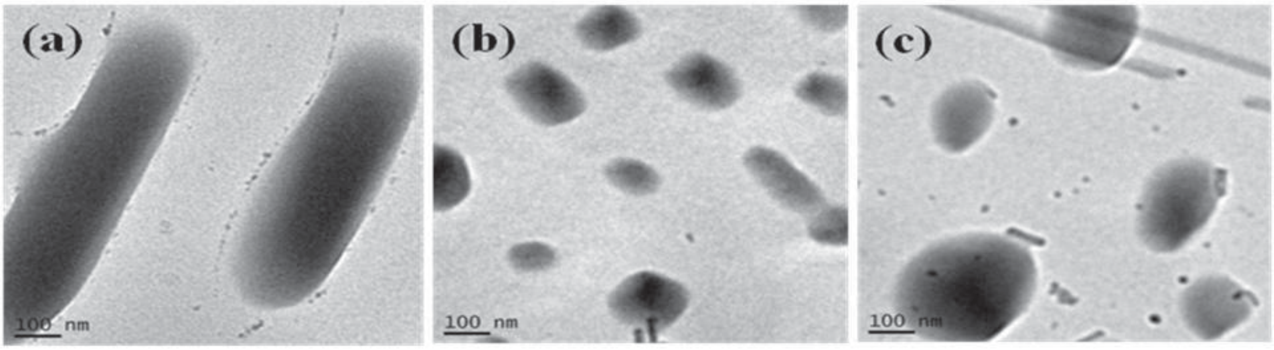

Fig. 2: TEM image of CdSe NPs synthesized upon electron beam irradiation in de-aerated CTAB ME with W_0 = 10 (a), 30 (b), 40 (c) and [precursor] = 5 mM. Dose = 25 kGy. *Taken from Ref. [6]*

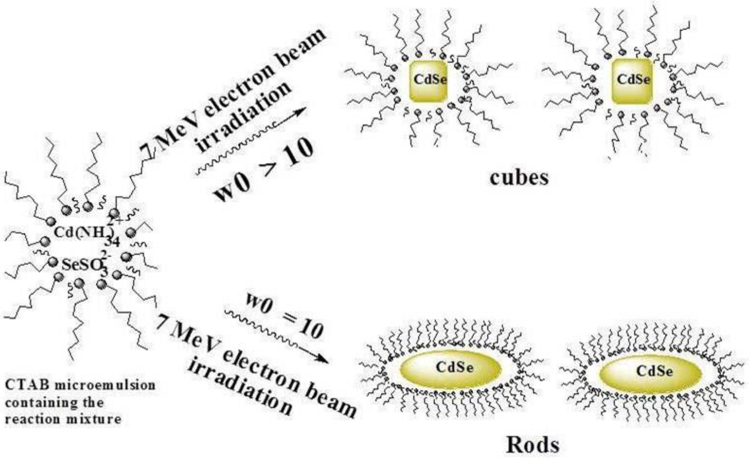

Fig. 3: The schematic representation of the formation of rod and cubic shaped CdSe NPs inside the water pool of water-in-oil CTAB MEs through electron beam irradiation. *Taken from Ref. [6]*

irradiation were found to be unstable and decomposed in ambient conditions [4]. The enhancement in their stability was attributed to the microenvironments provided by the small water pools inside the surfactant aggregates in the bulk organic phase. The schematic representation of the formation of the rod and cube shaped CdSe NPs grown in water-in-oil CTAB MEs is shown in Fig. 3.

Conclusions

In summary, we have successfully synthesized CdSe NPs of different shapes in *water-in-oil* CTAB MEs using electron beam irradiation. In the case of MEs with lower water content, W_0 = 10, the rod shaped CdSe NPs with aspect ratio 3 to 5 were produced. Whereas, cubic shaped CdSe NPs of dimensions about 100 nm were formed upon increase in the water content (higher W_0 values) of these MEs. These cubes further get separated with increase in the W_0 values. Thus, a tuning of the shape of CdSe NPs synthesized through electron beam irradiation was achieved by varying the W_0 values of the *water-in-oil* MEs. These materials were fairly stable at ambient conditions. It is therefore, expected that this method of synthesis along with a shape tuning would be of great interest in the area of nanotechnology.

Acknowledgements

Ms. Shalini Singh acknowledges Bhabha Atomic Research Centre, for providing her a research fellowship. The authors acknowledge Mr. R. S. Gholap, National Chemical Laboratory, Pune for his help in the TEM measurements.

References

1. Xie Y, Qiao Z, Chen M, Liu X, Qian Y. *Adv Mater 11* (1999): 1512–1514.
2. Biswal J, Ramnani SP, Tewari R, Dey GK, Sabharwal S. *Radiat Phys Chem* 79 (2010): 441–445.
3. Singh S, Rath MC, Singh AK, Mukherjee T, Jayakumar OD, Tyagi AK, Sarkar SK. *Radiat Phys Chem.* 80 (2011): 736-741.
4. Singh S, Rath MC, Singh AK, Sarkar SK, Mukherjee T. *Mater Chem Phys* 124 (2010): 6–9.
5. Curri ML, Agostiano A, Manna L, Monica MD, Catalano M, Chiavarone L, et al. J Phys Chem B 104 (2000): 8391–8397.
6. Singh S, Guleria A, Rath M C, Singh A K, Adhikari S, Sarkar S K. *Mat. Lett.* 65 (2011): 1815–1818.
7. Li X, Li T, Wu C, Zhang Z. J *Nano Res* 9 (2007): 1081–1086.
8. Guleria A, Singh S, Rath M C, Singh A K, Adhikari S, Sarkar S K. *J Luminescence* 132 (2012): 652–658.

MONTE CARLO SIMULATION & MEASUREMENT OF X-RAY DOSE FROM A 9 MeV RF ELECTRON LINAC FOR CARGO SCANNING

Nishant Chaudhary, D. Bhattacharjee, V. Yadav, S. Acharya,
K.P. Dixit and K.C. Mittal
Accelerator & Pulse Power Division
and
S.D. Sharma
Radiological Physics & Advisory Division

This paper received the Best Poster Presentation Award at the Conference on Accelerator Radiation Safety, (CARS 2011), held at Mumbai from November, 16-18, 2011

Abstract

A 9 MeV RF Electron Linear Accelerator (Linac) is operational at Electronic Corporation of India Limited (ECIL), Hyderabad to demonstrate cargo-scanning applications to prevent the transport of contraband objects. The interrogation is done by a fanned x-ray beam produced by impinging an energetic electron beam on tantalum (Ta) target. The desired dose rate for this purpose is 22 Gy/min at 1 m from the x-ray source. It is required to determine the x-ray dose rate at one meter distance from the x-ray converter for a given set of beam parameters. Monte Carlo simulations have been done for the x-ray dose rate measurement by using Geant4 software toolkit. X-ray dose rate values at 1 m distance from x-ray target have been estimated at various polar angles with respect to the direction of the incident beam. The plot shows angular distribution of significant x-ray intensity in a cone of 15^0 half- angle. The maximum x-ray emission is in the forward direction of the beam and the dose-rate is estimated to be 19.40 Gy/min when the beam parameters are i) 9 MeV energy ii) 60 mA peak beam current and iii) 250 Hz pulse repetition frequency (PRF).

Experiments have also been carried out using air ionization chamber to obtain x-ray dose-rate at 1 m distance from target. The measured value without an electron-stopper after the target is 20.63 Gy/min at 1 m distance which is close to the required dose rate for the actual cargo scanning purposes. The simulated results also closely match with the experimental observations, implying that the present simulation model is suitable for the characterization of an x-ray source for cargo scanning applications.

Keywords: GEANT4, Monte Carlo, ionization chamber, cargo-scanning

Introduction

Cargo scanning systems are employed at ports, to interrogate the cargos to prevent the transport of contraband objects. A high energy x-ray source is required to inspect the cargo container in a short time without manual opening. A 9 MeV electron Linac based x-ray source has been designed and developed which is suitable for penetration depth of 430 mm steel. The RF Electron Linac at ECIL, Hyderabad generates 60 mA, 5.8 μs current pulses with a pulse repetition rate of 250 Hz. A solenoid is employed to focus the beam to about 2-3 mm size on a Ta target. The accelerator is operated in x-ray mode which is obtained by high energy electron beam falling on a 2 mm thick Ta target. The electron beam is focused on the Ta target to keep x-ray spot size minimum so that the desired quality of imaging can be realized.

A simulation has been done for the x-ray dose rate measurement by using GEANT4 software code which is based upon Monte Carlo technique. [1] The x-ray dose-rate was also experimentally measured by using air ionization chamber.

Monte Carlo simulation

A spherical shaped geometry consisting of water phantoms is assumed as detector in the simulation. The water phantoms were arranged on the surface of the sphere having radius 1 meter and the center coinciding with that of the x-ray converter. For 60 mA peak beam current of 5.8 μs pulse duration, the number of electrons in one pulse is 2.18 X 10 ^{12} and the number of pulses per minute is 15000 as PRF is 250 Hz. We have chosen number of particles as 10^5 in a minute for realistic computation time.

The absorbed energy was then appropriately scaled for comparison with experimental results. The scaling factor is 3.94 X 10^{11} (=15000 X 2.18 X 10^{12}/ 10^5). The simulated dose rate profile (in Gy/min) at 1 meter distance from the bremsstrahlung converter has been plotted in the form of a polar graph shown in Fig. 1. Monte Carlo simulations have been carried out with varying peak beam current of accelerator at fixed PRF of 10 Hz. The peak beam current was varied from 10 mA to 60 mA at interval of 10 mA. The variations in dose rate with peak beam current are shown in Fig. 2.

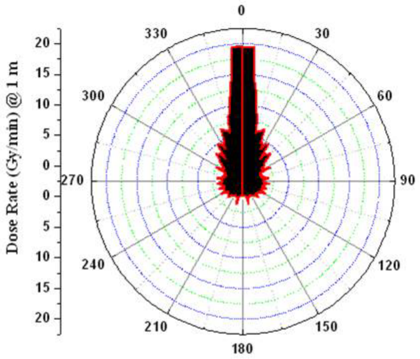

Fig.1: Polar dose rate profile of x-rays generated at 1 m from a Ta target on bombardment of 9 MeV electron beam

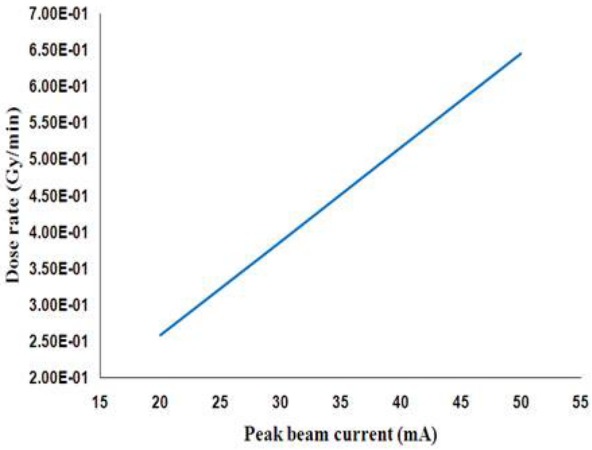

Fig.2: Simulated x-ray dose-rate at 1 m from Ta target at 9 MeV, 10 Hz for various peak beam currents.

The simulation has also been done for different PRF values changing from 50 Hz to 250 Hz under the all other parameters being constant. This simulated result has been shown in Fig. 3 for the fixed peak beam current 60 mA.

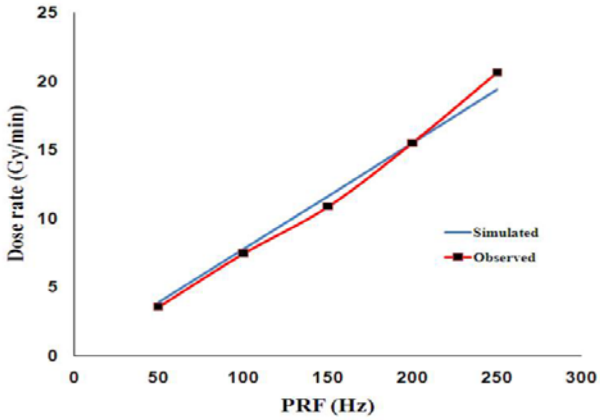

Fig.3: X-ray dose rate with varying PRF at 1 m from the source at 9MeV, 60mA.

X-ray measurements

The dose rate of x-ray, produced after hitting Ta target by 9 MeV electron beam, has been measured by using air ionization chamber. The radiant energy ionizes the air within the chamber. The ionization chamber used is model no. CC13 make IBA Dosimetry, Germany and its active volume is 0.13 cc. An electrometer, model Dose1, make-IBA is used for generating bias voltage of 300 V and measuring the ion current. The applied bias voltage results in accumulation of ions and electrons on respective opposite electrodes. The rate of charge accumulated on electrodes gives the dose rate by using a calibration factor having unit in Grey/coulomb (Gy/C).

In our experiment, the detector has been kept at 1m distance from the x-ray source and the PRF of accelerator was varied from 50 Hz to 250 Hz at the step of 50 Hz keeping all the other parameters fixed. The variation in dose-rate with respect to PRF has been plotted and it is shown in Fig. 3 as observed results.

Results and discussion

The polar plot of x-ray profile generated by Monte-Carlo simulation shows that the maximum dose rate is 19.40 Gy/min in the beam direction and it is reduced to half at an angle of about 15^0 symmetrically. The x-ray is generated from 9 MeV electron beam in fanned form and the cone has a 15^0 half- angle. [2] Thus in a particular plane, either horizontal or vertical the x-ray generated by 9 MeV electron beam makes a cone of angle 30^0. The variation in the x-ray dose rate shows a linear trend with peak beam current when all the other accelerator parameters are fixed. Similarly it also follows a linear relationship with pulse repetition rate as all other parameters are kept constant. The maximum x-ray dose rate observed is about 20.63 Gy/min at 1 m distance under the parameters 9 MeV, 60 mA and 250 Hz of beam energy, peak beam current and PRF respectively. The x-ray dose rate obtained by Monte-Carlo simulations nearly match with the experimentally observed values under the same beam parameters. However, the agreement may be fortuitous at the moment and the agreement should be viewed with some caution. No electron stopper was introduced after the target and it is likely that a portion of dose recorded by the ionization chamber might be due to electrons coming out of the target.

Conclusion

The simulated results show the x-ray dose rates are close to the experimentally observed values which validates our computational model. Thus it is suitable for these types of applications. At the moment, the experimental results indicate that x-ray dose rates are around the value of 22 Gy/min at 1 m distance, which is sufficient for imaging.

The existing system can be utilized for the demonstration of jobs related to cargo inspections. There are several issues, other than the x-ray dose rate, which are equally important to achieve the x-ray imaging of real cargos at ports. For example the design of collimators, the sensitivity of imaging detector arrays, image processing etc.

Further experiments and simulation studies will be conducted after introducing an electron stopper of suitable thickness to avoid the chances of leakage electron contribution in x-ray dose rate measurements.

References

1. Book for Application Development of GEANT4 http://geant4.web.cern.ch/geant4/G4UserDocuments/UsersGuides/ForApplicationDeveloper/html (2005).
2. E. A. Abramyan, *Industrial electron accelerator and applications,* Hemisphere Publishing Corporation, United States of America, (1988).

HIGH TEMPERATURE STRUCTURAL PHASE TRANSITIONS IN FEAS BASED COMPOUNDS

S.K. Mishra, R. Mittal, P.U. Sastry and S.L. Chaplot
Solid State Physics Division

This paper received the Best Poster Award at the 56th DAE Solid State Physics Symposium, held at SRM University, Kattankulathur, Chennai from December 20-23, 2011

Abstract

We report high temperature powder x-ray diffractions studies for MFe_2As_2 (M=Ca, Sr, Eu and Ba) compounds. All these compounds undergo a structural phase transition from tetragonal phase to an unknown phase with temperature. Coexistence of both phases suggests that the phase transition is first order in nature. At high temperatures, the tetragonal and unknown phases coexist over a large temperature regime, which is in contrast to the reported sharp transition at low temperature from the tetragonal to orthorhombic phase.

Keywords: Superconducting materials, Crystallographic aspects of phase transformations

PACS: 74.70.-b, 61.50.Ks, 72.80.Ga

Introduction

Knowledge of the structure of high *Tc* superconductors is basic to a fundamental understanding of microscopic origin of pairing mechanism. Recently, diffraction and magnetic measurements of the structural and superconducting properties in FeAs based materials have been reported [1,5]. These measurements show that these compounds undergo phase transitions from tetragonal to collapse tetragonal or orthorhombic structures based on different conditions like: dopant, temperature and pressure, and are mainly characterized by the distortion of $FeAs_4$ tetrahedra.

A wide variety of techniques have been used to understand the structural phase transitions driven by temperature, chemical pressure and pressure, below room temperature. No attempt has been made to investigate the structural phase transition behaviour above room temperature. We have carried out high temperature powder X-ray diffraction studies for FeAs based compounds namely: $CaFe_2As_2$, $SrFe_2As_2$, $BaFe_2As_2$ and $EuFe_2As_2$. Detailed analysis of diffraction data reveals that all compounds undergo transition from the tetragonal to an unknown phase with temperature. Presence of both phases (tetragonal and unknown) at high temperature clearly suggests that transition is first order in nature.

Experimental

The samples MFe_2As_2 (M: Ca, Sr, Eu and Ba) were prepared by a solid state reaction of MAs (M: Ca, Sr, Eu and Ba) and Fe_2As: $MAs + Fe_2As \rightarrow MFe_2As_2$. The high-temperature x-ray diffraction studies were carried out using a 18 kW rotating Cu anode-based powder diffractometer with a high- temperature attachment and a curved-crystal monochromator. The temperature was stable within ± 1 K during these measurements. The structural refinements were performed using the Rietveld refinement program FULLPROF.

Results and Discussion

Fig. 1 shows diffraction patterns for FeAs based compounds (Ca, Sr, Eu and Ba) at 300 and 873 K. It is evident from the figure that diffraction profiles show dramatic change with change of the M atom at ambient condition. To investigate the effect of ionic size on structural parameters, we refined room temperature powder diffraction data and results are shown in Fig. 2. It is evident from this figure that lattice parameters increases with increasing ionic size and show anomaly for $EuFe_2As_2$. The anomalous behaviour of lattice parameters for $EuFe_2As_2$ (open circle in Fig. 2) may be due to magnetic nature of Eu that has variable oxidation state, in contrast to other Ca, Sr, Ba which are non-magnetic.

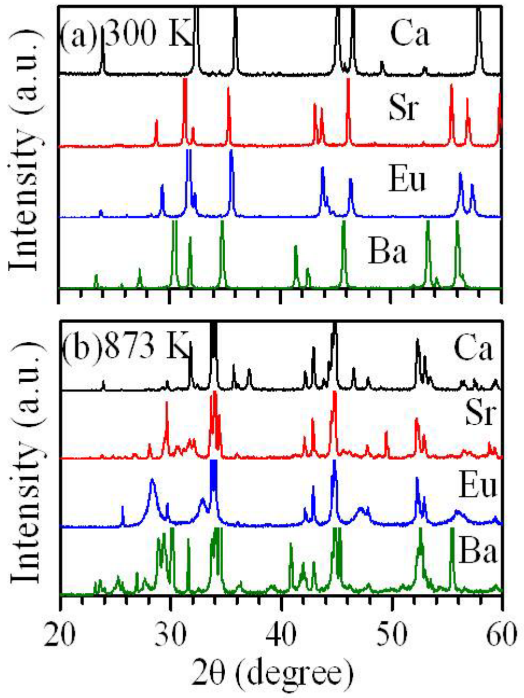

Fig. 1: X-ray diffraction patterns of MFe_2As_2 (M= Ca, Sr, Eu and Ba) at 300 and 873 K.

Fig. 3 (a) shows the temperature dependent x-ray diffraction data for $BaFe_2As_2$ compound at selected temperatures. It is clear from the figure as temperature increases above 723 K; additional peaks appear around $2\theta = 30$ and 34 degrees. These additional peaks cannot be indexed with tetragonal symmetry with *I4/mmm* space group. Thus, presence of additional peaks clearly suggests the existence of another unknown phase. To identify the correct symmetry and space group, we have explored various possibilities like: different cell size, various space groups belong with cubic and tetragonal symmetries, and its phase coexistence. But all the attempts were unsuccessful. The assignment of correct structure is in progress. It is important to notice that these additional peaks are present in all the four compounds at 873 K as shown in figure 1 (b). However, the presence of unknown phase also with the tetragonal phase provides unambiguous signature for the first order nature of structural phase transition.

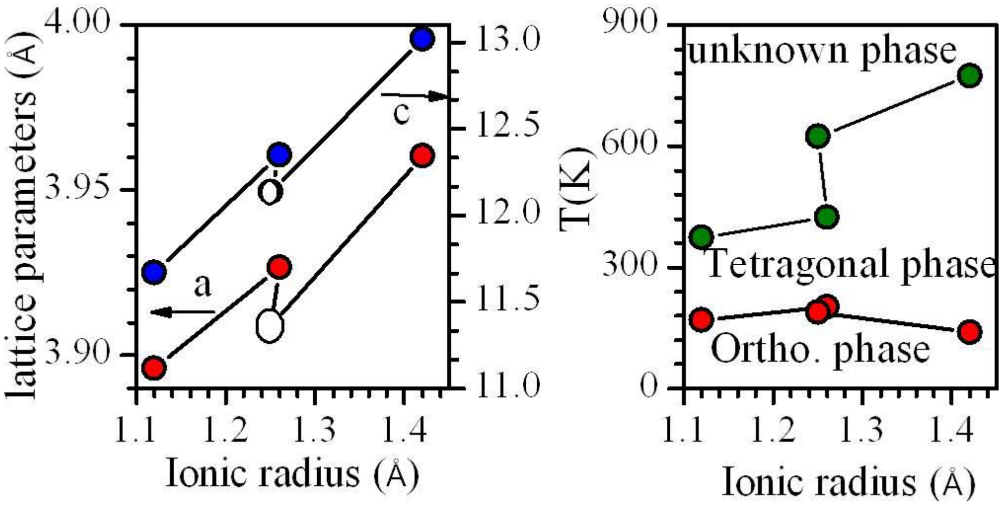

Fig. 2: Evolution of lattice parameters and structural phase transition temperature with ionic radii of MFe_2As_2 (A= Ca, Sr, Eu and Ba). Here, transition temperature for tetragonal to unknown phase is taken as the temperature where phase coexistence begins. However, the tetragonal to orthorhombic phase transition temperatures is taken from literature [1-4].

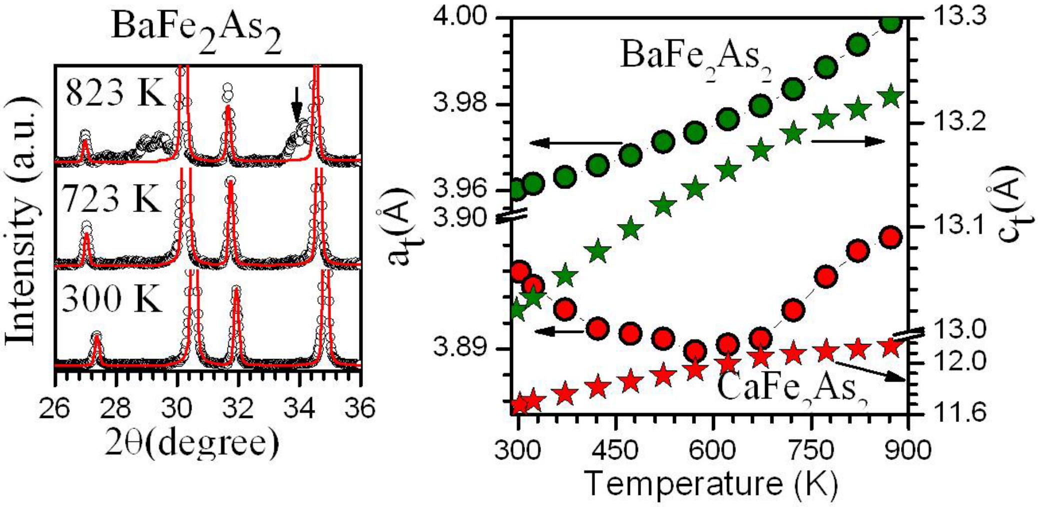

Fig. 3: (a) Powder x-ray diffraction patterns of $BaFe_2As_2$ at selected temperatures. Evolution of lattice parameters for $CaFe_2As_2$ and $BaFe_2As_2$ compounds with temperature are shown in (b) for the tetragonal phase only.

Fig. 3 (b) depicts the evolution of structural parameters with temperature for $BaFe_2As_2$ and $CaFe_2As_2$ compounds respectively. Lattice parameters for $BaFe_2As_2$ monotonically increase with temperature for the tetragonal phase. In contrast to $BaFe_2As_2$, the temperature dependence a_t lattice parameter of $CaFe_2As_2$ first decreases (up to 700 K) with temperature and then increases with increasing the temperature. On the other hand, c_t lattice parameter monotonically increases with temperature.

In this paper we have shown presence of a new phase and phase coexistence at high temperature in MFe_2As_2 compounds. This transition temperature increases with radius of the M-ion. On the other hand, another transition from tetragonal to the orthorhombic phase is known at low temperature in these compounds. This low temperature transition does not show any systematic behaviour with ionic radii. This may have electronic origin attributed to magnetic ordering.

References

1. Johnpierre Paglione and Richard L. Greene, High-temperature superconductivity in iron-based materials, *Nat. Phys.* **6**, (2010) 645-658.
2. Kamihara Y., Watanabe T. Hirano M. and Hosono H.,Iron-Based Layered Superconductor La[$O_{1-x}F_x$]FeAs(x=0.05-0.12) with T_c=26 K, *J. Am. Chem. Soc.* **130**, (2008) 3296-3297.
3. Rotter M. Tegel M, and Johrendt D, Superconductivity at 38 K in the Iron arsenide $(Ba_{1-x}K_x)Fe_2As_2$ *Phys. Rev. Lett.* **101**, (2008) 107006.
4. Kimber S A J, Kreyssig A, Zhang Yu-Zhong, Jeschke H O, Valentí R, Yokaichiya F, Colombier E, Yan J, Hansen T, Chatterji T, McQueeney R J, Canfield P C, Goldman A I and Argyriou D N., Similarities between structural distortions under pressure and chemical doping in superconducting $BaFe_2As_2$ *Nature Materials* **8**, (2009) 471-475.
5. Mittal R., Mishra S K, Chaplot S L, Ovsyannikov S. V., Greenberg E, Trots D M, Dubrovinsky L, Su Y, Brueckel Th, Matsuishi S, Hosono H, and Garbarino G., Ambient- and low-temperature synchrotron x-ray diffraction study of $BaFe_2As_2$ and $CaFe_2As_2$ at high pressures up to 56 GPa, Phys. Rev. B 83, (2011) 054503 and refrences their in.

EFFECT OF FAST NEUTRON IRRADIATION ON THE MAGNETO-DYNAMICS OF THE METAMAGNETIC TRANSITION IN $Ce(Fe_{0.96}Ru_{0.04})_2$

C.L. Prajapat, V. Dube, P.K. Mishra, M.R. Singh, G. Ravikumar and S.K. Gupta
Technical Physics Division
and
A.K. Rajarajan
Solid State Physics Division
and
S.V. Thakare and K.C. Jagadeesan
Radiopharmaceuticals Division
and
P.L. Paulose
Tata Institute of Fundamental Research, Mumbai

This paper received the Best Poster Award at the 56th DAE Solid State Physics Symposium held at SRM University, Kattankulathur, Tamil Nadu from 19-23 Dec., 2011

Abstract

Magnetic field induced Anti-ferromagnetic (AFM) to ferromagnetic (FM) phase transition on a sample of $Ce(Fe_{0.96}Ru_{0.04})_2$ is studied by magnetic measurements before and after fast neutron irradiation performed in CIRUS reactor at BARC, Trombay. Irradiation induced material defects caused the transition to move to lower fields, increased the zero field magnetic susceptibility and suppressed the logarithmic relaxation rate in the hysteretic transition region.

Keywords: Magnetic relaxation, Energy barrier, First order transition

PACS: 76.50.+g, 75.30.-m, 75.30.Kz

Field induced antiferromagnetic (AFM) to ferromagnetic (FM) transition observed in magnetic systems such as doped $CeFe_2$ is first order in nature [1]. While the undoped compound is FM with a transition temperature at 220K, a small substitution of Ru (4% Ru in place of Fe) makes the FM phase unstable below 80K, favoring AFM phase. However, application of a magnetic field restores the FM phase. Hysteresis under increasing and decreasing magnetic field cycles is attributed to quenched disorder due to local variation in the dopant concentration. Logarithmic magnetization relaxation accompanying the hysteresis indicates the presence of energy barriers hindering the system from attaining thermodynamic equilibrium.

Disorder induced first order (order-disorder or O/D) transition is also known in the context of weakly pinned superconductors, where a quasi-ordered Bragg glass vortex phase undergoes a transition to disordered solid phase as the field (or temperature) is varied [2]. A recent study on the effect of Li^{3+} ion irradiation induced pinning on superconducting $Tl_2Ca_2Ba_2Cu_3O_{10}$ crystals revealed that the O/D transition shifts to lower fields with increasing irradiation dose [3]. While the pinning force in the ordered phase increases with irradiation dose, the disordered phase is unaffected by the irradiation.

In the present work, we investigated the effect of fast neutron irradiation on the first order AFM-FM transition in Ce($Fe_{0.96}Ru_{0.04}$)$_2$. The sample is irradiated in CIRUS reactor at BARC, Trombay for 1 Hour at 10^{15} neutrons/cm^2 of energy greater than 1 MeV.

Zero field cooled (ZFC) magnetic moment (m) vs temperature (T) data measured under a magnetic field (H) of 20 Oe is presented in the inset of figure 1 for both pristine and fast neutron irradiated samples. While the main AFM to FM transition occurs in both the samples at 80 K, irradiated sample exhibits a much larger magnetic susceptibility below 80K than that of the pristine sample. m vs T data on the irradiated sample also exhibits perceptible deviation above 80K as well. The focus here is to compare field induced transition in pristine and that of the irradiated sample.

Main panel of Fig. 1 shows m vs H data recorded on pristine and irradiated samples at 30 K, where the field induced transition of the irradiated sample is advanced to lower fields, while m-H curves of the two samples merge into each other at higher fields. Detailed hysteresis loops at other temperatures will be presented later.

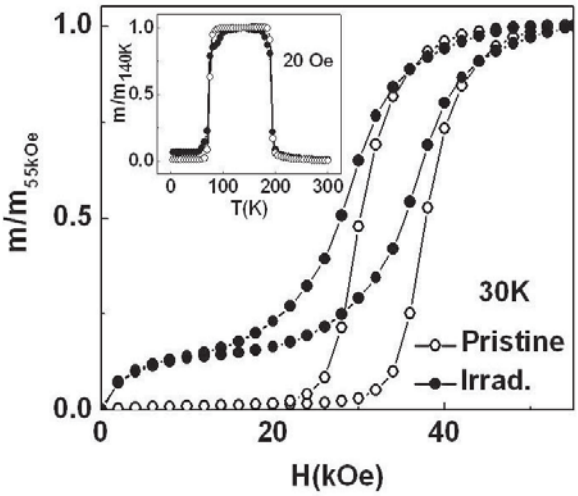

Fig. 1: *m vs H* loops at 30 K measured for pristine and irradiated samples. Inset shows the ZFC m vs T measurement under 20 Oe field.

We have also performed detailed magnetic relaxation measurements at different fields in the hysteretic regime. It is observed that the behavior is logarithmic in time as shown in Fig. 2. Importantly, logarithmic relaxation rate dropped precipitously upon irradiation as shown in Fig. 3.

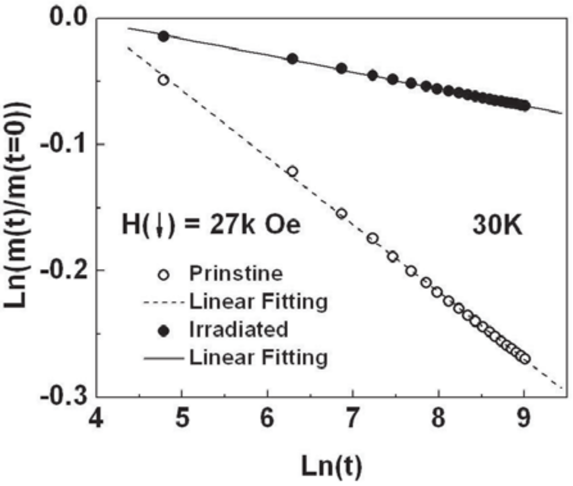

Fig. 2: m vs Time data at 30 K (normalized by initial magnetic moment) for pristine and irradiated samples recorded at 27 kOe on the decreasing field cycle. The dotted lines are linear fits.

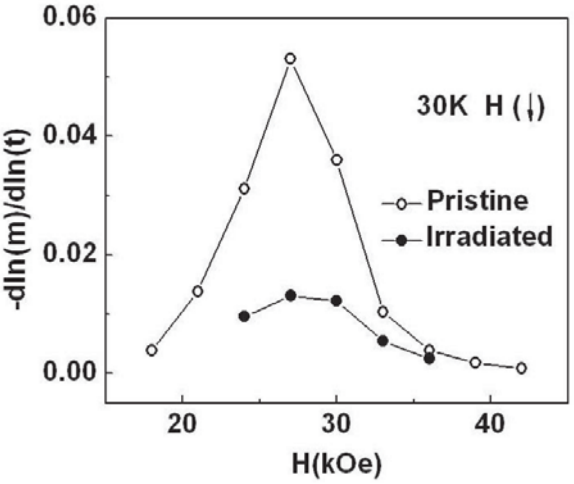

Fig.3: A comparison of the field dependent logarithmic relaxation rates measured on pristine and irradiated samples.

The low field susceptibility is significantly enhanced in the irradiated sample (main panel of figure 1), which is understood by the following arguments. We believe that the AFM-FM transition (or vice versa) occurs in a series of thermally activated events. In each event a microscopic correlation volume δV of the AFM phase transforms into FM phase, *a la flux creep* in hard type II superconductors [4], by overcoming an energy barrier U_0, presumably arising from the underlying quenched disorder. Larkin- Ovchinikov theory suggests that U_0 is an increasing function of δV [5]. Application of magnetic field only promotes the relaxation process by effectively lowering the barrier. Disruption of the AFM (or FM) correlations by irradiation induced defects (smaller δV) is perhaps responsible for increased susceptibility and reduced transition temperature. These arguments lead us to a conclusion that the relaxation should increase upon irradiation, contrary to our experimental results. This contradiction can be explained by the possibility that the time window over which relaxation data is recorded being quite different for the two samples as the intrinsic time scales ($\sim \exp[-U_0/kT]$) for two samples are different.

References

1. S. B. Roy, P. Chaddah, V. K. Perchansky, and K. S. Gschneidner Jr, Acta Materialia **56** (2008) 5895.
2. G.Ravikumar et al, Phys. Rev. B **63** (2001) 024505.
3. M.R. Singh et al, Nucl. Inst. Meth. B **269** (2011) 1117.
4. Y. Yeshurun, A. P. Malozemoff, and A. Shaulov, Rev. Mod. Phys. **68** (1996) 911.
5. A. I. Larkin, and Yu N. Ovchinikov, J. Low Temp. Phys. 34 (1979) 409.

AUTHOR INDEX

Dr. Homi J. Bhabha at the Cirus Construction site

Edited & Published by :
Dr. K. Bhanumurthy,
Head, Scientific Information Resource Division,
Bhabha Atomic Research Centre, Trombay, Mumbai 400 085.
Computer Graphics & Layout : B.S. Chavan, SIRD, BARC
BARC Newsletter is also available at URL: http://www.barc.gov.in